# SYNTHESIS AND CHARACTERIZATION OF METAL OXIDE/METAL SULFIDE NANOCOMPOSITES

**Ph.D. THESIS**

**by**

**SUDHEER KUMAR YADAV**



**DEPARTMENT OF CHEMISTRY**
**INDIAN INSTITUTE OF TECHNOLOGY ROORKEE**
**ROORKEE - 247 667 (INDIA)**
**FEBRUARY, 2016**

# SYNTHESIS AND CHARACTERIZATION OF METAL OXIDE/METAL SULFIDE NANOCOMPOSITES

**A THESIS**

*Submitted in partial fulfilment of the
requirements of the award of the degree
of*
DOCTOR OF PHILOSOPHY
in
CHEMISTRY

**by**

**SUDHEER KUMAR YADAV**



**DEPARTMENT OF CHEMISTRY
INDIAN INSTITUTE OF TECHNOLOGY ROORKEE
ROORKEE - 247 667 (INDIA)
FEBRUARY, 2016**

# INDIAN INSTITUTE OF TECHNOLOGY ROORKEE
# ROORKEE

## CANDIDATE'S DECLARATION

I hereby certify that the work which is being presented in the thesis entitled **"SYNTHESIS AND CHARACTERIZATION OF METAL OXIDE/METAL SULFIDE NANOCOMPOSITES"** in partial fulfilment of the requirements for the award of the degree of Doctor of Philosophy and submitted in the Department of Chemistry of the Indian Institute of Technology Roorkee, Roorkee is an authentic record of my own work carried out during the period from July, 2011 to February, 2016 under the supervision of Dr. P. Jeevanandam, Associate Professor, Department of Chemistry, Indian Institute of Technology Roorkee, Roorkee.

The matter presented in the thesis has not been submitted by me for the award of any other degree of this or any other Institute.

**(SUDHEER KUMAR YADAV**)

This is to certify that the above statement made by the candidate is correct to the best of my knowledge.

**(**P. Jeevanandam)

Supervisor

Date:

# CONTENTS

# ABSTRACT

Nanoscale materials exhibit size dependent physicochemical properties such as optical, magnetic, catalytic, etc, which vary significantly from that of bulk materials. Nanocomposites are multi-phase materials in which at least one of the phases possesses dimension in nanometer range. Nanocomposites are important because of their multifunctional properties and they have potential applications in diverse areas such as environmental remediation, catalysis, sensors, biomedical and photo-electronics. Various physical and chemical methods have been reported for the synthesis of nanocomposites which include chemical vapour deposition, ball milling, spray pyrolysis, laser ablation, sol-gel, thermal decomposition, precipitation, hydrothermal, and sonochemical methods.

In the present thesis, synthesis of different nanocomposites, their characterization and studies on their optical and magnetic properties have been carried out. After thorough characterization, some applications of the nanocomposites have been explored. In the present study, three different types of nanocomposites on the basis of matrix used have been synthesized; (i) $NiO-Al_2O_3$ and $PbS-Al_2O_3$ nanocomposites, (ii) $CdS-TiO_2$ and $Ag_2S-TiO_2$ nanocomposites and (iii) $CdS-\gamma-Fe_2O_3$ and $ZnO@\gamma-Fe_2O_3$ nanocomposites. The nanocomposites were synthesized using a facile sol-gel process, a two-step sol-gel process followed by thermal decomposition approach and also a one-step thermal decomposition approach. The synthesized nanocomposites were characterized using an array of analytical techniques. After thorough characterization, the nanocomposites were explored for a few applications such as oxidation of styrene, photocatalytic degradation of rhodamine B, photo-reduction of Cr(VI) and photocatalytic degradation of congo red in aqueous solutions. The thesis consists of seven chapters and a brief description on each chapter is given below.

**Chapter 1** deals with a brief historical background on nanotechnology, general introduction of nanoscale materials their types and synthetic methods. A description has been given on the nanocomposites, their types and different preparation methods. Various size and shape dependent properties of nanocomposites have been discussed with the help of suitable examples. At the end, applications of different nanocomposites depending on their optical, magnetic and electrical properties have been discussed.

**Chapter 2** deals with the various analytical techniques that were employed for the characterization of the synthesized nanocomposites. The techniques that were used include powder X-ray diffraction, Fourier transform infrared spectroscopy, Raman spectroscopy,

thermal gravimetric analysis, atomic absorption spectroscopy, field emission-scanning electron microscopy coupled with energy dispersive X-ray analysis, transmission electron microscopy, selected area electron diffraction, diffuse reflectance spectroscopy, UV-visible spectroscopy, photoluminescence spectroscopy and surface area measurements. The magnetic properties of the synthesized nanocomposites were investigated using a superconducting quantum interference device (SQUID) or a vibrating sample magnetometer (VSM) as a function of magnetic field and temperature. The applications of the nanocomposites were studied using gas chromatography coupled with mass spectroscopy and UV-visible spectroscopy.

**Chapter 3** deals with the synthesis and characterization of nickel oxide-alumina and lead sulfide-alumina nanocomposites. These nanocomposites have been discussed in two separate sections.

In the first section, $NiO-Al_2O_3$ nanocomposites were prepared by sol-gel method. XRD results indicate that the $NiO-Al_2O_3$ nanocomposites consist of small NiO crystallites (mean size ~ 2.6 nm) and FT-IR results on the nanocomposites show characteristic bands due to nickel oxide and alumina. Raman spectroscopy results show characteristic bands due to nickel oxide. EDX analysis shows the presence of oxygen, aluminium and nickel in the nanocomposites. TEM results indicate uniform distribution of NiO nanoparticles in the $Al_2O_3$ matrix. Increase in the band gap of NiO in the nanocomposites compared to pure NiO nanoparticles is observed and the nanocomposites show superparamagnetic behaviour at room temperature.

In the second section, $PbS-Al_2O_3$ nanocomposites were prepared by the sol-gel the method. X-ray diffraction results indicate that the $PbS-Al_2O_3$ nanocomposites consist of PbS nanocrystallites (18.2 to 40.5 nm). FT-IR results on the nanocomposites show characteristic bands due to lead sulfide and alumina and Raman spectroscopy results show characteristic bands due to lead sulfide. EDX analysis shows the presence of oxygen, aluminium, lead and sulfur in the nanocomposites. Transmission electron microscopy images show cube-like and flake-like morphology for pure PbS and $Al_2O_3$, respectively and TEM images of the nanocomposites indicate uniform distribution of PbS nanoparticles on the $Al_2O_3$ matrix. Diffuse reflectance spectral studies on the nanocomposites indicate near infrared (NIR) absorption and they exhibit blue shift of the band gap of PbS compared to pure PbS nanoparticles. The photoluminescence studies show characteristic peaks due to excitonic emission of PbS nanoparticles in the $PbS-Al_2O_3$ nanocomposites.

**Chapter 4** deals with the synthesis and characterization of cadmium sulfide-titanium dioxide and silver sulfide-titanium dioxide nanocomposites. These nanocomposites have been discussed in two separate sections.

In the first section, CdS-TiO$_2$ nanocomposites were prepared by a two-step method. In the first step, the TiO$_2$ nanoparticles were prepared by sol-gel method. In the second step, CdS-TiO$_2$ nanocomposites were prepared by the thermal decomposition of cadmium acetate, thiourea and TiO$_2$ nanoparticles in diphenyl ether at 150 $^o$C. The effect of using four different types of TiO$_2$ (as-prepared sol–gel TiO$_2$ nanoparticles, sol–gel TiO$_2$ after calcination at 500 $^o$C, sol–gel TiO$_2$ after calcination at 700 $^o$C and macro-crystalline TiO$_2$) on the structure and optical properties of the nanocomposites was investigated. The CdS–TiO$_2$ nanocomposites consist of nanocrystallites of cubic CdS and anatase TiO$_2$ when as-prepared sol-gel TiO$_2$ nanoparticles, sol-gel TiO$_2$ calcined at 500 $^o$C and macro-crystalline TiO$_2$ were used. On the other hand, when sol-gel TiO$_2$ after calcination at 700 $^o$C was used, the CdS-TiO$_2$ nanocomposites were found to consist of rutile TiO$_2$. In the nanocomposites prepared using as-prepared sol-gel TiO$_2$ nanoparticles and sol-gel TiO$_2$ after calcination at 500 $^o$C, FE-SEM and TEM results indicate uniform distribution of CdS nanoparticles (10.5 ± 1.6 nm) on the TiO$_2$ matrix. In the CdS-TiO$_2$ nanocomposites, a blue shift of the band gap of CdS compared to bulk CdS is observed.

In the second section, Ag$_2$S-TiO$_2$ nanocomposites were prepared by a two-step method. In the first step, TiO$_2$ nanoparticles were prepared by sol-gel method. In the second step, Ag$_2$S-TiO$_2$ nanocomposites were prepared by the thermal decomposition of silver acetate, thiourea and TiO$_2$ nanoparticles (calcined at 500 $^o$C) in diphenyl ether at 220 $^o$C. The XRD results indicate that the Ag$_2$S-TiO$_2$ nanocomposites consist of nanocrystallites of Ag$_2$S and TiO$_2$. The FE-SEM images showed that the Ag$_2$S-TiO$_2$ nanocomposites consist of more or less uniform particles with close to spherical morphology while the energy dispersive X-ray analysis studies indicate the presence of silver, sulfur, titanium and oxygen in the nanocomposites. TEM results indicate uniform distribution of Ag$_2$S nanoparticles (8.8 ± 1.9 nm) in the TiO$_2$ matrix. A blue shift of band gap of Ag$_2$S in the Ag$_2$S-TiO$_2$ nanocomposites compared to bulk Ag$_2$S is observed.

**Chapter 5** deals with the synthesis and characterization of cadmium sulfide-iron oxide nanocomposites and zinc oxide@iron oxide core-shell nanocomposites prepared by the thermal decomposition approach. These systems have been discussed in two separate sections.

In the first section, CdS-γ-Fe$_2$O$_3$ nanocomposites have been prepared by a facile single step thermal decomposition approach which involves thermal decomposition of iron

acetylacetonate, cadmium acetate and thiourea in diphenyl ether at 200 °C. The effect of varying the concentration of iron acetylacetonate, cadmium acetate and thiourea during synthesis of the nanocomposites on the crystal phases, microstructure and properties of the CdS-γ-Fe$_2$O$_3$ nanocomposites was investigated. The XRD results confirm the presence of CdS nanocrystals (1.2 to 2.9 nm) in the CdS-γ-Fe$_2$O$_3$ nanocomposites. FT-IR results on the nanocomposites show characteristic bands due to γ-Fe$_2$O$_3$ and CdS. FE-SEM results indicate more or less uniform particles with close to spherical morphology while the energy dispersive X-ray analysis studies indicate the presence of cadmium, sulfur, iron and oxygen in the nanocomposites. TEM results indicate formation of agglomerated sphere-like particles in the nanocomposites. The CdS-γ-Fe$_2$O$_3$ nanocomposites show band gap absorption (1.8 to 2.5 eV) and characteristics photoluminescence in the visible region, and exhibit superparamagnetic behaviour at room temperature.

In the second section, ZnO@γ-Fe$_2$O$_3$ core-shell nanocomposites were prepared by a thermal decomposition approach. ZnO nanorods were first synthesized by the calcination of zinc acetate at 300 °C. γ-Fe$_2$O$_3$ nanoparticles were then deposited on the surface of ZnO nanorods by the thermal decomposition of iron acetylacetonate at 200 °C in diphenyl ether. XRD studies on as prepared and calcined samples suggest the phase of as prepared iron oxide nanoparticles as γ-Fe$_2$O$_3$. FT-IR results on the as prepared iron oxide nanoparticles and ZnO@γ-Fe$_2$O$_3$ core-shell nanocomposites show IR bands due to γ-Fe$_2$O$_3$. FE-SEM images indicate the formation of shell of iron oxide on the ZnO nanorods while the energy dispersive X-ray analysis studies indicate the presence of zinc, iron and oxygen in the nanocomposites. Transmission electron microscopy studies clearly show that the ZnO possesses rod morphology (length = 1.1 ± 0.1 μm, diameter = 40 ± 7 nm) and TEM images of the ZnO@γ-Fe$_2$O$_3$ nanocomposites show uniform shell formation of γ-Fe$_2$O$_3$ on the surface of ZnO nanorods and thickness of the γ-Fe$_2$O$_3$ shell varies from 10 to 20 nm. The diffuse reflectance spectra of ZnO@γ-Fe$_2$O$_3$ nanocomposites reveal extended optical absorption in the visible range (400–600 nm) and the photoluminescence spectra indicate that the ZnO@γ-Fe$_2$O$_3$ nanocomposites exhibit enhanced defect emission. The magnetic measurements on the ZnO@γ-Fe$_2$O$_3$ nanocomposites reveal superparamagnetic behaviour at room temperature with characteristic blocking temperature which indicates the presence of iron oxide nanoparticles shell on the ZnO nanorods.

**Chapter 6** deals with the various applications that were explored using the synthesized nanocomposites in the present study. NiO-Al$_2$O$_3$ nanocomposites were used as the catalyst in the oxidation of styrene. The nanocomposites show better catalytic activity for the oxidation of styrene using tert-butyl hydroperoxide as the oxidant and also show higher selectivity for styrene oxide with higher total conversion compared to pure NiO nanoparticles. The CdS-TiO$_2$ nanocomposites were explored as photocatalyst for the photodegradation of rhodamine B and reduction of Cr(VI) in aqueous solutions in the presence of sunlight. The CdS–TiO$_2$ nanocomposites act as good catalyst for the photodegradation of rhodamine B and reduction of Cr(VI) compared to pure CdS and TiO$_2$ nanoparticles. The Ag$_2$S-TiO$_2$ nanocomposites were found to act as better photocatalyst for the photodegradation of rhodamine B in aqueous solution compared to pure Ag$_2$S and TiO$_2$ nanoparticles. The CdS-γ-Fe$_2$O$_3$ nanocomposites and ZnO@γ-Fe$_2$O$_3$ core-shell nanocomposites were explored for the photocatalytic degradation of congo red in aqueous solutions in the presence of sunlight. The CdS-γ-Fe$_2$O$_3$ nanocomposites show better photocatalytic activity compared to pure γ-Fe$_2$O$_3$ and CdS nanoparticles. Also, the ZnO@γ-Fe$_2$O$_3$ core-shell nanocomposites show better photocatalytic performance compared to pure ZnO nanorods and γ-Fe$_2$O$_3$ nanoparticles.

**Chapter 7** deals with the overall summary of the work done in the thesis and also discusses the future prospects.

# ACKNOWLEDGMENTS

**List of Figures**

images of flower-like NiCoP/ZnO nanocomposite prepared by the hydrothermal method [95].

1.24   (a) Schematic representation of sonochemical synthesis of GO–$Mn_3O_4$ composite, (b) and (c) TEM and (d) HRTEM images of GO–$Mn_3O_4$ nanocomposite and its SAED pattern [96].

1.25   (a) Table with values of tensile strength, flexural strength and impact strength, (b) histogram and (c) plot showing increase in the mechanical properties of F-nAl epoxy nanocomposites in comparision with pure TGBAPSB [102].

1.26   (a) Energy bands of bulk semiconductor ($E_g$) and for a quantum dot (QD) [101], (b) visual images of samples excited by a broadband UV lamp and (c) UV-visible absorption (black) and PL emission (red) spectra (excitation at 350 nm) of CdSe quantum dots with different sizes [102].

1.27   (a) SEM image and (b) UV-visible absorption spectra of CdS/ZnO nanocomposites and photoluminescence (PL) spectra of the CdS/ZnO nanocomposites with an excitation wavelength of (c) 420 nm , and (d) 320 nm, respectively [103].

1.28   Different kinds of nanocomposites heterojunctions [104].

1.29   Schematic representation of the charge transfer and separation in $In_2S_3$/$MoS_2$/CdS heterostructures under visible light [106].

1.30   (a) Cross-sectional HAADF image, (b) HRTEM image and (c) temperature dependence of resistivity of the Au–LNO nanocomposite thin film [112].

1.31   (a) Schematic representation of the typical hysteresis loops of magnetic metal oxide nanoparticles [117] and (b) M-H curves of cobalt iron oxide nanocomposites with different Co/Fe ratio ((a) 0/1, (b) 1/2, (c) 1/1 and (d) 2/1) [116].

1.32   (a) TEM image, (b) HRTEM image and (c) SAED pattern of $NiFe_2O_4$@silica nanofibrous (SNF), (d) $N_2$ adsorption–desorption isotherms of SNF, gelatin/SNF, and $NiFe_2O_4$@SNF and (e) magnetic hysteresis of $NiFe_2O_4$@SNF measured at 300 K [125].

1.33   (a) SEM image, (b) and (c) HRTEM images of 5CoO/$CoFe_2O_4$ nanocomposites, (d) first three charge–discharge profiles of 5CoO/$CoFe_2O_4$ cycled between 0.01–3.0 V under a current density of 100 mA $g^{-1}$ and (e) cycling behavior of A, B, C, D (5CoO/$CoFe_2O_4$) and E (3CoO/$CoFe_2O_4$) at a rate of 100 mA $g^{-1}$ [133].

**1.34** (a) Cyclic voltammetry of modified electrodes in the presence of $Fe_2O_3$, Ag NPs and Ag@iron oxide nanocomposite in presence of 20 mM $NO^{3-}$ ions, and (b) schematic of the sensing mechanism on Ag@iron oxide nanocomposites [140].

**1.35** (a) HRTEM image of $Cu/Al_2O_3$ nanocomposite, (b) simple pathways for the hydrogenation of methyl formate and (c) results on the selective hydrogenation of various formate esters into methanol over fresh $20-Cu/Al_2O_3$ nanocomposite as the catalyst [149].

**1.36** (a) The degradation rate of rhodamine B under solar radiation in the presence of pure ZnO, CdS and ZnO/CdS hierarchical heterostructures and (b) schematic illustration of the energy band structure and electron–hole pair separation in ZnO/CdS hierarchical heterostructures [152].

**1.37** Fundamental mechanism of photocatalytic water splitting [104].

**1.38** (a) TEM image of $\alpha$-$Fe_2O_3$-$TiO_2$ nanocomposite with its HRTEM image (inset), (b) schematic of transfer and separation of visible light excited electrons in the $TiO_2$-$Fe_2O_3$ nanocomposite, and (c) I-V curves in 1 M NaOH (pH = 13.6) under visible light irradiation [165].

**1.39** (a) J−V curves and (b) IPCE data from CdS and CuS/CdS sensitized cells. A schematic representation of charge transfer at the interface is shown in inset of (a) [170].

**1.40** (a) Schematic representation of biolabelling of HeLa cells with $Fe_3O_4/NaYF_4$ nanocomposites using EDC/NHS coupling chemistry and images of live HeLa cells after being incubated with $Fe_3O_4/NaYF_4$ nanocomposites biolabeled with transferrin (b), after being incubated with $Fe_3O_4/NaYF_4$ nanocomposites without transferrin conjugation (c), and without incubating with any nanoparticles (d) [182]. The left rows are bright field images, the central rows show fluorescent images in dark field and the right rows are the overlays of the left and central rows.

**1.41** (a) and (b) TEM images of $Fe_3O_4/YVO_4$:$Eu^{3+}$@$SiO_2$ nanocomposite, (c) schematic representation of the adsorption and separation process for methylene blue removal using $Fe_3O_4/YVO_4$:$Eu^{3+}$@$SiO_2$ composites, (d) magnetic hysteresis loops for $Fe_3O_4$ and $Fe_3O_4/YVO_4$:$Eu^{3+}$@$SiO_2$ and (e) magnetic response of multifunctional composites under UV-irradiation [187].

**List of Schemes**

**List of Tables**

**List of Publications**

1. Sudheer Kumar Yadav and P. Jeevanandam, 'Synthesis of $Ag_2S$-$TiO_2$ nanocomposites and their catalytic activity towards rhodamine B photodegradation, *Journal of Alloys and Compounds,* **649,** 483–490 (2015).

2. Sudheer Kumar Yadav and P. Jeevanandam, 'Synthesis of PbS–$Al_2O_3$ nanocomposites by sol–gel process and studies on their optical properties', *Optical Materials,* **46,** 209–215 (2015).

3. Sudheer Kumar Yadav and P. Jeevanandam, 'Thermal decomposition approach for the synthesis of CdS–$TiO_2$ nanocomposites and their catalytic activity towards degradation of rhodamine B and reduction of Cr(VI)' *Ceramics International,* **41,** 2160-2167 (2015).

4. Sudheer Kumar Yadav and P. Jeevanandam, 'Synthesis of NiO–$Al_2O_3$ nanocomposites by sol–gel process and their use as catalyst for the oxidation of styrene', *Journal of Alloys and Compounds,* **610,** 567–574 (2014).

5. Sudheer Kumar Yadav and P. Jeevanandam, 'Synthesis of $\gamma$-$Fe_2O_3$-CdS nanocomposites with enhanced photocatalytic activity by thermal decomposition approach', *Journal of Nanoscience and Nanotechnology, Accepted (2016)*

6. Sudheer Kumar Yadav and P. Jeevanandam, Synthesis of ZnO@$\gamma$-$Fe_2O_3$ core-shell nanocomposites by a facile thermal decomposition approach and their application in photocatalytic degradation of congo red, *Manuscript submitted to Journal of Nanoparticle Research.*

**List of Conference Proceedings**

1. Sudheer Kumar Yadav and P. Jeevanandam, Poster presentation (accepted) on 'Synthesis of $\gamma$-$Fe_2O_3$-CdS nanocomposites by thermal decomposition method and their application in the photodegradation of congo red, *International Conference on Advanced Materials for Energy, Environment and Health (ICAM-2016)*, Department of Chemistry, Indian Institute of Technology Roorkee, Roorkee, India, March 04-07, 2016.

2. Sudheer Kumar Yadav and P. Jeevanandam, Poster presentation on 'Synthesis of CdS-$TiO_2$ nanocomposites by thermal decomposition approach', *International Union of Materials Research Societies-International Conference in Asia (IUMRS-ICA 2013)*, Indian Institute of Science, Bangalore, India, December 16-20, 2013.

3. Sudheer Kumar Yadav and P. Jeevanandam, Oral presentation on 'NiO–$Al_2O_3$ nanocomposites by a simple sol-gel process', *$1^{st}$ Winter workshop on Engineering at Nanoscale: From Materials to Bio-sensors*, Indian Institute of Technology, Indore, India, $10^{th}$ to $12^{th}$ December, 2012.

# 1    Introduction

# 2     Experimental Techniques

# 5   Synthesis and Characterization of CdS-γ-Fe₂O₃ and ZnO@γ-Fe₂O₃ Nanocomposites by Thermal Decomposition Approach

# 6     Applications of Nanocomposites

# CHAPTER 1

## *Introduction*

## 1.1 Nanotechnology: Historical background

Nanotechnology can be defined as the technology that deals with fabrication, characterization and exploitation of materials with at least one dimension in nanometer range (1 nm = $10^{-9}$ m) [1]. Nanoscience involves the study of natural and manmade materials possessing size between 1 and 100 nm [2]. The physicochemical properties of nanoscale materials are different from that of bulk materials [3,4]. Nanomaterials were used by people unknowingly in the past. For example, 'The Lycurgus Cup' consisting of gold and silver alloy nanoparticles (Fig. 1.1(a)) were used in the Roman period. This cup shows different colors depending on the source of light. If it is illuminated from outside light (reflected light), the cup appears green and if it is illuminated from within (transmitted light), it appears red [5]. In 1856, Michael Faraday prepared colloidal gold to investigate its optical properties and discussed the results in his paper entitled "Experimental relation of gold (and other metals) to light" published in Philosophical Transactions [6]. The colloidal solution prepared by Michael Faraday is still preserved in the Royal Institution (Fig. 1.1(b)).



**Fig. 1.1:** Use of nanomaterials in ancient times; (a) The Lycurgus Cup [5] and (b) the gold colloid prepared by Michael Faraday [6].

The idea of nanotechnology was given first by noble prize winning physicist 'Richard Feynman' in 29th December 1959. He delivered a lecture titled "There's Plenty of Room at the Bottom, An Invitation to Enter a New Field of Physics" in the Annual meeting of the American Physical Society at the California Institute of Technology. In his talk, he suggested the

possibility of fabrication of nano-sized materials with the use of atoms as the building blocks [3]. The term nanotechnology was proposed by Professor Norio Taniguchi at the International Conference on Industrial Production in Tokyo in 1974. He described nanotechnology as the field of fabrication and processing of materials by manipulating them at their atomic or molecular level [7]. Later in 1980, nanotechnology was extensively promoted by Eric Drexler through his book *"Engines of Creation: The Coming Era of Nanotechnology"* in which he talks about the creation of nanometer size machines, robots and tiny computers [8].

## 1.2 Nanomaterials

Nanomaterials are materials with characteristic properties and functions having at least one dimension in less than 100 nanometers range [9]. Nanomaterials possess physicochemical properties different than that of microscopic and bulk materials due to surface and quantum size effects [10,11]. In nanomaterials, as the particle size decreases, the volume fraction of atoms at the surface and interfaces increases as compared to the bulk materials. The surface atoms possess less number of atoms in their surroundings, i.e., lower coordination and thus have higher average binding energy per atom. The changes in the physicochemical properties is due to an increase in the surface to volume ratio of nanomaterials [10]. In metals and semiconductors, the conduction band electrons are described using 'particle in a box' model and the density of states and energy of particle depend on the size of box. As the size decreases to nano level, the electronic levels form discontinuous states known as discrete energy levels in contrast to continuous energy levels in the bulk materials. This is known as quantization effect (Fig. 1.2) [12]. The modification of surface properties and discontinuities in the band energy levels lead to variation in the properties of nanomaterials such as band gap, density of states, electron affinity, ionization potential, mechanical, magnetic, electrical and thermal conductivity [10,13]. Other properties of materials such as melting point, lattice constant and stabilization of crystallographic phases are also affected by reduction in size to nano level [10].
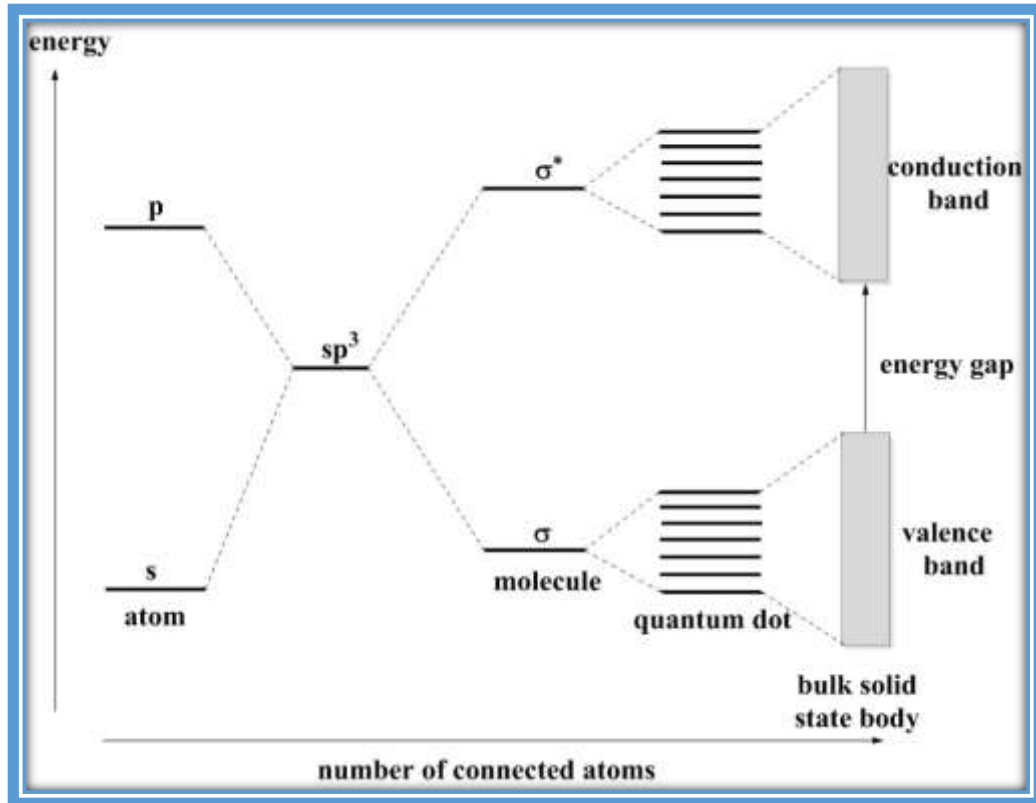
**Fig. 1.2:** Electronic energy levels in a semiconductor depending on the number of bound atoms (adapted from ref. [12]).

### 1.2.1 Types of nanomaterials

The nanomaterials, depending on their size, shape and composition, have been classified into different categories [1,14].

**Nanoparticles:**

Nanoparticles are particles that have atleast one dimension in the 1-100 nm range and examples are shown in Fig. 1.3. They often possess unexpected interesting optical and magnetic properties due to their small size [4]. The nanoparticles can be further classified into:

i) 0 dimensional nanoparticles (0 D), e.g. Quantum dots

ii) 1 dimensional nanoparticles (1 D), e.g. nanowires, nanotubes, nanorods

iii) 2 dimensional nanoparticles (2 D), e.g. nanorice, nanobars

iv) 3 dimensional nanoparticles (3 D), e.g. dendrimers, graphene
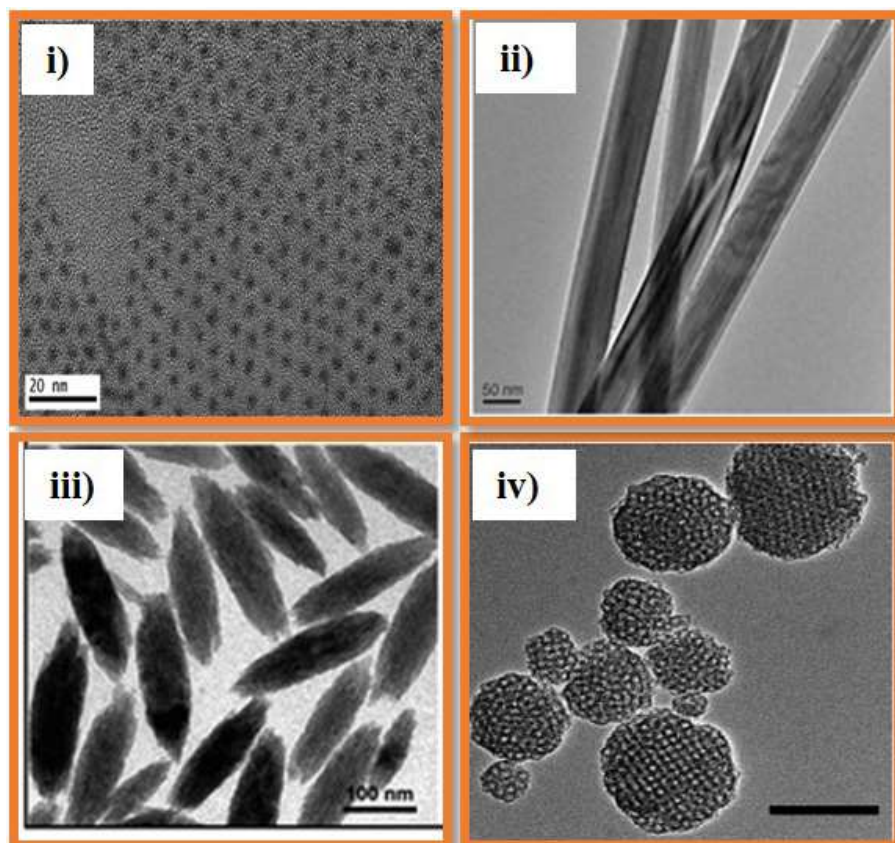
**Fig. 1.3:** TEM images elucidating different types of nanoparticles: i) PbS quantum dots [15], ii) ZnO nanorods [16], iii) rice-shaped NaLnF$_4$ [17] and iv) Poly (2-dimethylaminoethyl acrylate) (PDMAEA) dendrimers [18].

**Nanocomposites:**

Nanocomposites are materials made up of two or more components with distinct physical and chemical properties. At least one of the components should possess one of its dimensions in the nanometer range (1-100 nm) [19]. Fig 1.4(a) shows the schematic diagram of a polymer nanocomposite, where inorganic nanoparticles (red) are dispersed on the polymeric matrix (blue). Fig 1.4(b) show the SEM image of polystyrene/Ag nanowire nanocomposite as the example of polymer nanocomposite [20], Fig 1.4(c) shows the schematic diagram for a ceramic nanocomposite, glass mixed with nanoparticles to obtain different colours [21] and Fig 1.4(d) shows the TEM image of GaPd$_2$/SiO$_2$ as an example of ceramic nanocomposite [22].
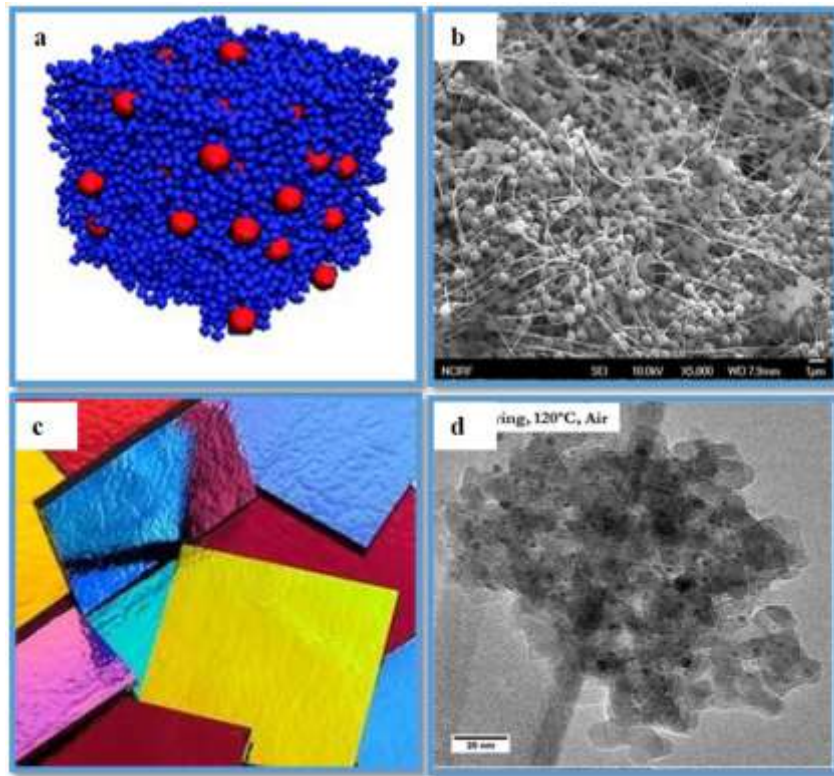
**Fig. 1.4:** (a) Schematic diagram of a polymer nanocomposite, (b) SEM image of polystyrene/Ag nanowire nanocomposite, (c) schematic diagram for a ceramic nanocomposite and (d) TEM image of GaPd$_2$/SiO$_2$ nanocomposite [21].

**Graphene:**

Graphene is an allotrope of carbon in which carbon atoms are bonded (sp$^2$) to each other in a hexagonal honeycomb structure. Fig 1.5(a) and 1.5(b) show the schematic representation and HRTEM image of a monolayer graphene sheet [23,24].
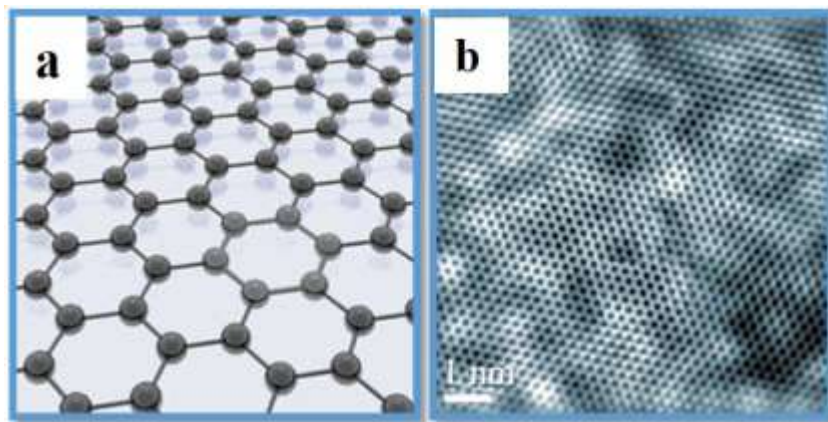


**Fig. 1.5:** (a) Schematic representation and (b) HRTEM image of a monolayer graphene sheet [23,24].

5

**Dendrimers:**

Dendrimers are highly branched mono disperse polymers with dimensions in the nanoscale range. Due to their unique structure, they are used in different areas of biology and material science, e.g. drug delivery, gene transfection, catalysis, photocatalysis activity, molecular weight and size determination [25]. Fig. 1.6 shows a schematic representation and TEM image of an arene-cored, PEG terminated dendrimers encapsulated gold nanoparticles [26].
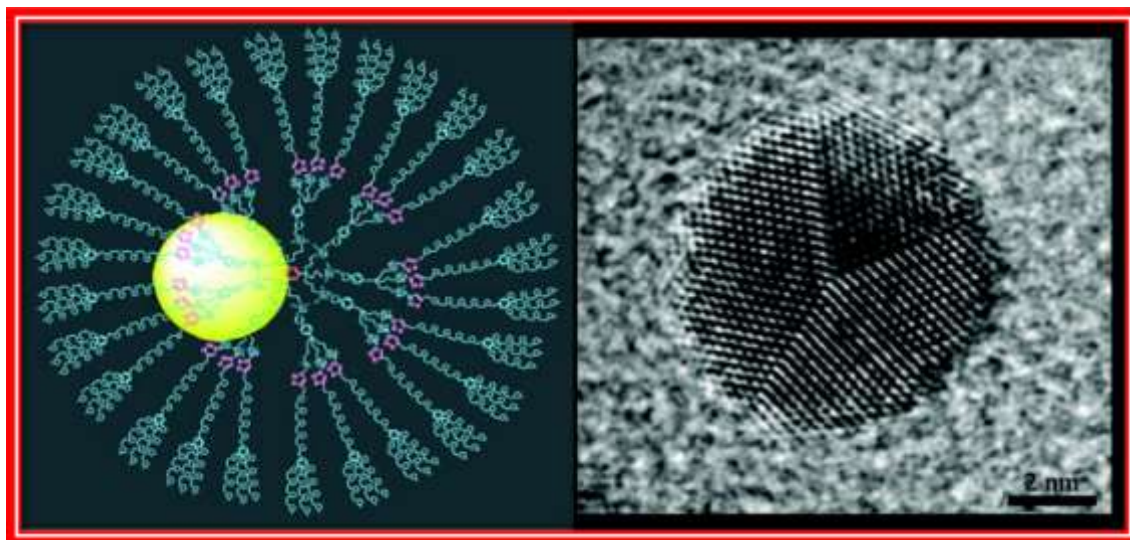


**Fig. 1.6:** Schematic representation and TEM image of an arene-cored, PEG terminated dendrimers encapsulated gold nanoparticles [26].

**Carbon Nanotubes:**

Carbon nanotube is an allotrope of carbon. Carbon nanotubes have drawn immense research attention and have shown great potential applications in many fields due to their exceptional structural, mechanical, and electronic properties. Functionalization of CNT with different functional groups containing oxygen, organic molecules, polymers, proteins, metal nanoparticles, etc., has attracted great interest over the past many years and produced various composite materials with specific applications [27,28]. CNTs are mainly classified into two types: single-walled carbon nanotubes (SWCNTs) and multi-walled carbon nanotubes (MWCNTs). MWCNTs consist of cylindrical tubes of sp$^2$ carbons produced by rolling up of single or multi-layered graphene (Fig. 1.7) [29].
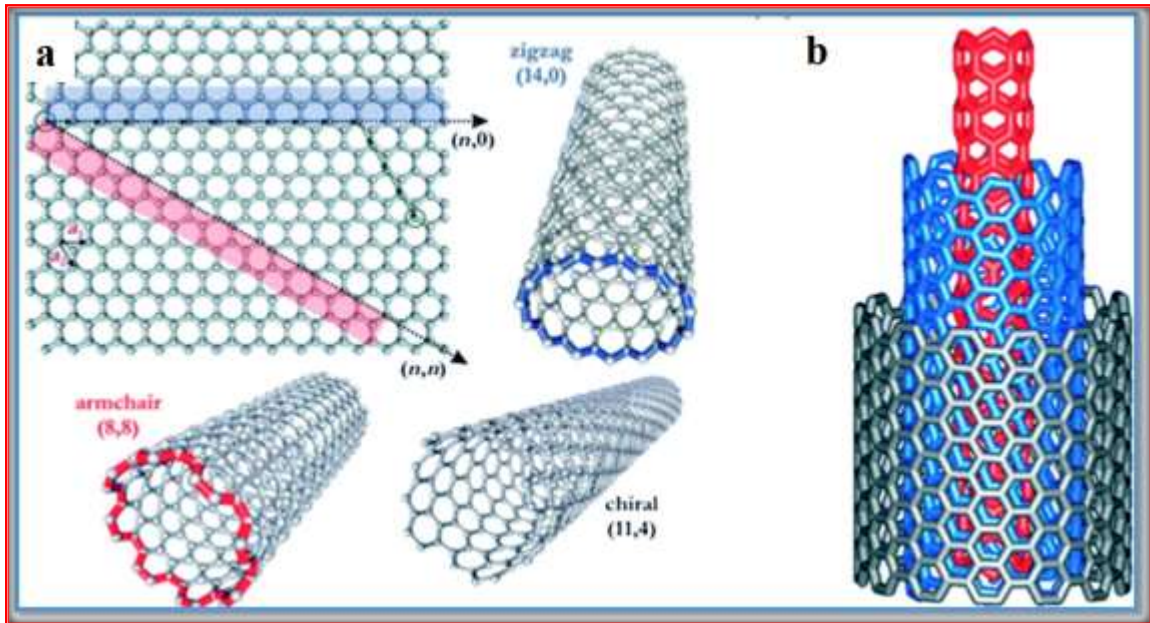
**Fig. 1.7:** (a) Roll-up of a graphene sheet leading to three different types of SWCNT and (b) structure of a multi-walled carbon nanotube [29].

### 1.2.2 General synthetic methods for the preparation of nanoparticles

The synthesis of nanoparticles is generally classified into two major approaches (Fig. 1.8) [30]:

1. Top down approach
2. Bottom up approach

**Top down approach**

Top down approach involves breaking down larger particles into nano sized particles with the help of physical methods such as vapor deposition, high energy ball milling, sputtering, laser ablation, ion implantation, arc method, pyrolysis and pulsed laser deposition.

**Bottom up approach**

Bottom up approach involves creation of atoms or molecule species by reduction of metal salts or from organometallic precursor complexes by chemical means such as reduction or decomposition. The generated species are further aggregated into nanoparticles. The chemical means of synthesis of nanoparticles are sol-gel synthesis, micro-emulsion method, sonochemical synthesis, co-precipitation, reverse micelle method, hydrothermal method, etc. Out of the two synthetic approaches, bottom up approach (chemical method) is less wasteful and the most commonly used.
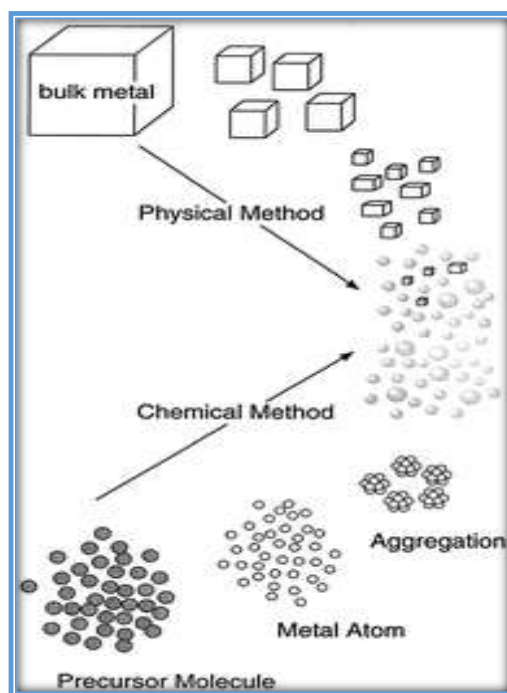
**Fig 1.8:** Schematic representation of top-down and bottom-up approaches for the synthesis of nanomaterials [30].

## 1.3 An Introduction to Nanocomposites

The field of nanocomposites involves the study of multi-phase materials where at least one of the constituent phases has alteast one dimension in 1 to 100 nm range. The structures have nanometer scale repeat interfaces between different phases of the contituents [19]. The mechanical, electrical, optical, electrochemical, catalytic, and structural properties of the nanocomposites differ significantly from that of the individual components. The physicochemical properties of the materials show improvement in their properties when the particle size of the materials is less than a particular size called "the critical size" [31]. Some of the properties of the nanocomposites get enhanced due to interaction of the constituents at their interface [32]. Nanocomposites possess many interfaces due to their high surface area. The speciality of nanocomposites is their multifunctional properties which arise from the combination of different nanomaterials with dissimilar properties [33].

The nanocomposites are mainly composed of an inorganic solid dispersed in an organic component or vice versa or composed of two or more inorganic phases or organic phases with at least one of the phases having at least one of the dimensions in the nanosize range. According to their matrix materials, nanocomposites can be classified under three different categories [34]:

1. Ceramic matrix nanocomposites

2. Metal matrix nanocomposites

3. Polymer matrix nanocomposites

### 1.3.1 Ceramic matrix nanocomposites

In ceramic composites, the major part of the material is a ceramic, i.e. a chemical compound from the group of oxides, nitrides, borides, silicides, etc. Ceramic materials have properties such as good wear resistance and high thermal and chemical stability, but they are brittle. In order to overcome this shortcoming, ceramic nanocomposites have been incorporated with different materials such as metals, semiconductors and polymers for achieving significant enhancement of their mechenical properties [35]. Both the components are finely dispersed in each other in order to enhance the desired properties. Ceramic nanocomposites by combination of different contituents have been obtained with improved mechanical, optical, electrical and magnetic properties. For example, Parchoviansky et al. have studied ceramic nanocomposite such as $Al_2O_3/SiC$ with improved mechanical property [36]. They have reported strengthening of $Al_2O_3$ matrix ($655 \pm 90$ MPa) after addition of a low volume fraction of SiC particles (20%) of suitable size and hot pressing of the resulting mixture (Fig. 1.9).
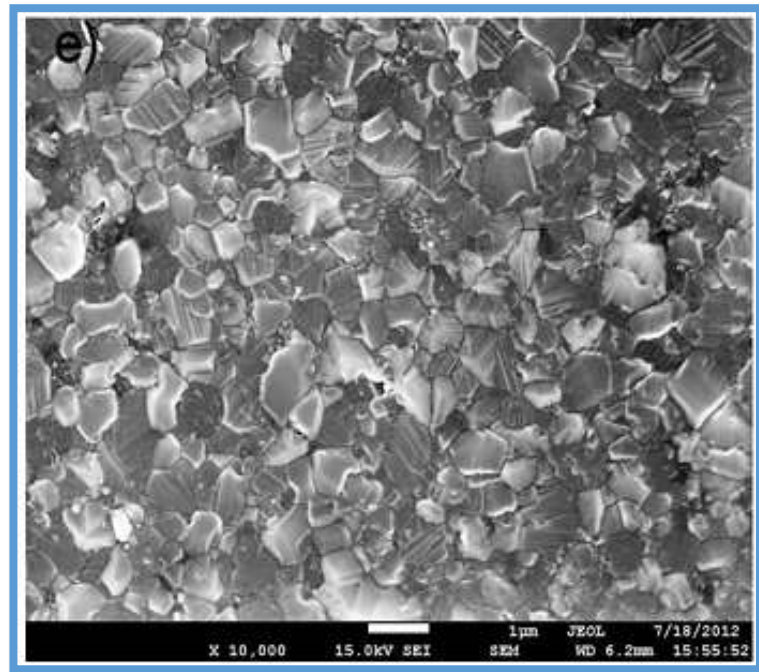


**Fig. 1.9:** SEM image of $Al_2O_3/SiC$ nanocomposite containing 20 vol.% SiC [36].

### 1.3.2 Metal matrix nanocomposites

Metal matrix nanocomposites are composed of a ductile metal or alloy as the matrix in which nanosized reinforcement materials are incorporated [34]. These composites consist of a metal matrix filled with nanoparticles having physical and mechanical properties completely different from that of the matrix [37]. They show potential applications in many areas such as heavy metal industries including aeronautical industries, motor industries and in the development of structural materials [38,39]. Fig. 1.10 shows the TEM image of example of Au/Ge bilayer metal matrix nanocomposite. It was found that the Ge nanocrystals embedded in the Au matrix show interesting fractal morphologies [40].
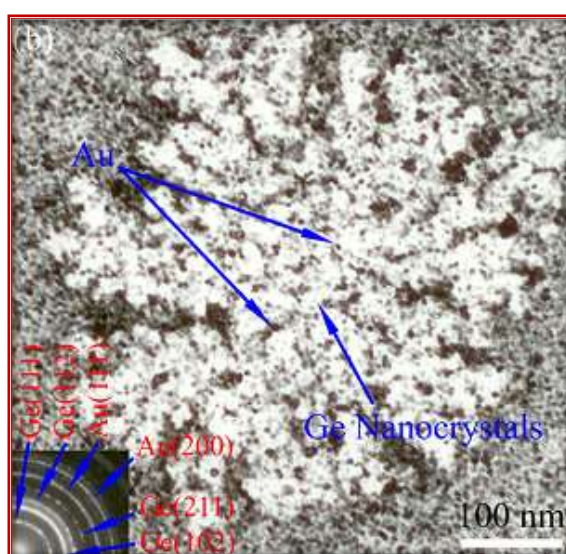


**Fig. 1.10:** Au/Ge nanocomposite bilayer with interesting fractal Ge nanocrystals [40].

### 1.3.3 Polymer-matrix nanocomposites

Polymers are long chain macromolecules composed of repeating units of identical structure. They are widely used because of their easy production, light weight and ductile nature [41]. Polymers have been used as matrix materials incorporated with different reinforcement materials having dimension in the nanometer range. Polymer nanocomposites are obtained with enhanced properties such as heat and impact resistance and mechanical strength. The reinforecement also leads to reduction in flammability, electrical conductivity and gas permeability of the polymer nanocomposites [42]. The incorporation of a reinforcement in polymer may also impart biodegradation ability to make the polymer ecofriendly [34,43]. Fig. 1.11 shows the TEM images of Au/polyaniline nanocomposites with different morphologies.
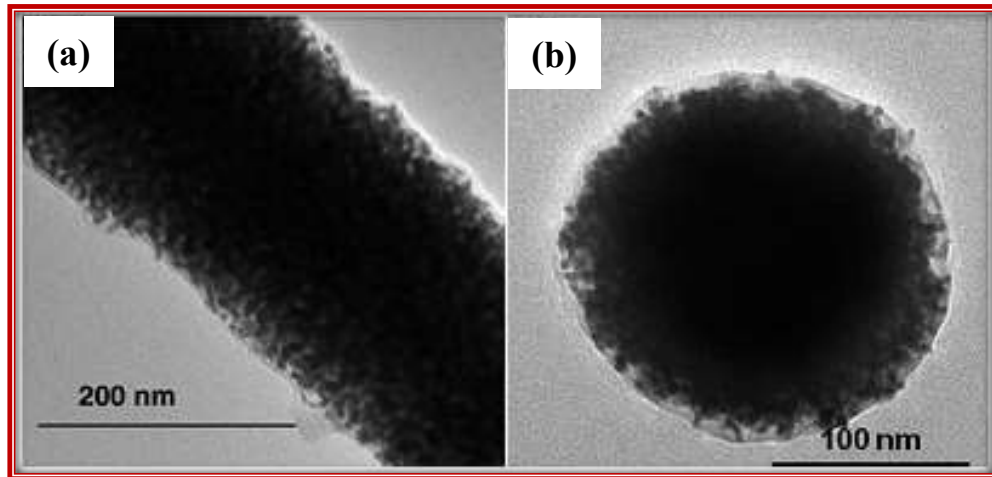
**Fig. 1.11:** TEM images of a nanorod (a) and nanosphere (b) of Au/PANI nanocomposites clearly showing Au nanoparticles embedded in the polymer matrix [44].

**1.4 General methods of synthesis of nanocomposites** (Fig. 1.12).

Synthesis of nanocomposites is classified into two categories:

1. Physical method of synthesis (Top-down)

2. Chemical method of synthesis (Bottom-up)
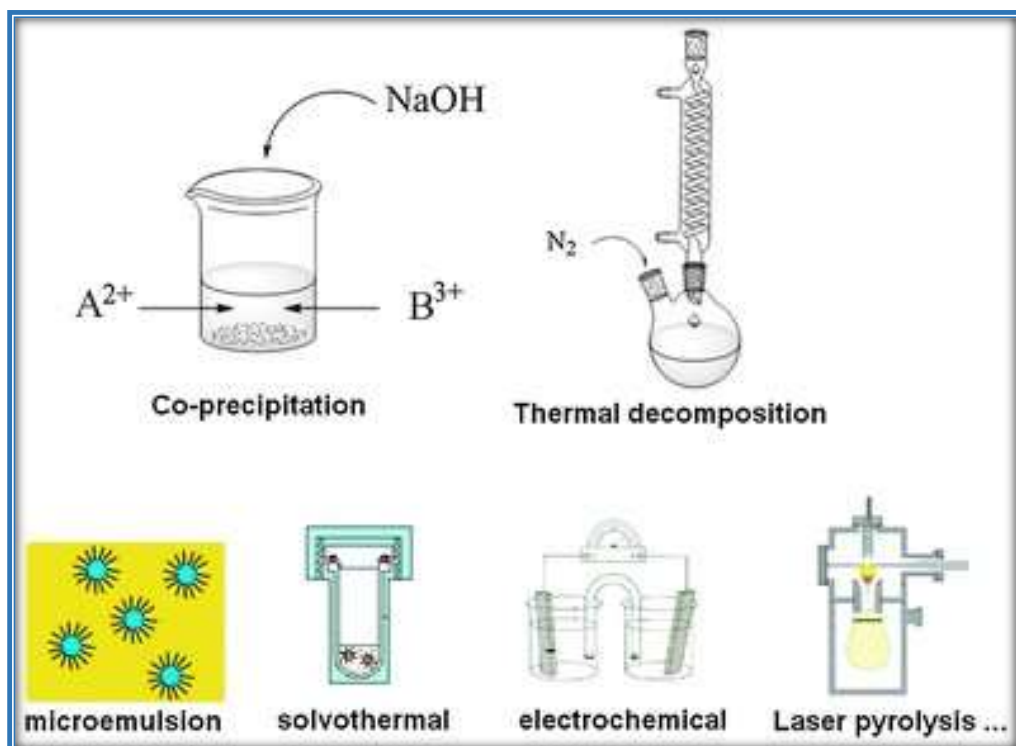


**Fig. 1.12:** Schematic representation of different methods used for the preparation of nanocomposites [45].

### 1.4.1 Physical methods

### 1.4.1.1 Chemical vapour deposition

Chemical vapour deposition (CVD) is a widely used method for the synthesis of nanocomposites. In chemical vpour depostion, volatile molecular precursors are deposited from vapour phase on substrate materials under controlled conditions. The advantages of CVD are large scale manufacturing, high growth rate, high flexibility and good control over the synthesis process [46]. The saturated vapour of molecules or atoms can be produced by different methods such as sputtering [47], laser ablation [48] and thermal evaporation [49]. Fig. 1.13(a) shows the HR-TEM image of $Fe_2O_3$–$TiO_2$ nanocomposites prepared using CVD method [46]. The Fourier transform (FT) patterns from regions 1 and 2 prove the presence of $\alpha$-$Fe_2O_3$ and anatase $TiO_2$, respectively. Fig. 1.13(b) shows the HAADF-STEM image of the $Fe_2O_3$–$TiO_2$ nanocomposite at the interface region.
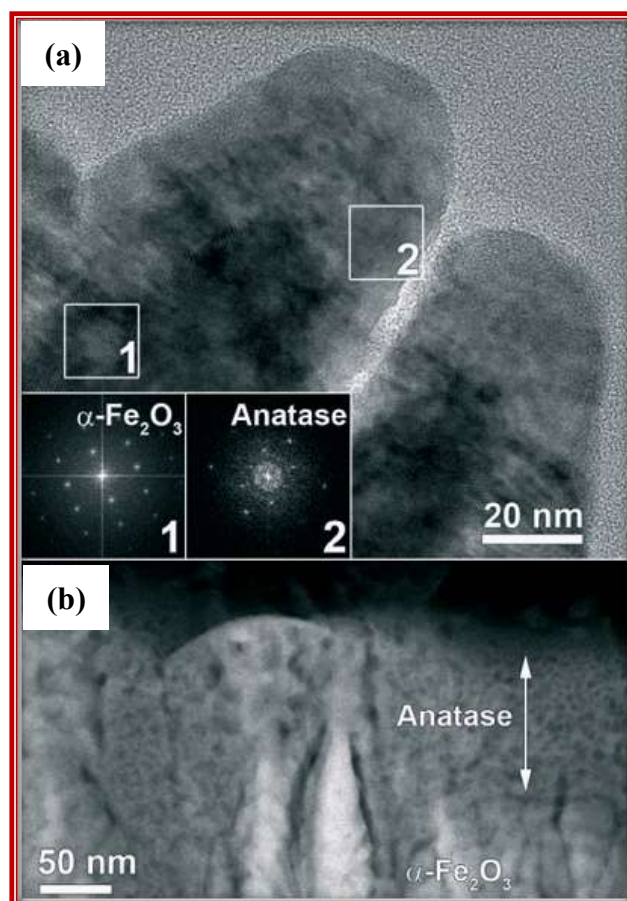


**Fig. 1.13:** (a) HR-TEM image and FT patterns for $Fe_2O_3$–$TiO_2$ nanocomposite and (b) HAADF-STEM image of the $Fe_2O_3$–$TiO_2$ nanocomposite at the interface region [50].

### 1.4.1.2. Ball milling

Ball milling is a mechanical grinding process. In this method, nanocomposites are formed by breaking and joining of constituent particles in a cylindrical vessel in the presence of steel balls (Fig. 1.14(a)). By this process, it is easy to produce nanocomposites in large scale but homogeneity interms of size, shape and purity of the nanocomposites produced remain a challenge [19]. Some of the examples of nanocomposites prepared by the ball milling method are Cu-ZrO$_2$ [51], Ni-Al$_2$O$_3$ [52], NiAl-Al$_2$O$_3$ [53], etc. Fig. 1.14(b) shows the HRTEM image and SAED pattern of C$_{60}$/Co nanocomposites prepared via the ball milling method [54].
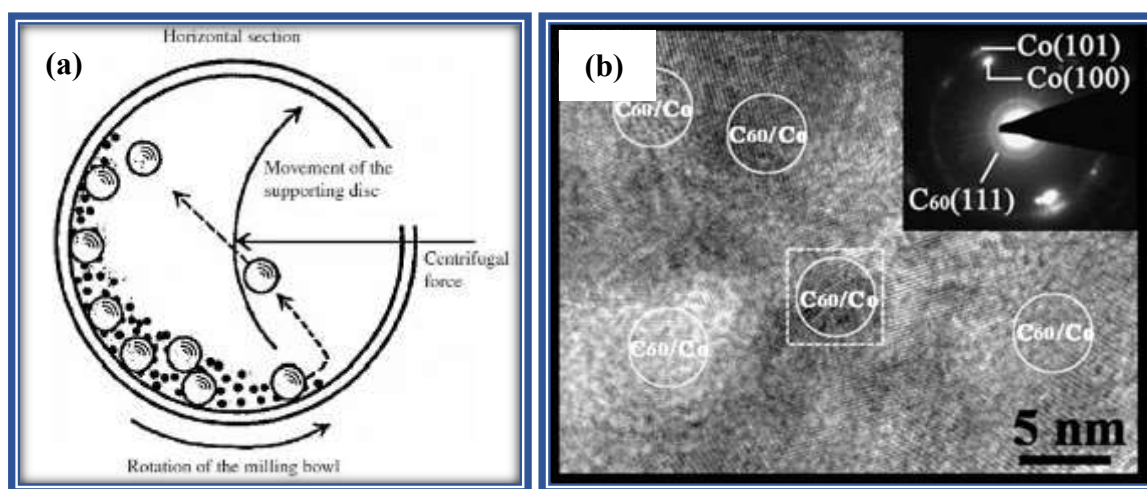


**Fig. 1.14:** (a) Schematic view of motion of the ball and powder mixture in ball milling [55] and (b) HRTEM image and SAED pattern of C$_{60}$/Co nanocomposite [54].

### 1.4.1.3 Spray pyrolysis

Spray pyrolysis is a very simple and cost-effective method for the deposition of nanocrystalline thin films. The steps involved in the spray pyrolysis method are atomization of precursor solution to form aerosol droplets, moving of the resultant aerosol to the substrate and decomposition of the precursor on substrate to form powder or film [56]. Some of the nanocomposites prepared via spray pyrolysis method are Mn$_3$O$_4$-C [57], Al$_2$O$_3$-ZrO$_2$ [58] and Au/TiO$_2$ [59]. Fig. 1.15 shows the two steps fabrication and SEM image of ZnO-SnO$_2$:F nanocomposite by spray pyrolysis.
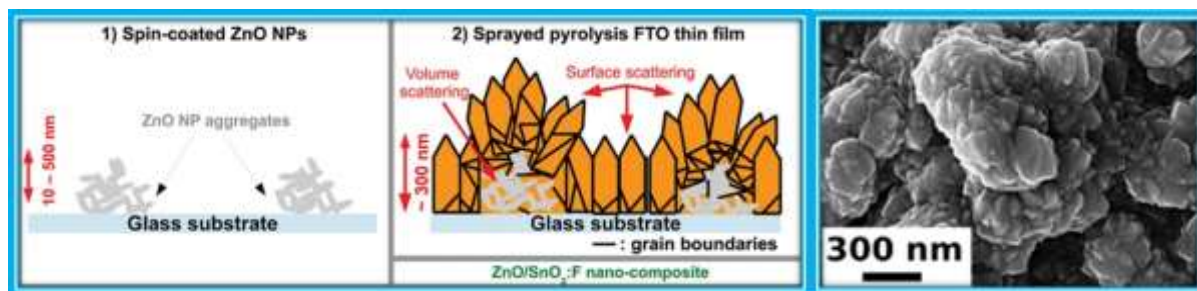
**Fig. 1.15:** Schematic representation of the two-step fabrication process of ZnO-SnO$_2$:F nanocomposite thin film by spray pyrolysis and the FE-SEM image of ZnO-SnO$_2$:F nanocomposite [60].

### 1.4.1.4 Laser ablation method

In laser ablation technique, a pulse laser having wavelength in the range of 1064 nm is allowed to irradiate a solid target either on a substrate or in a liquid medium [61]. The irradiated surface is heated up and gets vapourized. At an adequate laser flux, the vapourized material transforms into a plasma plume which contains several energetic species including electrons, atoms, molecules, ions, clusters, etc. The plasma has characterisitics such as high temperature, high pressure and high density. The plasma plume due to pressure difference between the plume and the sorrounding atmosphere expands rapidly and cools down. This rapid cooling and condensation of plasma plume leads to nucleation and growth of different nanoparticles, nanostructures and nanocomposites. The laser ablation setup can be designed in different environments namely, vacuum, gaseous and liquid [62]. If the the setup chamber is designed in vacuum or gaseous environment to produce thin films, the technique is known as pulse laser deposition (PLD). If the synthesis process is carried out in liquid environment to produce colloids of nanoparticles, the technique is known as laser ablation liquid (LAL). Some examples of the nanocomposites prepared using laser ablation techniques are Sn@SnS [62], Ag-SiO$_2$ [63], Ag-Al$_2$O$_3$ [64], graphene oxide (GO)-ZnFe$_2$O$_4$ [65], BiFeO$_3$-MgFe$_2$O$_4$ [66], etc. Fig. 1.16(a) shows the schematic representation of preparation of SnO$_2$-rGO nanocomposites by LAL method using a Nd:YAG laser (1064 nm) with 10 Hz pulse repetition rate, 10 ns pulse duration and 100 mJ per pulse. Fig. 1.16(b) shows the TEM image and SAED pattern, and (c) the HRTEM image of the SnO$_2$-rGO nanocomposite [67].
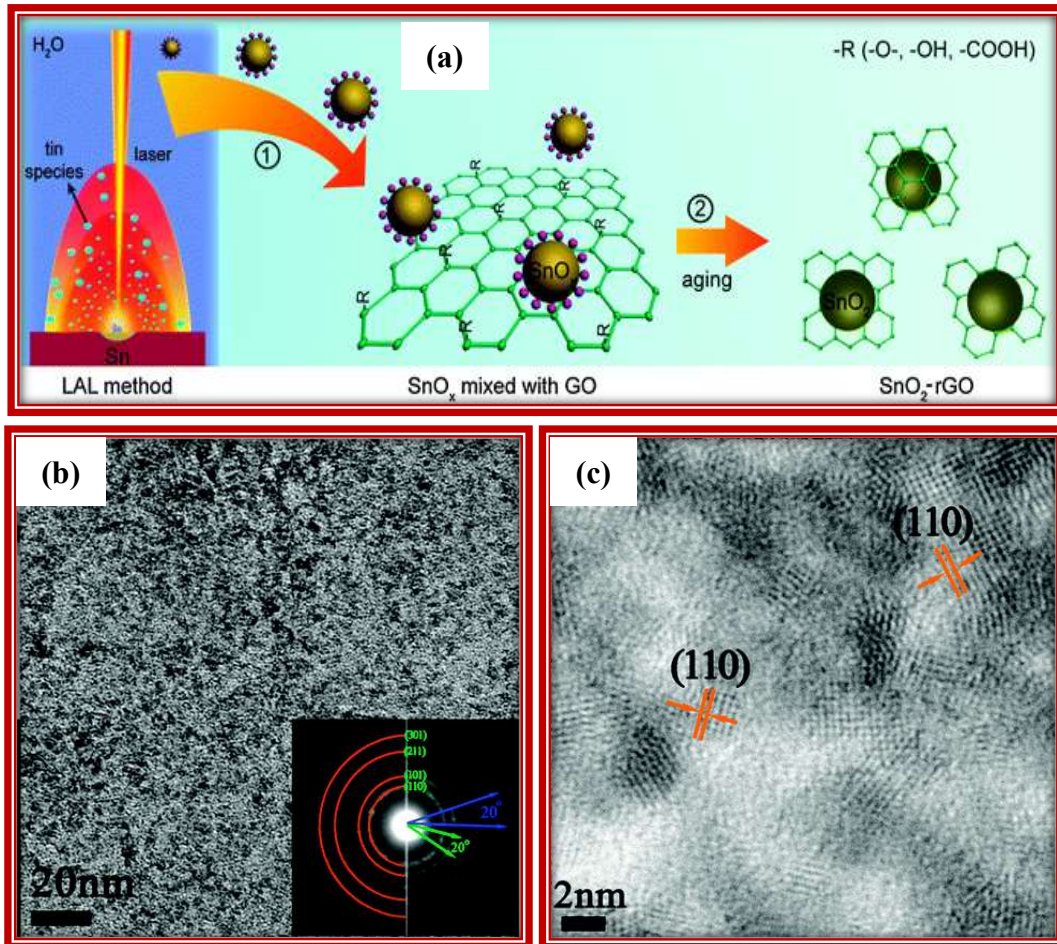
**Fig. 1.16:** (a) Schematic representation of LAL (laser ablation liquid) -assisted fabrication of SnO$_2$–rGO nanocomposite, (b) TEM image and SAED pattern and (c) HRTEM image of the SnO$_2$–rGO nanocomposite [67].

### 1.4.1.5 Ion implantation

In this technique, the matrix materials are targeted with ions. The ions are highly energetic as they are accelerated with 10 to 1000 kilovolts of electric field. Ions get saturated to form a layer below the target surface layer [68]. The saturation layer can extend from 10 nm upto 1μm, and this depends on energy of the ions and composition of the target [69]. Further, individual nanoparticles are precipitated by annealing, or bombardment with other ions or electrons (Fig. 1.17).
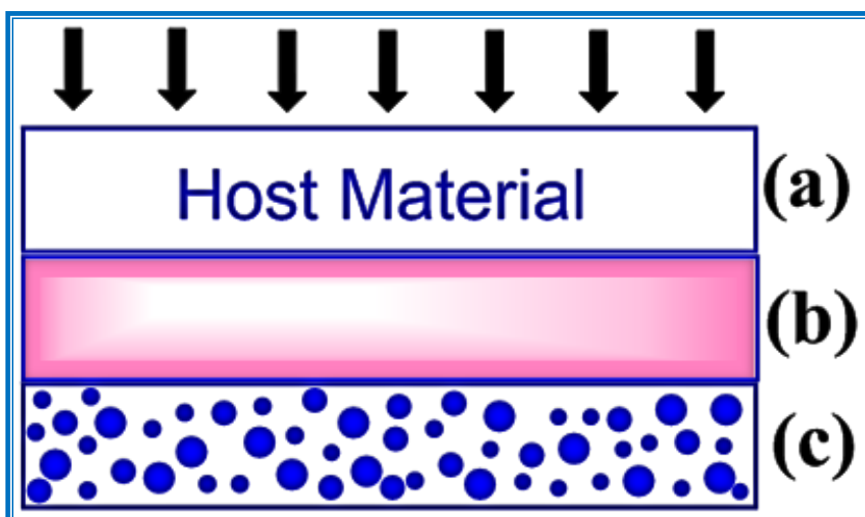
**Fig. 1.17:** Representation of the ion implantation technique for producing implanted nanoparticles, (a) The host matrix is implanted with energetic ions (arrows), (b) a supersaturated solid solution is formed below the surface region and (c) the implanted material is precipitated into a layer of isolated nanoparticles with varying size [68].

Some of the examples of nanocomposites prepared using ion implantation techniques are $\alpha$-$Fe_2O_3$-$TiO_2$ [69], Fe-$SiO_2$ [70], Au@Ag [71], CdSe-$SiO_2$ [72], PbS-$SiO_2$ [73], and Au-polyimide [74]. Fig. 1.18 shows the TEM and HRTEM images for Fe-$SiO_2$ nanocomposite prepared using ion implantation method.
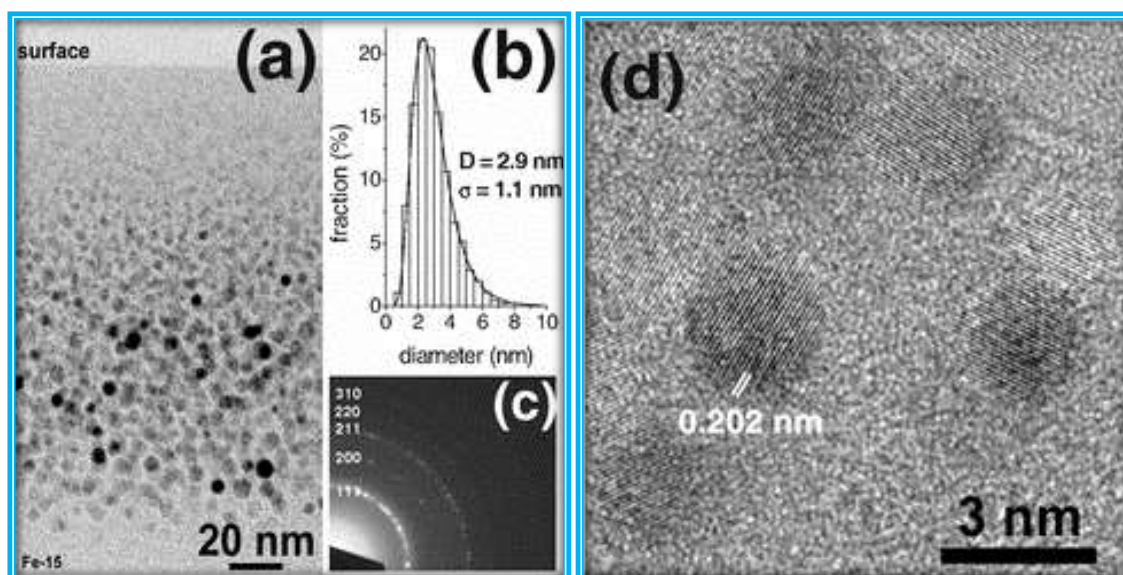


**Fig. 1.18:** (a) TEM image of Fe-$SiO_2$ nanocomposite prepared by ion implantation method, (b) corresponding particle size distribution, (c) SAED pattern showing the presence of Fe and (d) HRTEM image of the Fe-$SiO_2$ nanocomposite [70].

### 1.4.2 Chemical methods

### 1.4.2.1 Sol-gel

Sol-gel process is one of the most widely used techniques for the synthesis of nanocomposites. It can be defined as hydrolysis and polycondensation of a liquid precusor to solid. Sol-gel process involves dissolution of precursor metal salts in a liquid to form a sol. Further, a gel is formed by formation of three dimensional polymeric network of metal hydroxide and metal alkoxide through oxygen bond formation [75]. Densification and decomposition of the gel at high temperature leads to destruction of the metal hydroxide and metal alkoxide network to form a solid product. Advantages of sol-gel method include high yield of product, homogeneity, low reaction temperature and low production cost [4,76]. Sol-gel method has been used to synthesize materials with different shapes including porous structures, fibers, dense powders and thin films (Fig. 19(i)) [77]. Heat treatment of gel leads to the formation of xerogel due to collaspe of the gel network [75]. When the heating is carried out under controlled conditions, the three dimensional gel network is retained leading to the formation of an aerogel. In the case of nanocomposites, sol-gel process is either used as a single process or in combination with two-step processes. Some examples of nanocomposites synthesized via sol-gel process are $SiO_2$-$TiO_2$ [78], $NiTiO_3$/$NiO$ [79] and $Au$/$ZnO$ [80]. Fig. 1.19(ii) shows the SEM, TEM, and HRTEM images and SAED pattern of $Ag$/$TiO_2$ nanocables prepared by the sol-gel method [81].
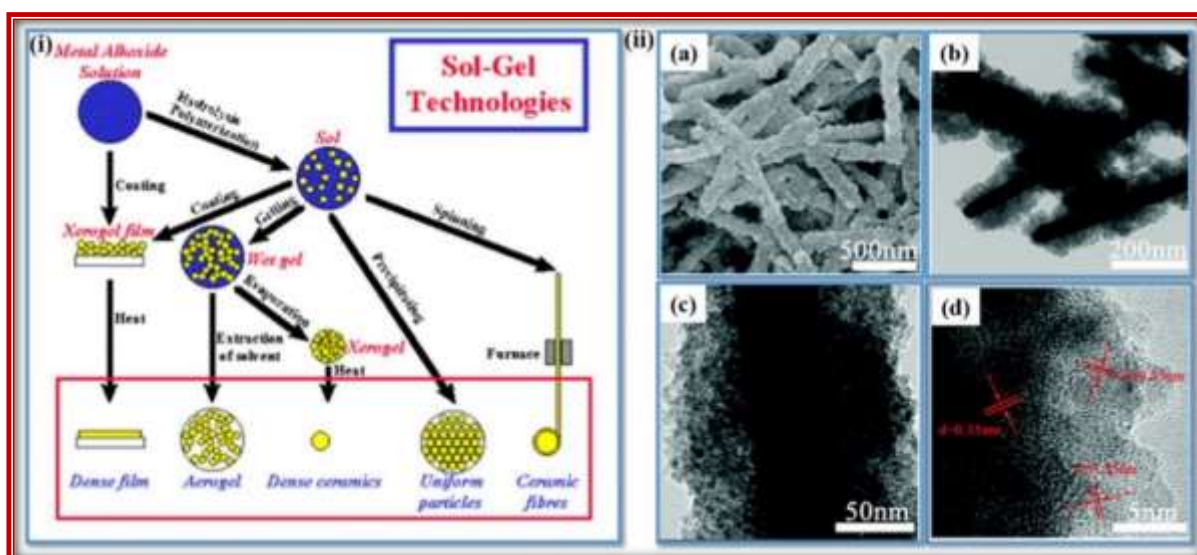


**Fig. 1.19:** (i) Sol-gel method and its products [77] and (ii) SEM (a), TEM (b and c) and HRTEM (d) images of $Ag$/$TiO_2$ nanocables [81].

### 1.4.2.2. Thermal decomposition

In thermal decomposition approach for the synthesis of nanocomposites, two or more organometallic metal precursors such as metal acetate, metal acetylacetonate and metal carbonyl are decomposed in high boiling solvents (e.g. diphenyl ether, oleic acid, 1-octadecene, etc.) at temperatures higher than the decompostion temperature of the precursors (e. g. 150 $^{o}$C to 350 $^{o}$C). Nanocomposites with tunable optical and magnetic properties can be prepared by varying the reaction parameters such as time, temperature and concentration of the precursors. Thermal decompostion method can be used solely or in combination with other methods for the synthesis of the nanocomposites. Some examples of nanocomposites prepared by the thermal decomposition methods are $Ag_2S$-$TiO_2$ [82], Au-$Cu_2S$ [83], ZnO-$FeWO_4$ [84], $Co_3O_4$/ZnO [85], etc. Fig.1.20(i) illustrates the one pot synthesis of EuS-CdS hetronanostrucutures [86]. Fig. 1.20(ii) shows the TEM images of $Ag_2S$-$TiO_2$ and $Ag_2S$-$SiO_2$ nanocomposites prepared by a two step thermal decompositon method, where $TiO_2$ and $SiO_2$ were prepared by the sol-gel process [82].
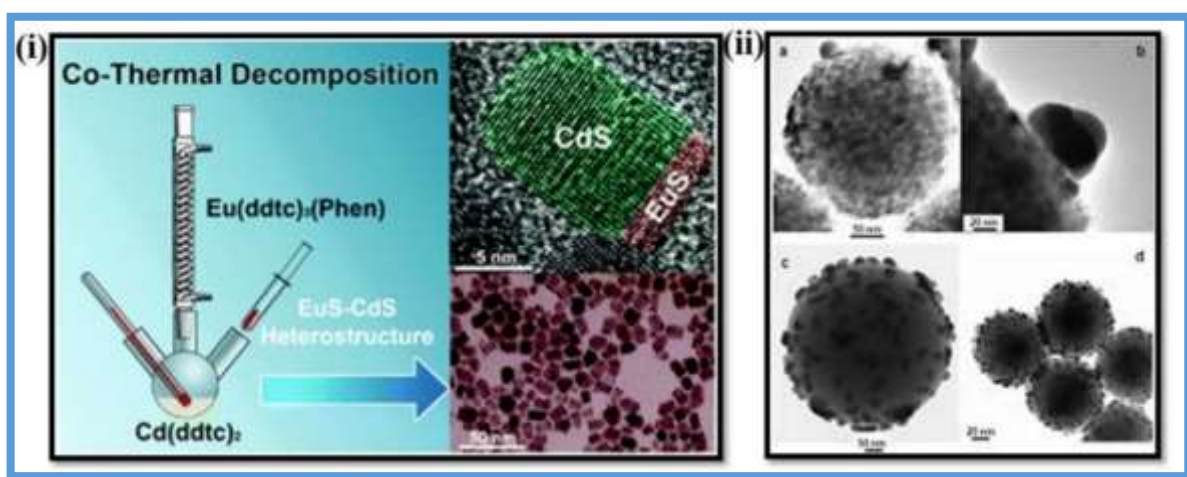


**Fig. 1.20:** (i) Schematic representation of co-thermal decomposition synthesis, TEM and HRTEM images of EuS–CdS heterostructured nanocrystals [86], and (ii) TEM images of nanosized islands of $Ag_2S$ on the surface of $TiO_2$ particles (a and b) and on the surface of amorphous $SiO_2$ particles (c and d) [82].

### 1.4.2.3 Pricipitation method

Precipitation method (co-precipitation/homogeneous precipitation) is generally used for the synthesis of metal oxide-metal oxide nanocomposites. This method involves hydrolysis of aqueous solution of metal salt precursors (e.g. chlorides, nitrates, sulfates, acetates, etc.) in the presence of water or precipitating agents such as urea, sodium hydroxide, ammonium

hydroxide etc., at room temperature or at elevated temperatures leading to the formation of metal hydroxides [87]. Metal oxide is formed by further heat treatment of the metal hydroxide [88]. When urea is used as the precipitating agent, the method is known as homogeneous precipitation. Figs. 1.21(a), (b) and (c) show the TEM and HRTEM images of $CeO_2/Fe_2O_3$ composite nanospindles prepared by the co-precipitation method [89] and Figs. 1.21(d) and (e) show SEM and TEM images of $\alpha$-Ni(OH)$_2$/graphite nanosheet composite prepared by the homogeneous precipitation method [90].
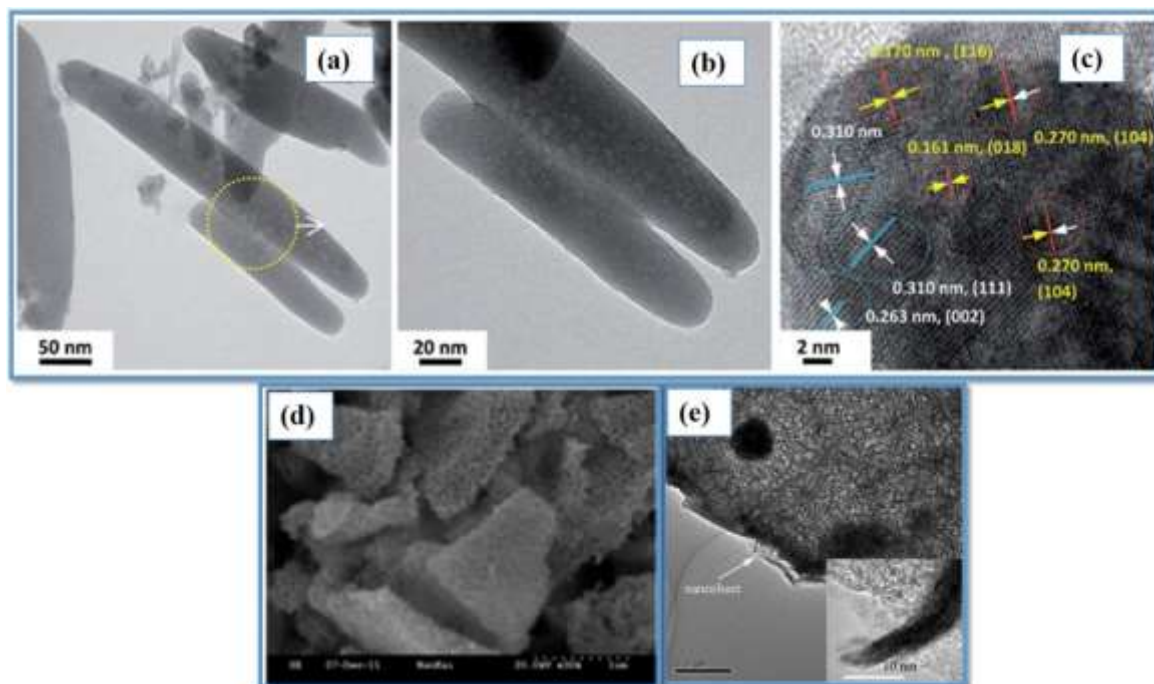


**Fig. 1.21:** (a), (b) and (c) TEM and HRTEM images of $CeO_2/Fe_2O_3$ composite nanospindles and (d) and (e) SEM and TEM images of $\alpha$-Ni(OH)$_2$/graphite nanosheet composite [89,90].

### 1.4.2.4 Micro-emulsion method

Microemulsion method offers a good way to prepare nanocomposites with controlled surface and size. Preparation of nanocomposites by microemulsion method involves two steps. First step is the preparation of nanoparticles in a water in oil (W/O) emulsion. (W/O) emulsion is a surfactant stabilized transparent isotropic liquid medium consisting of nanosized water droplets dispersed in oil phase. The surfactant protected water droplets act as micro-reactors for the synthesis of nanocomposites and prevent aggregation of particles. The other step in the synthesis is to crystallize the nanocomposites by increasing the annealing temperature [91,92].

Fig. 1.22(a) shows schematic of the preparation of PVP-modified composite silica coated gold nanospheres and quantum dots probe (Au@SiO$_2$-QDs/SiO$_2$-PVP). Figs. 1.22(b) and (c) show the TEM images of the composites Au@SiO$_2$ and Au@SiO$_2$-QDs/SiO$_2$-PVP prepared using the microemulsion method [93].
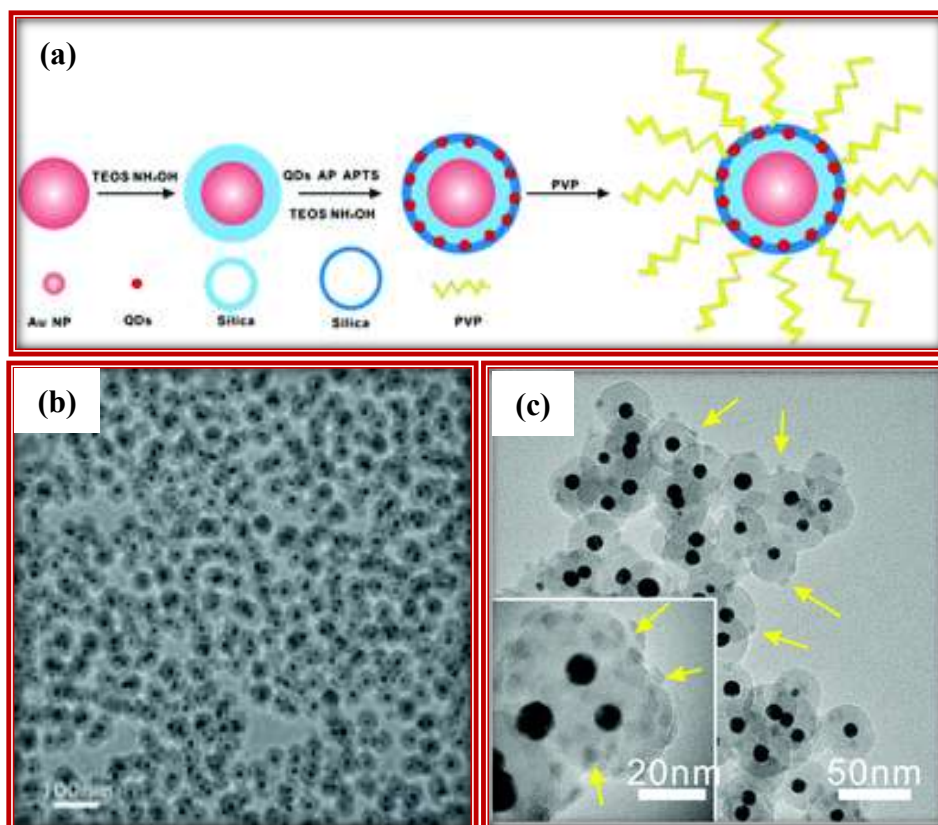


**Fig. 1.22:** (a) Schematic for the preparation of the PVP modified silica coated gold nanosphere composite and quantum dots probe (Au@SiO$_2$-QDs/SiO$_2$-PVP), (b) TEM image of Au@SiO$_2$ composite and (c) TEM image of composite Au@SiO$_2$-QDs/SiO$_2$-PVP prepared using the micro-emulsion method [93].

### 1.4.2.5 Solvothermal/Hydrothermal synthesis

In this method, the nanocomposites are prepared in a closed vessel known as autoclave by chemical reactions under controlled temperature and pressure conditions. Solvents get heated above their boiling point by the increase in generated pressures due to heating. When the solvent is water, the method is known as hydrothermal. Fig 1.23 shows the TEM and HRTEM images of the vertically aligned Bi$_2$Ti$_2$O$_7$-TiO$_2$ composite nanowire arrays prepared via solvothermal method [94] and flower-like NiCoP/ZnO nanocomposite prepared via hydrothermal method [95].
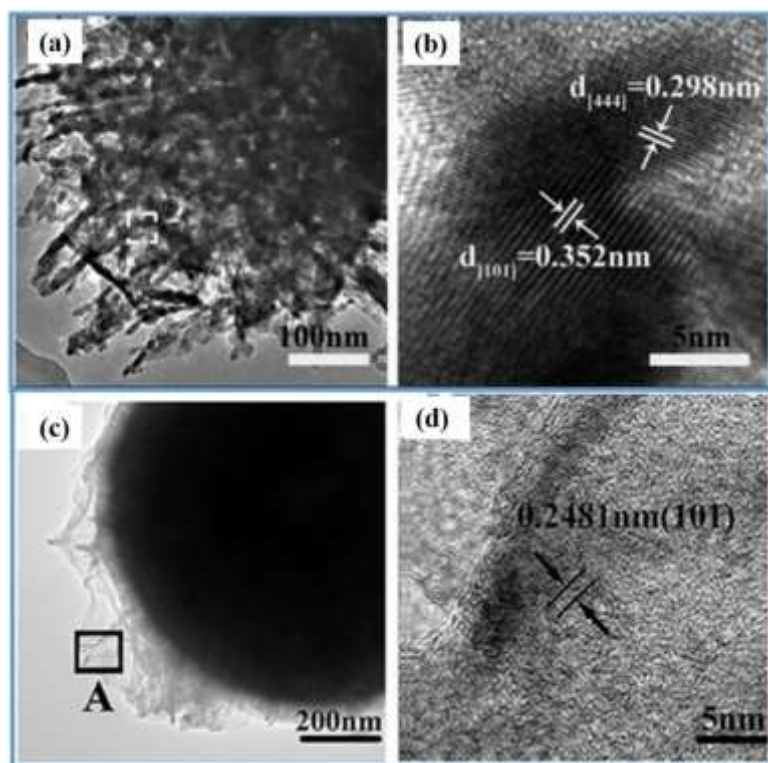
**Fig. 1.23:** (a) TEM and (b) HRTEM images of the vertically aligned $Bi_2Ti_2O_7$-$TiO_2$ composite nanowire arrays [94] prepared by the solvothermal method, (c) TEM and (d) HRTEM images of flower-like NiCoP/ZnO nanocomposite prepared by the hydrothermal method [95].

### 1.4.2.6 Sonochemical synthesis

Sonochemistry is one of the earliest known methods for the synthesis of nanocomposites [13]. In sonochemical synthesis, molecules undergo chemical reaction in the presence of ultrasound radiation (20 kHz-10 MHz). The main event that occurs in sonochemical synthesis is the formation, growth and destruction of the solvent bubbles in the liquid and this is known as acoustic cavitation. The bubbles formed are of nanometer size. During the synthesis, the solute vapour diffuses into the solvent bubbles and when the size of the bubbles increases beyond a certain size they get destroyed. During the destruction of bubbles, very high temperature (e.g. 5000 K) is aquired, which is sufficient for breaking of the chemical bonds in the solute [96]. Since, the destruction of bubble ocurs in less than a nanosecond, a high cooling rate (e.g. 1011 K/s) is obtained. Sonochemical synthesis products are amorphous because the breaking of bonds takes place in gaseous medium and also high cooling rate prevents crystallization of the products [91]. Fig. 1.24(a) shows a schematic presentation of sonochemical preparation of the GO-$Mn_3O_4$ composite. Figs. 1.24(b), (c) and (d) show TEM and HRTEM images of GO-$Mn_3O_4$ nanocomposite [96].
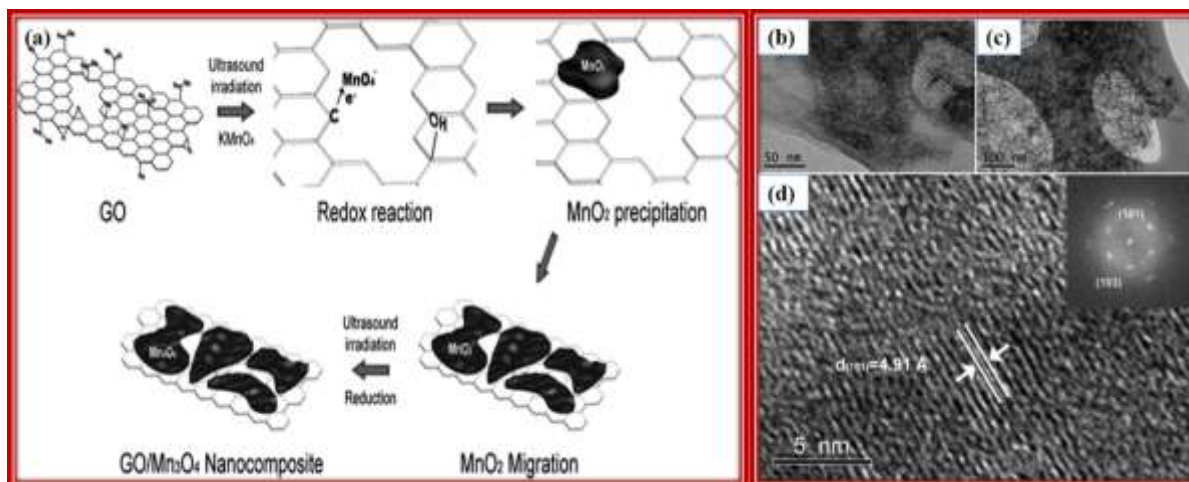
**Fig. 1.24:** (a) Schematic representation of sonochemical synthesis of GO–$Mn_3O_4$ composite, (b) and (c) TEM and (d) HRTEM image of GO–$Mn_3O_4$ nanocomposite and its SAED pattern [96].

## 1.5 Properties of nanocomposites

### 1.5.1 Mechanical properties

The interesting mechanical properties of nanocomposites are hardness and fracture toughness. These properties depend on nature of the matrix and reinforcement and their interaction at the interface throughout the material [34]. Fig. 1.25(a) shows a table with values of tensile strength, flexural strength and impact strength of pure 1,4-bis (4-amine-phenoxy) sulphone benzene epoxy resin (TGBAPSB) and TGBAPSB epoxy resin reinforced with different weight percentages (1-5 wt%) of functionalized alumina (F-nAl) nanoparticles [97]. A significant enhancement in tensile strength, flexural strength, impact strength (Fig. 1.25(b)) and storage modulus (Fig. 1.25(c)) was observed when F-nAl was introduced into the epoxy matrix. In the case of F-nAl (5 wt%) reinforced nanocomposite, the mechanical properties were found to be decreased compared to the other nanocomposites (1-3%). This is attributed to irregular dispersion of alumina nanoparticles within the epoxy matrix [97].

| (a) System | TGBAPSB/%F-nAl | Tensile Strength (MPa) | Flexural strength (MPa) | Impact strength (J/m) |
|---|---|---|---|---|
| a | 100/0 | 84.3±5 | 170.3±1 | 197.4±3 |
| b | 100/1 | 104.5±2 | 191.4±3 | 218.3±1 |
| c | 100/3 | 124.5±3 | 212.5±1 | 238.4±2 |
| d | 100/5 | 106.4±2 | 189.5±1 | 216.3±3 |
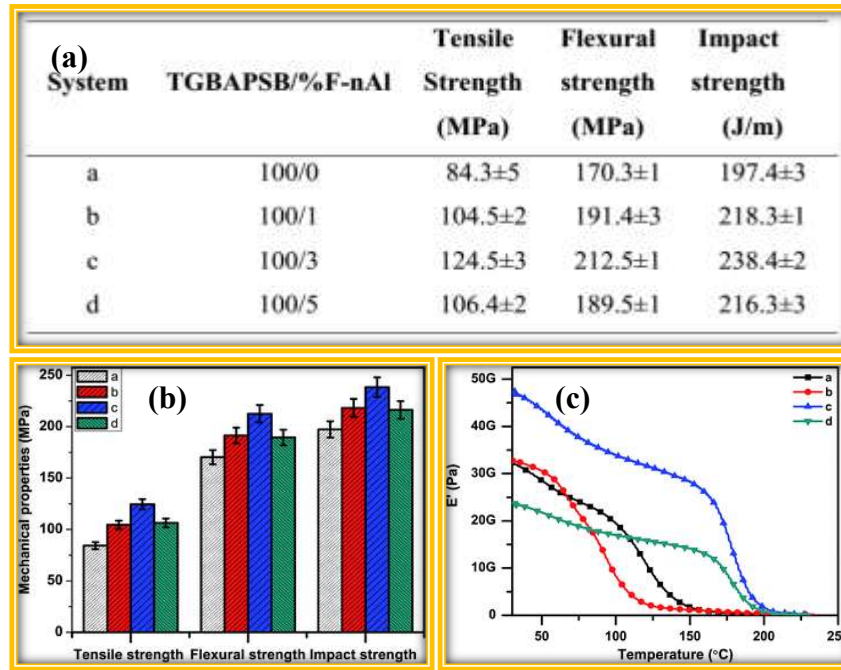
**Fig. 1.25:** (a) Table with values of tensile strength, flexural strength and impact strength, (b) histogram and (c) plot showing increase in the mechanical properties of F-nAl epoxy nanocomposites in comparision with pure TGBAPSB [97].

## 1.5.2 Optical properties

Nanocomposites are widely used as optically interesting materials. Reinforcement of semiconductors in different matrix materials such as polymer, ceramic or another semiconductor improve many of their optical properties including, absorption, flourescence, luminescence and non-linearity [68,69]. The optical properties of nanocomposites can be influenced by varying the particle size of constituents and the interaction at their interface. If particle size of a semiconductor is below the Bohr radius of both the holes and electrons, strong quantum confinement will occur. The quantum confinement will lead to breaking of continuous energy levels into discrete energy levels. The band gap and the spacing between these energy levels increases with decrease in the particle size of the semiconductor. Thus, the optical absorption peak shifts towards higher energies as the particle size decreases [100]. Fig. 1.26(a) shows schematic presentation of energy bands of a bulk semiconductor showing the continuity of conduction and valence bands separated by a bandgap, $E_g$. For quantum dots, the continuity of energy bands is broken into discrete atomic like energy levels whose energy is determined by size of the quantum dot [101]. Figs. 1.26(b) and (c) show visual images of CdSe quantum dots excited by a broadband UV lamp and UV-visible absorption (black) and PL emission (red) spectra of CdSe quantum dots with different sizes, respectively [102].
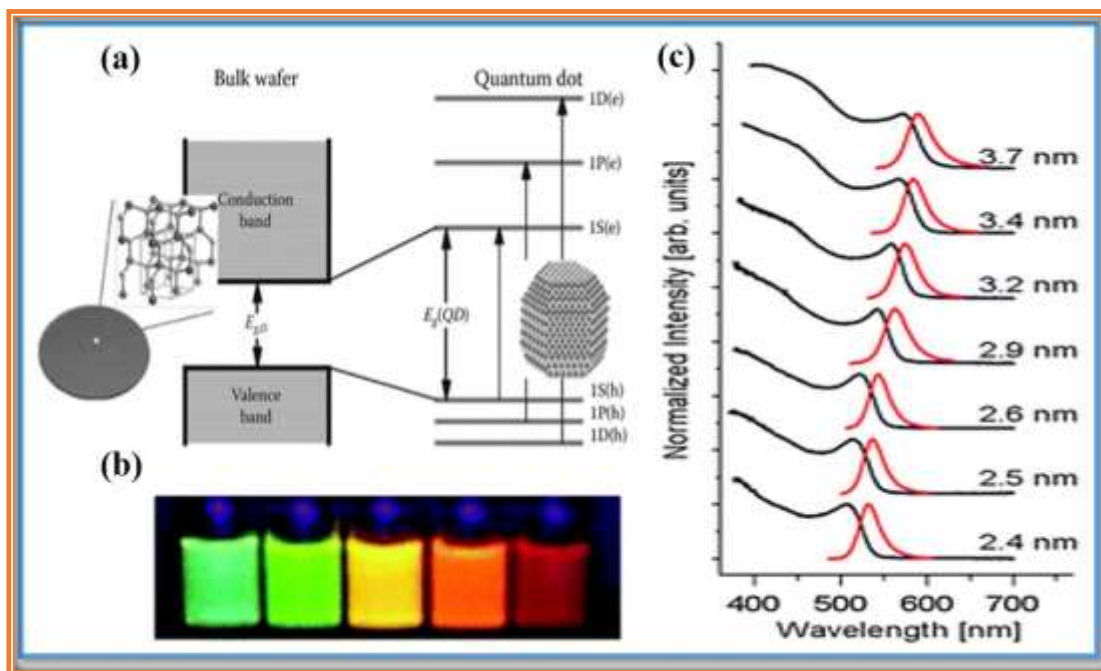
**Fig. 1.26:** (a) Energy bands of bulk semiconductor ($E_g$) and for a quantum dot (QD) [101], (b) visual images of samples excited by a broadband UV lamp and (c) UV-visible absorption (black) and PL emission (red) spectra (excitation at 350 nm) of CdSe quantum dots with different sizes [102].

Optically interesting nanocomposites are usually prepared by combining optically functional materials with processable transparent matrix materials, for example, hierarchical CdS/ZnO nanocomposites as shown in Fig. 1.27 [103]. Pure CdS nanoparticles have absorption in the visible region whereas ZnO have absorption in the UV region. It is clearly seen in Fig. 1.27(b) that the hierarchical CdS/ZnO (CZ) nanocomposites show enhanced visible light absorption compared to pure CdS and ZnO in the range 250–750 nm. Figs. 1.27(c) and (d) show the PL spectra for hierarchical CdS/ZnO nanocomposite with excitation wavelengths of 420 nm and 320 nm, respectively [103]. The luminescence intensity of CdS/ZnO nanocomposite is lower than that of pure CdS and ZnO. The enhancement in visible light absorption and decrease in the luminescence intensity of hierarchical CdS/ZnO nanocomposites is attributed to sensitization of the ZnO nanorods by CdS [100,103].
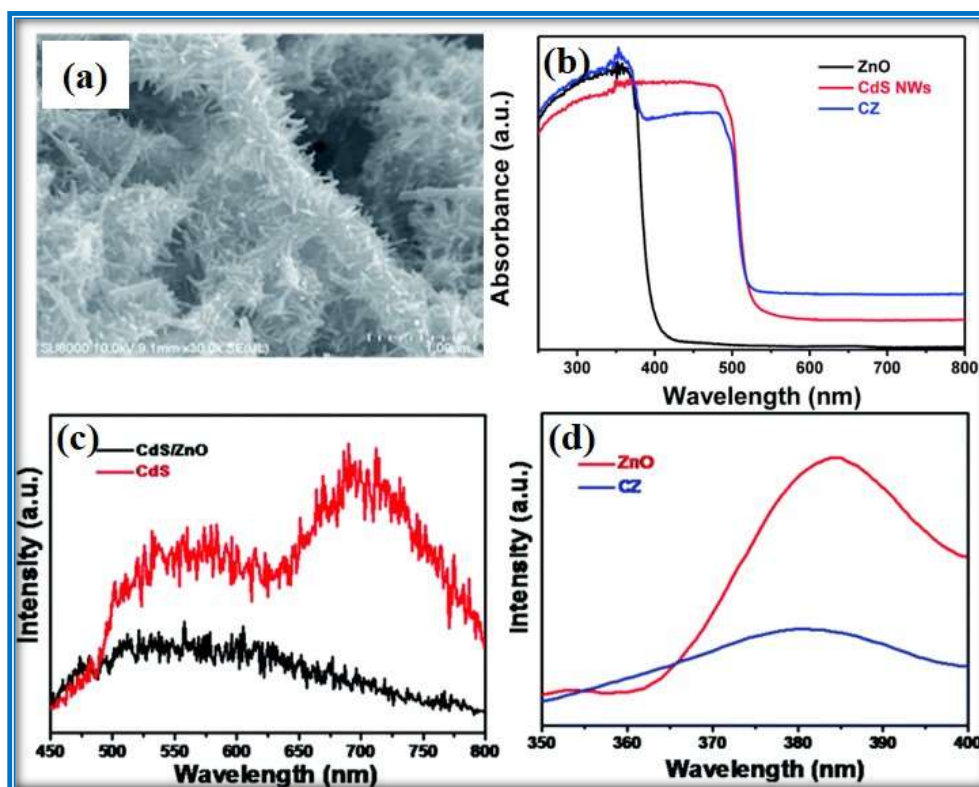
**Fig. 1.27:** (a) SEM image and (b) UV-visible absorption spectra of CdS/ZnO nanocomposites and photoluminescence (PL) spectra of the CdS/ZnO nanocomposites with an excitation wavelength of (c) 420 nm, and (d) 320 nm, respectively [103].

The optical properties of nanocomposites depend on electron transfer from one semiconductor to an other depending on their band edge positions. Based on the band edge positions, nanocomposites are broadly classified into three types, as demonstrated in Fig. 1.28 [104]. In type I, the band edge positions of semiconductors 1 and 2 are such that all the excited electrons and holes are transferred from semiconductor 1 to 2. This type of nanocomposites are not photocatalytically useful due to accumulation of elctrons and holes on a single semiconductor, e.g. CdTe/ZnSe [105]. In type II nanocomposites, the band edge positions of semiconductors 1 and 2 are such that the conduction band of semiconductor 1 is lower than that of semiconductor 2 and the valence band of semiconductor 1 is higher than that of semiconductor 2. Thus, the excited electrons can easily move from conduction band of semiconductor 1 to semiconductor 2 and holes can move from valence band of semiconductor 2 to 1. This will decrease the recombination tendency leading to efficient charge separation. Thus, the charge carriers will have longer life-time which results in higher phototocatalytic activity.
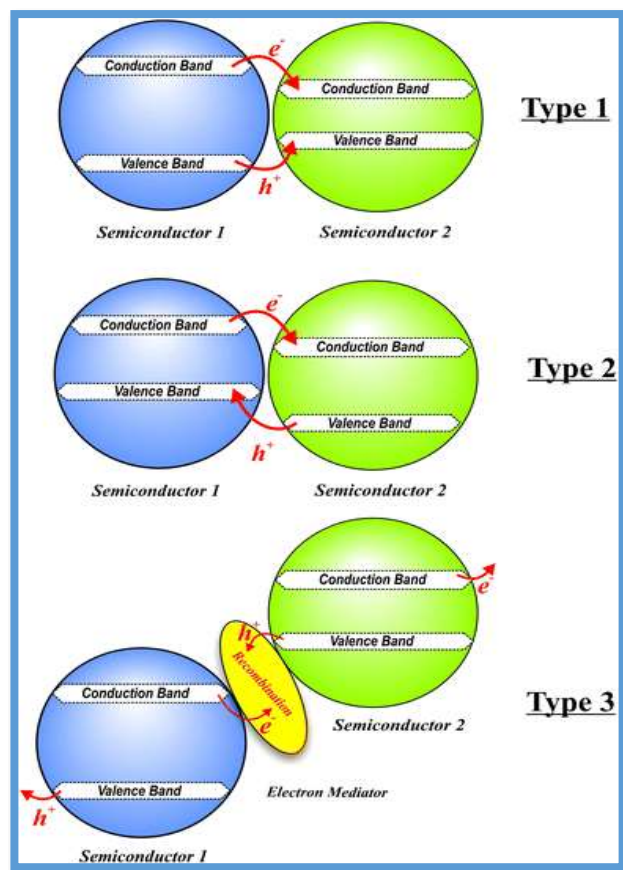
**Fig. 1.28:** Different kinds of nanocomposites heterojunctions [104].

In type III nanocomposites, both the valence and conduction bands of semiconductor 1 are lower than the valence band and conduction bands of semiconductor 2, as shown in Fig. 1.28. Such combination of semiconductors are used in Z scheme systems where there is an electron mediator or some type of link that connects the two semiconductors. For example, Jiang et al. have synthesized $In_2S_3/MoS_2/CdS$ heterostructured nanocomposites (Fig. 1.29) and $MoS_2$ acts as the charge-carrier link between $In_2S_3$ and CdS [106].
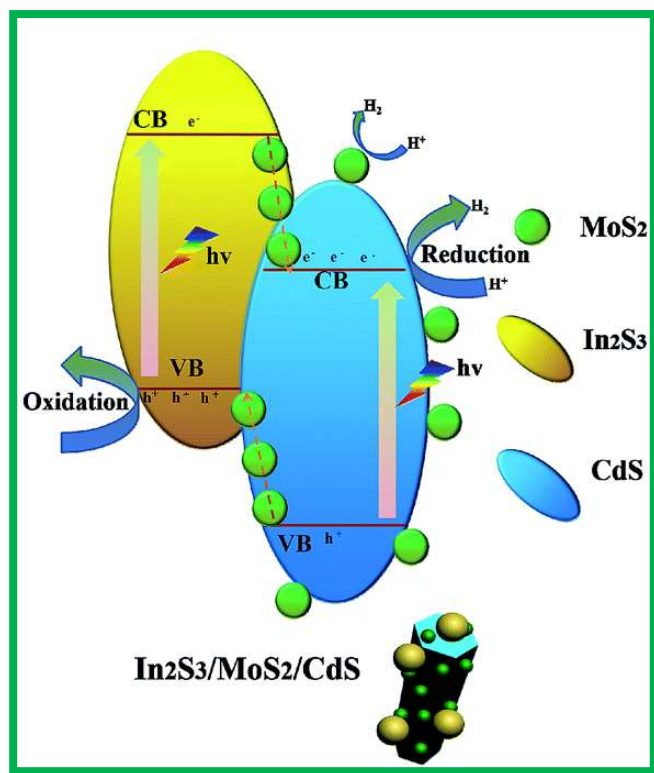
**Fig. 1.29:** Schematic representation of the charge transfer and separation in $In_2S_3/MoS_2/CdS$ heterostructures under visible light [106].

## 1.5.3 Electrical properties

The incorporation of metal nanoparticles, CNT, graphene and conductive polymers in non conducting matix materials lead to nanocomposites with enhanced electrical conducting properties [107–109]. Some of the nanocomposites reported with enhanced electrical properties are ZnO-graphene oxide [110], and graphene/polyurethane nanocomposites [111]. Wang et al. have reported an enhancement of electrical conductivity of Au–LaNiO$_3$ nanocomposite film as compared to LNO film [112]. The resistivity of Au–LNO film was 313 $\mu\Omega$ cm which was much lower than that of the LNO film (1221 $\mu\Omega$ cm). Fig. 1.30(a) and Fig. 1.30(b) show the cross-sectional HAADF and HRTEM images for the Au–LNO nanocomposite film, respectively. Fig. 1.30(c) shows the plot of variation of electrical resestivity with temperature for LNO and Au-LNO nanocomposite thin films. Both the films exhibit metallic behaviour at high temperature.
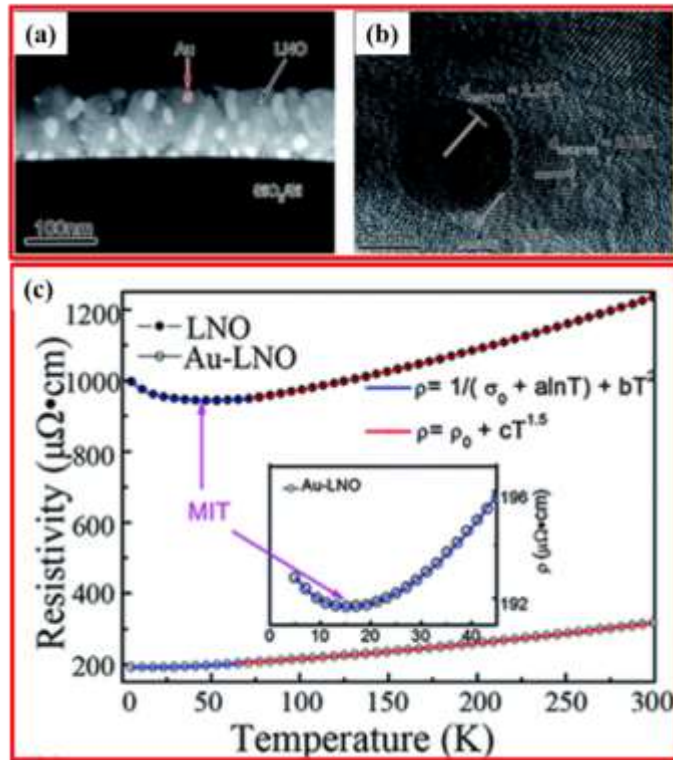
**Fig. 1.30:** (a) Cross-sectional HAADF image, (b) HRTEM image and (c) temperature dependence of resistivity of the Au–LNO nanocomposite thin film [112].

### 1.5.4 Magnetic properties

The magnetic properties of nanoparticles are different than that of bulk materials and the properties depend on their size, shape and composition. Bulk materials exhibiting ferro or ferri magnetic nature contain several magnetic domains. However, nanoparticles having size comparable to the thickness of a domain consist of a single domain. When the single domain particles become much smaller, they show superparamagnetism [113]. Nanoparticles showing superparamagnetism are easily magnetized as paramagnets under the influence of an external magnetic field but they have much higher magnetic susceptibility compared to the paramagnets [88].

Nowadays, magnetic nanocomposites have been explored because of their potential applications in many areas such as biology, medicine, data storage, parmanent magnet, etc. Nanocomposites are magnetic when magnetic species are dispersed in magnetic or nonmagnetic matrix materials. Magnetic nanocomposites having both the components as magnetic are important because they have higher remanance magnetization and large energy product in comparison to typical magnetic materials [19]. The coercivity of nanocomposites also increases with the particle size when the particle size is below the critical domain size.

Howerever, it starts decreasing with the particle size when the particle size is more than critical domain size [20,84,85]. The saturation magnetization and blocking temperature of the nanocomposites depend on the composition and particle size of the magnetic species [113,115,116]. The magnetic properties of nanocomposites are determined by hysteresis loops (M–H) and zero-field cooled/field cooled (ZFC/FC, M–T) curves. As shown in Fig. 1.31(a), the saturation magnetization ($M_S$), remanence magnetization ($M_r$), and coercivity ($H_c$) can be obtained from the hysteresis loop [117]. The variation of magnetization of cobalt-iron oxide nanocomposites with field is shown in Fig. 1.31(b) [116].
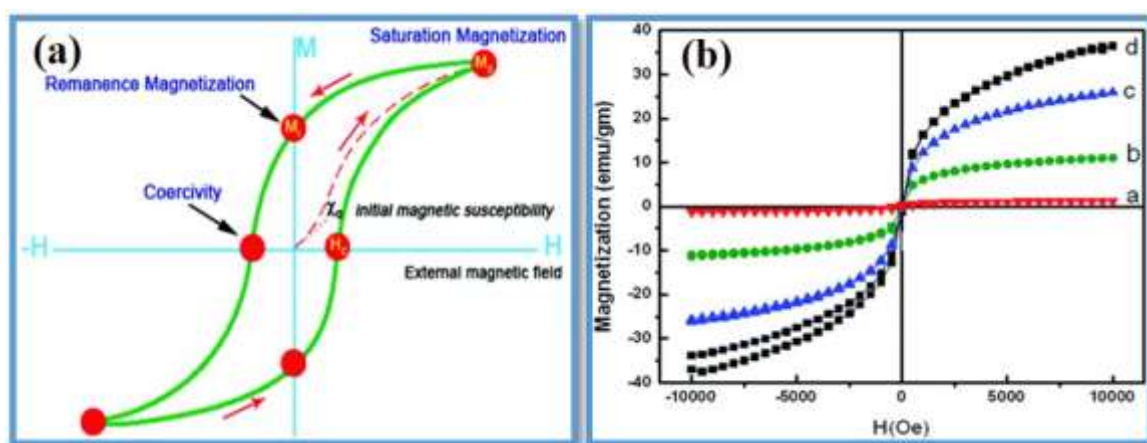


**Fig. 1.31:** (a) Schematic representation of the typical hysteresis loops of magnetic metal oxide nanoparticles [117] and (b) M-H curves of cobalt iron oxide nanocomposites with different Co/Fe ratios ((a) 0/1, (b) 1/2, (c) 1/1 and (d) 2/1) [116].

Nanocomposites not only provide an improved stability to magnetic nanoparticulates, but also introduce new physical properties and multi-functional behaviour. Some of the well studied magnetic nanocomposites are $Fe_2O_3$-$TiO_2$ [118], $Fe_2O_3$-$CuO$ [119], $Co_3O_4$/$ZnFe_2O_4$ [120], $ZnO$/$Co_3O_4$ [121], $Fe_3O_4$@$MnO_2$@$Pt$ [122], $Fe_3O_4$-$SiO_2$ [123], $CuO$@$Fe_3O_4$ [124], etc. As shown in Fig. 1.32(a-c), Si et al. have synthesized magnetic silica nanofibrous membranes (SNF) with multifunctional properties such as magnetic responsiveness, dye adsorption, and emulsion separation [125]. Introduction of $NiFe_2O_4$ NPs into pristine SNF create a hierarchical porous structure with increased porosity and surface area. In the adsorption-desorption isotherm, the $NiFe_2O_4$@SNF nanocomposite shows H1 hysteresis in the $P/P_0$ region of 0.5–0.9, indicating its mesoporous nature (Fig.1.32(d)). Fig. 1.32(e) shows M-H curve for $NiFe_2O_4$@SNF nanocomposite with saturation magnetiztion of 13.7 emu $g^{-1}$ which is less than that of pure $NiFe_2O_4$ (50 emu $g^{-1}$).
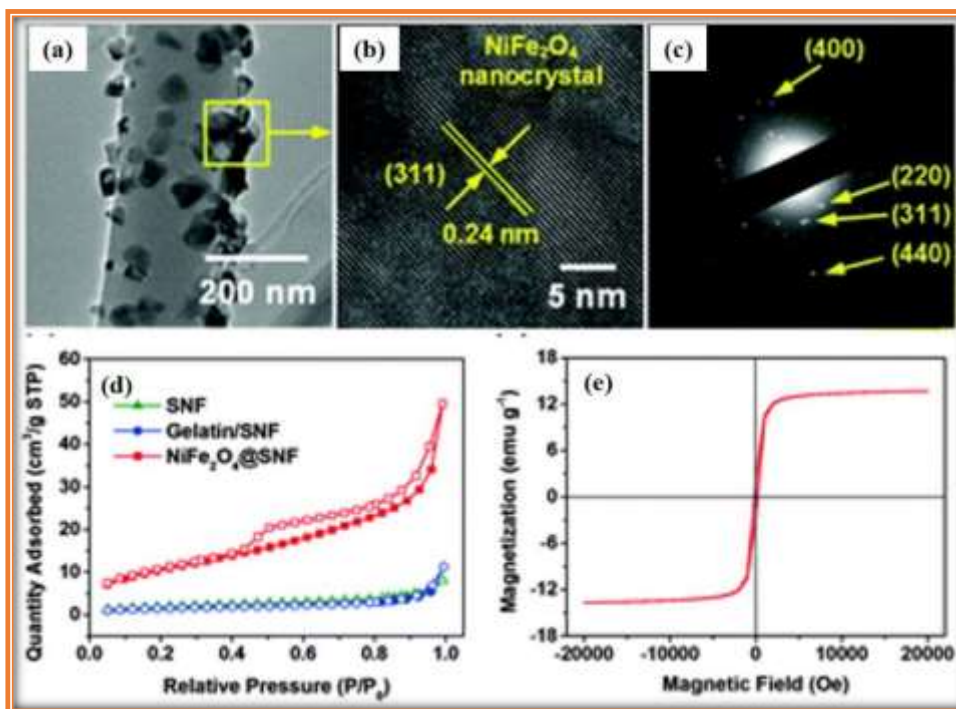
**Fig. 1.32:** (a) TEM image, (b) HRTEM image and (c) SAED pattern of $NiFe_2O_4$@silica nanofibers (SNF), (d) $N_2$ adsorption–desorption isotherms of SNF, gelatin/SNF, and $NiFe_2O_4$@SNF and (e) magnetic hysteresis of $NiFe_2O_4$@SNF measured at 300 K [125].

## 1.6 Applications of nanocomposites

### 1.6.1 Electrochemical application

Nowadays, due to an increase in consumption of energy there is increasing need for harnessing pollution free renewable sources, their proper storage and distribution. Significant amount of research has been carried out on development of materials for energy storage applications [126]. Rechargable lithium-ion batteries are frequently used in energy storage and energy conversion devices [127,128]. Nanocomposites offer great potential in the development of lithium-ion batteries (LIBs) [126]. Some of the nanocomposites reported as anode materials for lithium-ion batteries are $\alpha$-$Fe_2O_3$-$SnO_2$ [129], $Co_3O_4$/$Fe_2O_3$ [130], graphene/Ir [131], graphene/Au [132], etc. Fig. 1.33 shows the FE-SEM image (a), HRTEM images (b) and (c), and the electrochemical measurements (d) and (e), performed for $CoO$/$CoFe_2O_4$ nanocomposite ($CoO$/$CoFe_2O_4$ molar ratio 5:1 and the control materials (A = $CoO$, B = physical mixture 5$CoO$/$CoFe_2O_4$, C = $CoFe_2O_4$) [133]. The first charge specific capacities for 5$CoO$/$CoFe_2O_4$ nanocomposite, $CoO$, $CoFe_2O_4$ and physical mixture are 844, 475, 1200, 679 mA h g$^{-1}$ at a current density of 100 mA g$^{-1}$, respectively (Fig. 1.33(d)). Also, an overlap

was identified only for 5CoO/CoFe$_2$O$_4$ through subsequent two discharge/charge cycles (Fig. 1.33(d)), indicating that the reversible capacity of 5CoO/CoFe$_2$O$_4$ is almost constant. After 30 cycles, the charge capacities of the control materials dropped to 132, 453, and 150 mA h g$^{-1}$ (Fig. 1.33(e), A, B, and C). In contrast, the charge capacity of 5CoO/CoFe$_2$O$_4$ remained constant at 735 mA h g$^{-1}$ (Fig. 1.33(e), D), a value indicative of highly enhanced capacity and cycle stability in comparison with the control materials.
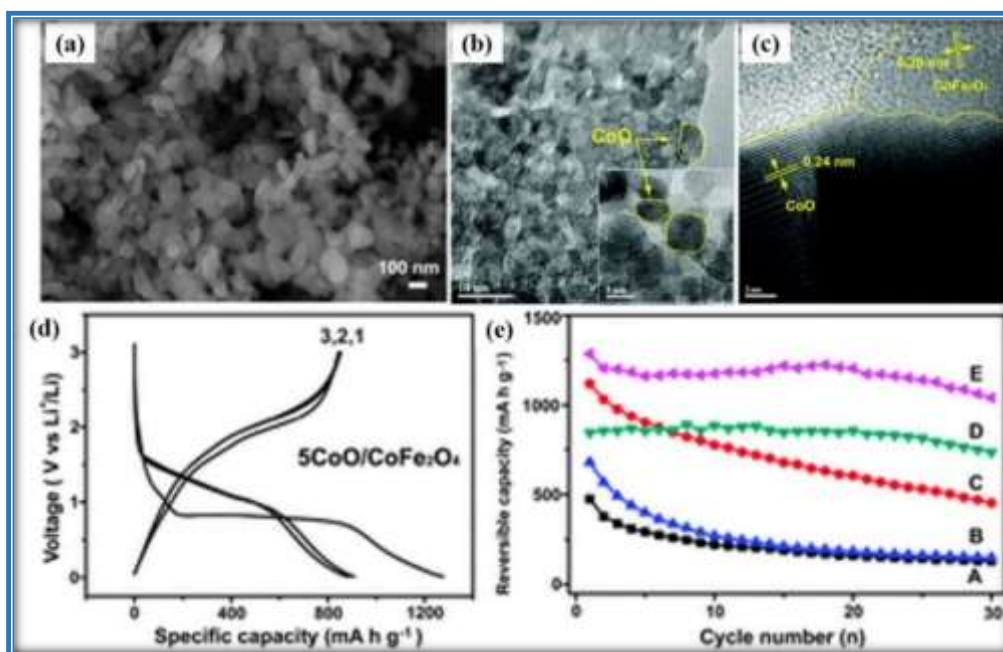


**Fig. 1.33:** (a) SEM image, (b) and (c) HRTEM images of 5CoO/CoFe$_2$O$_4$ nanocomposites, (d) first three charge–discharge profiles of 5CoO/CoFe$_2$O$_4$ cycled between 0.01–3.0 V under a current density of 100 mA g$^{-1}$ and (e) cycling behavior of A, B, C, D (5CoO/CoFe$_2$O$_4$) and E (3CoO/CoFe$_2$O$_4$) at a rate of 100 mA g$^{-1}$ [133].

### 1.6.2 Sensors

Electrochemical gas sensors are gas detectors which work on the principle that when some gas is oxided or reduced on an electrode, there is a change in the current across the electrodes. Gas detectors are important and useful for medical diagnosis, bioprocesses, beverage industry, and pharmaceutical analysis and for sensing potential industrial pollutants such as nitric oxide, ethane, and ammonia [134]. Semiconductor gas sensors are highly sensitive at the low ppm level. Nanocomposites have potential applications in gas sensing because of enhancement in sensors response and good reproducibility due to their high surface area [135]. Some of the nanocomposites employed for sensing applications are Cu@Cu$_2$O for glucose detection [136], CuO/Co$_3$O$_4$ for fructose sensing [137], WO$_3$-SnO$_2$ nanocomposites for ammonia detection

[138] and ZnO–SnO$_2$ for H$_2$ and CO detection [139]. The performance of Ag@iron oxide modified electrode for the detection of nitrate was tested by cyclic voltammetry measurements [140]. Fig. 1.34(a) shows the cylic voltammetry results for electrodes modified with Fe$_2$O$_3$, Ag nanoparticles and Ag@iron oxide in the presence of 20 mM NO$^{3-}$ ions. The Ag@iron oxide nanocomposite modified electrode shows a large peak current at lower negative potential (-0.75 V), in the presence of NO$^{3-}$ ions compared to the Fe$_2$O$_3$ modified electrode. A more prominent background current was observed for Ag@iron oxide than that for Fe$_2$O$_3$ modified electrode due to larger capacitance of double electric layer of the Ag@iron oxide nanocomposite. The electrocatalytic activity towards nitrate reduction using the Ag@iron oxide nanocomposite modified electrode is higher than that of Fe$_2$O$_3$ modified electrode. The mechanism for sensing of nitrate ions is shown in Fig. 1.34(b). The improved performance of the nanocomposite is due to enhanced adsorption of the analyte on the iron sites. The adsorbed nitrate species undergo further reduction by adjacent Ag nanoparticles [140].
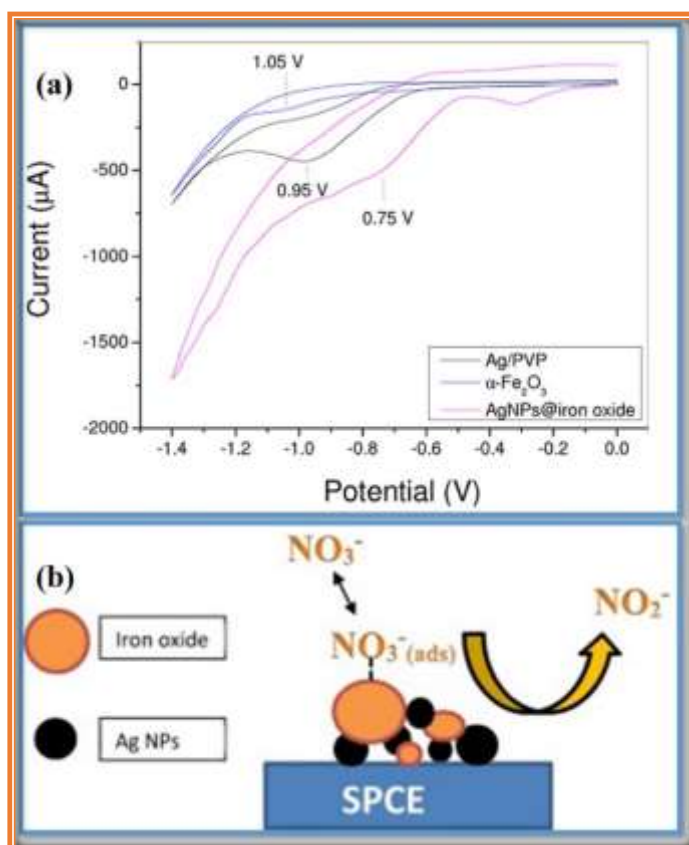


**Fig. 1.34:** (a) Cyclic voltammetry of modified electrodes in the presence of Fe$_2$O$_3$, Ag NPs and Ag@iron oxide nanocomposite in presence of 20 mM NO$^{3-}$ ions, and (b) schematic of the sensing mechanism on Ag@iron oxide nanocomposites [140].

### 1.6.3 Catalysis

The benefit of heterogeneous catalysts is that they are easily separated and they have excellent reusability. In general, catalysts based on nanocomposites consist of one or more catatytically active constituents and a functional support. The interaction of catalytically active constituents with the support can improve many properties of the composites including enhancement in catalytic activity, life time, selectivity for a specific product and chemical stability [141,142]. Nanocomposites show enhanced catalytic activity due to high surface area, high density of active sites and synergetic catalytic effect. The synergetic catalytic effect is described as cooperative interaction between different constituents and/or active sites of one contituents due to which there is enhancement in the catalytic activity of the nanocomposites in comparison with the respective individual constituents [141,143]. Some of the recently reported nanocomposites used in heterogeneous catalytic reactions are $CuO@Fe_3O_4$ for the degradation of 2,4-dichlorophenol [124], $Cu-SiO_2$ for production of methanol by hydrogenation of cyclic carbonates [144], chitosan-stabilised $Cu-Fe_3O_4$ for azide–alkyne cycloaddition reactions [145], $V_2O-WO_3$ for oxidation of aryl alcohols [146], $MgO-ZrO_2$ for cross aldol reactions [147], $Au-SiO_2$ for reduction of nitrophenols [148], etc. Xian-Long Du et al. have reported selective hydrogenation of carbon dioxide to methanol by using a simple $Cu-Al_2O_3$ as the heterogeneous catalyst [149]. Fig. 1.35(a) shows the HRTEM image of the nanocomposite and Fig. 1.35(b) shows the scheme for possible products formed on hydrogenation of methyl formates. It was found that $Cu/Al_2O_3$ nanocomposites with 20% loading of Cu act as better catalyst for the selective production of methanol from methyl formates. The table in Fig 1.35(c) lists the results on the synthesis of methanol from different formate esters in the presence of $Cu/Al_2O_3$ nanocomposite with 20% Cu loading as the catalyst. For example, ethyl, propyl, and butyl formates were selectively hydrogenated to methanol, and the corresponding alcohols were obtained in high yield.
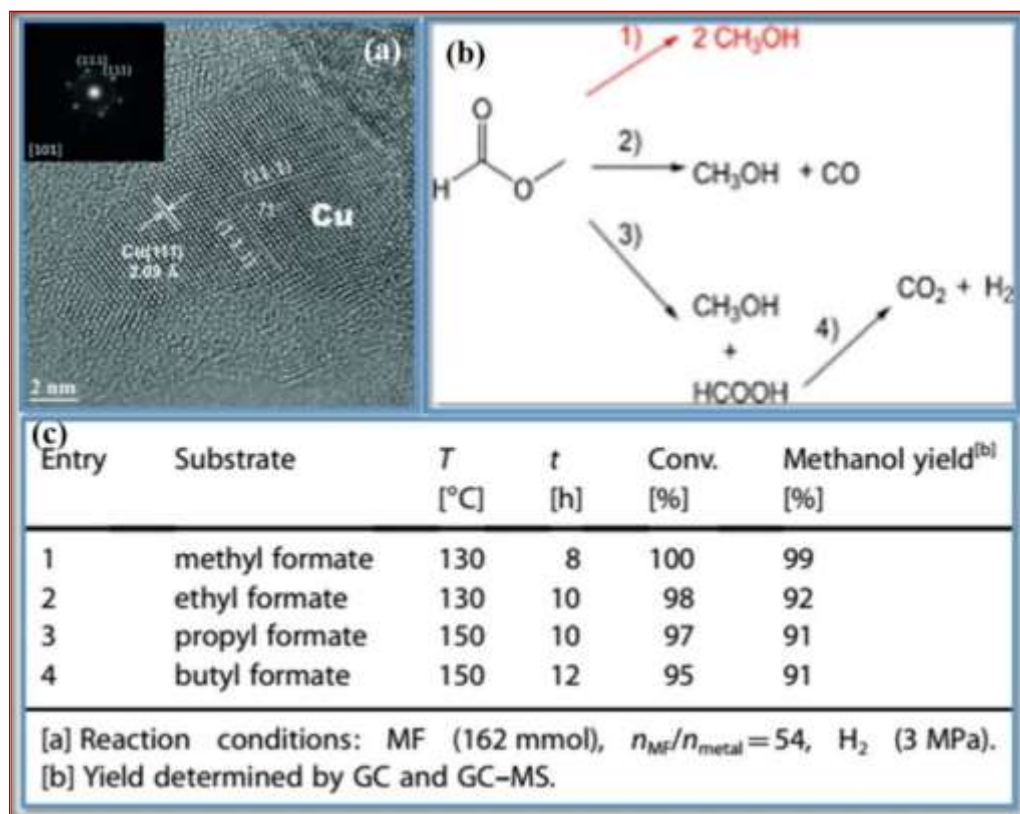
**Fig. 1.35:** (a) HRTEM image of Cu/Al$_2$O$_3$ nanocomposite, (b) simple pathways for the hydrogenation of methyl formate and (c) results on the selective hydrogenation of various formate esters into methanol over fresh 20-Cu/Al$_2$O$_3$ nanocomposite as the catalyst [149].

### 1.6.4 Photocatalysis

The basic requirement for photocatalysis is the fabrication of efficient photocatalysts which must fulfill several conditions such as wide range of solar absorption, effective charge separation and high chemical and photochemical stability [104]. The combination of appropriate semiconductors can produce composites with enhanced light absorption, effective charge separation and improved photostability. These properties of the nanocomposites are due to effective band gap arrangements of the constituents and the synergestic interactions at their interface. Electrons-holes pairs are produced in semiconductors on light irradiation which could be used for carrying out photocatalytic oxidation or reduction [99]. Photocatalytic reactions are widely used in green chemistry, e.g. for the (i) photodegradation of various pollutants (organic dyes, phenol, etc.) and (ii) splitting of water. They are briefly described below.

**1.6.4.1 Photodegradation of organic dyes**

Some of the recent nanocomposites reported as phtocatalysts for the photodegradation of organic dyes are $Cu_2O$-$TiO_2$ [150], CuS-ZnS [151], CdS-ZnO [152], $MoS_2$-$TiO_2$ [153], ZnO–$FeWO_4$ [84], ZnO/$Fe_2O_3$/$MnO_2$ [154], polyvinyl acetate/$TiO_2$ [155], ZnS-CdS-$TiO_2$ [156], CdS-ZnS [157], etc. Fig. 1.36(a) shows the degradation rate of rhodamine B (RhB) under solar light irradiation in the presence of pure ZnO, CdS and ZnO/CdS heterostructures [152]. The enhancement of photocatalytic activity of the ZnO/CdS hierarchical heterostructures is attributed to the coupling of ZnO and CdS nanoparticles. As shown in the schematic representation (Fig. 1.36(b)), the band position of CdS and ZnO has a type-II structure. The type II band arrangement can effectivley separate electron–hole pairs that are photogenerated at the ZnO/CdS interface and inhibits their recombination. When the ZnO/CdS photocatalyst is illuminated in the presence of sunlight, the photogenerated electrons are transfered from the conduction band of photoexcited CdS to that of ZnO [158]. In this way, better charge separation is achieved. Meanwhile, the photogenerated holes transfer from valence band (VB) of ZnO to that of CdS. Thus a high concentration of holes in the VB of the CdS nanoparticles is obtained. Holes in the valence band of CdS react with $OH^-$ adsorbed on the surface of the CdS nanoparticles to form highly reactive hydroxyl radicals ($OH^{\bullet}$). The CB electrons ($e^-$) concentrated on the surface of ZnO interact with dissolved oxygen molecules in water to yield oxidative species such as superoxide radical anion ($O_2^{\bullet-}$) and hydroxyl radical ($OH^{\bullet}$) which help in the decomposition of organic pollutants effectively.
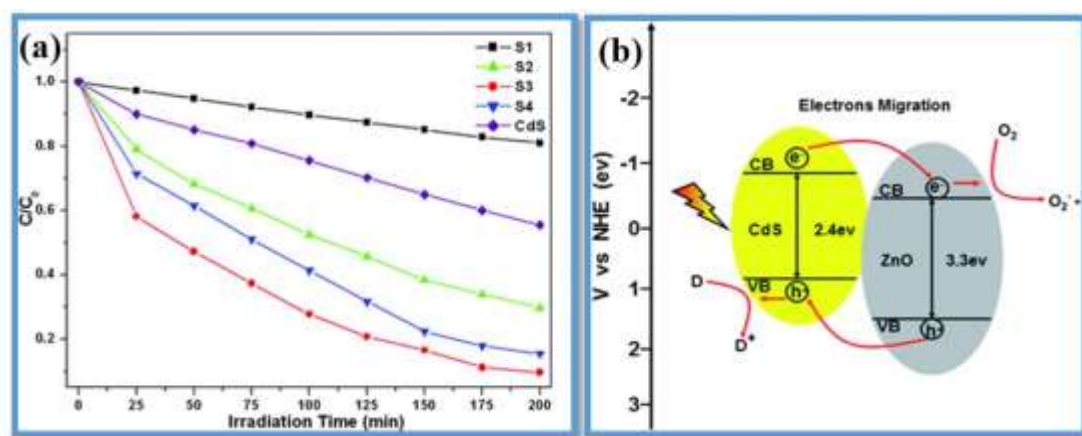


**Fig. 1.36:** (a) The degradation rate of rhodamine B under solar radiation in the presence of pure ZnO, CdS and ZnO/CdS hierarchical heterostructures and (b) schematic illustration of the energy band structure and electron–hole pair separation in ZnO/CdS hierarchical heterostructures [152].

## 1.6.4.2 Water splitting

Production of hydrogen by water splitting in the presence of sunlight has enormous energy and environmental applications. Photoinduced water splitting in the presence of sunlight involves three steps. In the first step, the photocatalyst absorbs sunlight and produces excited electrons and holes. In the second step, these excited electrons and holes come to the photocatalyst surface. Finally, on the surface of the photocatalyst, the holes oxidize water to $O_2$ and the electrons reduce protons to $H_2$. Fig. 1.37 illustrates the three main steps in water splitting [104].
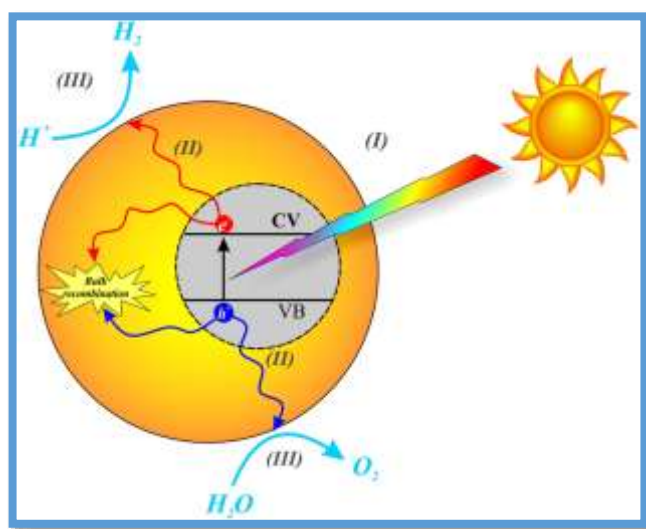


**Fig. 1.37:** Fundamental mechanism of photocatalytic water splitting [104].

Some of the reported nanocomposites exhibiting water splitting activity are $NiO/TiO_2$ [159], $TiO_2$-$Fe_2O_3$ [160], $CaMn_4O_5$-lactate [161], $CdS$-$TiO_2$ [162], $Au@r$-$GO/TiO_2$ [163], $M-Au/TiO_2$ (M = Ag, Pd and Pt) [164], etc. Fig. 1.38(a) shows the TEM and HRTEM images of $Fe_2O_3$-$TiO_2$ nanocomposite [165]. Fig. 1.38(b) shows a schematic for charge transfer and separation in $\alpha$-$Fe_2O_3$-$TiO_2$ nanocomposite. The photogenerated electrons will be excited from VB of $\alpha$-$Fe_2O_3$ to its CB under visible light irradiation. Further, these photoexcited electrons transfer to the CB of rutile $TiO_2$ leading to effective charge separation. The photocurrent density of $\alpha$-$Fe_2O_3$ under visible irradiation gradually increases with increase in the amount of $TiO_2$. The nanocomposite with 20 wt% of $TiO_2$ shows the largest photocurrent density as 0.3 mA/cm$^2$ at 0.4 V vs Ag/AgCl, over 10-fold enhancement compared to $\alpha$-$Fe_2O_3$. If the amount of coupled $TiO_2$ is increased further, the photocurrent density of $\alpha$-$Fe_2O_3$-$TiO_2$ nanocomposite begins to decrease. According to the inset of Fig. 1.38(c), a large photocurrent density corresponds to large detector response for produced $O_2$ in the photoelectrochemical water splitting.
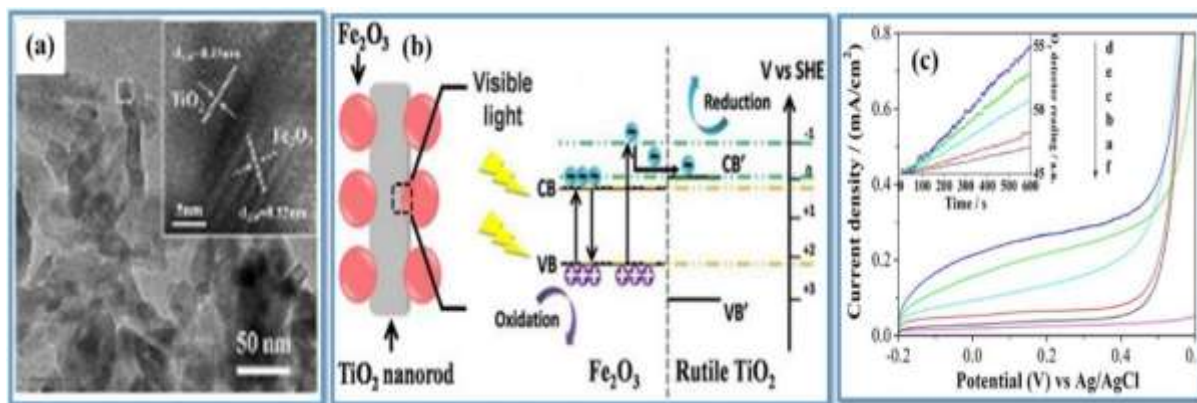
**Fig. 1.38:** (a) TEM image of $\alpha$-$Fe_2O_3$-$TiO_2$ nanocomposite with its HRTEM image (inset), (b) schematic of transfer and separation of visible light excited electrons in the $TiO_2$-$Fe_2O_3$ nanocomposite, and (c) I-V curves in 1 M NaOH (pH = 13.6) under visible light irradiation [165].

## 1.6.5 Photovoltaic cell

Nowadays, quantum dot-sensitized solar cells (QDSSCs) are widely studied because of their exceptional optical and electronic properties such as tunable band gap, multiple excitons generation leading to better energy conversion and enhanced extinction coefficient [166]. Some of the nanocomposite based sensitizers for quantum dot solar cells with visible-light absorption are $SnO_2$-$TiO_2$ [167], CdS-$TiO_2$ [166], graphene-PbS [168], ZnO-Ag [169], CuS-ZnS [170], $CuInS_2$-ZnO [171], CdTe-$TiO_2$ [172], etc.

Fig. 1.39(a) shows the current–voltage characterisitic curves for CdS and CuS/CdS sensitized solar cells. There is an increase in the overall power conversion efficiency from 2.82% to 3.60% due to a large increase in current density ($J_{sc}$), when CuS/CdS composite sensitized electrode was used instead of CdS. From the measurements of IPCE (incident photon-to-current efficiency) it was concluded that the CuS/CdS composite has more sensitization efficiency in the visible region due to generation of more photocurrent compared to pure CdS.
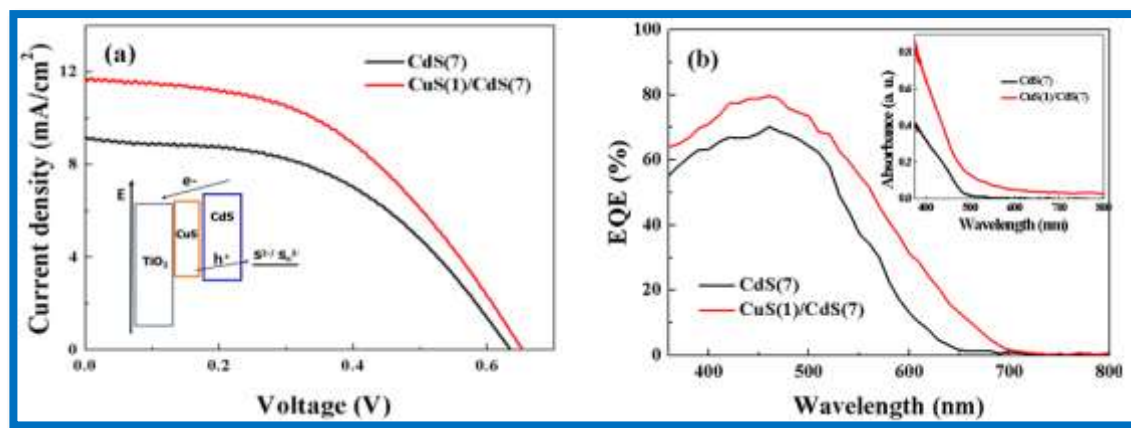
**Fig. 1.39:** (a) J−V curves and (b) IPCE data from CdS and CuS/CdS sensitized cells. A schematic representation of charge transfer at the interface is shown in inset [170].

### 1.6.6 Biological applications

For biological applications, nanocomposites are widely studied group of nanomaterials. Because of their characteristic properties such as tunable optical, electronic and magnetic properties, nanocomposites are of great interest [173,174]. Some of the nancomposites recently reported for biological applications are $SiO_2$-$TiO_2$ for selective improvement of phosphopeptides [175], Ag-GO for antibacterial activity [176], Ag-GaN for biosensing [177,178], $CeO_2$-$TiO_2$ for peroxidase-like activity [179], $Fe_3O_4$-$SiO_2$ for drug delivery [180], ZnSe/Au for bioimaging [181], etc. Mi et al. have reported biolabeling and fluorescent imaging of cancer cells (HeLa cells) using $Fe_3O_4$/$NaYF_4$ nanocomposite [182]. Fig. 1.40(a) shows a schematic representation of biolabelling of HeLa cells with $Fe_3O_4$/$NaYF_4$ nanocomposites using EDC/NHS (N-Ethyl-N-[3(dimethylamino)propyl] carbodiimide hydrochloride (EDC) and N-hydroxysuccinimide (NHS)) coupling chemistry. The cells which are incubated with $Fe_3O_4$/$NaYF_4$ nanocomposite labelled transferrin show strong green emission under 980 nm excitation, which means that if the nanocomposite is labeled with transferrin it is active and can recognize the receptors on the HeLa cells. $Fe_3O_4$/$NaYF_4$ nanocomposite moves inside the cells due to the transferrin-transferrin receptor interaction on the cell surface. The cell surface does not show green emission under 980 nm excitation in control experiments when treated with $Fe_3O_4$/$NaYF_4$ nanocomposites without in conjugation with transferrin (Fig. 1.40(c)). This means that transferrin conjugation is required for the HeLa cells recognition. As shown in Fig. 1.40(d), the HeLa cells without being incubated with any nanoparticles do not show any fluorescence which proves the benefit of using near infrared active nanocomposites for fluorescent imaging of biological samples.
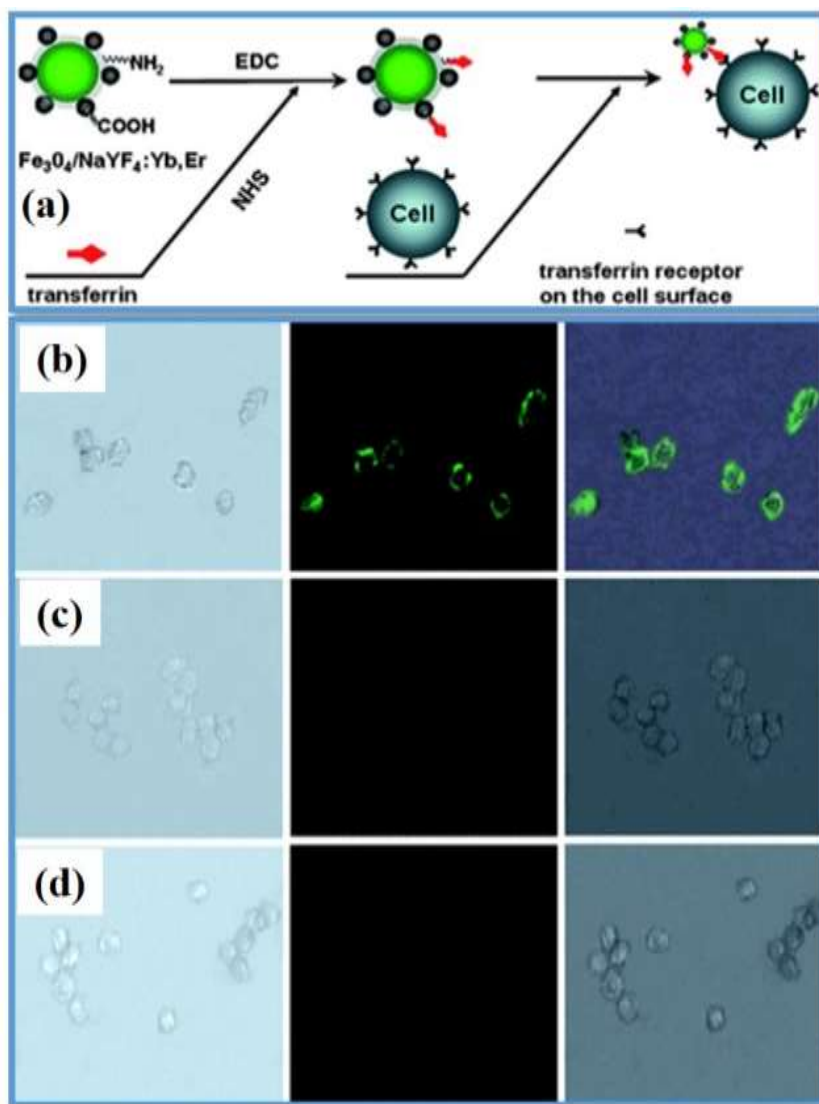
**Fig. 1.40:** (a) Schematic representation of biolabelling of HeLa cells with $Fe_3O_4/NaYF_4$ nanocomposites using EDC/NHS coupling chemistry and images of live HeLa cells after being incubated with $Fe_3O_4/NaYF_4$ nanocomposites biolabeled with transferrin (b), after being incubated with $Fe_3O_4/NaYF_4$ nanocomposites without transferrin conjugation (c), and without incubating with any nanoparticles (d) [182]. The left rows are bright field images, the central rows show fluorescent images in dark field and the right rows are the overlays of the left and central rows.

### 1.6.7 Multifunctional applications

Nowadays, fabrication of multifunctional nanocomposites are of great interest due to their diverse applications including catalysis, medicine, chemical sensors and adsorption [183]. Some of the recent nanocomposites reported having multifunctional applications are $Fe_3O_4$@C–Au [184], $Fe_3O_4$@$Ag_2Se$ [185], Fe-Au core-shell nanoparticles [186], etc. Shi et al. have reported multifunctional $Fe_3O_4$/$YVO_4$:$Eu^{3+}$@$SiO_2$ nanocomposites with mesoporous, magnetic and fluorescent properties [187]. Fig. 1.41(a) and (b) show the TEM images of multifunctional $Fe_3O_4$/$YVO_4$:$Eu^{3+}$@$SiO_2$ nanocomposites. Fig. 1.41(c), (d) and (e) show the adsorption, magnetic and luminescence properties of $Fe_3O_4$/$YVO_4$:$Eu^{3+}$@$SiO_2$ nanocomposite.
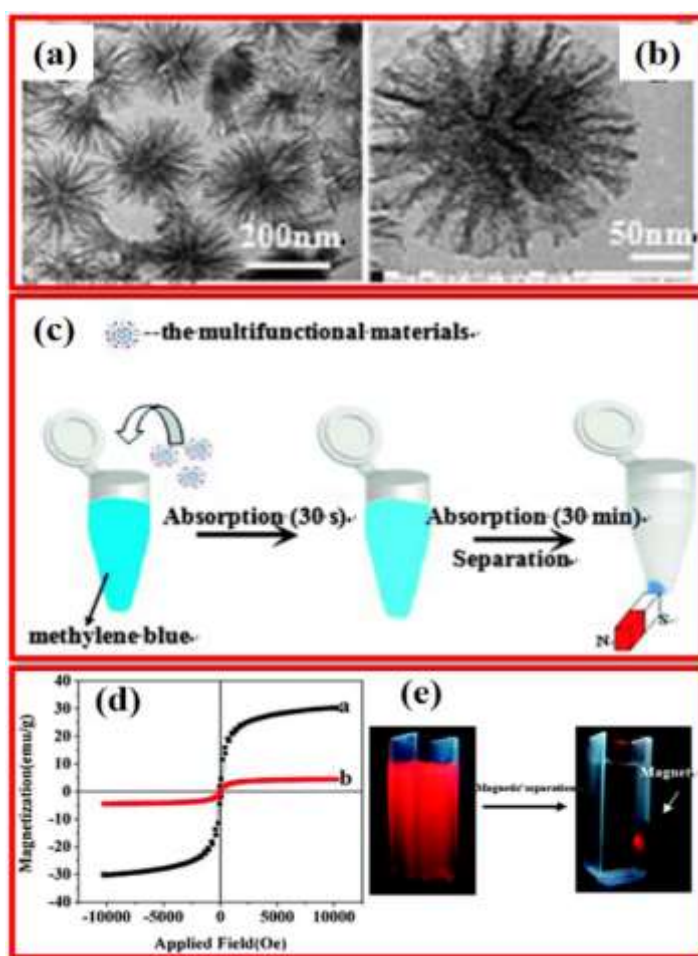


**Fig. 1.41:** (a) and (b) TEM images of $Fe_3O_4$/$YVO_4$:$Eu^{3+}$@$SiO_2$ nanocomposite, (c) schematic representation of the adsorption and separation process for methylene blue removal using $Fe_3O_4$/$YVO_4$:$Eu^{3+}$@$SiO_2$ composites, (d) magnetic hysteresis loops for $Fe_3O_4$ and $Fe_3O_4$/$YVO_4$:$Eu^{3+}$@$SiO_2$ and (e) magnetic response of multifunctional composites under UV-irradiation [187].

**Aim of the present study**

In the present work, nanocomposites with different compositions have been synthesized using (i) a facile sol-gel process, (ii) sol-gel process followed by thermal decomposition approach and (iii) one step thermal decomposition approach. Three different types of nanocomposites on the basis of different matrices have been synthesized: (i) $NiO-Al_2O_3$ and $PbS-Al_2O_3$ nanocomposites, (ii) $CdS-TiO_2$ and $Ag_2S-TiO_2$ nanocomposites and (iii) $CdS-\gamma-Fe_2O_3$ and $ZnO-Fe_2O_3$ nanocomposites. The synthesized nanocomposites were characterized using various analytical techniques such as powder XRD, TGA-DTA, FT-IR, Raman, AAS, BET, DRS, FE-SEM, SQUID, TEM and VSM. The synthesized nanocomposites were explored for a few applications such as oxidation of styrene, photocatalytic degradation of rhodamine B and photocatalytic degradation of congo red in aqueous solutions.

**References**

1. Rao C. N. R., Muller A., Cheetham A.K., 'The chemistry of nanomaterials: Synthesis, properties and applications', *Wiley-VCH Verlag GmbH & Co. kGaA* (2004).

2. Hyeon T., Manna L., Wong S. S., 'Sustainable nanotechnology', *Chemical Society Reviews*, **44**, 5755–5757 (2015).

3. Pradeep T., 'Nano: The Essentials, understanding nanoscience and nanotechnology', *McGraw-Hill* (2007).

4. Kenneth J. Klabunde and Ryan M. Richards., 'Nanoscale materials in chemistry', *John Wiley & Sons, Inc.* (2009).

5. Freestone I., Meeks N., Sax M., Higgitt C., 'The lycurgus cup-A Roman nanotechnology', *Golden Bulletin*, **40**, 270–277 (2007).

6. Brongersma M. L., 'Introductory lecture: nanoplasmonics', *Faraday Discussions*, **178**, 9–36 (2015).

7. Taniguchi N., 'On the basic concept of 'nano-technology', *Proceedings of the International Conference of Production Engineering, Tokyo, Japan: Society of Precision Engineering*, (1974).

8. Drexler E., 'The coming era of nanotechnology', *Anchor Books* (1986).

9. Sharma N., Ojha H., Bharadwaj A., Pathak D. P., Sharma R. K., 'Preparation and catalytic applications of nanomaterials: A review', *RSC Advances*, **5**, 53381–53403 (2015).

10. Roduner E., 'Size matters: why nanomaterials are different', *Chemical Society Reviews*, **35**, 583–592 (2006).

11. TamilSelvan S., Aldeyab S. S., Zaidi J. S. M., Arivuoli D., Ariga K., Mori T., Vinu A., 'Preparation and characterization of highly ordered mesoporous SiC nanoparticles with rod shaped morphology and tunable pore diameters', *Journal of Materials Chemistry*, **21**, 8792–8799 (2011).

12. Alivisatos A. P., 'Nanocrystals: Building blocks for modern materials design',

*Endeavour*, **21**, 56–60 (1997).

13. Gunter Schmid., 'Nanoparticles: From theory to application', *Wiley-VCH Verlag GmbH & Co. kGaA* (2004).

14. Schaefer H. E., 'Nanoscience: The science of the small in physics, engineering, chemistry, biology and medicine', *Springer* (2010).

15. Niu G., Wang L., Gao R., Ma B., Dong H., Qiu Y., 'Inorganic iodide ligands in ex situ PbS quantum dot sensitized solar cells with $I^-/I^{3-}$ electrolytes', *Journal of Materials Chemistry*, **22**, 16914–16919 (2012).

16. Wang W., Wang L., Liu L., He C., Tan J., Liang Y., 'Morphology-controlled synthesis and growth mechanism of ZnO nanostructures via the NaCl nonaqueous ionic liquid route', *CrystEngComm*, **14**, 4997–5004 (2012).

17. Zhang M., Zhao A., Li D., Sun H., Wang D., Guo H., Gao Q., Gan Z., Tao W., 'A simple and highly efficient route to the synthesis of $NaLnF_4$–Ag hybrid nanorice with excellent SERS performances', *The Analyst*, **137**, 4584–4592 (2012).

18. Hartono S. B., Phuoc N. T., Yu M., Jia Z., Monteiro M. J., Qiao S., Yu C., 'Functionalized large pore mesoporous silica nanoparticles for gene delivery featuring controlled release and co-delivery', *Journal of Materials Chemistry B*, **2**, 718–726 (2014).

19. Ajayan P. M., Schadler L. S., Braun P. V., 'Nanocomposite science and technology', *Wiley-VCH Verlag GmbH Co. KGaA, Weinheim* (2003).

20. Sureshkumar M., Na H. Y., Ahn K. H., Lee S. J., 'Conductive nanocomposites based on polystyrene microspheres and silver nanowires by latex blending', *ACS Applied Materials and Interfaces*, **7**, 756–764 (2015).

21. www.lamp-project.eu/Edu/what-is-nanotechnology

22. Fiordaliso E. M., Sharafutdinov I., Carvalho H. W. P., Grunwaldt J. D., Hansen T. W., Chorkendorff I., Wagner J. B., Damsgaard C. D., 'Intermetallic $GaPd_2$ nanoparticles on $SiO_2$ for low pressure $CO_2$ hydrogenation to methanol: Catalytic performance and in situ characterization', *ACS Catalysis*, **5**, 5827−5836 (2015).

23. www.rsc.org/chemistryworld

24. Gu W., Zhang W., Li X., Zhu H., Wei J., Li Z., Shu Q., Wang C., Wang K., Shen W., Kang F., Wu D., 'Graphene sheets from worm-like exfoliated graphite', *Journal of Materials Chemistry*, **19**, 3367–3369 (2009).

25. Sowinska M., Urbanczyk-Lipkowska Z., 'Advances in the chemistry of dendrimers', *New Journal of Chemistry*, **38**, 2168–2203 (2014).

26. Boisselier E., Diallo A. K., Salmon L., Ruiz J., 'Encapsulation and stabilization of gold nanoparticles with 'Click' polyethyleneglycol dendrimers', *The Journal of the American Chemical Society*, **132**, 2729–2742 (2010).

27. Sinha N. N., Shivakumara C., Munichandraiah N., 'High rate capability of a dual-porosity LiFePO$_4$/C composite', *ACS Applied Materials and Interfaces*, **2**, 2031–2038 (2010).

28. Fuchs I., Fechler N., Antonietti M., Mastai Y., 'Enantioselective nanoporous carbon based on chiral ionic liquids', *Angewandte Chemie International Edition*, **55**, 408–412 (2016).

29. Gao C., Guo Z., Liu J. H., Huang X. J., 'The new age of carbon nanotubes: An updated review of functionalized carbon nanotubes in electrochemical sensors', *Nanoscale*, **4**, 1948–1963 (2012).

30. Toshima N., Yonezawa T., 'Bimetallic nanoparticles-novel materials for chemical and physical applications', *New Journal of Chemistry*, **22**, 1179–1201 (1998).

31. Komarneni S., 'Nanocomposites', *Jounal of Materials Chemistry*, **2**, 1219–1230 (1992).

32. Xia F., Kwon S., Lee W. W., Liu Z., Kim S., Song T., Choi K. J., Paik U., Park W. I., 'Graphene as an interfacial layer for improving cycling performance of Si nanowires in lithium-ion batteries', *Nano Letters*, **15**, 6658–6664 (2015).

33. Xu Z., Li C., Kang X., Yang D., Yang P., Hou Z., Lin J., 'Synthesis of a multifunctional nanocomposite with magnetic, mesoporous, and near-IR absorption properties', *The Journal of Physical Chemistry C*, **114**, 16343–16350 (2010).

34.  Henrique P., Camargo C., Satyanarayana K. G., Wypych F., 'Nanocomposites: Synthesis, structure, properties and new application opportunities', *Materials Research*, **12**, 1–39 (2009).

35.  Vollath D., Szabó D. V., Haußelt J., 'Synthesis and properties of ceramic nanoparticles and nanocomposites', *Journal of the European Ceramic Society*, **17**, 1317–1324 (1997).

36.  Parchovianský M., Galusek D., Sedláček J., Švančárek P., Kašiarová M., Dusza J., Šajgalík P., 'Microstructure and mechanical properties of hot pressed $Al_2O_3$/SiC nanocomposites', *Journal of the European Ceramic Society*, **33**, 2291–2298 (2013).

37.  Casati R., Vedani M., 'Metal matrix composites reinforced by nano-particles-A Review', *Metals*, **4**, 65–83 (2014).

38.  Zotti A., Borriello A., Zuppolini S., Antonucci V., Giordano M., Pomogailo A. D., Lesnichaya V. A., Golubeva N. D., Bychkov A. N., Dzhardimalieva G. I., Zarrelli M., 'Fabrication and characterization of metal-core carbon-shell nanoparticles filling an aeronautical composite matrix', *European Polymer Journal*, **71**, 140–151 (2015).

39.  El-Mahallawi I., Abdelkader H., Yousef L., Amer A., Mayer J., Schwedt A., 'Influence of $Al_2O_3$ nano-dispersions on microstructure features and mechanical properties of cast and T6 heat-treated Al Si hypoeutectic Alloys', *Materials Science and Engineering A*, **556**, 76–87 (2012).

40.  Wang W., Chen Z., Hou L., Hu P., Shek C. H., Wu C. M. L., Lai J. K. L., 'Formation and third-order optical nonlinearities of fractal Ge nanocrystals embedded in Au matrix', *The Journal of Physical Chemistry C*, **117**, 8903–8908 (2013).

41.  Yang C., Wei H., Guan L., Guo J., Wang Y., Yan X., Zhang X., Wei S., Guo Z., 'Polymer nanocomposites for energy storage, energy saving, and anticorrosion', *Journal of Materials Chemistry A*, **3**, 14929–14941 (2015).

42.  Duncan T. V, Pillai K., 'Release of engineered nanomaterials from polymer nanocomposites: Diffusion, dissolution and desorption', *ACS Applied Materials and Interfaces*, **7**, 2–19 (2015).

43.  Baruch-Teblum E., Mastai Y., Landfester K., 'Miniemulsion polymerization of

cyclodextrin nanospheres for water purification from organic pollutants', *European Polymer Journal*, **46**, 1671–1678 (2010).

44. Huang Y. F., Park Y. Il, Kuo C., Xu P., Williams D. J., Wang J., Lin C. W., Wang H. L., 'Low-temperature synthesis of Au/polyaniline nanocomposites: Toward controlled size, morphology, and size dispersity', *The Journal of Physical Chemistry C*, **116**, 11272–11277 (2012).

45. Gallo J., Long N. J., Aboagye E. O., 'Magnetic nanoparticles as contrast agents in the diagnosis and treatment of cancer', *Chemical Society Reviews*, **42**, 7816–7833 (2013).

46. Bekermann D., Barreca D., Gasparotto A., Maccato C., 'Multi-component oxide nanosystems by chemical vapor deposition and related routes: Challenges and perspectives', *CrystEngComm*, **14**, 6347–6358 (2012).

47. Warwick M. E. A., Barreca D., Bontempi E., Carraro G., Gasparotto A., Maccato C., Kaunisto K., Ruoko T. P., Lemmetyinen H., Sada C., Gönüllü Y., Mathur S., 'Pt-functionalized $Fe_2O_3$ photoanodes for solar water splitting: the role of hematite nano-organization and the platinum redox state', *Physical Chemistry Chemical Physics*, **17**, 12899–12907 (2015).

48. Venugopal R., Lin P. I., Chen Y. T., 'Photoluminescence and Raman scattering from catalytically grown $Zn_xCd_{1-x}Se$ alloy nanowires', *The Journal of Physical Chemistry B*, **110**, 11691–11696 (2006).

49. Mojić-Lanté B., Djenadic R., Chakravadhanula V. S. K., Kübel C., Srdić V. V., Hahn H., 'Chemical vapor synthesis of $FeO_x$-$BaTiO_3$ nanocomposites', *Journal of the American Ceramic Society*, **98**, 1724–1730 (2015).

50. Barreca D., Carraro G., Warwick M. E. A., Kaunisto K., Gasparotto A., Gombac V., Sada C., Turner S., Van Tendeloo G., Maccato C., Fornasiero P., '$Fe_2O_3$–$TiO_2$ nanosystems by a hybrid PE-CVD/ALD approach: Controllable synthesis, growth mechanism, and photocatalytic properties', *CrystEngComm*, **17**, 6219–6226 (2015).

51. Kang B. R., Yoon J. kook, Hong K. T., Shon I. J., 'Mechanical properties and rapid low-temperature consolidation of nanocrystalline Cu-$ZrO_2$ composites by pulsed current activated heating', *Metals and Materials International*, **21**, 698–703 (2015).

52. Arif T. M., Saheb N., 'Characterization of ball milled Ni–Al$_2$O$_3$ nanocomposite powders', *Powder Metallurgy and Metal Ceramics*, **53**, 541–548 (2015).

53. Beyhaghi M., Kiani-Rashid A. R., Kashefi M., Khaki J. V., Jonsson S., 'Effect of powder reactivity on fabrication and properties of NiAl/Al$_2$O$_3$ composite coated on cast iron using spark plasma sintering', *Applied Surface Science*, **344**, 1–8 (2015).

54. Bao D., Gao P., Shen X., Chang C., Wang L., Wang Y., Chen Y., Zhou X., Sun S., Li G., Yang P., 'Mechanical ball-milling preparation of fullerene/cobalt core/shell nanocomposites with high electrochemical hydrogen storage ability', *ACS Applied Materials and Interfaces*, **6**, 2902–2909 (2014).

55. W. Cao., 'Synthesis of nanomaterials by high energy ball milling', at www.understandingnano.com/nanomaterial-synthesis-ball-milling.html

56. Perednis D., Gauckler L. J., 'Thin film deposition using spray pyrolysis', *Journal of Electroceramics*, **14**, 103–111 (2005).

57. Ko Y. N., Park S. Bin, Choi S. H., Kang Y. C., 'One-pot synthesis of manganese oxide-carbon composite microspheres with three dimensional channels for Li-ion batteries', *Scientific Reports*, **4**, 5751/1–5751/7 (2014).

58. Karthik A., Arunmetha S., Srither S. R., Manivasakan P., Rajendran V., 'Nano alumina–zirconia blended epoxy polymeric composites for anticorrosive applications', *Journal of Sol-Gel Science and Technology*, **74**, 460–471 (2015).

59. Oja Acik I., Oyekoya N. G., Mere A., Loot A., Dolgov L., Mikli V., Krunks M., Sildos I., 'Plasmonic TiO$_2$: Au composite layers deposited in situ by chemical spray pyrolysis', *Surface and Coatings Technology*, **271**, 27–31 (2015).

60. Giusti G., Consonni V., Puyoo E., Bellet D., 'High performance ZnO-SnO$_2$:F nanocomposite transparent electrodes for energy applications', *ACS Applied Materials and Interfaces*, **6**, 14096–14107 (2014).

61. Zeng H., Du X. W., Singh S. C., Kulinich S. A., Yang S., He J., Cai W., 'Nanomaterials via laser ablation/irradiation in liquid: A review', *Advanced Functional Materials*, **22**, 1333–1353 (2012).

62.  Sun M. Y., Yang J., Lin T., Du X. W., 'Facile synthesis of SnS hollow nanoparticles via laser ablation followed by chemical etching', *RSC Advances*, **2**, 7824–7828 (2012).

63.  Santagata A., Guarnaccio A., Pietrangeli D., Szegedi Á., Valyon J., De Stefanis A., De Bonis A., Teghil R., Sansone M., Mollica D., Parisi G. P., 'Production of silver-silica core-shell nanocomposites using ultra-short pulsed laser ablation in nanoporous aqueous silica colloidal solutions', *Journal of Physics D: Applied Physics*, **48**, 205304/1–205304/12 (2015).

64.  Lambert M., May A., Akkan C. K., Agarwal N., Aktas O. C., 'Ag–$Al_2O_3$ optical nanocomposites with narrow particle size distribution prepared by pulsed laser deposition', *Materials Letters*, **137**, 405–408 (2014).

65.  Wu S., Wang P., Cai Y., Liang D., Ye Y., Tian Z., Liu J., Liang C., 'Reduced graphene oxide anchored magnetic $ZnFe_2O_4$ nanoparticles with enhanced visible-light photocatalytic activity', *RSC Advances*, **5**, 9069–9074 (2015).

66.  Kim D. H., Aimon N. M., Ross C. A., 'Self-assembled growth and magnetic properties of a $BiFeO_3$-$MgFe_2O_4$ nanocomposite prepared by pulsed laser deposition', *Journal of Applied Physics*, **113**, 17B510/1–17B510/3 (2013).

67.  Ye Y., Wang P., Dai E., Liu J., Tian Z., Liang C., Shao G., 'A novel reduction approach to fabricate quantum-sized $SnO_2$-conjugated reduced graphene oxide nanocomposites as non-enzymatic glucose sensors', *Physical Chemistry Chemical Physics*, **16**, 8801–8807 (2014).

68.  Meldrum A., Haglund R. F., Boatner L. A., White C. W., 'Nanocomposite materials formed by ion implantation', *Advanced Materials*, **13**, 1431–1444 (2001).

69.  Sun L., Wu W., Zhang S., Liu Y., Xiao X., Ren F., Cai G., Jiang C., 'Spindle-like α-$Fe_2O_3$ embedded with $TiO_2$ nanocrystalline: Ion implantation preparation and enhanced magnetic properties', *Journal of Nanoscience and Nanotechnology*, **13**, 5428–5433 (2013).

70.  Lobotka P., Dérer J., Vávra I., de Julián Fernández C., Mattei G., Mazzoldi P., 'Single-electron transport and magnetic properties of Fe-$SiO_2$ nanocomposites prepared by ion implantation', *Physical Review B*, **75**, 024423/1–024423/8 (2007).

71. Pena O., Pal U., Rodrıguez-Fernandez L., Silva-Pereyra H. G., Rodrıguez-Iglesias V., Cheang-Wong J. C., Arenas-Alatorre J., Oliver A., 'Formation of Au-Ag core-shell nanostructures in silica matrix by sequential ion', *The Journal of Physical Chemistry C*, **113**, 2296–2300 (2009).

72. Mangold H. M., Karl H., Krenner H. J., 'Site-selective ion beam synthesis and optical properties of individual CdSe nanocrystal quantum dots in a $SiO_2$ matrix', *ACS Applied Materials and Interfaces*, **6**, 1339–1344 (2014).

73. De Espiau Lamaestre R., Majimel J., Jomard F., Bernas H., 'Synthesis of lead chalcogenide nanocrystals by sequential ion implantation in silica', *The Journal of Physical Chemistry B*, **109**, 19148–19155 (2005).

74. Fernandez C. de J., Manera M. G., Spadavecchia J., Maggioni G., Quaranta A., Mattei G., Bazzan M., Cattaruzza E., Bonafini M., Nergo E., Vomiero A., Carturan S., Scian C., Mea G. Della, Rella R., Vasanelli L., Mazzoldi P., 'Study of the gas optical sensing properties of Au-polyimide nanocomposite films prepared by ion implantation', *Sensors and Actuators B*, **111-112**, 225–229 (2005).

75. Guglielmi M., Kickelbick G., Martucci A., 'Sol-gel nanocomposites', *Springer* (2014).

76. Larry L. Hench and Jon K. West., 'The sol-gel process', *Chemical Reviews*, **90**, 33–72 (1990).

77. www.centexbel.be/solgel-treatment

78. Islam S., Bidin N., Riaz S., Rahman R. A., Naseem S., Marsin F. M., 'Mesoporous $SiO_2$–$TiO_2$ nanocomposite for pH sensing', *Sensors and Actuators B: Chemical*, **221**, 993–1002 (2015).

79. Pal N., Saha B., Kundu S. K., Bhaumik A., Banerjee S., 'A highly efficient non-enzymatic glucose biosensor based on a nanostructured $NiTiO_3$/NiO material', *New Journal of Chemistry*, **39**, 8035–8043 (2015).

80. Lee Y. H., Kim D. H., Kim T. W., 'Enhanced current efficiency of organic light-emitting devices due to a broad localized surface plasmonic resonance of Au–ZnO nanocomposites', *Applied Surface Science*, **355**, 359–363 (2015).

81.  Qu G., Geng H., Guo J., Zheng J., Gu H., 'Facile synthesis of Ag nanowires/mesoporous $TiO_2$ core–shell nanocables with improved properties for lithium storage', *New Journal of Chemistry*, **39**, 7889–7894 (2015).

82.  Neves M. C., Monteiro O. C., Hempelmann R., Silva A. M. S., Trindade T., 'From single-molecule precursors to coupled $Ag_2S/TiO_2$ nanocomposites', *European Journal of Inorganic Chemistry*, **2008**, 4380–4386 (2008).

83.  Sinha S. K., Srivastava C., Sampath S., Chattopadhyay K., 'Morphology control synthesis of $Au–Cu_2S$ metal-semiconductor hybrid nanostructures by modulating reaction constituents', *RSC Advances*, **5**, 56629–56635 (2015).

84.  Ma Y., Guo Y., Jiang H., Qu D., Liu J., Kang W., Yi Y., Zhang W., Shi J., Han Z., 'Preparation of network-like $ZnO–FeWO_4$ mesoporous heterojunctions with tunable band gaps and their enhanced visible light photocatalytic performance', *New Journal of Chemistry*, **39**, 5612–5620 (2015).

85.  Dong C., Xiao X., Chen G., Guan H., Wang Y., 'Synthesis and photocatalytic degradation of methylene blue over p-n junction $Co_3O_4/ZnO$ core/shell nanorods', *Materials Chemistry and Physics*, **155**, 1–8 (2015).

86.  Gong X., Liu Z., Yan D., Zhao H., Li N., Zhang X., Du Y., 'EuS–CdS and EuS–ZnS heterostructured nanocrystals constructed by co-thermal decomposition of molecular precursors in the solution phase', *Journal of Materials Chemistry C*, **3**, 3902–3907 (2015).

87.  Rajendran R., Shrestha L. K., Minami K., Subramanian M., Jayavel R., Ariga K., 'Dimensionally integrated nanoarchitectonics for a novel composite from 0D, 1D, and 2D nanomaterials: $RGO/CNT/CeO_2$ ternary nanocomposites with electrochemical performance', *Jounal of Materials Chemistry A*, **2**, 18480–18487 (2014).

88.  Kenneth J Klabunde., 'Nanoscale materials in chemistry', *John wiley & Sons, Inc.* (2001).

89.  Sabari Arul N., Mangalaraj D., Rajendran R., Nirmala Grace A., Han J. I., 'Fabrication of $CeO_2/Fe_2O_3$ composite nanospindles for enhanced visible light driven photocatalyst and supercapacitor electrode', *Journal of Materials Chemistry A*, **3**, 15248–15258

(2015).

90. Zhang J. T., Liu S., Pan G. L., Li G. R., Gao X. P., 'A 3D hierarchical porous α-Ni(OH)$_2$/graphite nanosheet composite as an electrode material for supercapacitors', *Journal of Materials Chemistry A*, **2**, 1524 (2014).

91. Rodríguez J. A., Fernández-García M., 'Synthesis, properties, and applications of oxide nanomaterials', *John Wiley & Sons, Inc.* (2006).

92. Preiss L. C., Werber L., Fischer V., Hanif S., Landfester K., Mastai Y., Muñoz-Espí R., 'Amino-acid-based chiral nanoparticles for enantioselective crystallization', *Advanced Materials*, **27**, 2728–2732 (2015).

93. Song J. T., Yang X. Q., Zhang X. S., Yan D. M., Yao M. H., Qin M. Y., Zhao Y. Di., 'Composite silica coated gold nanosphere and quantum dots nanoparticles for X-ray CT and fluorescence bimodal imaging', *Dalton Transactions*, **44**, 11314–11320 (2015).

94. Liu H., Chen Y., Tian G., Ren Z., Tian C., Fu H., 'Visible-light-induced self-cleaning property of Bi$_2$Ti$_2$O$_7$-TiO$_2$ composite nanowire arrays', *Langmuir*, **31**, 5962–5969 (2015).

95. Liu S., Ma C., 'Synthesis and characterization of flower-like NiCoP/ZnO composites', *New Journal of Chemistry*, **39**, 6332–6337 (2015).

96. Park G., Bartolome L., Lee K. G., Lee S. J., Kim D. H., Park T. J., 'One-step sonochemical synthesis of a graphene oxide–manganese oxide nanocomposite for catalytic glycolysis of poly(ethylene terephthalate)', *Nanoscale*, **4**, 3879–3885 (2012).

97. Duraibabu D., Alagar M., Kumar S. A., 'Studies on mechanical, thermal and dynamic mechanical properties of functionalized nanoalumina reinforced sulphone ether linked tetraglycidyl epoxy nanocomposites', *RSC Advances*, **4**, 40132–40140 (2014).

98. Beecroft L. L., Ober C. K., 'Nanocomposite materials for optical applications', *Chemistry of Materials*, **9**, 1302–1317 (1997).

99. Rajeshwar K., Tacconi N. R. De, Chenthamarakshan C. R., 'Semiconductor-based composite materials: Preparation, properties, and performance', *Chemisty of Materials*, **13**, 2765–2782 (2001).

100. Su H., Xie Y., Gao P., Xiong Y., Qian Y., 'Synthesis of MS/TiO$_2$ (M = Pb, Zn, Cd) nanocomposites through a mild sol–gel process', *Journal of Materials Chemistry*, **11**, 684–686 (2001).

101. Debnath R., Bakr O., Sargent E. H., 'Solution-processed colloidal quantum dot photovoltaics: A perspective', *Energy and Environmental Science*, **4**, 4870–4881 (2011).

102. Siy J. T., Brauser E. M., Bartl M. H., 'Low-temperature synthesis of CdSe nanocrystal quantum dots', *Chemical Communications*, **47**, 364–366 (2011).

103. Liu S., Yang M., Tang Z., Xu Y., 'A nanotree-like CdS/ZnO nanocomposite with spatially branched hierarchical structure for photocatalytic fine-chemical synthesis', *Nanoscale*, **6**, 7193–7198 (2014).

104. Reza Gholipour M., Dinh C. T., Béland F., Do T. O., 'Nanocomposite heterojunctions as sunlight-driven photocatalysts for hydrogen production from water splitting', *Nanoscale*, **7**, 8187–8208 (2015).

105. Blackman B., Battaglia D., Peng X., 'Bright and water-soluble near IR-emitting CdSe/CdTe/ZnSe type-II/type-I nanocrystals, tuning the efficiency and stability by growth', *Chemistry of Materials*, **20**, 4847–4853 (2008).

106. Jiang W., Liu Y., Zong R., Li Z., Yao W., Zhu Y., 'Photocatalytic hydrogen generation on bifunctional ternary heterostructured In$_2$S$_3$/MoS$_2$/CdS composites with high activity and stability under visible light irradiation', *Journal of Materials Chemistry A*, **3**, 18406–18412 (2015).

107. Tjong S. C., 'Polymer composites with graphene nanofillers: Electrical properties and applications', *Journal of Nanoscience and Nanotechnology*, **14**, 1154–1168 (2014).

108. Davim J. P., Charitidis C. A., 'Nanocomposites', *Walter de Gruyter GmbH, Berlin/Boston* (2013).

109. Pardha-Saradhi P., Yamal G., Peddisetty T., Sharmila P., Singh J., Nagarajan R., Rao K. S., 'Root system of live plants is a powerful resource for the green synthesis of Au-nanoparticles', *RSC Advances*, **4**, 7361–7367 (2014).

110. Nam W. H., Kim B. B., Seo S. G., Lim Y. S., Kim J. Y., Seo W. S., Choi W. K., Park H. H., Lee J. Y., 'Structurally nanocrystalline-electrically single crystalline ZnO-reduced graphene oxide composites', *Nano Letters*, **14**, 5104–5109 (2014).

111. Kim H., Miura Y., Macosko C. W., 'Graphene/polyurethane nanocomposites for improved gas barrier and electrical conductivity', *Chemistry of Materials*, **22**, 3441–3450 (2010).

112. Wang H. L., Ning X. K., Wang Z. J., 'Enhanced electrical conductivity of Au–LaNiO$_3$ nanocomposite thin films by chemical solution deposition', *RSC Advances*, **5**, 76783–76787 (2015).

113. Cullity B. D., Graham C. D., 'Introduction to magnetic materials', *John Wiley & Sons, Inc.* (2009).

114. Nadeem K., Traussnig T., Letofsky-Papst I., Krenn H., Brossmann U., Würschum R., 'Sol-gel synthesis and characterization of single-phase Ni ferrite nanoparticles dispersed in SiO$_2$ matrix', *Journal of Alloys and Compounds*, **493**, 385–390 (2010).

115. Duan W. J., Lu S. H., Wu Z. L., Wang Y. S., 'Size effects on properties of NiO nanoparticles grown in alkali salts', *The Journal of Physical Chemistry C*, **116**, 26043–26051 (2012).

116. Saber O., Mohamed N. H., Arafat S. A., 'Conversion of iron oxide nanosheets to advanced magnetic nanocomposites for oil spill removal', *RSC Advances*, **5**, 72863–72871 (2015).

117. Wu W., Jiang C., Roy V. A. L., 'Recent progress in magnetic iron oxide–semiconductor composite nanomaterials as promising photocatalysts', *Nanoscale*, **7**, 38–58 (2015).

118. Lin Z., Liu P., Yan J., Yang G., 'Matching energy levels between TiO$_2$ and α-Fe$_2$O$_3$ in a core–shell nanoparticle for visible-light photocatalysis', *Journal of Materials Chemistry A*, **3**, 14853–14863 (2015).

119. Wang J. C., Zhang L., Fang W. X., Ren J., Li Y. Y., Yao H. C., Wang J., Li Z., 'Enhanced photoreduction CO$_2$ activity over direct Z-Scheme α-Fe$_2$O$_3$/Cu$_2$O heterostructures under visible light irradiation', *ACS Applied Materials and Interfaces*,

**7**, 8631–8639 (2015).

120. Hu X. W., Liu S., Qu B. T., You X. Z., 'Starfish-shaped $Co_3O_4$/$ZnFe_2O_4$ hollow nanocomposite: Synthesis, supercapacity and magnetic properties', *ACS Applied Materials and Interfaces*, **7**, 9972–9981 (2015).

121. Hu L., Zhang P., Sun Y., Bao S., Chen Q., '$ZnO$/$Co_3O_4$ porous nanocomposites derived from MOFs: Room-temperature ferromagnetism and high catalytic oxidation of CO', *ChemPhysChem*, **14**, 3953–3959 (2013).

122. Wu D., Ma H., Zhang Y., Jia H., Yan T., Wei Q., 'Corallite-like magnetic $Fe_3O_4$@$MnO_2$@Pt nanocomposites as multiple signal amplifiers for the detection of carcinoembryonic antigen', *ACS Applied Materials and Interfaces*, **7**, 18786−18793 (2015).

123. Egodawatte S., Datt A., Burns E. A., Larsen S. C., 'Chemical insight into the adsorption of chromium(III) on iron oxide/mesoporous silica nanocomposites', *Langmuir*, **31**, 7553–7562 (2015).

124. Sun C., Zhou R., E J., Sun J., Ren H., 'Magnetic $CuO$@$Fe_3O_4$ nanocomposite as a highly active heterogeneous catalyst of persulfate for 2,4-dichlorophenol degradation in aqueous solution', *RSC Advances*, **5**, 57058–57066 (2015).

125. Si Y., Yan C., Hong F., Yu J., Ding B., 'General strategy for fabricating flexible magnetic silica nanofibrous membranes with multifunctionality', *Chemical Communications*, **51**, 12521–12524 (2015).

126. Roy P., Srivastava S. K., 'Nanostructured anode materials for lithium ion batteries', *Journal of Materials Chemistry A*, **3**, 2454–2484 (2015).

127. Li G. R., Xu H., Lu X. F., Feng J. X., Tong Y. X., Su C. Y., 'Electrochemical synthesis of nanostructured materials for electrochemical energy conversion and storage.', *Nanoscale*, **5**, 4056–4069 (2013).

128. Singh K., Nowotny J., Thangadurai V., 'Amphoteric oxide semiconductors for energy conversion devices: A tutorial review.', *Chemical Society Reviews*, **42**, 1961–1972 (2013).

129. Zhou W., Cheng C., Liu J., Tay Y. Y., Jiang J., Jia X., Zhang J., Gong H., Hng H. H., Yu T., Fan H. J., 'Epitaxial growth of branched $\alpha$-Fe$_2$O$_3$/SnO$_2$ nano-heterostructures with improved lithium-ion battery performance', *Advanced Functional Materials*, **21**, 2439–2445 (2011).

130. Wu H., Xu M., Wang Y., Zheng G., 'Branched Co$_3$O$_4$/Fe$_2$O$_3$ nanowires as high capacity lithium-ion battery anodes', *Nano Research*, **6**, 167–173 (2013).

131. Kumar S., Chinnathambi S., Munichandraiah N., 'Ir nanoparticles-anchored reduced graphene oxide as a catalyst for oxygen electrode in Li-O$_2$ cells', *New Journal of Chemistry*, **39**, 7066–7075 (2015).

132. Kumar S., Selvaraj C., Munichandraiah N., Scanlon L. G., 'Gold nanoparticles anchored reduced graphene oxide as catalyst for oxygen electrode of rechargeable Li–O$_2$ cells', *RSC Advances*, **3**, 21706–21714 (2013).

133. Li M., Yin Y. X., Li C., Zhang F., Wan L. J., Xu S., Evans D. G., 'Well-dispersed bi-component-active CoO/CoFe$_2$O$_4$ nanocomposites with tunable performances as anode materials for lithium-ion batteries', *Chemical Communications*, **48**, 410–412 (2012).

134. Hodgkinson J., Tatam R. P., 'Optical gas sensing: A review', *Measurement Science and Technology*, **24**, 012004/1–012004/59 (2013).

135. Rumyantseva M. N., Kovalenko V. V., Gas'kov A. M., Pagnier T., 'Metal-oxide based nanocomposites as materials for gas sensors', *Russian Journal of General Chemistry*, **78**, 1081–1092 (2008).

136. Zhao Y., Fan L., Zhang Y., Zhao H., Li X., Li Y., Wen L., Yan Z., Huo Z., 'Hyper-branched Cu@Cu$_2$O coaxial nanowires mesh electrode for ultra-sensitive glucose detection', *ACS Applied Materials and Interfaces*, **7**, 16802–16812 (2015).

137. Wang Y., Wang W., Song W., 'Binary CuO/Co$_3$O$_4$ nanofibers for ultrafast and amplified electrochemical sensing of fructose', *Electrochimica Acta*, **56**, 10191–10196 (2011).

138. Nayak A. K., Ghosh R., Santra S., Guha P. K., Pradhan D., 'Hierarchical nanostructured WO$_3$-SnO$_2$ for selective sensing of volatile organic compounds', *Nanoscale*, **7**,

12460–12473 (2015).

139. Chen W., Li Q., Xu L., Zeng W., 'Gas sensing properties of ZnO–SnO$_2$ nanostructures', *Journal of Nanoscience and Nanotechnology*, **15**, 1245–1252 (2015).

140. Bonyani M., Mirzaei A., Leonardi S. G., Bonavita A., Neri G., 'Electrochemical properties of Ag@iron oxide nanocomposite for application as nitrate sensor', *Electroanalysis*, **27**, 1–10 (2015).

141. Shi J., 'On the synergetic catalytic effect in heterogeneous nanocomposite catalysis', *Chemical Reviews*, **113**, 2139–2181 (2013).

142. Pachfule P., Panda M. K., Kandambeth S., Shivaprasad S. M., Díaz D. D., Banerjee R., 'Multifunctional and robust covalent organic framework–nanoparticle hybrids', *Journal of Materials Chemistry A*, **2**, 7944–7952 (2014).

143. Zhu L., Jiang Y., Zheng J., Zhang N., Yu C., Li Y., Pao C. W., Chen J. L., Jin C., Lee J. F., Zhong C. J., Chen B. H., 'Ultrafine nanoparticle-supported Ru nanoclusters with ultrahigh catalytic activity', *Small*, **11**, 4385–4393 (2015).

144. Liu H., Huang Z., Han Z., Ding K., Liu H., Xia C., Chen J., 'Efficient production of methanol and diols via the hydrogenation of cyclic carbonates using copper–silica nanocomposite catalysts', *Green Chemistry*, **17**, 4281–4290 (2015).

145. Chetia M., Ali A. A., Bhuyan D., Saikia L., Sarma D., 'Magnetically recoverable chitosan-stabilised copper–iron oxide nanocomposite material as an efficient heterogeneous catalyst for azide–alkyne cycloaddition reactions', *New Journal of Chemistry*, **39**, 5902–5907 (2015).

146. Skliri E., Lykakis I. N., Armatas G. S., 'Ordered mesoporous V$_2$O$_5$/WO$_3$ composite catalysts for efficient oxidation of aryl alcohols', *RSC Advances*, **4**, 46170–46178 (2014).

147. Gawande M. B., Branco P. S., Parghi K., Shrikhande J. J., Pandey R. K., Ghumman C. A. A., Bundaleski N., Teodoro O. M. N. D., Jayaram R. V., 'Synthesis and characterization of versatile MgO–ZrO$_2$ mixed metal oxide nanoparticles and their applications', *Catalysis Science and Technology*, **1**, 1653–1664 (2011).

148. Ji Q., Hill J. P., Ariga K., 'Shell-adjustable hollow 'soft' silica spheres as a support for gold nanoparticles', *Journal of Materials Chemistry A*, **1**, 3600–3606 (2013).

149. Du X. L., Sun X. P., Jin C., Jiang Z., Su D. S., Wang J. Q., 'Efficient hydrogenation of alkyl formate to methanol over nanocomposite copper/alumina catalysts', *ChemCatChem*, **6**, 3075–3079 (2014).

150. Geng Z., Zhang Y., Yuan X., Huo M., Zhao Y., Lu Y., Qiu Y., 'Incorporation of $Cu_2O$ nanocrystals into $TiO_2$ photonic crystal for enhanced UV–visible light driven photocatalysis', *Journal of Alloys and Compounds*, **644**, 734–741 (2015).

151. Guan X. H., Yang L., Guan X., Wang G. S., 'Synthesis of a flower-like CuS/ZnS nanocomposite decorated on reduced graphene oxide and its photocatalytic performance', *RSC Advances*, **5**, 36185–36191 (2015).

152. Xu F., Yuan Y., Han H., Wu D., Gao Z., Jiang K., 'Synthesis of ZnO/CdS hierarchical heterostructure with enhanced photocatalytic efficiency under nature sunlight', *CrystEngComm*, **14**, 3615–3622 (2012).

153. Cravanzola S., Muscuso L., Cesano F., Agostini G., Damin A., Scarano D., Zecchina A., '$MoS_2$ nanoparticles decorating titanate-nanotube surfaces: combined microscopy, spectroscopy and catalytic studies', *Langmuir*, **31**, 5469–5478 (2015).

154. Tedla H., Diaz I., Kebede T., Taddesse A. M., 'Synthesis, characterization and photocatalytic activity of zeolite supported $ZnO/Fe_2O_3/MnO_2$ nanocomposites', *Journal of Environmental Chemical Engineering*, **3**, 1586–1591 (2015).

155. Abdal-hay A., Hamdy Makhlouf A. S., Khalil K. A., 'Novel, facile, single-step technique of polymer/$TiO_2$ nanofiber composites membrane for photodegradation of methylene blue', *ACS Applied Materials and Interfaces*, **7**, 13329–13341 (2015).

156. Mumin M. A., Moula G., Charpentier P. A., 'Supercritical $CO_2$ synthesized $TiO_2$ nanowires covalently linked with core–shell CdS–ZnS quantum dots: Enhanced photocatalysis and stability', *RSC Advances*, **5**, 67767–67779 (2015).

157. Xu X., Hu L., Gao N., Liu S., Wageh S., Al-Ghamdi A. A., Alshahrie A., Fang X., 'Controlled growth from ZnS nanoparticles to ZnS-CdS nanoparticle hybrids with

enhanced photoactivity', *Advanced Functional Materials*, **25**, 445–454 (2015).

158. Zirak M., Moradlou O., Bayati M. R., Nien Y. T., Moshfegh A. Z., 'On the growth and photocatalytic activity of the vertically aligned ZnO nanorods grafted by CdS shells', *Applied Surface Science*, **273**, 391–398 (2013).

159. Li L., Cheng B., Wang Y., Yu J., 'Enhanced photocatalytic $H_2$-production activity of bicomponent $NiO/TiO_2$ composite nanofibers', *Journal of Colloid and Interface Science*, **449**, 115–121 (2015).

160. Luan P., Xie M., Fu X., Qu Y., Sun X., Jing L., 'Improved photoactivity of $TiO_2$–$Fe_2O_3$ nanocomposites for visible-light water splitting after phosphate bridging and its mechanism', *Physical Chemistry Chemical Physics*, **17**, 5043–5050 (2015).

161. Walsh D., Sanchez-Ballester N. M., Ariga K., Tanaka A., Weller M., 'Chelate stabilized metal oxides for visible light photocatalyzed water oxidations', *Green Chemistry*, **17**, 982–990 (2015).

162. Zhu Y., Wang Y., Chen Z., Qin L., Yang L., Zhu L., Tang P., Gao T., Huang Y., Sha Z., Tang G., 'Visible light induced photocatalysis on CdS quantum dots decorated $TiO_2$ nanotube arrays', *Applied Catalysis A: General*, **498**, 159–166 (2015).

163. Wang M., Han J., Xiong H., Guo R., 'Yolk@shell nanoarchitecture of Au@r-GO/$TiO_2$ hybrids as powerful visible light photocatalysts', *Langmuir*, **31**, 6220–6228 (2015).

164. Melvin A. A., Illath K., Das T., Thirumalaiswamy R., Bhattacharyya S., Gopinath C. S., 'M-Au/$TiO_2$ (M = Ag, Pd, and Pt) nanophotocatalyst for overall solar water splitting: Role of interfaces', *Nanoscale*, **7**, 13477–13488 (2015).

165. Luan P., Xie M., Liu D., Fu X., Jing L., 'Effective charge separation in the rutile $TiO_2$ nanorod-coupled $\alpha$-$Fe_2O_3$ with exceptionally high visible activities', *Scientific Reports*, **4**, 6180/1–6180/7 (2014).

166. Wei L., Li F., Hu S., Li H., Chi B., Pu J., Jian L., 'CdS quantum dot-sensitized vertical $TiO_2$ nanorod arrays by a simple linker-assisted SILAR method', *Journal of the American Ceramic Society*, **98**, 3173–3178 (2015).

167. Gong J., Qiao H., Sigdel S., Elbohy H., Adhikari N., Zhou Z., Sumathy K., Wei Q., Qiao

Q., 'Characteristics of $SnO_2$ nanofiber/$TiO_2$ nanoparticle composite for dye-sensitized solar cells', *AIP Advances*, **5**, 067134/1–067134/10 (2015).

168. Tayyebi A., Tavakoli M. M., Outokesh M., Shafiekhani A., Simchi A., 'Supercritical synthesis and characterization of graphene–PbS quantum dots composite with enhanced photovoltaic properties', *Industrial and Engineering Chemistry Research*, **54**, 7382–7392 (2015).

169. Yuan K., Chen L., Chen Y., 'In situ photocatalytically heterostructured ZnO-Ag nanoparticle composites as effective cathode-modifying layers for air-processed polymer solar cells', *Chemistry-A European Journal*, **21**, 11899–11906 (2015).

170. Kim M., Altantuya U., Lee H. J., 'CuS/CdS quantum dot composite sensitizer and its applications to various $TiO_2$ mesoporous film-based solar cell devices', *Langmuir*, **31**, 7609–7615 (2015).

171. Scheunemann D., Wilken S., Parisi J., Borchert H., 'Investigation of the spatially dependent charge collection probability in $CuInS_2$/ZnO colloidal nanocrystal solar cells', *ACS Photonics*, **2**, 864–875 (2015).

172. Beshkar F., Sabet M., Salavati-Niasari M., 'Improving electron transfer from dye to $TiO_2$ by using CdTe nanostructure layers in dye-sensitized solar cells', *Journal of Materials Engineering and Performance*, **24**, 3107–3117 (2015).

173. Bagga K., Brougham D. F., Keyes T. E., Brabazon D., 'Magnetic and noble metal nanocomposites for separation and optical detection of biological species.', *Physical Chemistry Chemical Physics*, **17**, 27968–27980 (2015).

174. Dai X., Fan Z., Lu Y., Ray P. C., 'Multifunctional nanoplatforms for targeted multidrug-resistant-bacteria theranostic applications', *ACS Applied Materials and Interfaces*, **5**, 11348–11354 (2013).

175. Hu Y., Shan C. X., Wang J., Zhu J. M., Gu C. Q., Ni W. T., Zhu D., Zhang A. H., 'Fabrication of functionalized $SiO_2$/$TiO_2$ nanocomposites via amidation for the fast and selective enrichment of phosphopeptides', *New Journal of Chemistry*, **39**, 6540–6547 (2015).

176. Chen X., Huang X., Zheng C., Liu Y., Xu T., Liu J., 'Preparation of different sized nano-silver loaded on functionalized graphene oxide with highly effective antibacterial properties', *Jounal of Materials Chemistry B*, **3**, 7020–7029 (2015).

177. Siddhanta S., Thakur V., Narayana C., Shivaprasad S. M., 'Universal metal-semiconductor hybrid nanostructured SERS substrate for biosensing', *ACS Applied Materials and Interfaces*, **4**, 5807−5812 (2012).

178. Sharvani S., Upadhayaya K., Kumari G., Narayana C., Shivaprasad S. M., 'Nano-morphology induced additional surface plasmon resonance enhancement of SERS sensitivity in Ag/GaN nanowall network', *Nanotechnology*, **26**, 465701/1–465701/7 (2015).

179. Zhao H., Dong Y., Jiang P., Wang G., Zhang J., 'Highly dispersed $CeO_2$ on $TiO_2$ nanotube: A synergistic nanocomposite with superior peroxidase-like activity', *ACS Applied Materials and Interfaces*, **7**, 6451–6461 (2015).

180. Sharifabad M. E., Mercer T., Sen T., Sharifabad M. E., Mercer T., Sen T., 'The fabrication and characterization of stable core-shell superparamagnetic nanocomposites for potential application in drug delivery', *Journal of Applied Physics*, **117**, 17D139/1–17D139/4 (2015).

181. Pan J., Wei J., Shen J., Guo S., Sheng Y., Zhang X., Feng B., 'Green synthesis of surface plasmons photoluminescence enhancement ZnSe/Au nanocomposites and its bioimaging application', *Journal of Physics D: Applied Physics*, **47**, 045504/1–045504/6 (2014).

182. Mi C., Zhang J., Gao H., Wu X., Wang M., Wu Y., Di Y., Xu Z., Mao C., Xu S., 'Multifunctional nanocomposites of superparamagnetic ($Fe_3O_4$) and NIR-responsive rare earth-doped up-conversion fluorescent ($NaYF_4$: Yb, Er) nanoparticles and their applications in biolabeling and fluorescent imaging of cancer cells', *Nanoscale*, **2**, 1141–1148 (2010).

183. Wang Y., Gu H., 'Core-shell-type magnetic mesoporous silica nanocomposites for bioimaging and therapeutic agent delivery', *Advanced Materials*, **27**, 576–585 (2015).

184. Liu S., Lu F., Liu Y., Jiang L. P., Zhu J. J., 'Synthesis, characterization, and

electrochemical applications of multifunctional $Fe_3O_4$@C-Au nanocomposites', *Journal of Nanoparticle Research*, **15**, 1331/1–1331/8 (2013).

185. Wu Y., Yang H., Zhu L., Xie A., Li S., Song J., Shen Y., 'Multifunctional SERS substrates of $Fe_3O_4$@$Ag_2Se$/Ag: Construction, properties and application', *Analytical Methods*, **6**, 7083–7087 (2014).

186. Fan Z., Senapati D., Singh A. K., Ray P. C., 'Theranostic magnetic core-plasmonic shell star shape nanoparticle for the isolation of targeted rare tumor cells from whole blood, fluorescence imaging, and photothermal destruction of cancer', *Molecular Pharmaceutics*, **10**, 857–866 (2013).

187. Shi J., Ren X., Tong L., Chen X., Yang X., Yang H., 'In situ assembly of monodisperse, multifunctional silica microspheres embedded with magnetic and fluorescent nanoparticles and their application in adsorption of methylene blue', *Physical Chemistry Chemical Physics*, **15**, 18642–18648 (2013).

# CHAPTER 2

## *Experimental Techniques*

In the present study, different characterization techniques were used for the determination of various parameters such as phase, crystallinity, crystallite size, thermal decomposition behaviour, elemental composition, morphology, magnetic behaviour, optical properties and catalytic properties of the synthesized nanocomposites. The techniques used were powder X-ray diffraction (XRD), Fourier transform infrared spectroscopy (FT-IR), Raman spectroscopy, thermal gravimetric analysis (TGA), field emission-scanning electron microscopy (FE-SEM) coupled with energy dispersive X-ray analysis (EDXA), transmission electron microscopy (TEM), selected area electron diffraction (SAED), diffuse reflectance spectroscopy (DRS), photoluminescence spectroscopy (PL), surface area measurements (BET) and atomic absorption spectroscopy (AAS). The magnetic properties of the nanocomposites were investigated using a superconducting quantum interference device (SQUID) or a vibrating sample magnetometer (VSM). Catalytic applications of the nanocomposites were studied using gas chromatography coupled with mass spectroscopy (GC-MS) and UV-visible spectroscopy. More details on the sample preparation and data acquisition for each of the above techniques are discussed below.

## 2.1 Powder X-ray diffraction (XRD)

X-ray powder diffraction is a widely used technique in solid state chemistry for phase determination, structural information and crystallite size estimation [1]. This method is based on the principle that when parallel monochromatic X-rays are allowed to fall on a crystal plane with interplanar spacing $d$, the X-rays get diffracted at an angle $\theta$. The diffracted beam intensity is recorded on the detector as a function of diffraction angle. The wavelength of incident X-ray is related to the angle of diffraction by the following Bragg's equation (equation 1) [2]:

$$n\lambda = 2dsin\theta \qquad\qquad (1)$$

Where n is order of the diffraction. For n = 1, diffraction is first order, $\lambda$ is wavelength of X-rays and $\theta$ is the angle of diffraction.

In the present study, the X-ray diffraction patterns of the synthesized nanocomposites were recorded using a Brucker AXS-D8 diffractometer. The sample preparation was done by placing 50 to 100 mg of sample powder on the sample holder with a groove and were levelled using a glass slide. The instrumental parameters for the measurements and data evolution were given using DIFFRAC$^{plus}$ and EVA$^{®}$ software, respectively. The instrumental parameters during the powder XRD measurements of the samples were: Cu-K$\alpha$ radiation ($\lambda$ = 1.5406 Å) as the

X-ray source with 40 kV and 30 mA. The 2θ range was between 5° and 90° and the goniometer scan speed was 1°/min or 2°/min. The X-ray diffraction patterns recorded were evaluated using JCPDS (Joint committee on powder diffraction standards) database. The average crystallite size of the nanocomposites was estimated using the most intense reflections of the phases by Debye–Scherrer formula (equation 2) [3].

$$D = \frac{K\lambda}{\beta cos\theta} \qquad\qquad (2)$$

Where D is the crystallite size in nm, K is a dimensionless constant varying from 0.89 to 1.39 (K = 0.89 for two dimensional lattices), λ is the wavelength of X-rays, θ is the Bragg angle in radians and β is the full width at half maximum in radians.

**2.2 Fourier Transform Infrared Spectroscopy (FT-IR)**

Infrared spectroscopy is a versatile technique used for the determination of characteristic functional groups, metal-sulfide bonds, metal-oxide bonds etc., present in the materials. IR spectroscopy is useful as one of the characterization techniques in different areas of science and technology including chemical, biological, pharmaceuticals, materials, etc [4]. Infrared spectra can be recorded for any material (in solid, liquid or gaseous state) excluding metals. The infrared absorption is due to vibrational state of molecules having net dipole moment during their vibrational movement [5].

In the present study, a Thermo Nicolet infrared spectrometer was used for recording the IR spectra of NiO-$Al_2O_3$ nanocomposites (Chapter 2), PbS-$Al_2O_3$ nanocomposites (Chapter 2), CdS-γ-$Fe_2O_3$ nanocomposites (Chapter 5) and ZnO@γ-$Fe_2O_3$ core-shell nanocomposites (Chapter 5) in the range 4000 cm$^{-1}$ to 400 cm$^{-1}$ at room temperature. The IR spectral results were useful in the characterization of amorphous nanoparticles such as $Al_2O_3$ and $Fe_2O_3$ due to the presence of Al-O and Fe-O stretching bands in the corresponding IR spectra of the nanocomposites. Omnic® software was used to input the instrumental parameters for recording the IR spectra and their analysis. Potassium bromide (Aldrich®) was used for recording the background. The powder samples were mixed with KBr (KBr:sample = 100:1) and grounded with help of a pestle and mortar. The homogeneous mixtures were made into pellets using a hydraulic press (1500 psi). The pellets were placed inside the sample chamber of the IR spectrometer with the help of a sample holder to record the IR spectrum.

## 2.3 Raman Spectroscopy

Raman spectroscopy is used to study vibrational modes of a molecule [6]. This technique works on the principle of inelastic scattering of light from molecules. In inelastic scattering, when a monochromatic light fall on the sample there is shift in the frequency of the scattered light. The up or down shift in comparison to the incident light with monochromatic frequency depends on the nature of vibrational modes of the molecules. This shift is known as Raman shift. Raman spectroscopy can be used to study solid, liquid and gaseous samples [7]. It must be noted that Raman spectroscopy results are complementary to infrared spectroscopy results. Also, almost all molecules are Raman active, e.g., homo atomic molecules are Raman active but they are not IR active.

In the present study, Raman spectra for $NiO-Al_2O_3$ nanocomposites and $PbS-Al_2O_3$ nanocomposites (Chapter 3) were recorded at room temperature using a RENISHAW in Via Raman spectrophotometer with 514 nm Ar ion laser, a CCD (Charge Coupled Device) detector and a 50× objective lens. For the measurement, the powder sample was placed on a clean glass substrate under 50× objective lens and the measurement was carried out in the range 200 to 1400 $cm^{-1}$. All the spectra were recorded using a low laser power of 1 mW in order to prevent destruction of the samples. The instrument was calibrated before the sample measurements using a silicon reference at 520 $cm^{-1}$.

## 2.4 Thermal Gravimetric Analysis (TGA)

Thermal gravimetric analysis is an experimental technique in which weight or mass of the sample is recorded as a function of temperature. The sample is heated at constant rate in air or an inert atmosphere (e.g. $N_2$) and the result obtained is presented as TGA curve in which weight or mass percentage is plotted against temperature [8]. There is change in weight or mass of the sample due to different processes that occur during heating of the sample such as evaporation of water, oxidation of organic compounds, carbonization of organic matter, oxidation of metals, etc [9]. The TGA instrument comprises of a small sample holder pan attached with a high precision balance. In the present study, thermal gravimetric analysis (TGA) was carried out using a Perkin Elmer Pyris Diamond instrument for as-prepared nickel hydroxide-alumina nanocomposites (Chapter-3). About 10 mg of sample was used for the measurement under $N_2$ (flow rate = 200 mL/min) from 30 to 1000 °C with a heating rate of 10 °C $min^{-1}$. Thermal gravimetric analysis was also carried out for $CdS-\gamma-Fe_2O_3$ (Chapter 5) nanocomposites by using

an EXSTAR TG/DTA 6300 instrument under air (flow rate = 200 mL/min) from 25 to 1000 $^{\circ}$C with a heating rate of 10 $^{\circ}$C min$^{-1}$.

## 2.5 Atomic Absorption Spectroscopy (AAS)

Atomic absorption spectroscopy is useful for the quantitative determination of metals present at low concentrations (e.g. ppm) in the samples. It is a destructive technique and the working principle involves excitation of metal atoms present in the analyte vapour by suitable absorption of light at characteristic wavelengths [10].

In the present study, the amount of cadmium present in the CdS-$\gamma$-Fe$_2$O$_3$ nanocomposites (Chapter-5) and the cadmium present after photodegradation of congo red in an aqueous solution using CdS-$\gamma$-Fe$_2$O$_3$ nanocomposites (Chapter-6) were quantitatively determined using a Perkin Elmer AAnalyst 800 atomic absorption spectrometer. Cadmium solutions were prepared in the working concentration limit (upto 1.5 ppm) according to the specification of the instrument. The standard solutions were prepared by dissolving a known amount of AR grade cadmium acetate in Millipore$^{\circledR}$ water followed by dilution. The unknown solutions were prepared by digesting known amount of CdS-$\gamma$-Fe$_2$O$_3$ nanocomposites in conc. HNO$_3$ followed by dilution with Millipore$^{\circledR}$ water. The cadmium lamp ($\lambda$ = 228.8 nm) was inserted into the AAS instrument and the columns were washed with Millipore$^{\circledR}$ water before analyzing the samples. Mixture of air and acetylene was used to generate flame in the spectrometer. The input instrumental parameters were given using WIN lab$^{\circledR}$ software. Firstly, the AAS instrument was calibrated using the standard cadmium solutions. Then, the unknown solutions were analyzed and the concentrations of cadmium present in the unknown solutions were estimated using the calibration curve.

## 2.6 Field Emission Scanning Electron Microscope (FE-SEM) and Energy Dispersive X-ray Analysis (EDXA)

Field emission scanning electron microscopy (FE-SEM) is a microscopy technique used to study surface structure and morphology (topology) of the materials [11]. In the present study, the surface properties and morphology of the samples were studied using a FEI Quanta 200F or Carl Zeiss (ULTRA plus) electron microscope. FEI Quanta 200F electron microscope was operated at an accelerating voltage of 20 kV and the Carl Zeiss (ULTRA plus) electron microscope was operated at an accelerating voltage of 15 kV. The FE-SEM was coupled with an energy dispersive X-ray analysis (EDXA) facility for elemental analysis of the samples. The

samples were prepared on brass stubs which were cleaned with iso-amyl acetate (RANKEM®) and dried by blowing hot air. A small amount of sample powder was spread over the stubs with the help of a conducting carbon double sided tape. The sample surface was made conductive by gold sputtering for about 70 seconds and at 30 mA to prevent charging effect during the measurement. The SEM images of the samples were recorded under high vacuum of about $1\times10^{-7}$ Torr. Stigmation was done to remove optical aberration and images were captured at different magnifications using a CCD camera. To determine the atomic and weight percent of the elements present in the samples, energy dispersive X-ray analysis was carried out simultaneously on the FE-SEM images. The EDX analyses were carried out at least at three different spots of a single SEM image to determine the uniformity (homogeneity) of a sample in terms of elemental composition.

## 2.7 Transmission Electron Microscopy (TEM) and Selected Area Electron Diffraction (SAED)

Transmission electron microscope is used to acquire high resolution images. In this technique, a beam of electron is permitted to pass through a thin sample under vacuum. The electron beam is generated from a tungsten source accelerated through an electric field of 50-300 kV [12]. Series of electromagnetic lenses are used to focus the electron beam on to the sample and the transmitted electrons are captured on a scintillation screen or an electronic detector to produce an image [13].

In the present study, TEM images of the nanocomposites were acquired using a FEI TECNAI $G^2$ 20 S-TWIN electron microscope operating at an accelerating voltage of 200 kV. For the TEM measurements, the sample preparation was carried out as follows: about 5 mg each of the sample powders was dispersed in about 5 mL of ethanol with the help of a low power sonicator. Further, a drop of the prepared dispersion was placed on carbon coated copper grid using a micropipette and the grid was allowed to dry in air. The prepared sample grids were inserted inside the specimen holder once the desired vacuum ($1\times10^{-9}$ Torr) is achieved using ion getter pump and turbo molecular pump. The Z-height of the sample specimen was adjusted to center the electron beam on the sample specimen and afterwards, the TEM images were acquired. Selected area diffraction pattern (SAED) of the samples was also recorded using the same TEM instrument which gives information about crystallinity and characteristic lattice spacing.

## 2.8 Diffuse Reflectance Spectroscopy (DRS)

When light radiation is incident on a powder, it gets scattered in all directions. This is known as diffuse reflection. The reflectance and optical absorption characteristics of nanocomposites were investigated using diffuse reflectance spectroscopy. From the reflectance spectra, the absorbance of nanocomposites were calculated using Kubelka-Munk equation [14]:

$$f(R) = \frac{(1-R)^2}{2R} = \frac{k}{s} = \frac{AC}{s} \tag{3}$$

Where R is the reflectance, k is the molar absorption coefficient, s is the scattering coefficient, A is the absorbance and C is the concentration of absorbing species.

The band gap ($E_g$) and the absorption coefficient ($\alpha$) of a direct band gap semiconductor is associated through the equation [15]:

$$\alpha h\nu = C_1 (h\nu - E_g)^{1/2} \tag{4}$$

Where $\alpha$ is linear absorption coefficient of the material, $h\nu$ is the photon energy and $C_1$ is the proportionality constant.

In the present study, diffuse reflectance spectra of the nanocomposites $NiO-Al_2O_3$, $PbS-Al_2O_3$ (Chapter 3) and $CdS-TiO_2$ (Chapter 4) were recorded using a Shimadzu UV3600 UV–visible NIR spectrophotometer along with a diffuse reflectance accessory (model: ISR-3100). For the $Ag_2S-TiO_2$ (Chapter 4) and $CdS-\gamma-Fe_2O_3$ (Chapter 5) nanocomposites, the reflectance spectra were recorded using a Shimadzu UV–2450 UV–visible spectrophotometer along with a diffuse reflectance accessory. The instrumental parameters for the reflectance measurements were: mode; % reflectance, slid width; 5 nm, time constant; 0.2 sec. The wavelength range for the $PbS-Al_2O_3$ nanocomposites was 1000 to 1800 nm and for all the other nanocomposites, the wavelength range was 200 to 800 nm. The reflectance spectra for $ZnO@\gamma-Fe_2O_3$ core-shell nanocomposites (Chapter 5) were recorded on a Varian Cary 5000 UV-VIS-NIR spectrophotometer attached with a diffuse reflectance accessory. $BaSO_4$ (Aldrich®) was used as the reference material in all the measurements and baseline correction was accomplished using $BaSO_4$ before recording the reflectance spectra for the samples. For sample preparation, about 40 mg of each of the sample powder was mixed with about 4 g of $BaSO_4$ homogeneously using a pestle and mortar. The homogeneous mixture was placed in the groove of sample holder and pressed with the help of cylindrical glass slide to make it planar. The sample holder was then placed inside the reflectance accessory to record the DRS spectrum.

## 2.9 UV-Visible Spectroscopy

UV-visible spectroscopy was used for monitoring the photodegradation and catalytic reactions. In the present study, the UV-visible absorption measurements were carried out during the photodegradation of rhodamine B (Chapter 6) and congo red (Chapter 6) using a Shimadzu UV–2450 UV–visible spectrophotometer in the spectral range 200 to 800 nm. UV-visible spectroscopy measurements were also carried to determine the band gap absorption for as prepared iron oxide nanoparticles, $Fe_3O_4$ nanoparticles and $ZnO@\gamma\text{-}Fe_2O_3$ core-shell nanocomposite (Chapter 5). The input instrumental parameters were: mode; absorbance, slit width; 2 nm and time constant; 0.2 sec. Before recording absorbance of the samples, baseline correction was performed by taking Millipore® water in two quartz cuvettes placed in reference and sample compartments. Afterwards, the absorbance spectra of the samples were acquired by taking two quartz cuvettes one filled with Millipore water as reference and another filled with the sample solutions. More details on the photodegradation and photocatalytic experiments carried out are given in Chapter 6.

## 2.10 Photoluminescence Spectroscopy (PL)

Photoluminescence spectroscopy is used to study optical properties of the materials. Photoluminescence is the emission of light by a (solid, liquid and gas) after absorption of electromagnetic radiation. Photoluminescence spectroscopy works on the principle that on absorption of electromagnetic radiation, the electrons get excited to a higher energy level and when the electrons return to the ground state energy level, they emit radiation of a characteristic wavelength [10]. Fluorescence and phosphorescence are two types of photoluminescence. When the excited electron returns to the ground state in 'ns' time, the emission is known as fluorescence and when the emission takes more time, the emission is known as phosphorescence [16].

In the present study, photoluminescence properties of $PbS\text{-}Al_2O_3$ nanocomposites (Chapter 3) were studied using a FLS980 Fluorescence Spectrometer (Edinburgh Photonics). The excitation wavelength was selected as 700 nm and the emission wavelength range was between 900 and 1150 nm. The photoluminescence spectra for $CdS\text{-}TiO_2$ (Chapter 4) and $ZnO@\gamma\text{-}Fe_2O_3$ nanocomposites (Chapter 5) were recorded using a Shimadzu RF 5301 PC spectrofluorophotometer. The $CdS\text{-}TiO_2$ and $ZnO@\gamma\text{-}Fe_2O_3$ nanocomposites were excited with excitation wavelengths of 380 nm and 325 nm, respectively. The photoluminescence spectra for $CdS\text{-}\gamma\text{-}Fe_2O_3$ nanocomposites (Chapter 5) were measured using a HORIBA Fluoromax-4

spectrofluorophotometer. The excitation wavelength was selected as 360 nm and the emission wavelength range was between 350 and 700 nm.

The sample preparation for the fluorescence measurements was carried out as follows: About 5 mg of each of the powder samples was dispersed in about 5 mL of water and sonicated for 10 minutes at room temperature. Then, the suspensions were taken in a quartz cuvette and the PL spectra were recorded at room temperature.

## 2.11 Surface Area and Pore Size Analyzer (BET method)

BET (Brunauer Emmitt Teller) method is used for the determination of surface area of solid samples from adsorption isotherm measurements. The BET equation is as follows [17,18]:

$$\frac{1}{V(1-(P_O/P))} = \frac{1}{V_m C} + \frac{C-1}{V_m C}\left(\frac{P}{P_O}\right) \qquad (5)$$

Where V is the volume of the gas adsorbed at a relative pressure, $P/P_0$, and $V_m$ is the volume of adsorbate gas when the adsorbent surface is covered with a monolayer. The term C is the BET constant, which is related to the energy of adsorption in the first adsorbed layer and accordingly its value indicates magnitude of the adsorbent/adsorbate interactions.

In the present study, surface area of the nanocomposites was measured using a NOVA 2200e (Quantachrome) autosorb instrument. Prior to the analysis, precisely weighed sample powders were degassed in a glass bulb cell at 100 °C for about 2 h. The instrumental parameters for the measurement were given using the Quantachrome™ NOVA Win software. After degassing, the bulb cell filled with sample was placed on the measurement station dipped in a dewar filled with liquid nitrogen. The specific surface area was calculated from the linear part of the nitrogen adsorption isotherm [17].

## 2.12 Gas Chromatography-Mass Spectroscopy (GC-MS)

GC-MS is the combination of gas chromatography and mass spectroscopy. It is used to determine different organic constituents present in a sample. Gas chromatography separates compounds present in a mixture on the basis of time required for the individual constituents to appear at end of the column. MS identifies the species on the basis of mass to charge ratio (m/z) of ions produced when the compound is bombarded with different types of particles such as electrons [10]. In the present study, Gas chromatography–mass spectrometry (GC–MS) was used for the identification and the quantification of the products after oxidation of styrene by tert-butyl hydroperoxide (TBHP) in the presence of $NiO–Al_2O_3$ nanocomposites as the catalyst

(Chapter 3). The analysis was done on a Perkin–Elmer Clarus 680 gas chromatograph coupled with a Perkin–Elmer Clarus SQ 8T mass detector. The column (Elite 5MS) used was of length 30 m, i.d.0.25 mm, film thickness 0.25 μm and temperature range was 80–280°C. After the catalytic reaction, the products solution mixture was diluted using acetonitrile (1:10) and about 1-2 μL of the solution was injected into the GC column using a micro syringe for the analysis.

## 2.13 Superconducting Quantum Interference Device (SQUID)

SQUID is a superconducting device used to study magnetic properties of the materials. It measures magnetic flux and output voltage or current signal developed around superconducting loops consisting of Josephson junctions [19]. A Josephson junction consists of two superconductors separated by a thin insulating layer such that electrons can pass through it. The movement of current in the absence of applied voltage in the Josephson junction is known as Josephson tunneling. The maximum current that a Josephson junction can support without developing any voltage across it is called critical current ($I_c$). In the absence of applied voltage, the net magnetic flux across the loop is zero. This is because of opposite and equal magnetic flux against the applied magnetic field that develops due to Meissner effect. In the presence of a sample, a voltage will develop across the junction due to induced magnetization in the sample and the magnetic properties of the materials can be studied by varying the temperature or the magnetic field. SQUID is a sensitive device and it can measure low magnetic field up to the order of $10^{-18}$ T [20].

In the present study, magnetic measurements of the $NiO-Al_2O_3$ nanocomposites (Chapter 3) were carried out using the superconducting quantum interference device (Quantum Design, MPMS XL-7) by varying the field up to 7 Tesla at two different temperatures; 300 K and 5 K. Field cooled (FC) and zero field cooled (ZFC) magnetization measurements were carried out using the same instrument by varying the temperature from 300 K to 5 K under an applied field of 100 Oe.

The sample preparation for the magnetic measurement was done as follows: About 20 to 40 mg of the sample powder was compactly packed in a sample holder. The sample holder was attached to a sample rod with the help of a non-magnetic tape. The sample rod was then inserted into a homogeneous magnetic field due to which magnetization was induced in the sample. The instrumental parameters for the measurement were given to the magnetometer using MPMS multiVu® software. After that, the sample rod was moved along its axis to determine the position at which maximum magnetization is induced in the sample at a fixed applied field. Later, the magnetization values of the sample were recorded at that optimized position by

varying the temperature and the magnetic field. The sensitivity of the SQUID magnetometer was about $1 \times 10^{-9}$ emu.

## 2.14 Vibrating Sample Magnetometer (VSM)

Vibrating sample magnetometer is a technique which measures magnetic moment of a sample when it is vibrating perpendicularly under a uniform magnetic field [21]. VSM works on the principle of Faraday's Law of induction, which states that when magnetic field is changed around a coil it will induce an electric field in it. This electric field induced in the coil is measured as to get information about the changing magnetic field [22]. In VSM, the sample is subjected to a sinusoidal motion. The electric signal produced on vibration of the sample in changing magnetic field is received by pick-up coils. The electrical output signals have the same frequency as vibrational motion of the sample and its intensity is proportional to magnitude of the magnetic moment of the sample. The data acquired is collected by a computer to obtain the magnetization curves.

In the present study, magnetic measurements of CdS-$\gamma$-Fe$_2$O$_3$ nanocomposites (Chapter 5) and ZnO@$\gamma$-Fe$_2$O$_3$ core-shell nanocomposites (Chapter 5) were carried out using 3 Tesla cryogen free mini Vibrating Sample Magnetometer (VSM) with a pulse cryocooler (CRYOGENICS Ltd, UK). The variation of the magnetization with temperature was studied by the same instrument in the zero-field-cooled/field-cooled (ZFC/FC) mode under an applied magnetic field of 0.05 T, between 4 K and 300 K. The sample preparation for the magnetic measurements was carried out as follows: About 10 to 20 mg of the sample was compactly packed in the sample capsule. Then, the sample capsule was attached to a sample tube (straw) with the help of a non-magnetic tape. The sample tube was fixed with the sample probe vibrator again with the help of the non-magnetic tape. After that, the sample probe was placed inside the Cryostat magnet having constant magnetic field due to which the sample get magnetized. The input instrumental parameters were given using Cryogenics Limited Software which was created using the LabVIEW® graphical programming application developed by the National Instruments Corporation. The sample probe was moved along its axis under constant magnetic field to fix the position of maximum magnetization for the sample. Afterwards, the magnetization of the sample was recorded with respect to changing temperature or magnetic field. The temperature of the sample was controlled using a Lakeshore model-350 temperature controller.

**References**

1.  Cullity B. D., 'Elements of X-ray diffraction', *Addison-Wesley Publishing Company Inc.* (1956).

2.  Waseda Y., Matsubara E., Shinoda K., 'X-Ray diffraction crystallography', *Springer* (2011).

3.  Patterson A. L., 'The Scherrer formula for X-ray particle size determination', *Physical Review*, **56**, 978–982 (1939).

4.  Tasumi M., 'Introduction to experimental infrared spectroscopy', *John Wiley & Sons, Ltd.* (2015).

5.  Silverstein R. M., Webster F. X., Kiemle D. J., 'Spectrometric identification of organic compounds', *John Wiley & Sons, Inc.* (2005).

6.  Zheng X., Zong C., Xu M., Wang X., Ren B., 'Raman imaging from microscopy to nanoscopy, and to macroscopy', *Small*, **11**, 3395–3406 (2015).

7.  Colthup N. B., Daly L. H., Wiberley S. E., 'Introduction to infrared and Raman spectroscopy', *Academic Press* (1990).

8.  Broido A., 'A simple , sensitive graphical method of treating thermogravimetric analysis data', *Journal of Polymer Science, Part A-2 Polymer Chemistry*, **7**, 1761–1773 (1969).

9.  Bottom R., 'Thermogravimetric analysis, in principles and applications of thermal analysis', *Blackwell Publishing Ltd, Oxford, UK* (2008).

10. Skoog D. A., West D. M., Holler F. J., Crouch S. R., 'Fundamental of analytical chemistry', *Mary Finch* (2014).

11. Goldstein, J., Newbury, D.E., Joy, D.C., Lyman, C.E., Echlin, P., Lifshin, E., Sawyer, L., Michael J. R., 'Scanning electron microscopy and X-ray microanalysis', *Springer* (2003).

12. Pennycook S. J., Nellist P. D., 'Scanning transmission electron microscopy, imaging and analysis', *Springer* (2011).

13. Williams D. B., Carter C. B., 'Transmission electron microscopy. A textbook for material science', *Springer* (2009).

14. Kortum G., 'Reflectance spectroscopy principles, methods, applications', *Springer-Verlag New York* (1969).

15. Morales A. E., Mora S., Pal U., 'Use of diffuse reflectance spectroscopy for optical characterization of un-supported nanostructures', *Revista Mexicana de Física*, **53**, 18–22 (2007).

16. Shinde, K.N., Dhoble, S.J., Swart, H.C., Park K., 'Phosphate phosphors for solid-state lighting', *Springer-Verlag Berlin Heidelberg* (2012).

17. Dollimore D., Spooner P., Turner A., 'The BET method of analysis of gas adsorption data and its relevance to the calculation of surface areas', *Surface Technology*, **4**, 121–160 (1976).

18. Condon J. B., 'Surface area and porosity determinations by physisorption measurement and theory', *Elsevier B.V.* (2006).

19. Arndt M., Hornberger K., 'Testing the limits of quantum mechanical superpositions', *Nature Physics*, **10**, 271–277 (2014).

20. Wernsdorfer W., 'From micro- to nano-SQUIDs: Applications to nanomagnetism', *Superconductor Science and Technology*, **22**, 064013/1–064013/13 (2009).

21. Foner S., 'Versatile and sensitive vibrating-sample magnetometer', *The Review of Scientific Instruments*, **30**, 548–557 (1959).

22. Buschow K. H. J., Boer F. R. De., 'Physics of magnetism and magnetic materials', *Kluwer Academic/Plenum Publishers* (2004).

# CHAPTER 3

*Synthesis and Characterization of*

*NiO-Al$_2$O$_3$ and PbS-Al$_2$O$_3$*

*Nanocomposites by Sol-Gel Method*

**3.1 Synthesis and Characterization of NiO-Al$_2$O$_3$ Nanocomposites by Sol-Gel Method**

**3.1.1 Introduction**

Due to presence of many phases, nanocomposites possess multi-functional properties [1]. Different physical and chemical methods have been reported in the literature to prepare nanocomposites. They include chemical vapour deposition, ball milling, spray pyrolysis, co-precipitation, hydrothermal, homogeneous precipitation, thermal decomposition, and sol-gel methods [2–4]. Among these reported methods, sol–gel method has received considerable attention for the synthesis of metal oxides with specific textural and microstructural characteristics [5]. It offers many advantages such as good chemical homogeneity, high purity, lower calcination temperatures and control of particle size [6]. Some of the examples of metal oxide nanocomposites prepared using sol-gel method are Co$_3$O$_4$-TiO$_2$, MgO–Al$_2$O$_3$, Au-TiO$_2$, and ZnO-TiO$_2$ [7–10].

Nickel oxide is a binary transition metal oxide with a wide range of applications as a p-type semiconductor with a wide band gap (3.6–3.8 eV) [11]. Nanostructured NiO shows interesting optical, magnetic and electronic properties due to quantum confinement. Alumina is one of the most widely used ceramic materials as catalyst, support, adsorbent, and in wear resistant coating [12,13]. NiO-Al$_2$O$_3$ nanocomposites have been widely used as catalyst in industrial processes such as hydrogenation, dehydrogenation, petroleum refining, methanation, CO$_2$ reduction and fuel cells [14–19]. They also possess applications in protective barriers, electro chromic materials and sensors [20–23]. Different methods such as sol-gel [22–29], impregnation [30–33], co-precipitation [34], homogeneous precipitation [35], solid-state reaction [36], sonochemical method [37], hydrothermal [38,39], spray pyrolysis [40,41], chemical vapour deposition (CVD) [42] and pulse laser deposition [43] have been used for the preparation of NiO-Al$_2$O$_3$ nanocomposites. A brief summary on the synthesis of NiO-Al$_2$O$_3$ nanocomposites by the above mentioned methods are given in Table 3.1. A brief discussion on each of these methods is given below.

**Table 3.1:** Different reported methods for the synthesis of NiO-Al$_2$O$_3$ nanocomposites.

| Sl. No. | Method | Chemicals used | Morphology of the product | Size | Reference |
|---------|--------|----------------|---------------------------|------|-----------|
| 1. | Sol-gel process | Nickel nitrate and aluminum isopropoxide | Nanotubes | 8.5-12.8 nm | [29] |
| 2. | Impregnation | Nickel nitrate and aluminum scrap | Plates | 20-28 nm | [31] |
| 3. | Co-precipitation | Nickel nitrate, aluminium nitrate and ammonium hydroxide | Agglomerated particles | 20-40 nm | [34] |
| 4. | Homogeneous precipitation | Nickel nitrate and aluminium nitrate and urea | Needle-like crystals | 3 nm | [35] |
| 5. | Solid state reaction | Nickel oxide and $\gamma$-alumina | Powder | - | [36] |
| 6. | Sonochemical | Nickel tetracarbonyl and aluminum sec-butoxide | Spheres | 30 nm | [37] |
| 7. | Hydrothermal | Nickel nitrate, alum, and urea | Nano-flakes | 30 nm | [38] |
| 8. | Spray pyrolysis | Nickel nitrate, triethanolamine, and aluminum tris(sec-butoxide) | Spheres | 10-100 nm | [40] |
| 9. | Chemical vapour deposition | Nickel bis(1-dimethylamino-2-methyl-2-butanolate), and trimethylaluminium | Thin film | 15 nm | [42] |

| 10. | Pulse laser deposition | $Al_2O_3$ and Ni target | Thin film | - | [43] |
|-----|------------------------|-------------------------|-----------|---|------|

*Sol-gel process* [29]*:* The synthesis of NiO-$Al_2O_3$ nanocomposites by sol-gel process is illustrated in scheme 3.1. In a typical synthesis, first, polymer Pluronic F127 is dissolved in ethanol. Then specified amount of nitric acid, nickel nitrate and aluminium isopropoxide are added to the above solution with vigorous stirring. The resulting solution is covered with polyethylene film to prevent evaporation of ethanol and stirred for 5h at room temperature. After that, the solution is kept for drying at 60 °C for 48 hours in air. The collected powder samples are calcined at 400°C, 600°C, 700°C, 800°C for 4 h.
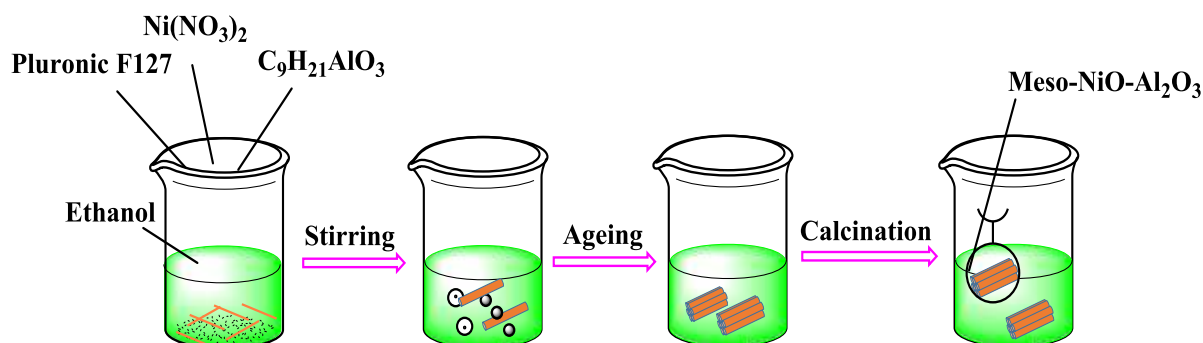


**Scheme 3.1:** Synthesis of NiO-$Al_2O_3$ nanocomposites by sol-gel process [29].

Crisan et al., [24] have used simultaneous gelation of nickel nitrate hexahydrate and aluminium isopropoxide. Shon et al. [26] have used P123 as an organic additive to increase the surface area of the NiO-$Al_2O_3$ nanocomposites. Zhang et al. [27] have prepared NiO-$Al_2O_3$ nanocomposites by combining sol-gel and impregnation methods. Tadanaga et al. have prepared NiO-$Al_2O_3$ films coated on soda-lime silica glass plates [28]. Fig. 3.1 shows TEM images of nanocomposites prepared using the sol-gel process [44–47].
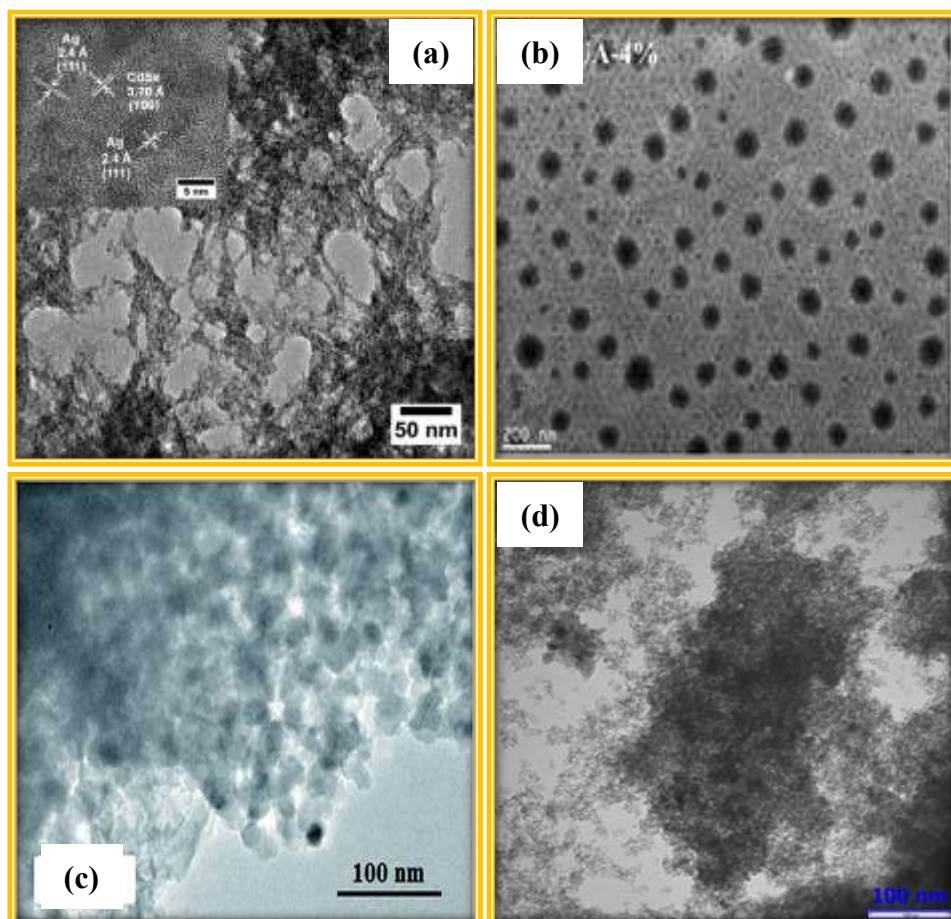
**Fig. 3.1:** TEM images of nanocomposites prepared using sol-gel-process; (a) CdSe-Ag hybrid nanocomposites (in the inset, HRTEM image), (b) polyurethane acrylate/silica (PUA/SiO$_2$) nanocomposite, (c) Cu-doped TiO$_2$–reduced graphene oxide nanocomposite, and (d) RuNi-doped TiO$_2$–Al$_2$O$_3$ nanocomposite [44–47].

*Impregnation* [31]*:* In this method, an aqueous solution of nickel nitrate is mixed with calcined sol-gel alumina at room temperature. The suspension is maintained at 80 $^o$C under reduced pressure for 24 h to completely remove the solvent. After that, the content is dried at 80 $^o$C (24 h) and then calcined at 750 $^o$C to the get NiO/Al$_2$O$_3$ nanocomposite.

*Co-precipitation* [34]*:* In this method, aqueous solutions of nickel nitrate and aluminium nitrate are mixed in specific proportions with the help of stirring at 60 $^o$C. The pH of the solution is increased to 9 by drop wise addition of 5% NH$_3$.H$_2$O solution. The temperature of the solution is further increased to 90 $^o$C and kept for 1 h with constant stirring. The precipitate obtained is filtered, washed with deionized water and dried in air.

*Homogeneous precipitation* [35]*:* In this method, the metal salt solutions are prepared by dissolving specified amounts of nickel nitrate and aluminium nitrate in distilled water. The precipitant solution is prepared by dissolving urea in distilled water. The metal solution and the precipitant solution are mixed and reacted at 85 $^{\circ}$C for 10 h. After this, the precipitates are filtered, washed and dried at 110 $^{\circ}$C overnight. The dry powders obtained are calcined at 650 $^{\circ}$C to get NiO-Al$_2$O$_3$ nanocomposites.

*Solid state reaction* [36]*:* In a typical synthesis, NiO and γ-alumina pre-heated at 600 $^{\circ}$C for 6 h are mixed in an agate mortar using acetone as a mixing aid and ethyl cellulose as a binder. The mixture is placed on alumina disk support and annealed three times in air at 1400 $^{\circ}$C for 24 h in a furnace to get NiO-Al$_2$O$_3$ nanocomposites.

*Sonochemical synthesis* [37]: Sonochemical coating of nanosized nickel has been carried out on submicrospherical alumina which is prepared by the hydrolysis of aluminum sec-butoxide in a dilute mixture of 1-octanol, 1-butanol, and acetonitrile in the presence of hydroxypropyl cellulose (dispersant). An appropriate amount of alumina spheres and nickel tetracarbonyl are added to a sonication cell filled with decalin under flowing argon. The irradiation of nickel tetracarbonyl and alumina spheres is carried out using a high-intensity ultrasonic Ti-Horn (Vibracell, 20 kHz, 100W/cm$^2$) under argon at 0 $^{\circ}$C for 1 h. The product is then washed thoroughly with hexane in a glove box. The samples obtained are heated at 550 and 700 $^{\circ}$C in air to get NiO coated Al$_2$O$_3$ microspheres.

*Spray pyrolysis method* [40]*:* In this method, first the precursors alumatrane and nickel propionate are prepared in high purity by complex chemical routes. Then, precise amount of alumatrane solution and nickel propionate solutions are mixed in ethanol. The resulting solution is atomized using an atomizer at ~60 mL/min to produce an oxygen rich aerosol. The aerosol is ignited through methane-oxygen pilot torch in the combustion chamber. The combustion of the aerosol occurs at temperatures greater than 1500 °C producing nanopowders and gaseous byproducts. The powders are collected in electrostatic precipitators. Fig. 3.2 shows the TEM images for NiO-Al$_2$O$_3$ nanocomposite prepared using spray pyrolysis method.
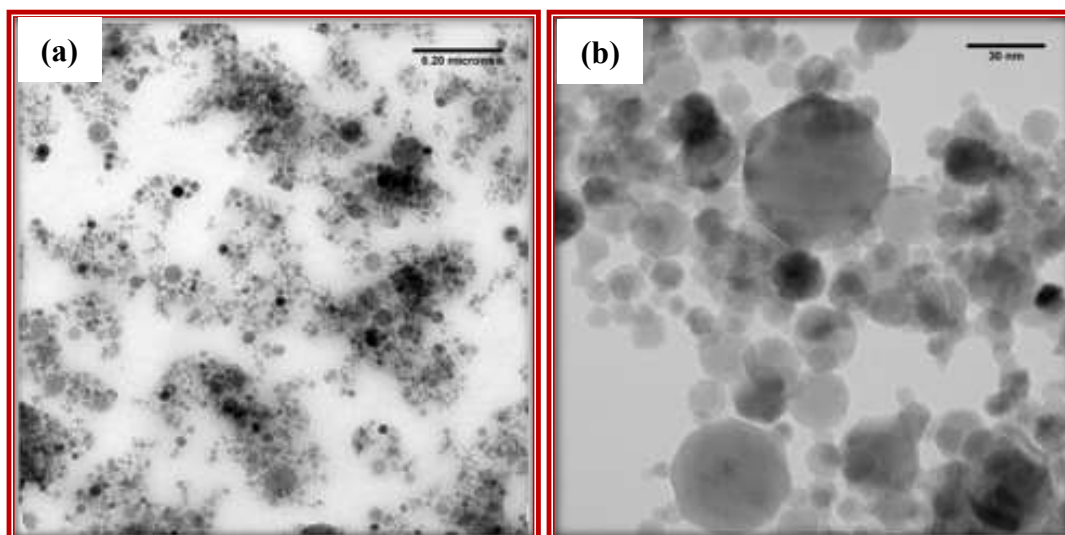
**Fig. 3.2:** TEM micrographs of NiO-Al$_2$O$_3$ nanocomposite prepared by spray pyrolysis method, (a) showing distribution of particles throughout the sample and (b) specific weak agglomerate showing average particle size < 30 nm [40].

*Hydrothermal synthesis* [38]*:* In this method, firstly NiAl-LDH precursors are synthesized by hydrothermal method and then calcined to get the NiO-Al$_2$O$_3$ nanocomposites. In a typical synthesis, specified amount of alum and urea are dissolved in an aqueous solution of nickel nitrate under vigorous stirring for 30 minutes at room temperature. After that the solution is transferred into a 50 mL Teflon-lined autoclave and heated at 180 $^{\circ}$C for 15 h. The precipitate obtained is washed and separated by centrifugation and then dried at 60 $^{\circ}$C for 4 h. The obtained NiAl-LDH powders are calcined at 800 $^{\circ}$C for 5 h to get NiO-γ-Al$_2$O$_3$ nanocomposites.

*Chemical vapour deposition* [42]*:* In this method, NiO layers are deposited using MOCVD (Metal Organic Chemical Vapour Deposition) from Ni(dmamb)$_2$ (dmamb = 1-dimethylamino-2-methyl-2-butanolate) in oxygen atmosphere at 315 $^{\circ}$C on a polycrystalline 12 nm thick Al$_2$O$_3$ layer.

*Pulse laser deposition* [43]*:* In this method, a KrF pulsed laser is used to ablate the target in a high vacuum chamber (vacuum ~7×10$^{-8}$ Torr). The wavelength of the excimer laser is 248 nm with a frequency of 5 Hz. The target consists of one piece of high-purity Al$_2$O$_3$ round target and a square piece of high-purity Ni target. The deposited thin film is annealed at 600 $^{\circ}$C in the chamber with an oxygen partial pressure of 5 ×10$^{-2}$ Torr or in ambient N$_2$ to get Ni/NiO core shell nanoparticles deposited on Al$_2$O$_3$.

Using the reported synthetic methods, it takes about three to six days to prepare the $NiO-Al_2O_3$ nanocomposites. In the present study, $NiO-Al_2O_3$ nanocomposites have been synthesized by single step sol-gel method using simple precursors (nickel acetate and aluminium isopropoxide) which takes shorter time (~48 hours) compared to the reported sol-gel methods and impregnation, solid state reaction and spray pyrolysis methods.

### 3.1.2 Experimental Details

**Chemicals**

The chemicals used for the synthesis of $NiO-Al_2O_3$ nanocomposites were aluminium isopropoxide (Aldrich), nickel acetate (Aldrich), toluene (Rankem), ammonia solution (Rankem), ethanol (Changshu Yangyuan Chemicals, China) and Millipore® water. All the chemicals were used as received.

**Synthesis**

The $NiO-Al_2O_3$ nanocomposites were prepared by sol-gel process. Scheme 3.2 shows the schematic representation of synthesis of $NiO-Al_2O_3$ nanocomposites by the sol-gel process. Nickel acetate and aluminium isopropoxide were taken in a beaker with different molar ratios (0.5:1, 1:1 and 2:1). Then, 80 mL ethanol and 1 mL water were added. The contents were stirred for 3 hours at room temperature. Then, 50 mL of toluene and 4 mL of aqueous ammonia solution were added with continuous stirring. After a period of 15 minutes, 2 mL of water was added for hydrolysis. The contents were kept for stirring for 23 hours at room temperature resulting in the formation of sol. The obtained sol was evaporated to get a gel and the gel was kept in an oven at 80 °C overnight for drying. The green coloured powder obtained was calcined at different temperatures (500 °C, 700 °C and 900 °C) in a muffle furnace to obtain the nanocomposites. The designation of various $NiO-Al_2O_3$ nanocomposites prepared under different synthetic conditions is given in Table 3.2.

```
┌──────────────┐     ┌──────────────┐     ┌──────────────┐     ┌──────────────┐
│ Ni(Ac)₂.4H₂O │  ✚  │  Al(iOPr)₃   │  ✚  │ EtOH (80 mL) │  ✚  │  H₂O (1 mL)  │
└──────────────┘     └──────────────┘     └──────────────┘     └──────────────┘
```

i) Stirred for 3h at RT
ii) Addition of 50 mL of toluene
   and 4 mL of 25% aq. NH₃ solution
iii) Stirred for 15 min at RT
iv) Addition of 2 mL of H₂O
v) Stirred for 23 h at RT

**Sol**

⇩ Evaporation at 80 °C

**Gel**

⇩ Dried in an oven at 80 °C

**As-prepared samples**

⇩ Calcined at 500 °C, 700 °C and 900 °C

**NiO–Al₂O₃ nanocomposites**
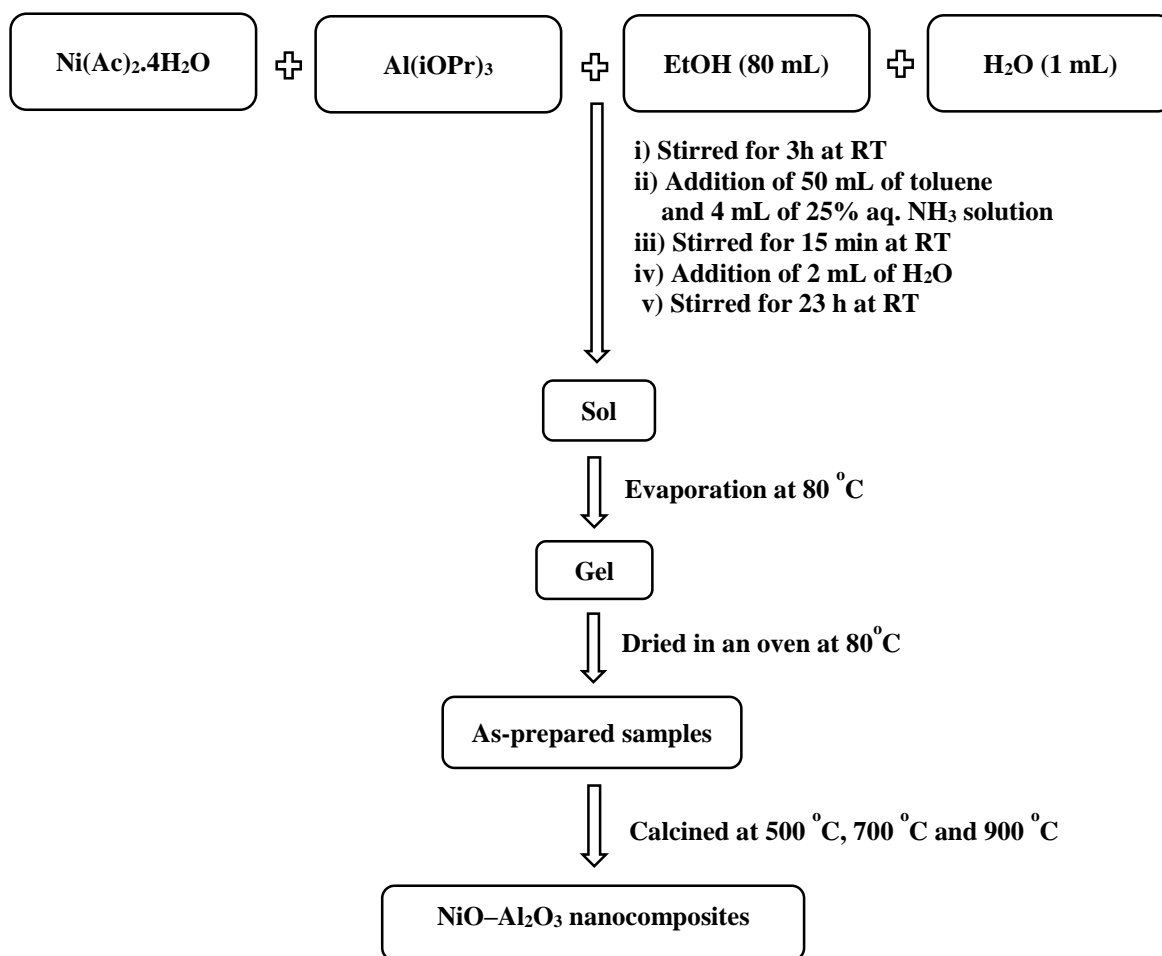
**Scheme 3.2:** Synthesis of NiO-Al$_2$O$_3$ nanocomposites by sol-gel process.

**Table 3.2:** Designation of various nanocomposites prepared in the present study.

| Nanocomposite | Amount of Ni(Ac)₂.4H₂O (mmol) | Amount of Al(iOPr)₃ (mmol) | $[Ni^{2+}]:[Al^{3+}]$ |
|---|---|---|---|
| LN1 | 4.5 | 9 | 0.5:1 |
| LN2 | 9 | 9 | 1:1 |
| LN3 | 18 | 9 | 2:1 |

### 3.1.3 Results and Discussion

### 3.1.3.1 XRD Results

Fig. 3.3(a) shows the XRD patterns of as-prepared $NiO-Al_2O_3$ nanocomposites and Figs. 3.3(b), (c) and (d) show the XRD patterns of nanocomposites after calcination of samples at 500 °C, 700 °C and 900 °C, respectively. The XRD patterns of all the as-prepared nanocomposites show peaks at $2\theta$ = 21.72°, 35.74°, and 61.27° due to $\alpha-Ni(OH)_2 0.75H_2O$ (JCPDS file no. = 38-0715). Nanocomposite LN3 shows an additional peak ($2\theta$ = 12.6°) due to nickel oxide hydroxide (JCPDS file no. = 40−1179), one peak ($2\theta$ = 13.8°) due to nickel acetate hydrate (JCPDS file no. = 49−1173) and one peak at $2\theta$ = 19.25° due to $\beta-Ni(OH)_2$ (JCPDS file no. 14−0117). The XRD patterns of the nanocomposites after calcination at 500 °C and 700 °C show peaks due to cubic NiO (JCPDS file No. 78−0643) whereas the XRD patterns recorded after calcination at 900 °C show peaks due to NiO and spinel $NiAl_2O_4$ (JCPDS file No. 01−1299). The crystallite size of pure and NiO in the nanocomposites was calculated using Debye−Scherer's formula. The crystallite size of pure NiO, after calcination at 500 °C and 700 °C, were 11.3 nm and 16.4 nm, respectively. The crystallite size of NiO in the nanocomposites after calcination at 500 °C varies from 2.6 to 3.5 nm. The crystallite size of NiO in the nanocomposites after calcination at 700 °C varies from 2.8 to 3.9 nm. The crystallite size of NiO in the nanocomposites increases with an increase in the calcination temperature. The crystallite size of NiO in the nanocomposites after calcination at 900 °C could not be calculated because at 900 °C nickel aluminate is formed and its XRD peaks overlap with that of NiO. Nickel aluminate is formed by incorporation of nickel in boehmite formed during the hydrolysis of aluminium isopropoxide followed by calcination at 900 °C [48].
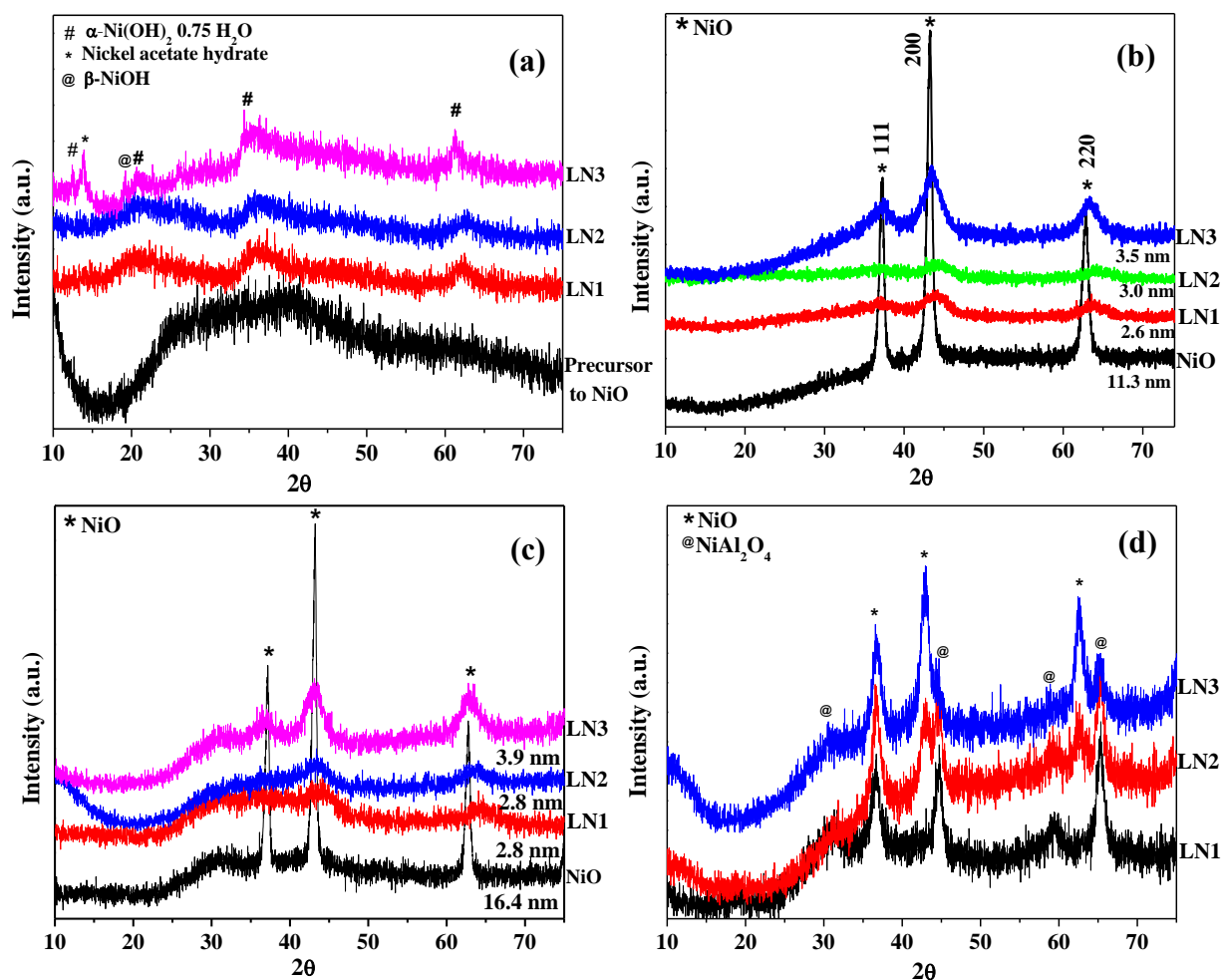
**Fig. 3.3:** XRD patterns of NiO-Al$_2$O$_3$ nanocomposites: (a) as prepared, (b) after calcination at 500 $^{\circ}$C, (c) after calcination at 700 $^{\circ}$C and (d) after calcination at 900 $^{\circ}$C.

### 3.1.3.2 FT-IR Results

Fig. 3.4 shows the IR spectra of NiO−Al$_2$O$_3$ nanocomposites. All the as-prepared and calcined nanocomposites show broad bands due to hydroxyl stretching due to physisorbed water at about 3400 cm$^{-1}$. The bands at 2929 cm$^{-1}$ and 2850 cm$^{-1}$ are attributed to C-H stretching. The band at 1640 cm$^{-1}$ is assigned to bending vibration of the water molecules. The band at 1410 cm$^{-1}$ is attributed to stretching mode of carbonate ions [49]. The bending vibrational mode of Al-OH appears at 1029 cm$^{-1}$ [50]. The IR band at 674 cm$^{-1}$ is assigned to Ni-OH bond [49]. After calcination at 500 $^{\circ}$C, the nanocomposites show bands at 811 cm$^{-1}$, 598 cm$^{-1}$ and 489 cm$^{-1}$. The band at 811 cm$^{-1}$ is attributed to vibrational mode of surface Al-O bond and the band at 598 cm$^{-1}$ is assigned to the stretching vibrational mode of octahedrally coordinated Al-O [24].

The band at 489 cm$^{-1}$ is due to characteristic Ni-O stretching present in pure NiO nanoparticles and in all the nanocomposites [24,51]. After calcination, the intensity of the bands at 3400 cm$^{-1}$, 2929 cm$^{-1}$, 1640 cm$^{-1}$ due to hydroxyl stretching, C-H stretching and O-H bending, respectively, decreases in the nanocomposites compared to the as-prepared nanocomposites. This is due to loss of water molecules and organic content at higher temperature. The FT-IR spectra of the nanocomposites, after calcination at 900 °C, show bands at 733 cm$^{-1}$ and 489 cm$^{-1}$. The band at 733 cm$^{-1}$ is attributed to tetrahedrally coordinated Al-O bond and the band at 489 cm$^{-1}$ is attributed to characteristic Ni-O stretching [24,51]. In the calcined NiO-Al$_2$O$_3$ nanocomposites, the IR bands due to Al-OH and Ni-OH are absent compared to the IR spectra of as prepared nanocomposites.
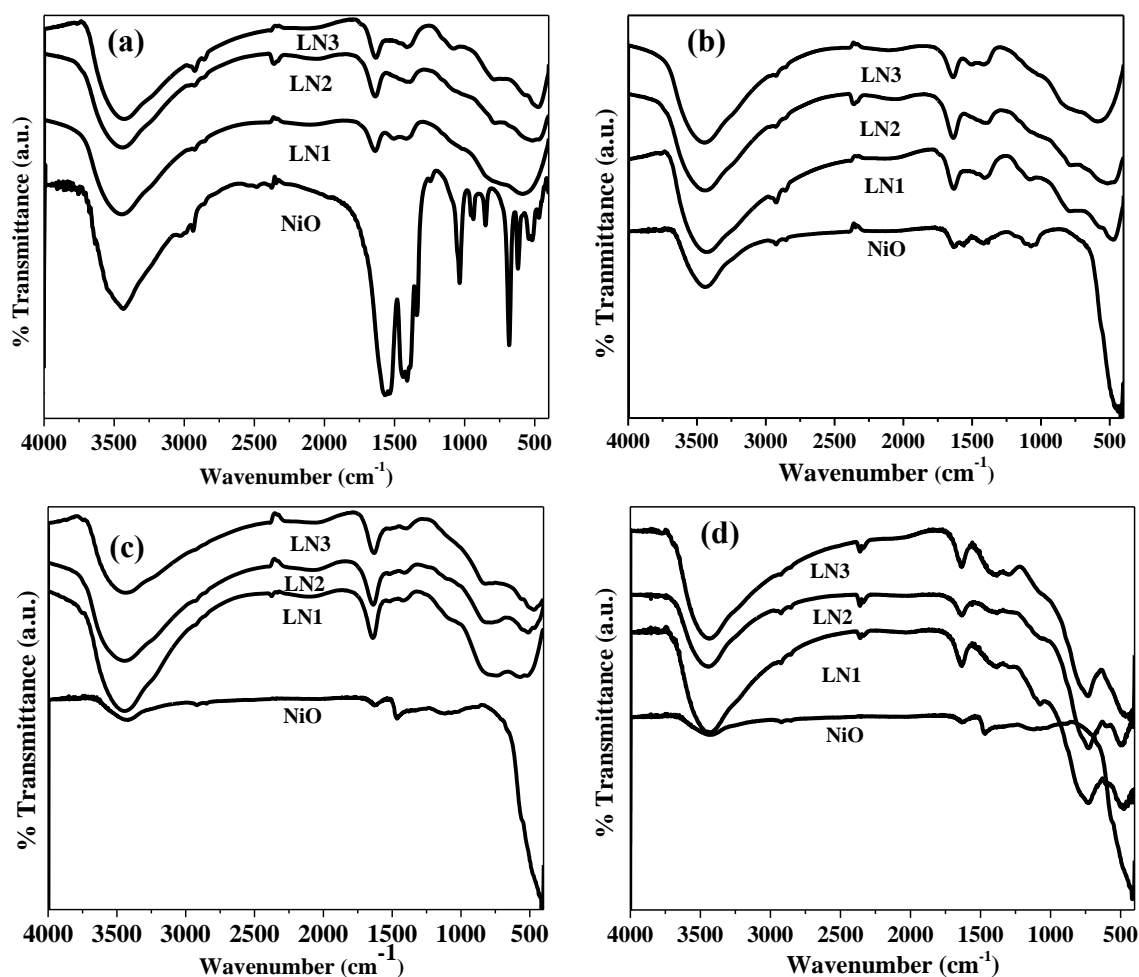


**Fig. 3.4:** IR spectra of NiO-Al$_2$O$_3$ nanocomposites: (a) as prepared and (b) after calcination at 500 °C, (c) after calcination at 700 °C and (d) after calcination at 900 °C.

### 3.1.3.3 Raman Spectroscopy Studies

Fig. 3.5 shows the Raman spectra of pure NiO nanoparticles and the NiO−$Al_2O_3$ nanocomposites. Pure NiO nanoparticles possess Raman bands at 360 cm$^{-1}$, 527 cm$^{-1}$, 690 cm$^{-1}$ and 1064 cm$^{-1}$. The bands at 360 cm$^{-1}$ and 527 cm$^{-1}$ are attributed to first order transverse optical (1TO) and longitudinal optical (1LO) phonon modes of NiO, respectively. The bands at 690 cm$^{-1}$ and 1064 cm$^{-1}$ are assigned to second order transverse optical (2TO) and longitudinal optical (2LO) phonon modes of NiO, respectively [52,53].

The Raman spectrum of nanocomposite LN1 shows bands at 576 cm$^{-1}$ and 822 cm$^{-1}$ that could be attributed to first order longitudinal optical phonon mode (1LO) and TO + LO mode of NiO [52,53]. Nanocomposite LN2 shows only one band at 576 cm$^{-1}$ that is attributed to first order longitudinal optical phonon mode (1LO). Nanocomposite LN3 shows bands at 360 cm$^{-1}$, 576 cm$^{-1}$, and 1050 cm$^{-1}$. The bands at 360 cm$^{-1}$ and 576 cm$^{-1}$ are attributed to first order transverse optical (1TO) and longitudinal optical (1LO) phonon modes of NiO, respectively. The band at 1050 cm$^{-1}$ is assigned to longitudinal optical (2LO) phonon mode of NiO [52,53]. The Raman shift of 1LO band at 527 cm$^{-1}$ in pure NiO nanoparticles to 576 cm$^{-1}$ in the NiO−$Al_2O_3$ nanocomposites is attributed to the decrease of size of NiO in the NiO−$Al_2O_3$ nanocomposites [54,55]. Yang et al. have ascribed the Raman shift to size-induced phonon confinement effect and surface relaxation [55]. The intensity of bands at 690 cm$^{-1}$ (2TO) and 1064 cm$^{-1}$ (2LO) decreases from nanocomposites LN3 to LN1. This is also attributed to decrease in the size of the NiO nanoparticles in the nanocomposites from LN3 (3.5 nm) to LN1 (2.6 nm) [54]. When the size of nanoparticles is comparable to exciton diameter of the semiconductor (for NiO, it is 7.7 nm) [54], the size confinement leads to a rapid decrease of 2LO frequency [54,55]. According to Gandhi et al. as the size of NiO nanoparticles decreases, the intensity of band at 1064 cm$^{-1}$ (2LO mode) rapidly decreases which is attributed to finite size-effect which confines the lattice vibrations [56]. Also, the intensity of one phonon modes (e.g. band 576 cm$^{-1}$) increases in the nanocomposites compared to pure NiO. This is attributed to decrease in the size of NiO in the nanocomposites. Mironova-Ulmane et al. have reported an increase in the intensity of one phonon mode bands with decrease in size of NiO and this is attributed to the presence of defects or surface effects [53].

85
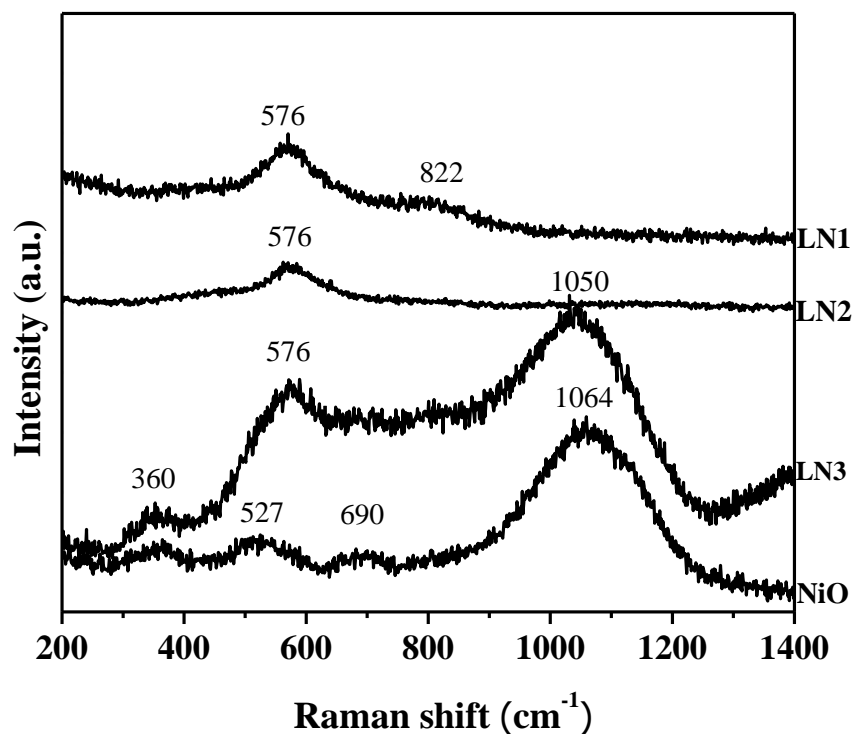
**Fig. 3.5:** Raman spectra of pure NiO and NiO-Al$_2$O$_3$ nanocomposites (LN1, LN2 and LN3).

## 3.1.3.4 TGA/DTG Analysis

Fig. 3.6(a-c) represents TGA patterns of as prepared NiO-Al$_2$O$_3$ nanocomposites. Composite LN1 shows a total weight loss of 49.1%. This weight loss occurs in three steps; the first step occurs upto 91 $^o$C with a weight loss of 7% due to removal of organic matter (e.g. ethanol), and physisorbed water. The second step in the temperature range 100 $^o$C to 250 $^o$C with a weight loss of 17.1% arises due to the evolution of interstitial water. The final step is upto 480 $^o$C with a weight loss of 26.2% and it is due to the dehydroxylation of boehmite and nickel hydroxide into Al$_2$O$_3$ and NiO, respectively [57–59]. Composites LN2 and LN3 show similar TGA patterns as that of LN1 with overall total weight losses of 52.2% and 53.1%, respectively.
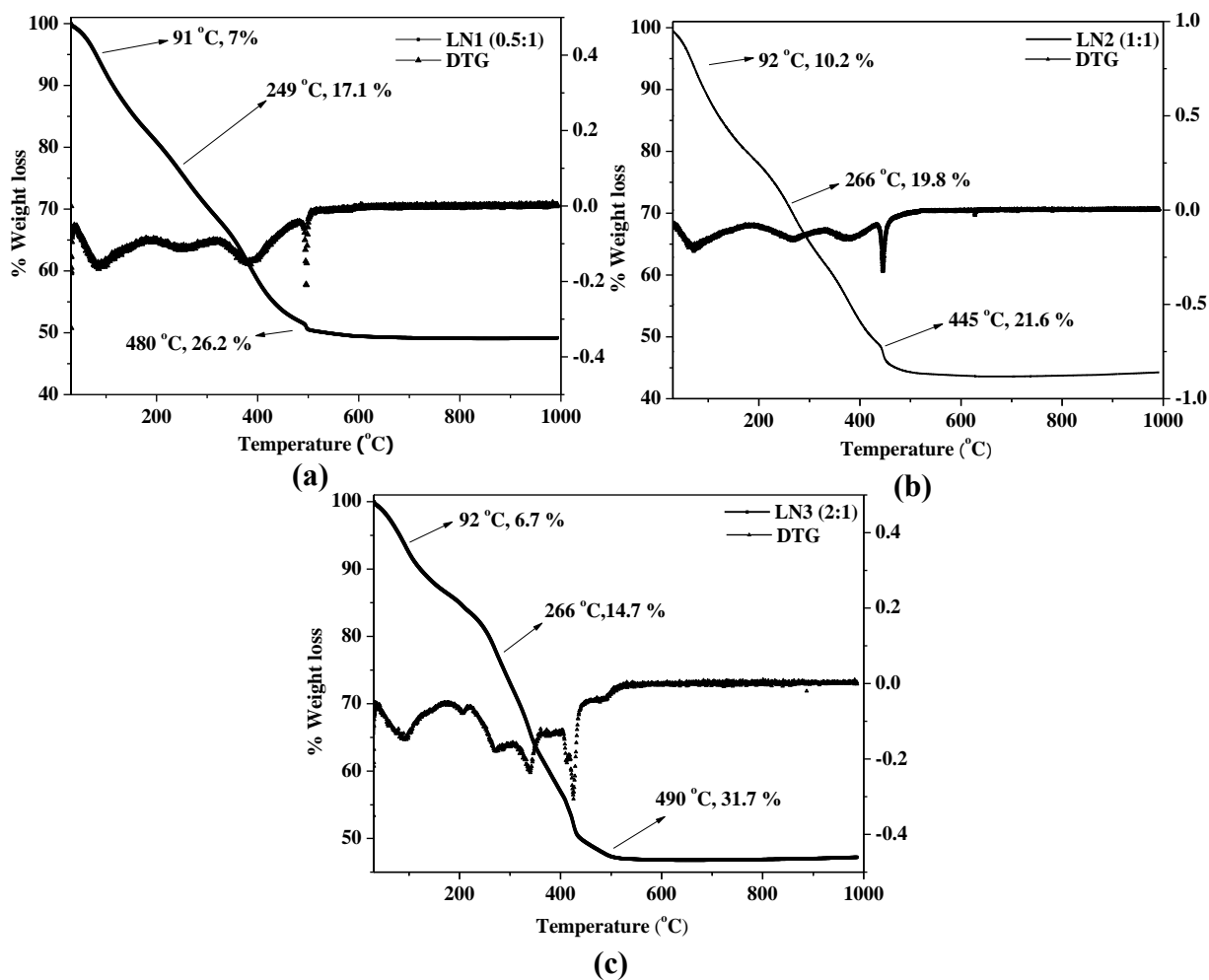
**Fig. 3.6:** TG-DTG curves of as-prepared nanocomposites LN1 (a), LN2 (b) and LN3 (c).

### 3.1.3.5 TEM and EDXA Results

TEM images of the NiO−Al$_2$O$_3$ nanocomposites are shown in Fig. 3.7. The TEM images of nanocomposites LN1 (Fig. 3.7(a)) and LN3 (Fig. 3.7(c)) show web-like structures. Nanocomposite LN2 (Fig. 3.7(b)) shows larger particles with agglomeration. Inset of image Fig. 3.7(a) corresponds to SAED pattern of the NiO where spots observed are due to (200), (111), (220) and (311) planes confirming the presence of single crystalline NiO. Inset of image Fig. 3.7(b) and Fig. 3.7(c) correspond to SAED patterns of the NiO where rings are observed confirming the presence of polycrystalline NiO.
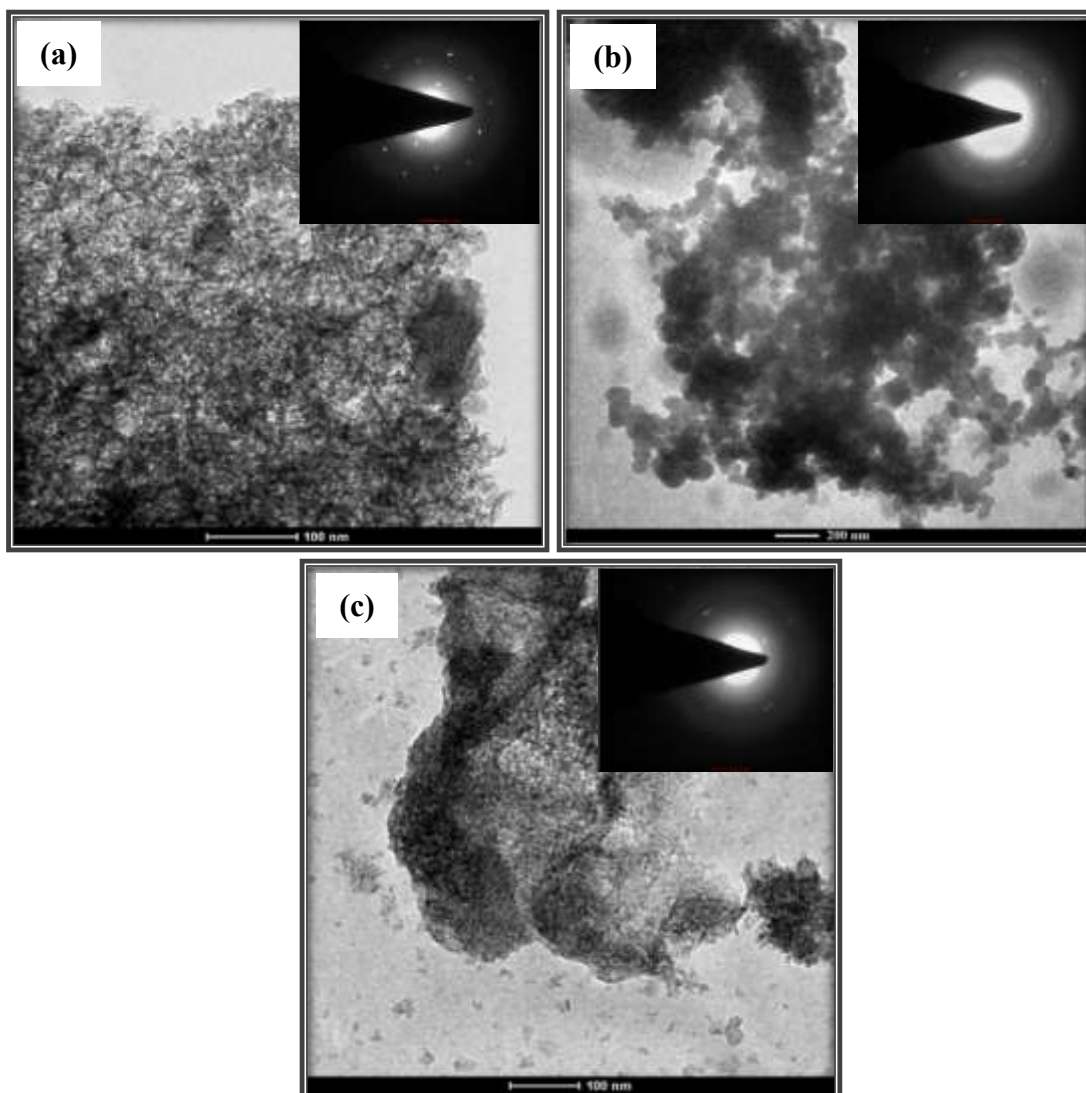
**Fig. 3.7:** TEM images of NiO-Al$_2$O$_3$ nanocomposites calcined at 500 $^\circ$C: (a) LN1, (b) LN2 and (c) LN3.

Fig. 3.8 shows the EDXA patterns of NiO-Al$_2$O$_3$ nanocomposites (LN1-LN3). The EDX analysis shows the presence of oxygen, aluminum and nickel in all the NiO-Al$_2$O$_3$ nanocomposites. Table 3.3 shows the EDX analysis results of the NiO-Al$_2$O$_3$ nanocomposites (LN1-LN3). Nanocomposite LN1 was found to have uniform elemental distribution compared to the other two nanocomposites LN2, and LN3 (Table 3.2). In LN1, the %wt. of aluminum varies from 25.3 to 25.8 and the %wt. of nickel varies from 39.5 to 40.7. In LN2, the %wt. of aluminium varies from 39.2 to 41.2 and the %wt. of nickel varies from 31.9 to 34.6 and in LN3, the %wt. of aluminium varies from 4.7 to 18.4 and the %wt. of nickel varies from 59.3 to 71.1.
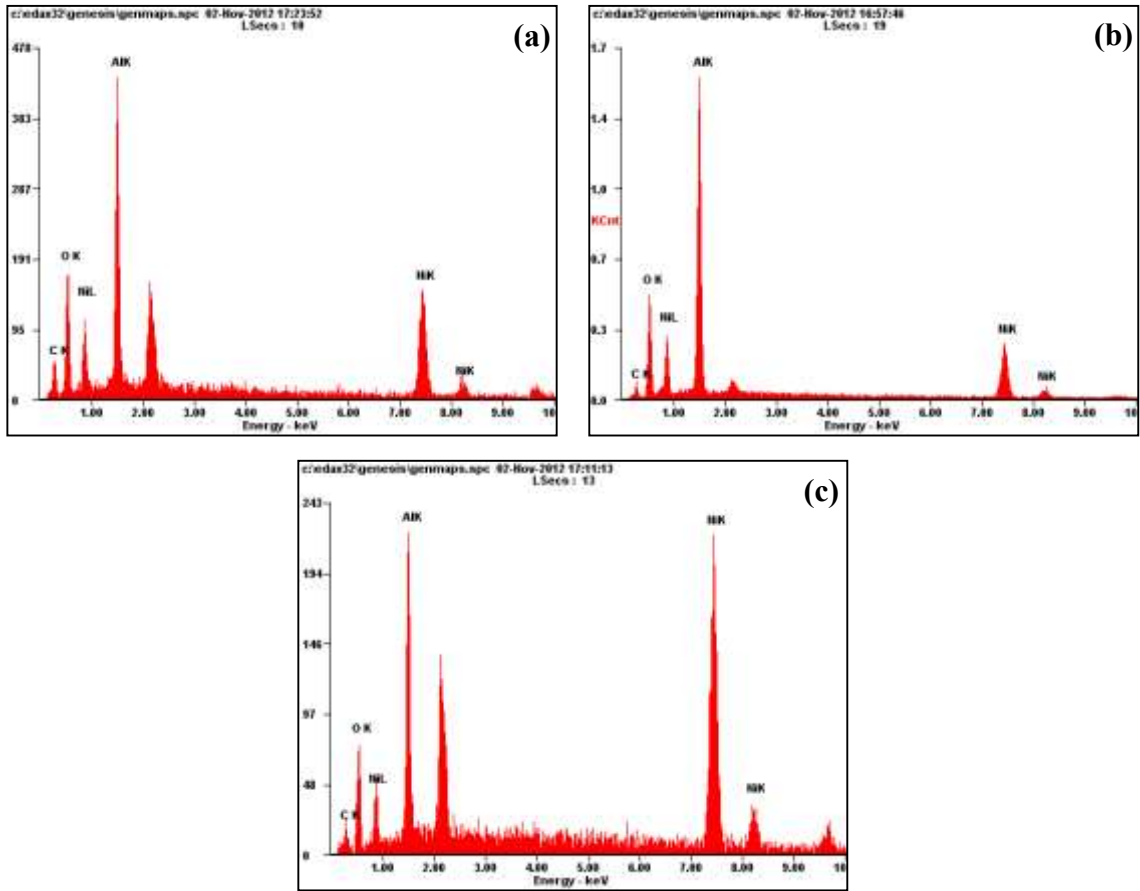
**Fig. 3.8:** EDXA patterns of NiO-Al$_2$O$_3$ nanocomposites calcined at 500 °C: (a) LN1, (b) LN2 and (c) LN3.

**Table 3.3** EDX analysis data of the NiO-Al$_2$O$_3$ nanocomposites.

| EDX Analysis Data | | | | | | | | |
|---|---|---|---|---|---|---|---|---|
| **Nanocomposite** | **C** | | **O** | | **Al** | | **Ni** | |
| | Wt% | At% | Wt% | At% | Wt% | At% | Wt% | At% |
| **LN1** | 8.2 | 17.7 | 19.2 | 30.9 | 25.8 | 24.3 | 40.7 | 18.2 |
| | 7.3 | 15.6 | 19.5 | 31.2 | 25.3 | 23.1 | 39.5 | 16.4 |
| **LN2** | 8.2 | 17.7 | 19.2 | 30.9 | 39.2 | 30.9 | 34.6 | 15.2 |
| | 7.3 | 15.6 | 19.5 | 31.2 | 41.2 | 39.2 | 31.9 | 13.9 |
| **LN3** | 10.3 | 26.1 | 11.9 | 22.5 | 18.4 | 20.7 | 59.3 | 30.6 |
| | 19.8 | 49.7 | 4.5 | 8.4 | 4.7 | 5.3 | 71.1 | 36.6 |

### 3.1.3.6 DRS Results

NiO is a semiconductor with a bulk band gap of 3.9-3.8 eV [11]. Fig. 3.9 shows the UV-visible diffuse reflectance spectral results of pure NiO nanoparticles and NiO−$Al_2O_3$ nanocomposites after calcination at 500 $^{\circ}$C. The band gap values of pure NiO and nanocomposites were calculated by using the formula as given below:

$$E_g = \frac{1240}{\lambda \ (nm)}$$

NiO nanoparticles show a band gap of 4.0 eV. Nanocomposite LN1, prepared using a molar ratio of nickel acetate and aluminium isopropoxide 0.5:1, shows the highest band gap (4.8 eV). Nanocomposite LN2, prepared using molar ratio of 1:1, shows a band gap of 4.6 eV and nanocomposite LN3, prepared using a molar ratio of 2:1, shows a band gap of 4.5 eV. The NiO−$Al_2O_3$ nanocomposites show an increase in the band gap with decrease in the concentration of nickel acetate used during the synthesis. The size of NiO nanoparticles in the NiO−$Al_2O_3$ nanocomposites decreases with the concentration of nickel acetate used during the sol-gel process (3.5 nm for LN3 to 2.6 nm for LN1). The increase in the band gap with decrease in size of NiO is attributed to quantum size effect. When the size of a particle becomes comparable to its Bohr radius (for NiO it is 7.7 nm), the continuous energy levels splits into discrete energy levels leading to an increase in the gap between the energy levels [54].
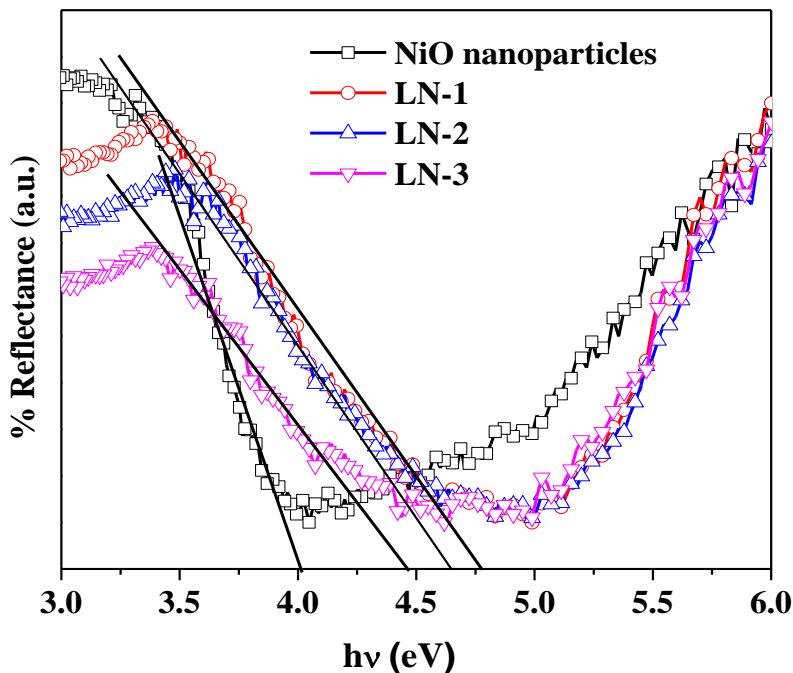
**Fig. 3.9:** UV-visible diffuse reflectance spectra of $NiO$-$Al_2O_3$ nanocomposites (calcination temp. = 500 $^{o}C$).

### 3.1.3.7 Magnetic Measurements

Fig. 3.10 shows the magnetization versus field curves (M-H) for pure nickel oxide nanoparticles and the $NiO-Al_2O_3$ nanocomposites. Bulk NiO is antiferromagnetic with a Neel temperature ($T_N$) of 523 K [60]. Pure NiO nanoparticles calcined at 500 $^{o}C$ show hysteresis at 5 K with a remanent magnetization ($M_r$) of 0.27 emu/g and coercivity ($H_c$) of 1000 Oe; no saturation of magnetization is observed (Fig. 3.10(a)). The M-H curve at 300 K shows superparamagnetic behaviour. All the $NiO-Al_2O_3$ nanocomposites show superparamagnetic behaviour with no saturation of magnetization at 5 K (Figs. 3.10(b), (c) and (d)). The non-saturation behaviour of the curves observed at 5 K and 300 K is associated with the antiferromagnetic core of the NiO nanoparticles [61]. At 5 K, the $M_r$ and $H_c$ values for the nanocomposite LN1 are negligible whereas nanocomposite LN2 shows a $M_r$ value of 0.17 emu/g and $H_c$ value of 151 Oe. Nanocomposite LN3 exhibits a $M_r$ value of 0.45 emu/g. The higher $M_r$ in the case of nanocomposite, LN3 compared to pure NiO nanoparticles, is attributed to smaller particle size of NiO in the nanocomposites [38]. The increase in the remanent magnetization in case of nanocomposite LN3, compared to nanocomposites LN1 and LN2, is due to an increase in the relative concentration of NiO in nanocomposite LN3 [43].
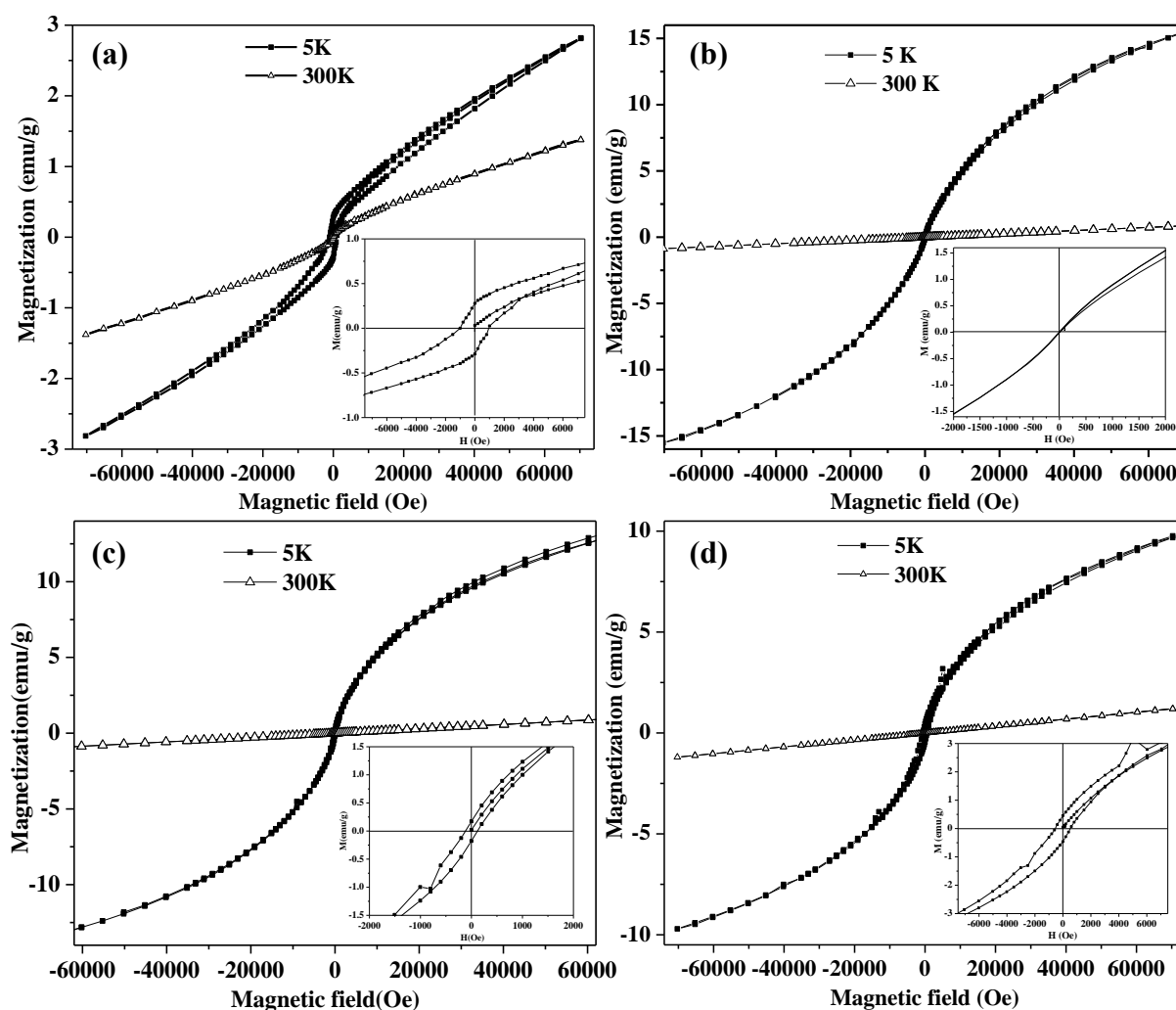
**Fig. 3.10:** M-H curves for (a) NiO nanoparticles and NiO-Al$_2$O$_3$ nanocomposites: (b) LN1, (c) LN2 and (d) LN3.

Fig. 3.11 shows the ZFC and FC curves measured for the NiO-Al$_2$O$_3$ nanocomposites under an applied field of 100 Oe. For the ZFC measurement, the samples were first cooled to 5 K in the absence of magnetic field. A field of 100 Oe was then applied and magnetization was measured with an increase in temperature up to 300 K. For the FC measurement, the sample was cooled in the presence of an external magnetic of 100 Oe and then, magnetization of the sample was measured with an increase in temperature under the same magnetic field. No peak is observed in the ZFC-FC curves for NiO nanoparticles (Fig. 3.11(a)). This is due to the absence of antiferromagnetic ordering [61]. A rapid increase in the magnetization at low temperatures is observed, which is attributed to the presence of uncorrelated spins on the surface of NiO nanoparticles. The ZFC and FC curves of NiO nanoparticles show bifurcation at about 225 K,

as reported in the literature [54]. The temperature at which bifurcation of the ZFC and FC curves occurs is called as irreversible temperature ($T_{irr}$) above which all the spins are unblocked [54,61]. The ZFC and FC curves for the nanocomposites LN1, LN2 and LN3 (Fig. 3.11(b-c)) show bifurcation at 65 K, 80 K and 110 K, respectively. The bifurcation temperature shifts to lower temperature with a decrease in the NiO particle size in the NiO−$Al_2O_3$ nanocomposites [54,61].
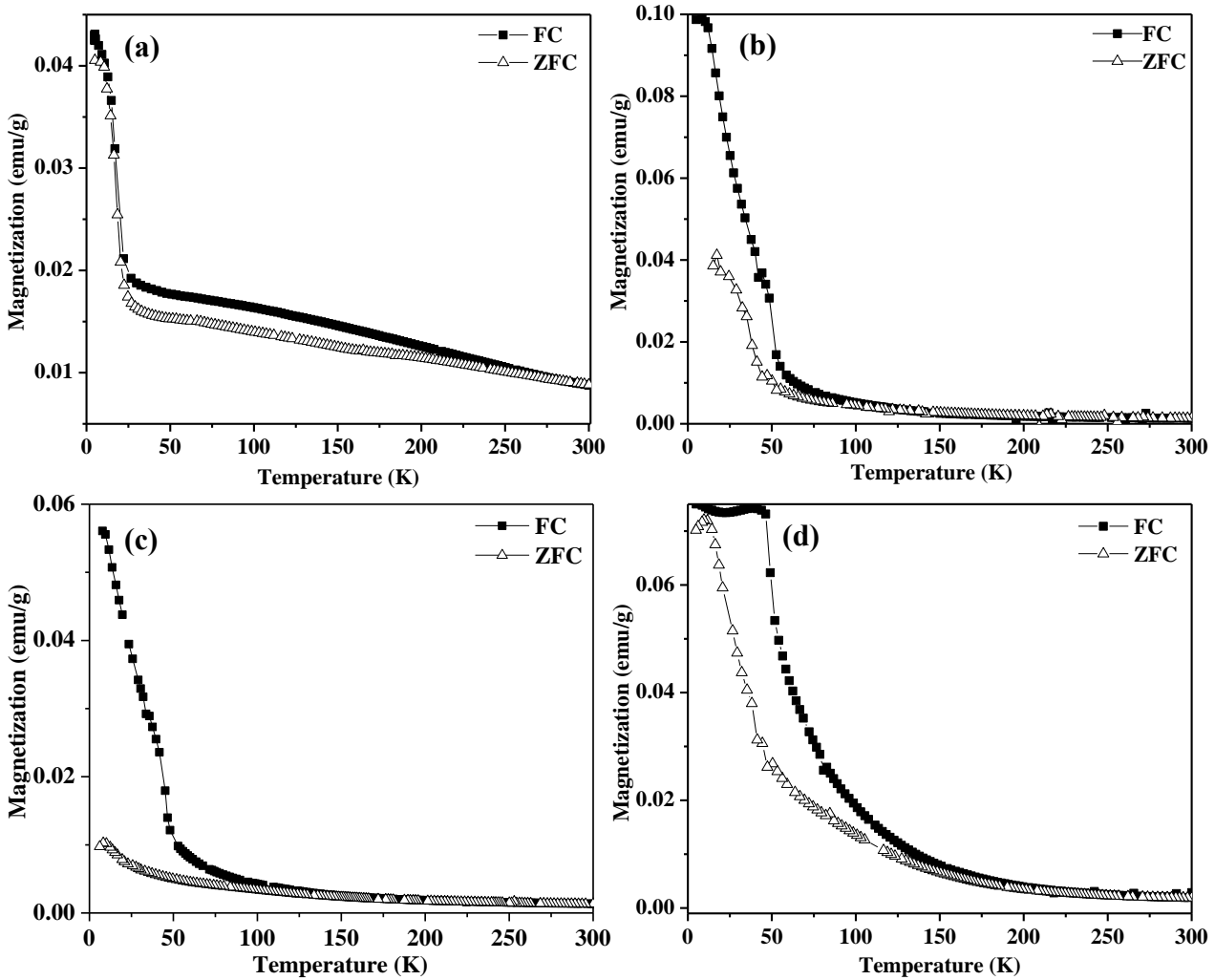


**Fig. 3.11:** ZFC-FC curves for (a) NiO nanoparticles and NiO-$Al_2O_3$ nanocomposites: (b) LN1, (c) LN2 and (d) LN3.

### 3.1.3.8 Surface Area Analysis (BET)

The BET surface area values for the NiO−Al$_2$O$_3$ nanocomposites LN1, LN2 and LN3 are 336.7 m$^2$/g, 293.7 m$^2$/g and 216.6 m$^2$/g, respectively. The NiO−Al$_2$O$_3$ nanocomposites possess higher surface area compared to pure alumina (267 m$^2$/g) and pure NiO nanoparticles (25.4 m$^2$/g). The surface area of the nanocomposites decreases as the concentration of nickel acetate, used during preparation of the nanocomposites, increases from LN1 to LN3. This is explained in terms of the formation of relatively larger NiO particles as the concentration of nickel acetate is increased [22].

### 3.1.3.9 Mechanism of formation of NiO-Al$_2$O$_3$ nanocomposites

NiO-Al$_2$O$_3$ nanocomposites are formed via hydrolysis of mixture of nickel acetate and aluminium isopropoxide in a mixture of ethanol and water. The hydrolysis of nickel acetate leads to the formation of Ni(OH)$_2$ [62,63].

$$Ni(CH_3COO)_2.4H_2O + 2H_2O \rightarrow Ni(OH)_2 + 2CH_3COOH + 4H_2O$$
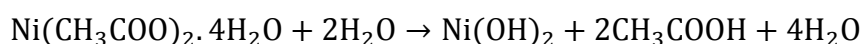
Aluminium isopropoxide is hydrolyzed to yield an alcohol (ROH, R = (CH$_3$)$_2$CH) and hydroxylated aluminium centers (Al–OH) [64]. The −Al–OH groups get linked to each other via polycondensation which leads to the formation of Al–O–Al network. The number of Al–O–Al bonds increases with time and individual molecules are aggregated to form sol, which further condenses to form gel of boehmite (AlO(OH)).

$$Al(OR)_3 + H_2O \rightarrow Al(OR)_2(OH) + ROH$$

$$Al(OR)_2(OH) + H_2O \rightarrow AlO(OH) + 2ROH$$

$$-Al(OH) + -Al(OH) \rightarrow Al-O-Al + H_2O$$
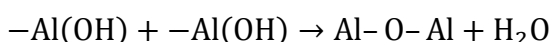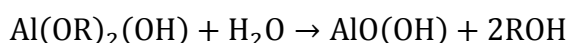
The dehydration of Ni(OH)$_2$ and AlO(OH) (boehmite) (present in as prepared samples as confirmed by the XRD results) by calcination (at 500 °C and 700 °C) leads to the formation of NiO-Al$_2$O$_3$ nanocomposites [64,65].

$$Ni(OH)_2 + 2AlO(OH) \xrightarrow{\Delta} NiO - Al_2O_3 + 2H_2O$$
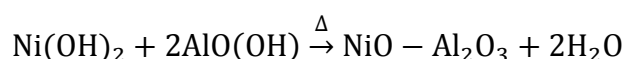
### 3.1.4 Conclusions

A sol-gel method for the synthesis of $NiO-Al_2O_3$ nanocomposites has been described. The nanocomposites were characterized using different sophisticated analytical techniques. XRD results confirm the presence of small NiO nanocrystallites in the nanocomposites. The crystallite size of NiO in the nanocomposites increases with an increase in concentration of nickel acetate used during the sol-gel process. EDXA and TEM results suggest uniform distribution of small NiO nanoparticles on the surface of alumina with web-like morphology for nanocomposites LN1 and LN3. Diffuse reflectance spectral studies indicate higher band gap of NiO in the nanocomposites compared to bulk NiO. The band gap of NiO in the nanocomposites increases with decrease in the particle size and this is attributed to quantum size effect. The nanocomposites exhibit superparamagnetism at 5K and show higher remanent magnetization compared to pure NiO nanoparticles. The $NiO-Al_2O_3$ nanocomposites are expected to be useful as good heterogeneous catalysts.

## 3.2 Synthesis and Characterization of PbS-Al$_2$O$_3$ Nanocomposites by Sol-Gel Method

### 3.2.1 Introduction

Synthesis of nanomaterials with tunable optical and photophysical properties has been a subject of intense interest [66,67]. Size dependence of band gap in semiconductor nanoparticles is well known and varying their size allows tunable optical properties for the semiconductor nanostructures [68,69]. Metal sulfides are important materials because of their wide applications in optoelectronics and catalysis [70–72]. PbS is an important IV-VI semiconductor with rock salt structure with a direct band gap of 0.41 eV. It has a small effective mass of charge carriers and a high value of dielectric constant [73]. PbS has a large exciton Bohr radius (18 nm) due to which quantum confinement effect is observed even for PbS with relatively large particle size [74]. By varying the size and shape of PbS nanoparticles, it has been possible to tune the band gap from 0.3 eV to 5.2 eV [74–76]. Due to their unique optical properties, PbS based nanomaterials possess various applications in lasers diodes [77], light-emitting diodes [78], detectors [79], nonlinear optics [80], single electron devices [81], optical switches [82], optical amplification [83], telecommunication [75] and biological imaging [84]. An exceptional third order nonlinear optical absorption for PbS nanoparticles has been reported [85]. Nanocomposites based on PbS have received considerable interest and PbS nanocomposites with Au [86], Ag [87], poly (vinyl alcohol) [88], polystyrene [89], CdS [90], Ag$_2$S [91], PbTe [92], PbSe [93], ZnS [94], TiO$_2$ [95] ZnO [96], SiO$_2$ [97] and Fe$_3$O$_4$ [98] have been reported. Fig. 3.12(a) shows room temperature PL spectra of apoferritin-PbS nanocomposites [99]. Their PL emission maxima are tunable by varying the diameter of PbS quantum dots from 2 to 8 nm. Inset of Fig. 3.12(a) shows PL of PbS solution injected within the peritoneal cavity of a mouse cadaver and this is an example of bio imaging application of apoferritin encapsulated PbS quantum dots. Fig. 3.12(b) shows TEM images of unstained and negatively stained apoferritin-PbS nanocomposite.
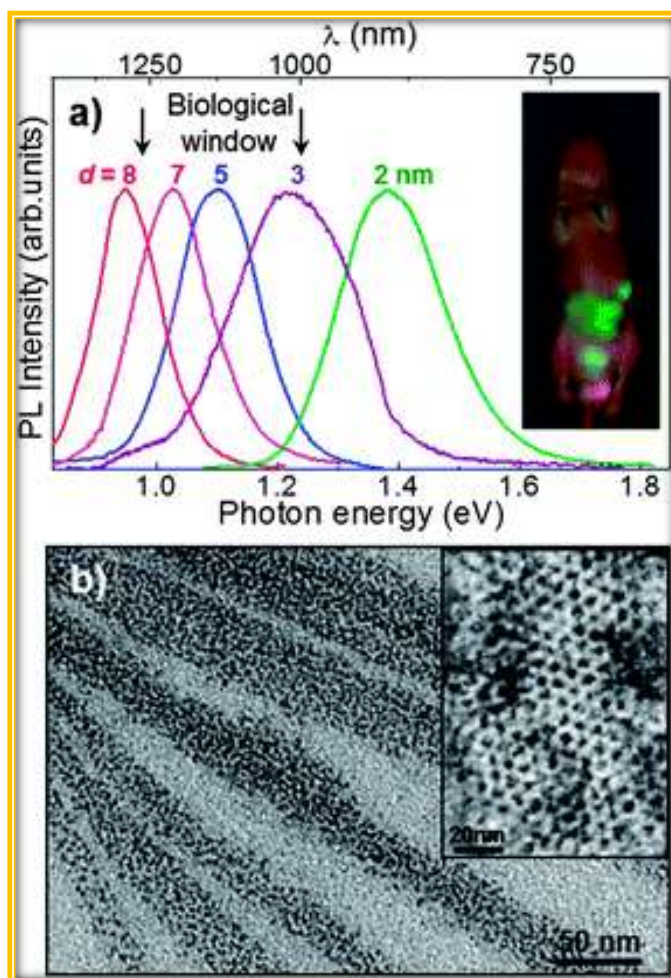
**Fig. 3.12:** (a) Room temperature PL spectra of PbS quantum dots with different sizes. Inset: the PL of PbS solution injected in mice via the peritoneal cavity, and (b) TEM images of unstained and (inset) negatively stained apoferritin-PbS [92].

Alumina is considered as one of the advanced materials for its wide applications in microelectronics, refractories, catalysis, and ceramics [100,101]. In recent times, a lot of work has been carried out on alumina supported metal sulfides, e.g. $CdS/Al_2O_3$ [102], $ZnS/Al_2O_3$ [103] and $NiMoS/Al_2O_3$ [104]. Alumina supported metal sulfides possess applications in water splitting [102], photocatalysis [105], $H_2$ production [103] and hydrogenation of tetralin [104]. Li et al. have explored photocatalytic application of $Al_2O_3/g$-$C_3N_4$ nanocomposite. Fig. 3.13(a) and (b) show TEM and HRTEM image of $g$-$C_3N_4$-$Al_2O_3$ nanocomposite. Fig. 3.13(c) shows a schematic representation of electron transfer and radical generation in $Al_2O_3/g$-$C_3N_4$ hetreojunction.

**Fig. 3.13:** (a) TEM and (b) HRTEM images of $Al_2O_3/g$-$C_3N_4$ nanocomposite and (c) schematic diagram of electron transfer and radical generation over $Al_2O_3/g$-$C_3N_4$ heterojunction [105].

Sol-gel method has been widely used to prepare metal oxide nanoparticles by hydrolysis of metal alkoxides or halides [100]. Materials obtained by this method possess high surface area, high porosity and high thermal stability [106]. The advantage of this method is the intimate molecular level mixing of the components [107]. Sol-gel method has been used for the preparation of PbS nanocomposites [108–111]. Different methods such as electrodeposition [112,113], atomic layer deposition [114–116], solid state reaction [117,118] have been used for the preparation of PbS-$Al_2O_3$ nanocomposites. A brief summary on the synthesis of PbS-$Al_2O_3$ nanocomposites by the above mentioned methods are describe below (Table 3.4).

**Table 3.4:** Different reported methods for the synthesis of PbS-$Al_2O_3$ nanocomposites.

| Sl. No. | Method | Chemicals used | Morphology of the product | Size | Reference |
|---------|--------|----------------|---------------------------|------|-----------|
| 1. | Electrodeposition | Al sheets, lead chloride and sulfur | Film | 30 nm | [112] |

| 2. | Atomic layer deposition | Trimethyl aluminum, lead oxide, and bis(trimethylsilyl) sulfide | Film | 30 nm | [115] |
|---|---|---|---|---|---|
| 3. | Solid state reaction | Alumino-alkali-silicate glass, lead chloride and sulfur | - | 5.8–9.7 nm | [117] |

*Electrodeposition method* [112]*:* PbS nanowires arrays fabricated into alumina membrane have been prepared by electrodeposition method. Porous alumina films which are used as templates are prepared by two-step anodization process [112]. For the PbS electrodeposition, the alumina film is deposited with a Pt film by sputtering to serve as a conductive electrode. Aligned PbS nanowire arrays in the anodized alumina membrane (AAM) templates are produced by applying AC 12 V (60 Hz) electrodeposition in a dimethylsulfoxide (DMSO) solution containing lead chloride and elemental sulfur. After the deposition, the AAM templates with PbS nanowires are washed and rinsed with dimethylsulfoxide and then with de-ionized water, and finally air dried at room temperature. Chen et al. [113] have also prepared PbS nanocrystals in porous alumina membranes.

*Atomic layer deposition method (ALD)* [114]*:* PbS colloidal quantum dots deposited on $Al_2O_3$ film have been prepared by atomic layer deposition (ALD). First, oleylamine coated PbS colloidal quantum dots are prepared by thermal decomposition of $PbCl_2$ and elemental sulfur at 125 $^{o}$C in $N_2$ atmosphere. Then, PbS photoelectrodes are prepared by layer by layer deposition on a silicon substrate. The PbS photoelectrodes are further passivated with $Al_2O_3$ in an ALD chamber. First, the ALD chamber is pumped by a turbo molecular pump to a base pressure of $10^{-4}$ Pa. Samples are then placed on a resistive heating element located at the center of the ALD chamber. The samples are successively exposed to trimethyl aluminum and water vapor each for a time period of 3 second at a pressure of $5 \times 10^{-1}$ Pa. Then, the chamber temperature is increased to 100 $^{o}$C to grow $Al_2O_3$. 300 ALD cycles are performed for the formation of 30 nm thick pinhole free alumina film.

*Solid state reaction:* Loiko et al. have prepared lead sulfide nanocrystals doped alumina–alkali–silicates glass [117,118]. The raw materials are weighed and thoroughly homogenized in large-volume (100 cm$^{-3}$) corundum crucible. The mixture is then heated at the maximum temperature of $\sim$1400 $\pm$ 50 $^{o}$C in a furnace for 2 h to carry out the synthesis. Further, the melt obtained is cast on a steel surface and then calcined at about 400 $^{\circ}$C in the muffle furnace for 2 h. The optical properties of nanocomposites are studied by annealing them at different temperatures (480 $^{o}$C, 490 $^{o}$C and 500 $^{o}$C) for different time intervals (60-150 h).

In the present study, PbS-Al$_2$O$_3$ nanocomposites were synthesized using lead acetate and thiourea using a facile sol-gel process. Sol-gel method has been used to prepare the PbS-Al$_2$O$_3$ nanocomposites for the first time.

### 3.2.2 Experimental Details

### Chemicals

The chemicals used for the synthesis of PbS-Al$_2$O$_3$ nanocomposites were aluminium isopropoxide (Aldrich), lead acetate trihydrate (Merck), thiourea (Rankem), ethanol (Changshu Yangyuan Chemicals, China), toluene (Rankem), ammonia solution (Rankem) and Millipore$^{®}$ water. All the chemicals were used as received.

### Synthesis

The PbS−Al$_2$O$_3$ nanocomposites were prepared by the sol-gel process [119]. Scheme 3.3 shows the schematic representation of the synthesis of PbS-Al$_2$O$_3$ nanocomposites by sol-gel process. Lead acetate, thiourea and aluminium isopropoxide were taken in a beaker with different molar ratios (0.25:0.25:9, 0.50:0.50:9 and 1:1:9). Then, 80 mL ethanol and 1 mL water were added. The contents were stirred for 3 hours at room temperature. Then, 50 mL of toluene and 4 mL of ammonia solution were added with continuous stirring to increase solubility of the precursors. After a period of 15 minutes, 2 mL of water was added for further hydrolysis. The contents were kept for stirring for about 23 hours at room temperature resulting in the formation of sol. The obtained sol was evaporated to get a gel. The gel was kept in an oven at 80 $^{o}$C overnight for drying. Black coloured powders were obtained. The designation of various PbS-Al$_2$O$_3$ nanocomposites, prepared in the present study, is given in Table 3.5.

| Pb(Ac)$_2$.3H$_2$O | ⊹ | Al(iOPr)$_3$ | ⊹ | EtOH (80 mL) | ⊹ | H$_2$O (1 mL) |

i) Stirred for 3h at RT
ii) Addition of 50 mL of toluene
    and 4 mL of 25% aq. NH$_3$ solution
iii) Stirred for 15 min at RT
iv) Addition of 2 mL of H$_2$O
 v) Stirred for 23 h at RT

**Sol**

Evaporation at 80 $^{\circ}$C

**Gel**

Dried in an oven at 80 $^{\circ}$C

**PbS–Al$_2$O$_3$ nanocomposites**
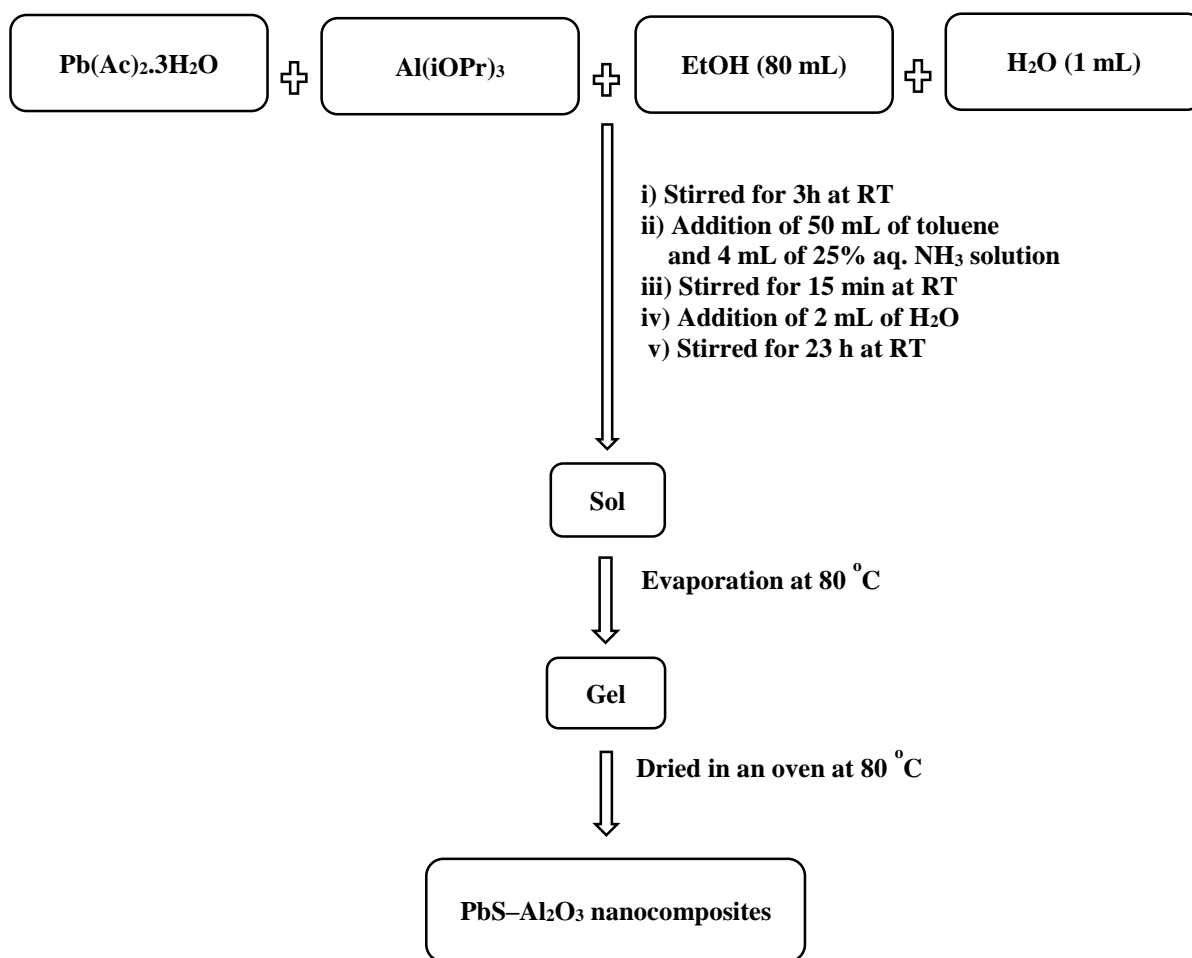
**Scheme 3.3:** Synthesis of PbS-Al$_2$O$_3$ nanocomposites by sol-gel method.

**Table 3.5:** Designation of different PbS-Al$_2$O$_3$ nanocomposites synthesized by sol-gel method.

| Nanocomposite | Pb(Ac)$_2$.3H$_2$O (mmol) | (NH$_2$)$_2$CS (mmol) | Al(iOPr)$_3$ (mmol) | Crystallite size of PbS (nm) (from XRD) |
|---|---|---|---|---|
| AP1 | 0.25 | 0.25 | 9 | 18.2 |
| AP2 | 0.5 | 0.5 | 9 | 28.4 |
| AP3 | 1 | 1 | 9 | 40.5 |

### 3.2.3 Results and Discussion

### 3.2.3.1 XRD Results

The phase structures of pure PbS, $Al_2O_3$ and $PbS-Al_2O_3$ nanocomposites were studied by XRD measurements. Fig. 3.14(a) represents the XRD patterns of pure PbS and $Al_2O_3$ nanoparticles. Characteristic diffraction peaks for PbS can be clearly noticed and the peaks at $2\theta$ values of 25.9°, 30.1°, 43.1°, 50.9°, 53.4°, 62.5°, 68.8°, 70.9°, 78.9° and 84.8° correspond to (111), (200), (220), (311), (222), (400), (331), (420), (422) and (511) planes of crystalline PbS (JCPDS No. 78-1901), respectively. Sol-gel alumina shows peaks due to aluminium oxide hydrate (JCPDS No. 25-0017). Fig. 3.14(b) shows the XRD patterns of $PbS-Al_2O_3$ nanocomposites (AP1, AP2 and AP3). Sharp peaks due to crystalline cubic PbS are observed in the nanocomposites. No other impurities were observed and the peaks due to alumina are absent in the nanocomposites. The crystallite size of PbS in the nanocomposites, estimated using the Debye−Scherrer's equation, increases from 18.2 to 40.5 nm (Table 3.5) with an increase in the concentration of lead acetate and thiourea used during the preparation of the nanocomposites.
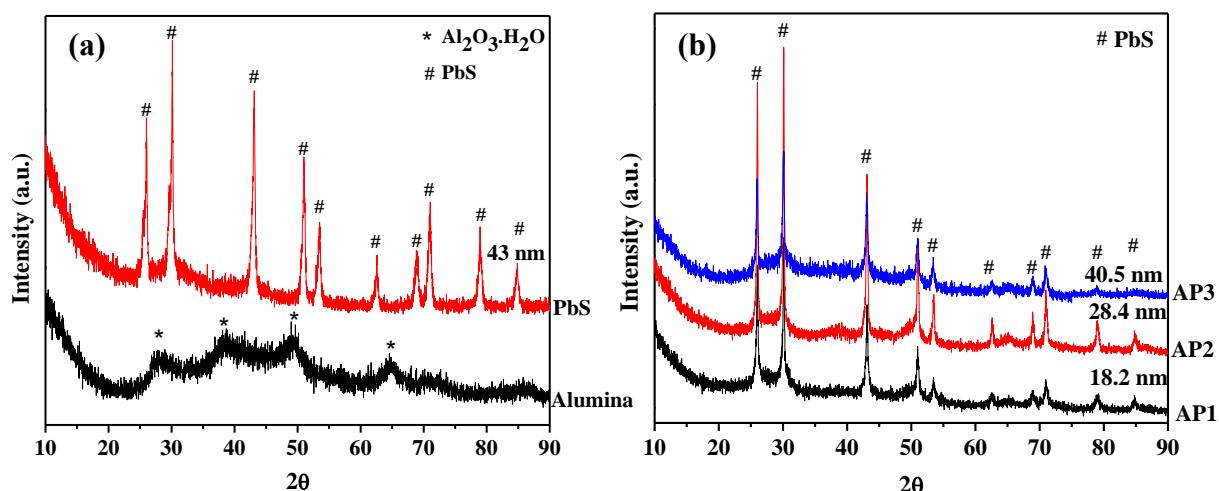


**Fig. 3.14:** XRD patterns of (a) pure PbS, alumina and (b) $PbS-Al_2O_3$ nanocomposites (AP1, AP2 and AP3).

### 3.2.3.2 FT-IR Results

The FT−IR spectral results of pure PbS nanoparticles, alumina and all the PbS−Al$_2$O$_3$ nanocomposites (AP1, AP2 and AP3) are shown in Fig. 3.15. The IR spectra of pure PbS, alumina and all the nanocomposites show a broad band at about 3334−3450 cm$^{-1}$ due to hydroxyl stretching of physisorbed water. The bands at about 2934 cm$^{-1}$ and 2854 cm$^{-1}$ are attributed to asymmetric and symmetric C−H stretching. The C-H stretching is attributed to the presence of small amount of adsorbed organic solvent molecules (e.g. toluene, ethanol) on the surface of PbS-Al$_2$O$_3$ nanocomposites. These solvents were used during the sol-gel preparation of the PbS-Al$_2$O$_3$ nanocomposites. The band at about 1644 cm$^{-1}$ is attributed to the bending vibration of water molecules. The bands at 1554 cm$^{-1}$ and 1412 cm$^{-1}$ are attributed to the stretching mode of carbonate ions and C−O bond, respectively [51]. The band at about 1070 cm$^{-1}$ is attributed to the deformation of O−H group. The bands at 827 cm$^{-1}$ and 780 cm$^{-1}$ are due to the stretching vibration of four coordinated Al−O of AlO$_4$. The bands at 630 cm$^{-1}$ and 470 cm$^{-1}$ are due to six-coordinated Al–O of AlO$_6$ [100]. The band at 670 cm$^{-1}$ in pure PbS nanoparticles is attributed to Pb−O stretching; PbO is the photo-oxidation product of PbS [95].
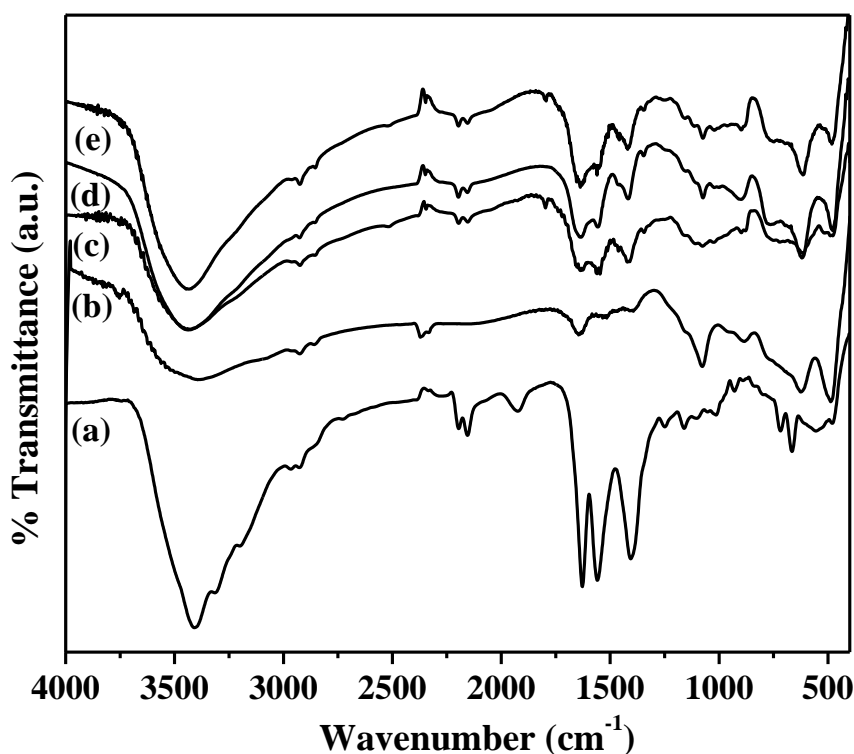


**Fig. 3.15:** FT-IR spectra of (a) pure PbS, (b) alumina, and (c-e) PbS-Al$_2$O$_3$ nanocomposites (AP1, AP2 and AP3, respectively).

### 3.2.3.3 Raman Spectroscopy Studies

Fig. 3.16 shows the Raman spectra of pure PbS and the PbS-Al$_2$O$_3$ nanocomposites (AP1, AP2 and AP3). The Raman spectrum of pure aluminium oxide did not show any characteristic band. The spectra of pure PbS and the nanocomposites reveal several bands at 72, 204, 351, 475 and 921 cm$^{-1}$. The intense narrow peak at 72 cm$^{-1}$ is attributed to the acoustic mode of PbS [120]. The peaks at 205 cm$^{-1}$ and 475 cm$^{-1}$ are attributed to first LO phonon and second LO phonon modes of PbS, respectively. The weak peak at 351 cm$^{-1}$ is due to crystal defects. The peak at 921 cm$^{-1}$ is the characteristic peak of oxidation product of PbS due to laser induced degradation [121]. Other modes such as the transverse optical (TO) and the surface phonon (SP) modes are absent in PbS-Al$_2$O$_3$ nanocomposites due to symmetry restrictions and their low intensities [110].
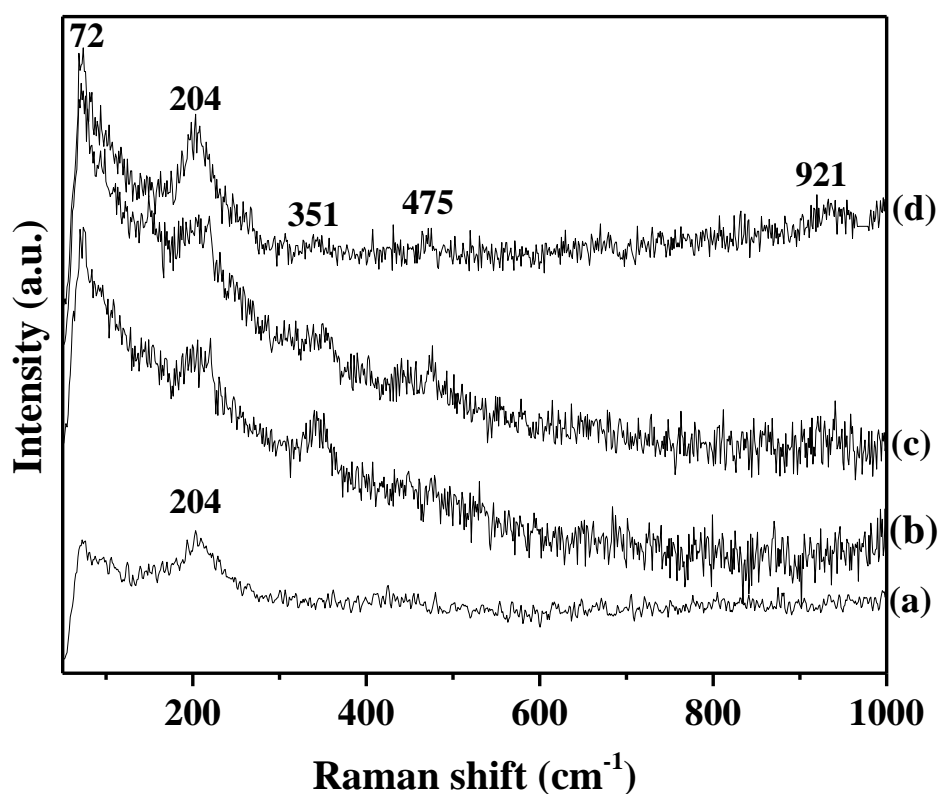


**Fig. 3.16:** Raman spectra of (a) pure PbS, and (b-d) PbS-Al$_2$O$_3$ nanocomposites (AP1, AP2 and AP3, respectively).

### 3.2.3.4 FE-SEM and EDXA Results

Fig. 3.17 shows the EDXA patterns of PbS-$Al_2O_3$ nanocomposites (AP1-AP3). The EDX analysis shows the presence of oxygen, aluminum, lead and sulfur in all the PbS-$Al_2O_3$ nanocomposites. Table 3.6 shows the EDX analysis results for all the PbS-$Al_2O_3$ nanocomposites. Nanocomposites AP1 and AP3 show uniform elemental distribution compared to nanocomposite (AP2). In nanocomposite AP1, the %wt. of aluminum varies between 19.8 and 20.6, the %wt. of sulfur varies between 28.6 and 29.9 and the %wt. of lead varies between 3.3 and 3.6. In the nanocomposite AP3, the %wt. of aluminum varies between 15.3 and 16.8, the %wt. of sulfur varies between 22.1 and 23.8 and the %wt. of lead varies between 5.0 and 5.5. In the nanocomposite AP2, the %wt. of aluminum varies between 21.8 and 24.2, the %wt. of sulfur varies between 32.3 and 36.9 and the %Wt. of lead varies between 3.6 and 4.2.
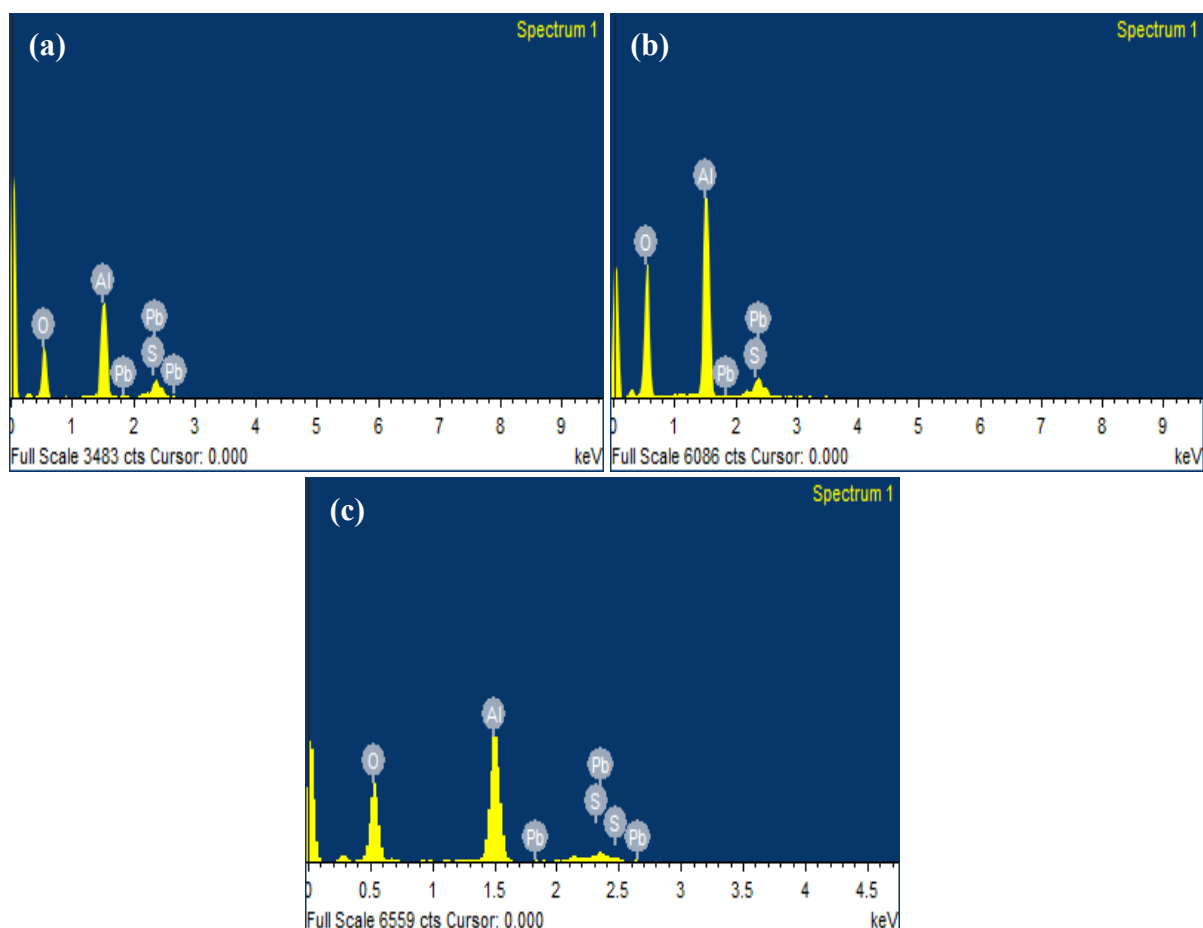


**Fig. 3.17:** EDXA patterns for PbS-$Al_2O_3$ nanocomposites; (a) AP1, (b) AP2 and (c) AP3.

**Table 3.6:** EDX analysis results of PbS-Al$_2$O$_3$ nanocomposites.

| EDX Analysis Data | | | | | | | | |
|---|---|---|---|---|---|---|---|---|
| **Nanocomposite** | **O** | | **Al** | | **S** | | **Pb** | |
| | Wt% | At% | Wt% | At% | Wt% | At% | Wt% | At% |
| AP1 | 61.5 | 73.9 | 19.8 | 17.8 | 28.6 | 10.3 | 3.5 | 1.7 |
| | 34.4 | 52.9 | 20.6 | 23.8 | 29.5 | 10.2 | 3.6 | 2.1 |
| | 36.6 | 55.5 | 19.9 | 22.7 | 29.9 | 10.8 | 3.3 | 1.8 |
| AP2 | 17.8 | 32.6 | 24.2 | 33.4 | 35.9 | 29.4 | 3.9 | 2.6 |
| | 17.4 | 34.0 | 21.8 | 32.0 | 32.3 | 28.1 | 4.2 | 3.1 |
| | 19.4 | 34.8 | 23.9 | 32.2 | 36.2 | 28.9 | 3.6 | 2.4 |
| AP3 | 31.4 | 56.4 | 15.3 | 19.3 | 22.1 | 18.5 | 5.0 | 3.0 |
| | 23.5 | 44.8 | 16.8 | 25.5 | 23.8 | 22.8 | 5.5 | 3.9 |
| | 19.3 | 38.9 | 16.7 | 25.3 | 23.8 | 28.8 | 5.1 | 3.8 |

## 3.2.3.5 TEM and SAED Results

Transmission electron microscopy (TEM) was employed to examine the morphology of pure PbS, Al$_2$O$_3$ and the PbS-Al$_2$O$_3$ nanocomposites. Fig. 3.18 shows the TEM images of pure PbS, and alumina nanoparticles. Pure PbS nanoparticles show cube-like particles with an average particle size of 26.2 ± 6.7 nm. The SAED pattern (inset of Fig. 3.18(a)) consists of rings attributed to (200), (220), (311), (420), (422) and (511) planes of polycrystalline PbS. Wang Z. L. [122] has reported that the shape of a cubic nanocrystals is determined by the ratio of the growth rate in the (100) direction to that in the (111) direction. According to Lee et al., when the growth rate is high along the (100) facets, PbS cubes are formed [123]. Pure alumina shows particles with flake-like morphology and the electron diffraction pattern indicates amorphous nature (Fig. 3.18(b)).
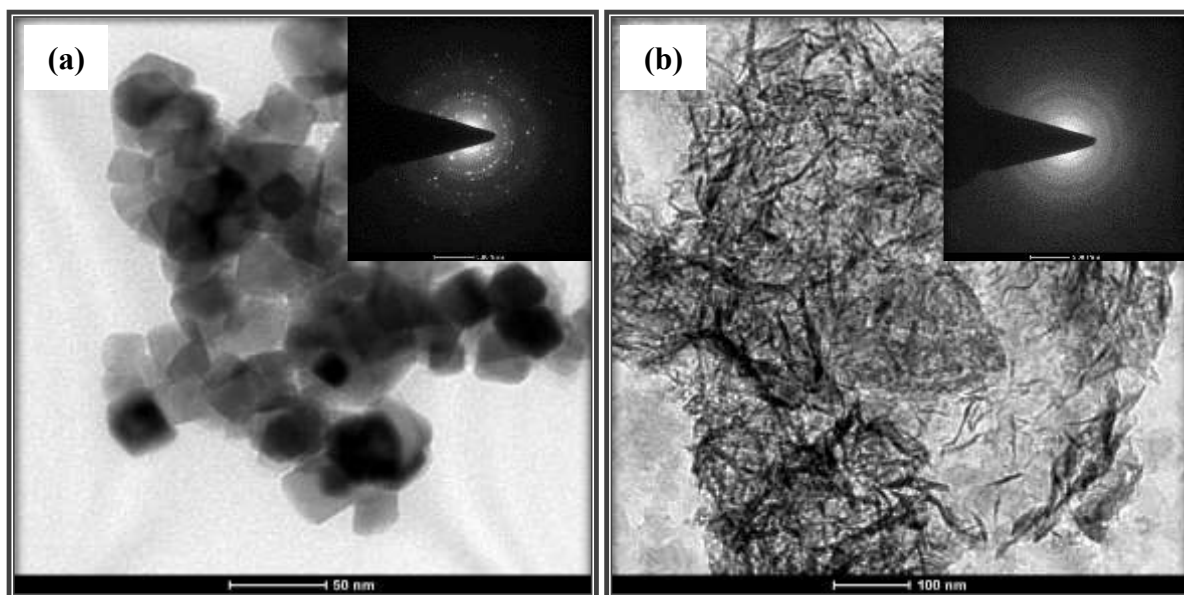
**Fig. 3.18:** TEM images of (a) pure PbS and (b) alumina nanoparticles.

The TEM images of PbS-Al$_2$O$_3$ nanocomposites AP1, AP2 and AP3 (Figs. 3.19(a), (b) and (c), respectively) show dispersion of lead sulfide nanoparticles (as dark spots) on the flakes of alumina. The inset of Fig. 3.19(a) corresponds to the SAED pattern of nanocomposite AP1 where no rings or spots due to PbS are observed. In the SAED pattern of nanocomposite AP2 (inset of Fig. 3.19(b)), the observed rings are attributed to (311), (220), (331) and (511) planes of polycrystalline PbS. In the SAED pattern of nanocomposite AP3 (inset of Fig. 3.19(d)), the observed rings are attributed to (220), (311), and (422) planes of polycrystalline PbS.
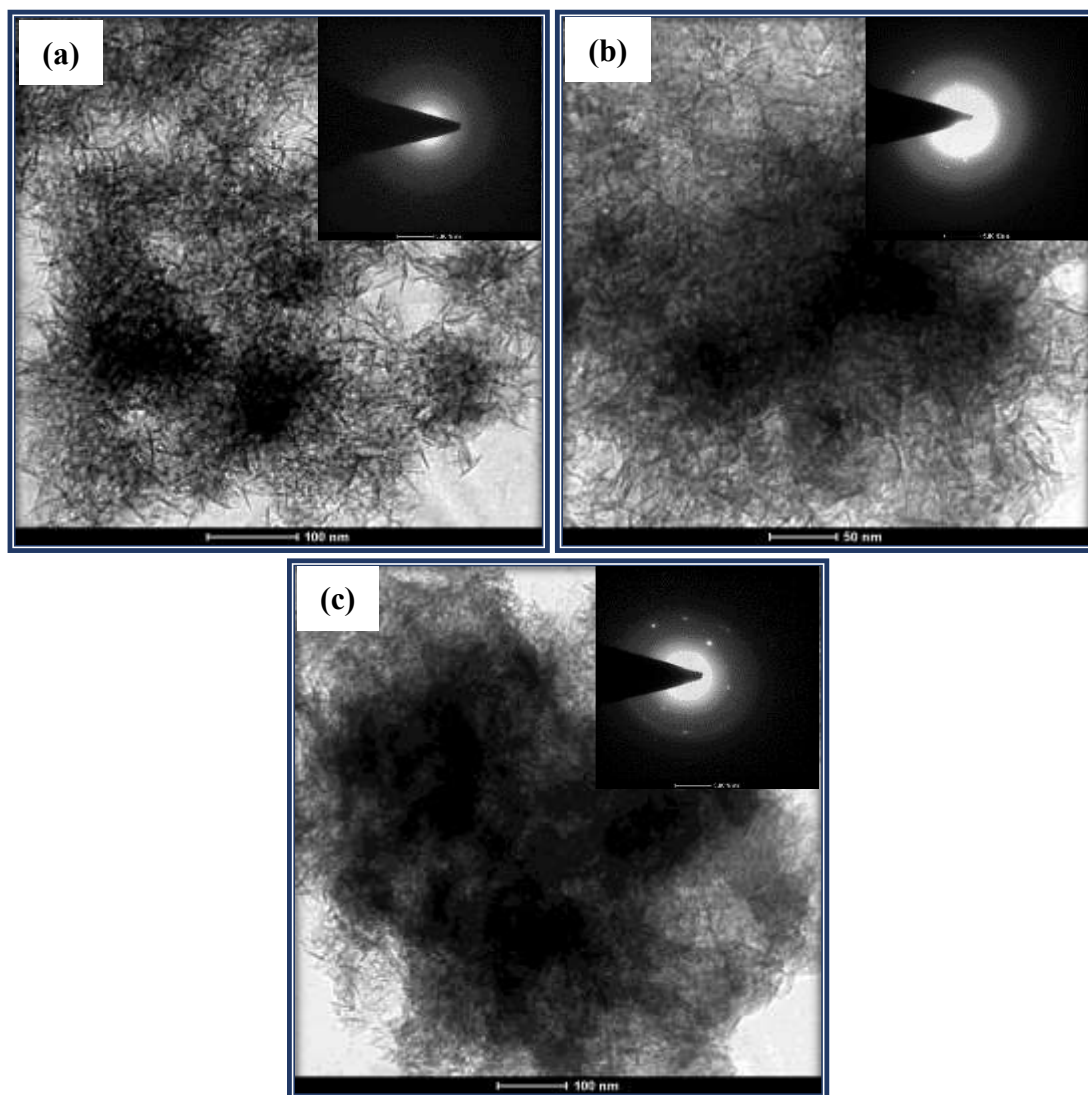
**Fig. 3.19:** TEM images of PbS-Al$_2$O$_3$ nanocomposites; (a) AP1, (b) AP2 and (c) AP3.

### 3.2.3.6 DRS Results

Fig. 3.20 depicts the diffuse reflectance spectra of PbS nanoparticles and PbS-Al$_2$O$_3$ nanocomposites (AP1, AP2 and AP3) in the range 1000 to 1800 nm. Pure PbS and all the nanocomposites show absorption in the near infrared (NIR) region.
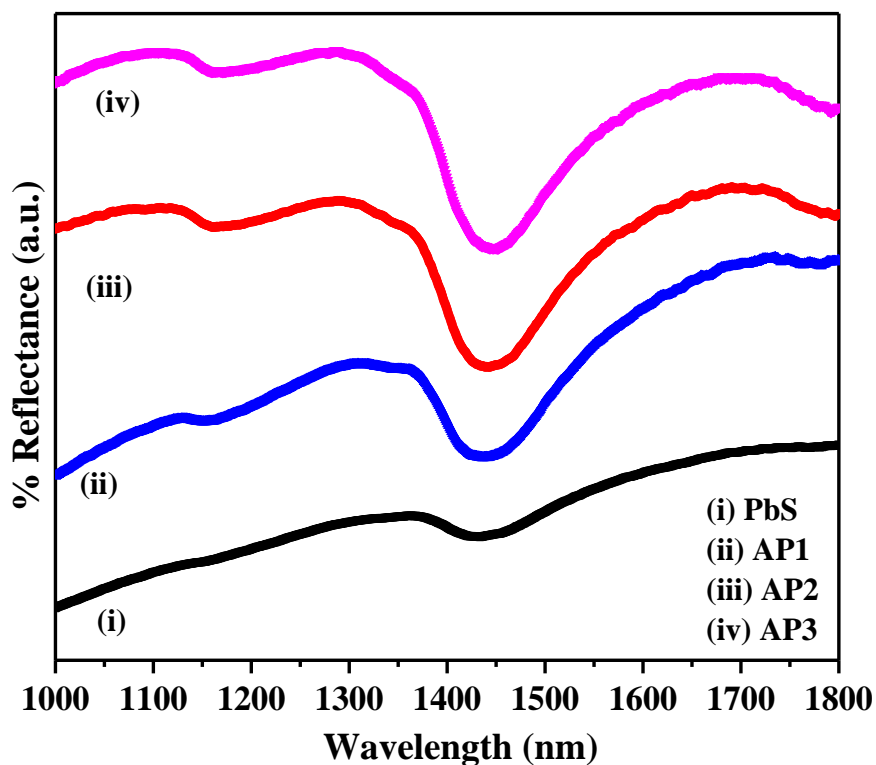
**Fig. 3.20:** Diffuse reflectance spectra of pure PbS and PbS-$Al_2O_3$ nanocomposites (AP1, AP2 and AP3).

The band gap was determined by plotting $(\alpha h \nu)^2$ vs. $h \nu$. Fig. 3.21 shows the Tauc plots of pure PbS and all the PbS-$Al_2O_3$ nanocomposites (AP1, AP2 and AP3). Pure PbS nanoparticles show band edge at about 0.85 eV and the band gap of bulk PbS is 0.41 eV. The band gap of PbS in the nanocomposites varies from 0.92 eV to 0.96 eV. There is blue shift in the band gap of PbS and PbS-$Al_2O_3$ nanocomposites compared to bulk PbS, which is attributed to quantum confinement effect. The broad band at about 1440 nm observed in PbS and in all the PbS-$Al_2O_3$ nanocomposites is due to absorption of water molecules present in these samples [124].
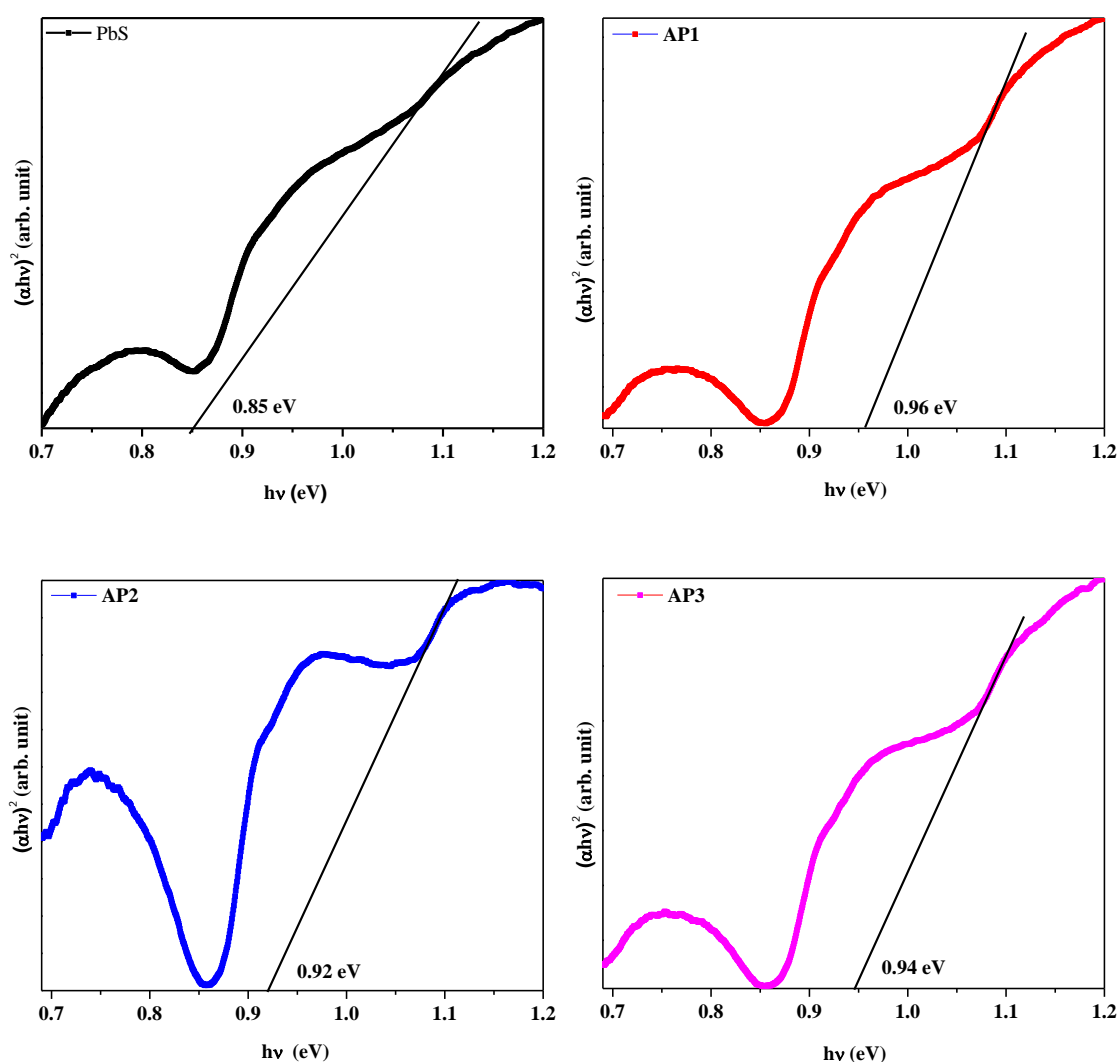
**Fig. 3.21:** Tauc plots of pure PbS and PbS-Al$_2$O$_3$ nanocomposites (AP1, AP2 and AP3).

### 3.2.3.7 Photoluminescence Spectroscopy Studies

Fig. 3.22 shows the photoluminescence spectra of pure PbS nanoparticles and PbS−Al$_2$O$_3$ nanocomposites (AP1, AP2 and AP3) at excitation wavelength of 700 nm. Two emission bands are observed at about 919 nm and 1007 nm. The sharp band at 919 nm is attributed to the band edge emission of PbS and the broad band at 1007 nm is due to the recombination of electrons trapped in sulfur vacancies with the holes of valence band of PbS [97,125]. A blue shift of PbS emission band compared to bulk PbS (∼3020 nm) is observed [126].
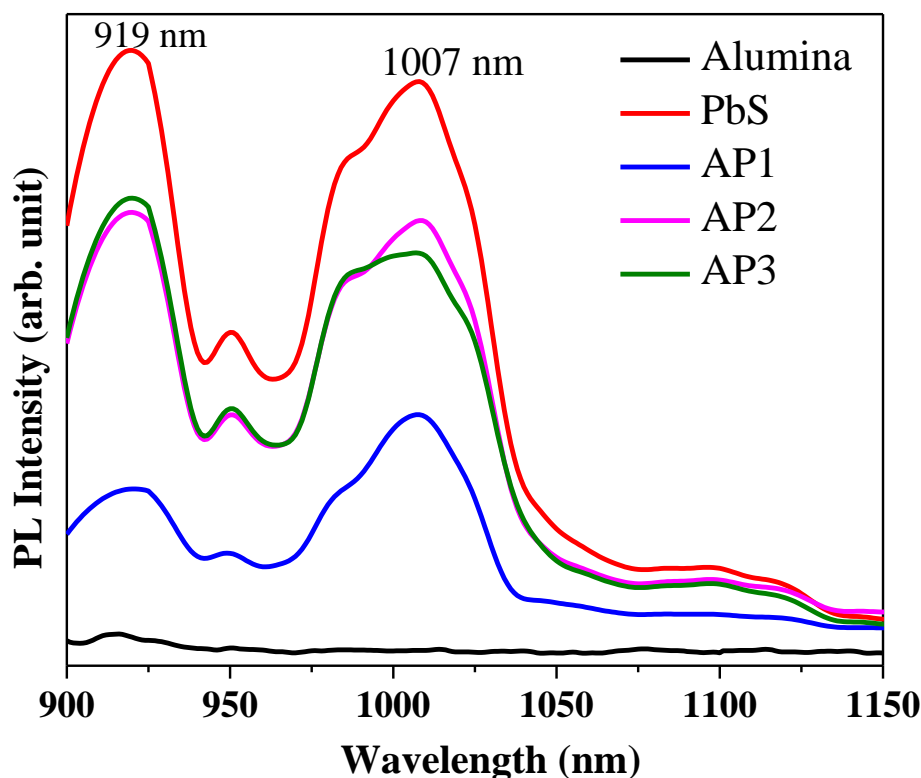
**Fig. 3.22:** Photoluminescence spectra of pure PbS and PbS-Al$_2$O$_3$ nanocomposites (AP1, AP2 and AP3) ($\lambda_{exc}$ = 700 nm).

Loiko et al. have reported the optical absorption and photoluminescence of novel alumina alkali-silicate glasses doped with PbS quantum dots in the NIR region (800−1400 nm) [118]. Saraidarov et al. have reported optical absorption of PbS−TiO$_2$ thin film nanocomposites in the NIR region (0.7 to 2.7 eV) [127]. Ntwaeaborwa et al. have reported NIR absorption of PbS−ZnO nanocomposites at 1015 nm (0.94 eV) and an excitonic emission due to PbS at 1396−1486 nm (0.88−0.83 eV) [128]. Acharaya et al. have reported absorbance and excitonic emission in the NIR region (800−1200 nm) for PbS−TiO$_2$ nanocomposites [95]. Turyanska et al. [129] and Bradshaw et al. [99] have reported emission in the NIR region (1000-1300 nm) for apoferritin-PbS nanocomposites. Chaudhuri et al. have reported band gap absorption in the NIR region (1200−1600 nm) for PbS-polystyrene nanocomposites [89]. Most of the PbS nanocomposites reported with NIR absorption and emission consist of semiconductor metal oxides or polymers and the size of PbS nanoparticles varies between 2 to 10 nm. In the present study, PbS-Al$_2$O$_3$ nanocomposites show NIR absorption and emission even though the nanocomposites consist of larger PbS nanoparticles (18.2 to 40.5 nm).

### 3.2.3.8 Mechanism for formation of PbS-Al₂O₃ nanocomposites

PbS-Al$_2$O$_3$ nanocomposites are produced by sol-gel method. Boehmite (AlO(OH)) is formed by the same mechanistic steps as discussed in the mechanism of formation of NiO-Al$_2$O$_3$ nanocomposites (Section 3.1.3.9). For PbS formation, lead acetate and thiourea were used as the precursors. Lead acetate is dissolved in a mixture of water and ethanol to give Pb$^{2+}$ ions [130], and thiourea slowly releases H$_2$S in the solution [131,132]. The reaction between Pb$^{2+}$ and H$_2$S leads to the formation of PbS. The temperature of the contents was raised to 80 $^o$C which results in slow dehydration of AlO(OH) leading to the formation of amorphous Al$_2$O$_3$. Formation of Al$_2$O$_3$ in the nanocomposites is confirmed by IR results (Section 3.2.3.2, Fig. 3.15). The FT-IR spectra of PbS-Al$_2$O$_3$ nanocomposites show bands at 827 cm$^{-1}$ and 780 cm$^{-1}$ attributed to stretching vibration of four coordinated Al–O of AlO$_4$, and bands at 630 cm$^{-1}$ and 470 cm$^{-1}$ attributed to six-coordinated Al–O of AlO$_6$. The proposed reactions related to the formation of PbS-Al$_2$O$_3$ nanocomposites are summarized as follows:

$$Pb(CH_3COO)_2.3H_2O \rightarrow Pb^{2+} + 2CH_3COO^- + 3H_2O$$

$$(NH_2)_2CS + 2H_2O \rightarrow H_2S + 2NH_3 + CO_2$$

$$Pb^{2+} + H_2S + 2AlO(OH) \xrightarrow{\Delta} PbS - Al_2O_3 + H_2O + 2H^+$$
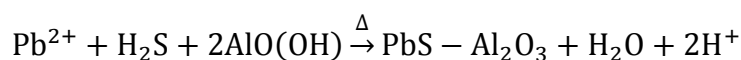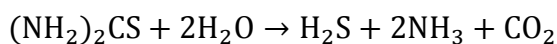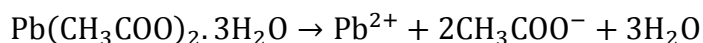
### 3.2.4 Conclusions

PbS-Al$_2$O$_3$ nanocomposites were prepared by a simple sol-gel method. The crystallite size of PbS in the nanocomposites varies from 18.2 to 40.5 nm. Raman spectral studies on the nanocomposites reveal characteristic peaks due to PbS nanoparticles and TEM studies indicate uniform distribution of lead sulfide nanoparticles on the alumina matrix. Optical studies on the nanocomposites indicate NIR absorption and emission. A blue shift of band gap of PbS in the nanocomposites compared to pure PbS nanoparticles and bulk PbS is observed. PL studies show characteristic peaks due to excitonic emission of PbS nanoparticles in all the nanocomposites. The PbS-Al$_2$O$_3$ nanocomposites can be used in Q-switching NIR lasers, luminescent markers, solar cells and photovoltaics.

## References

1.  Gao P. X., Shimpi P., Gao H., Liu C., Guo Y., Cai W., Liao K. T., Wrobel G., Zhang Z., Ren Z., Lin H. J., 'Hierarchical assembly of multifunctional oxide-based composite nanostructures for energy and environmental applications', *International Journal of Molecular Sciences*, **13**, 7393–7423 (2012).

2.  Henrique P., Camargo C., Satyanarayana K. G., Wypych F., 'Nanocomposites: Synthesis, structure, properties and new application opportunities', *Materials Research*, **12**, 1–39 (2009).

3.  Xiao G., Wang Y., Ning J., Wei Y., Liu B., Yu W. W., Zou G., Zou B., 'Recent advances in IV–VI semiconductor nanocrystals: Synthesis, mechanism, and applications', *RSC Advances*, **3**, 8104–8130 (2013).

4.  Tripathi V. K., Nagarajan R., 'Rapid synthesis of mesoporous, nano-sized $MgCr_2O_4$ and its catalytic properties', *Journal of the American Ceramic Society*, **2015**, 1–5 (2015).

5.  Sui R., Charpentier P., 'Synthesis of metal oxide nanostructures by direct sol−gel chemistry in supercritical fluids', *Chemical Reviews*, **112**, 3057–3082 (2012).

6.  Cui H., Zayat M., Levy D., 'A sol–gel route using propylene oxide as a gelation agent to synthesize spherical $NiAl_2O_4$ nanoparticles', *Journal of Non-Crystalline Solids*, **351**, 2102–2106 (2005).

7.  Chu Y., Feng J., Qian Y., Xiong S., 'Enhancing the electrode performance of $Co_3O_4$ through $Co_3O_4$@a-$TiO_2$ core–shell microcubes with controllable pore size', *RSC Advances*, **5**, 40899–40906 (2015).

8.  Bang Y., Han S. J., Kwon S., Hiremath V., Song I. K., Seo J. G., 'High temperature carbon dioxide capture on nano-structured $MgO$–$Al_2O_3$ and $CaO$–$Al_2O_3$ adsorbents: An experimental and theoretical study', *Journal of Nanoscience and Nanotechnology*, **14**, 8531–8538 (2014).

9.  Li B., Hao Y., Shao X., Tang H., Wang T., Zhu J., Yan S., 'Synthesis of hierarchically porous metal oxides and $Au/TiO_2$ nanohybrids for photodegradation of organic dye and catalytic reduction of 4-nitrophenol', *Journal of Catalysis*, **329**, 368–378 (2015).

10. Hussein A. M., Shende R. V., 'Enhanced hydrogen generation using $ZrO_2$-modified coupled $ZnO/TiO_2$ nanocomposites in the absence of noble metal co-catalyst',

*International Journal of Hydrogen Energy*, **39**, 5557–5568 (2014).

11. Shi C., Wang G., Zhao N., Du X., Li J., 'NiO nanotubes assembled in pores of porous anodic alumina and their optical absorption properties', *Chemical Physics Letters*, **454**, 75–79 (2008).

12. Seki T., Onaka M., 'Mesoporous alumina: Synthesis, characterization, and catalysis, in advanced nanomaterials', *Wiley-VCH Verlag GmbH & Co. kGaA* (2010).

13. Subramanian V., Gnanakumar E. S., Jeong D. W., Han W. B., Gopinath C. S., Roh H. S., 'A rationally designed $CuFe_2O_4$-mesoporous $Al_2O_3$ composite towards stable performance of high temperature water-gas shift reaction', *Chemical Communications*, **49**, 11257–11259 (2013).

14. Choi J., Zhang S., Hill J. M., 'Reducibility and toluene hydrogenation activity of nickel catalysts supported on γ-$Al_2O_3$ and κ-$Al_2O_3$', *Catalysis Science and Technology*, **2**, 179–186 (2012).

15. Zhang X., Liu J., Jing Y., Xie Y., 'Support effects on the catalytic behavior of $NiO/Al_2O_3$ for oxidative dehydrogenation of ethane to ethylene', *Applied Catalysis A: General*, **240**, 143–150 (2003).

16. Li J., Yan R., Xiao B., Liang D. T., Du L., 'Development of nano-$NiO/Al_2O_3$ catalyst to be used for tar removal in biomass gasification', *Environmental Science and Technology*, **42**, 6224–6229 (2008).

17. Xu L., Song H., Chou L., 'Carbon dioxide reforming of methane over ordered mesoporous $NiO–Al_2O_3$ composite oxides', *Catalysis Science and Technology*, **1**, 1032–1042 (2011).

18. Chen X., Zhao A., Shao Z., Li C., Williams C. T., Liang C., 'Synthesis and catalytic properties for phenylacetylene hydrogenation of silicide modified nickel catalysts', *The Journal of Physical Chemistry C*, **114**, 16525–16533 (2010).

19. Crişan M., Zaharescu M., Kumari V. D., Subrahmanyam M., Crian D., Drăgan N., Răileanu M., Jitianu M., Rusu A., Sadanandam G., Krishna Reddy J., 'Sol-gel based alumina powders with catalytic applications', *Applied Surface Science*, **258**, 448–455 (2011).

20. Abe O., Ohwa Y., 'Oxidation of $NiAl/Al_2O_3$ composites for controlled development of

surface layers and toughening', *Solid State Ionics*, **172**, 553–556 (2004).

21. Lin F., Nordlund D., Weng T. C., Moore R. G., Gillaspie D. T., Dillon A. C., Richards R. M., Engtrakul C., 'Hole doping in Al-containing nickel oxide materials to improve electrochromic performance', *ACS Applied Materials and Interfaces*, **5**, 301–309 (2013).

22. Makhlouf S., 'Humidity sensing properties of NiO/Al$_2$O$_3$ nanocomposite materials', *Solid State Ionics*, **164**, 97–106 (2003).

23. Ahmad M. M., Makhlouf S. A., Khalil K. M. S., 'Dielectric behavior and ac conductivity study of NiO/Al$_2$O$_3$ nanocomposites in humid atmosphere', *Journal of Applied Physics*, **100**, 094323/1–094323/8 (2006).

24. Crişan M., Zaharescu M., Kumari V. D., Subrahmanyam M., Crişan D., Drăgan N., Răileanu M., Jitianu M., Rusu A., Sadanandam G., Krishna Reddy J., 'Sol–gel based alumina powders with catalytic applications', *Applied Surface Science*, **258**, 448–455 (2011).

25. Zangouei M., Moghaddam A. Z., Arasteh M., 'The influence of nickel loading on reducibility of NiO/Al$_2$O$_3$ catalysts synthesized by sol-gel method', *Chemical Engineering Research Bulletin*, **14**, 97–102 (2010).

26. Shon B. Y., Jung M. W., 'Hydrogen permeability of NiO-doped alumina with nickel composites membrane', *Materials Science Forum*, **724**, 213–216 (2012).

27. Zhang Y., Xiong G., Sheng S., Yang W., 'Deactivation studies over NiO/γ-Al$_2$O$_3$ catalysts for partial oxidation of methane to syngas', *Catalysis Today*, **63**, 517–522 (2000).

28. Tadanaga K., Miyata A., Ando D., Yamaguchi N., Tatsumisago M., 'Preparation of Co–Al and Ni–Al layered double hydroxide thin films by a sol–gel process with hot water treatment', *Journal of Sol-Gel Science and Technology*, **62**, 111–116 (2012).

29. Ding C., Liu W., Wang J., Liu P., Zhang K., Gao X., Ding G., Liu S., Han Y., Ma X., 'One step synthesis of mesoporous NiO–Al$_2$O$_3$ catalyst for partial oxidation of methane to syngas: The role of calcination temperature', *Fuel*, **162**, 148–154 (2015).

30. Li G., Hu L., Hill J. M., 'Comparison of reducibility and stability of alumina-supported Ni catalysts prepared by impregnation and co-precipitation', *Applied Catalysis A:*

*General*, **301**, 16–24 (2006).

31.    Asencios Y. J. O., Elias K. F. M., Assaf E. M., 'Oxidative-reforming of model biogas over NiO/Al$_2$O$_3$ catalysts: The influence of the variation of support synthesis conditions', *Applied Surface Science*, **317**, 350–359 (2014).

32.    Garbarino G., Wang C., Valsamakis I., Chitsazan S., Riani P., Finocchio E., Flytzani-Stephanopoulos M., Busca G., 'A study of Ni/Al$_2$O$_3$ and Ni–La/Al$_2$O$_3$ catalysts for the steam reforming of ethanol and phenol', *Applied Catalysis B: Environmental*, **174-175**, 21–34 (2015).

33.    Liu Q., Gao J., Zhang M., Li H., Gu F., Xu G., Zhong Z., Su F., 'Highly active and stable Ni/γ-Al$_2$O$_3$ catalysts selectively deposited with CeO$_2$ for CO methanation', *RSC Advances*, **4**, 16094–16103 (2014).

34.    Hou X., Shen B., Zhao J., 'Reactive adsorption desulfurization of thiophene in n-hexane over oxides adsorbent of NiO-ZnO/Al$_2$O$_3$-SiO$_2$', *Applied Mechanics and Materials*, **455**, 43–47 (2013).

35.    Jung Y. S., Yoon W. L., Lee T. W., Rhee Y. W., Seo Y. S., 'A highly active Ni-Al$_2$O$_3$ catalyst prepared by homogeneous precipitation using urea for internal reforming in a molten carbonate fuel cell (MCFC): Effect of the synthesis temperature', *International Journal of Hydrogen Energy*, **35**, 11237–11244 (2010).

36.    Rotan M., Tolchard J., Rytter E., Einarsrud M. A., Grande T., 'On the solid solution of the spinel phase in the system NiO–Al$_2$O$_3$', *Journal of Solid State Chemistry*, **182**, 3412–3415 (2009).

37.    Zhong Z., Mastai Y., Koltypin Y., Zhao Y., Gedanken A., 'Sonochemical coating of nanosized nickel on alumina submicrospheres and the interaction between the nickel and nickel oxide with the substrate', *Chemistry of Materials*, **11**, 2350–2359 (1999).

38.    Zhang Q., Wu T., Zhang P., Qi R., Huang R., Song X., Gao L., 'Facile synthesis of hollow hierarchical Ni/γ-Al$_2$O$_3$ nanocomposites for methane dry reforming catalysis', *RSC Advances*, **4**, 51184–51193 (2014).

39.    Nagano T., Sato K., Saitoh T., Takahashi S., 'Hydrothermal stability of mesoporous Ni-doped γ-Al$_2$O$_3$', *Journal of the Ceramic Society of Japan*, **117**, 832–835 (2009).

40.    Azurdia J. A., Marchal J., Shea P., Sun H., Pan X. Q., Laine R. M., 'Liquid-feed flame

spray pyrolysis as a method of producing mixed-metal oxide nanopowders of potential interest as catalytic materials. Nanopowders along the NiO-Al$_2$O$_3$ tie line including (NiO)$_{0.22}$(Al$_2$O$_3$)$_{0.78}$, a new inverse spinel composition', *Chemistry of Materials*, **18**, 731–739 (2006).

41.  Baek J. I., Lee J. B., Eom T. H., Kim K. S., Yang S. R., Ryu C. K., 'Characterization of spray-dried NiO oxygen carriers supported on alpha alumina', *Energy Procedia*, **37**, 560–566 (2013).

42.  Chou H. Y., Badylevich M., Afanas'ev V. V., Houssa M., Stesmans A., Meersschaut J., Goux L., Kittl J. A., Wouters D. J., 'Electronic structure of NiO layers grown on Al$_2$O$_3$ and SiO$_2$ using metallo-organic chemical vapour deposition', *Journal of Applied Physics*, **110**, 113724/1–113724/5 (2011).

43.  Yuan C. L., 'Room-temperature coercivity of Ni/NiO core/shell nanoparticles fabricated by pulsed laser deposition', *The Journal of Physical Chemistry C*, **114**, 2124–2126 (2010).

44.  Nahar L., Esteves R. J. A., Hafiz S., Ozgur U., Arachchige I. U., 'Metal-semiconductor hybrid aerogels: Evolution of optoelectronic properties in a low-dimensional', *ACS Nano*, **9**, 9810–9821 (2015).

45.  Lv C., Hu L., Yang Y., Li H., Huang C., Liu X., 'Waterborne UV-curable polyurethane acrylate/silica nanocomposites for thermochromic coatings', *RSC Advances*, **5**, 25730–25737 (2015).

46.  Hasan M. R., Abd Hamid S. B., Basirun W. J., Meriam Suhaimy S. H., Che Mat A. N., 'A sol–gel derived, copper-doped, titanium dioxide–reduced graphene oxide nanocomposite electrode for the photoelectrocatalytic reduction of CO$_2$ to methanol and formic acid', *RSC Advances*, **5**, 77803–77813 (2015).

47.  Dai X., Liang J., Ma D., Zhang X., Zhao H., Zhao B., Guo Z., Kleitz F., Qiao S., 'Large-pore mesoporous RuNi-doped TiO$_2$–Al$_2$O$_3$ nanocomposites for highly efficient selective CO methanation in hydrogen-rich reformate gases', *Applied Catalysis B: Environmental*, **165**, 752–762 (2015).

48.  Osaki T., Horiuchi T., Sugiyama T., Suzuki K., Mori T., 'NiO-Al$_2$O$_3$ aerogel from (CH$_2$O)$_2$ Ni and AlOOH sol', *Journal of Non-Crystalline Solids*, **225**, 111–114 (1998).

49.  Giarola D. A., Catarini da Silva P. R., Urbano A., de Oliveira F. M., Texeira Tarley C. R., Dall'Antonia L. H., 'Surfactant effect on electrochemical-induced synthesis of α-Ni(OH)$_2$', *Journal of Solid State Electrochemistry*, **18**, 497–504 (2014).

50.  Meyer F., Hempelmann R., Mathur S., Veith M., 'Microemulsion mediated sol–gel synthesis of nano-scaled MAl$_2$O$_4$ (M= Co, Ni, Cu) alkoxide precursors', *Journal of Materials Chemistry*, **9**, 1755–1763 (1999).

51.  Jeevanandam P., Koltypin Y., Gedanken A., 'Preparation of nanosized nickel aluminate spinel by a sonochemical method', *Materials Science and Engineering: B*, **B90**, 125–132 (2002).

52.  Zhu G., Xi C., Xu H., Zheng D., Liu Y., Xu X., Shen X., 'Hierarchical NiO hollow microspheres assembled from nanosheet-stacked nanoparticles and their application in a gas sensor', *RSC Advances*, **2**, 4236–4241 (2012).

53.  Mironova-Ulmane N., Kuzmin A., Steins I., Grabis J., Sildos I., Pärs M., 'Raman scattering in nanosized nickel oxide NiO', *Journal of Physics: Conference Series*, **93**, 012039/1–012039/5 (2007).

54.  Duan W. J., Lu S. H., Wu Z. L., Wang Y. S., 'Size effects on properties of NiO nanoparticles grown in alkali salts', *The Journal of Physical Chemistry C*, **116**, 26043–26051 (2012).

55.  Yang C. C., Li S., 'Size-dependent Raman red shifts of semiconductor nanocrystals', *The Journal of Physical Chemistry B*, **112**, 14193–14197 (2008).

56.  Gandhi A. C., Pant J., Pandit S. D., Dalimbkar S. K., Chan T. S., Cheng C. L., Ma Y. R., Wu S. Y., 'Short-range magnon excitation in NiO nanoparticles', *The Journal of Physical Chemistry C*, **117**, 18666–18674 (2013).

57.  Gao T., Jelle B. P., 'Paraotwayite-type α-Ni(OH)$_2$ nanowires: Structural, optical, and electrochemical properties', *The Journal of Physical Chemistry C*, **117**, 17294–17302 (2013).

58.  Bae H. S., Shim E. H., Hoon Park J., Jung H., 'γ-ray irradiation synthesis and characterization of nickel hydroxide nanoparticles', *Journal of Physics and Chemistry of Solids*, **73**, 1456–1459 (2012).

59.  Ramsis M. N., Souaya E. R., Abd-El-Khalik M., Selim S. A., 'NiO-Al$_2$O$_3$ catalysts

prepared at high pH variation of structure and texture upon thermal treatment', *Journal of Materials Science*, **25**, 6–14 (1990).

60. Thota S., Kumar J., 'Sol–gel synthesis and anomalous magnetic behaviour of NiO nanoparticles', *Journal of Physics and Chemistry of Solids*, **68**, 1951–1964 (2007).

61. Proenca M. P., Sousa C. T., Pereira A. M., Tavares P. B., Ventura J., Vazquez M., Araujo J. P., 'Size and surface effects on the magnetic properties of NiO nanoparticles', *Physical Chemistry Chemical Physics*, **13**, 9561–9567 (2011).

62. Al-Kahlout A., Heusing S., Aegerter M. A., 'Electrochromism of NiO-TiO$_2$ sol-gel layers', *Journal of Sol-Gel Science and Technology*, **39**, 195–206 (2006).

63. Yang L. X., Zhu Y. J., Tong H., Liang Z. H., Li L., Zhang L., 'Hydrothermal synthesis of nickel hydroxide nanostructures in mixed solvents of water and alcohol', *Journal of Solid State Chemistry*, **180**, 2095–2101 (2007).

64. Teoh G. L., Liew K. Y., Mahmood W. A. K., 'Synthesis and characterization of sol-gel alumina nanofibers', *Journal of Sol-Gel Science and Technology*, **44**, 177–186 (2007).

65. Ghule A. V., Ghule K., Punde T., Liu J. Y., Tzing S. H., Chang J. Y., Chang H., Ling Y. C., 'In situ monitoring of NiO–Al$_2$O$_3$ nanoparticles synthesis by thermo-Raman spectroscopy', *Materials Chemistry and Physics*, **119**, 86–92 (2010).

66. Zhang J. Z., 'Interfacial charge carrier dynamics of colloidal semiconductor nanoparticles', *The Journal Physical Chemistry B*, **104**, 7239–7253 (2000).

67. Zhou X., Torabi M., Lu J., Shen R., Zhang K., 'Nanostructured energetic composites: Synthesis, ignition/combustion modeling, and applications', *ACS Applied Materials and Interfaces*, **6**, 3058–3074 (2014).

68. Mostafa A. El-Sayed., 'Small is different: Shape-,size-, and composition-dependent properties of some colloidal semiconductor nanocrystals', *Accounts of Chemical Research*, **37**, 326–333 (2004).

69. Kershaw S. V, Susha A. S., Rogach A. L., 'Narrow bandgap colloidal metal chalcogenide quantum dots: Synthetic methods, heterostructures, assemblies, electronic and infrared optical properties.', *Chemical Society Reviews*, **42**, 3033–87 (2013).

70. Rui X., Tan H., Yan Q., 'Nanostructured metal sulfides for energy storage', *Nanoscale*,

**6**, 9889–9924 (2014).

71.     Kim K., Son J., Han J. I., 'Metal sulfides as anode catalysts in direct alkaline sulfide fuel cell', *International Journal of Hydrogen Energy*, **39**, 10493–10497 (2014).

72.     Cingarapu S., Ikenberry M. A., Hamal D. B., Sorensen C. M., Hohn K., Klabunde K. J., 'Transformation of indium nanoparticles to β-indium sulfide: Digestive ripening and visible light-induced photocatalytic properties', *Langmuir*, **28**, 3569–3575 (2012).

73.     Kanazawa H., Adachi S., 'Optical properties of PbS', *Journal of Applied Physics*, **83**, 5997–6001 (1998).

74.     Kumar D., Agarwal G., Tripathi B., Vyas D., Kulshrestha V., 'Characterization of PbS nanoparticles synthesized by chemical bath deposition', *Journal of Alloys and Compounds*, **484**, 463–466 (2009).

75.     Wise F. W., 'Lead salt quantum dots: The limit of strong quantum confinement', *Accounts of Chemical Research*, **33**, 773–780 (2000).

76.     Machol J. L., Wise F. W., York N., Tanner B., 'Vibronic beats microcrystallites', *Physical Review B*, **48**, 2819–2822 (1993).

77.     Schnitzer I., Katzir A., Schiessl U., Riedel W. J., Tacke M., 'Fiber-optic-based evanescent field chemical sensor using tunable diode lasers for the midinfrared spectral region', *Journal of Applied Physics*, **66**, 5667–5670 (1989).

78.     Pal B. N., Robel I., Mohite A., Laocharoensuk R., Werder D. J., Klimov V. I., 'High-sensitivity p-n junction photodiodes based on PbS nanocrystal quantum dots', *Advanced Functional Materials*, **22**, 1741–1748 (2012).

79.     Saran R., Nordin M. N., Curry R. J., 'Facile fabrication of PbS nanocrystal: C$_{60}$ fullerite broadband photodetectors with high detectivity', *Advanced Functional Materials*, **23**, 4149–4155 (2013).

80.     Neo M. S., Venkatram N., Li G. S., Chin W. S., Wei J., 'Size-dependent optical nonlinearities and scattering properties of PbS nanoparticles', *The Journal of Physical Chemistry C*, **113**, 19055–19060 (2009).

81.     Jiang P., Liu Z., Wang Y., Cai S., 'Room temperature single electron tunneling in nanoparticle-STM tip assemblies', *Molecular Crystals and Liquid Crystals Science and*

*Technology. Section A. Molecular Crystals and Liquid Crystals*, **337**, 317–320 (1999).

82. Liu C., Kwon Y. K., Heo J., 'Optical modulation of near-infrared photoluminescence from lead sulfide quantum dots in glasses', *Applied Physics Letters*, **94**, 021103/1–021103/3 (2009).

83. Sargent E. H., 'Infrared quantum dots', *Advanced Materials*, **17**, 515–522 (2005).

84. Nakane Y., Tsukasaki Y., Sakata T., Yasuda H., Jin T., 'Aqueous synthesis of glutathione-coated PbS quantum dots with tunable emission for non-invasive fluorescence imaging in the second near-infrared biological window (1000–1400 nm)', *Chemical Communications*, **49**, 7584–7586 (2013).

85. Warner J. H., Heckenberg N., Rubinsztein-Dunlop H., 'Non-linear photoluminescence from purified aqueous PbS nanocrystals', *Materials Letters*, **60**, 3332–3334 (2006).

86. Yang J., Peng J., Zhang Q., Peng F., Wang H., Yu H., 'One-step synthesis and characterization of gold-hollow $PbS_x$ hybrid nanoparticles', *Angewandte Chemie International Edition*, **48**, 3991–3995 (2009).

87. Wang Y., Yang W., Zhang L., Hu Y., Lou X. W., 'Formation of MS–Ag and MS (M = Pb, Cd, Zn) nanotubes via microwave-assisted cation exchange and their enhanced photocatalytic activities', *Nanoscale*, **5**, 10864–10867 (2013).

88. Kuljanin J., Čomor M. I., Djoković V., Nedeljković J. M., 'Synthesis and characterization of nanocomposite of polyvinyl alcohol and lead sulfide nanoparticles', *Materials Chemistry and Physics*, **95**, 67–71 (2006).

89. Chaudhuri T. K., Kothari A. J., Tiwari D., Ray A., 'Photoconducting nanocomposite films of PbS nanocrystals in insulating polystyrene', *Physica Status Solidi A*, **210**, 356–360 (2013).

90. Kovalenko M. V, Schaller R. D., Jarzab D., Loi M. A., Talapin D. V., 'Inorganically functionalized PbS/CdS colloidal nanocrystals: Integration into amorphous chalcogenide glass and luminescent properties', *The Journal of the American Chemical Society*, **134**, 2457–2460 (2012).

91. Wang H. J., Yu X. H., Cao Y., Zhou B., Wang C. F., 'Controllable synthesis and adjustable antineoplastic activity of bovine serum albumin-conjugated $PbS/Ag_2S$ core/shell nanocomposites', *Journal of Inorganic Biochemistry*, **113**, 40–46 (2012).

92. Girard S. N., Schmidt-Rohr K., Chasapis T. C., Hatzikraniotis E., Njegic B., Levin E. M., Rawal A., Paraskevopoulos K. M., Kanatzidis M. G., 'Analysis of phase separation in high performance PbTe-PbS thermoelectric materials', *Advanced Functional Materials*, **23**, 747–757 (2013).

93. Xu Y., Sun W., Liu C., Chu Y., 'Facile solvothermal preparation and photoluminescence properties of PbS, PbSe nanocrystals and PbS/PbSe alloyed heterostructures on lead substrates', *Materials Research Bulletin*, **50**, 1–6 (2014).

94. Bouet C., Laufer D., Mahler B., Nadal B., Heuclin H., Pedetti S., Dubertret B., 'Synthesis of zinc and lead chalcogenide core and core/shell nanoplatelets using sequential cation exchange reactions', *Chemistry of Materials*, **26**, 3002–3008 (2014).

95. Acharya K. P., Hewa Kasakarage N. N., Alabi T. R., Nemitz I., Khon E., Ullrich B., Anzenbacher P., Zamkov M., 'Synthesis of PbS/TiO$_2$ colloidal heterostructures for photovoltaic applications', *The Journal of Physical Chemistry C*, **114**, 12496–12504 (2010).

96. Liang Y., Novet T., Thorne J. E., Parkinson B. A., 'Photosensitization of ZnO single crystal electrodes with PbS quantum dots', *Physica Status Solidi A*, **211**, 1954–1959 (2014).

97. Chahadih A., El Hamzaoui H., Bernard R., Boussekey L., Bois L., Cristini O., Le Parquier M., Capoen B., Bouazaoui M., 'Direct-writing of PbS nanoparticles inside transparent porous silica monoliths using pulsed femtosecond laser irradiation', *Nanoscale Research Letters*, **6**, 542/1–542/7 (2011).

98. Liu X., Hu Q., Zhang X., Fang Z., Wang Q., 'Generalized and facile synthesis of Fe$_3$O$_4$/MS (M = Zn, Cd, Hg, Pb, Co, and Ni) nanocomposites', *The Journal Physical Chemistry C*, **112**, 12728–12735 (2008).

99. Bradshaw T. D., Junor M., Patanè A., Clarke P., Thomas N. R., Li M., Mann S., Turyanska L., 'Apoferritin-encapsulated PbS quantum dots significantly inhibit growth of colorectal carcinoma cells', *Journal of Materials Chemistry B*, **1**, 6254–6260 (2013).

100. Du X., Zhao S., Liu Y., Li J., Chen W., Cui Y., 'Facile synthesis of monodisperse α-alumina nanoparticles via an isolation-medium-assisted calcination method', *Applied Physics A Materials Science and Processing*, **116**, 1963–1969 (2014).

101. Pannu K. G. S., Pannu T., Fürstenhaupt T., Thangadurai V., 'Electrical properties of ionic liquid and double perovskite-type metal oxide composites-A new method to tailor grain-boundary impedance of ceramic electrolytes', *Solid State Ionics*, **232**, 106–111 (2013).

102. Roelofs K. E., Brennan T. P., Dominguez J. C., Bailie C. D., Margulis G. Y., Hoke E. T., McGehee M. D., Bent S. F., 'Effect of $Al_2O_3$ recombination barrier layers deposited by atomic layer deposition in solid-state CdS quantum dot-sensitized solar cells', *The Journal of Physical Chemistry C*, **117**, 5584–5592 (2013).

103. Zhao L., Wang Y., Sun Z., Wang A., Li X., Song C., Hu Y., 'Synthesis of highly dispersed metal sulfide catalysts via low temperature sulfidation in dielectric barrier discharge plasma', *Green Chemistry*, **16**, 2619–2626 (2014).

104. Ferraz S. G. A., Zotin F. M. Z., Araujo L. R. R., Zotin J. L., 'Influence of support acidity of NiMoS catalysts in the activity for hydrogenation and hydrocracking of tetralin', *Applied Catalysis A: General*, **384**, 51–57 (2010).

105. Li F., Xue Y., Li B., Hao Y., Wang X., Liu R., Zhao J., 'Precipitation synthesis of mesoporous photoactive $Al_2O_3$ for constructing $g$-$C_3N_4$ based heterojunctions with enhanced photocatalytic activity', *Industrial and Engineering Chemistry Research*, **53**, 19540–19549 (2014).

106. Kobayashi Y., Ishizaka T., Kurokawa Y., 'Preparation of alumina films by the sol-gel method', *Journal of Materials Science*, **40**, 263–283 (2005).

107. Liu J., Zou S., Li S., Liao X., Hong Y., Xiao L., Fan J., 'A general synthesis of mesoporous metal oxides with well-dispersed metal nanoparticles via a versatile sol–gel process', *Journal of Materials Chemistry A*, **1**, 4038–4047 (2013).

108. Park H., Ryu I., Kim J., Jeong S., Yim S., Jang S., 'PbS quantum dot solar cells integrated with sol−gel derived ZnO as an n-type charge-selective layer', *The Journal of Physical Chemistry C*, **118**, 17374–17382 (2014).

109. Ullah K., Meng Z. Da, Ye S., Zhu L., Oh W. C., 'Synthesis and characterization of novel PbS–graphene/$TiO_2$ composite with enhanced photocatalytic activity', *Journal of Industrial and Engineering Chemistry*, **20**, 1035–1042 (2014).

110. Dhlamini M. S., Terblans J. J., Ntwaeaborwa O. M., Joubert H. D., Swart H. C.,

'Preparations and luminescent properties of PbS nanoparticle phosphors incorporated in a $SiO_2$ matrix', *Physica Status Solidi C*, **5**, 598–601 (2008).

111. Cheng X. L., Jiang J. Sen, Hu M., Mao G. Y., Bu F. X., Lin C. C., Zeng Y., Zhang Q. H., 'Controlled synthesis of novel flowerlike α-$Fe_2O_3$ nanostructures via a one-step biphasic interfacial reaction route', *CrystEngComm*, **14**, 7701–7708 (2012).

112. Wu C., Shi J. B., Chen C. J., Lin J. Y., 'Synthesis and optical properties of ordered 30 nm PbS nanowire arrays fabricated into sulfuric anodic alumina membrane', *Materials Letters*, **60**, 3618–3621 (2006).

113. Chen J. H., Chao C. G., Ou J. C., Liu T. F., 'Growth and characteristics of lead sulfide nanocrystals produced by the porous alumina membrane', *Surface Science*, **601**, 5142–5147 (2007).

114. Hu C., Gassenq A., Justo Y., Devloo-Casier K., Chen H., Detavernier C., Hens Z., Roelkens G., 'Air-stable short-wave infrared PbS colloidal quantum dot photoconductors passivated with $Al_2O_3$ atomic layer deposition', *Applied Physics Letters*, **105**, 171110/1–171110/5 (2014).

115. Brennan T. P., Trejo O., Roelofs K. E., Xu J., Prinz F. B., Bent S. F., 'Efficiency enhancement of solid-state PbS quantum dot-sensitized solar cells with $Al_2O_3$ barrier layer', *Journal of Materials Chemistry A*, **1**, 7566–7571 (2013).

116. So H. M., Choi H., Shim H. C., Lee S. M., Jeong S., Chang W. S., 'Atomic layer deposition effect on the electrical properties of $Al_2O_3$-passivated PbS quantum dot field-effect transistors', *Applied Physics Letters*, **106**, 093507/1–093507/5 (2015).

117. Loiko P. A., Rachkovskaya G. E., Zacharevich G. B., Gurin V. S., Gaponenko M. S., Yumashev K. V., 'Optical properties of novel PbS and PbSe quantum-dot-doped alumino-alkali-silicate glasses', *Journal of Non-Crystalline Solids*, **358**, 1840–1845 (2012).

118. Loiko P. A., Rachkovskaya G. E., Zacharevich G. B., Yumashev K. V., 'Wavelength-tunable absorption and luminescence of $SiO_2$–$Al_2O_3$–ZnO–$Na_2O$–$K_2O$–NaF glasses with PbS quantum dots', *Journal of Luminescence*, **143**, 418–422 (2013).

119. Yadav S. K., Jeevanandam P., 'Synthesis of NiO–$Al_2O_3$ nanocomposites by sol–gel process and their use as catalyst for the oxidation of styrene', *Journal of Alloys and*

*Compounds*, **610**, 567–574 (2014).

120. Khanmohammadi M., Fard H. G., Garmarudi A. B., Khoddami N., 'Fourier transform infrared spectroscopic monitoring of sol–gel process in synthesis of PbS–TiO₂ hybrid nanostructures', *Thin Solid Films*, **518**, 6729–6732 (2010).

121. Deng B., Zhong S. L., Wang D. H., Wang S. S., Zhang T. K., Qu W. G., Xu A. W., 'High yield synthesis of matchstick-like PbS nanocrystals using mesoporous organosilica as template', *Nanoscale*, **3**, 1014–1021 (2011).

122. Wang Z. L., 'Transmission electron microscopy of shape-controlled nanocrystals and their assemblies', *The Journal of Physical Chemistry B*, **104**, 1153–1175 (2000).

123. Lee S. M., Cho S. N., Cheon J., 'Anisotropic shape control of colloidal inorganic nanocrystals', *Advanced Materials*, **15**, 441–444 (2003).

124. Viger M. L., Sheng W., Doré K., Alhasan A. H., Carling C. J., Lux J., De Gracia Lux C., Grossman M., Malinow R., Almutairi A., 'Near-infrared-induced heating of confined water in polymeric particles for efficient payload release', *ACS Nano*, **8**, 4815–4826 (2014).

125. Souici A. H., Keghouche N., Delaire J. A., Remita H., Etcheberry A., Mostafavi M., 'Structural and optical properties of PbS nanoparticles synthesized by the radiolytic method', *The Journal Physical Chemistry C*, **113**, 8050–8057 (2009).

126. Ka I., Ma D., El Khakani M. A., 'Tailoring the photoluminescence of PbS-nanoparticles layers deposited by means of the pulsed laser ablation technique', *Journal of Nanoparticle Research*, **13**, 2269–2274 (2011).

127. Saraidarov T., Reisfeld R., 'Synthesis and characterization of lead sulfide nanoparticles in zirconia-silica-urethane thin films prepared by the sol-gel process', *Journal of Sol-Gel Science and Technology*, **26**, 533–540 (2003).

128. Ntwaeaborwa O. M., Kroon R. E., Kumar V., Dubroca T., Ahn J. P., Park J. K., Swart H. C., 'Ex situ synthesis and optical properties of ZnO–PbS nanocomposites', *Journal of Physics and Chemistry of Solids*, **70**, 1438–1442 (2009).

129. Turyanska L., Bradshaw T. D., Li M., Bardelang P., Drewe W. C., Fay M. W., Mann S., Patanè A., Thomas N. R., 'The differential effect of apoferritin-PbS nanocomposites on cell cycle progression in normal and cancerous cells', *Journal of Materials Chemistry*,

**22**, 660–665 (2012).

130. Wang X., Shi J., Yang Y., 'Synthesis and optical properties of PbS/ZnO composite films', **95**, 4791–4794 (2004).

131. Shnidman L., 'The solubility of thiourea in water, methanol, and ethanol', *The Journal of Physical Chemistry*, **37**, 693–700 (1933).

132. Wang S., Pan A., Yin H., He Y., Lei Y., Xu Z., Zou B., 'Synthesis of PbS microcrystals via a hydrothermal process', *Materials Letters*, **60**, 1242–1246 (2006).

# CHAPTER 4

*Synthesis and Characterization of CdS-TiO$_2$ and Ag$_2$S-TiO$_2$ Nanocomposites by Thermal Decomposition Approach*

## 4.1 Synthesis and Characterization of CdS-TiO$_2$ Nanocomposites by Thermal Decomposition Approach

### 4.1.1 Introduction

Semiconductor metal oxide nanoparticles offer simple ways to tailor their physicochemical properties. One of the methods is sensitization with other metal oxide and metal sulfide nanoparticles [1]. Modification of a semiconductor metal oxide with another semiconductor can enhance charge separation and hence promote interfacial charge transfer [2]. In recent times, metal oxide nanocomposites have received enormous interest due to their applications in diverse areas such as photocatalysis, environmental remediation and energy generation [2–5]. TiO$_2$ has been extensively used as a photocatalyst due to its strong oxidizing ability, high stability and non-toxicity [6,7]. It possesses applications in various areas such as environmental remediation, solar energy conversion and hydrogen generation [8–11]. The use of TiO$_2$ as the photocatalyst is limited since it absorbs only about 5% of sunlight in the UV region due to its wide band gap (3.2 eV for anatase and 3.0 eV for rutile). The high recombination rate of photo-generated electrons and holes drastically reduces its quantum efficiency. In order to extend the light absorption of TiO$_2$ to visible region, a number of new TiO$_2$ based photocatalysts have been developed. A variety of methods such as hydrogenation [12], doping with metal/non-metal [13–15], sensitization with dyes [9] and combining with narrow band gap semiconductors [6,16] have been reported for the modification of TiO$_2$. Among the modified TiO$_2$ photocatalysts, coupling of a narrow band gap semiconductor with TiO$_2$ to form nanocomposites is considered as one of the most promising ways for harvesting sunlight with enhancement of quantum yield [17]. Some of the semiconductors with narrow band gap that have been coupled with TiO$_2$ are PbS [18], CdTe [19], CdSe [20], ZnFe$_2$O$_4$ [21], Cu$_2$O [22] and CdS [23–25].

CdS–TiO$_2$ nanocomposites show good optical absorption in the visible region due to sensitization with CdS. CdS has a high quantum efficiency in the visible region due to its low band gap (E$_g$ ≈ 2.40 eV) [26]. The conduction band of CdS (−0.7 eV) is more cathodic than that of TiO$_2$ (−0.5 eV) [27]; higher the difference between the conduction bands of two semiconductors, higher is the driving force of electron transfer [28]. On irradiation with light, TiO$_2$ accepts photoelectrons generated from the CdS and thus effectively inhibits the recombination of photoelectrons and holes. CdS–TiO$_2$ nanocomposites possess various photocatalytic applications such as degradation of organic pollutants (e.g. methyl orange, rhodamine B, methylene blue) [29–31], reduction of nitrobenzene derivatives [32], selective

oxidation of alcohols [33], water splitting [34] and reduction of Cr(VI) [35]. CdS–TiO$_2$ nanocomposites with different morphologies such as CdS quantum dots on TiO$_2$ nanotubes [32], core–shell [33], CdS/TiO$_2$ branched nanoarrays [34] and nanospheres [36] have been reported (Fig. 4.1). The nanocomposites have been synthesized by various methods such as hydrothermal [23,37–41], solvothermal [30,36,42], precipitation [28,43,44], chemical bath deposition [34,45,46], sol–gel [47,48], reverse micellar route [49], self-assembly [32,50], sonochemical [51,52], successive ionic layer adsorption and reaction (SILAR) [53–55], electrodeposition [56] and electrospinnig and photodeposition [57]. A brief summary on the synthesis of CdS-TiO$_2$ nanocomposites by the above mentioned methods are given in Table 4.1. A brief discussion on some of these methods is given below.
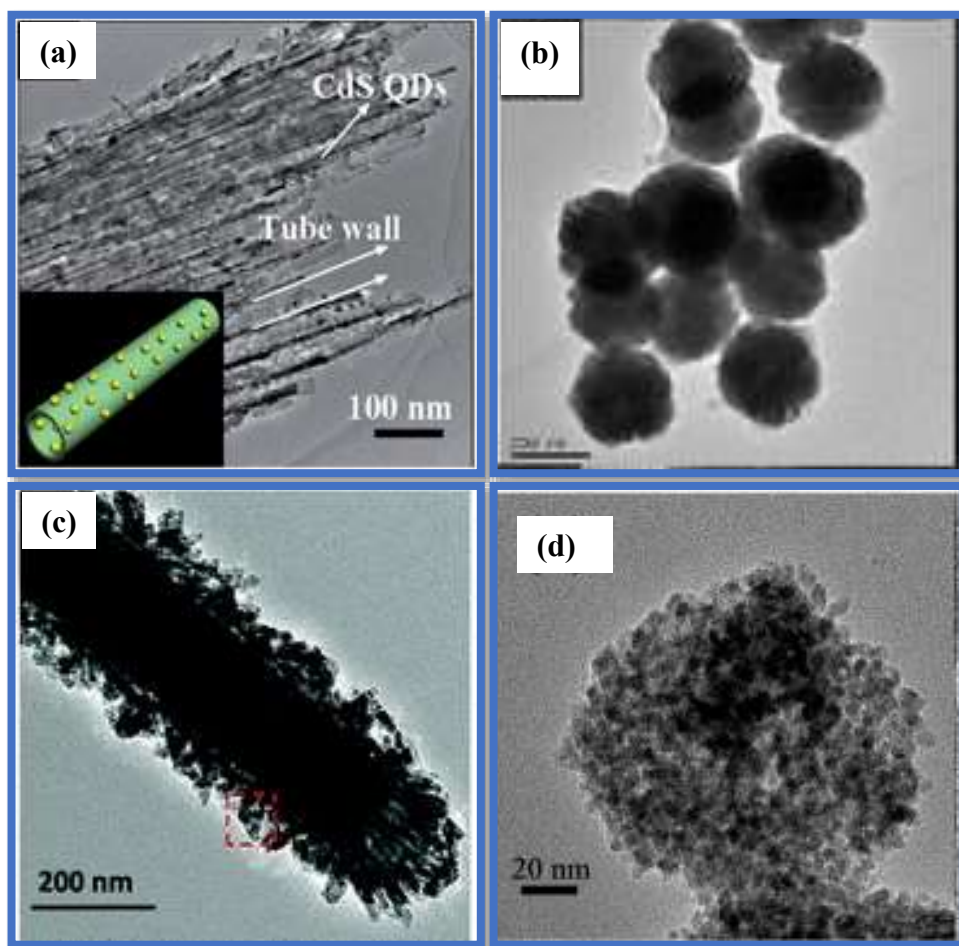


**Fig. 4.1:** CdS-TiO$_2$ nanocomposites with different morphologies; (a) CdS quantum dots on TiO$_2$ nanotubes [32], core–shell [33], CdS/TiO$_2$ branched nanoarrays [34] and nanospheres [36].

**Table 4.1:** Different reported methods for the synthesis of CdS-TiO$_2$ nanocomposites.

| Sl. No. | Method | Chemicals used | Morphology of the nanocomposites | Size | Reference |
|---|---|---|---|---|---|
| 1. | Hydrothermal | Cadmium acetate, thiourea and tetrabutyl titanate | Core-shell | CdS core = 200 nm, TiO$_2$ shell = 7-50 nm | [39] |
| 2. | Solvothermal | Cadmium chloride, sodium sulfide, PVP K-30 and titanium n-butoxide | Hybrid nanospheres | 100 nm | [36] |
| 3. | Precipitation | Cadmium chloride, sodium sulfide, P25 and L-cysteine | Powder | 6-10 nm | [43] |
| 4. | Chemical bath deposition | Cadmium nitrate, sodium sulfide and titanium butoxide | Branched nanoarrays | TiO$_2$ = 200 nm, CdS = 5-10 nm | [34] |
| 5. | Sol-gel | Cadmium nitrate, thiourea, and titanium isopropoxide | Powder | 9-40 nm | [47] |
| 6. | Reverse micellar | Cadmium nitrate, thiourea, and titanium tetra-isopropoxide | Core-shell | CdS core = 3-5 nm, TiO$_2$ shell = 1 nm | [49] |
| 7. | Self-assembly | Cadmium chloride, sodium sulfide and titanium sheets | Nanobelts | Diameter = 450 nm | [50] |
| 8. | Sonochemical | Cadmium chloride, thiourea and titanium tetra-isopropoxide | Core-shell | 11 nm | [52] |

| | | | | | |
|---|---|---|---|---|---|
| 9. | Successive ionic layer adsorption and reaction (SILAR) | Cadmium perchlorate, sodium sulfide and TiO$_2$ | Film | 4 nm | [55] |
| 10. | Electrodeposition | Cadmium chloride, sodium thiosulphate and titanium tetra-isopropoxide | Film | - | [56] |
| 11. | Electrospinning and photodeposition | Cadmium chloride, sulfur and titanium tetra-isopropoxide | Nanofibers | Diameter = 150 nm | [57] |
| 12. | Thermal decomposition method | Cadmium chloride, potassium ethyl xanthate and commercial TiO$_2$ | Film | - | [58] |

*Hydrothermal synthesis* [39]*:* In this method, synthesized CdS nanoparticles (hydrothermal) are dispersed in ethanol followed by addition of specified amounts of tetrabultyl titanate. Then, water is added drop wise to the solution with vigorous magnetic stirring. The mixture is kept stirring for 2 h and is transferred to a Teflon-lined autoclave (100 mL). Afterwards, hydrothermal reaction is conducted at 180 °C for 24 h. Finally, the samples are washed, and then dried in vacuum oven at 60 °C for 6 h.

*Solvothermal synthesis* [36]*:* The formation of CdS/TiO$_2$ nanocomposites by solvothermal method is illustrated in scheme 4.1 [36]. In this method, specified amounts of titanium butoxide, poly vinyl pyrrolidone (PVP) and already prepared CdS nanoparticles are dispersed in ethanol with magnetic stirring for 2 h. Then, 1:1 (v/v) mixture of n-propyl ethanol:water is added into the solution with stirring due to which the solution turns milky. The milky solution is stirred for another 2 h at 70 °C. After that, the milky solution is transferred to a 50 mL Teflon lined stainless-steel autoclave. The autoclave is maintained at 160 °C for 12 h and then cooled to room temperature. The product obtained is centrifuged, washed with ethanol and deionized water, and vacuum dried at 60 °C.
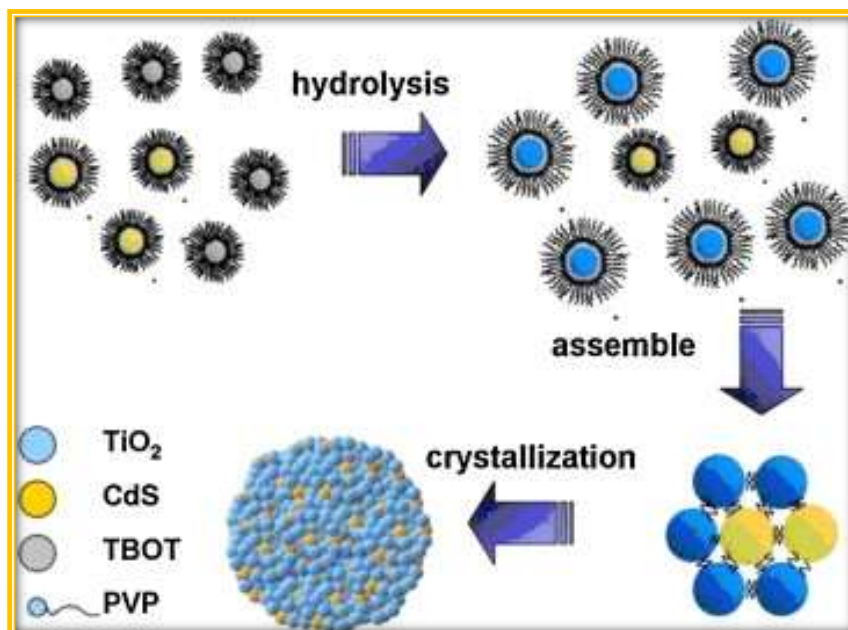
**Scheme 4.1:** Schematic illustration of the formation of CdS/TiO$_2$ hybrid nanostructures by solvothermal method [36].

*Precipitation* [43]*:* In this method, an aqueous solution of precursors is formed by mixing specific ratio of L-cysteine, P25 and CdCl$_2$ under vigorous stirring. Thereafter, the pH value of the solution is adjusted to 12.5 with 1 M NaOH solution and Na$_2$S aqueous solution is slowly added. The solution is then refluxed at 383 K for 5 h. The composite obtained is centrifuged and washed with distilled water and dried at 353 K for 12 h.

*Self-assembly* [50]*:* The formation of CdS/TiO$_2$ nanocomposites by self-assembly is illustrated in Scheme 4.2. In this method, amine functionalized TiO$_2$ nanobelts are immersed in an aqueous solution of thioglycolic acid capped CdS quantum dots for 2 h to produce TiO$_2$ nanobelt–CdS quantum dot heterostructures.
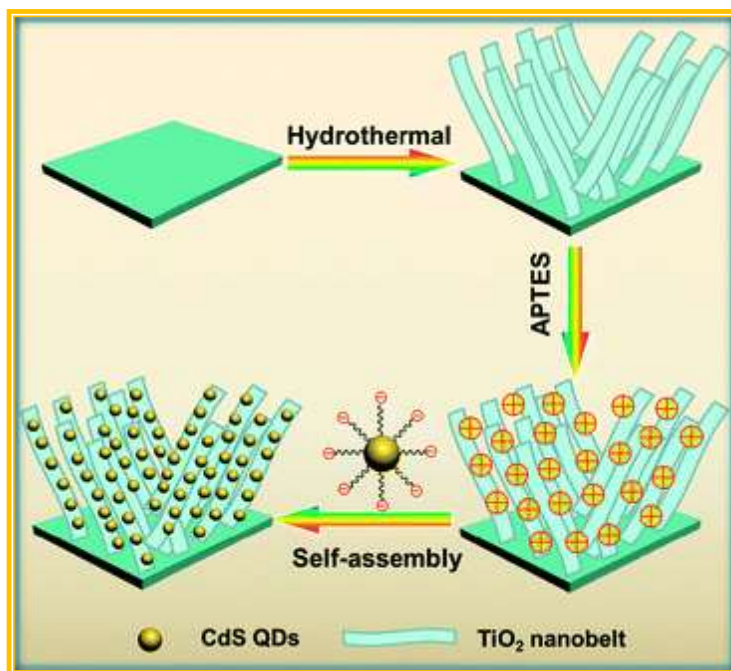
**Scheme 4.2:** Schematic representation of self-assembly of $TiO_2$ nanobelt–CdS quantum dot heterostructures [50].

*Thermal decomposition method:* Lutz et al. [58] have reported the preparation of CdS sensitized $TiO_2$ films by controlled thermal decomposition of a metal xanthate precursor. The films are prepared by decomposing pyridine adduct of cadmium ethylxanthate at 200 ºC under nitrogen atmosphere. Tristao et al. [59] have reported the thermal decomposition of cadmium thiourea complex impregnated on $TiO_2$ at 300 ºC under nitrogen atmosphere. In most of the reported methods, the synthesis of CdS–$TiO_2$ nanocomposites has been carried out at high temperatures (200 to 600 ºC) and in inert atmosphere (e.g. $N_2$), and the time required for the synthesis is about 3 to 4 days.

In the present study, CdS–$TiO_2$ nanocomposites have been prepared by a two-step method. Nanocrystalline $TiO_2$ was first prepared by sol–gel method [60]. In the second step, CdS–$TiO_2$ nanocomposites were synthesized by the thermal decomposition of cadmium acetate and thiourea in diphenyl ether in the presence of $TiO_2$ at about 150 ºC for one hour. The effect of using four different types of $TiO_2$ (as-prepared sol–gel $TiO_2$ nanoparticles, sol–gel $TiO_2$ after calcination at 500 ºC, sol–gel $TiO_2$ after calcination at 700 ºC and macro-crystalline $TiO_2$) on the structure, and optical properties of the nanocomposites was investigated.

### 4.1.2 Experimental Details

### Chemicals

The chemicals used were cadmium acetate (Himedia), titanium(IV) isopropoxide (Aldrich), thiourea (Rankem), titanium(IV) oxide (Aldrich), diphenyl ether (Aldrich), nitric acid (Rankem), ethanol (Changshu Yangyuan Chemicals, China), methanol (Rankem) and Millipore$^{®}$ water. All the chemicals were used as received.

### Synthesis

The CdS–TiO$_2$ nanocomposites were synthesized by the thermal decomposition method. Nanocrystalline TiO$_2$ was first synthesized by sol–gel method as reported by Choi et al [60]. A mixture of titanium(IV) isopropoxide (30 mL) and absolute ethanol (5 mL) was added to an aqueous solution (180 mL) containing 2 mL of concentrated HNO$_3$ under vigorous stirring. The suspension was stirred at 80 °C for about six hours and then evaporated to obtain a yellowish TiO$_2$ powder (Scheme 4.3).

| Ti (IV) isopropoxide (30 mL) | + | Ethanol (5 mL) | + | $H_2O$ (180 mL) | + | $HNO_3$ (2 mL) |

Stirring
↓

**Suspension**

$80^{\circ}C$, Stirred for 6h
↓

**Sol**

Evaporation at 80 °C
↓

**$TiO_2$ (Yellow powder)**

Calcined at 500 °C and 700 °C
↓

**$TiO_2$ (Crystalline)**
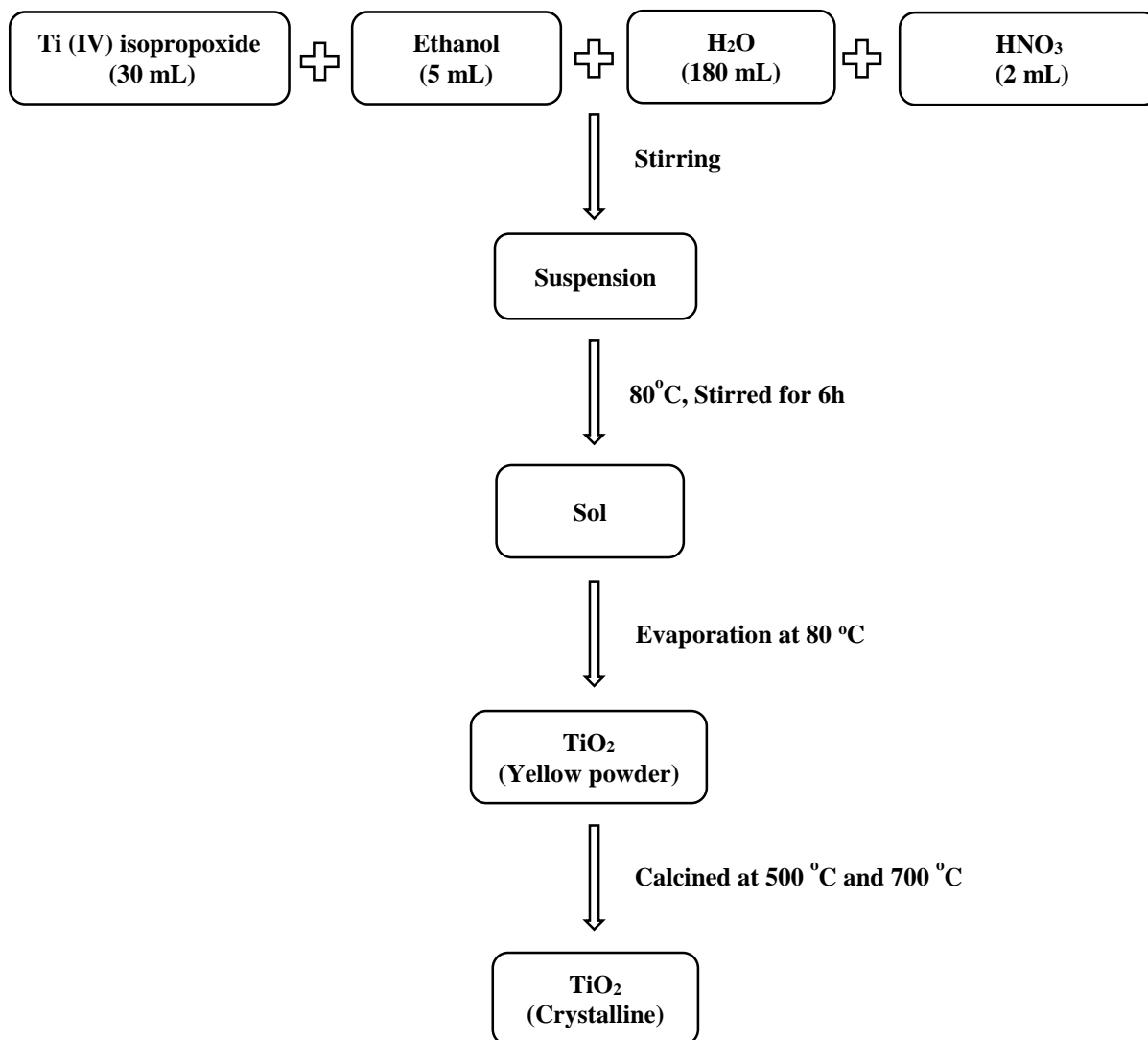
**Scheme 4.3:** Synthesis of $TiO_2$ nanoparticles by sol-gel process [60].

In the second step, the CdS–$TiO_2$ nanocomposites were prepared by refluxing a mixture of cadmium acetate and thiourea in different molar ratios in the presence of about 300 mg of $TiO_2$ (as-prepared sol-gel $TiO_2$, after calcination at 500 °C, after calcination at 700 °C and macro-crystalline $TiO_2$) in diphenyl ether (boiling point = 257 °C) at about 150 °C for one hour. The precipitates obtained were centrifuged, washed with methanol and dried overnight under vacuum to obtain the CdS–$TiO_2$ nanocomposite powders. Scheme 4.4 shows the schematic diagram of the synthesis of CdS-$TiO_2$ nanocomposites via thermal decomposition approach. Four different nanocomposites were prepared using each $TiO_2$ by varying the concentrations of cadmium acetate and thiourea. The designation of various CdS–$TiO_2$ nanocomposites, prepared under different synthetic conditions, is given in Table 4.2.

**Cadmium acetate + Thiourea + TiO$_2$ + Diphenyl ether** → **Refluxed at 150 $^o$C 60 min** → **Slurry**

i) Allowed to cool
ii) Precipitatation
   with methanol

**Yellow precipitate**

**CdS-TiO$_2$ nanocomposites** ← **Dried under vacuum**
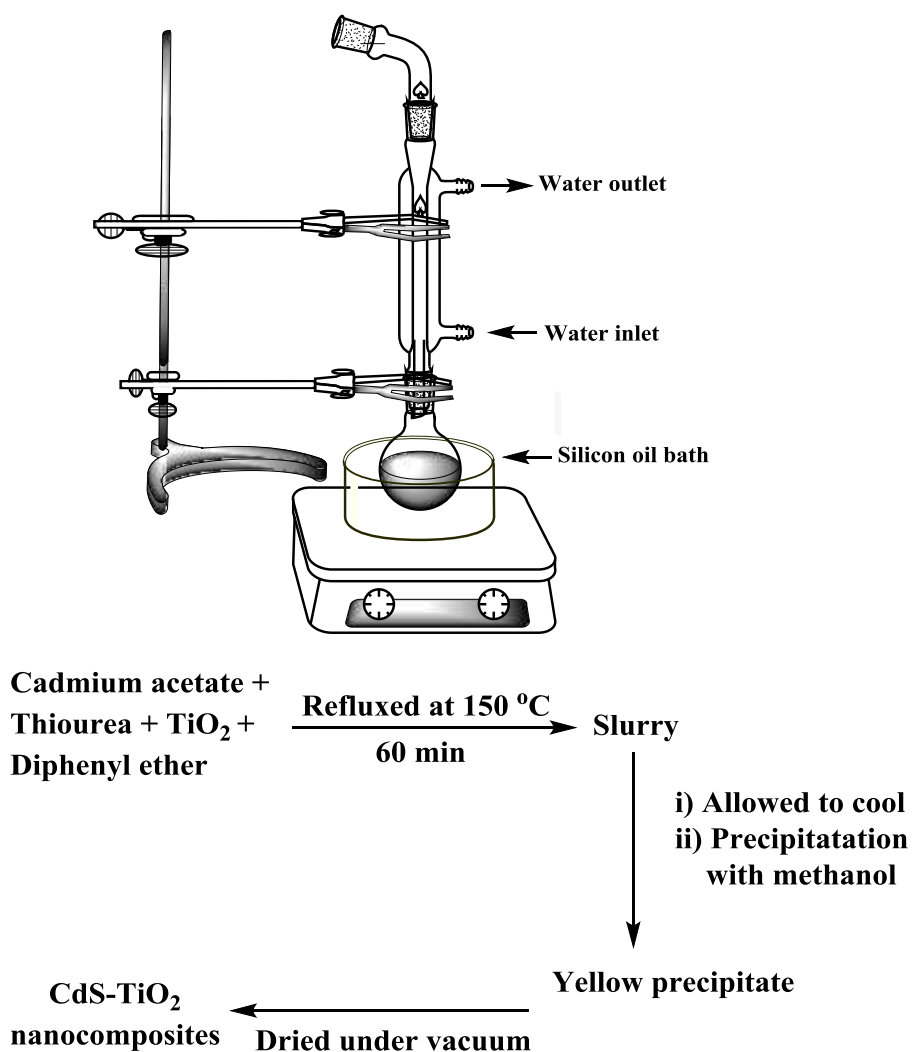
**Scheme 4.4:** Schematic diagram for the synthesis of CdS-TiO$_2$ nanocomposites via thermal decomposition approach.

**Table 4.2:** Designation of various CdS-TiO$_2$ nanocomposites prepared using different synthetic conditions.

| Sample code | TiO$_2$ used | Cadmium acetate (mmol) | Thiourea (mmol) |
|:---:|:---:|:---:|:---:|
| CdS | - | 1 | 1 |
| CTA1 | as-prepared sol-gel TiO$_2$ | 1 | 1 |
| CTA2 | ,, | 0.5 | 0.5 |
| CTA3 | ,, | 0.25 | 0.25 |
| CTA4 | ,, | 0.15 | 0.15 |
| CT1 | Sol-gel TiO$_2$ (500 $^\circ$C) | 1 | 1 |
| CT2 | ,, | 0.5 | 0.5 |
| CT3 | ,, | 0.25 | 0.25 |
| CT4 | ,, | 0.15 | 0.15 |
| CTR1 | Sol-gel TiO$_2$ (700 $^\circ$C) | 1 | 1 |
| CTR2 | ,, | 0.5 | 0.5 |
| CTR3 | ,, | 0.25 | 0.25 |
| CTR4 | ,, | 0.15 | 0.15 |
| C1 | Macro-crystalline TiO$_2$ | 1 | 1 |
| C2 | ,, | 0.5 | 0.5 |
| C3 | ,, | 0.25 | 0.25 |
| C4 | ,, | 0.15 | 0.15 |

### 4.1.3 Results and Discussion

### 4.1.3.1 XRD Results

Fig. 4.2 shows the XRD patterns of as-prepared sol–gel $TiO_2$, after calcination at 500 °C and 700 °C and commercial (macro-crystalline) $TiO_2$. In the XRD patterns of as-prepared sol-gel $TiO_2$ and $TiO_2$ after calcination at 500 °C, distinct peaks at $2\theta$ = 25.33°, 37.84°, 48.07°, 53.95°, 62.75°, 70.34°, 75.12° and 82.75° corresponding to (101), (004), (200), (105), (204), (220), (215) and (224) planes of anatase (JCPDS file no. 84-1286) are observed. The XRD pattern of sol-gel $TiO_2$ after calcination at 700 °C shows peaks at $2\theta$ = 27.55°, 36.06°, 41.30°, 44.16°, 54.44°, 56.80°, 62.92°, 64.2°, 69.1°, 69.8° and 82.53° corresponding to (110), (101), (111), (210), (211), (220), (002), (310), (301), (112) and (321) planes of rutile phase (JCPDS no. 78-1510). The XRD pattern of commercial (macro-crystalline) $TiO_2$ shows peaks at 25.33°, 36.7°, 37.84°, 38.5°, 48.07°, 53.95°, 62.75°, 70.34°, 75.12° and 82.75° corresponding to (101), (103), (004), (112), (200), (105), (204), (220), (215), (301) and (224) planes of anatase (JCPDS file no. 84-1286). The crystallite size values for as prepared sol–gel $TiO_2$, sol-gel $TiO_2$ calcined at 500 °C, sol-gel $TiO_2$ calcined at 700 °C and commercial (macro-crystalline) $TiO_2$, calculated using Debye-Scherrer equation, are 4.8 nm, 10 nm, 28 nm and 120 nm, respectively.
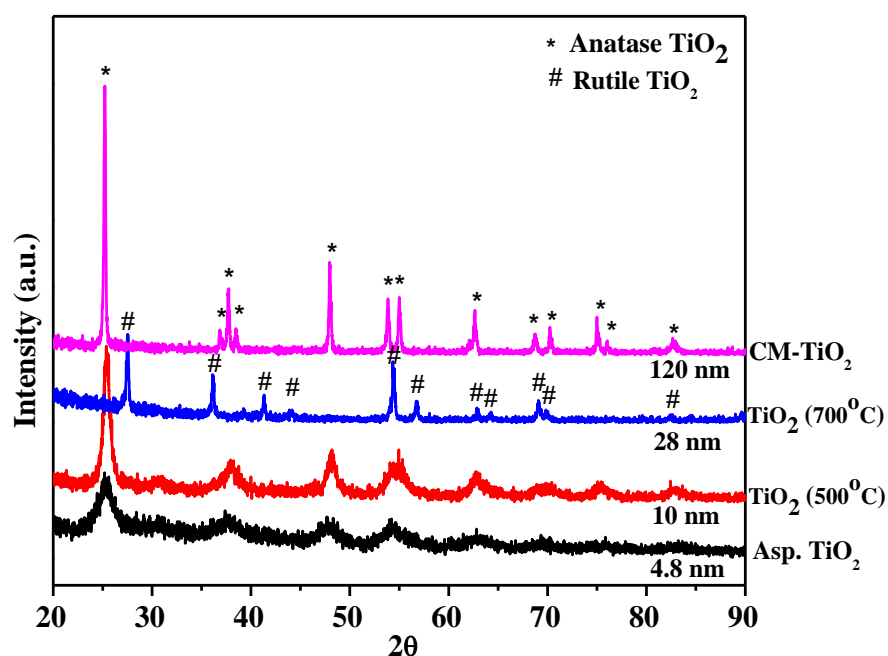


**Fig. 4.2:** XRD patterns of as-prepared sol-gel $TiO_2$ and after calcination at 500 °C and 700 °C. The XRD pattern of macro-crystalline $TiO_2$ (Aldrich, CM-$TiO_2$) is also shown.

Fig. 4.3(a) shows the XRD patterns of pure CdS and the CdS–TiO$_2$ nanocomposites prepared using as-prepared sol–gel TiO$_2$ (CTA1-CTA4). Peaks due to CdS (JCPDS file no. 75-1546) and anatase are present in the nanocomposites. Figs. 4.3(b) and (d) show the XRD patterns of nanocomposites prepared using sol-gel TiO$_2$ after calcination at 500 $^o$C (CT1-CT4) and macro-crystalline TiO$_2$ (C1-C4), respectively. Peaks due CdS and anatase are present in all these nanocomposites, too. Fig. 4.3(c) shows the XRD patterns of CdS-TiO$_2$ nanocomposites prepared using sol–gel TiO$_2$ after calcination at 700 $^o$C (CTR1-CTR4). Peaks due CdS and rutile phase are present in all these nanocomposites. The crystallite size of CdS, TiO$_2$ and CdS in the CdS–TiO$_2$ nanocomposites was calculated using Debye–Scherrer formula (Table 4.5). The crystallite size of pure CdS nanoparticles is 2.3 nm. The crystallite size of CdS in the nanocomposites prepared using as-prepared sol–gel TiO$_2$ varies from 3.9 to 5.5 nm. In the nanocomposites prepared using TiO$_2$ after calcination at 500 $^o$C and 700 $^o$C, the crystallite size of CdS varies from 3 to 6 nm and 8.8 to 12.0 nm, respectively. The crystallite size of CdS in the nanocomposites prepared using macro-crystalline TiO$_2$ varies from 13.3 to 18 nm. In the nanocomposites, the crystallite size of CdS decreases with decrease in the concentration of cadmium acetate and thiourea used during their preparation (Table 4.2).
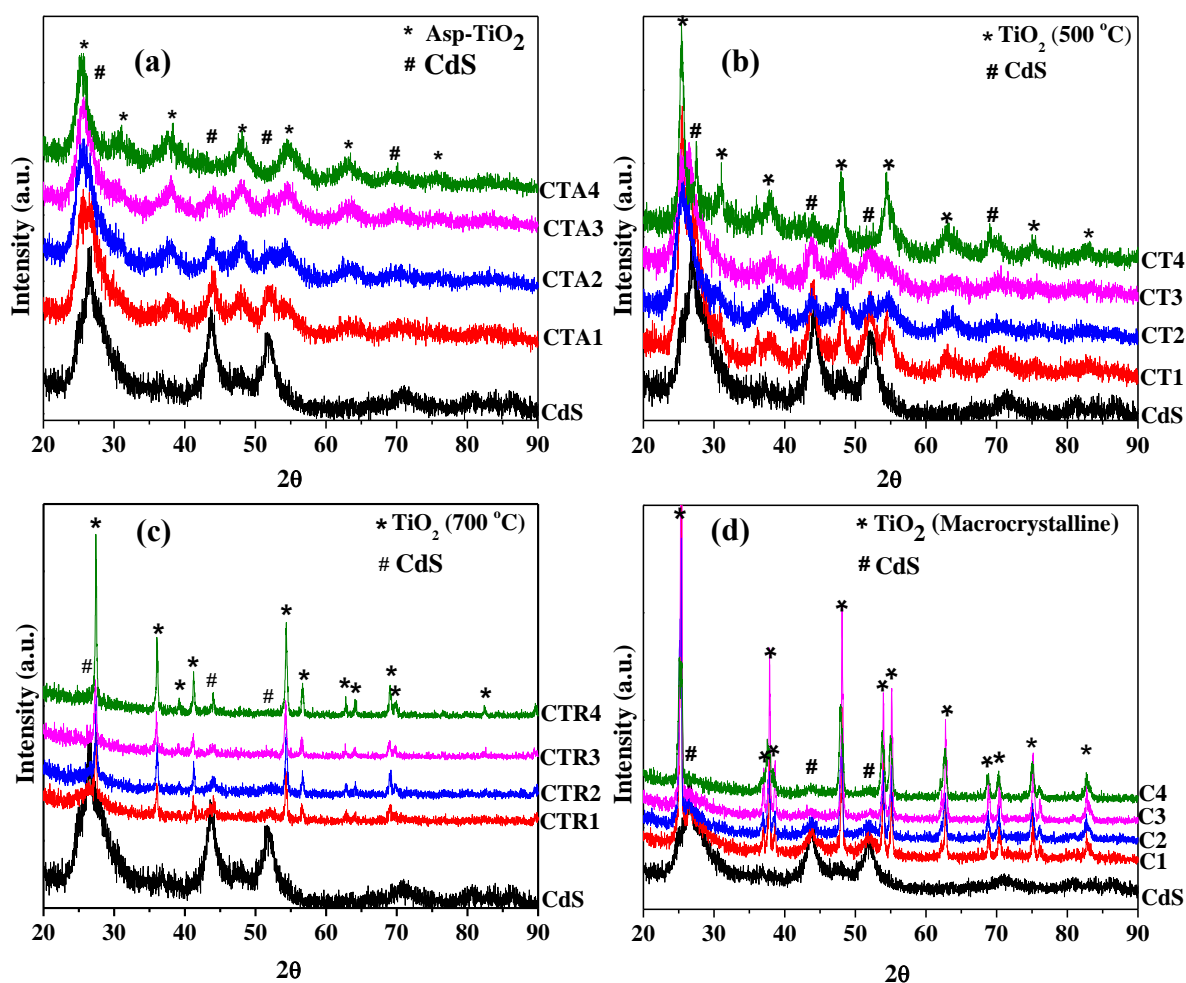
**Fig. 4.3:** XRD patterns of CdS–TiO$_2$ nanocomposites prepared using (a) as-prepared sol-gel TiO$_2$ nanoparticles, (b) sol-gel TiO$_2$ after calcination at 500 $^o$C, (c) sol-gel TiO$_2$ after calcination at 700 $^o$C and (d) macro-crystalline TiO$_2$.

## 4.1.3.2 FE-SEM and EDXA Results

The FE-SEM images of pure CdS indicate that it consists of agglomerated small particles with irregular morphology (Fig. 4.4). The as-prepared sol–gel TiO$_2$, sol-gel TiO$_2$ after calcination at 500 $^o$C, sol-gel TiO$_2$ after calcination at 700 $^o$C and macro-crystalline TiO$_2$ showed agglomerated particles.
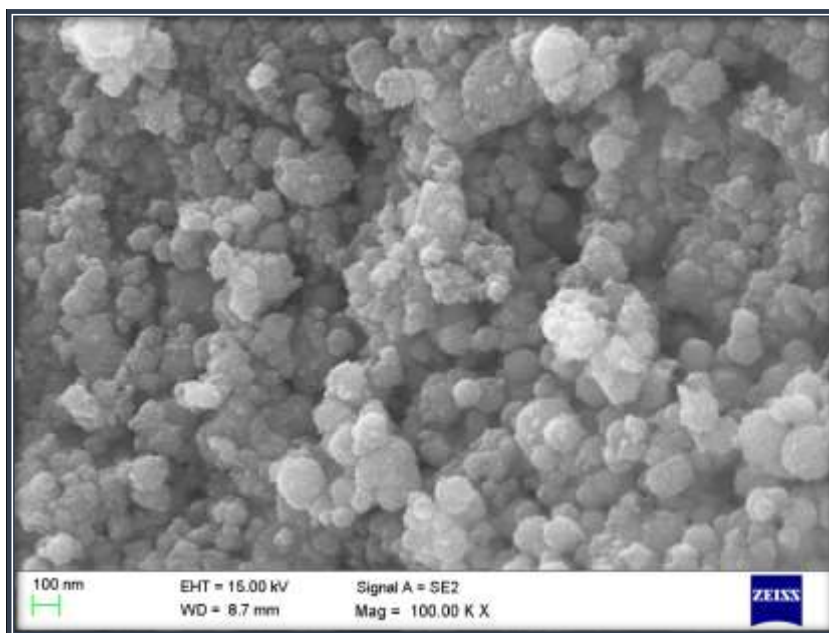
**Fig. 4.4:** FE-SEM image of CdS nanoparticles.

Fig. 4.5 shows the FE-SEM images of CdS–TiO$_2$ nanocomposites prepared using as-prepared sol–gel TiO$_2$ (CTA1-CTA4). Small particles which are highly agglomerated can be noticed and it was found that the agglomeration decreases with decrease in the concentration of cadmium acetate and thiourea used during the preparation of the nanocomposites.
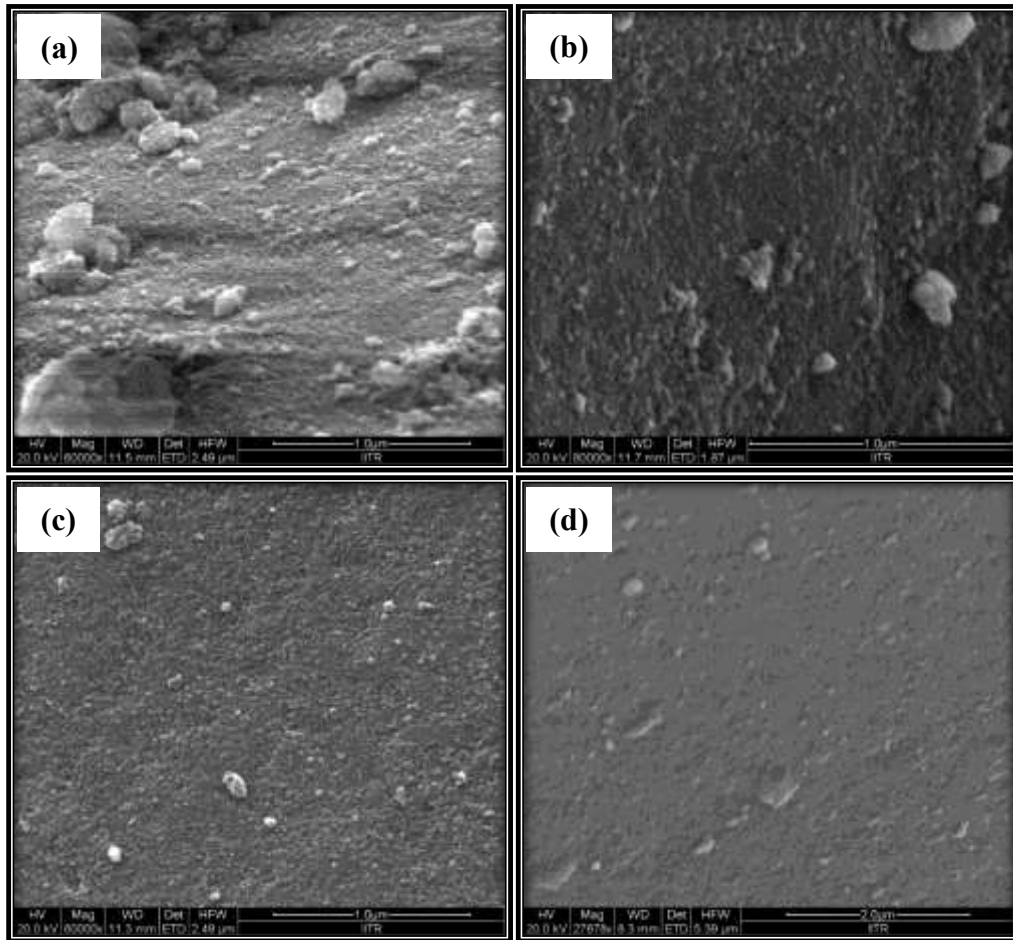
**Fig. 4.5:** FE-SEM images of CdS−TiO$_2$ nanocomposites prepared using as-prepared sol-gel TiO$_2$ nanoparticles: (a) CTA1, (b) CTA2, (c) CTA3 and (d) CTA4.

Fig. 4.6 and Fig. 4.7 show the FE-SEM images of CdS−TiO$_2$ nanocomposites prepared using sol−gel TiO$_2$ after calcination at 500 $^o$C and 700 $^o$C, respectively. Well dispersed small particles with close to spherical morphology can be noticed.
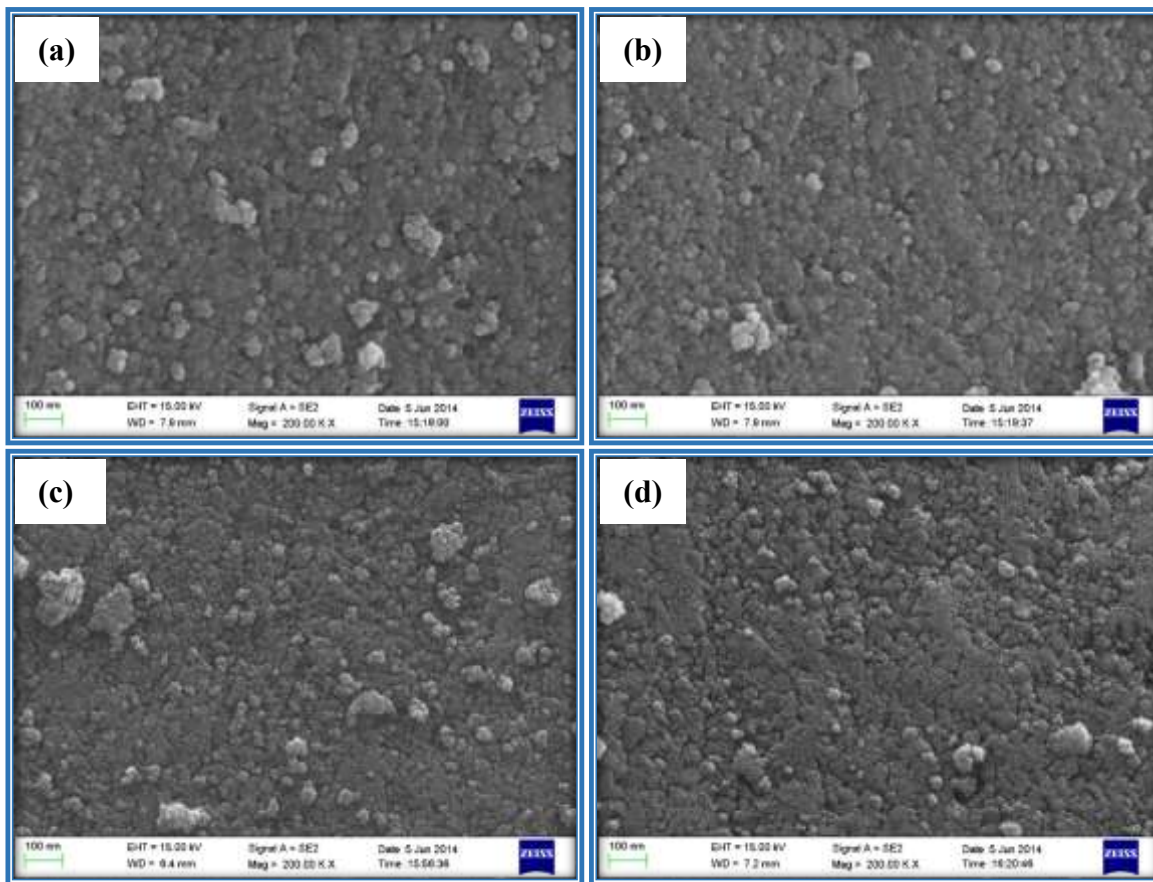
**Fig. 4.6:** SEM images of CdS−TiO$_2$ nanocomposites prepared using sol-gel TiO$_2$ nanoparticles after calcination at 500 $^o$C: (a) CT1 (b) CT2 (c) CT3 and (d) CT4.
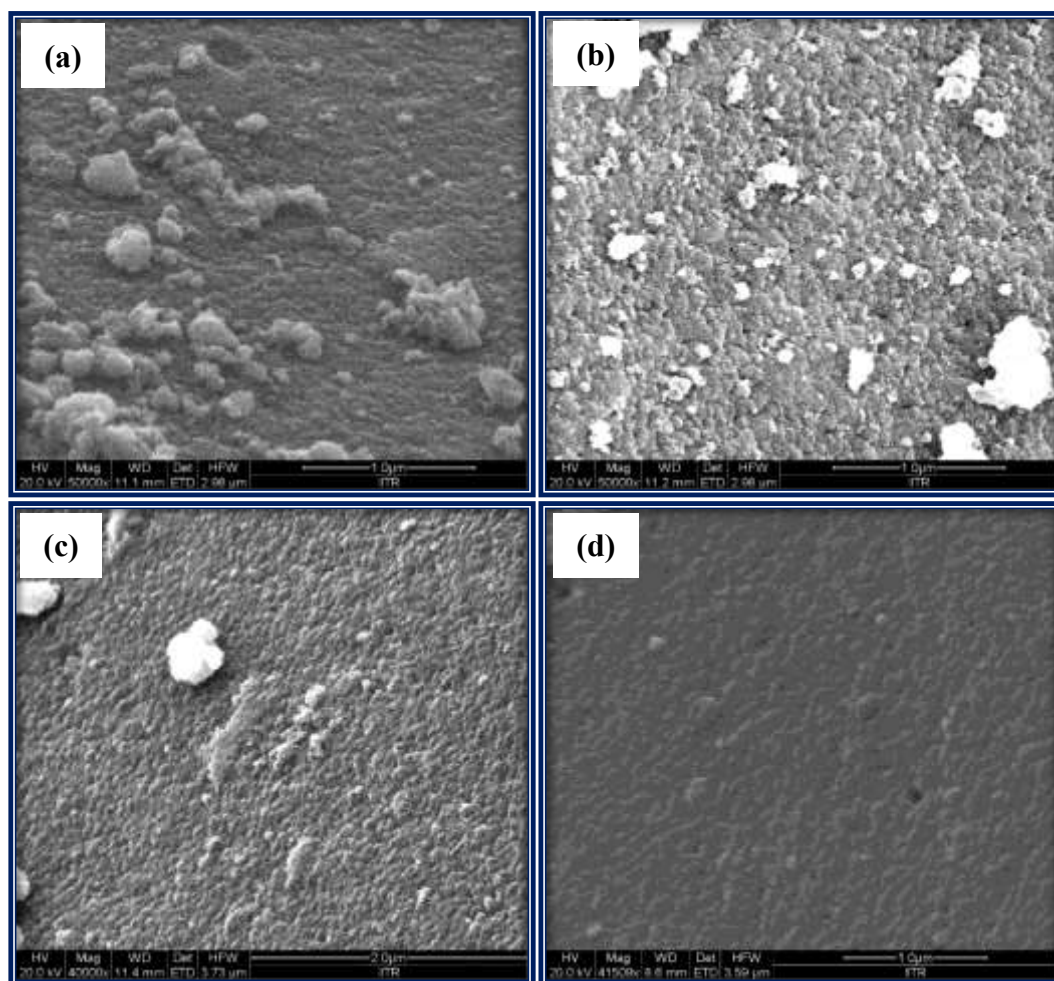
**Fig. 4.7:** SEM images of CdS−TiO$_2$ nanocomposites prepared using sol-gel TiO$_2$ nanoparticles after calcination at 700 $^{\circ}$C: (a) CTR1, (b) CTR2, (c) CTR3 and (d) CTR4.

Fig. 4.8 shows the FE-SEM images of CdS-TiO$_2$ nanocomposites prepared using macro-crystalline TiO$_2$ in which agglomerated large particles with no particular morphology can be noticed.
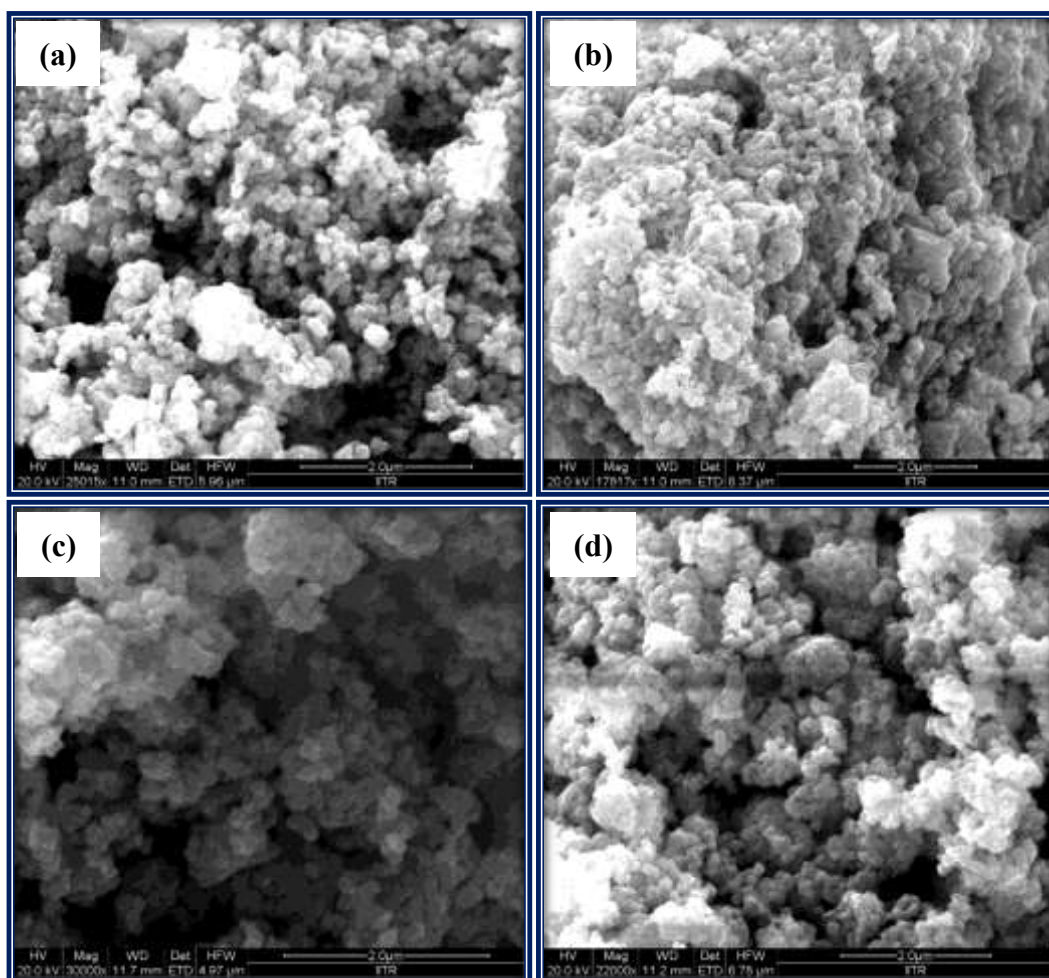
**Fig. 4.8:** SEM images of CdS−TiO$_2$ nanocomposites prepared using macro-crystalline TiO$_2$: (a) C1, (b) C2, (c) C3 and (d) C4.

Figs. 4.9 to 4.12 show the EDXA patterns of CdS-TiO$_2$ nanocomposites prepared using different TiO$_2$ (as-prepared sol-gel TiO$_2$, sol-gel TiO$_2$ after calcination at 500 $^{\circ}$C and 700 $^{\circ}$C, and macro-crystalline TiO$_2$). The EDX analysis shows the presence of oxygen, titanium, cadmium and sulfur in all the CdS-TiO$_2$ nanocomposites.
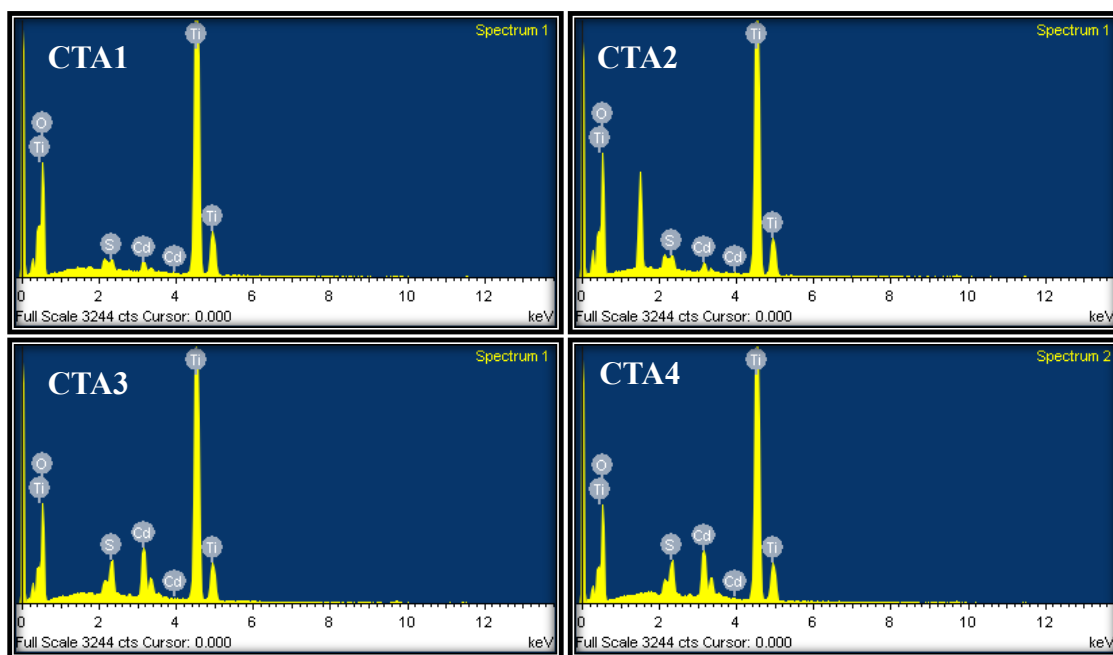
**Fig. 4.9:** EDXA patterns of CdS-TiO$_2$ nanocomposites prepared using as-prepared sol-gel TiO$_2$ nanoparticles.
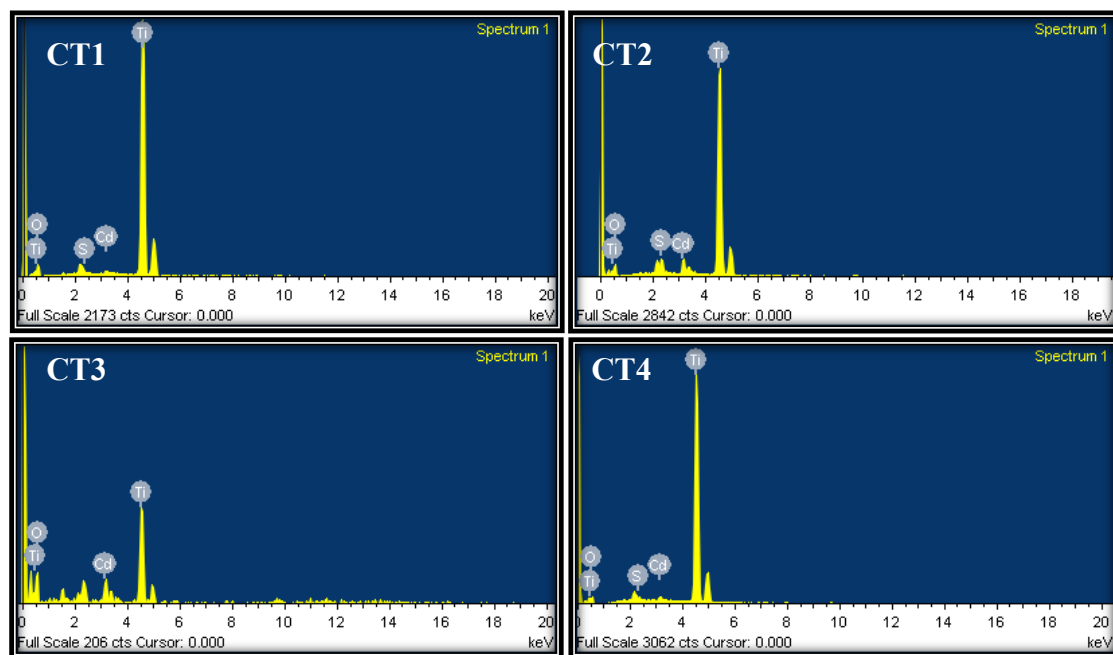


**Fig. 4.10:** EDXA patterns of CdS-TiO$_2$ nanocomposites prepared using sol-gel TiO$_2$ nanoparticles after calcination at 500 ºC.
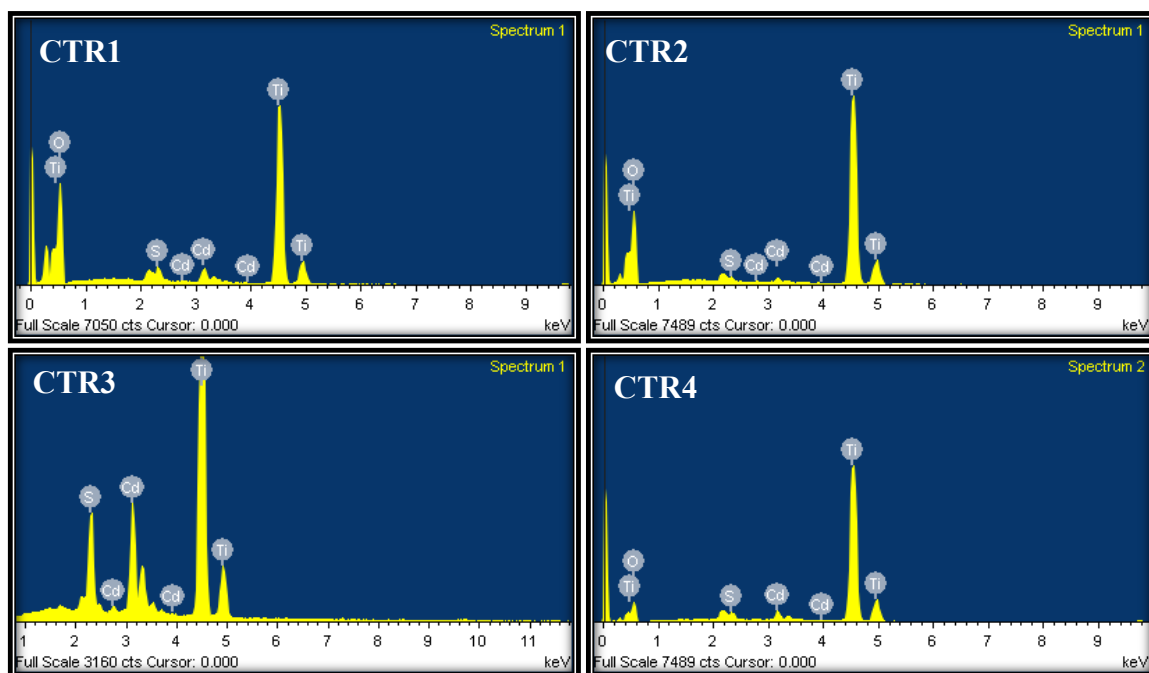
**Fig. 4.11:** EDXA patterns of CdS-TiO$_2$ nanocomposites prepared using sol-gel TiO$_2$ nanoparticles after calcination at 700 $^o$C.
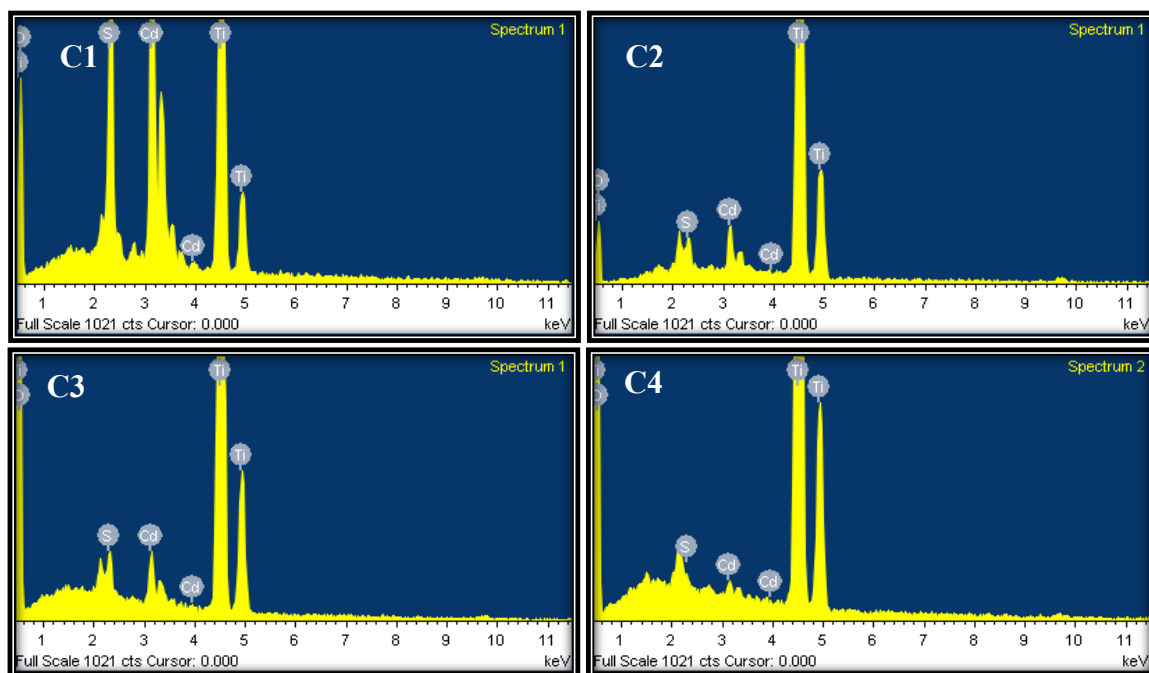


**Fig. 4.12:** EDXA patterns of CdS-TiO$_2$ nanocomposites prepared using macro-crystalline TiO$_2$.

Tables 4.3 and 4.4 show the EDX analysis results of the CdS-TiO$_2$ nanocomposites prepared using as-prepared sol–gel TiO$_2$ nanoparticles, sol-gel TiO$_2$ after calcination at 500 °C, sol-gel TiO$_2$ after calcination at 700 °C and macro-crystalline TiO$_2$. The nanocomposites prepared using [Cd$^{2+}$]:[S$^{2-}$] = 1:1 molar ratio and all the four different types of TiO$_2$ exhibit uniform elemental distribution. The nanocomposites prepared using [Cd$^{2+}$]:[S$^{2-}$] = 0.5:0.5 and 0.25:0.25 and all the four types of TiO$_2$ samples show non-uniform elemental distribution. The nanocomposites prepared using [Cd$^{2+}$]:[S$^{2-}$] = 0.15:0.15 and sol–gel TiO$_2$ (after calcination at 500 °C and 700 °C) show uniform elemental distribution. On the other hand, the nanocomposites prepared using ([Cd$^{2+}$]:[S$^{2-}$] = 0.15:0.15) and as-prepared sol–gel TiO$_2$ and macro-crystalline TiO$_2$ show non-uniform elemental distribution.

**Table 4.3:** EDX analysis data for CdS-TiO$_2$ nanocomposites prepared using as-prepared sol-gel TiO$_2$ and sol-gel TiO$_2$ calcined at 500 °C.

| Nanocomposite | TiO$_2$ used | Weight% | | | | Atomic% | | | | Comment |
|---|---|---|---|---|---|---|---|---|---|---|
| | | O | S | Ti | Cd | O | S | Ti | Cd | |
| CTA1 | TiO$_2$ as-prepared | 50.6 to 51.5 | 1.2 to 1.5 | 46.2 to 46.9 | 1.7 to 1.9 | 75.7 to 76.3 | 0.3 to 0.4 | 22.9 to 23.5 | 0.2 to 0.4 | Uniform |
| CTA2 | ,, | 54.5 to 55.6 | 1.6 to 1.7 | 41.6 to 43.1 | 1.6 to 2.0 | 78.4 to 79.2 | 0.1 to 0.5 | 19.8 to 20.7 | 0.3 to 0.4 | Non-uniform |
| CTA3 | ,, | 47.4 to 47.9 | 1.9 to 2.1 | 40.8 to 40.9 | 1.5 to 1.6 | 74.7 to 75.0 | 0.5 to 0.6 | 21.4 to 21.5 | 2.0 to 2.2 | Uniform |
| CTA4 | ,, | 24.8 to 42.9 | 0.4 to 0.9 | 55.7 to 73.6 | 0.7 to 1.1 | 49.9 to 69.3 | 0.4 to 0.8 | 30.0 to 49.3 | 0.2 to 0.3 | Non-uniform |
| CT1 | TiO$_2$ (Calcined at 500 °C) | 38.5 to 41.0 | 3.8 to 3.9 | 41.3 to 43.5 | 1.3 to 1.4 | 75.7 to 76.3 | 1.2 to 1.5 | 22.9 to 23.5 | 0.2 to 0.4 | Uniform |

| Nanocomposite | TiO₂ used | O | S | Ti | Cd | O | S | Ti | Cd | Comment |
|---|---|---|---|---|---|---|---|---|---|---|
| CT2 | ,, | 54.5 to 55.6 | 2.3 to 2.8 | 41.6 to 43.1 | 1.6 to 2.0 | 78.4 to 79.2 | 1.9 to 2.4 | 19.8 to 20.7 | 0.3 to 0.4 | Non-uniform |
| CT3 | ,, | 45.5 to 48.6 | 2.1 to 2.3 | 36.7 to 41.9 | 1.6 to 1.9 | 74.2 to 76.3 | 1.7 to 1.8 | 19.2 to 22.8 | 2.4 to 2.9 | Uniform |
| CT4 | ,, | 34.8 to 35.2 | 0.9 to 1.0 | 58.0 to 59.6 | 4.7 to 4.9 | 62.1 to 63.3 | 0.8 to 0.9 | 33.9 to 34.8 | 1.0 to 1.2 | Uniform |

**Table 4.4:** EDX analysis data for CdS-TiO₂ nanocomposites prepared using sol-gel TiO₂ calcined at 700 °C and macro-crystalline TiO₂.

| Nanocomposite | TiO₂ used | Weight% | | | | Atomic% | | | | Comment |
|---|---|---|---|---|---|---|---|---|---|---|
| | | O | S | Ti | Cd | O | S | Ti | Cd | |
| CTR1 | TiO₂ (Calcined at 700 ºC ) | 57.4 to 58.3 | 0.9 to 1.1 | 36.6 to 37.3 | 4.0 to 4.2 | 80.8 to 81.5 | 0.6 to 0.8 | 17.0 to 17.5 | 0.7 to 0.8 | Uniform |
| CTR2 | ,, | 54.7 to 58.0 | 0.3 to 0.8 | 43.6 to 45.6 | 0.7 to 1.4 | 78.5 to 84.6 | 0.1 to 0.2 | 20.1 to 21.3 | 0.2 to 0.3 | Non-uniform |
| CTR3 | ,, | 8.2 to 13.6 | 0.2 to 0.4 | 84.4 to 89.1 | 1.8 to 2.7 | 21.4 to 32.2 | 0.3 to 0.5 | 70.6 to 84.4 | 0.6 to 0.9 | Uniform |
| CTR4 | ,, | 28.9 to 29.7 | 0.2 to 0.3 | 60.5 to 60.6 | 4.9 to 5.0 | 59.0 to 61.1 | 0.8 to 0.9 | 59.0 to 61.1 | 1.2 to 1.3 | Uniform |
| C1 | Macro-crystalline TiO₂ | 46.3 to 47.9 | 4.9 to 6.9 | 31.0 to 33.0 | 7.4 to 8.4 | 74.2 to 75.4 | 3.5 to 4.5 | 16.3 to 16.7 | 4.0 to 6.0 | Uniform |

| | | | | | | | | | | |
|---|---|---|---|---|---|---|---|---|---|---|
| C2 | ,, | 28.0 to 41.4 | 5.4 to 9.4 | 30.7 to 33.5 | 9.7 to 1.9 | 59.0 to 71.2 | 4.6 to 9.8 | 19.3 to 21.6 | 4.8 to 9.6 | Non-uniform |
| C3 | ,, | 14.7 to 28.7 | 0.6 to 0.9 | 65.7 to 78.4 | 4.9 to 6.0 | 34.8 to 55.6 | 0.6 to 1.0 | 42.5 to 65.0 | 1.3 to 2.0 | Non-uniform |
| C4 | ,, | 58.0 to 59.0 | 0.4 to 0.7 | 77.9 to 82.6 | 2.6 to 3.3 | 77.9 to 81.6 | 0.3 to 0.5 | 17.5 to 20.8 | 0.5 to 0.7 | Non-uniform |

### 4.1.3.3 TEM and SAED Results

Fig. 4.13(a) shows the TEM image of pure CdS nanoparticles. Agglomerated small particles with mean size $6.3 \pm 0.6$ nm can be observed. Fig 4.13(b) shows the TEM image of as-prepared sol–gel $TiO_2$ nanoparticles. Well dispersed uniform sized ($13.8 \pm 2.9$ nm) particles can be observed. Fig. 4.13(c) and (d) show the TEM images of sol–gel prepared $TiO_2$ samples after calcination at 500 °C and 700 °C, respectively. Irregular shaped small as well as large particles can be noticed. The particle size of sol-gel $TiO_2$ after calcination at 500 °C is $25.4 \pm 15.7$ nm whereas that of $TiO_2$ after calcination at 700 °C is $32.0 \pm 9.5$ nm. Insets of Fig. 4.13(a), (c) and (d) show the SAED patterns of CdS and $TiO_2$ indicating their polycrystalline nature. The SAED pattern of as-prepared sol-gel $TiO_2$ (Fig. 4.13(b)) indicates that it is less crystalline compared to the other $TiO_2$ samples.
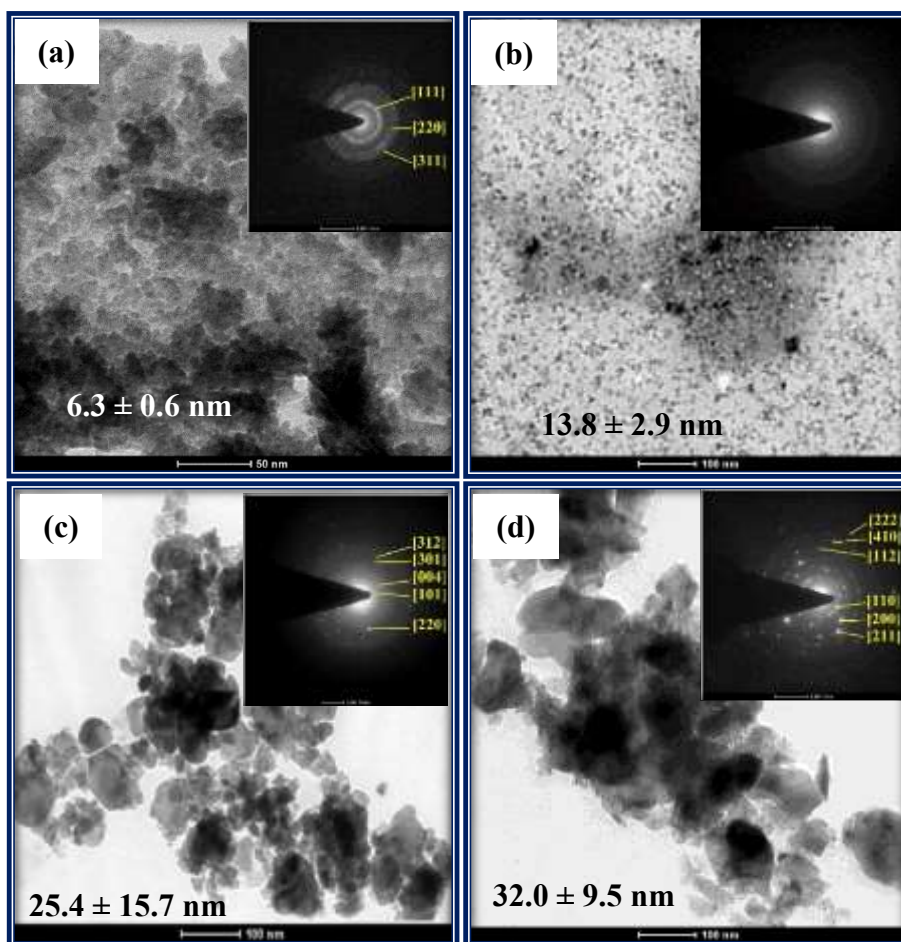
**Fig. 4.13:** TEM images and SAED patterns of (a) pure CdS nanoparticles, (b) as-prepared sol-gel $TiO_2$ nanoparticles, (c) sol-gel $TiO_2$ nanoparticles after calcination at 500 $^{\circ}$C and (d) $TiO_2$ nanoparticles after calcination at 700 $^{\circ}$C.

Fig. 4.14 shows the TEM images of CdS–$TiO_2$ nanocomposites (CTA1-CTA4) prepared using as-prepared sol-gel $TiO_2$ nanoparticles. The particle size of the nanocomposites decreases from 10.4 to 5.2 nm with decrease in the concentration of cadmium acetate and thiourea used during the preparation of the nanocomposites. The inset of Fig. 4.14(a) corresponds to the SAED pattern of nanocomposite CTA1 where the observed rings are attributed to (111), (220), (311) planes of polycrystalline CdS along with a ring due to (101) plane of anatase. The inset of Fig. 4.14(c) corresponds to the SAED pattern of nanocomposite CTA3 where the observed rings are attributed to (111), (220), (222) planes of polycrystalline CdS along with rings due to (101), (211), (004) planes of anatase. In the SAED patterns of nanocomposites CTA2 and CTA4 (Insets of Fig. 4.14(b) and Fig. 4.14(d)), the observed rings are attributed to (111), (220), (222), (200) planes of polycrystalline CdS along with rings due to (101), (211) planes of anatase.
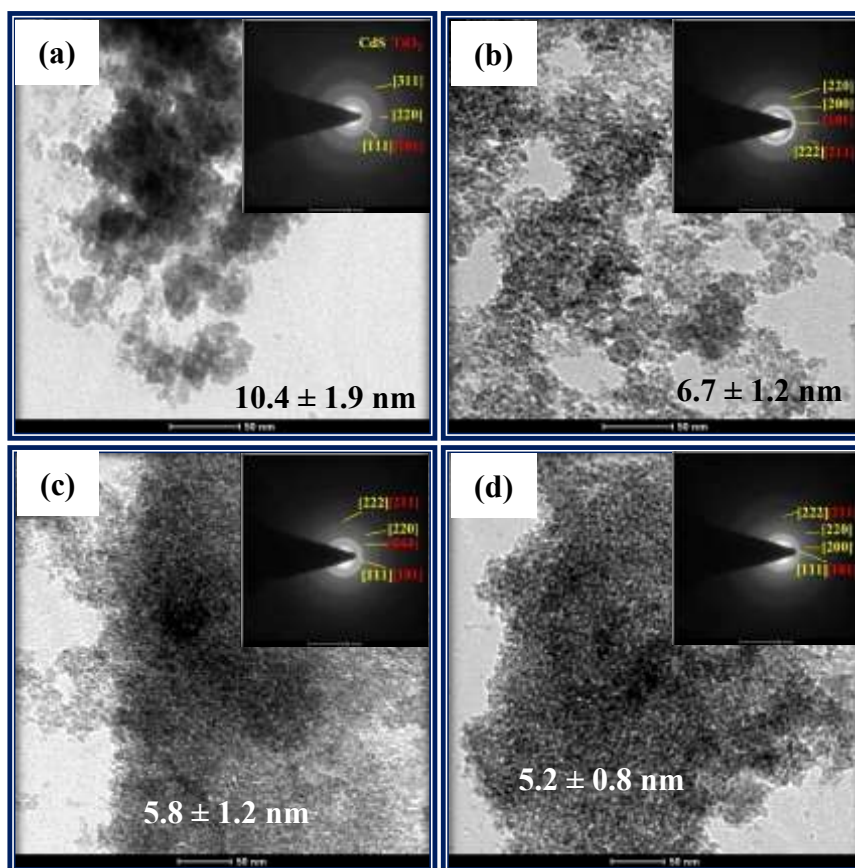
**Fig. 4.14:** TEM images and SAED patterns of CdS−TiO$_2$ nanocomposites prepared using as-prepared sol-gel TiO$_2$: (a) CTA1, (b) CTA2, (c) CTA3 and CTA4.

Fig. 4.15 shows the TEM images of CdS−TiO$_2$ nanocomposites (CT1-CT4) prepared using sol-gel TiO$_2$ calcined at 500 $^o$C. Particles of the nanocomposites, prepared using higher concentration of cadmium acetate and thiourea (CT1 and CT2), are more agglomerated as compared to those prepared using lower concentration of cadmium acetate and thiourea (CT3 and CT4). The particle size of the nanocomposites decreases from 12.6 to 10.5 nm with decrease in the concentration of cadmium acetate and thiourea used during the preparation of the nanocomposites. The inset of Fig. 4.15(a) corresponds to the SAED pattern of nanocomposite CT1 where the observed rings are attributed to (111), (220), (311), (206) planes of polycrystalline CdS along with rings due to (101), (107) and (224) planes of polycrystalline anatase. The observed rings in the SAED patterns of nanocomposites CT2 and CT3 (Insets of Fig. 4.15(b) and Fig. 4.15(c)) are attributed to (111), (220), (311) planes of polycrystalline CdS and (101), (105) and (213) planes of anatase. The inset of Fig. 4.15(d) corresponds to SAED pattern of nanocomposite CT4 where the rings and spots observed are due to (111), (222), (311), (331) planes of polycrystalline CdS and (101), (103), (112) and (105) planes of polycrystalline anatase.
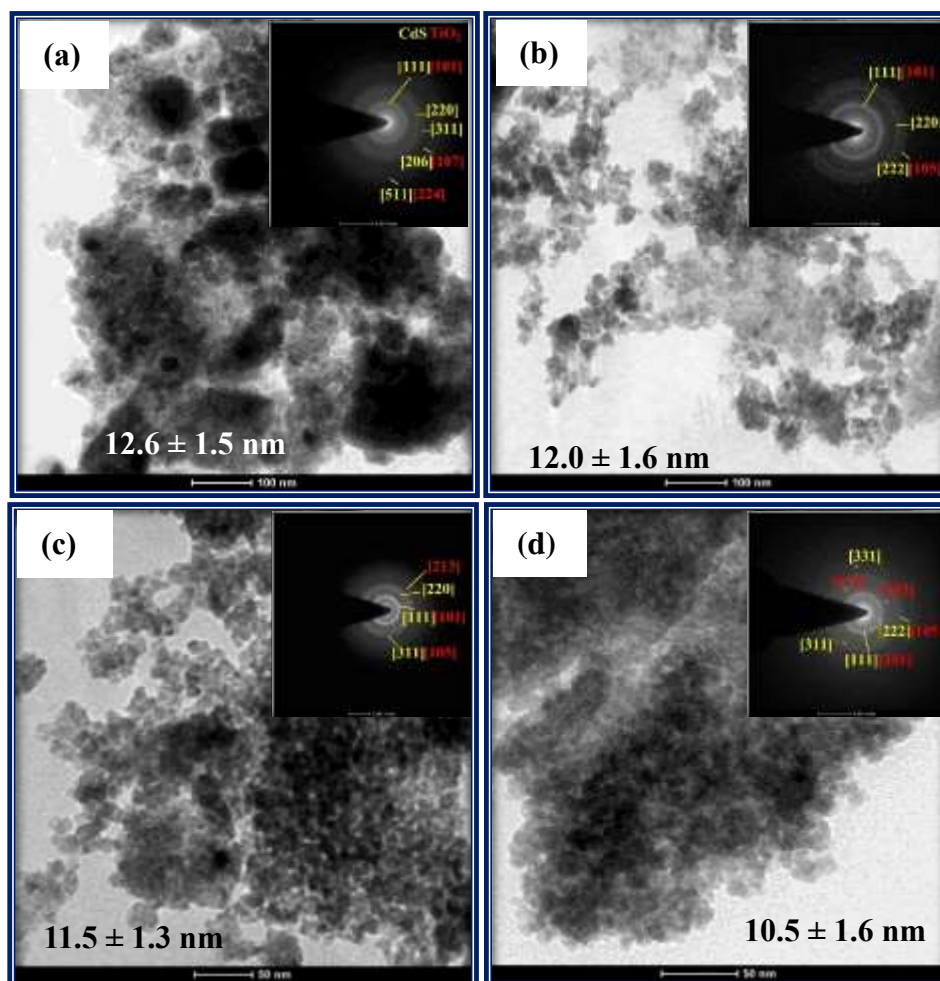
**Fig. 4.15:** TEM images and SAED patterns of CdS−TiO$_2$ nanocomposites prepared using sol-gel TiO$_2$ after calcination at 500 °C: (a) CT1, (b) CT2, (c) CT3 and CT4.

Nanocomposites CT1-CT4 show uniform elemental composition with better photocatalytic activity in photodegradation of rhodamine B dye compared to other nanocomposites (See Chapter 6). Thus HRTEM measurements were done and the high resolution TEM images (HRTEM) of nanocomposites CT1, CT2, CT3 and CT4 are shown in Fig. 4.16. The interplanar spacing of 0.35 nm and 0.33 nm, correspond to (101) plane of anatase and (111) plane of CdS, respectively.
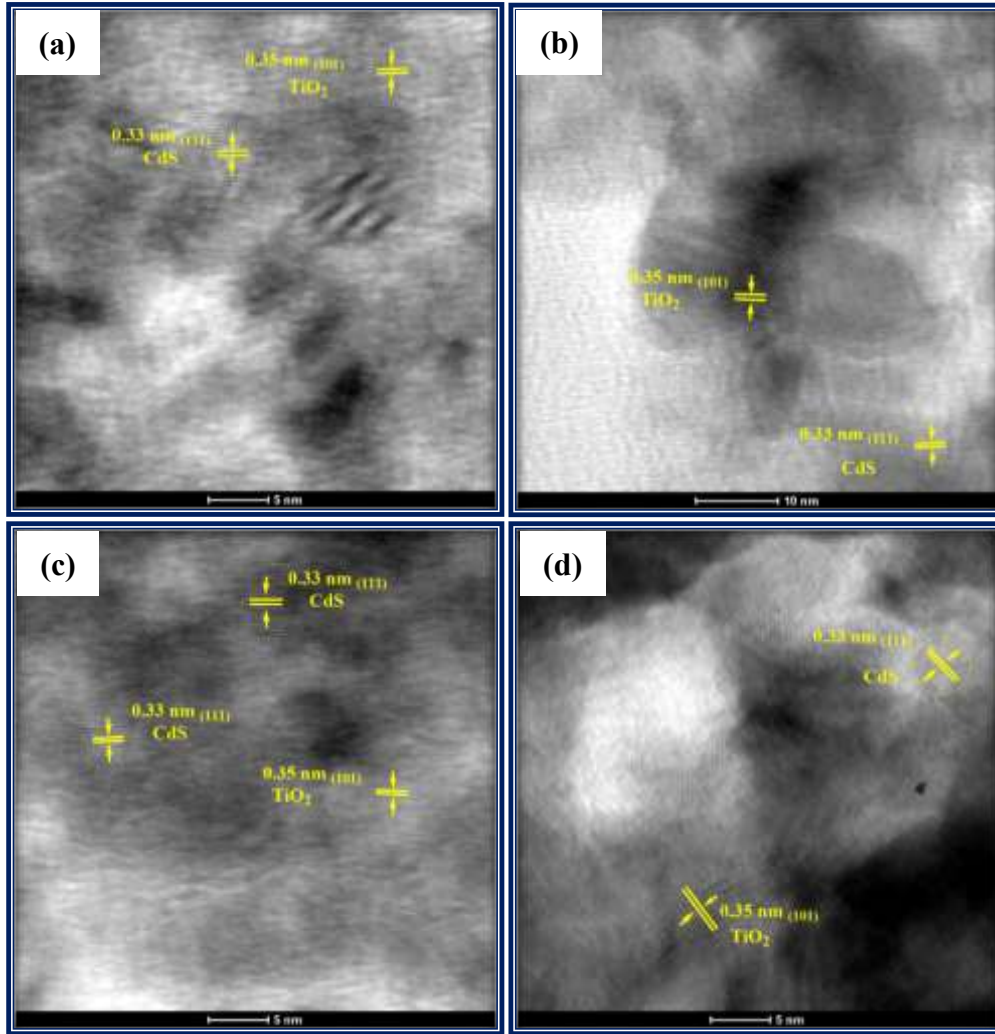
**Fig. 4.16:** HRTEM images of CdS-TiO$_2$ nanocomposites: (a) CT1, (b) CT2, (c) CT3 and CT4.

### 4.1.3.4 DRS Results

The optical properties of CdS, TiO$_2$ samples and the CdS−TiO$_2$ nanocomposites were investigated by UV−visible diffuse reflectance spectroscopy. The band gaps of all the samples were estimated from the DRS spectra using the following formula [24]:

$$\alpha h\nu = A\big(h\nu - E_g\big)^{1/2}$$

Where h is Planck's constant, $\nu$ is frequency of light, $\alpha$ is absorption coefficient, E$_g$ is the band gap and A is the proportional constant. Fig. 4.17 shows the DRS spectra of CdS nanoparticles and different TiO$_2$ samples. Fig. 4.18 shows the DRS spectra of the CdS-TiO$_2$ nanocomposites prepared using different TiO$_2$ samples. Plotting ($\alpha h\upsilon$)$^2$ versus h$\upsilon$ gives the Tauc plots from which the band gap values were obtained. Table 4.5 lists the crystallite size and band gap of CdS, TiO$_2$ and all the CdS-TiO$_2$ nanocomposites.

**Table 4.5:** Variation of band gap with crystallite size of CdS in the CdS-TiO$_2$ nanocomposites.

| Sample | Crystallite size of CdS/TiO$_2$ (nm) | Band gap (eV) |
|---|---|---|
| CdS | 2.3 (CdS) | 2.5 |
| As-prepared sol-gel TiO$_2$ | 4.8 (TiO$_2$) | 3.3 |
| Sol-gel TiO$_2$ (500 $^\circ$C) | 10 (TiO$_2$) | 3.1 |
| Sol-gel TiO$_2$ (700 $^\circ$C) | 28 (TiO$_2$) | 2.9 |
| Macro-crystalline TiO$_2$ | 120 (TiO$_2$) | 3.2 |
| CTA1 | 5.5 (CdS) | 2.51 (CdS), 3.4 (TiO$_2$) |
| CTA2 | 5.1 (CdS) | 2.6 (CdS), 3.3 (TiO$_2$) |
| CTA3 | 4.3 (CdS) | 2.41 (CdS) |
| CTA4 | 3.9 (CdS) | 3.4 (TiO$_2$) |
| CT1 | 6 (CdS) | 2.4 (CdS) |
| CT2 | 5 (CdS) | 2.41 (CdS) |
| CT3 | 4.5 (CdS) | 2.55 (CdS) |
| CT4 | 3 (CdS) | 2.52 (CdS), 3.1 (TiO$_2$) |
| CTR1 | 12 (CdS) | 2.5 (CdS) |
| CTR2 | 10.8 (CdS) | 2.53 (CdS) |
| CTR3 | 9.3 (CdS) | 2.5 (CdS) |
| CTR4 | 8.8 (CdS) | 2.55 (CdS), 3.0 (TiO$_2$) |
| C1 | 18.0 (CdS) | 2.5 (CdS), 3.3 (TiO$_2$) |
| C2 | 15.2 (CdS) | 2.52 (CdS), 3.2 (TiO$_2$) |
| C3 | 14.3 (CdS) | 2.56 (CdS), 3.2 (TiO$_2$) |
| C4 | 13.3 (CdS) | 2.57 (CdS), 3.2 (TiO$_2$) |

Pure CdS nanoparticles show band gap absorption at 2.5 eV. The as-prepared sol–gel TiO$_2$, sol-gel TiO$_2$ after calcination at 500 $^\circ$C and after calcination at 700 $^\circ$C show band gap value of 3.3 eV, 3.1 eV and 2.9 eV, respectively. Macro-crystalline TiO$_2$ shows a band gap of 3.2 eV. Pure TiO$_2$ samples absorb only UV light and the band gap of sol-gel TiO$_2$ decreases with increase in the calcination temperature which is due to increase in the crystallite size.
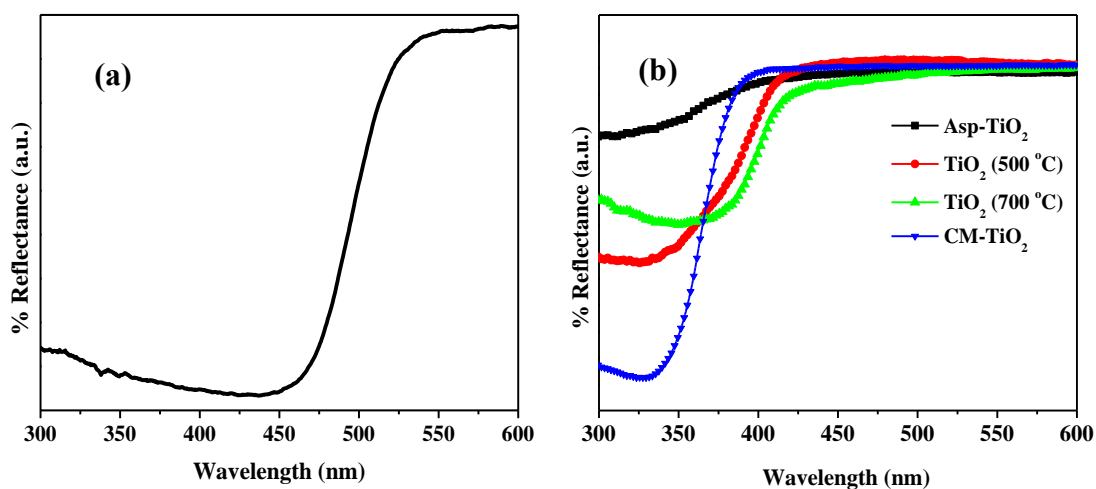
**Fig. 4.17:** Diffuse reflectance spectra of (a) CdS nanoparticles and (b) different TiO$_2$ samples.

The nanocomposites prepared using as-prepared sol-gel TiO$_2$ (CTA1-CTA4) show absorption in the visible region with CdS band gap varying from 2.41 to 2.6 eV. Nanocomposite CTA4 shows band gap absorption only due to TiO$_2$. This is due to lower concentration of cadmium acetate and thiourea used during the preparation of the nanocomposite. The nanocomposites prepared using sol-gel TiO$_2$ after calcination at 500 $^o$C (CT1-CT4) show absorption in the visible region with CdS band gap varying from 2.4 to 2.55 eV. The nanocomposites prepared using sol-gel TiO$_2$ after calcination at 700 $^o$C (CTR1-CTR4) show absorption in the visible region with CdS band gap varying from 2.5 to 2.55 eV. The nanocomposites prepared using macro-crystalline TiO$_2$ (C1-C4) show absorption in the visible region with CdS band gap varying from 2.5 to 2.57 eV and TiO$_2$ band gap varies from 3.2 to 3.3 eV. Nanocomposites (CTA3, CTA4, CT1, CT2, CT3, CTR1, CTR2 and CTR3) in which there is sufficient sensitization of TiO$_2$ by CdS possess single band gap absorption in the visible region. This is due to synergistic interaction between CdS and TiO$_2$. Nanocomposites (CTA1, CTA2, CT4 and CTR4) and all the nanocomposites prepared using macro-crystalline TiO$_2$ (C1-C4) show band gap absorption due to both CdS and TiO$_2$ because there is no sensitization of TiO$_2$ by the CdS [23,24,61]. Nanocomposites (CTA1, CTA2, CTA4, CT3, CT4, CTR2 and CTR4) show blue shift of CdS band gap with respect to pure CdS nanoparticles which is attributed to quantum confinement effect. These nanocomposites possess CdS crystallite size comparable to the Bohr radius of CdS (5 nm) [24]. The blue shift of CdS band gap absorption in the nanocomposites, prepared using macro-crystalline TiO$_2$ (C2, C3 and C4), can be attributed to the electronic coupling between CdS and TiO$_2$ [61]; the crystallite size of CdS in these nanocomposites is in the range 10 to 20 nm.
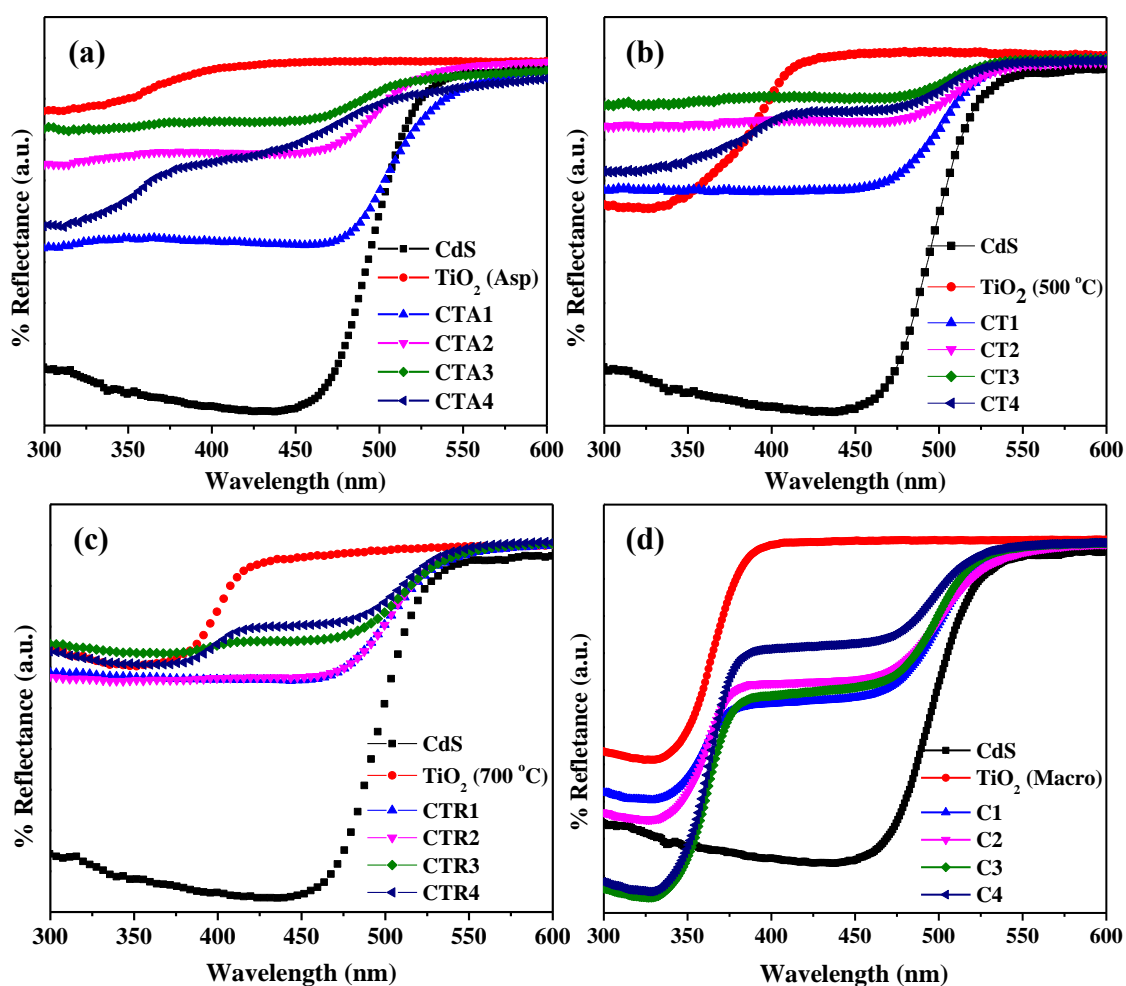
**Fig. 4.18:** Diffuse reflectance spectra of CdS-TiO$_2$ nanocomposites prepared using (a) as-prepared sol-gel TiO$_2$, (b) sol-gel TiO$_2$ after calcination at 500 $^o$C, (c) sol-gel TiO$_2$ after calcination at 700 $^o$C and (d) macro-crystalline TiO$_2$.

### 4.1.3.5 Photoluminescence Spectroscopy Results

Fig. 4.19 shows the photoluminescence spectra of different TiO$_2$ samples. The PL spectra of as-prepared sol-gel TiO$_2$ nanoparticles, and sol-gel TiO$_2$ after calcination at 500 $^o$C show emission around 411 nm (3.0 eV) which is due to the near band edge emission of TiO$_2$ [62]. The PL spectrum of sol-gel TiO$_2$ calcined at 700 $^o$C shows near band edge emission at 428 nm (2.9 eV) [62,63]. In all the TiO$_2$ samples, two emission bands are observed at about 451 nm (2.75 eV) and 470 nm (2.64 eV) which are attributed to the oxygen vacancies [64,65]. The other two emission bands at 481 nm and 493 nm are attributed to luminescence of free excitons and self-trapped excitons [63,64].
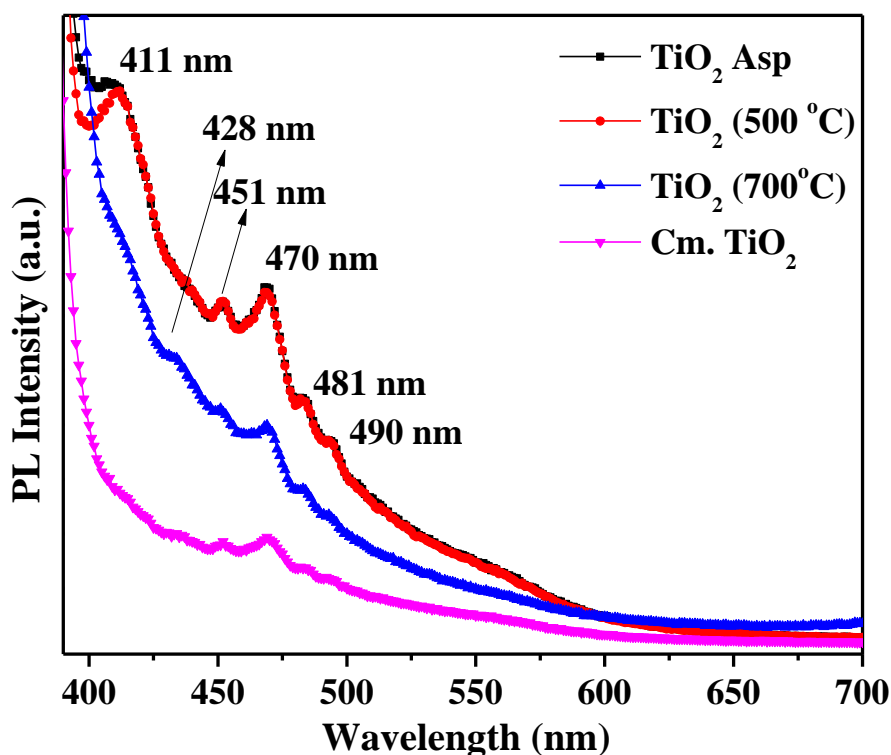
**Fig. 4.19:** Photoluminescence spectra of different sol-gel prepared $TiO_2$ nanoparticles and macro-crystalline $TiO_2$.

Fig. 4.20 shows the photoluminescence spectra of pure CdS nanoparticles and CdS–$TiO_2$ nanocomposites prepared using different $TiO_2$ samples. Pure CdS nanoparticles show band edge emission at 530 nm with a broad shoulder at 560 nm which is attributed to surface-states-induced recombination and vacancies ($Cd^{2+}$ or $S^{2-}$) [66]. The nanocomposites prepared using as-prepared sol-gel $TiO_2$ (CTA1, CTA2, CTA3 and CTA4) show band edge emission due to CdS at 530 nm, 525 nm, 517 nm and 516 nm, respectively. The nanocomposites CT1, CT2, CT3 and CT4 show band edge emission due to CdS at 529 nm, 526 nm, 525 nm and 520 nm, respectively. The nanocomposites CTR1, CTR2, CTR3 and CTR4 show band edge emission due to CdS at 530 nm, 527 nm, 523 nm and 520 nm, respectively. The nanocomposites C1, C2, C3 and C4 show band edge emission at 530 nm, 525 nm, 525 nm, and 520 nm, respectively.
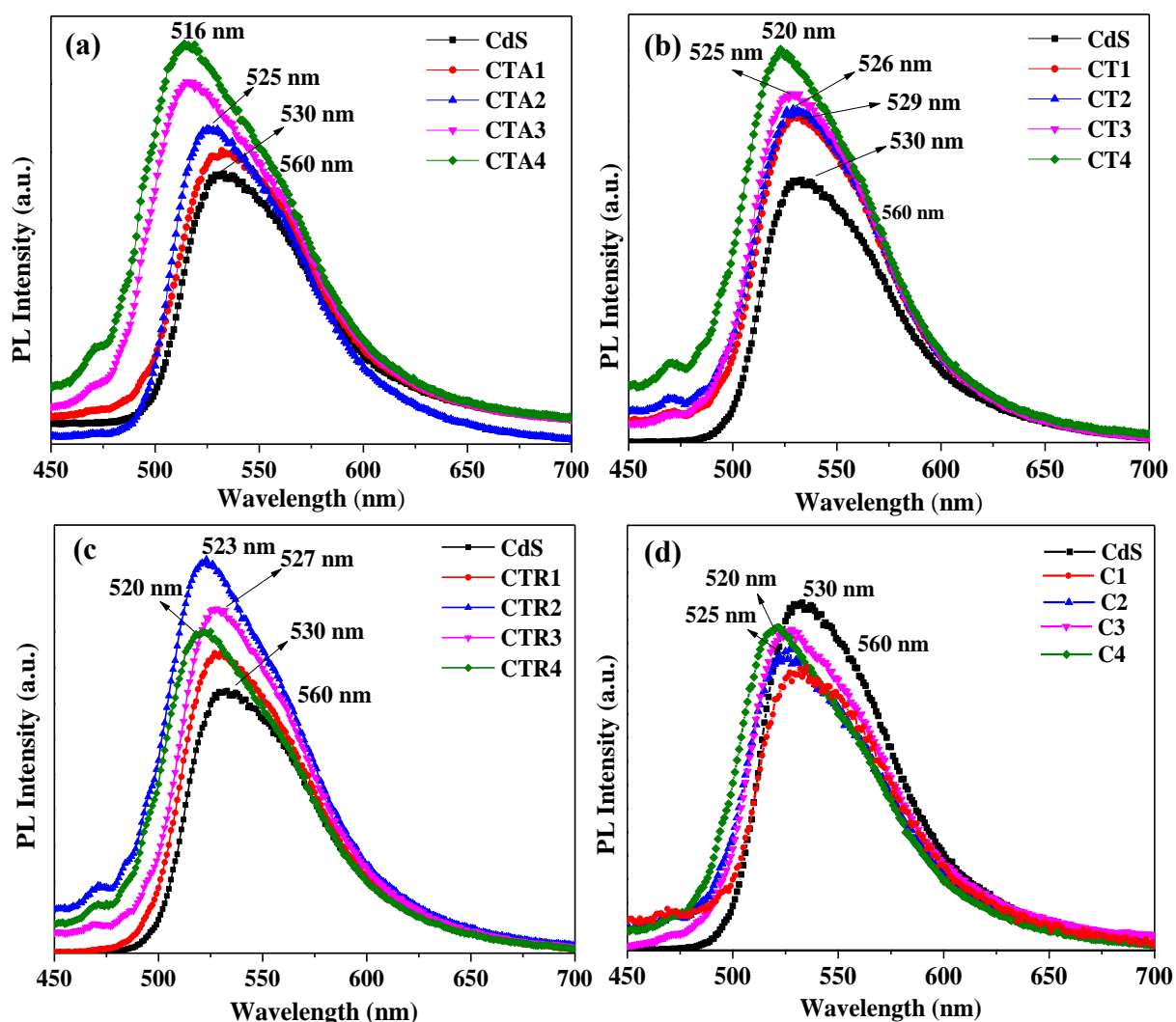
**Fig. 4.20:** Photoluminescence spectra of CdS-TiO$_2$ nanocomposites prepared using (a) as-prepared sol-gel TiO$_2$, (b) sol-gel TiO$_2$ after calcination at 500 $^o$C, (c) sol-gel TiO$_2$ after calcination at 700 $^o$C and (d) macro-crystalline TiO$_2$.

The nanocomposites prepared using sol-gel as-prepared TiO$_2$, sol-gel TiO$_2$ after calcination at 500 $^o$C and 700 $^o$C show blue shift of band edge emission of CdS. This blue shift is attributed to quantum confinement due to decrease in the particle size of CdS with decrease in the concentration of cadmium acetate and thiourea used during the preparation of the nanocomposites [67]. The PL emission bands of CdS-TiO$_2$ nanocomposites, prepared using macro-crystalline TiO$_2$, exhibit blue shift of band edge emission of CdS with weaker PL intensity compared to that of CdS. This decrease in photoluminescence intensity indicates photoluminescence quenching due to coupling of CdS and TiO$_2$ [25,61].

### 4.1.3.6 Mechanism for the synthesis of CdS-TiO$_2$ nanocomposites

CdS-TiO$_2$ nanocomposites were synthesized by a two-step method. In the first step, TiO$_2$ nanoparticles were prepared by sol-gel method. Following reactions are involved in the hydrolysis of titanium isopropoxide $(Ti(OR)_4$, $(R= (CH_3)_2CH))$ in a mixture of ethanol and water [68]:

$$Ti(OR)_4 + H_2O \rightarrow Ti(OR)_3(OH) + ROH$$

$$Ti(OR)_3(OH) + H_2O \rightarrow Ti(OR)_2(OH)_2 + ROH$$

$$Ti(OR)_2(OH)_2 + H_2O \rightarrow Ti(OR)(OH)_3 + ROH$$

$$Ti(OR)_2(OH)_2 \rightarrow TiO_2 + 2ROH$$

$$Ti(OR)(OH)_3 \rightarrow TiO_2 + H_2O + ROH$$
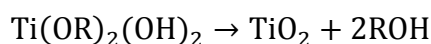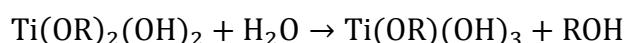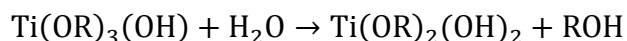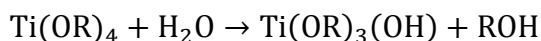
The as prepared TiO$_2$ nanoparticles were calcined at 500 $^oC$ and 700 $^oC$ to obtain crystalline anatase and rutile TiO$_2$ nanoparticles, respectively. The second step for the synthesis of TiO$_2$-CdS nanocomposites involves thermal decomposition of cadmium acetate and thiourea at about 150 $^oC$ in the presence of TiO$_2$ nanoparticles in diphenyl ether. Reaction of cadmium acetate and thiourea leads to the formation of bis(thiourea)cadmium acetate complex which on heating decomposes to give CdS nanoparticles [69,70]. The proposed reactions involved during the formation of CdS-TiO$_2$ nanocomposites are summarized as follows:

$$Cd(CH_3COO)_2 + 2(NH_2)_2CS \rightarrow Cd(SC(NH_2)_2)_2(CH_3COO)_2$$

$$TiO_2 + Cd(SC(NH_2)_2)_2(CH_3COO)_2 \xrightarrow{\Delta} TiO_2 - CdS + NH_3 + HCNS + CH_3COCH_3$$

$$+ CH_2CO + CO + H_2O$$
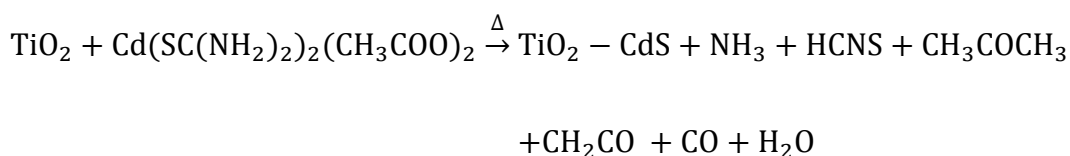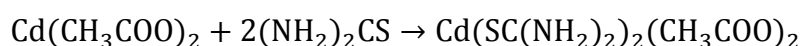
### 4.1.4 Conclusions

A simple thermal decomposition approach for the synthesis of CdS−TiO$_2$ nanocomposites with four different TiO$_2$ samples has been described. The nanocomposites were characterized using different analytical techniques. XRD results confirm the presence of CdS and TiO$_2$ nanocrystallites in the composites. The crystallite size of CdS in the nanocomposites increases with an increase in the concentration of CdS precursors (cadmium acetate and thiourea) used during the preparation of nanocomposites. SEM and TEM results indicate uniform distribution of small CdS nanoparticles on the surface of TiO$_2$ in the case of nanocomposites prepared using lower concentration of CdS precursors ([Cd$^{2+}$:S$^{2-}$] = 0.15:0.15) and as-prepared sol−gel TiO$_2$ and sol−gel TiO$_2$ nanoparticles after calcination at 500 $^\circ$C. Diffuse reflectance spectral studies indicate higher band gap of CdS in all the nanocomposites with respect to bulk CdS. Photoluminescence studies indicate blue shift in band edge emission of the nanocomposites compared to pure CdS nanoparticles.

## 4.2 Synthesis and Characterization of Ag₂S-TiO₂ Nanocomposites by Thermal Decomposition Approach

### 4.2.1 Introduction

A number of binary and ternary nanocomposites with variable particle size and controlled morphologies have been synthesized by different synthetic methods [3]. Using different synthetic methods, multi-functional nanocomposites with unique magnetic, electrical, optical and catalytic properties have been explored [71,72].

Titanium dioxide ($TiO_2$) is an important wide band gap semiconductor which has been extensively investigated due to its applications in solar energy conversion and photocatalysis [6,73,74]. $TiO_2$ (anatase) has a large band gap (3.2 eV). It absorbs in the UV region and much effort has been devoted to improve its photoresponse in the visible region [74,75]. One of the ways to do this is to combine $TiO_2$ with another semiconductor with narrow band gap (sensitization) such as CdS, CdSe, PbS, PbSe, $Ag_2S$ and CdTe [76–81]. Compared to the other sensitizers, semiconductors have unique advantages. The band gap of semiconductors can be easily tuned by varying the particle size. Another important advantage of semiconductor nanoparticles is their use in photocatalysis [82]. Nanocrystalline $Ag_2S$ is a good candidate for the photosensitization of $TiO_2$ and $Ag_2S$ is a direct band gap semiconductor with a low band gap (~1.0 eV). It is a promising material which responds in the whole solar energy spectrum [80]. Moreover, the conduction band of $Ag_2S$ is less anodic (−0.3 eV) than that of $TiO_2$ (−0.1 eV). The valence band of $Ag_2S$ is more cathodic (+0.7 eV) than that of $TiO_2$ (+3.1 eV) [83], and $Ag_2S$ has a large absorption coefficient in the visible region [84].

$Ag_2S$ possesses good photoelectric and thermoelectric properties along with good chemical stability due to which it has been used in a number of optoelectronic devices such as photovoltaic cells, infrared detectors, etc [85–88]. It possesses various photocatalytic applications such as photodegradation of pollutant dyes (e.g. rhodamine B, methylene blue and methyl orange) [89–91] and industrial pollutants (e.g. phenol, p-xylene and chlorophenol) [83,92].

Nagasuna et al. [93] have reported photoelectrochemical measurements on $TiO_2$-$Ag_2S$ mixed system under simulated sunlight illumination. They observed that $Ag_2S/TiO_2$/fluorine-doped $SnO_2$ photoanode cell yields $H_2$ at a rate of 0.8 mL h⁻¹ with a total conversion efficiency of 0.29%, while $Ag/TiO_2$/fluorine-doped $SnO_2$ photoanode is inactive. Xie et al. [94] have used $Ag_2S$ quantum dots to sensitize $TiO_2$ nanotube arrays (TNAs) in the visible range and they have observed a photo current response of about 120 μA cm⁻². Gholami et al. [80] have used

$Ag_2S$-$TiO_2$ nanocomposites for water splitting in the visible region and they have reported a photocurrent density of about 840 $\mu A$ $cm^{-2}$ using the TNA-$Ag_2S$ photoanode. Neves et al. [83] and Zhu et al. [89,90] have reported the photocatalytic degradation of phenol, rhodamine B and methylene blue over $Ag_2S$-$TiO_2$ nanocomposites under visible light irradiation. Mossalayi et al. [92] have reported the photocatalytic degradation of p-xylene and chlorophenol over $Ag_2S$-$TiO_2$ nanocomposites. Liu et al. have reported the photocatalytic production of hydrogen in the presence of $Ag_2S$ sensitized $TiO_2$ nanotube arrays [95]. Fig. 4.21(a) shows the degradation kinetics for the methyl orange degradation in the presence of $Ag_2S$-$TiO_2$ nanocomposites and 3-$Ag_2S$-$TiO_2$ (3 cycles of $Ag_2S$ loading on $TiO_2$) nanocomposite shows better photocatalytic activity. Fig. 4.21(b) shows the schematic diagram for charge-transfer process between $Ag_2S$ and $TiO_2$ during methyl orange photodegradation under UV-visible irradiation [91].
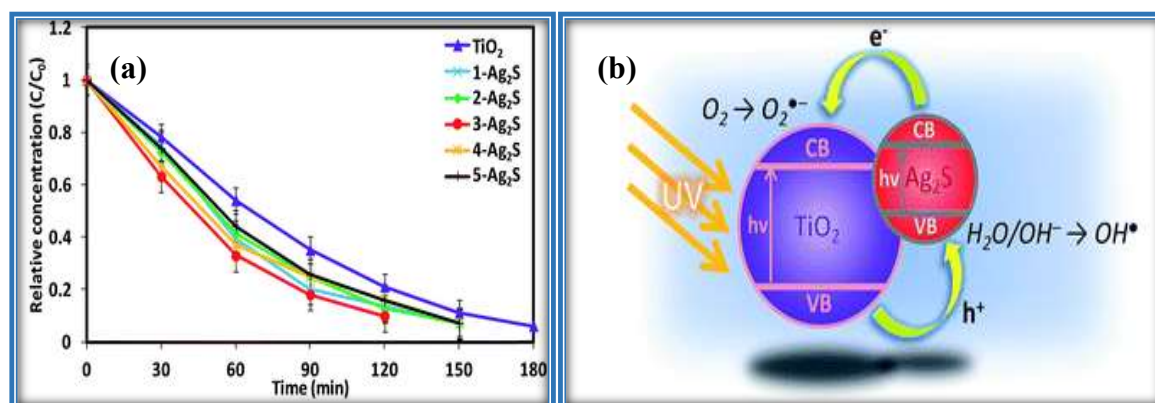


**Fig. 4.21:** Photodegradation of methyl orange in the presence of $Ag_2S$-$TiO_2$ nanocomposites and (b) schematic representation of the charge-transfer between $Ag_2S$ and $TiO_2$ during photodegradation [91].

$Ag_2S$-$TiO_2$ nanocomposites have been prepared by different synthetic methods which involve two steps. For example, electrochemical anodization of Ti foil for the formation of titanium oxide nanotube arrays followed by sequential chemical bath deposition of $Ag_2S$ [80,94,96,97], hydrothermal method for the preparation of titanium oxide nanotube arrays followed by photodeposition of $Ag_2S$ [98], electrochemical anodization of Ti foil for titanium nanotube arrays followed by photodeposition of $Ag_2S$ [93], refluxing mixture of precursors under nitrogen atmosphere followed by ultrasound irradiation [89], sol-gel method for $TiO_2$ followed by subsequent SILAR process for $Ag_2S$ deposition [99], hydrothermal method for titanium nanotube arrays followed by SILAR method [86], sol-gel method for $TiO_2$ followed by thermal decomposition [83,100], electrochemical anodization of Ti foil for titanium oxide nanotube

arrays followed by deposition of Ag-Ag$_2$S nanoparticles on TiO$_2$ by hydrothermal method [101] and electrochemical anodization of Ti foil for titanium oxide nanotube arrays followed by electrodeposition of Ag nanoparticles and in situ sulfurization leading to Ag$_2$S deposition [95]. Porous Ag$_2$S sensitized TiO$_2$ nanocomposites have been prepared by the hydrothermal method [90]. A brief summary on the synthesis of Ag$_2$S-TiO$_2$ nanocomposites by the above mentioned methods is given in Table 4.6. A brief discussion on some of the synthetic methods is given below.

**Table 4.6:** Different reported methods for the synthesis of Ag$_2$S-TiO$_2$ nanocomposites.

| Sl. No. | Method | Chemicals used | Morphology of the product | Size | Reference |
|---------|--------|----------------|---------------------------|------|-----------|
| 1. | Electrochemical anodization and sequential chemical bath deposition | Titanium (Ti) sheet, silver nitrate and sodium sulfide | Nanotube arrays | 10 -30 nm | [80] |
| 2. | Sol-gel method and Thermal decomposition | Titanium tetraethoxide, silver nitrate and sodium diethyldithiocarbamate | Nanospheres | 100-600 nm | [83] |
| 3. | Hydrothermal and successive ionic layer adsorption and reaction (SILAR) | Tetrabutyl titanate, silver nitrate and sodium sulfide | Nanotube arrays | 5-25 nm | [86] |
| 4. | Thermal decomposition and sonochemical | Titanium butoxide, silver nitrate and sodium sulfide | Powder | 10-15 nm | [89] |
| 5. | Hydrothermal | Commercial TiO$_2$, silver nitrate and sodium sulfide | Powder | 15-20 nm | [90] |
| 6. | Photodeposition | Anatase TiO$_2$, silver nitrate and sulfur | Film | 9.7-13.2 nm | [93] |
| 7. | Electrochemical anodization, electrodeposition and *in situ* sulfurization | Titanium foils, silver wire and sulfur | Nanotube arrays | 10 nm | [95] |

| 8. | Hydrothermal and photodeposition | Titanium butoxide, silver nitrate and sodium sulfide | Nanotube arrays | 10 nm | [98] |
|---|---|---|---|---|---|
| 9. | Sol-gel and successive ionic layer adsorption and reaction (SILAR) | Commercial TiO$_2$, silver nitrate and sodium sulfide | Film | - | [99] |
| 10. | Electrochemical anodization and hydrothermal | Titanium foils, silver nitrate and sodium sulfide | Nanotube arrays | 100 nm | [101] |
| 11. | Electrochemical anodization and successive ionic layer adsorption and reaction (SILAR) | Titanium foils, silver nitrate and sodium sulfide | Nanotube arrays | 100-120 nm | [102] |
| 12. | Solvothermal and sequential ionic deposition (SID) | Titanium n-butoxide, silver nitrate and thiourea | Hierarchical spheres | 5-12.5 nm | [91] |

*Electrochemical anodization followed by sequential chemical bath deposition* [80]*:* Gholami et al., have prepared Ag$_2$S incorporated TiO$_2$ nanotube arrays by a two-step method. TiO$_2$ nanotube arrays are prepared by anodization of titanium sheets (Ti). The electrolyte for the anodization consists of de-ionized water and ethylene glycol solution with the volume ratio of 10:90, containing 0.5 M NH$_4$F. The pH of the solution is adjusted to 5.7 by adding a few drops of 1 M H$_3$PO$_4$ aqueous solution. The anodization process is performed at an optimized voltage of 60 V for a total time of 200 min. Then, the grown structures are crystallized by heating at 500 $^o$C for 80 min at a heating rate of 10 $^o$C min$^{-1}$. Surface modification of titania nanotube arrays (TNA) is done by fabricating Ag$_2$S nanoparticles by using sequential-chemical bath deposition method (Scheme 4.5). In this method, cationic precursor solution is prepared by adding suitable amount of AgNO$_3$ to ethanol (0.1 M). The anionic precursor solution is prepared by adding sodium sulfide to methanol (0.1 M). Then, the TNA sample is immersed in cationic solution for 1 min. After that the sample is washed by ethanol to remove loosely bound and excess precursor on its surface. Afterwards, the sample is immersed in an anionic solution for 3 min to deposit Ag$_2$S nanoparticles. Then, the sample is washed with ethanol again. These sequential four steps are considered as one cycle.
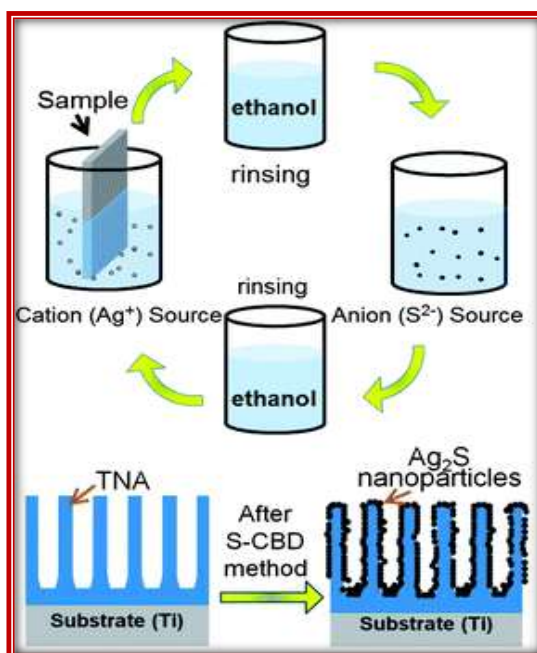
**Scheme 4.5:** Schematic of sequential-chemical bath deposition (S-CBD) process for the deposition of $Ag_2S$ nanoparticles on $TiO_2$ nanotube arrays [80].

*Hydrothermal synthesis* [90] : Zhu et al. have prepared porous $Ag_2S$-$TiO_2$ nanocomposites by hydrothermal method. Scheme 4.6 shows the schematic diagram for the preparation of $Ag_2S$-$TiO_2$ nanocomposites by hydrothermal method. First, suitable amount of $TiO_2$ and silver nitrate are added to distilled water and ultrasonicated for 20 min. The already prepared solution of sodium sulfide is added to the above solution and stirred for 8 h at 80 °C. The resulting solution is then transferred into a Teflon-lined stainless steel autoclave. The contents are then heated at 140 °C for 10 h. The precipitate obtained is filtered and washed with water and ethanol, and vacuum dried at 100 °C.
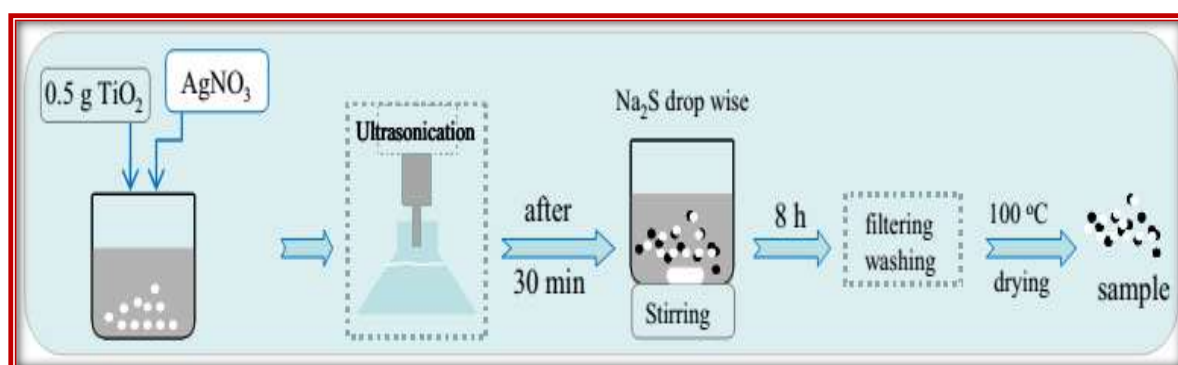


**Scheme 4.6:** Schematic diagram for the preparation of $Ag_2S$-$TiO_2$ nanocomposites by hydrothermal method [87].

*Sol-gel method followed by thermal decomposition* [83,100]: Silver complexes (e.g. silver(I) diethyldithiocarbamate) are first prepared. The silver complexes are then decomposed to produce silver sulfide nanoparticles in the presence of $TiO_2$ under inert atmosphere to yield the $Ag_2S$-$TiO_2$ nanocomposites. The silver dithiocarbamate complex is prepared by the reacting sodium diethyldithiocarbamate ($Na[S_2CN(CH_2CH_3)_2]$) with silver nitrate in water. $TiO_2$ (anatase) particles (spherical) are prepared by the controlled hydrolysis of titanium tetraethoxide in ethanol. Then, suitable amount of $Ag_2S$ precursor and $TiO_2$ particles are added to a mixture of ethylenediamine and acetone. The suspension is refluxed for different time intervals in $N_2$ atmosphere to obtain the $Ag_2S$-$TiO_2$ nanocomposites.

Most of the reported methods for the preparation of the $Ag_2S$-$TiO_2$ nanocomposites require inert atmosphere (e.g. $N_2$) and the thermal decomposition time varies between 2 to 8 hours [83,92,100]. In the present study, $Ag_2S$-$TiO_2$ nanocomposites have been prepared by a two-step method. Nanocrystalline $TiO_2$ was first prepared by sol-gel method [60]. In the second step, $Ag_2S$-$TiO_2$ nanocomposites were synthesized by the thermal decomposition of silver acetate and thiourea in diphenyl ether in the presence of $TiO_2$ at about 220 $^o$C for one hour. Nanocomposites prepared were thoroughly characterized using different analytical techniques.

**4.2.2 Experimental Details**

**Chemicals**

The chemicals used were silver acetate (SRL), titanium(IV) isopropoxide (Aldrich), thiourea (Rankem), diphenyl ether (Aldrich), nitric acid (Rankem), ethanol (Changshu Yangyuan Chemicals, China), methanol (Rankem) and Millipore$^®$ water. All the chemicals were used as received.

**Synthesis**

$Ag_2S$-$TiO_2$ nanocomposites were synthesized by the thermal decomposition method. Scheme 4.7 shows the schematic diagram of the synthesis of $Ag_2S$-$TiO_2$ nanocomposites via thermal decomposition approach. Nanocrystalline $TiO_2$ was first synthesized by sol-gel method as already discussed in section 4.1.2 [60]. In the second step, $Ag_2S$-$TiO_2$ nanocomposites were synthesized by refluxing a mixture of silver acetate, thiourea in different ratios and $TiO_2$ nanoparticles (calcined at 500 $^o$C) in diphenyl ether (boiling point = 257 $^o$C) at about 220 $^o$C for one hour. The precipitates obtained were centrifuged, washed with methanol and dried

overnight under vacuum to obtain the $Ag_2S$-$TiO_2$ nanocomposite powders. Four different nanocomposites were prepared by varying the concentrations of silver acetate and thiourea. The designation of various $Ag_2S$-$TiO_2$ nanocomposites, prepared under different synthetic conditions, is given in Table 4.7.

**Table 4.7:** Designation of various $Ag_2S$-$TiO_2$ nanocomposites prepared under different synthetic conditions.

| Sample ID | Concentration of silver acetate (mmol) | Concentration of thiourea (mmol) | Amount of $TiO_2$ nanoparticles (mmol) |
|---|---|---|---|
| A1 | 2 | 1 | 3.8 |
| A2 | 1 | 0.5 | 3.8 |
| A3 | 0.50 | 0.25 | 3.8 |
| A4 | 0.30 | 0.15 | 3.8 |
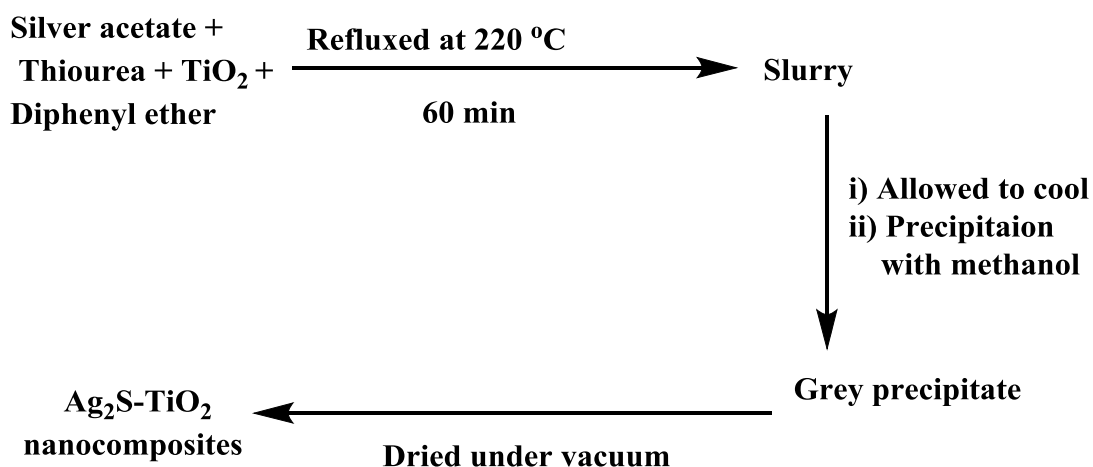


**Scheme 4.7:** Schematic diagram of the synthesis of $Ag_2S$-$TiO_2$ nanocomposites via thermal decomposition approach.

### 4.2.3 Results and Discussion

### 4.2.3.1 XRD Results

Fig. 4.22(a) shows the XRD patterns of pure $Ag_2S$, as prepared $TiO_2$ and calcined $TiO_2$ nanoparticles. Distinct peaks at $25.33°$, $37.84°$, $48.07°$, $53.95°$, $62.75°$, $70.34°$, $75.12°$ and $82.75°$ corresponding to (101), (004), (200), (105), (204), (220), (215) and (224) reflections of anatase (JCPDS file no. 84-1286) are observed in the XRD pattern of $TiO_2$. Silver sulfide is known to exist in two main polymorphs; monoclinic $\alpha$-$Ag_2S$ (acanthite) and body centered cubic $\beta$-$Ag_2S$ (argentite). Pure $Ag_2S$ nanoparticles show XRD peaks at $26.32°$, $28.96°$, $31.5°$, $34.38°$, $36.55°$, $36.80°$, $37.71°$, $40.8°$ and $43.45°$ due to acanthite (JCPDS file no. 14-0072) corresponding to (012), (111), ($\bar{1}$21), (112), (121), ($\bar{1}$03) , (031), (200) reflections, respectively. Fig. 4.22(b) shows the XRD patterns of all the $Ag_2S$-$TiO_2$ nanocomposites (A1-A4). Peaks due to acanthite $Ag_2S$ and $TiO_2$ (anatase) are present in all the nanocomposites. The crystallite size values of $TiO_2$ and $Ag_2S$ in the nanocomposites were calculated using the Debye–Scherrer formula. The crystallite size values of pure $TiO_2$ and $Ag_2S$ nanoparticles were found to be 10 nm and 41 nm, respectively. The crystallite size values of $Ag_2S$ in the $Ag_2S$-$TiO_2$ nanocomposites A1, A2, A3 and A4 are 35.3 nm, 28.7 nm, 22.4 nm and 16 nm, respectively. It decreases with decrease in the concentration of silver acetate and thiourea used during the synthesis of the $Ag_2S$-$TiO_2$ nanocomposites.
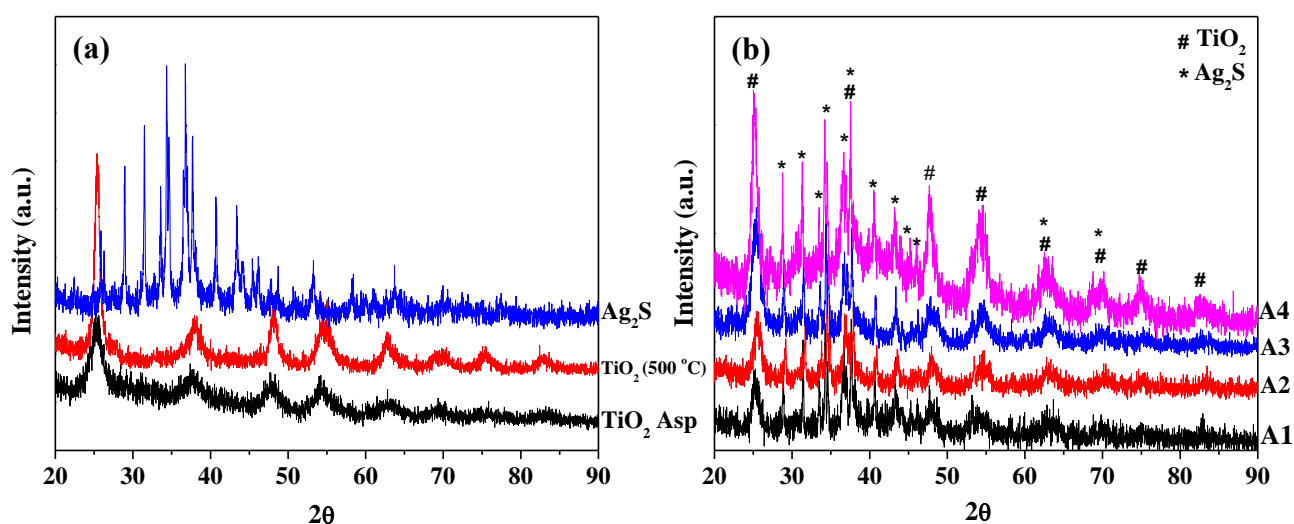


**Fig. 4.22:** XRD patterns of (a) as-prepared $TiO_2$, $Ag_2S$ and calcined $TiO_2$ nanoparticles (500 ºC) and (b) $Ag_2S$-$TiO_2$ nanocomposites (A1-A4).

### 4.2.3.2 FE-SEM and EDXA Results

Fig. 4.23 shows the FE-SEM images of pure $Ag_2S$, $TiO_2$ nanoparticles and all the $Ag_2S$-$TiO_2$ nanocomposites (A1, A2, A3 and A4). From the images, it can be noticed that pure $Ag_2S$ and $TiO_2$ nanoparticles are agglomerated with irregular morphology whereas the $Ag_2S$-$TiO_2$ nanocomposites consist of more or less uniform particles with close to spherical morphology.
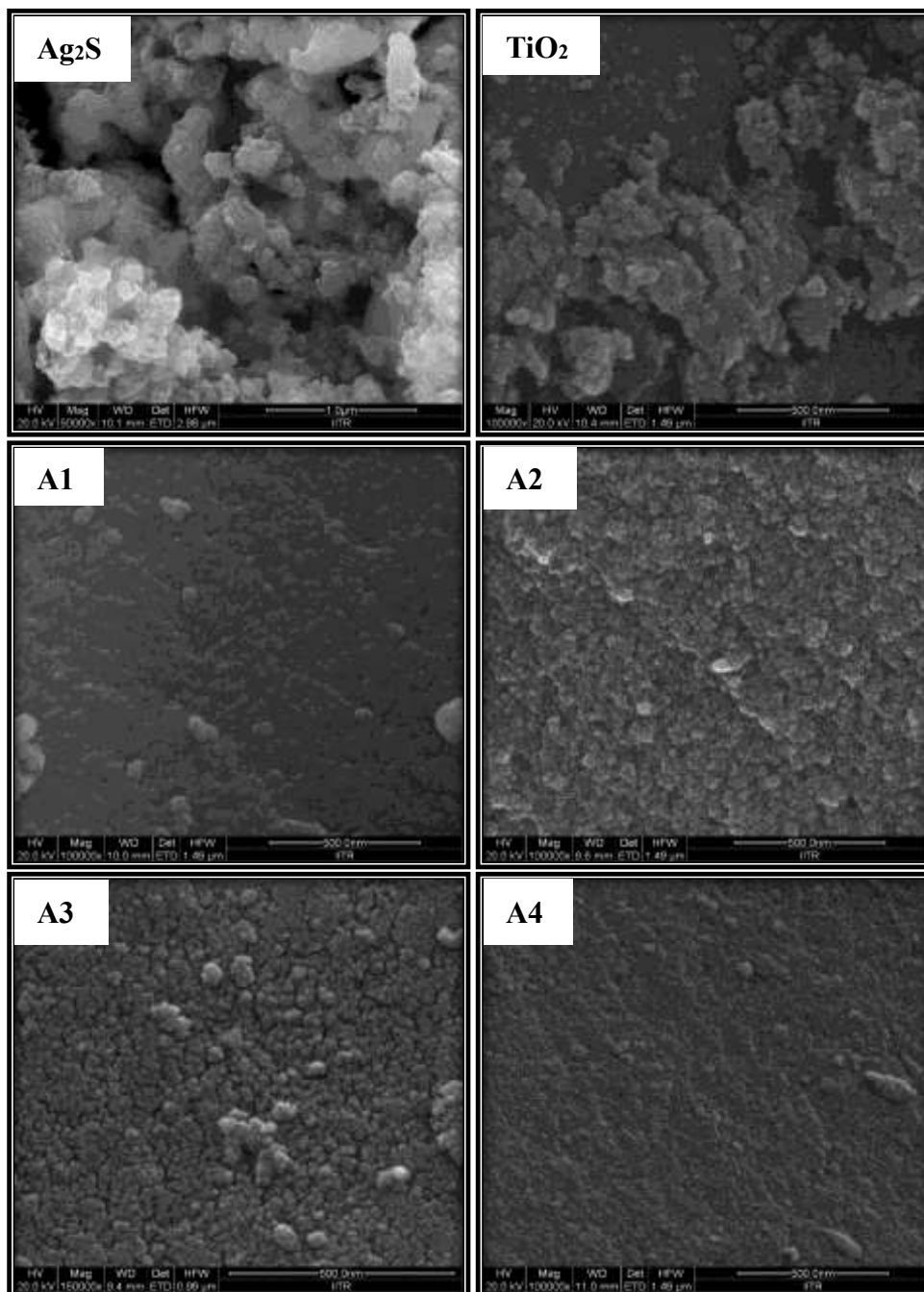


**Fig. 4.23:** FE-SEM images of pure $Ag_2S$, $TiO_2$ nanoparticles and $Ag_2S$-$TiO_2$ nanocomposites (A1-A4). For more details on the samples, see Table 4.7.

Fig. 4.24 shows the EDXA patterns of $Ag_2S$-$TiO_2$ nanocomposites (A1 to A4). The EDX analysis indicates the presence of oxygen, titanium, silver and sulfur in all the $Ag_2S$-$TiO_2$ nanocomposites. Table 4.8 shows the EDX analysis results for all the nanocomposites observed at three different spots. Nanocomposite A4 has uniform elemental (Ag, Ti, S and O) distribution compared to the other three nanocomposites (A1, A2 and A3).
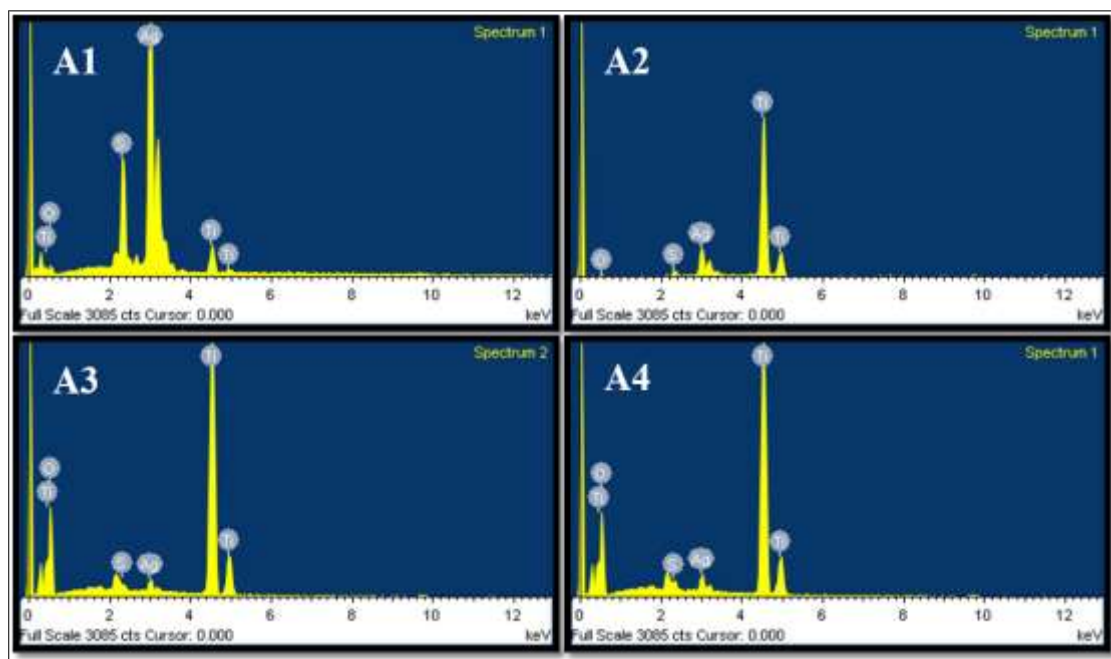


**Fig. 4.24:** EDXA patterns of the $Ag_2S$-$TiO_2$ nanocomposites (A1, A2, A3 and A4).

**Table 4.8:** EDX analysis data of $Ag_2S$-$TiO_2$ nanocomposites. The analysis was carried at three different spots.

| EDX Analysis Data | | | | | | | | |
|---|---|---|---|---|---|---|---|---|
| **Nanocomposite** | **O** | | **S** | | **Ti** | | **Ag** | |
| | Wt% | At% | Wt% | At% | Wt% | At% | Wt% | At% |
| | 50.8 | 75.9 | 7.2 | 13.1 | 47.0 | 23.4 | 1.9 | 0.4 |
| A1 | 51.9 | 76.6 | 9.1 | 16.1 | 46.9 | 23.2 | 1.1 | 0.2 |
| | 46.9 | 63.7 | 8.2 | 14.2 | 42.8 | 19.4 | 1.9 | 0.5 |
| | 33.0 | 59.6 | 1.1 | 2.1 | 66.9 | 40.4 | 2.2 | 1.0 |
| A2 | 34.5 | 61.3 | 1.2 | 2.5 | 65.2 | 38.7 | 2.4 | 1.1 |
| | 8.5 | 24.6 | 2.2 | 3.2 | 62.9 | 60.9 | 2.5 | 1.3 |

| | | | | | | | | |
|---|---|---|---|---|---|---|---|---|
| | 36.9 | 53.7 | 0.9 | 0.6 | 36.0 | 17.5 | 1.9 | 1.1 |
| A3 | 34.5 | 63.3 | 0.4 | 0.3 | 35.8 | 22.3 | 1.6 | 0.4 |
| | 35.8 | 15.7 | 0.6 | 12.6 | 36.8 | 13.3 | 1.5 | 0.8 |
| | 47.8 | 68.9 | 0.2 | 0.3 | 48.6 | 23.7 | 1.4 | 0.7 |
| A4 | 48.0 | 74.9 | 0.3 | 0.6 | 47.1 | 24.0 | 1.3 | 0.8 |
| | 49.3 | 75.1 | 0.3 | 0.2 | 46.7 | 23.8 | 1.6 | 0.8 |

### 4.2.3.3 TEM and SAED Results

Fig. 4.25 shows the TEM images of $Ag_2S$ and $TiO_2$ nanoparticles. From the images, it can be noticed that pure $Ag_2S$ and $TiO_2$ nanoparticles show irregular agglomerated particles. The average particle size of $Ag_2S$ and $TiO_2$ nanoparticles are $45.6 \pm 16.4$ nm and $29.7 \pm 10.1$ nm, respectively.
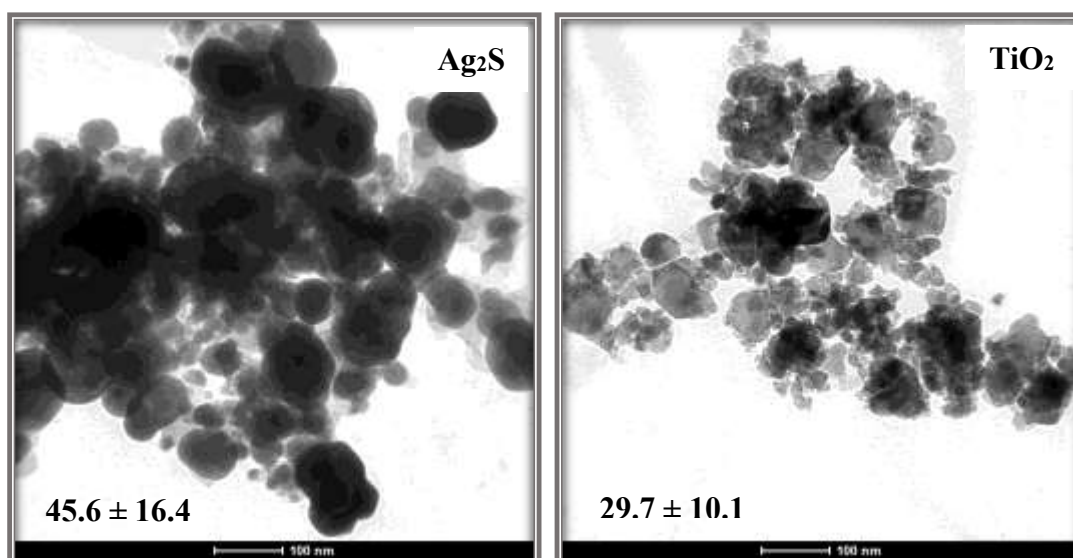


**Fig. 4.25:** TEM images of pure $Ag_2S$ and $TiO_2$ nanoparticles after calcination at 500 ºC.

Fig. 4.26 shows the TEM images of $Ag_2S$-$TiO_2$ nanocomposites (A1-A4). The TEM images show well dispersed spherical $Ag_2S$ nanoparticles in the $TiO_2$ matrix. The particle size of $Ag_2S$ in the nanocomposites varies from 8.8 to 16.3 nm.
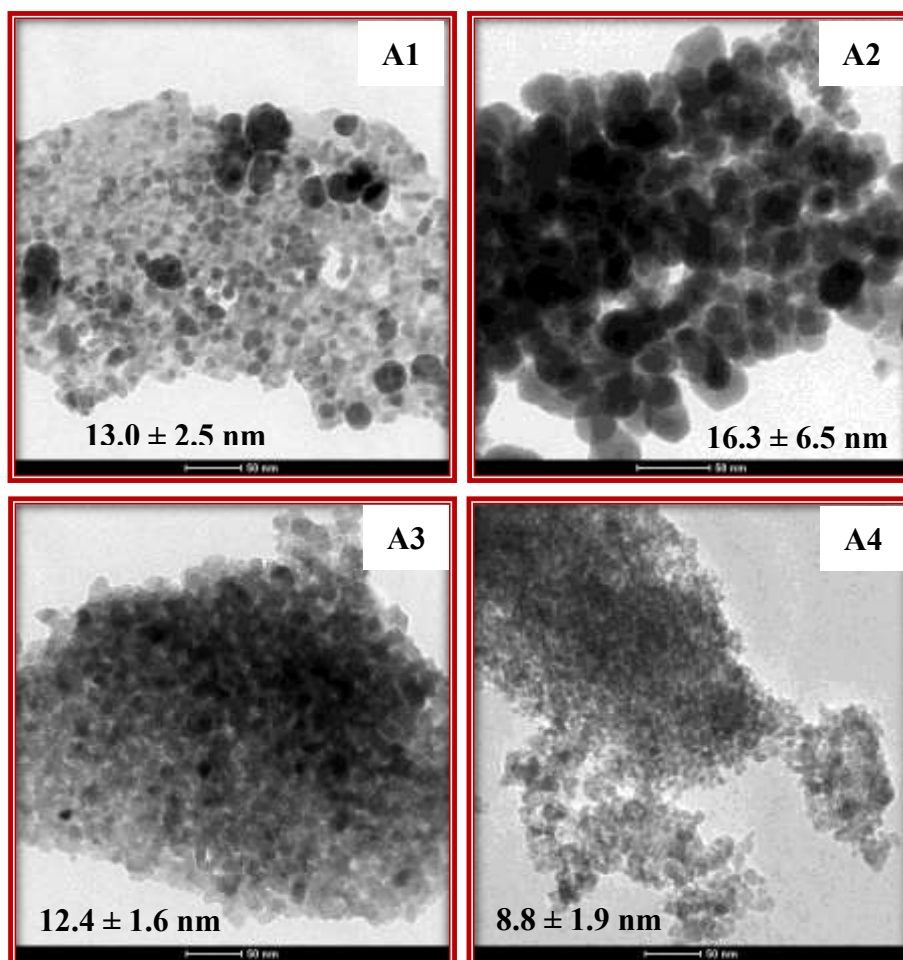
**Fig. 4.26:** TEM images of $Ag_2S$-$TiO_2$ nanocomposites (A1-A4).

Fig. 4.27 shows the HRTEM image and SAED pattern for the A4 nanocomposite. The observed lattice spacing of 0.35 nm is attributed to that of (101) plane of anatase. The HRTEM image also shows evidence for the presence of $Ag_2S$ nanoparticles. The observed 0.31 nm lattice spacing is attributed to (111) plane of α-$Ag_2S$. The selected area electron diffraction (SAED) pattern of nanocomposite A4 shows diffraction rings, which could be indexed to (312), (105), (200), (103), (220) and (204) planes of anatase. The SAED pattern also shows the presence of crystalline $Ag_2S$ with spots due to ($\bar{1}$21), (121), (031), ($\bar{2}$13) and (014) planes.

172
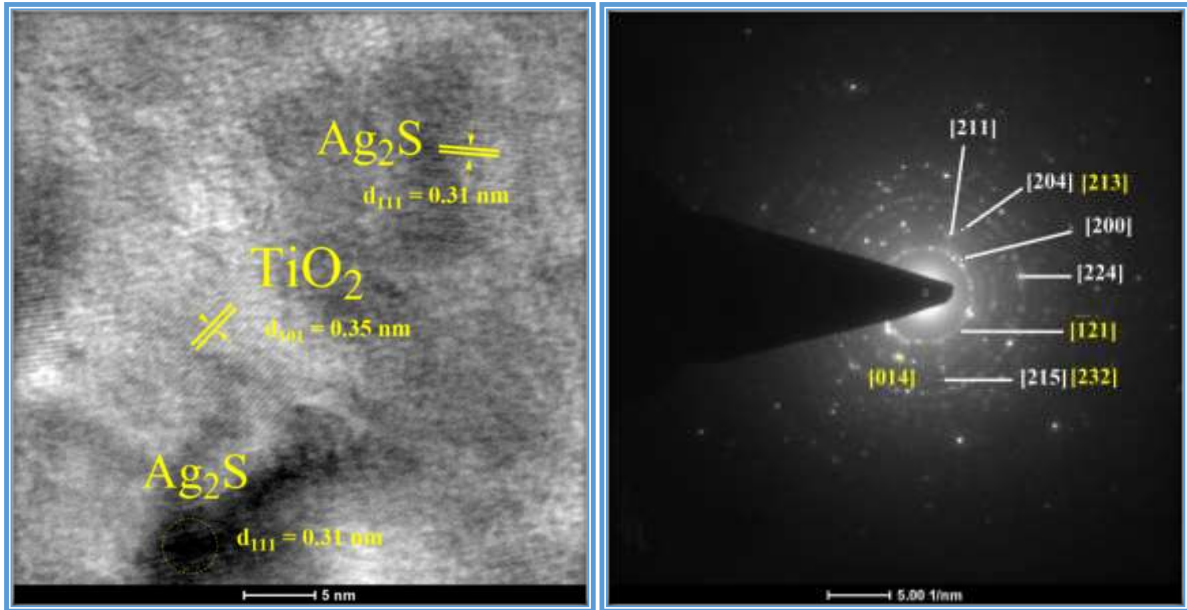
**Fig. 4.27:** HRTEM image and SAED pattern for $Ag_2S$-$TiO_2$ nanocomposite A4.

### 4.2.3.4 DRS Results

Diffuse reflectance spectral analysis in the UV-visible region was carried out for pure $Ag_2S$, $TiO_2$ and all the $Ag_2S$-$TiO_2$ nanocomposites (A1-A4). The reflectance values were converted to absorbance using the Kubelka-Munk function [93].

$$F(R_\infty) = \frac{(1 - R)^2}{2R}$$

Where R is the measured reflectance (%), and $F(R_\infty)$ is the Kubelka-Munk function. Fig. 4.28 shows the diffuse reflectance spectra of $TiO_2$, $Ag_2S$ and the $Ag_2S$-$TiO_2$ nanocomposites (A1-A4). Pure $TiO_2$ exhibits an absorption edge around 400 nm, which corresponds to its band gap (3.2 eV). Pure $Ag_2S$ nanoparticles show an absorption edge in the visible region around 560 nm, which corresponds to its band gap of 2.2 eV. This is higher than the bulk band gap of $Ag_2S$ (1 eV). All the $Ag_2S$-$TiO_2$ nanocomposites show absorption in the visible region (455 to 480 nm). The band gap of $Ag_2S$ in the nanocomposites varies from 2.2 to 2.7 eV and the increase in the band gap compared to that of bulk $Ag_2S$ is attributed to quantum size effect. The crystallite size of $Ag_2S$ in the nanocomposites decreases from 35.3 to 16 nm with decrease in the concentration of precursors (silver acetate and thiourea) used during the preparation of the nanocomposites (Table 4.7). This leads to an increase in the band gap of $Ag_2S$ in the $Ag_2S$-$TiO_2$ nanocomposites.
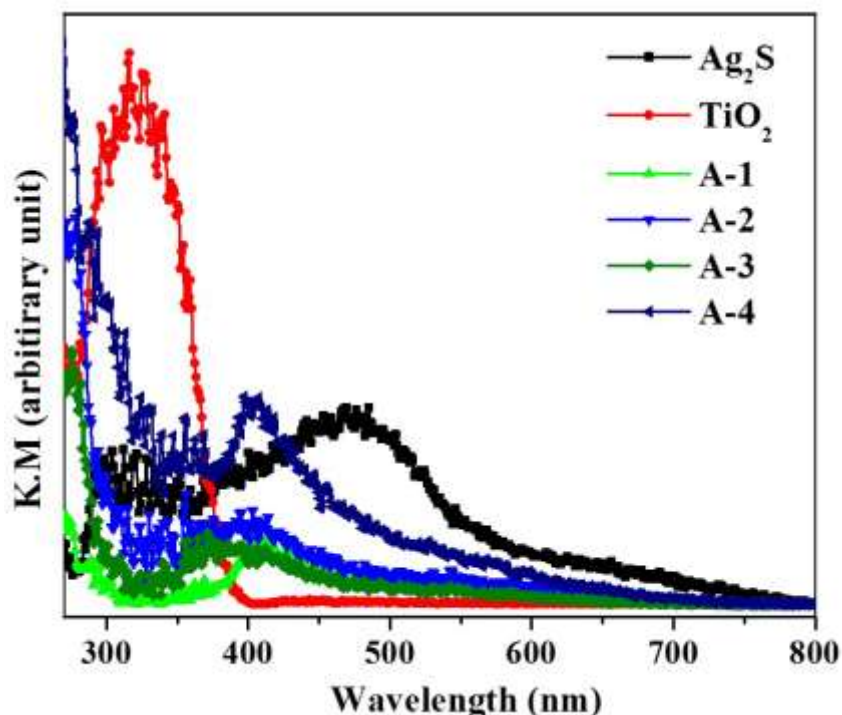
**Fig. 4.28:** Diffuse reflectance spectra of $Ag_2S$-$TiO_2$ nanocomposites (A1-A4).

Neves et al. [83,100] have reported an absorption band around 400-450 nm for the $Ag_2S$-$TiO_2$ nanocomposites. Zhu et al. [89,90] have reported a band gap of 1.95 eV for the $Ag_2S$-$TiO_2$ nanocomposites. Gholami et al. [80] have reported the diffuse reflectance spectra of $Ag_2S$ nanoparticles incorporated in $TiO_2$ nanotube arrays in the visible region. They report an increase in the optical absorption of the samples in the visible region (450–650 nm) with an increase in the deposition of $Ag_2S$ nanoparticles on the surface of $TiO_2$ nanotube arrays. Liu et al. [103] have reported that $Ag_2S$ QD-modified $TiO_2$ nanorod films absorb in the region, 400-500 nm. Xie et al. [94] have reported that $Ag_2S$ QDs-sensitized $TiO_2$ nanotube arrays absorb in the region, 400-650 nm. Ji et al. [97] have reported the diffuse reflectance spectra of $TiO_2$ nanotube arrays, $Ag_2S$, N3 dye and $Ag_2S$ and N3 sensitized $TiO_2$ nanotube arrays. Compared to the pristine $TiO_2$, the absorption of $Ag_2S$, N3 and $Ag_2S$ & N3 dye sensitized $TiO_2$ nanotube arrays is significantly enhanced in the visible region. $Ag_2S$ and N3 co-sensitized $TiO_2$ nanotube arrays have absorption in the region 400 to700 nm and the absorption is higher than that of $Ag_2S$ or N3 sensitized $TiO_2$ nanotube arrays. Hu et al. [98] have reported that $Ag_2S$ QDs deposited on $TiO_2$ nanotube arrays absorb in the region 400 to 520 nm. Fan et al. [101] have reported that Ag–$Ag_2S$ hybrid nanoparticles deposited on $TiO_2$ nanotube arrays absorb in the region 400–550 nm. Liu et al. [95] have reported that TNAs sensitized with $Ag_2S$ nanoparticles have remarkable absorption capability in the visible as well as UV region. In the present study, the synthesized $Ag_2S$-$TiO_2$ nanocomposites show absorption in the range 455–480 nm.

### 4.2.3.5 Surface area Analysis (BET)

The BET surface area values for the $Ag_2S$-$TiO_2$ nanocomposites, A1, A2, A3 and A4 are 12.8 $m^2$/g, 27.6 $m^2$/g, 41.3 $m^2$/g and 54.5 $m^2$/g, respectively. The $Ag_2S$-$TiO_2$ nanocomposites possess higher surface area compared to pure $Ag_2S$ (5.8 $m^2$/g) and $TiO_2$ nanoparticles (22.6 $m^2$/g). The surface area of the nanocomposites increases as the concentration silver acetate and thiourea used during preparation of the nanocomposites decreases from A1 to A4 (Table 4.7). The decrease in surface area is explained in terms of the formation of larger $Ag_2S$ particles as the concentrations of silver acetate and thiourea are increased during the preparation of the nanocomposites. From FE-SEM, TEM and EDX analyses, it was found that nanocomposite A4 has uniform distribution of smaller silver sulphide nanoparticles (8.8 ± 1.9 nm) over the $TiO_2$ matrix. The nanocomposite A4 possesses the highest surface area (54.5 $m^2$/g) among the nanocomposites and hence possesses more active adsorption sites for rhodamine B, which improves the photocatalytic activity [104,105].

Neves et al. [83,100] have prepared $Ag_2S$-$TiO_2$ nanocomposites by thermal decomposition approach. Silver(I) diethyldithiocarbamate complex was used as the source for $Ag_2S$ and $TiO_2$ submicron particles were used as the substrate. The nanocomposites were prepared by adding ethylenediamine drop wise to an acetone solution of Ag(I) dithiocarbamato complex and $TiO_2$ particles. The suspension formed was then refluxed with stirring under $N_2$ for different time intervals (2-8 h). The authors have reported photodegradation of phenol by the $Ag_2S$-$TiO_2$ nanocomposites. Mossalayi et al. [92] have also synthesized $Ag_2S$-$TiO_2$ nanocomposites by the thermal decomposition approach. The nanocomposites were prepared by refluxing a suspension of silver thiobenzoate precursor dissolved in trioctylphosphine with a warm mixture containing hexadecylamine and $TiO_2$ under nitrogen at 60-120°C for 2 h. They have used the $Ag_2S$-$TiO_2$ nanocomposites for the photodegradation of p-xylene and chlorophenol. The reported thermal decomposition methods have used silver complexes as the precursors for the preparation of $Ag_2S$ nanoparticles.

In the present study, simple precursors like silver acetate and thiourea have been used for the preparation of $Ag_2S$ nanoparticles and no inert atmosphere is required. The precursors were decomposed in diphenyl ether in the presence of $TiO_2$ at about 220 °C for one hour to get the $Ag_2S$-$TiO_2$ nanocomposites.

### 4.2.3.6 Mechanism of the formation of Ag₂S-TiO₂ nanocomposites

Ag₂S-TiO₂ nanocomposites were synthesized by a two-step method. In the first step, TiO₂ nanoparticles were prepared by sol-gel method as discussed in Section 4.1.3.6. The second step involves thermal decomposition of silver acetate and thiourea at about 220 °C in the presence of TiO₂ nanoparticles (calcined at 500 °C) in diphenyl ether. Reaction of silver acetate and thiourea at temperature less than 150 °C leads to the formation of silver acetate-thiourea complex which on further heating decomposes to give Ag₂S nanoparticles [70,106]. The proposed reactions involved during the synthesis of Ag₂S-TiO₂ nanocomposites are as follows:

$$(CH_3COO)Ag + (NH_2)_2CS \rightarrow CH_3COOAg-S-C(NH_2)_2 + CH_3COOH$$

$$TiO_2 + 2CH_3COOAg-S-C(NH_2)_2 \xrightarrow{\Delta} Ag_2S - TiO_2 + CS(NH_2)_2 + N \equiv CNH_2 + 2CH_3COOH$$
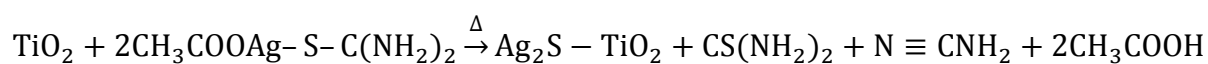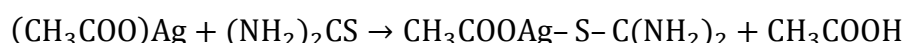
### 4.2.4 Conclusions

A simple thermal decomposition method for the synthesis of Ag₂S-TiO₂ nanocomposites has been described. The nanocomposites were characterized using different analytical techniques. XRD results confirm the presence of both Ag₂S and TiO₂ nanocrystallites in the composites. The crystallite size of Ag₂S in the nanocomposites increases with an increase in the concentration of precursors (silver acetate and thiourea) used during the preparation of Ag₂S-TiO₂ nanocomposites. FE-SEM and TEM results indicate uniform distribution of small Ag₂S nanoparticles on the surface of TiO₂ and diffuse reflectance spectral studies indicate higher band gap of Ag₂S in the nanocomposites compared to bulk Ag₂S. The band gap of Ag₂S in the nanocomposites increases with decrease in the size of Ag₂S nanoparticles.

**References**

1.  Xiao G., Wang Y., Ning J., Wei Y., Liu B., Yu W. W., Zou G., Zou B., 'Recent advances in IV–VI semiconductor nanocrystals: Synthesis, mechanism, and applications', *RSC Advances*, **3**, 8104–8130 (2013).

2.  Zhang H., Chen G., Bahnemann D. W., 'Photoelectrocatalytic materials for environmental applications', *Journal of Materials Chemistry*, **19**, 5089 (2009).

3.  Henrique P., Camargo C., Satyanarayana K. G., Wypych F., 'Nanocomposites: Synthesis, structure, properties and new application opportunities', *Materials Research*, **12**, 1–39 (2009).

4.  Liu S., Bai S. Q., Zheng Y., Shah K. W., Han M. Y., 'Composite metal-oxide nanocatalysts', *ChemCatChem*, **4**, 1462–1484 (2012).

5.  Roy N., Park Y., Sohn Y., Leung K. T., Pradhan D., 'Green synthesis of anatase $TiO_2$ nanocrystals with diverse shapes and their exposed facets-dependent photoredox activity', *ACS Applied Materials and Interfaces*, **6**, 16498–16507 (2014).

6.  Chen X., Mao S. S., 'Titanium dioxide nanomaterials: Synthesis, properties, modifications, and applications', *Chemical Reviews*, **107**, 2891–2959 (2007).

7.  Roy N., Park Y., Sohn Y., Pradhan D., 'Controlled synthesis and facets-dependent photocatalysis of $TiO_2$ nanocrystals', *Semiconductor Science and Technology*, **30**, 044005/1–044005/8 (2015).

8.  Yang G., Jiang Z., Shi H., Jones M. O., Xiao T., Edwards P. P., Yan Z., 'Study on the photocatalysis of F–S co-doped $TiO_2$ prepared using solvothermal method', *Applied Catalysis B: Environmental*, **96**, 458–465 (2010).

9.  Jin H. Y., Kim J. Y., Ah Lee J., Lee K., Yoo K., Lee D. K., Kim B., Young Kim J., Kim H., Jung Son H., Kim J., Ah Lim J., Jae Ko M., 'Rapid sintering of $TiO_2$ photoelectrodes using intense pulsed white light for flexible dye-sensitized solar cells', *Applied Physics Letters*, **104**, 143902/1–143902/5 (2014).

10. Zhang Y., Xia T., Shang M., Wallenmeyer P., Katelyn D., Peterson A., Murowchick J., Dong L., Chen X., 'Structural evolution from $TiO_2$ nanoparticles to nanosheets and their photocatalytic performance in hydrogen generation and environmental pollution removal', *RSC Advances*, **4**, 16146–16152 (2014).

11. Sivaranjani K., RajaAmbal S., Das T., Roy K., Bhattacharyya S., Gopinath C. S., 'Disordered mesoporous $TiO_{2-x}N_x$+Nano-Au: An electronically integrated nanocomposite for solar $H_2$ generation', *ChemCatChem*, **6**, 522–530 (2014).

12. Xia T., Chen X., 'Revealing the structural properties of hydrogenated black $TiO_2$ nanocrystals', *Journal of Materials Chemistry A*, **1**, 2983–2989 (2013).

13. Chang S., Liu W., 'The roles of surface-doped metal ions (V, Mn, Fe, Cu, Ce, and W) in the interfacial behavior of $TiO_2$ photocatalysts', *Applied Catalysis B: Environmental*, **156-157**, 466–475 (2014).

14. Lin T., Yang C., Wang Z., Yin H., Lü X., Huang F., Lin J., Xie X., Jiang M., 'Effective nonmetal incorporation in black titania with enhanced solar energy utilization', *Energy and Environmental Science*, **7**, 967–972 (2014).

15. Sivaranjani K., Agarkar S., Ogale S. B., Gopinath C. S., 'Toward a quantitative correlation between microstructure and DSSC efficiency: A case study of $TiO_{2-x}N_x$ nanoparticles in a disordered mesoporous framework', *The Journal of Physical Chemistry C*, **116**, 2581–2587 (2012).

16. Linsebigler A. L., Lu G., Yates J. T., 'Photocatalysis on $TiO_2$ surfaces: Principles, mechanisms, and selected results', *Chemical Reviews*, **95**, 735–758 (1995).

17. Hayden S. C., Allam N. K., El-Sayed M. A., '$TiO_2$ nanotube/CdS hybrid electrodes: Extraordinary enhancement in the inactivation of Escherichia coli', *The Journal of the American Chemical Society*, **132**, 14406–14408 (2010).

18. Tao L., Xiong Y., Liu H., Shen W., 'High performance PbS quantum dot sensitized solar cells via electric field assisted in situ chemical deposition on modulated $TiO_2$ nanotube arrays', *Nanoscale*, **6**, 931–938 (2014).

19. Gao X. F., Li H. B., Sun W., Chen Q., Tang F. Q., Peng L. M., 'CdTe quantum dots-sensitized $TiO_2$ nanotube array photoelectrodes', *The Journal of Physical Chemistry C*, **113**, 7531–7535 (2009).

20. Fitzmorris B. C., Larsen G. K., Wheeler D. A., Zhao Y., Zhang J. Z., 'Ultrafast charge transfer dynamics in polycrystalline CdSe/$TiO_2$ nanorods prepared by oblique angle codeposition', *The Journal of Physical Chemistry C*, **116**, 5033–5041 (2012).

21. Wang M., Sun L., Cai J., Huang P., Su Y., Lin C., 'A facile hydrothermal deposition of

$ZnFe_2O_4$ nanoparticles on $TiO_2$ nanotube arrays for enhanced visible light photocatalytic activity', *Journal of Materials Chemistry A*, **1**, 12082–12087 (2013).

22. Rühle S., Barad H. N., Bouhadana Y., Keller D. A., Ginsburg A., Shimanovich K., Majhi K., Lovrincic R., Anderson A. Y., Zaban A., 'Combinatorial solar cell libraries for the investigation of different metal back contacts for $TiO_2$–$Cu_2O$ hetero-junction solar cells', *Physical Chemistry Chemical Physics*, **16**, 7066–7073 (2014).

23. Guo E., Yin L., Zhang L., 'CdS quantum dot sensitized anatase $TiO_2$ hierarchical nanostructures for photovoltaic application', *CrystEngComm*, **16**, 3403–3413 (2014).

24. Song G., Xin F., Chen J., Yin X., 'Photocatalytic reduction of $CO_2$ in cyclohexanol on CdS–$TiO_2$ heterostructured photocatalyst', *Applied Catalysis A: General*, **473**, 90–95 (2014).

25. Vu T. T. D., Mighri F., Ajji A., Do T. O., 'Synthesis of titanium dioxide/cadmium sulfide nanosphere particles for photocatalyst applications', *Industrial and Engineering Chemistry Research*, **53**, 3888–3897 (2014).

26. Yan H., Yang J., Ma G., Wu G., Zong X., Lei Z., Shi J., Li C., 'Visible-light-driven hydrogen production with extremely high quantum efficiency on Pt–PdS/CdS photocatalyst', *Journal of Catalysis*, **266**, 165–168 (2009).

27. Flood R., Enright B., Allen M., Barry S., Dalton A., Doyle H., Tynan D., Fitzmaurice D., 'Determination of band edge energies for transparent nanocrystalline $TiO_2$-CdS sandwich electrodes prepared by electrodeposition', *Solar Energy Materials and Solar Cells*, **39**, 83–98 (1995).

28. Bessekhouad Y., Robert D., Weber J. V., '$Bi_2S_3$/$TiO_2$ and CdS/$TiO_2$ heterojunctions as an available configuration for photocatalytic degradation of organic pollutant', *Journal of Photochemistry and Photobiology A: Chemistry*, **163**, 569–580 (2004).

29. Liu L., Lv J., Xu G., Wang Y., Xie K., Chen Z., Wu Y., 'Uniformly dispersed CdS nanoparticles sensitized $TiO_2$ nanotube arrays with enhanced visible-light photocatalytic activity and stability', *Journal of Solid State Chemistry*, **208**, 27–34 (2013).

30. Yang G., Yang B., Xiao T., Yan Z., 'One-step solvothermal synthesis of hierarchically porous nanostructured CdS/$TiO_2$ heterojunction with higher visible light photocatalytic activity', *Applied Surface Science*, **283**, 402–410 (2013).

31. Meng Z. Da, Peng M. M., Zhu L., Oh W. C., Zhang F. J., 'Fullerene modification CdS/TiO$_2$ to enhancement surface area and modification of photocatalytic activity under visible light', *Applied Catalysis B: Environmental*, **113-114**, 141–149 (2012).

32. Xiao F. X., Miao J., Wang H. Y., Liu B., 'Self-assembly of hierarchically ordered CdS quantum dots–TiO$_2$ nanotube array heterostructures as efficient visible light photocatalysts for photoredox applications', *Journal of Materials Chemistry A*, **1**, 12229–12238 (2013).

33. Chen Z., Xu Y., 'Ultrathin TiO$_2$ layer coated-CdS spheres core−shell nanocomposite with enhanced visible-light photoactivity', *ACS Applied Materials and Interfaces*, **5**, 13353–13363 (2013).

34. Su F., Lu J., Tian Y., Ma X., Gong J., 'Branched TiO$_2$ nanoarrays sensitized with CdS quantum dots for highly efficient photoelectrochemical water splitting', *Physical Chemistry Chemical Physics*, **15**, 12026–12032 (2013).

35. Liu S., Zhang N., Tang Z. R., Xu Y. J., 'Synthesis of one-dimensional CdS@TiO$_2$ core-shell nanocomposites photocatalyst for selective oxidation: The dual role of TiO$_2$ shell', *ACS Applied Materials and Interfaces*, **4**, 6378−6385 (2012).

36. Guo X., Chen C., Song W., Wang X., Di W., Qin W., 'CdS embedded TiO$_2$ hybrid nanospheres for visible light photocatalysis', *Journal of Molecular Catalysis A: Chemical*, **387**, 1–6 (2014).

37. Gao B., Yuan X., Lu P., Lin B., Chen Y., 'Enhanced visible-light-driven photocatalytic H$_2$ -production activity of CdS-loaded TiO$_2$ microspheres with exposed (001) facets', *Journal of Physical and Chemistry of Solids*, **87**, 171–176 (2015).

38. Rao S. S., Durga I. K., Gopi C. V. V. M., Venkata Tulasivarma C., Kim S. K., Kim H. J., 'The effect of TiO$_2$ nanoflowers as a compact layer for CdS quantum-dot sensitized solar cells with improved performance', *Dalton Transactions*, **44**, 12852–12862 (2015).

39. Han S., Pu Y. C., Zheng L., Zhang J. Z., Fang X., 'Shell-thickness dependent electron transfer and relaxation in Type-II core-shell CdS/TiO$_2$ structures with optimized photoelectrochemical performance', *Journal of Materials Chemistry A*, **3**, 22627–22635 (2015).

40. Mazumdar S., Bhattacharyya A. J., 'One-pot synthesis of a TiO$_2$–CdS nano-

heterostructure assembly with enhanced photocatalytic activity', *RSC Advances*, **5**, 34942–34948 (2015).

41. Li X., Chen X., Niu H., Han X., Zhang T., Liu J., Lin H., Qu F., 'The synthesis of CdS/TiO$_2$ hetero-nanofibers with enhanced visible photocatalytic activity', *Journal of Colloid and Interface Science*, **452**, 89–97 (2015).

42. Wang B., Zhang H., Lu X. Y., Xuan J., Leung M. K. H., 'Solar photocatalytic fuel cell using CdS–TiO$_2$ photoanode and air-breathing cathode for wastewater treatment and simultaneous electricity production', *Chemical Engineering Journal*, **253**, 174–182 (2014).

43. Chang P., Cheng H., Li W., Zhuo L., He L., Yu Y., Zhao F., 'Photocatalytic reduction of o-chloronitrobenzene under visible light irradiation over CdS quantum dot sensitized TiO$_2$', *Physical Chemistry Chemical Physics*, **16**, 16606–16614 (2014).

44. Jang J. S., Ji S. M., Bae S. W., Son H. C., Lee J. S., 'Optimization of CdS/TiO$_2$ nano-bulk composite photocatalysts for hydrogen production from Na$_2$S/Na$_2$SO$_3$ aqueous electrolyte solution under visible light ($\lambda \geq 420$ nm)', *Journal of Photochemistry and Photobiology A: Chemistry*, **188**, 112–119 (2007).

45. Li L., Wang L., Hu T., Zhang W., Zhang X., Chen X., 'Preparation of highly photocatalytic active CdS/TiO$_2$ nanocomposites by combining chemical bath deposition and microwave-assisted hydrothermal synthesis', *Journal of Solid State Chemistry*, **218**, 81–89 (2014).

46. Bjelajac A., Petrovic R., Nedeljkovic, M. J., Djokic V., Radetic T., Cirkovic J., Janackovic D., 'Ex-situ sensitization of ordered TiO$_2$ nanotubes with CdS quantum dots', *Ceramics International*, **41**, 7048–7053 (2015).

47. Bessekhouad Y., Chaoui N., Trzpit M., Ghazzal N., Robert D., Weber J. V., 'UV–vis versus visible degradation of Acid Orange II in a coupled CdS/TiO$_2$ semiconductors suspension', *Journal of Photochemistry and Photobiology A: Chemistry*, **183**, 218–224 (2006).

48. Liu Y., Zhang P., Tian B., Zhang J., 'Enhancing the photocatalytic activity of CdS nanorods for selective oxidation of benzyl alcohol by coating amorphous TiO$_2$ shell layer', *Catalysis Communications*, **70**, 30–33 (2015).

49.    Vaidya S., Patra A., Ganguli A. K., 'CdS@TiO$_2$ and ZnS@TiO$_2$ core–shell nanocomposites: Synthesis and optical properties', *Colloids and Surfaces A: Physicochemical and Engineering Aspects*, **363**, 130–134 (2010).

50.    Zhang J., Xiao F. X., Xiao G., Liu B., 'Assembly of a CdS quantum dot–TiO$_2$ nanobelt heterostructure for photocatalytic application: Towards an efficient visible light photocatalyst via facile surface charge tuning', *New Journal of Chemistry*, **39**, 279–286 (2015).

51.    Xue C., Wang T., Yang G., Yang B., Ding S., 'A facile strategy for the synthesis of hierarchical TiO$_2$/CdS hollow sphere heterostructures with excellent visible light activity', *Journal of Materials Chemistry A*, **2**, 7674–7679 (2014).

52.    Ghows N., Entezari M. H., 'Sono-synthesis of core–shell nanocrystal (CdS/TiO$_2$) without surfactant', *Ultrasonics Sonochemistry*, **19**, 1070–1078 (2012).

53.    Lu N., Su Y., Li J., Yu H., Quan X., 'Fabrication of quantum-sized CdS-coated TiO$_2$ nanotube array with efficient photoelectrochemical performance using modified successive ionic layer absorption and reaction (SILAR) method', *Science Bulletin*, **60**, 1281–1286 (2015).

54.    Esparza D., Zarazúa I., López-Luke T., Cerdán-Pasarán A., Sánchez-Solís A., Torres-Castro A., Mora-Sero I., De la Rosa E., 'Effect of different sensitization technique on the photoconversion efficiency of CdS quantum dot and CdSe quantum rod sensitized TiO$_2$ solar cells', *The Journal of Physical Chemistry C*, **119**, 13394–13403 (2015).

55.    Nakamura R., Makuta S., Tachibana Y., 'Electron injection dynamics at the SILAR deposited CdS quantum dot/TiO$_2$ interface', *The Journal of Physical Chemistry C*, **119**, 20357–20362 (2015).

56.    Yang X., Li J., Fu J., 'A novel photoelectrochemical sensor for the detection of α-fetoprotein based on a mesoporous TiO$_2$–CdS QD composite film', *Analytical Methods*, **7**, 1328–1332 (2015).

57.    Qin N., Liu Y., Wu W., Shen L., Chen X., Li Z., Wu L., 'One-dimensional CdS/TiO$_2$ nanofiber composites as efficient visible-light-driven photocatalysts for selective organic transformation: Synthesis, characterization, and performance', *Langmuir*, **31**, 1203–1209 (2015).

58.    Lutz T., MacLachlan A., Sudlow A., Nelson J., Hill M. S., Molloy K. C., Haque S. A., 'Thermal decomposition of solution processable metal xanthates on mesoporous titanium dioxide films: A new route to quantum-dot sensitised heterojunctions', *Physical Chemistry Chemical Physics*, **14**, 16192–16196 (2012).

59.    Tristão J. C., Magalhães F., Corio P., Sansiviero M. T. C., 'Electronic characterization and photocatalytic properties of CdS/TiO₂ semiconductor composite', *Journal of Photochemistry and Photobiology A: Chemistry*, **181**, 152–157 (2006).

60.    Choi S. K., Kim S., Lim S. K., Park H., 'Photocatalytic comparison of TiO₂ nanoparticles and electrospun TiO₂ nanofibers: Effects of mesoporosity and interparticle charge transfer', *The Journal of Physical Chemistry C*, **114**, 16475–16480 (2010).

61.    Zhang J., Zhu Z., Tang Y., Müllen K., Feng X., 'Titania nanosheet-mediated construction of a two-dimensional titania/cadmium sulfide heterostructure for high hydrogen evolution activity', *Advanced Materials*, **26**, 734–738 (2014).

62.    Liu Y., Claus R. O., 'Blue light emitting nanosized TiO₂ colloids', *The Journal of the American Chemical Society*, **119**, 5273–5274 (1997).

63.    Cheng X., Pan G., Yu X., Zheng T., 'Preparation of CdS NCs decorated TiO₂ nano-tubes arrays photoelectrode and its enhanced photoelectrocatalytic performance and mechanism', *Electrochimica Acta*, **105**, 535–541 (2013).

64.    Liqiang J., Xiaojun S., Weimin C., Zili X., Yaoguo D., Honggang F., 'The preparation and characterization of nanoparticle TiO₂/Ti films and their photocatalytic activity', *Journal of Physics and Chemistry of Solids*, **64**, 615–623 (2003).

65.    Das K., De S. K., 'Optical properties of the Type-II core−shell TiO₂@CdS nanorods for photovoltaic applications', *The Journal of Physical Chemistry C*, **113**, 3494–3501 (2009).

66.    Lozada-Morales R., Zelaya-Angel O., Torres-Delgado G., 'Photoluminescence in cubic and hexagonal CdS films', *Applied Surface Science*, **175-176**, 562–566 (2001).

67.    Li C. X., Jiang Z. H., Yao Z. P., 'Self-assembly of large scale CdS/TiO₂ film photocatalyst', *Advanced Materials Research*, **512-515**, 1692–1698 (2012).

68.    Courtecuisse V. G., Chhor K., Bocquet J. F., Pommier C., 'Kinetics of the titanium isopropoxide decomposition in supercritical isopropyl alcohol', *Industrial and*

*Engineering Chemistry Research*, **35**, 2539–2545 (1996).

69. Patel J. D., Mighri F., Ajji A., Chaudhuri T. K., 'Development of CdS nanostructures by thermal decomposition of aminocaproic acid-mixed Cd-thiourea complex precursor: Structural, optical and photocatalytic characterization', *Journal of Nanoscience and Nanotechnology*, **15**, 2733–2741 (2015).

70. Zhang Y., Shen S., Wang Q., 'Controllable growth of $Ag_2S$–CdS heteronanostructures', *CrystEngComm*, **16**, 9501–9505 (2014).

71. Nguyen T. D., Tran T. H., 'Multicomponent nanoarchitectures for the design of optical sensing and diagnostic tools', *RSC Advances*, **4**, 916–942 (2014).

72. Gao P. X., Shimpi P., Gao H., Liu C., Guo Y., Cai W., Liao K. T., Wrobel G., Zhang Z., Ren Z., Lin H. J., 'Hierarchical assembly of multifunctional oxide-based composite nanostructures for energy and environmental applications', *International Journal of Molecular Sciences*, **13**, 7393–7423 (2012).

73. Weng Z., Guo H., Liu X., Wu S., Yeung K. W. K., Chu P. K., 'Nanostructured $TiO_2$ for energy conversion and storage', *RSC Advances*, **3**, 24758–24775 (2013).

74. Pelaez M., Nolan N. T., Pillai S. C., Seery M. K., Falaras P., Kontos A. G., Dunlop P. S. M., Hamilton J. W. J., Byrne J. A., O'Shea K., Entezari M. H., Dionysiou D. D., 'A review on the visible light active titanium dioxide photocatalysts for environmental applications', *Applied Catalysis B: Environmental*, **125**, 331–349 (2012).

75. Roy N., Leung K. T., Pradhan D., 'Nitrogen doped reduced graphene oxide based Pt−$TiO_2$ nanocomposites for enhanced hydrogen evolution', *The Journal of Physical Chemistry C*, **119**, 19117−19125 (2015).

76. Kozlova E. A., Kozhevnikova N. S., Cherepanova S. V., Lyubina T. P., Gerasimov E. Y., Kaichev V. V., Vorontsov A. V., Tsybulya S. V., Rempel A. A., Parmon V. N., 'Photocatalytic oxidation of ethanol vapors under visible light on CdS–$TiO_2$ nanocatalyst', *Journal of Photochemistry and Photobiology A: Chemistry*, **250**, 103–109 (2012).

77. Hassan Y., Chuang C. H., Kobayashi Y., Coombs N., Gorantla S., Botton G. A., Winnik M. A., Burda C., Scholes G. D., 'Synthesis and optical properties of linker-free $TiO_2$/CdSe nanorods', *The Journal of Physical Chemistry C*, **118**, 3347–3358 (2014).

78.  Bubenhofer S. B., Schumacher C. M., Koehler F. M., Luechinger N. A., Grass R. N., Stark W. J., 'Large-scale synthesis of PbS–TiO$_2$ heterojunction nanoparticles in a single step for solar cell application', *The Journal of Physical Chemistry C*, **116**, 16264–16270 (2012).

79.  Acharya K. P., Hewa Kasakarage N. N., Alabi T. R., Nemitz I., Khon E., Ullrich B., Anzenbacher P., Zamkov M., 'Synthesis of PbS/TiO$_2$ colloidal heterostructures for photovoltaic applications', *The Journal of Physical Chemistry C*, **114**, 12496–12504 (2010).

80.  Gholami M., Qorbani M., Moradlou O., Naseri N., Moshfegh A. Z., 'Optimal Ag$_2$S nanoparticle incorporated TiO$_2$ nanotube array for visible water splitting', *RSC Advances*, **4**, 7838–7844 (2014).

81.  Gholap H., Patil R., Yadav P., Banpurkar A., Ogale S., Gade W., 'CdTe–TiO$_2$ nanocomposite: An impeder of bacterial growth and biofilm', *Nanotechnology*, **24**, 195101/1–195101/14 (2013).

82.  Kisch H., 'Semiconductor photocatalysis-mechanistic and synthetic aspects', *Angewandte Chemie - International Edition*, **52**, 812–847 (2013).

83.  Neves M. C., Nogueira J. M. F., Trindade T., Mendonça M. H., Pereira M. I., Monteiro O. C., 'Photosensitization of TiO$_2$ by Ag$_2$S and its catalytic activity on phenol photodegradation', *Journal of Photochemistry and Photobiology A: Chemistry*, **204**, 168–173 (2009).

84.  Grozdanov I., 'Solution growth and characterization of silver sulfide films', *Applied Surface Science*, **84**, 325–329 (1995).

85.  Tubtimtae A., Wu K. L., Tung H. Y., Lee M. W., Wang G. J., 'Ag$_2$S quantum dot-sensitized solar cells', *Electrochemistry Communications*, **12**, 1158–1160 (2010).

86.  Liu B., Wang D., Zhang Y., Fan H., Lin Y., Jiang T., Xie T., 'Photoelectrical properties of Ag$_2$S quantum dot-modified TiO$_2$ nanorod arrays and their application for photovoltaic devices', *Dalton Transactions*, **42**, 2232–2237 (2013).

87.  Du Y., Xu B., Fu T., Cai M., Li F., Zhang Y., Wang Q., 'Near-infrared photoluminescent Ag$_2$S quantum dots from a single source precursor', *The Journal of the American Chemical Society*, **132**, 1470–1471 (2010).

88. Shrestha L. K., Shrestha R. G., Vilanova N., Rodriguez-Abreu C., Ariga K., 'In-situ formation of silver nanoparticles using nonionic surfactant reverse micelles as nanoreactors', *Journal of Nanoscience and Nanotechnology*, **14**, 2238–2244 (2014).

89. Zhu L., Meng Z. Da, Oh W. C., 'MWCNT-Based $Ag_2S$-$TiO_2$ nanocomposites photocatalyst: Ultrasound-assisted synthesis, characterization, and enhanced catalytic efficiency', *Journal of Nanomaterials*, **2012**, 1–10 (2012).

90. Zhu L., Meng Z., Trisha G., Oh W. C., 'Hydrothermal synthesis of porous $Ag_2S$ sensitized $TiO_2$ catalysts and their photocatalytic activities in the visible light range', *Chinese Journal of Catalysis*, **33**, 254–260 (2012).

91. Ong W. L., Lim Y. F., Ting Ong J. L., Ho G. W., 'Room temperature sequential ionic deposition (SID) of $Ag_2S$ nanoparticles on $TiO_2$ hierarchical spheres for enhanced catalytic efficiency', *Journal of Materials Chemistry A*, **3**, 6509–6516 (2015).

92. Mossalayi H., A.Moghimi., 'Fabrication of $TiO_2$/$Ag_2S$ nano-composites via a new method for photocatalytic degradation of p-xylene & chlorophenol', *Journal of Chemical and Pharmaceutical Research*, **3**, 718–724 (2011).

93. Nagasuna K., Akita T., Fujishima M., Tada H., 'Photodeposition of $Ag_2S$ quantum dots and application to photoelectrochemical cells for hydrogen production under simulated sunlight', *Langmuir*, **27**, 7294–7300 (2011).

94. Xie Y., Yoo S. H., Chen C., Cho S. O., '$Ag_2S$ quantum dots-sensitized $TiO_2$ nanotube array photoelectrodes', *Materials Science and Engineering: B*, **177**, 106–111 (2012).

95. Liu X., Liu Z., Lu J., Wu X., Chu W., 'Silver sulfide nanoparticles sensitized titanium dioxide nanotube arrays synthesized by in situ sulfurization for photocatalytic hydrogen production', *Journal of Colloid and Interface Science*, **413**, 17–23 (2014).

96. Chen C., Xie Y., Ali G., Yoo S. H., Cho S. O., 'Improved conversion efficiency of $Ag_2S$ quantum dot-sensitized solar cells based on $TiO_2$ nanotubes with a ZnO recombination barrier layer.', *Nanoscale Research Letters*, **6**, 462/1–462/9 (2011).

97. Ji G., Liu Z., Guan D., Yang Y., '$Ag_2S$ quantum dots and N3 dye co-sensitized $TiO_2$ nanotube arrays for a solar cell', *Applied Surface Science*, **282**, 695–699 (2013).

98. Hu H., Ding J., Zhang S., Li Y., Bai L., Yuan N., 'Photodeposition of $Ag_2S$ on $TiO_2$ nanorod arrays for quantum dot-sensitized solar cells', *Nanoscale Research Letters*, **8**,

10/1–10/7 (2013).

99. Zhang Y., Zhang W., Xie T., Wang D., Song X. M., 'A novel research approach on the dynamic properties of photogenerated charge carriers at $Ag_2S$ quantum-dots-sensitized $TiO_2$ films by a frequency-modulated surface photovoltage technology', *Materials Research Bulletin*, **48**, 3242–3246 (2013).

100. Neves M. C., Monteiro O. C., Hempelmann R., Silva A. M. S., Trindade T., 'From single-molecule precursors to coupled $Ag_2S/TiO_2$ nanocomposites', *European Journal of Inorganic Chemistry*, **2008**, 4380–4386 (2008).

101. Fan W., Jewell S., She Y., Leung M. K. H., 'In situ deposition of $Ag–Ag_2S$ hybrid nanoparticles onto $TiO_2$ nanotube arrays towards fabrication of photoelectrodes with high visible light photoelectrochemical properties', *Physical Chemistry Chemical Physics*, **16**, 676–680 (2014).

102. Liu Z., Ji G., Guan D., Wang B., Wu X., 'Enhanced charge-carrier transfer by CdS and $Ag_2S$ quantum dots co-sensitization for $TiO_2$ nanotube arrays', *Journal of Colloid and Interface Science*, **457**, 1–8 (2015).

103. Liu Y., Jiang J., Xu Q., Li M., Guo L., 'Photoelectrochemical performance of CdS nanorods grafted vertically aligned $TiO_2$ nanorods', *Materials Research Bulletin*, **48**, 4548–4554 (2013).

104. Wu J. M., Zhang T. W., 'Photodegradation of rhodamine B in water assisted by titania films prepared through a novel procedure', *Journal of Photochemistry and Photobiology A: Chemistry*, **162**, 171–177 (2004).

105. Tang J., Gong W., Cai T., Xie T., Deng C., Peng Z., Deng Q., 'Novel visible light responsive $Ag@(Ag_2S/Ag_3PO_4)$ photocatalysts: Synergistic effect between Ag and $Ag_2S$ for their enhanced photocatalytic activity', *RSC Advances*, **3**, 2543–2547 (2013).

106. Armelao L., Colombo P., Fabrizio M., Gross S., Tondello E., 'Sol–gel synthesis and characterization of $Ag_2S$ nanocrystallites in silica thin film glasses', *Journal of Materials Chemistry*, **9**, 2893–2898 (1999).

# CHAPTER 5

*Synthesis and Characterization of CdS-γ-Fe₂O₃ and ZnO@γ-Fe₂O₃ Nanocomposites by Thermal Decomposition Approach*

## 5.1 Synthesis and Characterization of CdS-γ-Fe₂O₃ Nanocomposites by Thermal Decomposition Approach

### 5.1.1. Introduction

Metal oxide-metal sulfide nanocomposites are of current technological interest due to their wide applications in solar energy conversion, optoelectronic devices, and photocatalysis [1]. Metal sulfide semiconductor nanocrystals such as CdS, ZnS, CuS and PbS have been coupled with metal oxide semiconductors such as $TiO_2$, $SnO_2$, ZnO and $Fe_2O_3$ to extend their photo response to visible region. The coupling facilitates charge separation by accumulating electrons and holes in separate particles [2,3]. Some of the recently reported metal oxide-metal sulfide nanocomposites that are useful for the photocatalytic degradation of organic dye pollutants include CdS-$TiO_2$, $Fe_3O_4$-ZnS, CuS-ZnO, CdS-$Fe_2O_3$ and PbS-$TiO_2$ [4–8].

Synthesis of iron oxide based semiconductor nanocomposites is of immense interest recently [9–11]. Because of their low cost, easy production, environmental friendliness and good chemical stability, iron oxide nanoparticles have been extensively investigated for a wide variety of applications such as catalysis, water treatment, sensors, magnetic materials, pigments, drug delivery and lithium ion batteries [12–19]. With low band gap (~2.0 to 2.2 eV), γ-$Fe_2O_3$ absorbs in the visible region and it is one of the most promising photocatalysts in this region [20]. However, the photo-induced electron-hole pairs in γ-$Fe_2O_3$ easily undergo recombination which inhibits its application as an efficient photocatalyst. To overcome this drawback, composites of γ-$Fe_2O_3$ with other semiconductors such as CdS [7], $SnO_2$ [18], and $TiO_2$ [21] have been prepared. CdS is a semiconductor with a direct band gap of 2.42 eV and regarded as one of the most important photocatalysts in the visible region. However, CdS is susceptible to photo corrosion in aqueous media due to which it is not preferred for applications in environmental remediation [22]. In recent times, attempts have been made to prepare CdS based nanocomposites [7]. CdS is coupled with another semiconductor with lower but closely lying conduction band and appropriate valence band. Charge separation occurs at the interface of the two semiconductors and the photo generated carriers interact with the reactants efficiently at the interface [23]. CdS-$Fe_2O_3$ hetreojunctions are good photocatalysts for the degradation of hazardous organic dyes such as methylene blue and congo red, and photocatalytic reduction of Cr(VI), and hydrogen production [24–27].

CdS-$Fe_2O_3$ nanocomposites with different morphologies have been reported (Fig. 5.1). Wu et al. have prepared CdS nanowires decorated with $Fe_2O_3$ nanoparticles by a two-step

solvothermal method [7]. Wang et al. have synthesized CdS nanowires decorated with $Fe_3O_4$ microspheres by the same method [24]. Shi et al. have grown CdS nanoparticles on single crystalline $\alpha$-$Fe_2O_3$ nanorods by hydrothermal and solution routes [28]. Wu et al. have synthesized CdS urchin-like micro-spheres decorated with hematite/magnetite nanoparticles by the solvothermal method [29]. Zhang et al. have synthesized hierarchical $\alpha$-$Fe_2O_3$/CdS microflowers with $\alpha$-$Fe_2O_3$ core and CdS shell through chemical bath deposition [26]. Preethi et al. have synthesized $Fe_2O_3$@CdS@ZnS core-shell nanoparticles by a multi-step solution route [27]. Chen et al. have deposited CdS nanoparticles on $Fe_2O_3$ nanorods via a three step hydrothermal method [30]. Kwon et al. have synthesized hetero-structured nanocrystals of $\gamma$-$Fe_2O_3$ and CdS by airless thermal decomposition of $Fe(CO)_5$ in octyl ether in the presence of oleic acid [31]. Liu et al. have synthesized $Zn_{1-x}Cd_xS$/$\gamma$-$Fe_2O_3$ nanocomposites (x = 0 to 1) by a solution combustion method [32]. Most of the reported methods for the preparation of CdS-$Fe_2O_3$ nanocomposites consist of multi-steps with long reaction time and the methods often require expensive reagents. A brief summary on the synthesis of CdS-$Fe_2O_3$ nanocomposites by the above mentioned methods are given in Table 5.1.
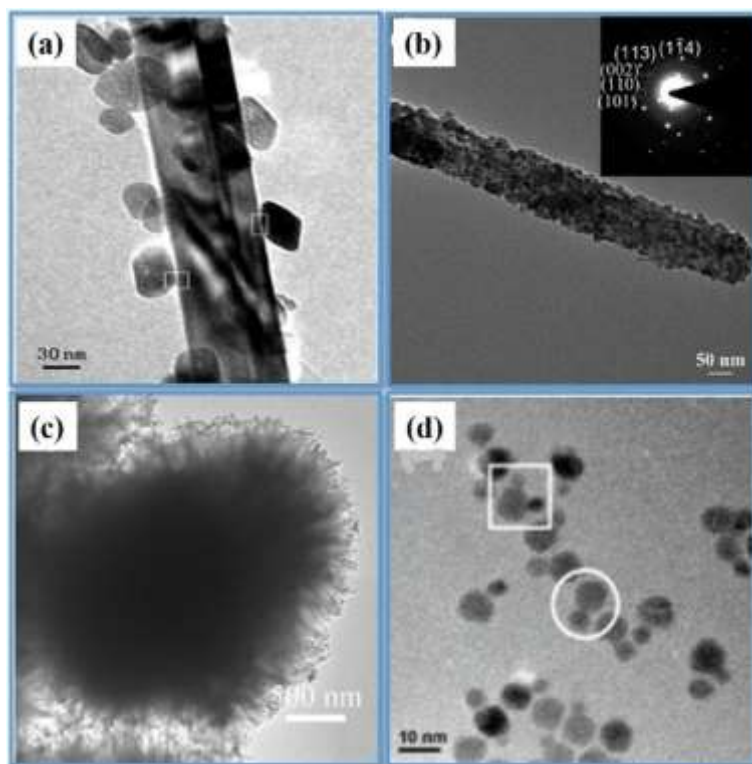


**Fig. 5.1:** CdS-$Fe_2O_3$ nanocomposites with different morphologies: (a) CdS nanowires decorated with $\alpha$-$Fe_2O_3$ nanoparticles [24], (b) corn like $\alpha$-$Fe_2O_3$/CdS nanocomposites [28], (c) CdS urchin-like microsphere decorated $\alpha$-$Fe_2O_3$ nanoparticles [29] and (d) $\gamma$-$Fe_2O_3$/CdS hetreojunctions [31].

**Table 5.1:** Different reported methods for the synthesis of $CdS$-$Fe_2O_3$ nanocomposites.

| Sl. No. | Method | Chemicals used | Morphology of the product | Size | Reference |
|---|---|---|---|---|---|
| 1. | Solvothermal synthesis | Ferric nitrate, PVP, cadmium nitrate and sulfur | $\alpha$-$Fe_2O_3$ decorated CdS nanowires | 20-30 nm | [7] |
| 2. | Solvothermal synthesis | Ferric nitrate, cadmium chloride, sodium diethyl dithiocarbamate and PVP | $\alpha$-$Fe_2O_3$ decorated CdS nanowires | 40-50 nm | [24] |
| 3. | Hydrothermal synthesis | Maghemite, cadmium chloride and sulfocarbamide | Powder | 18-30 nm | [25] |
| 4. | Hydrothermal and chemical bath method | Ferric chloride, urea, cadmium sulfate and thiourea | CdS deposited $\alpha$-$Fe_2O_3$ microflowers | $\alpha$-$Fe_2O_3$ = 1-2 $\mu$m, CdS = 3-5 nm | [26] |
| 5. | Solution route | Ferric nitrate, PVA, cadmium acetate and sodium sulfate | Core-shell | - | [27] |
| 6. | Hydrothermal and solution method | Ferric chloride, cadmium sulfate and thiourea | Corn-like | $\alpha$-$Fe_2O_3$ = 50-400 nm and CdS = 20 nm | [28] |
| 7. | Solvothermal synthesis | Ferrous sulphate, cadmium acetate and thiourea | CdS urchin-like microspheres decorated with haematite or magnetite | CdS = 2 $\mu$m $\alpha$-$Fe_2O_3$ = 20 nm, $Fe_3O_4$ = 30 nm | [29] |

| 8. | Hydrothermal synthesis | Ferric chloride, cadmium nitrate and thiourea | Hierarchical | $\alpha$-$Fe_2O_3$ diameter = 30-150 nm and length = 0.5-1.5 $\mu$m, CdS diameter =15-30 nm and length = 40-60 nm | [30] |
| 9. | Thermal decomposition | Iron pentacarbonyl, cadmium acetylacetonate and sulfur | Core-shell | $\gamma$-$Fe_2O_3$ = 8 nm and CdS = 4.6 nm | [31] |

A brief discussion on some of the synthetic methods is given below.

*Solvothermal synthesis* [29]*:* Wu et al., have prepared CdS/$\alpha$-$Fe_2O_3$ and CdS/$Fe_3O_4$ by two step solvothermal method. In the first step, urchin-like CdS microspheres are prepared. In this method, a specific amount of cadmium acetate is dissolved in mixed solvents of 1, 6-hexanediamine and ammonia with a volume ratio of 1:3 (total volume = 40 mL). Then, thiourea is added and stirred for dissolution. After that, the resulting solution is transferred into a 50 mL autoclave and maintained at 150 °C for 10 h. The yellow precipitate obtained is washed with distilled water and absolute ethanol several times, then dried in vacuum at 50 °C for 10 h. In the second step, the prepared CdS urchin-like microspheres are dispersed in the mixed solvents of ethylene glycol and water with the volume ratio of 1:3 (total volume = 40 mL) for preparation of CdS/$\alpha$-$Fe_2O_3$ and with a volume ratio of 1:1 (total volume = 40 mL) for the preparation of CdS/$Fe_3O_4$. After that, a specific amount of ferrous sulfate is added and stirred for 15 min at room temperature. Then, the resulting solution is transferred to a 50 mL autoclave and maintained at 150 °C for 12 h. The final product obtained is washed with distilled water and absolute ethanol several times and dried in vacuum at 50 °C for 10 h.

*Hydrothermal and solution method* [28]*:* Shi et al. have prepared $\alpha$-$Fe_2O_3$/CdS corn-like nanorods by a two-step hydrothermal and solution method. In the first step, $\alpha$-$Fe_2O_3$ is prepared by hydrothermal method. In this method, a specific amount of ferric chloride is dissolved in

distilled water and an aqueous solution of NaOH (2 M) is added to get the precipitate. The precipitate obtained is washed with distilled water and again dispersed in an aqueous solution of NaOH (2 M). Then, the resulting suspension is transferred to an autoclave and maintained at 160 $^{\circ}$C for 20 h. The product obtained is cooled to room temperature and is washed with distilled water and ethanol. After that, the α-Fe$_2$O$_3$ nanorods obtained are dried and calcined at 400 $^{\circ}$C for 3 h. In the second step, certain amount of α-Fe$_2$O$_3$ nanorods are dispersed in distilled water under magnetic stirring and then specified amount of CdSO$_4$, thiourea and ammonia are added into the suspension. The resulting mixture is kept at 60 °C under vigorous magnetic stirring for 3 h. The obtained product is washed with deionized water and ethanol, and then vacuum dried at 70°C for 3 h.

*Hydrothermal and chemical bath method* [26]*:* Zhang et al. have prepared hierarchical CdS/α-Fe$_2$O$_3$ by a two-step hydrothermal and chemical bath method. In the first step, hierarchical α-Fe$_2$O$_3$ microflowers are prepared by hydrothermal method. In this method, specified amounts of ferric chloride and urea are dissolved in ethylene glycol under stirring. Then, the suspension is transferred to a 200 mL autoclave and is heated at 160 °C for 8 h. The product obtained is washed with absolute ethanol, and vacuum dried at 60 °C for 6 h. The powders are then calcined at 500 °C for 10 min in air. In the second step, CdS/α-Fe$_2$O$_3$ nanocomposite is prepared by chemical bath method. In this method, certain amount of α-Fe$_2$O$_3$ microflowers is dispersed in deionized water under constant stirring and then cadmium sulfate, thiourea and ammonia are added to the suspension. The resulting mixture is kept at 60 $^{\circ}$C for 3 h under vigorous magnetic stirring. The obtained product is washed with distilled water and ethanol, and dried at 40 $^{\circ}$C for overnight.

*Thermal decomposition* [31]*:* Kwon et al. have prepared γ-Fe$_2$O$_3$/CdS hetreojunctions by two step thermal decomposition method (Scheme 5.1). First, γ-Fe$_2$O$_3$ nanocrystals are synthesized by thermal decomposition of iron pentacarbonyl at 290 $^{\circ}$C for 60 min in the presence of oleic acid and octyl ether in N$_2$ atmosphere. In the second step, specified amount of sulfur is added to the solution containing γ-Fe$_2$O$_3$ nanocrystals at 100 $^{\circ}$C and is stirred for 5 min. After that cadmium acetylacetonate, 1, 2-hexadecanediol and trioctylphosphine oxide are added at 80 $^{\circ}$C with constant stirring. The mixture is then refluxed at 230-280 $^{\circ}$C for a few minutes to several hours. The final product is precipitated with methanol and is dissolved in hexane or chloroform.
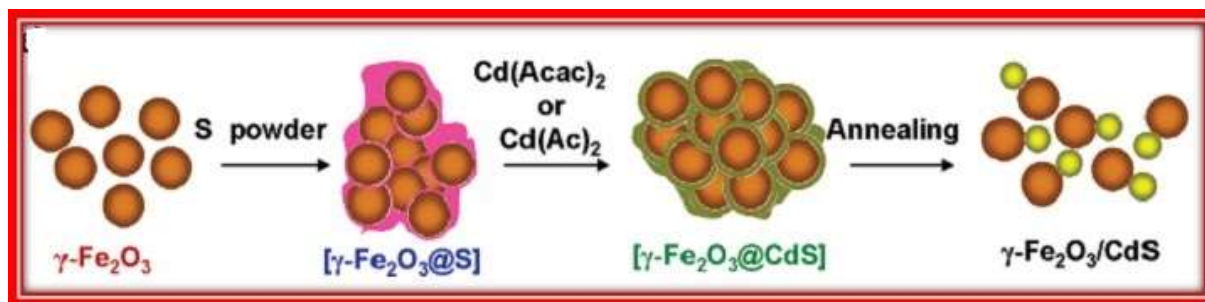
**Scheme 5.1:** Illustration of the synthesis of γ-Fe₂O₃/CdS nanocomposites by thermal decomposition approach [31].

In the present study, CdS-γ-Fe₂O₃ nanocomposites were synthesized by a single step thermal decomposition of iron acetylacetonate, cadmium acetate and thiourea in diphenyl ether at about 200 ºC for 35 min. The CdS-γ-Fe₂O₃ nanocomposites were characterized by different techniques and their optical and magnetic properties were studied.

### 5.1.2 Experimental Details

**Chemicals**

The chemicals used were cadmium acetate (Himedia), thiourea (Rankem), iron(III) acetylacetonate (ACROS), diphenyl ether (Aldrich), and methanol (Rankem). All the chemicals were used as received. The CdS-γ-Fe₂O₃ nanocomposites were synthesized by the thermal decomposition method and more details are as follows.

**Synthesis**

Six different CdS-γ-Fe₂O₃ nanocomposites (Table 5.2) were prepared by varying the concentration of cadmium acetate, thiourea and iron acetylacetonate and also by varying the thermal decomposition time. The reagents (iron acetylacetonate, cadmium acetate and thiourea) were added to 10 mL of diphenyl ether in a round bottom flask and refluxed in air at about 200 ºC for 35 min or 70 min. Then, 30 mL methanol was added to the contents to get the precipitate. The precipitates obtained were centrifuged, washed with methanol and dried overnight under vacuum to obtain the CdS-γ-Fe₂O₃ nanocomposite powders (Scheme 5.2). For comparison purpose, pure CdS and Fe₂O₃ nanoparticles were also prepared using the similar synthetic procedure.

```
┌──────────────────┐   ┌──────────────┐   ┌──────────────┐   ┌──────────────────┐
│      Iron        │ ✛ │   Cadmium    │ ✛ │   Thiourea   │ ✛ │  Diphenyl ether  │
│  acetylacetonate │   │   acetate    │   │              │   │     (10 mL)      │
└──────────────────┘   └──────────────┘   └──────────────┘   └──────────────────┘
```

**Refluxed at 200 °C, 35 min or 70 min**

```
                    ┌──────────┐
                    │  Slurry  │
                    └──────────┘
```

i) Allowed to cool
ii) Precipitation with methanol

```
               ┌────────────────────┐
               │    Dark brown      │
               │    Precipitate     │
               └────────────────────┘
```

**Dried under vacuum**

```
               ┌────────────────────┐
               │   CdS-γ-Fe₂O₃       │
               │   nanocomposite    │
               └────────────────────┘
```
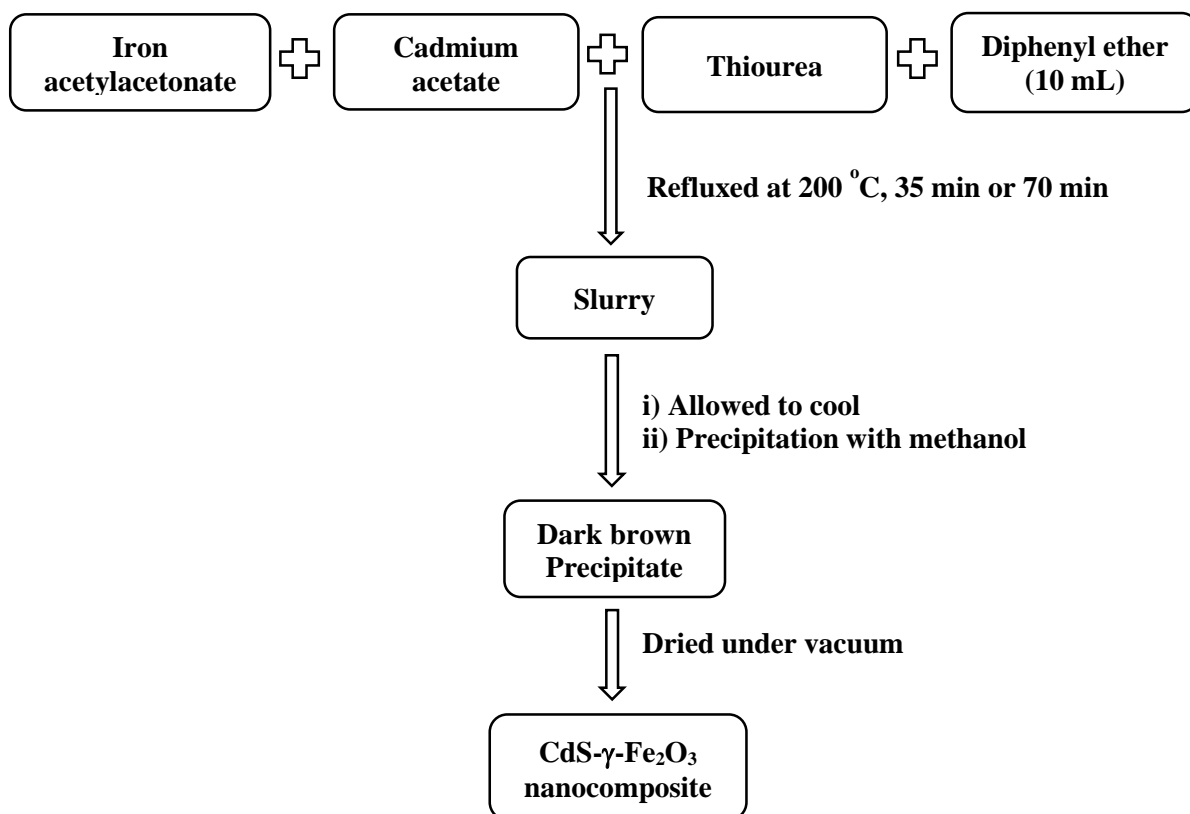
**Scheme 5.2:** Synthesis of CdS-γ-Fe$_2$O$_3$ nanocomposites by thermal decomposition approach.

**Table 5.2:** Designation of various CdS-γ-Fe$_2$O$_3$ nanocomposites prepared using different synthetic conditions.

| Sample code | Fe(acac)$_3$ (mmol) | Cd(Ac)$_2$ (mmol) | Thiourea (mmol) | Thermal decomposition time (min) |
|---|---|---|---|---|
| Fe$_2$O$_3$ | 1 | - | - | 35 |
| CdS | - | 1 | 1 | 35 |
| FC1 | 1 | 0.1 | 0.1 | 35 |
| FC2 | 1 | 0.25 | 0.25 | 35 |
| FC3 | 1.25 | 1 | 1 | 35 |
| FC4 | 1 | 0.1 | 0.1 | 70 |
| FC5 | 1 | 0.25 | 0.25 | 70 |
| FC6 | 1.25 | 1 | 1 | 70 |

### 5.1.3 Results and Discussion

### 5.1.3.1 XRD results

The X-ray diffraction patterns of pure $Fe_2O_3$, CdS nanoparticles and all the CdS-$\gamma$-$Fe_2O_3$ nanocomposites (FC1-FC6) are shown in Fig. 5.2. Pure iron oxide nanoparticles do not show any feature in the XRD pattern. Since the thermal decomposition of iron acetylacetonate was carried out in the presence of air and under refluxing conditions in diphenyl ether, the product obtained is proposed to be $\gamma$-$Fe_2O_3$ [33]. Further evidence for the presence $\gamma$-$Fe_2O_3$ comes from transmission electron microscopy (TEM) measurement and selected area electron diffraction (SAED) results discussed later. Pure CdS nanoparticles and all the CdS-$\gamma$-$Fe_2O_3$ nanocomposites show peaks at $2\theta$ values of 24.8°, 26.53°, 28.2°, 36.28°, 43.9°, 47.9°, 51.9° and 70.8° corresponding to (100), (002), (101), (102), (110), (103), (112) and (211) reflections of wurtzite CdS (JCPDS no. 41-1049). The crystallite size of CdS in the nanocomposites, calculated using Debye-Scherrer formula, varies from 1.2 to 2.9 nm while the crystallite size of pure CdS nanoparticles is about 5.7 nm. In general, the crystallite size of CdS in the nanocomposites increases with an increase in the concentration of cadmium acetate and thiourea used during their synthesis.
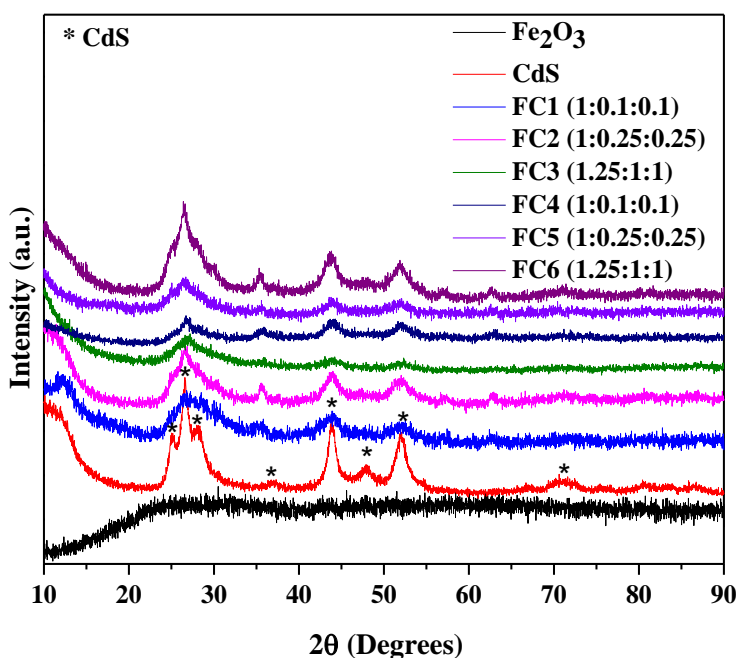


**Fig. 5.2:** XRD patterns of pure $Fe_2O_3$, CdS nanoparticles and CdS-$\gamma$-$Fe_2O_3$ nanocomposites (FC1-FC6).

## 5.1.3.2 FT-IR Results

The IR spectra of pure $Fe_2O_3$, CdS nanoparticles and all the nanocomposites are shown in Fig. 5.3. All the samples show bands near 3400 $cm^{-1}$ and 1630 $cm^{-1}$ attributed to O–H stretching and bending, respectively, due to physisorbed water molecules [34]. The IR bands in the 3000–2500 $cm^{-1}$ range in the nanocomposites are attributed to C–H stretching. The IR bands in the range 2500-2000 $cm^{-1}$ are attributed to $CO_2$ present in the chamber of IR spectrometer during the spectral measurements and the band at 1049 $cm^{-1}$ is attributed to C–O–C stretching [35]. The band at 1421 $cm^{-1}$ is attributed to the stretching vibration of $COO^-$ [36]. These bands suggest the presence of organic content adsorbed on the surface of the CdS-$\gamma$-$Fe_2O_3$ nanocomposites [36,37]. The band at 503 $cm^{-1}$ is attributed to Cd–S stretching [38] and the IR bands at about 553 and 480 $cm^{-1}$ are attributed to the characteristic vibrations of $\gamma$-$Fe_2O_3$ [20].
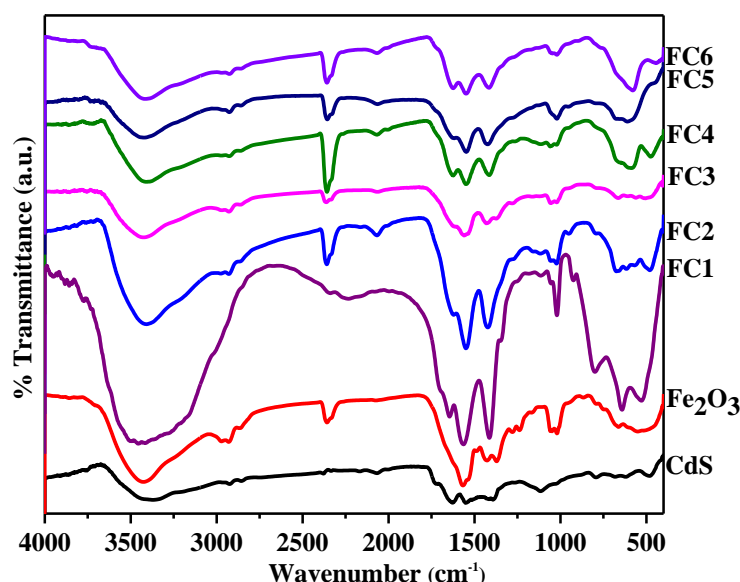


**Fig. 5.3:** FT-IR spectra of pure $Fe_2O_3$, CdS nanoparticles and CdS-$\gamma$-$Fe_2O_3$ nanocomposites (FC1-FC6).

## 5.1.3.3 TGA Results

TGA measurements were carried out for pure $\gamma$-$Fe_2O_3$, CdS and the nanocomposites (FC1-FC6) (Fig. 5.4). Pure iron oxide shows a weight loss of 23.1% and pure CdS shows a weight loss of 12.2% in the range 25 °C to 400 °C. The weight loss is attributed to the removal of organic molecules (e.g. diphenyl ether, acetylacetonate, methanol etc.) from the nanocomposites. The nanocomposites FC1, FC2, FC3, FC4, FC5 and FC6 exhibit %wt loss of

30.8, 18.4, 6.6, 45.5, 6.7 and 3.9, respectively. The nanocomposites FC1 and FC4 show more weight loss compared to the other nanocomposites and this is attributed to the presence of more organic moieties and some undecomposed precursors (e.g. iron acetylacetonate) in these nanocomposites. At about 450 °C, there is weight gain in pure CdS and all the CdS-$\gamma$-Fe$_2$O$_3$ nanocomposites. The pure CdS and all the nanocomposites (FC1, FC2, FC3, FC4, FC5 and FC6) show weight gain of 4.0, 5.6, 6.3, 16.7, 2.1, 6.0 and 15.6%, respectively, and this weight gain in all the cases is attributed to the formation of CdO and CdSO$_4$ [39,40]. After 840 °C pure CdS and all the nanocomposites (FC1-FC6) show continuous weight loss due to the decomposition of CdO.
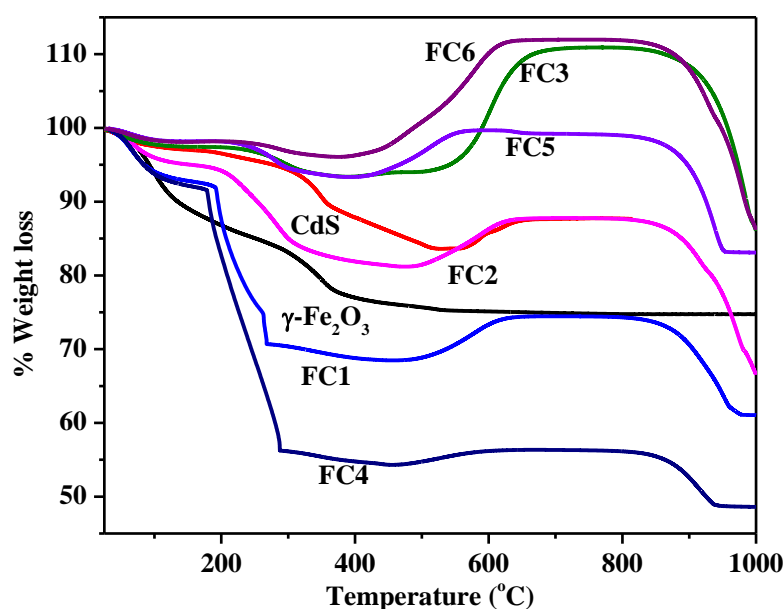


**Fig. 5.4:** TGA curves of pure $\gamma$-Fe$_2$O$_3$, CdS nanoparticles and all the CdS-$\gamma$-Fe$_2$O$_3$ nanocomposites (FC1-FC6).

### 5.1.3.4 FE-SEM and EDXA Results

Fig 5.5 shows the FE-SEM images of pure $\gamma$-Fe$_2$O$_3$, CdS nanoparticles and all the CdS-$\gamma$-Fe$_2$O$_3$ nanocomposites (FC1-FC6). Pure $\gamma$-Fe$_2$O$_3$ (Fig. 5.5(a)) shows small agglomerated nanoparticles with no regular morphology and pure CdS (Fig. 5.5(b)) shows agglomerated sphere-like particles. The nanocomposites FC1 and FC4 (Figs. 5.5(c) and 5.5(f)) show agglomerated particles with no particular morphology. On the other hand, nanocomposites FC2, FC3, FC5 and FC6 (Fig. 5.5(d), (e), (g) and (h), respectively) show agglomerated sphere-like particles.
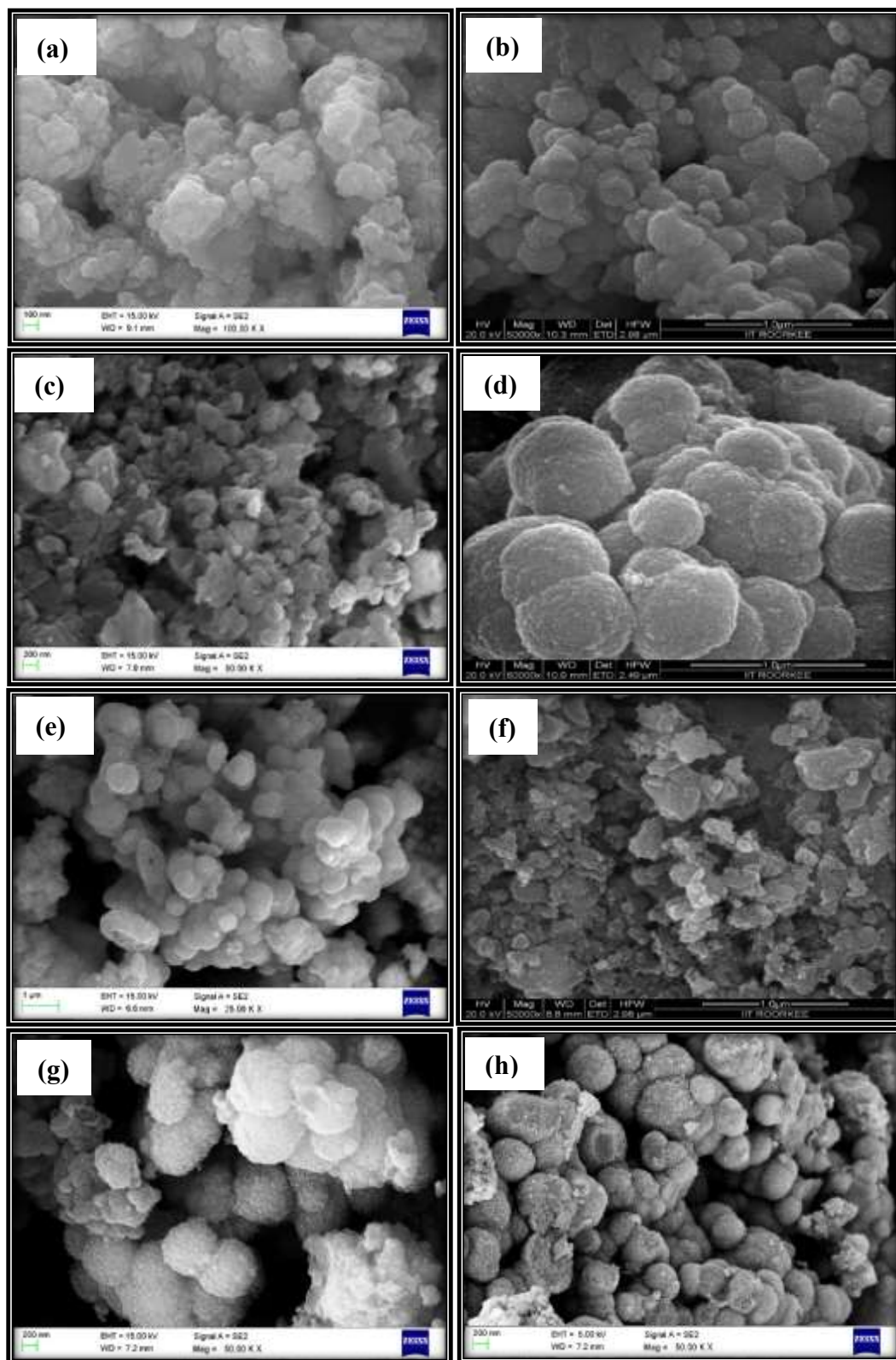
**Fig. 5.5:** FE-SEM images of (a) pure $Fe_2O_3$, (b) CdS nanoparticles and the CdS-$\gamma$-$Fe_2O_3$ nanocomposites; (c) FC1, (d) FC2, (e) FC3, (f) FC4, (g) FC5 and (h) FC6.

Fig. 5.6 shows the EDXA patterns of CdS-$\gamma$-Fe$_2$O$_3$ nanocomposites (FC1- FC6). The EDX analysis shows the presence of oxygen, iron, cadmium and sulfur in all the CdS-$\gamma$-Fe$_2$O$_3$ nanocomposites.
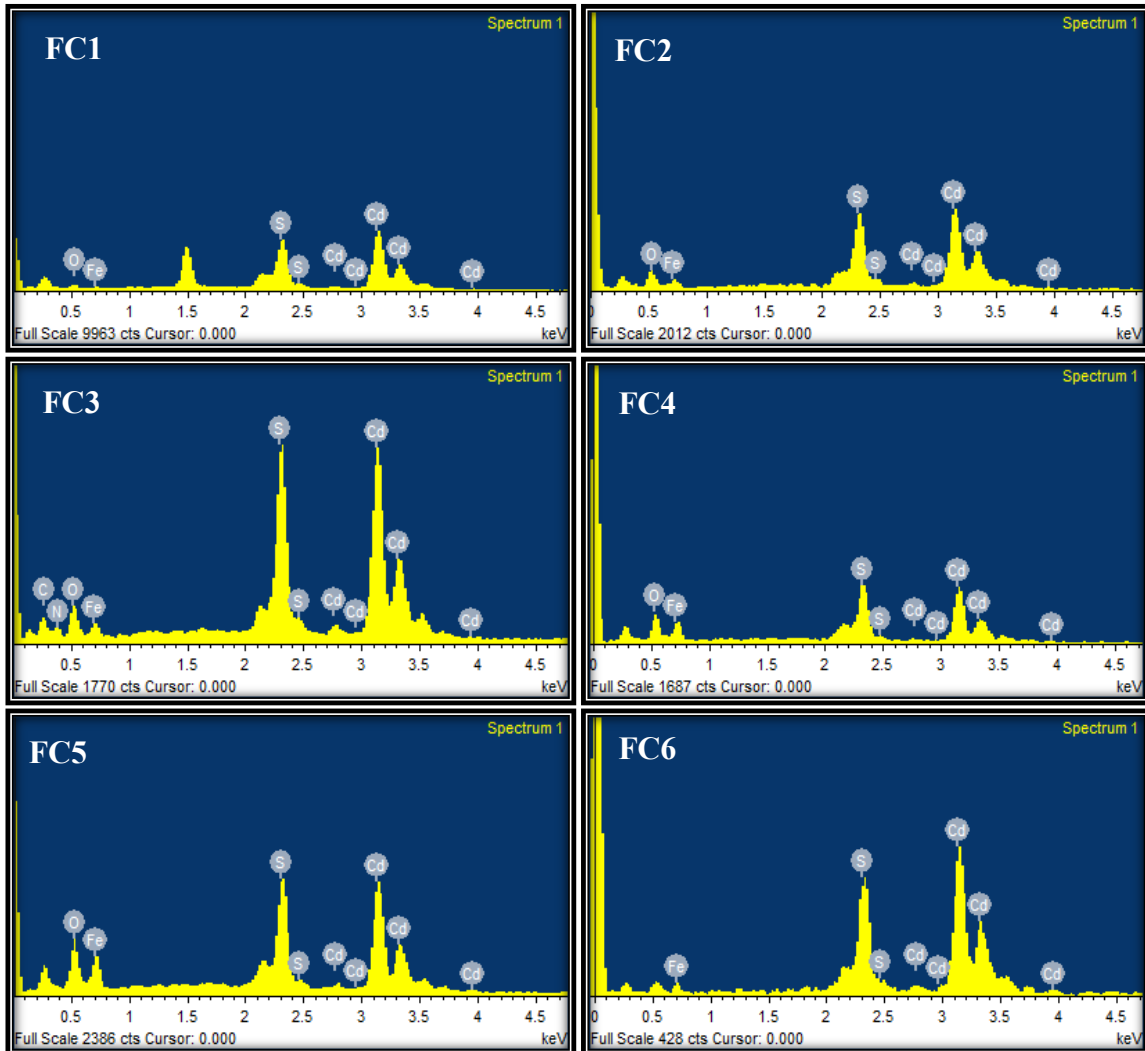


**Fig. 5.6:** EDXA patterns of CdS-$\gamma$-Fe$_2$O$_3$ nanocomposites (FC1-FC6).

Table 5.3 shows the energy dispersive X-ray (EDX) analysis results on the CdS-$\gamma$-Fe$_2$O$_3$ nanocomposites. The nanocomposites FC1, FC2, FC3, FC5 and FC6 show fairly uniform elemental distribution and nanocomposite FC4 exhibits non-uniform elemental distribution.

**Table 5.3:** EDX analysis data for the CdS-$\gamma$-Fe$_2$O$_3$ nanocomposites.

| Nanocomposite | Cd | | S | | Fe | | O | | Comment |
|---|---|---|---|---|---|---|---|---|---|
| | Wt% | At% | Wt% | At% | Wt% | At% | Wt% | At% | |
| FC1 | 11.1 | 6.0 | 9.0 | 8.3 | 39.9 | 15.7 | 37.9 | 69.8 | Uniform |
| | 11.8 | 2.7 | 5.3 | 4.2 | 39.8 | 16.0 | 47.9 | 77.0 | |
| | 11.0 | 2.6 | 8.9 | 7.6 | 38.8 | 15.0 | 41.2 | 70.6 | |
| FC2 | 60.7 | 27.1 | 23.6 | 36.9 | 5.9 | 5.3 | 9.7 | 30.6 | Uniform |
| | 60.2 | 31.4 | 24.8 | 43.2 | 5.6 | 6.6 | 5.4 | 18.8 | |
| | 60.5 | 31.1 | 24.2 | 43.8 | 6.1 | 6.2 | 5.8 | 17.8 | |
| FC3 | 70.9 | 34.7 | 14.9 | 25.6 | 2.6 | 3.6 | 10.5 | 35.9 | Uniform |
| | 71.6 | 40.4 | 18.5 | 35.6 | 2.2 | 2.5 | 5.5 | 21.4 | |
| | 71.9 | 39.5 | 18.9 | 36.0 | 2.4 | 2.6 | 5.7 | 21.9 | |
| FC4 | 9.3 | 3.5 | 4.8 | 6.3 | 71.9 | 53.8 | 23.9 | 36.4 | Non-uniform |
| | 14.1 | 1.3 | 3.8 | 4.3 | 69.9 | 54.8 | 22.1 | 49.5 | |
| | 15.5 | 5.8 | 11.5 | 14.8 | 69.6 | 45.8 | 12.7 | 33.6 | |
| FC5 | 45.8 | 16.6 | 16.2 | 20.8 | 17.0 | 14.8 | 18.5 | 47.7 | Uniform |
| | 46.1 | 31.2 | 21.2 | 36.7 | 18.9 | 18.9 | 6.7 | 23.2 | |
| | 46.2 | 18.2 | 16.2 | 21.4 | 17.7 | 13.5 | 17.7 | 46.9 | |
| FC6 | 28.7 | 11.2 | 14.1 | 19.3 | 44.8 | 35.9 | 12.4 | 34.1 | Uniform |
| | 28.8 | 11.1 | 14.2 | 19.2 | 43.8 | 34.2 | 13.2 | 35.4 | |
| | 28.6 | 12.8 | 14.7 | 18.2 | 45.7 | 34.1 | 13.2 | 35.7 | |

### 5.1.3.5 TEM and SAED Results

The particle size and morphology of the CdS-$\gamma$-Fe$_2$O$_3$ nanocomposites were investigated by transmission electron microscopy (TEM) analysis. The TEM images for pure $\gamma$-Fe$_2$O$_3$ and CdS nanoparticles are shown in Fig. 5.7. The TEM image of Fe$_2$O$_3$ (Fig. 5.7(a)) shows that the nanoparticles are very small ($\sim$2 nm) and they are agglomerated. The selected area electron diffraction (SAED) pattern of $\gamma$-Fe$_2$O$_3$ nanoparticles (Fig. 5.7(b)) shows rings that are attributed to (311), (410), (511) and (440) planes of $\gamma$-Fe$_2$O$_3$ (JCPDS no. 39-1346). The TEM image of CdS nanoparticles (Fig. 5.7(c)) shows agglomerated nanoparticles with no particular shape. Fig. 5.7(d) shows the SAED pattern of CdS nanoparticles and the observed rings are attributed to (103), (100), (110) and (300) planes of polycrystalline hexagonal CdS.
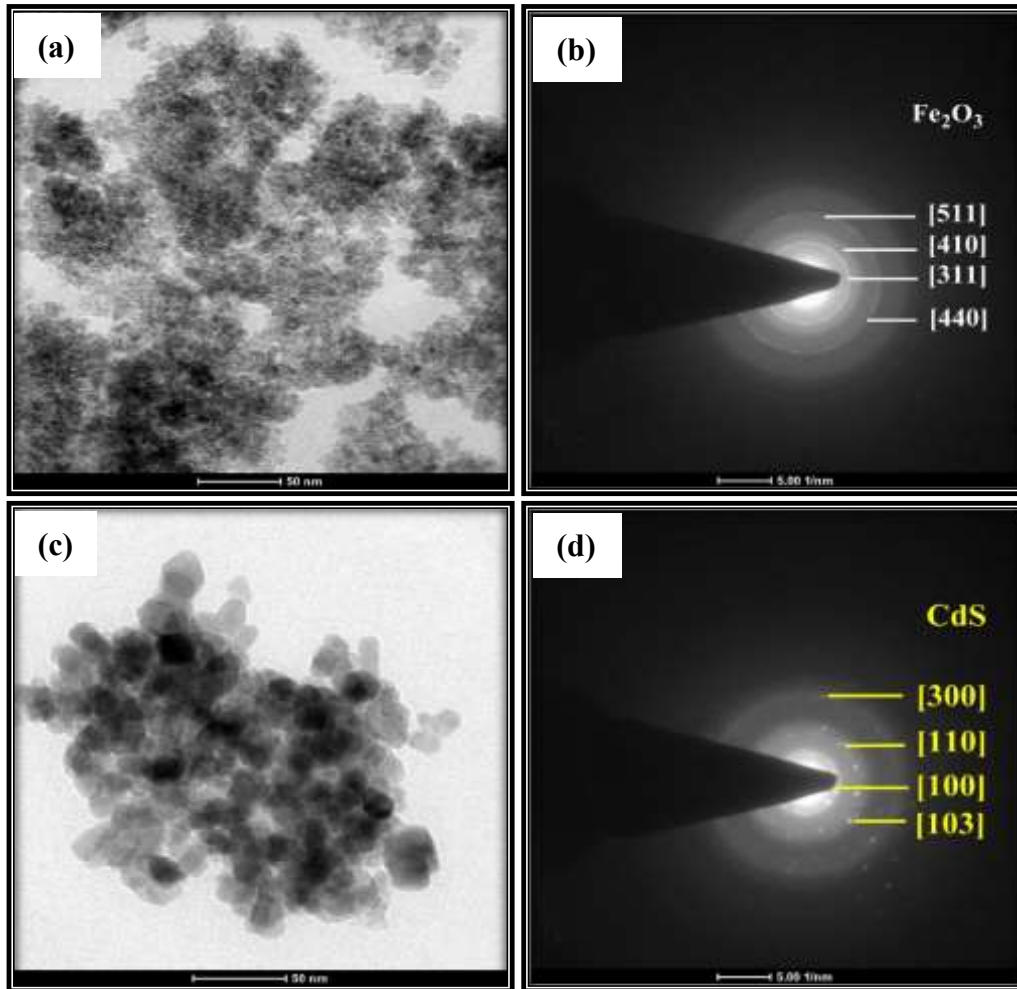
**Fig. 5.7:** TEM images and SAED patterns of pure $Fe_2O_3$ ((a) and (b)), and CdS nanoparticles ((c) and (d)).

Fig. 5.8 shows the TEM images of CdS-$\gamma$-$Fe_2O_3$ nanocomposites FC1, FC2, FC3, FC5 and FC6. The images reveal that small nanoparticles are agglomerated to produce particles with close to spherical morphology. Nanocomposites FC4, FC5 and FC6 were prepared in order to understand the effect of thermal decomposition time on the morphology of final products. It was found from FE-SEM images and electron microscopy studies of FC2 and FC5, and, FC3 and FC6 that there is not much difference in the morphology of nanocomposites when the thermal decomposition time is increased from 35 to 70 minutes.
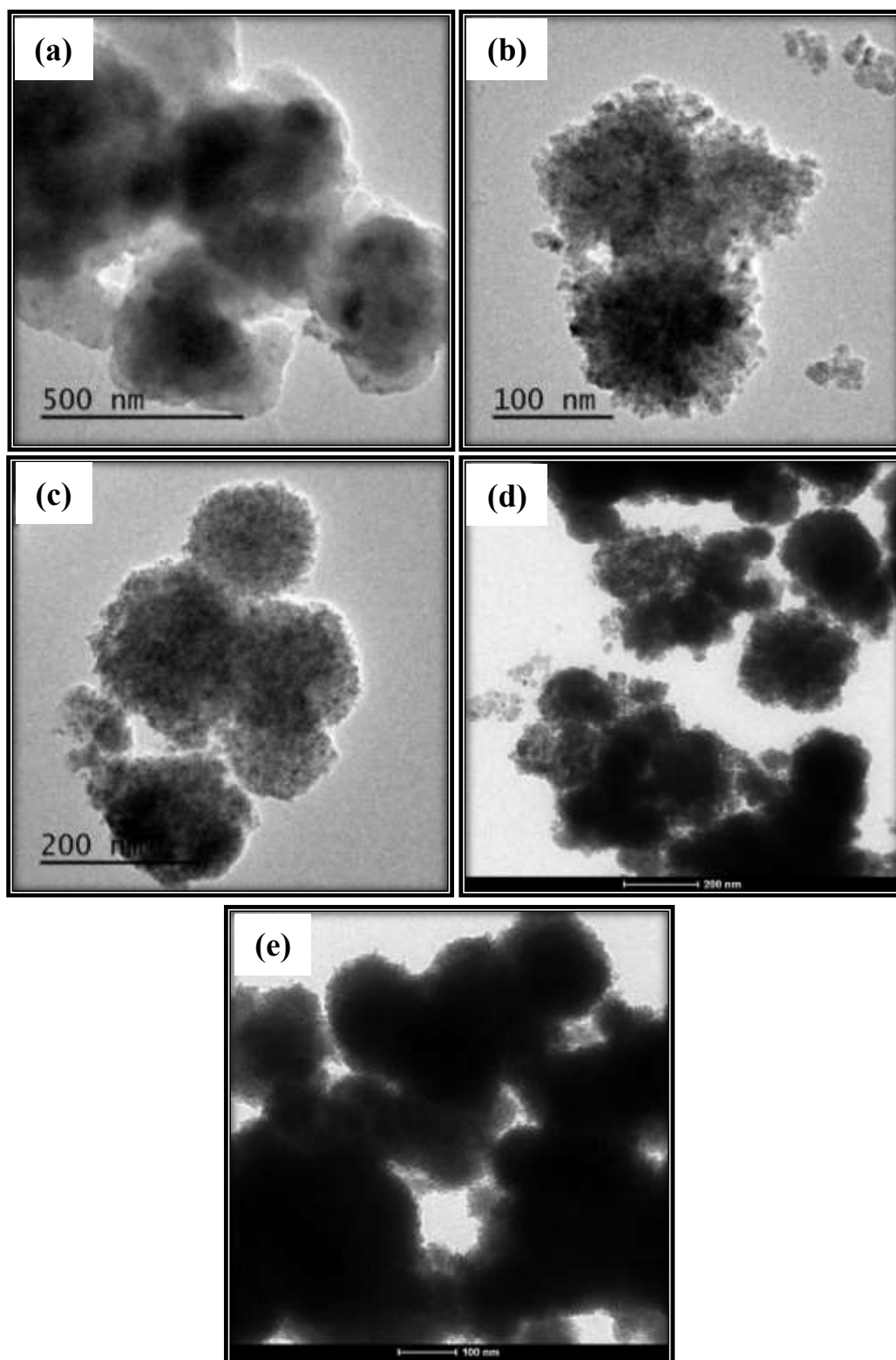
**Fig. 5.8:** TEM images and SAED patterns of CdS-$\gamma$-Fe$_2$O$_3$ nanocomposites; (a) FC1, (b) FC2, (c) FC3, (d) FC5 and (e) FC6.

Fig. 5.9 shows the SAED patterns of CdS-$\gamma$-Fe$_2$O$_3$ nanocomposites FC1, FC2, FC3, FC5 and FC6. The SAED pattern of nanocomposite FC1 shows rings attributed to (311) and (440) planes of $\gamma$-Fe$_2$O$_3$. The SAED patterns of nanocomposites FC2 and FC3 show rings that are attributed to (103), (100), (101) planes of polycrystalline hexagonal CdS and (311), (440) planes of $\gamma$-Fe$_2$O$_3$. The SAED patterns of nanocomposites FC5 and FC6 show rings that are attributed to (103), (100), (101) planes of polycrystalline hexagonal CdS and (311), (511), (440) planes of $\gamma$-Fe$_2$O$_3$.
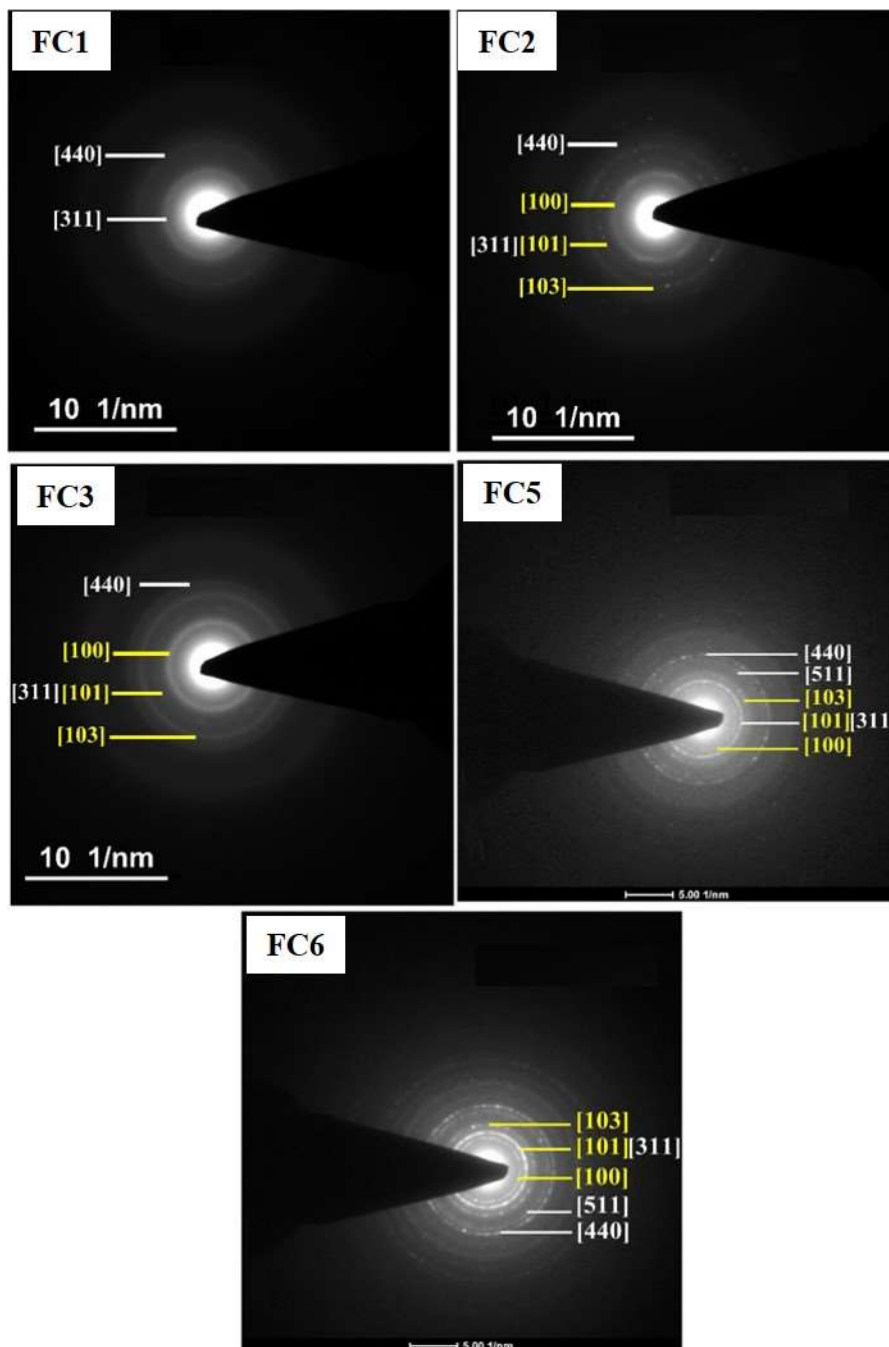


**Fig. 5.9:** SAED patterns of CdS-$\gamma$-Fe$_2$O$_3$ nanocomposites FC1, FC2, FC3, FC5 and FC6.

The high resolution TEM images (HRTEM) of nanocomposites FC1, FC2 and FC3 are shown in Fig. 5.10. The observed interplanar spacing of 0.35 nm in nanocomposites FC1, FC2 and FC3 corresponds to (100) plane of hexagonal CdS. The interplanar spacing of 0.37 nm in Fig. 5.10(a), 0.34 nm in Fig. 5.10(b) and 0.25 nm in Fig. 5.10(c) corresponds to (210), (211) and (311) planes of γ-$Fe_2O_3$, respectively.
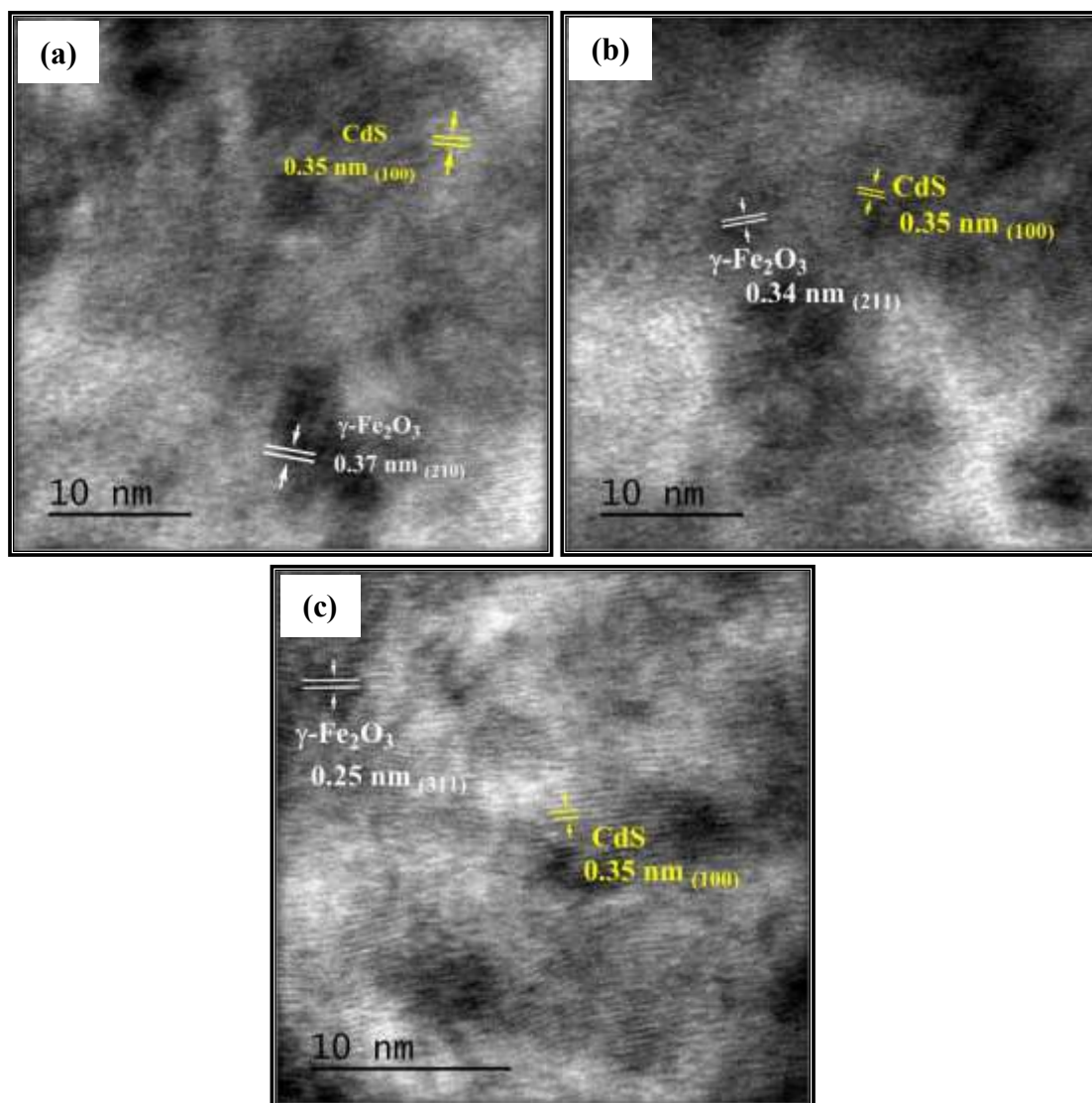


**Fig. 5.10:** HRTEM images of CdS-γ-$Fe_2O_3$ nanocomposites; (a) FC1, (b) FC2 and (c) FC3.

### 5.1.3.6 DRS Results

The diffuse reflectance spectra (DRS) of pure γ-$Fe_2O_3$, CdS nanoparticles and the CdS-γ-$Fe_2O_3$ nanocomposites (FC1-FC6) are shown in Fig. 5.11. The CdS-γ-$Fe_2O_3$ nanocomposites exhibit optical absorption in the visible region.
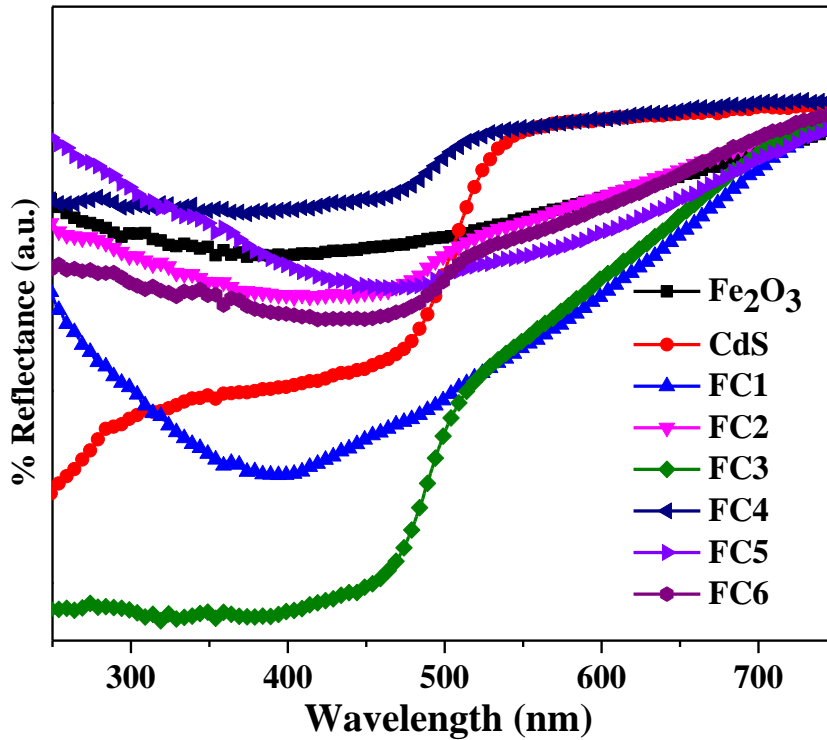
**Fig. 5.11:** DRS spectra of $\gamma$-$Fe_2O_3$, CdS nanoparticles and the CdS-$\gamma$-$Fe_2O_3$ nanocomposites (FC1-FC6).

The optical band gap of $\gamma$-$Fe_2O_3$, CdS nanoparticles and the CdS-$\gamma$-$Fe_2O_3$ nanocomposites was estimated by plotting $(\alpha h\nu)^2$ vs. $h\nu$ (Tauc plots) using the relation:

$$\alpha h\nu = A\left(h\nu - E_g\right)^{1/2}$$

Where $\alpha$ is the absorption coefficient, $h\nu$ is the photon energy, $E_g$ the optical band gap and A is a constant. From the Tauc plots (Fig. 5.12), $E_g$ was estimated by extrapolating a straight line from the absorption curve to the X-axis. Pure $\gamma$-$Fe_2O_3$ and CdS nanoparticles have band gap of 1.9 eV and 2.45 eV, respectively. The nanocomposites FC1, FC2, FC3, FC4 and FC6 show band gap absorption at about 1.8 eV, 2.1 eV, 2.45 eV, 2.2 eV, and 2.35 eV, respectively. Nanocomposite FC5 possesses nearly the same band gap as that of FC2 (2.1 eV). In general, the band gap of nanocomposites increases with an increase in the concentration of CdS (FC1 to FC3).
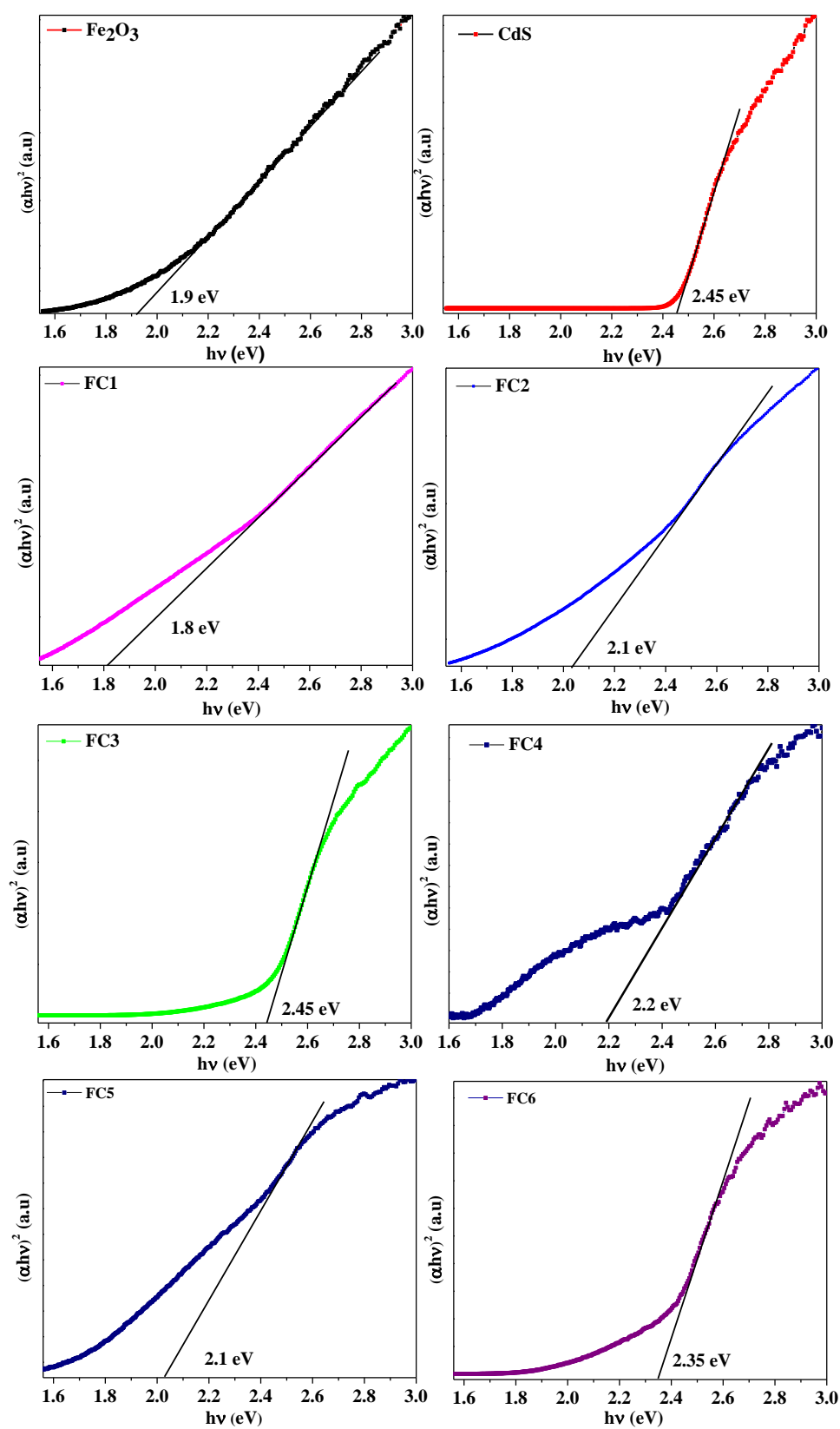
**Fig. 5.12:** Tauc plots of pure γ-Fe₂O₃, CdS nanoparticles and the CdS-γ-Fe₂O₃ nanocomposites (FC1-FC6).

### 5.1.3.7 Photoluminescence Spectroscopy Results

Fig. 5.13 shows the photoluminescence spectra of pure $\gamma$-Fe$_2$O$_3$, CdS nanoparticles and the CdS-$\gamma$-Fe$_2$O$_3$ nanocomposites (FC1-FC6). The spectra for the nanocomposites were normalized with respect to the amount of CdS present in the nanocomposites, as determined by the atomic absorption spectroscopy (AAS) analysis. Pure $\gamma$-Fe$_2$O$_3$ shows a small emission hump at 470 nm which is attributed to the presence of oxygen vacancies, defects and other structural impurities [41]. Pure CdS nanoparticles show band edge emission at about 529 nm with a broad shoulder at 560 nm attributed to Cd$^{2+}$ and S$^{2-}$ vacancies [42]. Nanocomposites FC1 and FC5 show band edge emission due to CdS at about 510 nm and nanocomposites FC3 and FC6 show band edge emission at about 475 nm. Nanocomposite FC2 shows band edge emission due to CdS at 465 nm and nanocomposite FC4 shows band edge emission due to CdS at 504 nm and a broad shoulder at 560 nm attributed to vacancies. There is a blue shift of the CdS band edge emission in the CdS-$\gamma$-Fe$_2$O$_3$ nanocomposites compared to pure CdS nanoparticles. The blue shift is attributed to quantum size effect due to decrease in the particle size of CdS in the nanocomposites. The blue shift is more in the case of nanocomposites FC2 and FC3 as compared to that in FC1 and FC5 in spite of the larger crystallite size of CdS and this is attributed to the presence of defects [26,42]. The CdS-$\gamma$-Fe$_2$O$_3$ nanocomposites contain CdS content (from AAS analysis) of 0.93%, 26.3%, 60.3%, 7.2%, 25.9% and 10.9% for FC1, FC2, FC3, FC4, FC5 and FC6, respectively. In general, the PL intensity of the CdS-$\gamma$-Fe$_2$O$_3$ nanocomposites decreases as compared to pure CdS nanoparticles which is attributed to an efficient charge separation in the nanocomposites [7,26]. Nanocomposite FC3 exhibits the highest PL emission intensity among the nanocomposites. The nanocomposites FC2 and FC5 exhibit less emission intensity compared to FC3 due to decrease in the CdS content. The nanocomposites FC1, FC4 and FC6 have less CdS content and thus exhibit lower emission intensity compared to the other nanocomposites (FC2, FC3 and FC5). The presence of a broad emission band at 475 nm in the nanocomposite FC6 is attributed to the transfer of excited electrons from the conduction band of CdS to the empty surface oxygen vacancies on the surface of iron oxide. Although nanocomposites FC1 and FC4 contain appreciable amount of iron oxide, they possess less amount of CdS compared to FC6 (see Table 5.3). The decrease in emission intensity at 475 nm in nanocomposite FC6 compared to FC1 and FC4 is attributed to the presence of smaller amount of CdS in these nanocomposites.
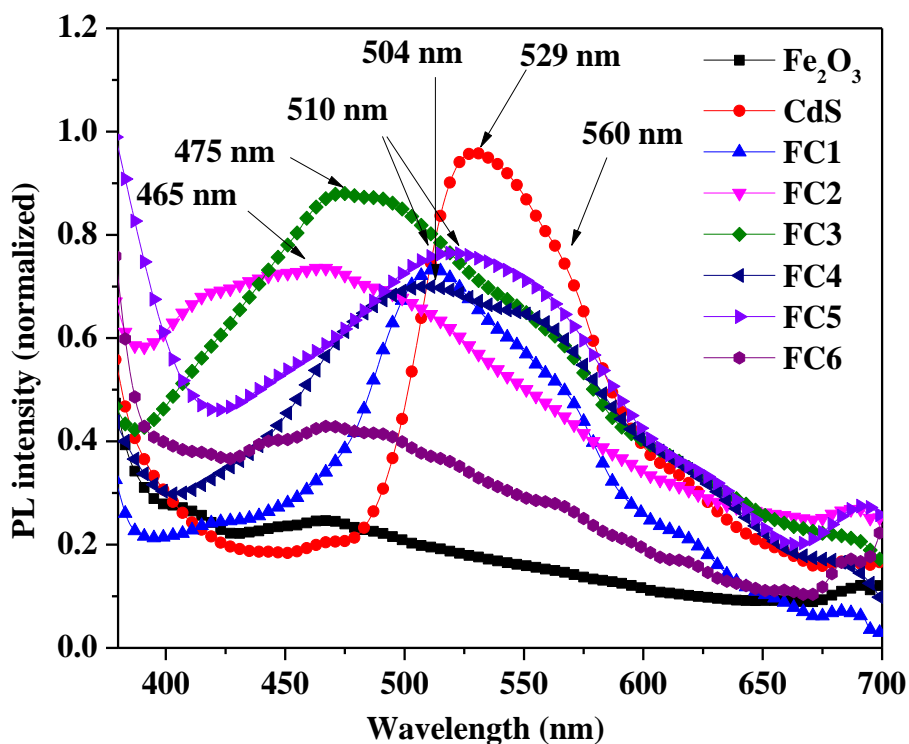
**Fig. 5.13:** Photoluminescence spectra of pure $\gamma$-Fe$_2$O$_3$, CdS nanoparticles and the CdS-$\gamma$-Fe$_2$O$_3$ nanocomposites (FC1-FC6).

### 5.1.3.8 Magnetic Measurements

Typical field dependent magnetization (M-H) plots for pure iron oxide nanoparticles and the CdS-$\gamma$-Fe$_2$O$_3$ nanocomposites with uniform elemental distribution (FC1 and FC2) at 300 K and 5 K are shown in Fig. 5.14. Pure $\gamma$-Fe$_2$O$_3$ nanoparticles show superparamagnetic behaviour at 300 K, while at 5 K, weak ferromagnetic behaviour is observed with $M_r$ and $H_c$ values of 0.32 emu/g and 0.03 T, respectively. At 300 K, the magnetization of $\gamma$-Fe$_2$O$_3$ nanoparticles saturates with a $M_s$ value of 0.61 emu/g while at 5 K, the magnetization does not saturate at a maximum field of 3 Tesla. The CdS-$\gamma$-Fe$_2$O$_3$ nanocomposites FC1 and FC2 show superparamagnetic behaviour at 300 K, weak ferromagnetic behaviour at 5 K and saturation of magnetization is not observed in these nanocomposites at 5 K. Pure iron oxide nanoparticles and all the nanocomposites show coercivity at 5 K but not at 300 K and this is attributed to thermal fluctuation of the blocked moments across the anisotropy barrier [43,44]. Nanocomposite FC1 shows higher coercivity (0.05 T) compared to pure iron oxide nanoparticles which is attributed to lager particle size of iron oxide in the nanocomposite which

increases the anisotropic energy in the single domain [39]. On the other hand, nanocomposite FC2 exhibits lower coercivity (0.033 T) compared to nanocomposite FC1 due to the formation of particles in multi-domain size range [45]. The remanent magnetization ($M_r$) for the nanocomposite FC1 (1.65 emu/g) is higher compared to that of pure $\gamma$-Fe$_2$O$_3$ nanoparticles. Nanocomposite FC2 shows decrease in the remanent magnetization (0.23 emu/g) compared to that of pure iron oxide nanoparticles. At room temperature, the $M_s$ values for the nanocomposites FC1 (4.4 emu/g) and FC2 (0.65 emu/g) are higher compared to that of pure $\gamma$-Fe$_2$O$_3$ nanoparticles. In general, the CdS-$\gamma$-Fe$_2$O$_3$ nanocomposites show lower saturation magnetization values compared to that of bulk $\gamma$-Fe$_2$O$_3$ ($M_s$ = 76 emu/g). This is attributed to the presence of disordered or canted spins on the surface of nanocomposites and superparamagnetic relaxation [46,47].
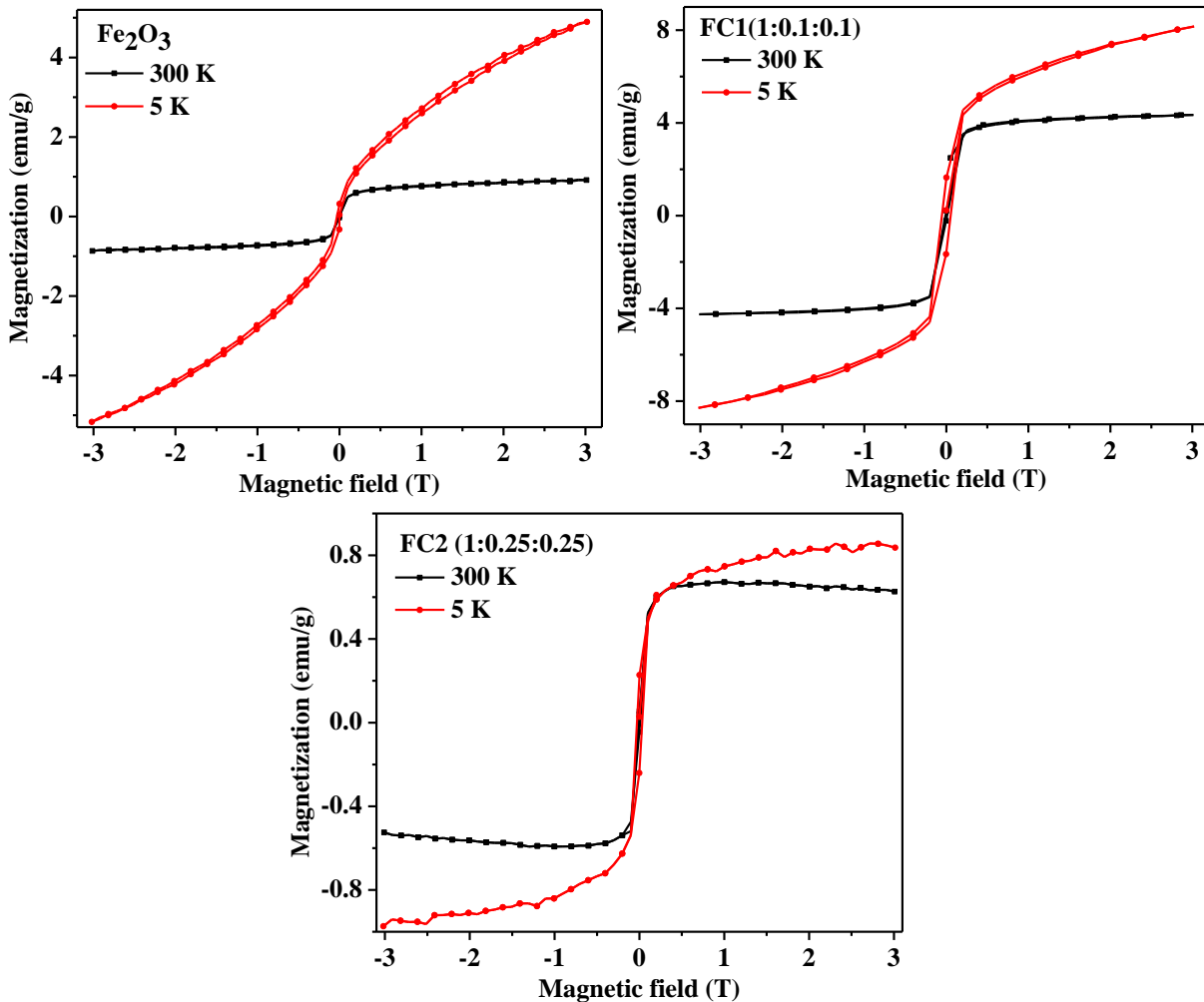


**Fig. 5.14:** Typical M-H curves for pure Fe$_2$O$_3$ nanoparticles and CdS-$\gamma$-Fe$_2$O$_3$ nanocomposites (FC1 and FC2) at 300 K and 5 K.

### 5.1.3.9 Surface area Analysis

The BET surface area values for the CdS-$\gamma$-Fe$_2$O$_3$ nanocomposites FC1, FC2, FC3, FC4, FC5 and FC6 are 29.8 m$^2$/g, 52 m$^2$/g, 59.8 m$^2$/g, 30.7 m$^2$/g, 66.1 m$^2$/g and 65.2 m$^2$/g, respectively. The CdS-$\gamma$-Fe$_2$O$_3$ nanocomposite FC5 possesses higher surface area than that of pure $\gamma$-Fe$_2$O$_3$ (51.1 m$^2$/g), CdS nanoparticles (58.9 m$^2$/g) and all the other nanocomposites.

### 5.1.3.10 Mechanism of formation of CdS-$\gamma$-Fe$_2$O$_3$ nanocomposites

CdS-$\gamma$-Fe$_2$O$_3$ nanocomposites were synthesized by a single step thermal decomposition method. Cadmium acetate, thiourea and iron acetylacetonate were mixed in specified ratios and refluxed at 200 $^o$C in diphenyl ether.

The formation of CdS nanoparticles follows the same reaction mechanism as discussed in the section on the synthesis of CdS-TiO$_2$ nanocomposites (Chapter 4, section 4.1.3.6). $\gamma$-Fe$_2$O$_3$ nanoparticles are formed by the thermal decomposition of iron(III) acetylacetonate along with by-products such as carbon monoxide, carbon dioxide, methane and water. The proposed reactions during the formation of CdS-$\gamma$-Fe$_2$O$_3$ nanocomposites are as follows [48–50]:

$$4(C_5H_7O_2)_3Fe + 17O_2 \rightarrow 2Fe_2O_3 + 30CO + 10CO_2 + 20CH_4 + 2H_2O$$

$$Cd(SC(NH_2)_2)_2(CH_3COO)_2 + Fe_2O_3 \rightarrow CdS - Fe_2O_3 + NH_3 + HCNS + CH_3COCH_3$$

$$+CH_2O + CO + H_2O$$
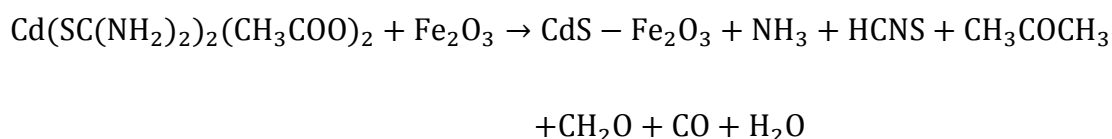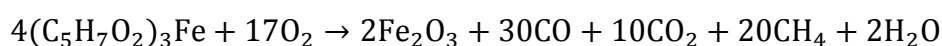
### 5.1.4 Conclusions

CdS-$\gamma$-Fe$_2$O$_3$ nanocomposites were successfully prepared by a simple and facile thermal decomposition approach. The nanocomposites were characterized using different analytical techniques. XRD results confirm the presence of CdS nanocrystals (1.2 to 2.9 nm) in the nanocomposites and TEM results indicate formation of agglomerated sphere-like particles in the nanocomposites. Diffuse reflectance spectral studies of CdS-$\gamma$-Fe$_2$O$_3$ nanocomposites indicate absorbance in the visible region (1.8 to 2.5 eV) and the nanocomposites show blue shift of band edge emission compared to pure CdS due to quantum size effect.

## 5.2 Synthesis of ZnO@γ-Fe₂O₃ Core-Shell Nanocomposites by a Thermal Decomposition Approach

### 5.2.1 Introduction

Nowadays, research efforts are being focused on the use of semiconductor photocatalysts for the degradation of toxic organic compounds discharged from different industries [51–53]. Among the various metal oxide semiconductor photocatalysts used for this purpose, ZnO has been of tremendous interest due to its high photosensitivity and wide band gap (3.2 eV) with major absorption in the UV range. ZnO possesses several advantages which include low cost, high quantum efficiency and high photocatalytic activity. There are two drawbacks associated with ZnO as the photocatalyst, namely, high charge recombination rate and low efficiency when utilized under solar light [54]. Various methods have been developed to reduce the recombination rate of photogenerated electrons and holes in ZnO and increase the utilization rate of visible light. Hybrid semiconductor nanostructures have been very promising for the removal of toxic organic pollutants from waste water [55]. The combination of semiconductors with small band gap with wide band gap semiconductors increases the probability of absorption of radiation in the visible range. $\gamma$-Fe$_2$O$_3$, a narrow band gap (1.9 to 2.2 eV) n-type semiconductor with absorption in the visible region, is a possible candidate which can act as a sensitizer under sunlight irradiation since it is able to transfer electrons to the conduction band of large band gap semiconductors such as ZnO. The enhanced photocatalytic efficiency is explained by fast transfer of photogenerated electrons and holes from $\gamma$-Fe$_2$O$_3$ to ZnO [56].

ZnO-Fe$_2$O$_3$ nanocomposites have been intensively investigated for a variety of applications such as waste water treatment, water splitting, sensors, magnetic materials, lithium ion batteries and solar cells [56–62]. ZnO-Fe$_2$O$_3$ heterostructured nanocomposites have been prepared by different methods (Fig. 5.15). Liu et al. have synthesized ZnO-Fe$_2$O$_3$ core-shell heterostructures using microwave irradiation followed by thermal decomposition method [56]. Hsu et al. have synthesized ZnO@Fe$_2$O$_3$ core-shell nanoparticles by a two-step hydrothermal and wet chemical method [57]. Guskos et al. have synthesized ZnO-Fe$_2$O$_3$ nanocomposites by a wet chemical method [59]. Reda, Maya-Treviño et al. and Hernandez et al. have synthesized ZnO-Fe$_2$O$_3$ nanocomposites by sol-gel method [61,63,64]. Yin et al. have synthesized $\alpha$-Fe$_2$O$_3$ decorated ZnO nanorods by acetone assisted impregnation deposition method [65]. Mirzaie et al. have synthesized ZnO-Fe$_2$O$_3$ nanocomposites by a solid state reaction [66]. Liu et al. have synthesized ZnO-Fe$_2$O$_3$ nanotube composites by photochemical deposition

under UV light [67]. Fu et al. have synthesized ZnO-$\gamma$-Fe$_2$O$_3$ nanocomposites by a solution route [68]. Si et al. have prepared ZnO-Fe$_2$O$_3$ core-shell nanorods by a solution phase hydrolysis method [69]. Balti et al. have synthesized Fe$_2$O$_3$ decorated ZnO nanorods by a polyol method [70]. Zhou et al. have synthesized Fe$_2$O$_3$-ZnO core-shell heterostructures by a solvothermal method [71]. Chu et al. have synthesized ZnO microrods coated with iron oxide nanoparticles by a low temperature hydrothermal method [72]. Mo et al. have synthesized ZnO/FeO$_x$ core-shell nanorods by thermal decomposition of Fe(acac)$_3$ at 265 $^o$C under nitrogen atmosphere [73]. Most of the methods reported so far involve multi-steps with reaction time of 3 to 4 h and require often special conditions such as an inert atmosphere. A brief summary on the synthesis of ZnO-$\gamma$-Fe$_2$O$_3$ nanocomposites by the above reported methods are given in Table 5.4. A brief discussion on some of the synthetic methods is given below.
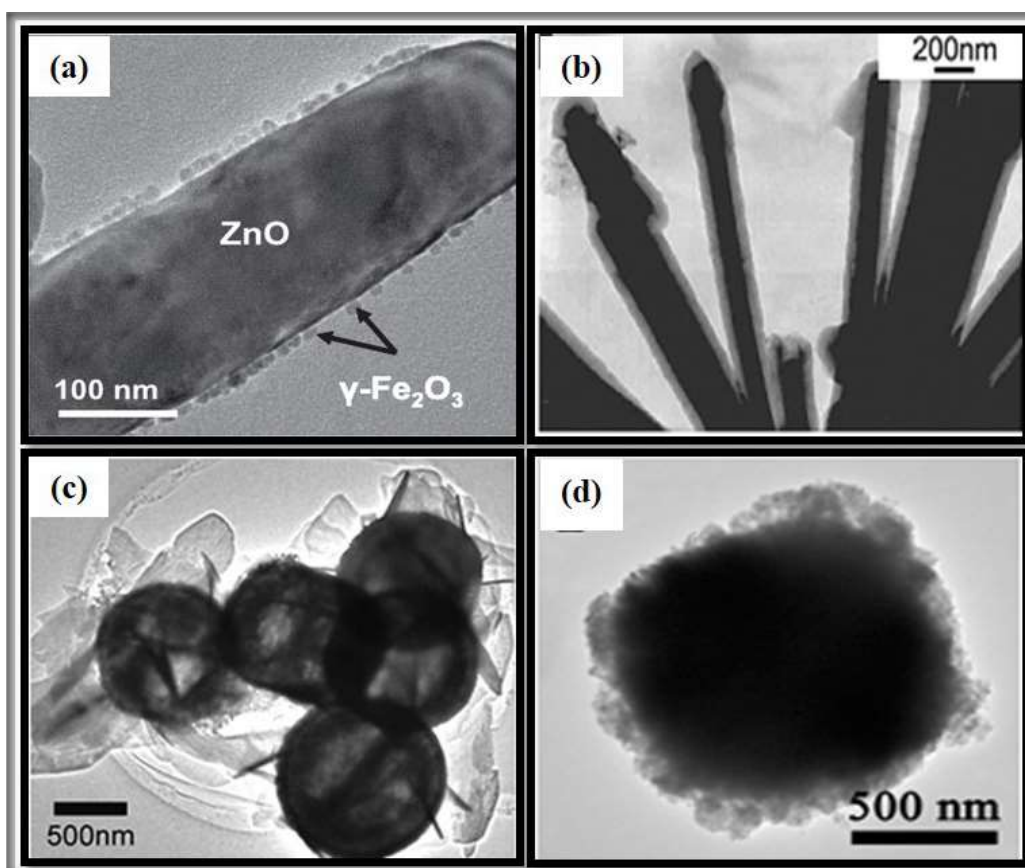


**Fig. 5.15:** ZnO-Fe$_2$O$_3$ nanocomposites with different morphologies: (a) ZnO nanorods decorated with $\gamma$-Fe$_2$O$_3$ nanoparticles [70], (b) ferric oxide deposited on ZnO nanorods [73], (c) $\gamma$-Fe$_2$O$_3$/ZnO nest-like hollow nanostructures [56] and (d) ZnO deposited $\alpha$-Fe$_2$O$_3$ hexahedrons [71].

**Table 5.4:** Different reported methods for the synthesis of $ZnO$-$Fe_2O_3$ nanocomposites.

| Sl. No. | Method | Chemicals used | Morphology of the product | Size | Reference |
|---|---|---|---|---|---|
| 1 | Microwave irradiation and thermal decomposition | Zinc acetate, ferric nitrate and thioacetamide | ZnO nanoflakes grown on the surface of $\gamma$-$Fe_2O_3$ hollow spheres | 1 $\mu$m | [56] |
| 2. | Hydrothermal synthesis and dip coating | Zinc acetate, zinc nitrate and ferric chloride | Core-shell | ZnO nanowires, diameter = 80 nm, $Fe_2O_3$ shell = 5 nm | [57] |
| 3. | Wet chemical method | Zinc nitrate and ferric nitrate | Nanopowder | 20 nm | [59] |
| 4. | Sol-gel | Zinc chloride and iron chloride | Nanopowder | 20 nm | [61] |
| 5. | Sol-gel | Zinc acetate dihydrate and iron acetylacetonate | Nanopowder | 23.8 nm | [63] |
| 6. | Hydrothermal and impregnation method | Zinc acetate and ferric nitrate | $\alpha$-$Fe_2O_3$ decorated ZnO nanorod | Shell = 300-500 nm | [65] |

| 7. | Solid state reaction | Zinc acetate and α-$Fe_2O_3$ | $Fe_2O_3$/ZnO nanorods and nanoflowers | $Fe_2O_3$ = 16 nm, ZnO = 16 nm | [66] |
|---|---|---|---|---|---|
| 8. | Hydrothermal and photochemical deposition | Zinc chloride and ferric chloride | ZnO nanorods decorated with $Fe_2O_3$ | ZnO nanorods diameter = 500 nm, length = 4 μm | [67] |
| 9. | Solution method | Zinc nitrate, ferric chloride and ferrous chloride | Spheres | 300-400 nm | [68] |
| 10. | Solution phase controlled hydrolysis method | Zinc acetate and ferric chloride | Core/shell nanorods | Width = 30-35 nm, length = 110-150 nm | [69] |
| 11. | Polyol method | Zinc acetate and iron acetate | ZnO nanorods decorated with γ-$Fe_2O_3$ | ZnO nanorods diameter = 80 nm, length = 200 nm, γ-$Fe_2O_3$ = 5 nm | [70] |

| 12. | Solvothermal method | Zinc acetate and ferric chloride | ZnO/α-Fe$_2$O$_3$ hexahedrons | ZnO = 15-20 nm | [71] |
|---|---|---|---|---|---|
| 13. | Hydrothermal synthesis | Zinc acetate dihydrate and ferrous chloride tetrahydrate | ZnO microrods decorated with γ-Fe$_2$O$_3$ | ZnO microrods diameter = 2 μm, length = 6 μm | [72] |
| 14. | Hydrothermal and thermal decomposition | Zinc nitrate and iron acetylacetonate | ZnO/FeO$_x$ core/shell nanorods | ZnO nanorods diameter = 150 nm, length = 5-6 μm | [73] |

*Microwave irradiation and thermal decomposition* [56]*:* Liu et al. have prepared nest-like γ-Fe$_2$O$_3$/ZnO double-shelled hollow structures, as shown in Scheme 5.3. Firstly, C/FeS$_x$ is prepared by microwave irradiation. In this method, specific amount of ferric nitrate is dissolved in a solvent (ethanol and water). Then, specified amount of carbon spheres (obtained by hydrothermal method) are added to the above solution and kept at 60 °C for 12 h. The product obtained is washed with water and ethanol and dried at 80 °C for 4 h. The above-obtained solid product and thioacetamide are refluxed in a microwave at 400 W for 30 min, which results in the formation of carbon/FeS$_x$ core–shell composite spheres. In the second step, specified amount of C/FeS$_x$ spheres and zinc acetate are dispersed in diethylene glycol and refluxed at 170 °C for 1 h to get C/FeS$_x$/ZnO spheres. The as prepared product is finally calcined at 500 °C for 2 h to get γ-Fe$_2$O$_3$/ZnO nest-like double-shelled hollow nanostructures.
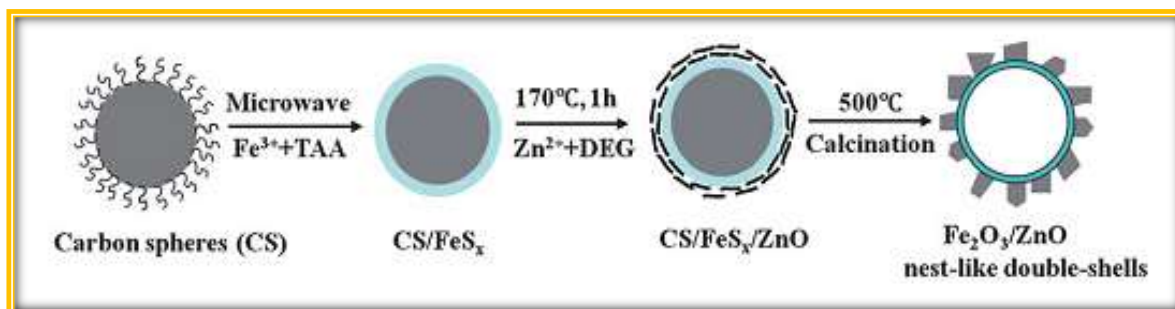
**Scheme 5.3:** Schematic illustration of the formation of γ-Fe$_2$O$_3$/ZnO nest-like double-shelled hollow nanostructures [56].

*Sol-gel* [63]*:* Trevino et al. have prepared ZnO-Fe$_2$O$_3$ nanocomposite by sol-gel method. In this method, specific proportions of zinc acetate and iron acetylacetonate are dissolved in water and isopropyl alcohol, respectively. The solutions are mixed together and concentrated NH$_4$OH is added with continuous stirring. The pH of the solution is adjusted to 7 and the reaction mixture is kept at room temperature until a gel is formed. The gel is aged for 3 days and then dried in water bath at 45 °C. Finally, the product is calcined at 450 °C for 4 h.

*Polyol method* [70]*:* Balti et al. have prepared rod-like ZnO decorated with γ-Fe$_2$O$_3$ nanoparticles by a two-step polyol method. In this method, specific proportions of zinc acetate dihydrate, sodium acetate trihydrate and water are dissolved in diethylene glycol (DEG). The resulting mixture is heated at 245 °C for 4 h and then the mixture is cooled to room temperature to obtain a white homogeneous suspension. To the above suspension, a solution of iron acetate in DEG is injected and the mixture is heated at 245 °C for 4 h. The dark brown precipitate obtained is washed in ethanol and acetone and then dried in vacuum at 50 °C.

*Solvothermal method* [71]*:* Zhou et al. have prepared ZnO/α-Fe$_2$O$_3$ hexahedron composites by a two-step solvothermal method. In the first step, specific amount of iron chloride hexahydrate is dissolved in a mixture of ethanol and deionized water under vigorous magnetic stirring. Subsequently, hexamethylenetetramine is added to the above solution. The resulting solution is transferred to an autoclave and maintained at 160 °C to 6 h. The product is naturally cooled to room temperature, washed with ethanol and water, and finally dried at 80 °C for 12 h. In the second step, specific amount of zinc acetate and pre-synthesized α-Fe$_2$O$_3$ hexahedrons are added in ethylene glycol with vigorous stirring for 30 min. The resulting solution is then transferred to an autoclave which is kept at 180 °C for 12 h. The product obtained is naturally cooled to room temperature, washed with ethanol and water, and finally dried at 80 °C for 12 h.

*Hydrothermal method* [72]*:* Chu et al. have prepared ZnO microrods coated with $Fe_3O_4$ and $Fe_2O_3$ nanoparticles by a two-step hydrothermal method. In the first step, specified amount of zinc acetate dihydrate is mixed with aqueous hexamethylenetetramine (HMT) with magnetic stirring. The mixture is then transferred to the autoclave and is hydrothermally treated for 5 h at 90 °C. The white solid product obtained is washed with distilled water and dried under vacuum at 40 °C. In the second step, an aqueous solution of ferrous chloride is added in equal volume of ZnO suspension either containing HMT or not. Then, the mixture is transferred to the autoclave and kept at 90 °C for 5 h. The product obtained is washed with deionized water and dried under vacuum. When HMT is used in the second step of reaction, the product formed is $ZnO/Fe_3O_4$ nanocomposite and when HMT is not used in the reaction, the product formed is $ZnO/Fe_2O_3$ (Scheme 5.4).
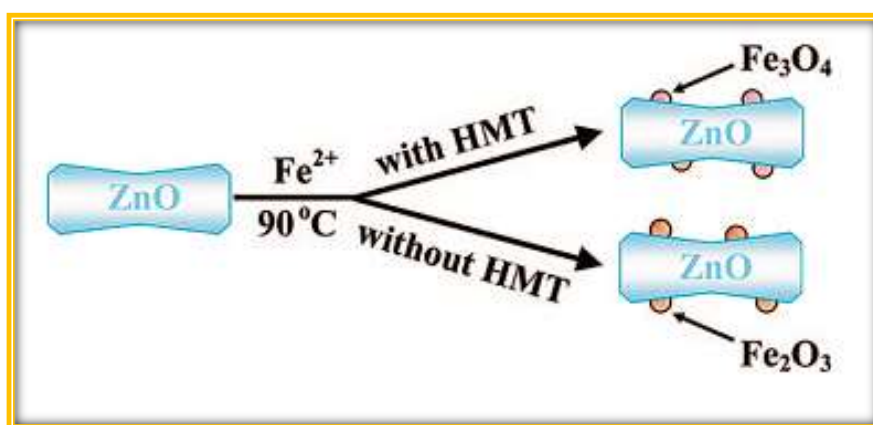


**Scheme 5.4:** Schematic representation of the growth mechanism of the ZnO/iron oxide heterostructured composites [72].

*Hydrothermal and thermal decomposition* [73]: Mo et al. have prepared $ZnO/FeO_x$ core/shell nanorods by a two-step method. Firstly, ZnO nanorods are prepared by hydrothermal method. In the second step, specific amount of ZnO nanorods and iron acetylacetonate are added in phenyl ether and refluxed at 265 °C under the flow of nitrogen. The dark brown precipitate obtained is washed with cyclohexane and ethanol. The product obtained is annealed at different temperatures to get $ZnO/FeO_x$ core-shell nanocomposites.

In the present study, $ZnO@\gamma-Fe_2O_3$ core-shell nanocomposites have been prepared by a novel two-step thermal decomposition method. ZnO nanorods with diameter $40.1 \pm 7$ nm and length $1.1 \pm 0.1$ μm were prepared by heating zinc acetate dihydrate at 300 °C for 3 h in air. Uniform layer of $\gamma-Fe_2O_3$ was deposited by the thermal decomposition of $Fe(acac)_3$ in diphenyl ether at 200 °C in the presence of ZnO nanorods.

### 5.2.2 Experimental Details

### Chemicals

The chemicals used were zinc acetate dihydrate (RANKEM), iron acetylacetonate (Fe(acac)$_3$) (ACROS), diphenyl ether (Aldrich) and methanol (Rankem). All the chemicals were used as received.

### Synthesis

The ZnO@γ-Fe$_2$O$_3$ nanocomposites were prepared via a two-step method: The first step was the preparation of ZnO nanorods by solid state thermal decomposition [74]. 2.0 g of zinc acetate dihydrate was crushed with the help of a pestle and mortar and was heated in a muffle furnace at 300 ºC for 3 h in air at a heating rate of 2 ºC/min. Then, the synthesis of ZnO@γ-Fe$_2$O$_3$ core-shell nanocomposites by the thermal decomposition of Fe(acac)$_3$ in diphenyl ether at 200 °C was carried out in the presence of ZnO nanorods (Scheme 5.5). Four different core-shell nanocomposites (ZF1, ZF2, ZF3 and ZF4) were prepared by varying the concentration of Fe(acac)$_3$ (Table 5.5). The reagents were added to 10 mL of diphenyl ether (boiling point = 257 ºC) in a round bottom flask and refluxed in air at about 200 ºC for 35 min. The precipitates obtained were centrifuged, washed with methanol and dried overnight under vacuum to obtain the ZnO@γ-Fe$_2$O$_3$ core-shell nanocomposites. For comparison, pure γ-Fe$_2$O$_3$ nanoparticles were also synthesized using the same method.

```
┌─────────────────┐      ┌─────────────────┐      ┌─────────────────┐
│                 │  ┌┐  │      Iron       │  ┌┐  │  Diphenyl ether │
│  ZnO nanorods   │  ╬   │ acetylacetonate │  ╬   │     (10 mL)     │
│                 │      │                 │      │                 │
└─────────────────┘      └─────────────────┘      └─────────────────┘
                                  │
                                  ▼  Refluxed at 200 °C, 35 min
                         ┌─────────────────┐
                         │     Slurry      │
                         └─────────────────┘
                                  │     i)   Allowed to cool
                                  ▼     ii)  Precipitation with methanol
                         ┌─────────────────┐
                         │   Dark brown    │
                         │   Precipitate   │
                         └─────────────────┘
                                  │
                                  ▼  Dried under vacuum
                         ┌─────────────────┐
                         │  ZnO@γ-Fe₂O₃    │
                         │  nanocomposites │
                         └─────────────────┘
```
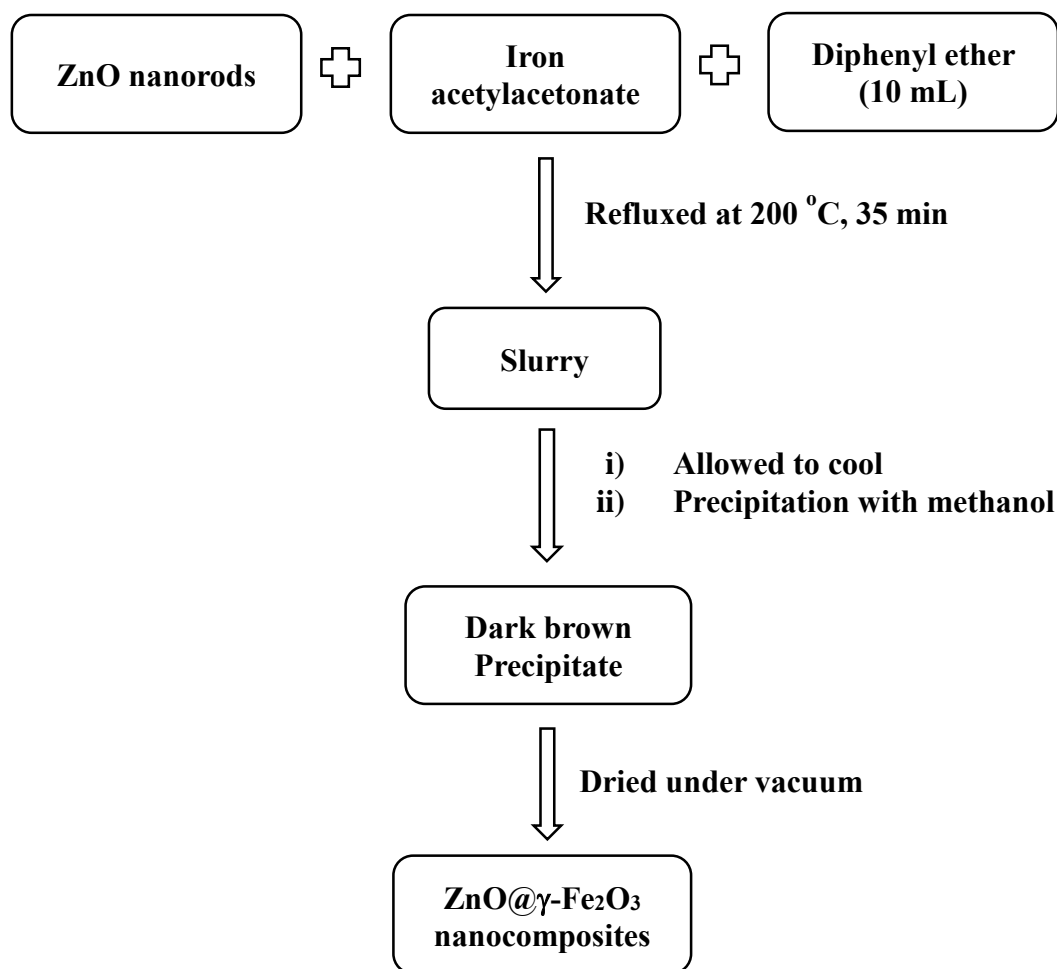
**Scheme 5.5:** Synthesis of ZnO@$\gamma$-Fe$_2$O$_3$ nanocomposites by thermal decomposition approach.

**Table 5.5:** Designation of various ZnO@$\gamma$-Fe$_2$O$_3$ nanocomposites prepared using different molar ratios of Fe(acac)$_3$ and ZnO.

| Sample code | ZnO (mmol) | Fe(acac)$_3$ (mmol) |
|:---:|:---:|:---:|
| Fe$_2$O$_3$ | - | 1 |
| ZF1 | 1 | 0.25 |
| ZF2 | 1 | 0.5 |
| ZF3 | 1 | 0.75 |
| ZF4 | 1 | 1 |

### 5.2.3 Results and Discussion

### 5.2.3.1 XRD Results

The XRD patterns of pure iron oxide nanoparticles, ZnO nanorods and ZnO@$\gamma$-Fe$_2$O$_3$ core-shell nanocomposites (ZF1, ZF2, ZF3 and ZF4) are shown in Fig 5.16. The XRD patterns of pure ZnO and all the nanocomposites show peaks at 31.7°, 34.2°, 36.1°, 47.6°, 56.5°, 62.7°, 66.3°, 67.7°, 72.5°, 76.9° and 81.50° corresponding to (100), (002), (101), (102), (110), (103), (200), (112), (201), (004), (202), (104) planes of wurtzite ZnO (JCPDS no. 80-0075). In the XRD patterns of the nanocomposites as well as that of pure iron oxide nanoparticles, reflections due to iron oxide are not observed. This is attributed to the presence of very small nanocrystals of iron oxide that are not detectable by X-ray diffraction. The proof for the presence of $\gamma$-Fe$_2$O$_3$ comes from SAED, and magnetic measurements (discussed latter). The mean crystallite size of pure ZnO and ZnO in the core-shell nanocomposites was estimated using the Scherrer equation [69]. The crystallite size of pure ZnO is 9.8 nm and the crystallite size of ZnO in the nanocomposites varies from 20.6 nm to 27.7 nm.
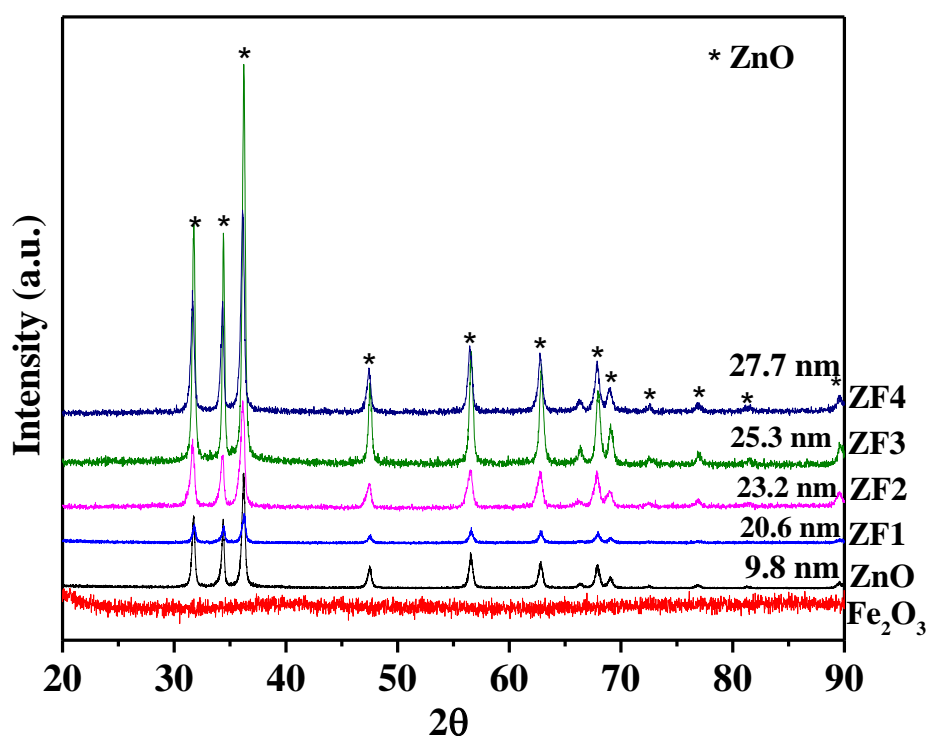


**Fig. 5.16:** XRD patterns of ZnO, $\gamma$-Fe$_2$O$_3$ and the ZnO@$\gamma$-Fe$_2$O$_3$ core-shell nanocomposites (ZF1-ZF4).

To identify the phase of iron oxide nanoparticles prepared by the thermal decomposition method, $Fe_3O_4$ nanoparticles were prepared for comparison using a reported method [75]. $Fe^{2+}$ and $Fe^{3+}$ salts (ferrous sulfate and ferric nitrate) were mixed in distilled water in appropriate proportions and co-precipitated with the help of aqueous ammonia at 70 °C. The XRD patterns of as prepared iron oxide prepared by the thermal decomposition method and the $Fe_3O_4$ nanoparticles are shown in Fig.5.17. The XRD pattern of as prepared iron oxide shows a single peak at 35.6° attributed to (311) reflection of $\gamma$-$Fe_2O_3$ (JCPDS No. 39-1346). The XRD pattern of $Fe_3O_4$ nanoparticles show peaks at 35.5°, 63.1° and 84.6° corresponding to (311), (440) and (642) planes of $Fe_3O_4$ (JCPDS no. 85-1436). It is difficult to distinguish $\gamma$-$Fe_2O_3$ and $Fe_3O_4$ from the XRD patterns. The as prepared iron oxide nanoparticles and $Fe_3O_4$ nanoparticles were calcined at 400 °C. The XRD pattern of as prepared iron oxide calcined at 400 °C shows peaks at 33.1°, 35.4°, 40.7°, 43.3°, 49.5°, 54.1°, 62.4° and 64.1° corresponding to (121), (110), (120), (020), (220), (132), (130) and (211) planes of $\alpha$-$Fe_2O_3$ (JCPDS No. 85-0987). The XRD pattern of $Fe_3O_4$ nanoparticles calcined at 400 °C show peaks at 35.6° and 63.8° corresponding to (311) and (440) planes of $\gamma$-$Fe_2O_3$ (Fig. 5.17); when $\gamma$-$Fe_2O_3$ is heated at 400 °C in air, it transforms to $\alpha$-$Fe_2O_3$ and when $Fe_3O_4$ is heated at 400 °C in air it transforms to $\gamma$-$Fe_2O_3$ [75–77]. Based on the XRD results after calcination, the as prepared iron oxide nanoparticles are proposed to be $\gamma$-$Fe_2O_3$ which on calcination transforms to $\alpha$-$Fe_2O_3$.
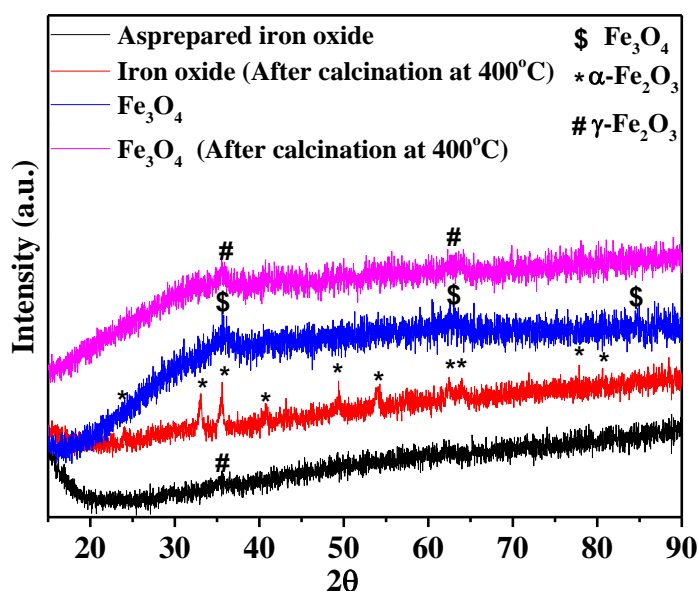


**Fig. 5.17:** XRD patterns of as prepared iron oxide and after calcination at 400 °C. The XRD patterns of as prepared $Fe_3O_4$ nanoparticles and after calcination at 400 °C are also shown.

### 5.2.3.2 FT-IR Results

The IR spectra of pure ZnO nanorods, $\gamma$-Fe$_2$O$_3$ nanoparticles (prepared by thermal decomposition method) and ZnO@$\gamma$-Fe$_2$O$_3$ core-shell nanocomposites were recorded (Fig. 5.18). Two broad bands at 3434 cm$^{-1}$ and 1600 cm$^{-1}$ are attributed to O–H stretching and bending, respectively due to adsorbed water molecules. The IR bands near 2920 cm$^{-1}$ and 2840 cm$^{-1}$ are due to C–H stretching and are attributed to the presence of organic molecules adsorbed on the surface of the ZnO@$\gamma$-Fe$_2$O$_3$ core-shell nanocomposites [64]. The band at 1432 cm$^{-1}$ is attributed to the stretching vibration of the COO$^-$ group [37]. The band at 1096 cm$^{-1}$ is due to C–O–C bond [36]. These bands suggest the presence of organic content adsorbed on the surface of the nanocomposites [36,37]. The bands at 553 cm$^{-1}$ and 453 cm$^{-1}$ are attributed to characteristic absorption of $\gamma$-Fe$_2$O$_3$ and the band at 444 cm$^{-1}$ is attributed to ZnO [78,79].
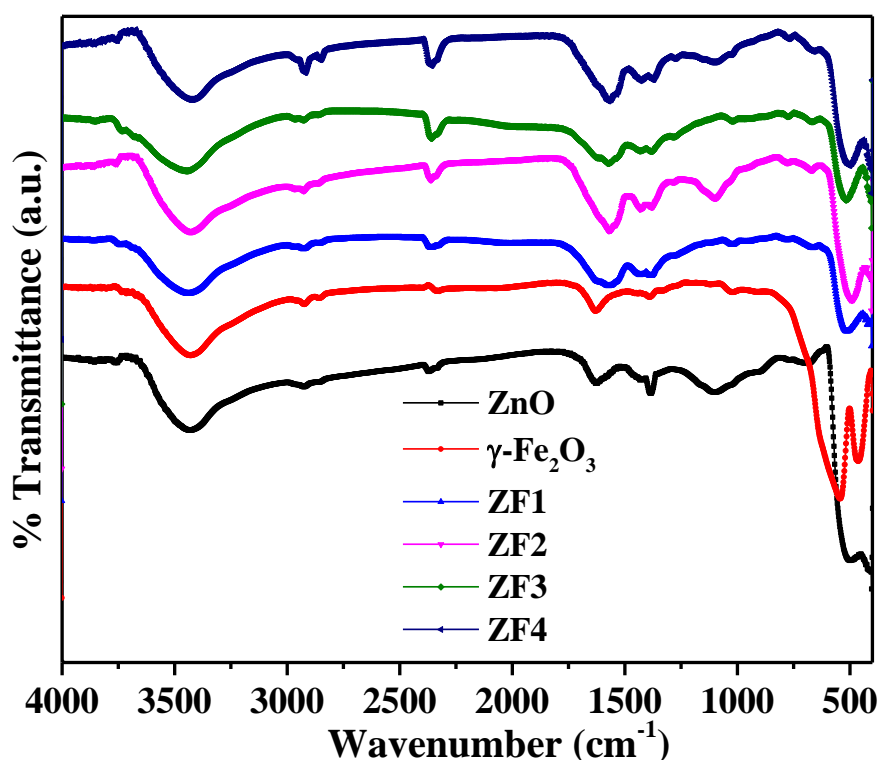


**Fig. 5.18:** FT-IR spectra for pure ZnO, $\gamma$-Fe$_2$O$_3$ (prepared by thermal decomposition method) and the ZnO@$\gamma$-Fe$_2$O$_3$ core-shell nanocomposites (ZF1-ZF4).

Fig. 5.19 shows the FT-IR spectra for as prepared iron oxide nanoparticles prepared by thermal decomposition, as prepared iron oxide nanoparticles calcined at 400 °C and as prepared $Fe_3O_4$ nanoparticles. The as prepared $Fe_2O_3$ nanoparticles show IR bands at 453 cm$^{-1}$ and 553 cm$^{-1}$ attributed to Fe-O bond of γ-$Fe_2O_3$ [78,80]. The iron oxide nanoparticles (prepared by thermal decomposition method) calcined at 400 °C show IR bands at 480 cm$^{-1}$ and 549 cm$^{-1}$ which are attributed to Fe-O bond of α-$Fe_2O_3$ [20,44,81]. $Fe_3O_4$ nanoparticles show characteristic IR bands at 426 cm$^{-1}$ and 580 cm$^{-1}$ [82,83]. The IR spectra of as prepared iron oxide nanoparticles and iron oxide nanoparticles calcined at 400 °C show IR bands at 1390 cm$^{-1}$ and 1031 cm$^{-1}$ attributed to the stretching vibration of COO$^-$ and C–O–C, respectively [36,37]. These bands are due to the presence of organic molecules adsorbed on the surface of iron oxide nanoparticles.
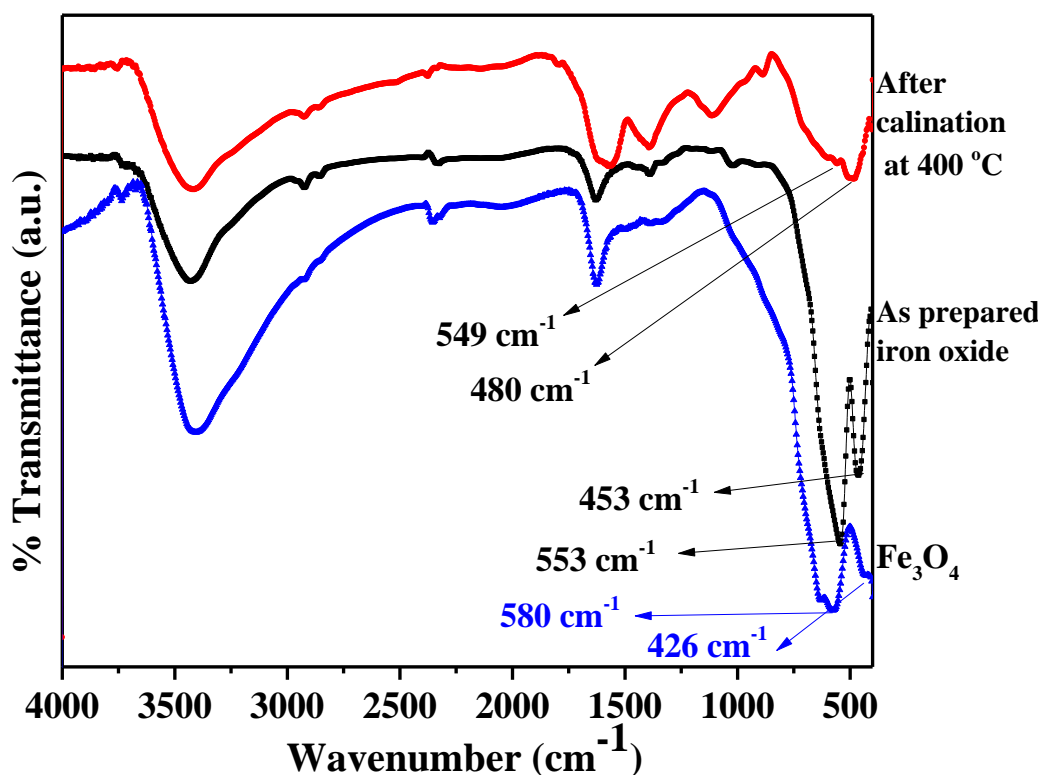


**Fig. 5.19:** FT-IR spectra of iron oxide nanoparticles prepared by thermal decomposition method (as prepared and after calcination at 400 °C). The IR spectrum for $Fe_3O_4$ nanoparticles is also shown.

### 5.2.3.3 FE-SEM and EDXA Results

FE-SEM and TEM measurements were performed to investigate the morphology and size of ZnO, $\gamma$-$Fe_2O_3$ and the ZnO@$\gamma$-$Fe_2O_3$ core-shell nanocomposites. Fig. 5.20 shows the FE-SEM images of pure ZnO, $\gamma$-$Fe_2O_3$ nanoparticles and the ZnO@$\gamma$-$Fe_2O_3$ core-shell nanocomposites (ZF1-ZF4). Pure ZnO exhibits nanorods and $\gamma$-$Fe_2O_3$ shows small agglomerated nanoparticles. After the deposition of $\gamma$-$Fe_2O_3$, the shape of ZnO is retained but the surface of ZnO nanorods is not smooth. Nanocomposites ZF1 and ZF2 show uniform shell formation of $\gamma$-$Fe_2O_3$ over the ZnO nanorods. Nanocomposites ZF3 and ZF4 show non-uniform shell formation of $\gamma$-$Fe_2O_3$ over the ZnO nanorods. Aggregation of $\gamma$-$Fe_2O_3$ nanoparticles increases as one increases the amount of Fe(acac)$_3$ used during the synthesis of the core-shell nanocomposites (ZF1 to ZF4).
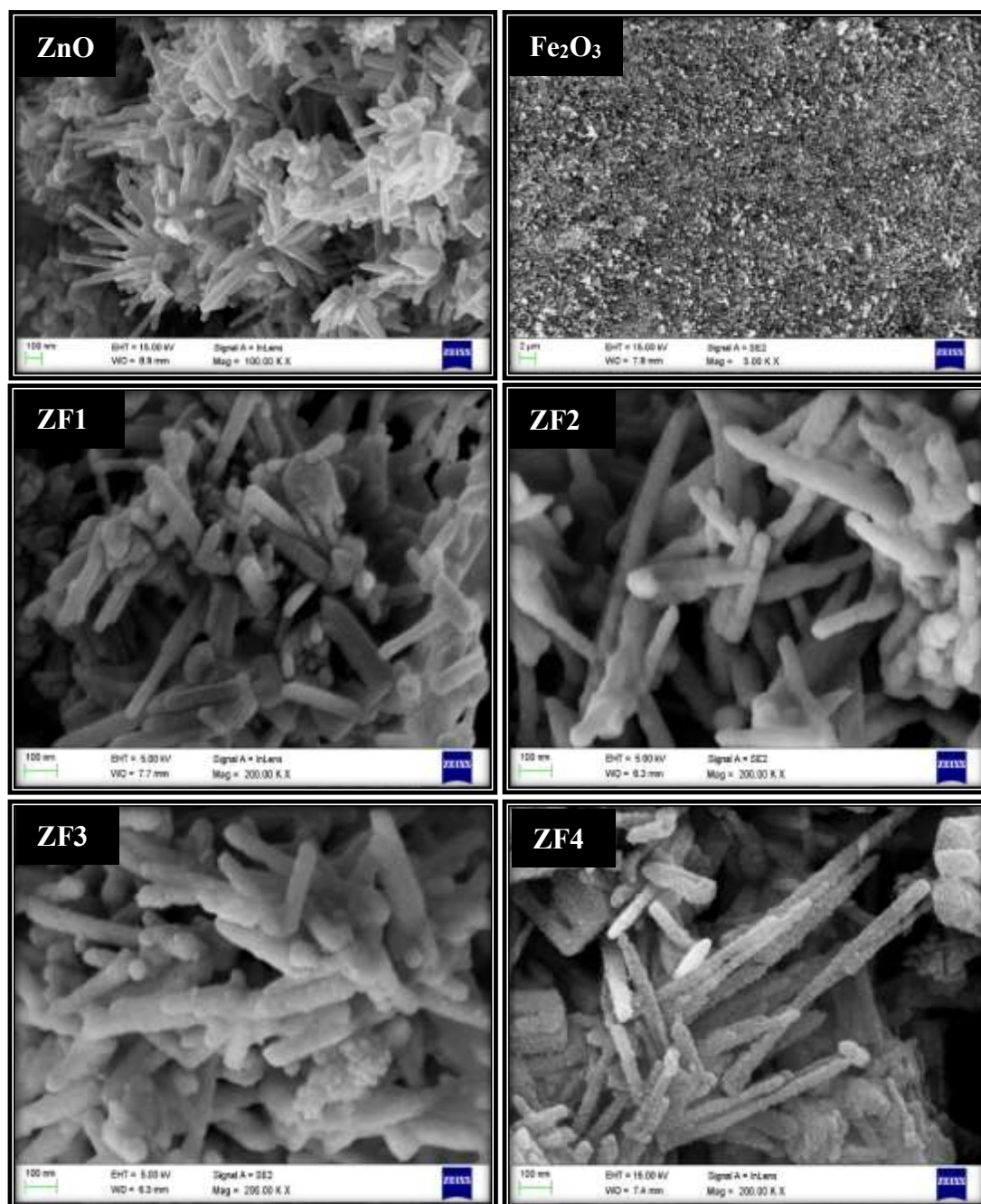
**Fig. 5.20:** FE-SEM images of ZnO nanorods, $\gamma$-$Fe_2O_3$ nanoparticles and the ZnO@$\gamma$-$Fe_2O_3$ core-shell nanocomposites (ZF1, ZF2, ZF3 and ZF4).

Fig. 5.21 shows the EDXA patterns of ZnO@$\gamma$-$Fe_2O_3$ nanocomposites ZF1, ZF2, ZF3 and ZF4. The EDX analysis shows the presence of oxygen, iron and zinc in all the ZnO@$\gamma$-$Fe_2O_3$ nanocomposites.
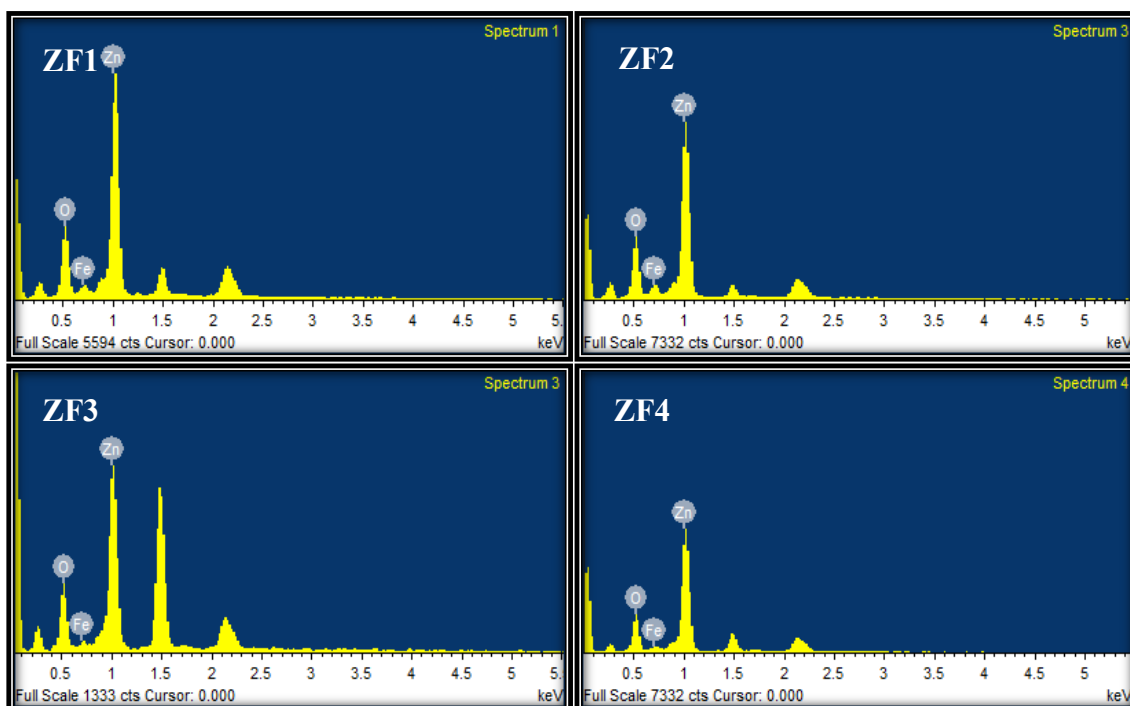
**Fig. 5.21:** EDXA patterns of ZnO@$\gamma$-Fe$_2$O$_3$ core-shell nanocomposites (ZF1-ZF4).

Table 5.6 shows the EDX analysis results on the ZnO@$\gamma$-Fe$_2$O$_3$ core-shell nanocomposites. The nanocomposites ZF1, ZF2 and ZF4 show uniform elemental distribution as compared to nanocomposite ZF3.

**Table 5.6:** EDX analysis data for the ZnO@$\gamma$-Fe$_2$O$_3$ core-shell nanocomposites. The analysis was done at three different spots.

| Nanocomposite | Zn | | Fe | | O | | Comment |
|---|---|---|---|---|---|---|---|
| | Wt% | At% | Wt% | At% | Wt% | At% | |
| ZF1 | 70.3 | 40.2 | 2.6 | 2.7 | 20.8 | 56.1 | Uniform |
| | 71.2 | 40.8 | 2.5 | 2.6 | 20.5 | 50.5 | |
| | 70.8 | 40.4 | 2.2 | 2.9 | 21.1 | 58.7 | |
| ZF2 | 71.9 | 41.2 | 3.8 | 3.6 | 23.2 | 54.8 | Uniform |
| | 71.4 | 41.9 | 3.4 | 3.9 | 23.3 | 55.1 | |
| | 71.8 | 40.8 | 3.5 | 3.7 | 23.6 | 55.5 | |

| | | | | | | | |
|---|---|---|---|---|---|---|---|
| | 78.4 | 55.1 | 3.9 | 3.9 | 14.6 | 40.9 | |
| ZF3 | 80.8 | 56.3 | 5.0 | 3.9 | 16.2 | 43.8 | Non-uniform |
| | 81.6 | 57.1 | 4.7 | 3.9 | 13.6 | 38.9 | |
| | 78.8 | 51.5 | 4.3 | 3.3 | 16.9 | 45.2 | |
| ZF4 | 78.8 | 50.2 | 4.8 | 3.1 | 18.3 | 47.6 | Uniform |
| | 79.7 | 52.3 | 4.5 | 2.9 | 16.8 | 45.0 | |

### 5.2.3.4 TEM and SAED Results

Fig. 5.22 shows the TEM images and high resolution TEM images (HRTEM) images of ZnO and $\gamma$-$Fe_2O_3$ nanoparticles. ZnO nanorods (Fig. 5.22(a)) are $1.1 \pm 0.1$ $\mu$m in length and $40.1 \pm 7$ nm in width. The SAED pattern of ZnO (inset of Fig. 5.22(a)) shows spots attributed to (101), (103), (202), (004) and (002) planes of wurtzite ZnO (JCPDS no. 80-0075). Fig. 5.22(b) shows well dispersed $Fe_2O_3$ nanoparticles ($2.1 \pm 0.3$ nm) and the SAED pattern (Inset of Fig. 5.22(b)) shows rings attributed to (311), (421) and (440) planes of $\gamma$-$Fe_2O_3$ (JCPDS no. 39-1346). The HRTEM images of pure ZnO nanorod (Fig. 5. 22(c)) and pure $\gamma$-$Fe_2O_3$ nanoparticles (Fig. 5.22(d)) exhibit interplanar spacing of 0.24 nm and 0.48 nm which are attributed to (101) plane of ZnO and (111) plane of $\gamma$-$Fe_2O_3$, respectively.
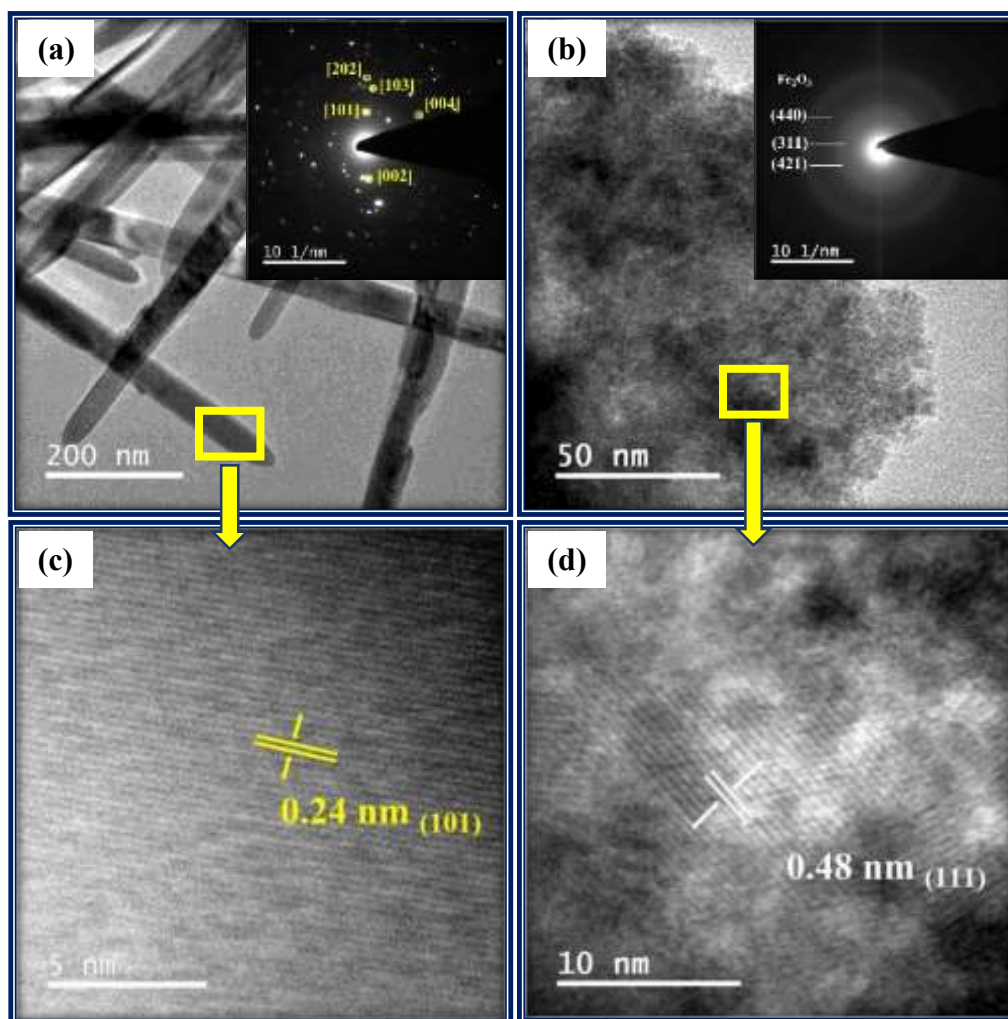
**Fig. 5.22:** TEM images of (a) ZnO nanorods, (b) $\gamma$-$Fe_2O_3$ nanoparticles, (c) HRTEM image of ZnO nanorods and (d) HRTEM image of $\gamma$-$Fe_2O_3$ nanoparticles.

The TEM and HRTEM images of ZnO@$\gamma$-$Fe_2O_3$ core-shell nanocomposites ZF1 and ZF2 are shown in Fig. 5.23. The core-shell nanocomposites ZF1 (Fig. 5.23(a)) and ZF2 (Fig. 5.23(c)) show formation of uniform shell of $\gamma$-$Fe_2O_3$ on the surface of ZnO nanorods. The inset of Fig. 5.23(a) shows the TEM image of single nanorod of core-shell nanocomposite ZF1 coated uniformly with a shell of $\gamma$-$Fe_2O_3$ ($\sim$15 nm). The HRTEM image of nanocomposite ZF1 (Fig. 5.23(b)) shows interplanar spacing values of 0.24 nm and 0.48 nm for the core and shell regions corresponding to ZnO (101) and $\gamma$-$Fe_2O_3$ (111) planes, respectively. This indicates that the $\gamma$-$Fe_2O_3$ shell with (111) plane is deposited on crystalline ZnO nanorod core with (101) plane. The inset of Fig. 5.23(c) shows the TEM image of single nanorod of core-shell nanocomposite ZF2 coated uniformly with a shell of $\gamma$-$Fe_2O_3$ ($\sim$20 nm). The HRTEM image of core-shell nanocomposite ZF2 (Fig. 5.23(d)) exhibits 0.24 nm interplanar spacing attributed to (101) plane of ZnO.
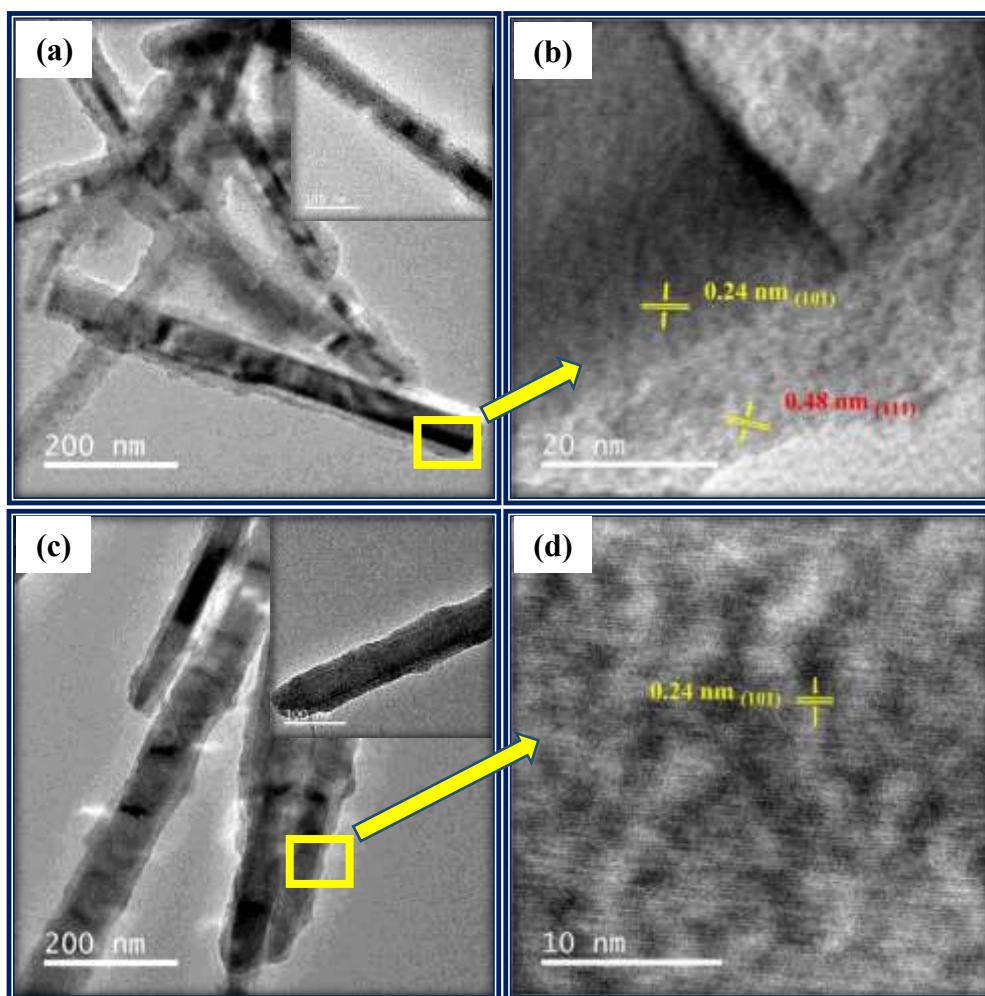
**Fig. 5.23:** TEM and HRTEM images of ZnO@γ-Fe$_2$O$_3$ core-shell nanocomposites ZF1 (a) and (b), and ZF2 (c) and (d).

Fig. 5.24 shows the TEM and HRTEM images of ZnO@γ-Fe$_2$O$_3$ core-shell nanocomposites ZF3 and ZF4. The core-shell nanocomposites ZF3 (Fig. 5.24(a)) and ZF4 (Fig. 5.24(c)) show formation of γ-Fe$_2$O$_3$ shell on the ZnO nanorods. The insets of Fig. 5.24(a) and 5.24(c) show the TEM images of single nanorods of core-shell nanocomposites ZF3 and ZF4 coated with a γ-Fe$_2$O$_3$ shell of thickness 10 and 15 nm, respectively. The HRTEM image of core-shell nanocomposite ZF3 (Fig. 5.24(c)) exhibits 0.24 nm interplanar spacing attributed to (101) plane of ZnO and the HRTEM image of core-shell nanocomposite ZF4 (Fig. 5.24(d)) exhibits interplanar spacing values of 0.24 nm and 0.48 nm for the core and shell regions corresponding to ZnO (101) and γ-Fe$_2$O$_3$ (111) planes, respectively. This indicates that the γ-Fe$_2$O$_3$ shell with (111) plane is deposited on crystalline ZnO nanorod core with (101) plane.

**Fig. 5.24:** TEM and HRTEM images of ZnO@$\gamma$-Fe$_2$O$_3$ core-shell nanocomposites; ZF3 (a) and (b), and ZF4 (c) and (d).

The SAED patterns of core-shell nanocomposites ZF1, ZF2, ZF3 and ZF4 are shown in Fig. 5.25. The SAED pattern of nanocomposite ZF1 (Fig. 5.25(a)) shows spots which are attributed to (101), (102), (200), (002), (004) planes of hexagonal ZnO and rings due to (311), (440) and (310) planes of $\gamma$-Fe$_2$O$_3$. The SAED pattern of nanocomposite ZF2 (Fig. 5.25(b)) shows spots which are attributed to (101), (102), (103), (002), (004), (104) planes of hexagonal ZnO and rings due to (311), (440), (310) planes of $\gamma$-Fe$_2$O$_3$. The SAED pattern of nanocomposite ZF3 (Fig. 5.25(c)) shows spots which are attributed to (101), (102), (103), (002), (004) planes of hexagonal ZnO and rings due to (311) and (440) planes of $\gamma$-Fe$_2$O$_3$. The SAED pattern of nanocomposite ZF4 (Fig. 5.25(d)) shows spots which are attributed to (101), (110), (103), (201), (202) planes of hexagonal ZnO and rings due to (311), (440), (321) planes of $\gamma$-Fe$_2$O$_3$.
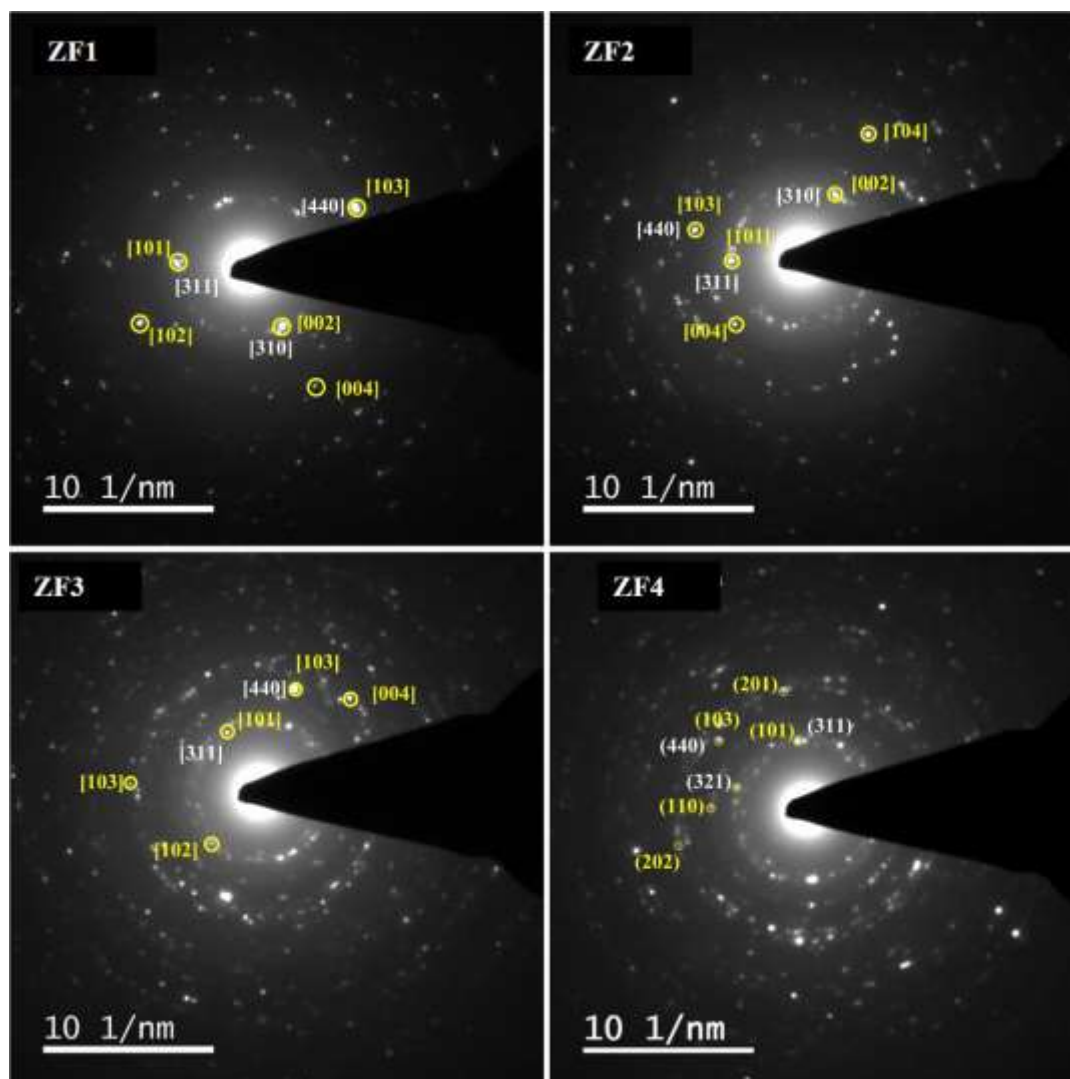
**Fig. 5.25:** SAED patterns of ZnO@$\gamma$-Fe$_2$O$_3$ core-shell nanocomposites (ZF1-ZF4).

### 5.2.3.5 DRS Results

Diffuse reflectance spectra of pure ZnO nanorods, $\gamma$-Fe$_2$O$_3$ nanoparticles and the ZnO@$\gamma$-Fe$_2$O$_3$ core-shell nanocomposites (ZF1, ZF2, ZF3 and ZF4) are shown in Fig. 5.26. ZnO shows absorption in the UV region at around 385 nm. Pure $\gamma$-Fe$_2$O$_3$ nanoparticles show absorption at around 653 nm. The ZnO@$\gamma$-Fe$_2$O$_3$ core-shell nanocomposites reveal an extended optical absorption in the visible region. One can observe two absorption bands in the diffuse reflectance spectra of ZnO@$\gamma$-Fe$_2$O$_3$ core-shell nanocomposites. The first one is observed at low energy in the visible region (between 550 and 655 nm) which is due to the absorption of $\gamma$-Fe$_2$O$_3$. The second absorption band (at about 380 nm) is attributed to the absorption of ZnO.
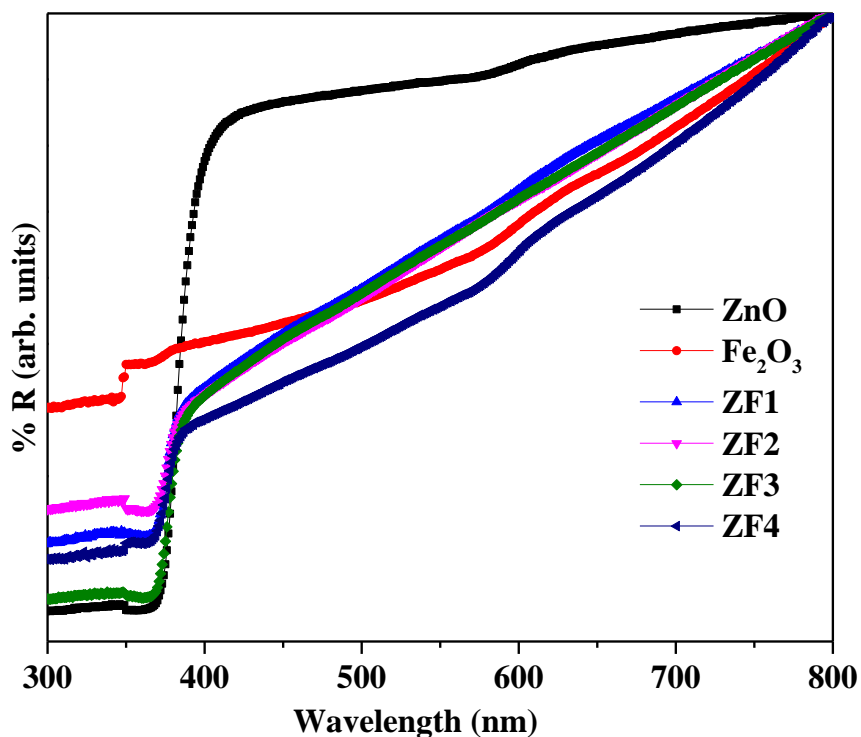
**Fig. 5.26:** Diffuse reflectance spectra of ZnO nanorods, γ-Fe₂O₃ nanoparticles and the ZnO@γ-Fe₂O₃ core-shell nanocomposites (ZF1-ZF4).

The absorption of ZnO@γ-Fe₂O₃ core–shell nanocomposites in the visible region increases with an increase in the concentration of precursor for γ-Fe₂O₃ (i.e. Fe(acac)₃) used during the synthesis of the nanocomposites. The band gap of ZnO nanorods, γ-Fe₂O₃ nanoparticles and ZnO@γ-Fe₂O₃ core-shell nanocomposites was estimated by plotting $(\alpha h\nu)^2$ vs. $h\nu$ (Tauc plots) using the relation [9]:

$$\alpha h\nu = A\big(h\nu - E_g\big)^{1/2}$$

Where $\alpha$ is the absorption coefficient, $h\nu$ is the photon energy, $E_g$ the optical band gap energy and A is a constant. From the Tauc plots (Fig. 5.27), $E_g$ was estimated by extrapolating a straight line from the linear portion of the absorption curve to the X-axis. The band gap of pure ZnO nanorods and pure γ-Fe₂O₃ nanoparticles are 3.2 eV and 1.9 eV, respectively. Band gap values of 2.24 eV, 2.2 eV, 2.18 eV and 1.9 eV due to γ-Fe₂O₃ were observed for ZnO@γ-Fe₂O₃ core-shell nanocomposites ZF1, ZF2, ZF3 and ZF4, respectively. The insets of Tauc plots in Fig. 5.27 of ZnO@γ-Fe₂O₃ core-shell nanocomposites (ZF1, ZF2, ZF3 and ZF4) show band

gap value of 3.3 eV due to ZnO. The band gap of $\gamma$-Fe$_2$O$_3$ in the core-shell nanocomposites shows red shift from ZF1 to ZF4. This red shift is attributed to an increase in particle size of $\gamma$-Fe$_2$O$_3$ with an increase in the precursor concentration of $\gamma$-Fe$_2$O$_3$ (i.e. Fe(acac)$_3$) used during the synthesis of the ZnO@$\gamma$-Fe$_2$O$_3$ nanocomposites [64,65].
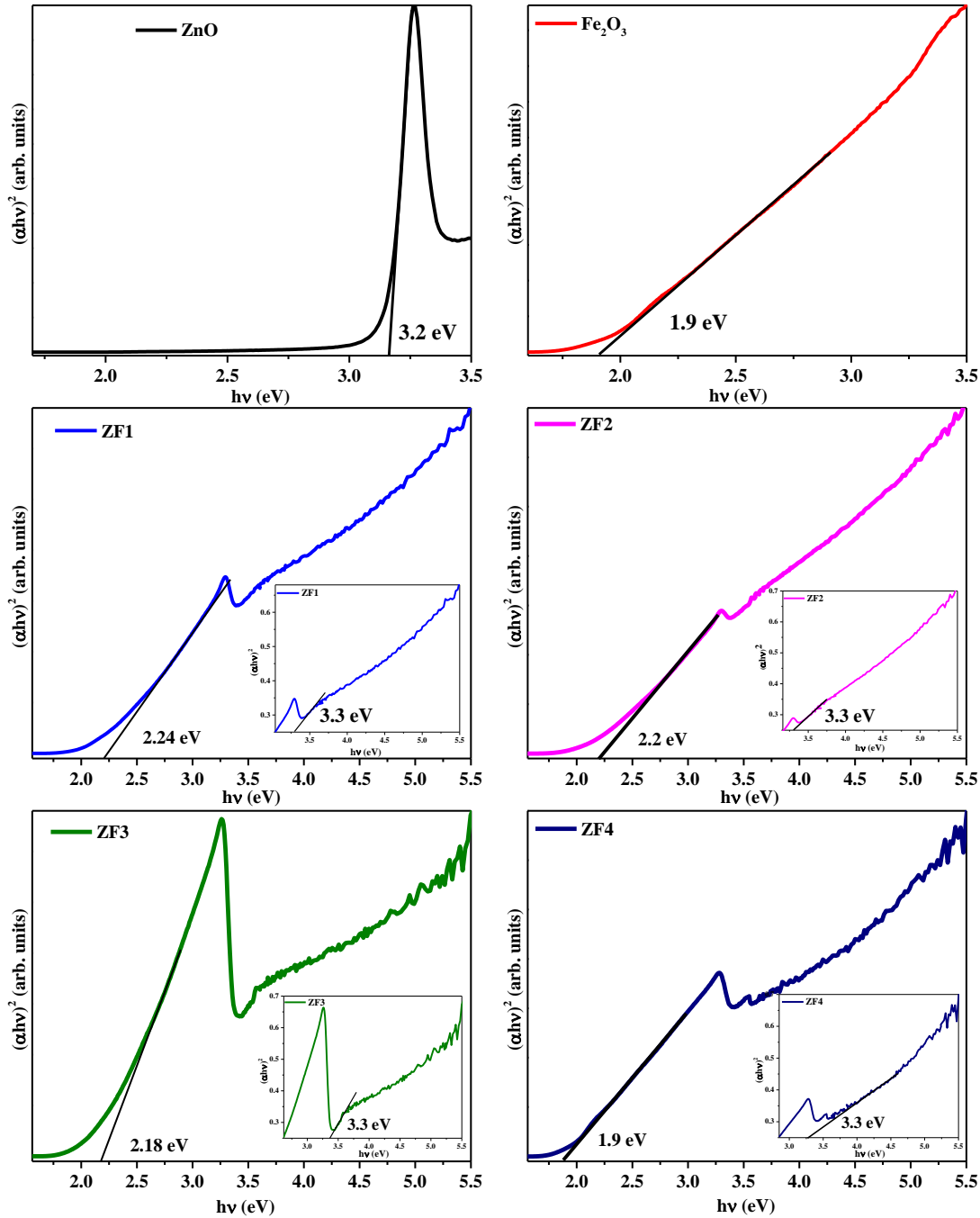


**Fig. 5.27:** Tauc plots (($\alpha$h$\nu$)$^2$ vs. h$\nu$) for ZnO nanorods, Fe$_2$O$_3$ nanoparticles and the ZnO@$\gamma$-Fe$_2$O$_3$ core-shell nanocomposites (ZF1, ZF2, ZF3 and ZF4).

### 5.2.3.6 UV-Visible Spectroscopy Studies

The UV-Visible absorption spectra of pure ZnO nanorods, iron oxide nanoparticles (as prepared by the thermal decomposition method, calcined at 400 $^{o}$C and $Fe_3O_4$) and the ZnO@$\gamma$-$Fe_2O_3$ core-shell nanocomposite ZF1 are shown in Fig. 5.28. The spectra were recorded using the dispersions in ethanol. The absorption spectrum of ZnO shows band edge absorption at about 376 nm (3.3 eV) which is blue shifted from that of bulk ZnO (3.2 eV) due to quantum confinement [64]. The as prepared iron oxide nanoparticles (prepared by the thermal decomposition method) show absorption in the visible region (400-800 nm) with a broad band at about 440 nm which corresponds to that of $\gamma$-$Fe_2O_3$ nanoparticles [84]. The absorption spectrum of iron oxide nanoparticles calcined at 400 $^{o}$C shows absorption at about 575 nm characteristic of $\alpha$-$Fe_2O_3$ [44,81]. $Fe_3O_4$ nanoparticles show band edge absorption at about 503 nm [84]. The absorption spectrum of ZnO@$\gamma$-$Fe_2O_3$ core-shell nanocomposite ZF1 shows a small shoulder at about 565 nm and a band edge absorption at about 376 nm (3.3 eV) attributed to $\gamma$-$Fe_2O_3$ and ZnO, respectively [46,61,64]. The absorption studies suggest that the phase of as prepared iron oxide nanoparticles, prepared by the thermal decomposition method, as $\gamma$-$Fe_2O_3$.
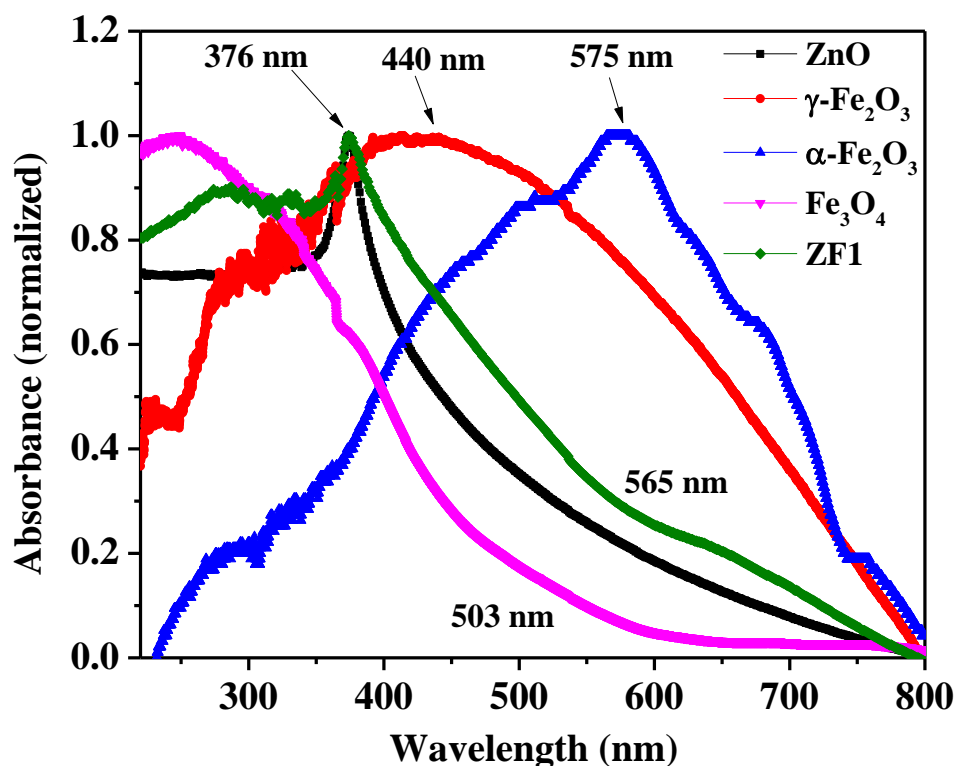
**Fig. 5.28:** UV-visible absorption spectra of iron oxide nanoparticles (as prepared using the thermal decomposition method, after calcination at 400 °C and $Fe_3O_4$) and $ZnO@\gamma$-$Fe_2O_3$ core-shell nanocomposite ZF1.

### 5.2.3.7 Photoluminescence Spectroscopy Studies

Fig. 5.29 shows the photoluminescence spectra of pure ZnO nanorods, $\gamma$-$Fe_2O_3$ nanoparticles (prepared by the thermal decomposition method) and the $ZnO@\gamma$-$Fe_2O_3$ core-shell nanocomposites (ZF1, ZF2, ZF3 and ZF4). The PL spectra of pure ZnO and $ZnO@\gamma$-$Fe_2O_3$ core-shell nanocomposites show emission bands around 382 nm and 469 nm. The emission band at about 382 nm is due to band-edge emission of ZnO resulting from the recombination of free excitons. The broad green emission centered at 469 nm, observed in ZnO nanorods, $\gamma$-$Fe_2O_3$ nanoparticles and all the core-shell nanocomposites (ZF1, ZF2, ZF3 and ZF4) is attributed to the presence of oxygen vacancies and defects [56]. In the $ZnO@\gamma$-$Fe_2O_3$ core-shell nanocomposites, the defect emission at 469 nm is enhanced as compared to pure ZnO nanorods and $\gamma$-$Fe_2O_3$ nanoparticles. A possible reason is the reduction in the number of hydroxyls groups on the surface of ZnO nanorods due to the formation of $\gamma$-$Fe_2O_3$ shell. Depletion of hydroxyls groups is known to lead to increase of oxygen vacancies and surface

defects on the surface of ZnO nanorods [72]. The oxygen vacancies/defects are very good electron scavengers and thus would improve the photocatalytic activity [66]. The defect emission decreases in the core-shell nanocomposites from ZF1 to ZF4 with an increase in the concentration of Fe(acac)$_3$ used during the preparation of the core-shell nanocomposites. The presence of more and more γ-Fe$_2$O$_3$ nanoparticles on the surface of ZnO nanorods due to increase in the concentration of Fe(acac)$_3$ decreases the surface defects and oxygen vacancies on the surface of ZnO nanorods [85].
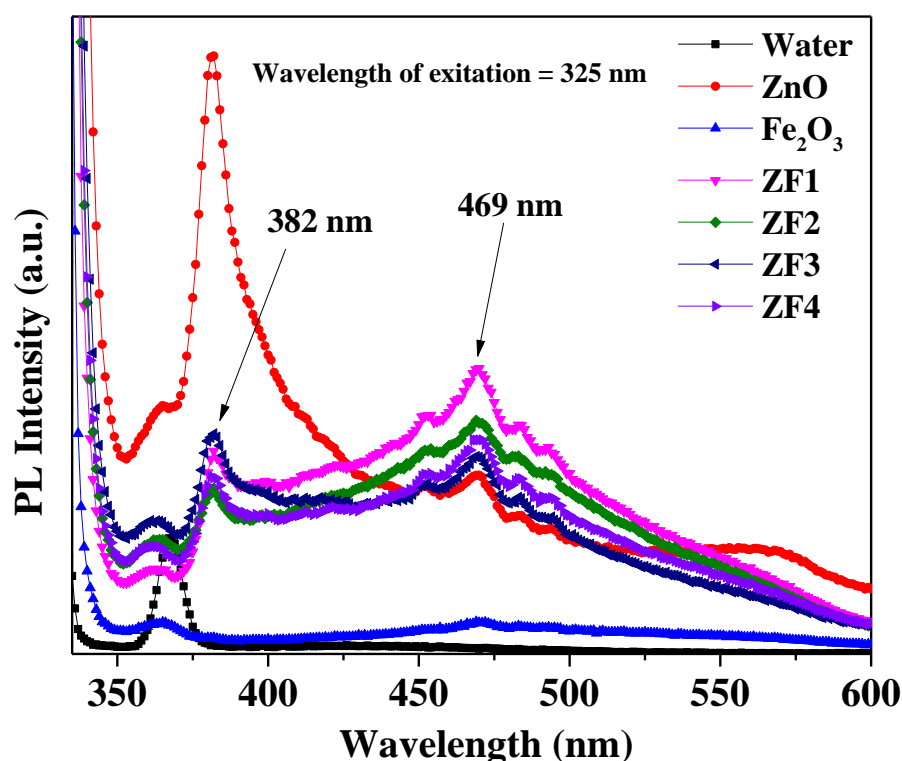


**Fig. 5.29:** Photoluminescence spectra for ZnO nanorods, γ-Fe$_2$O$_3$ nanoparticles (prepared by the thermal decomposition method) and the ZnO@γ-Fe$_2$O$_3$ core-shell nanocomposites (ZF1, ZF2, ZF3 and ZF4).

**5.2.3.8 Magnetic Measurements**

Magnetic measurements were carried out for pure γ-Fe$_2$O$_3$ nanoparticles prepared by the thermal decomposition method and the ZnO@γ-Fe$_2$O$_3$ core-shell nanocomposites which exhibit uniform elemental distribution (ZF1, ZF2 and ZF4). The magnetization versus magnetic field (M-H) plots for pure γ-Fe$_2$O$_3$ nanoparticles and the core-shell nanocomposites (ZF1, ZF2

and ZF4) are shown in Fig. 5.30. All the samples exhibit superparamagnetic behaviour at 300 K. At 5 K, however, the samples exhibit weak ferromagnetic behavior with a small coercivity ($H_c$) and remanent magnetization ($M_r$). For a superparamagnetic system, the coercivity and remanent magnetization in general increases below the superparamagnetic-ferromagnetic transition temperature [46,86]. The observed magnetic behavior and the magnetic parameters for pure $\gamma$-Fe$_2$O$_3$ nanoparticles and the ZnO@$\gamma$-Fe$_2$O$_3$ core–shell nanocomposites are summarized in Table 5.7. The coercivity of pure $\gamma$-Fe$_2$O$_3$ nanoparticles (0.05 T), and the core-shell nanocomposites ZF1 (0.05 T) and ZF2 (0.055 T) are almost the same. The coercivity of core-shell nanocomposite ZF4 (0.045 T) is less than that of pure $\gamma$-Fe$_2$O$_3$, ZF1 and ZF2. This is attributed to an increase in the particle size of iron oxide nanoparticles in the nanocomposite ZF4 [45]. Remanent magnetization is lower in all the core-shell nanocomposites as compared to pure $\gamma$-Fe$_2$O$_3$ nanoparticles (2.7 emu/g). This is due to the presence of diamagnetic ZnO nanorods, which decreases the effective mass of iron oxide [37,87]. Remanent magnetization values for the nanocomposites ZF1 (1:0.25), ZF2 (1:0.5) and ZF4 (1:1) are 0.33 emu/g, 0.88 emu/g and 0.66 emu/g, respectively. The unexpectedly high remanent magnetization in case of nanocomposite ZF2 is attributed to the formation of the thickest shell of iron oxide (~20 nm) over ZnO nanorods as compared to the other nanocomposites (ZF1 and ZF4) [88]. At 300 K, the saturation magnetization values of the core-shell nanocomposites are less than the saturation magnetization of $\gamma$-Fe$_2$O$_3$ nanoparticles and bulk maghemite (76 emu/g). The decrease of $M_s$ in the core–shell nanocomposites is attributed to the presence of diamagnetic ZnO, surface spin disorder and canting [86,87]. The saturation magnetization increases with an increase in the iron content of the nanocomposites ZF1 to ZF4 (Table 5.7). Also, there is an increase in the particle size of $\gamma$-Fe$_2$O$_3$ nanoparticles in the core-shell nanocomposites with an increase in the concentration of precursor for iron oxide (Fe(acac)$_3$) used during the synthesis [48]. Fig. 5.30 reveals that the magnetization at 5 K does not saturate for pure $\gamma$-Fe$_2$O$_3$ nanoparticles and also the core-shell nanocomposites at 3 Tesla. This is attributed to frozen spins on the surface as has been recently reported for maghemite nanoparticles [70,89].
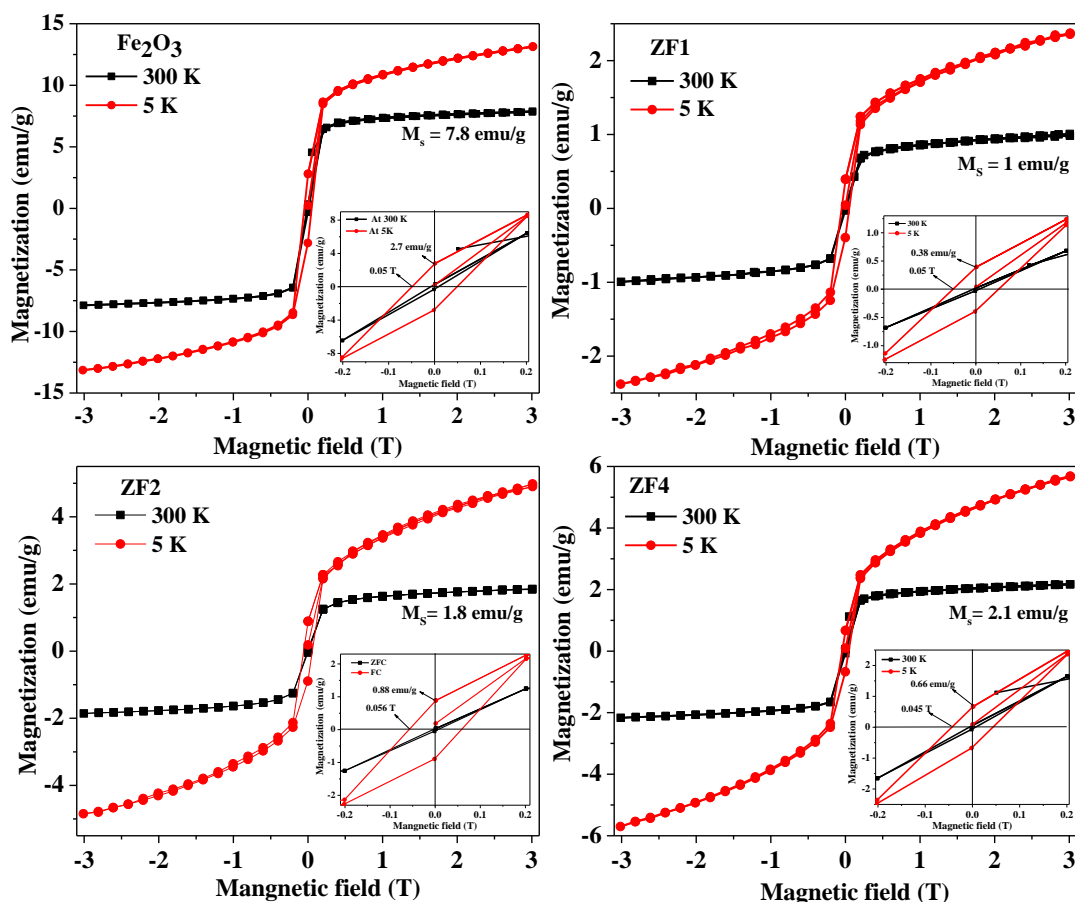
**Fig. 5.30:** M-H curves of pure γ-Fe$_2$O$_3$ nanoparticles prepared by the thermal decomposition method and the ZnO@γ-Fe$_2$O$_3$ core-shell nanocomposites ZF1, ZF2 and ZF4.

The zero-field-cooled (ZFC) and field-cooled (FC) magnetization curves for pure γ-Fe$_2$O$_3$ nanoparticles and for the ZnO@γ-Fe$_2$O$_3$ core–shell nanocomposites (ZF1, ZF2 and ZF4) under an applied field of 0.05 Tesla are shown in Fig. 5.31. Pure γ-Fe$_2$O$_3$ nanoparticles and all the core-shell nanocomposites (ZF1, ZF2 and ZF4) show broad maxima in the ZFC curve (Table 5.7). This temperature called as the blocking temperature (T$_B$), corresponds to the superparamagnetic transition of iron oxide nanoparticles.

**Table 5.7:** Magnetic parameters for pure iron oxide nanoparticles and the ZnO@$\gamma$-Fe$_2$O$_3$ core–shell nanocomposites.

| Sample | H$_c$ (T) | | M$_r$ (emu/g) | | M$_s$ (emu/g) | | T$_B$ (K) | T$_M$ (K) | Particle size of $\gamma$-Fe$_2$O$_3$ from T$_B$ (nm) |
|---|---|---|---|---|---|---|---|---|---|
| | 5 K | 300 K | 5 K | 300 K | 5 K | 300 K | | | |
| $\gamma$-Fe$_2$O$_3$ | 0.05 | - | 2.7 | - | - | 7.8 | 43 | 266 | 18.2 |
| ZF1 | 0.05 | - | 0.38 | - | - | 1.0 | 30 | 265 | 16.2 |
| ZF2 | 0.055 | - | 0.88 | - | - | 1.8 | 45 | 266 | 18.5 |
| ZF4 | 0.045 | - | 0.66 | - | - | 2.1 | 55 | 260 | 19.8 |

At temperatures higher than the T$_B$, the magnetization decreases and follows a Curie-Weiss law [90]. The observed blocking temperature for pure $\gamma$-Fe$_2$O$_3$ nanoparticles is 43 K and for the core-shell nanocomposites ZF1, ZF2 and ZF4, the T$_B$ values are 30 K, 45 K and 55 K, respectively. The increase in the blocking temperature in the nanocomposites ZF2 and ZF4 compared to ZF1 is attributed to increase in dipolar interaction due to increase in the particle volume [91]. The $\gamma$-Fe$_2$O$_3$ nanoparticles and all the core-shell nanocomposites (ZF1, ZF2 and ZF4) show broad maxima in the ZFC curves indicating broad particle size distribution of iron oxide nanoparticles [48]. The particle volume (V) can be calculated from T$_B$ using the following equation [92].

$$T_B = \frac{K_{eff}V}{25k_B}$$

Where K$_{eff}$ is the effective anisotropy constant (for bulk maghemite, K$_{eff}$ = 4.7 $\times$ 10$^4$ erg cm$^{-3}$) and k$_B$ is the Boltzmann constant. The average particle size of $\gamma$-Fe$_2$O$_3$ calculated from the blocking temperature of pure $\gamma$-Fe$_2$O$_3$ nanoparticles and the core-shell nanocomposites ZF1, ZF2, ZF4 are 18.2 nm, 16.2 nm, 18.5 nm and 19.8 nm, respectively. The ZFC curves of pure Fe$_2$O$_3$ and nanocomposites ZF1, ZF2 and ZF4 show Morin transition at about 266 K, 265 K, 266 K and 260 K, respectively. The observation of Morin transition is attributed to the presence of a small amount of $\alpha$-Fe$_2$O$_3$ nanoparticles due to the structural transformation of $\gamma$-Fe$_2$O$_3$ into $\alpha$-Fe$_2$O$_3$ nanoparticles [93]. In $\alpha$-Fe$_2$O$_3$, Morin transition is a phase transition in which a weakly ferromagnetic state converts to an antiferromagnetic state [94].
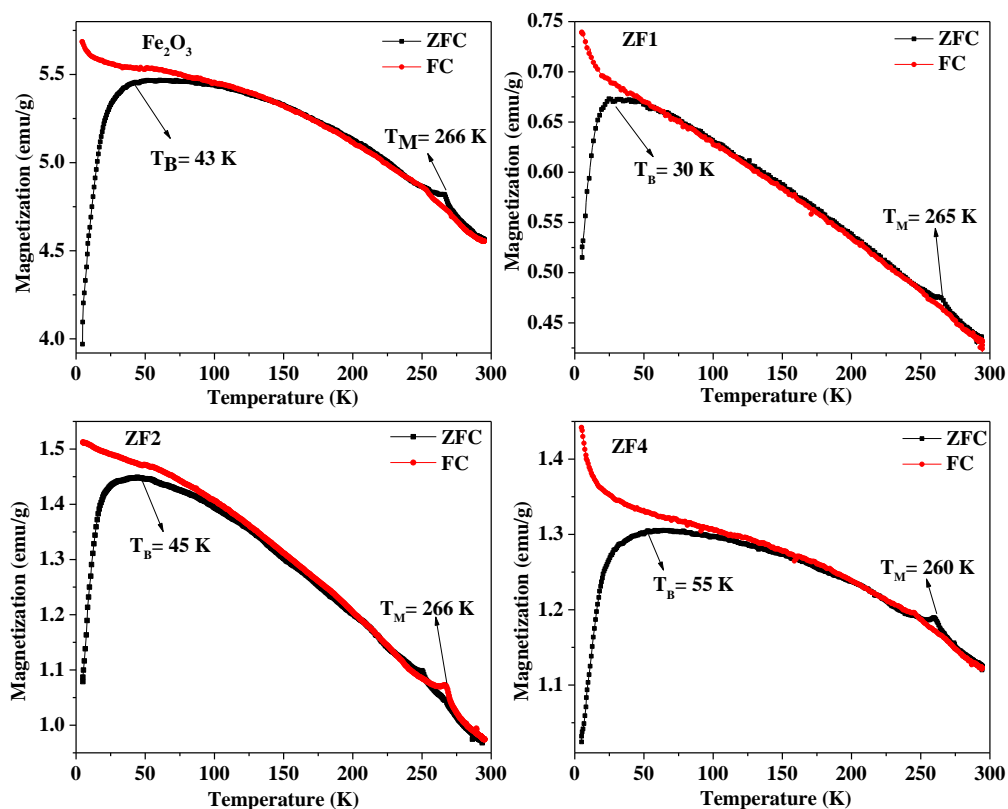
**Fig. 5.31:** ZFC and FC curves of pure $\gamma$-Fe$_2$O$_3$ nanoparticles prepared by the thermal decomposition method and ZnO@$\gamma$-Fe$_2$O$_3$ core-shell nanocomposites ZF1, ZF2 and ZF4.

Fig. 5.32 shows M-H curves for iron oxide nanoparticles prepared by the thermal decomposition method and calcined at 400 $^o$C (i.e. $\alpha$-Fe$_2$O$_3$) and ZnO@$\gamma$-Fe$_2$O$_3$ core-shell nanocomposite ZF1 calcined at 400 $^o$C, and Fe$_3$O$_4$ nanoparticles. The observed magnetic parameters such as coercivity (H$_c$), remanent magnetization (M$_r$) and saturation magnetization (M$_s$) have been summarized in Table 5.8. Pure iron oxide nanoparticles calcined at 400 $^o$C show weak ferromagnetic behaviour at both 300 K and 5 K with H$_c$ values of 0.016 and 0.65 T, respectively. The magnetization does not completely saturate at both the temperatures at a maximum field of 3 Tesla. The magnetic behaviour of iron oxide nanoparticles calcined at 400 $^o$C is similar to that reported for $\alpha$-Fe$_2$O$_3$ nanoparticles [44,76,95]. The core-shell nanocomposite ZF1 (after calcination at 400 $^o$C) shows superparamagnetic behaviour at room temperature. At 5 K, the nanocomposite ZF1 (after calcination at 400 $^o$C) shows weak ferromagnetic behaviour with a H$_c$ value of 0.1 T. The M-H curve of Fe$_3$O$_4$ nanoparticles shows superparamagnetic behaviour at room temperature and weak ferromagnetic behaviour at 5 K with H$_c$ and M$_r$ values of 0.48 T and 21.4 emu/g, respectively. The saturation magnetization at 300 K and 5 K are 73 emu/g and 89 emu/g, respectively.

**Table 5.8:** Magnetic parameters of iron oxide nanoparticles prepared by the thermal decomposition method, after calcination at 400 °C, $Fe_3O_4$ nanoparticles and $ZnO@\gamma\text{-}Fe_2O_3$ core-shell nanocomposite ZF1 (calcined at 400 °C).

| Sample | $H_c$ (T) | | $M_r$ (emu/g) | | $T_B$ (K) | $T_M$ (K) | $M_s$ at (emu/g) | | Particle size (estimated from $T_B$) |
|---|---|---|---|---|---|---|---|---|---|
| | 5 K | 300 K | 5 K | 300 K | | | 300 K | 5 K | |
| As prepared iron oxide nanoparticles (thermal decomposition method) | 0.05 | - | 2.7 | - | 43 | 266 | 7.8 | - | 18.2 nm |
| After calcination at 400 °C | 0.65 | 0.016 | 4.9 | 0.95 | 200 | - | - | - | 19.5 nm |
| $ZnO@\gamma\text{-}Fe_2O_3$ nanocomposite ZF1 (400 °C) | 0.1 | - | 0.8 | - | 52.5 | 262 | - | - | 30.4 nm |
| $Fe_3O_4$ nanoparticles | 0.48 | - | 21.4 | - | 39 | - | 73 | 89 | 17.6 nm |
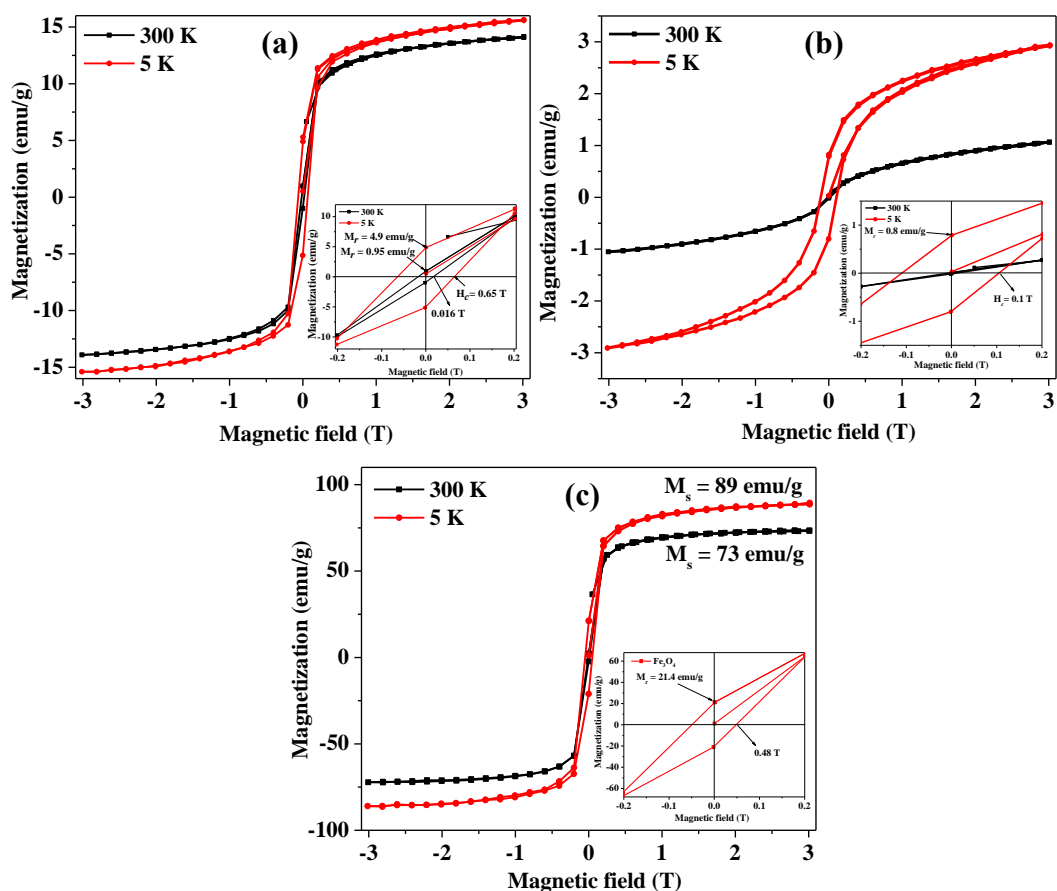
**Fig.5.32:** M-H curves of (a) iron oxide nanoparticles prepared by the thermal decomposition method and calcined at 400 °C, (b) ZnO@$\gamma$-Fe$_2$O$_3$ core-shell nanocomposite ZF1 calcined at 400 °C and (c) Fe$_3$O$_4$ nanoparticles.

The ZFC/FC curves of iron oxide nanoparticles prepared by thermal decomposition method followed by calcination at 400 °C, ZnO@$\gamma$-Fe$_2$O$_3$ core-shell nanocomposite ZF1 calcined at 400 °C, and Fe$_3$O$_4$ nanoparticles are shown in Fig. 5.33. The ZFC curve for iron oxide nanoparticles calcined at 400 °C (Fig. 5.33(a)) shows a broad maximum around 200 K, corresponding to the blocking temperature. The FC curve departs from the ZFC curve at T$_{irr}$ (blocking temperature of the largest particle) and remains constant with decrease in temperature and this is due to strong inter-particle interactions [96]. The ZFC curve for the ZnO@$\gamma$-Fe$_2$O$_3$ core-shell nanocomposite ZF1 (Fig. 5.33(b)) calcined at 400 °C shows sharper peak at 52.5 K indicating the superparamagnetic blocking transition. Also, the ZFC curve shows a small hump at 262 K due to Morin transition confirming the formation of $\alpha$-Fe$_2$O$_3$. Pure iron oxide nanoparticles prepared by the thermal decomposition method and after calcination at 400 °C do not show Morin transition. According to Zysler et al. [97], when iron oxide is prepared in the form of small particles, the Morin transition is a more complicated

phenomenon due to the presence of strain and defects. The Morin transition temperature reduces as the particle size decreases and vanishes for iron oxide particles smaller than 8-20 nm [98]. In the present case, the size of $\alpha$-$Fe_2O_3$ nanoparticles is 19.5 nm. The particle size values of iron oxide nanoparticles prepared by the thermal decomposition method and calcined at 400 °C and ZnO@$\gamma$-$Fe_2O_3$ core-shell nanocomposite ZF1 calcined at 400 °C estimated from their blocking temperature, are 19.5 nm and 30.4 nm, respectively. The ZFC curve for $Fe_3O_4$ nanoparticles (Fig. 5.33(c)) shows a broad maximum around 39 K and this is the superparamagnetic blocking temperature. The FC curve is more or less constant after the blocking temperature due to strong inter-particle interactions [99]. The particle size of $Fe_3O_4$ nanoparticles, calculated from the blocking temperature, is 17.6 nm. In general, the saturation magnetization at room temperature reported for $\gamma$-$Fe_2O_3$ nanoparticles is between 1.3 emu/g and 69.6 emu/g [70,72,78,85,87] and for $Fe_3O_4$ nanoparticles the $M_s$ value is between 20 emu/g and 84 emu/g [72,100,101]. The coercivity at 5 K reported for $\gamma$-$Fe_2O_3$ nanoparticles is between 0.005T and 0.413 T [97,102] and for $Fe_3O_4$ nanoparticles the value is between 0.01 T and 0.058 T [83,103]. The remanent magnetization values at 5 K reported for $\gamma$-$Fe_2O_3$ nanoparticles are between 0.62 emu/g and 16.7 emu/g [33,104] and for $Fe_3O_4$ nanoparticles the values are between 13 emu/g and 18.8 emu/g [76,104]. From the above results, one can conclude that there is difference in the magnetic properties of $\gamma$-$Fe_2O_3$ and $Fe_3O_4$ nanoparticles. In spite of having nearly same particle size for as prepared iron oxide nanoparticles prepared by the thermal decomposition method (18.2 nm) and $Fe_3O_4$ nanoparticles (17.6 nm), there is difference in their magnetic behaviour. For the as prepared iron oxide nanoparticles, the coercivity ($H_c$ = 0.05 T) and remanent value ($M_r$ = 2.7 emu/g) at 5 K and saturation magnetization ($M_s$ = 7.8 emu/g) at room temperature are less than that of $Fe_3O_4$ nanoparticles ($H_c$ = 0.48 T, $M_r$ = 21.4 emu/g and $M_s$ = 73 emu/g). This suggests that the phase of as prepared iron oxide nanoparticles prepared by the thermal decomposition method as $\gamma$-$Fe_2O_3$.
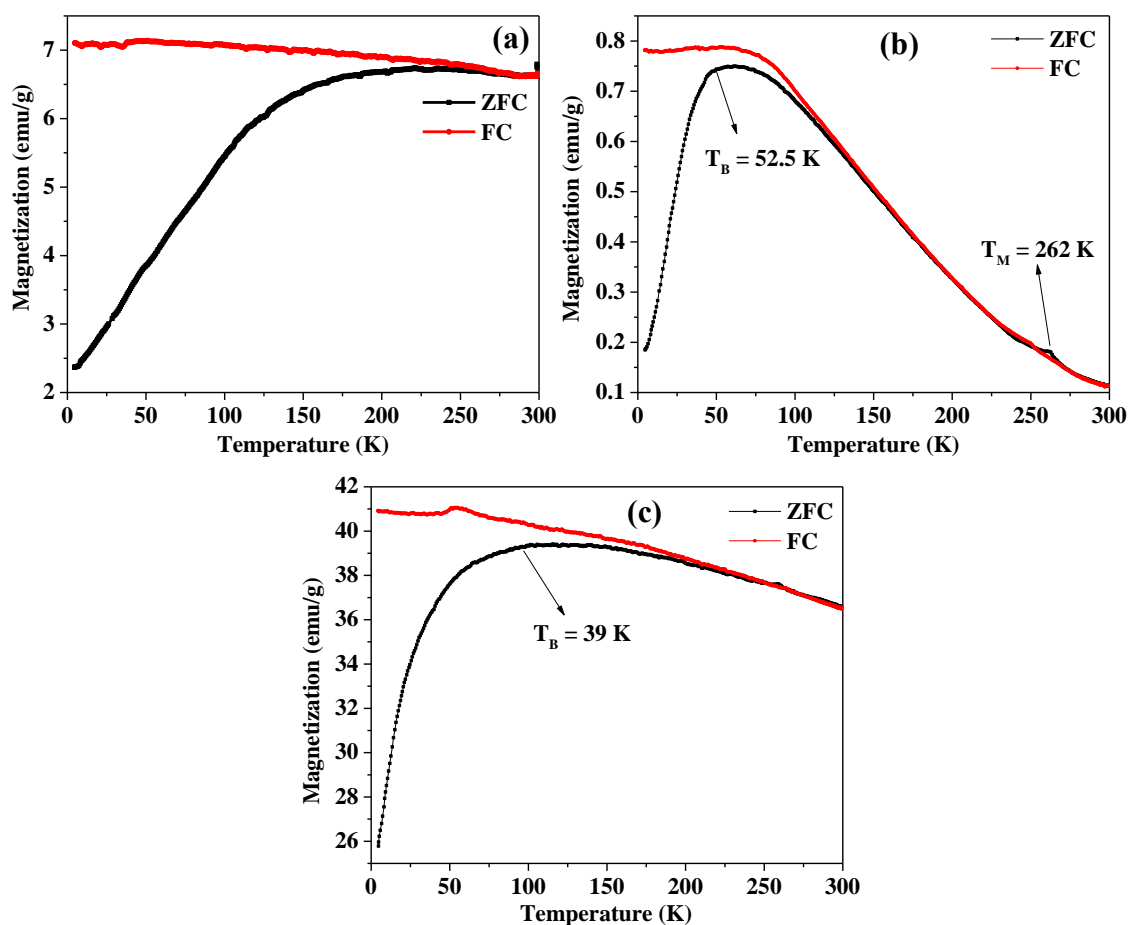
**Fig. 5.33:** ZFC/FC curves for (a) pure iron oxide nanoparticles prepared by the thermal decomposition method and calcined at 400 °C, (b) ZnO@γ-Fe$_2$O$_3$ core-shell nanocomposite ZF1 calcined at 400 °C and (c) Fe$_3$O$_4$ nanoparticles.

### 5.2.3.9 Surface Area Measurements

The BET surface area values for the ZnO@γ-Fe$_2$O$_3$ core-shell nanocomposites ZF1, ZF2, ZF3 and ZF4 are 62.1 m$^2$/g, 53.3 m$^2$/g, 50.3 m$^2$/g and 38.2 m$^2$/g, respectively. The surface area of ZF1 core-shell nanocomposite is higher than that of pure ZnO (24.4 m$^2$/g), as prepared Fe$_2$O$_3$ (51.1 m$^2$/g) and all the other nanocomposites.

### 5.2.3.10 Mechanism for the formation ZnO@γ-Fe$_2$O$_3$ core-shell nanocomposites

Zinc oxide nanorods possess hydroxyl groups on their surface [74]. During the formation of the ZnO@γ-Fe$_2$O$_3$ core-shell nanocomposites, iron(III) acetylacetonate interacts with the surface of ZnO via hydrogen bonding between the π-system of acetyl acetone ligand and protons of the hydroxyl groups present on the surface of ZnO (Scheme 5.6).
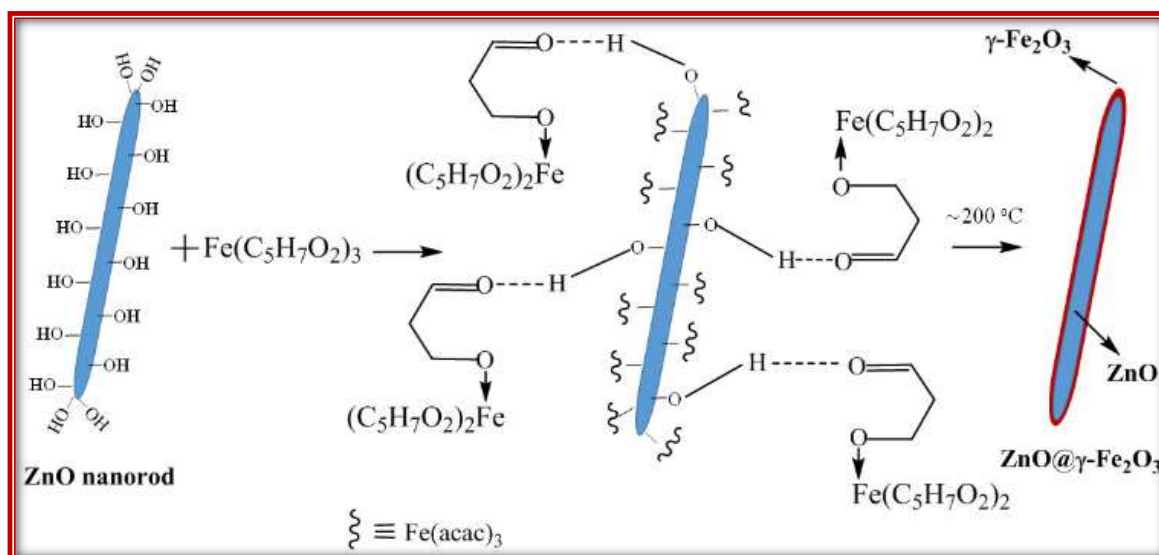
**Scheme 5.6:** Attachment of iron(III) acetylacetonate (Fe(acac)$_3$) on the surface of ZnO nanorods and its further decomposition to yield iron oxide nanoparticles.

Iron(III) acetylacetonate decomposes in air, at about 200°C, to produce iron oxide nanoparticles (maghemite) with by-products [43].

$$4(C_5H_7O_2)_3Fe + 17O_2 \xrightarrow{\sim 200\ ^\circ C} 2\ \gamma{-}Fe_2O_3 + 30CO + 10CO_2 + 20CH_4 + 2H_2O$$
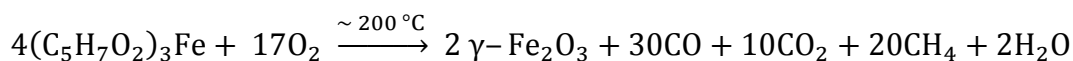
Since the thermal decomposition is carried out at 200 °C in diphenyl ether in the presence of ZnO nanorods, ZnO@$\gamma$-Fe$_2$O$_3$ core-shell nanocomposites are produced.

## 5.2.4 Conclusions

ZnO@$\gamma$-Fe$_2$O$_3$ core-shell nanocomposites were synthesized by a novel two-step thermal decomposition approach. The nanocomposites were characterized with the help of X-ray diffraction, FT-IR spectroscopy, scanning electron microscopy, transmission electron microscopy, diffuse reflectance UV–visible spectroscopy, photoluminescence spectroscopy, vibrating sample magnetometry and surface area measurements. XRD results confirm the presence of hexagonal wurtzite ZnO and XRD studies on as prepared and calcined samples suggest the phase of as prepared iron oxide nanoparticles as $\gamma$-Fe$_2$O$_3$. FT-IR results on as prepared iron oxide and ZnO@$\gamma$-Fe$_2$O$_3$ core-shell nanocomposites show characteristic IR bands due to $\gamma$-Fe$_2$O$_3$ and FE-SEM images show uniform shell formation of iron oxide on the ZnO nanorods. Transmission electron microscopy studies show that ZnO exhibits rod like morphology with ~40 nm diameter and length 1.1 μm. The ZnO@$\gamma$-Fe$_2$O$_3$ core-shell nanocomposites show uniform shell due to $\gamma$-Fe$_2$O$_3$ nanoparticles coated on the ZnO nanorods

and the thickness of $Fe_2O_3$ shell varies from 10 to 20 nm. HRTEM observations demonstrate that the constituents of the nanocomposites are crystalline with characteristics lattice spacing due to $\gamma$-$Fe_2O_3$ (0.48 nm) and ZnO (0.24 nm). The diffuse reflectance spectra of ZnO@$\gamma$-$Fe_2O_3$ core-shell nanocomposites reveal extended optical absorption in the visible range 400–600 nm. The core-shell nanocomposites show red shift of the band gap absorption due to iron oxide from 2.24 to 1.9 eV with increase in the precursor concentration of $\gamma$-$Fe_2O_3$. The photoluminescence spectral studies indicate that the ZnO@$\gamma$-$Fe_2O_3$ nanocomposites exhibit enhanced defect emission which is expected to increase its photocatalytic activity. The ZnO@$\gamma$-$Fe_2O_3$ core-shell nanocomposites exhibit superparamagnetic behaviour at room temperature with maximum saturation magnetization of 2.1 emu/g.

# References

1. Shen S., Wang Q., 'Rational tuning the optical properties of metal sulfide nanocrystals and their applications', *Chemistry of Materials*, **25**, 1166–1178 (2013).

2. Aldakov D., Lefrancois A., Reiss P., 'Ternary and quaternary metal chalcogenide nanocrystals: Synthesis, properties and applications', *Journal of Materials Chemistry C*, **1**, 3756–3776 (2013).

3. Sharma H., Sharma S. N., Singh S., Mehra N. C., Singh G., Shivaprasad S. M., 'Comparison of the properties of composition-tunable CdSe-ZnSe and $Zn_xCd_{1-x}Se$ nanocrystallites: Single- and double-pot synthesis approach', *Materials Chemistry and Physics*, **124**, 670–680 (2010).

4. Yadav S. K., Jeevanandam P., 'Thermal decomposition approach for the synthesis of $CdS–TiO_2$ nanocomposites and their catalytic activity towards degradation of rhodamine B and reduction of Cr(VI)', *Ceramics International*, **41**, 2160–2179 (2015).

5. Chang C. J., Lee Z., Wei M., Chang C. C., Chu K. W., 'Photocatalytic hydrogen production by magnetically separable $Fe_3O_4@ZnS$ and $NiCo_2O_4@ZnS$ core–shell nanoparticles', *International Journal of Hydrogen Energy*, **40**, 11436–11443 (2015).

6. Zhang W., Sun Y., Xiao Z., Li W., Li B., Huang X., Liu X., Hu J., 'Heterostructures of CuS nanoparticle/ZnO nanorod arrays on carbon fibers with improved visible and solar light photocatalytic properties', *Journal of Materials Chemistry A*, **3**, 7304–7313 (2015).

7. Wu J., Li Z., Li F., 'Synthesis and visible-light-driven photocatalytic activity of one-dimensional $CdS/\alpha-Fe_2O_3$', *Superlattices and Microstructures*, **54**, 146–154 (2013).

8. Qu X., Hou Y., Wang C., Du F., Cao L., 'Fabrication of $TiO_2$/MS (M = Pb, Zn) core–shell coaxial nanotube arrays and their photocatalytic properties', *RSC Advances*, **5**, 5307–5311 (2015).

9. Machala L., Tucek J., Zboril R., 'Polymorphous transformations of nanometric iron(III) oxide: A review', *Chemistry of Materials*, **23**, 3255–3272 (2011).

10. Zubir N. A., Zhang X., Yacou C., Costa J. C. D. da., 'Fenton-like degradation of acid orange 7 using graphene oxide-iron oxide nanocomposite', *Science of Advanced Materials*, **6**, 1382–1388 (2014).

11. Fan Z., Yust B., Priya B., Nellore V., Sinha S. S., Kanchanapally R., Crouch R. A., Pramanik A., Chavva S. R., Sardar D., Ray P. C., 'Accurate identification and selective removal of rotavirus using a plasmonic−magnetic 3D graphene oxide architecture', *Journal of Physical Chemistry Letters*, **5**, 3216–3221 (2014).

12. Hudson R., Feng Y., Varma R. S., Moores A., 'Bare magnetic nanoparticles: sustainable synthesis and applications in catalytic organic transformations', *Green Chemistry*, **16**, 4493–4505 (2014).

13. Hao C., Feng F., Wang X., Zhou M., Zhao Y., Ge C., Wang K., 'The preparation of $Fe_2O_3$ nanoparticles by liquid phase-based ultrasonic-assisted method and its application as enzyme-free sensor for the detection of $H_2O_2$', *RSC Advances*, **5**, 21161–21169 (2015).

14. Cheng W., Xu J., Wang Y., Wu F., Xu X., Li J., 'Dispersion–precipitation synthesis of nanosized magnetic iron oxide for efficient removal of arsenite in water', *Journal of Colloid and Interface Science*, **445**, 93–101 (2015).

15. Wang J., Li R., Zhang Z., Sun W., Xu R., Xie Y., Xing Z., Zhang X., 'Efficient photocatalytic degradation of organic dyes over titanium dioxide coating upconversion luminescence agent under visible and sunlight irradiation', *Applied Catalysis A: General*, **334**, 227–233 (2008).

16. Dengxin L., Guolong G., Fanling M., Chong J., 'Preparation of nano-iron oxide red pigment powders by use of cyanided tailings', *Journal of Hazardous Materials*, **155**, 369–377 (2008).

17. Mattingly S. J., O'Toole M. G., James K. T., Clark G. J., Nantz M. H., 'Magnetic nanoparticle-supported lipid bilayers for drug delivery', *Langmuir*, **31**, 3326–3332 (2015).

18. Liu S., Wang R., Liu M., Luo J., Jin X., Sun J., Gao L., '$Fe_2O_3$@$SnO_2$ nanoparticle decorated graphene flexible films as high-performance anode materials for lithium-ion batteries', *Journal of Materials Chemistry A*, **2**, 4598–4604 (2014).

19. Penki T. R., Shivakumara S., Minakshi M., Munichandraiah N., 'Porous flower-like α-$Fe_2O_3$ nanostructure: A high performance anode material for lithium-ion batteries', *Electrochimica Acta*, **167**, 330–339 (2015).

20. Apte S. K., Naik S. D., Sonawane R. S., Kale B. B., Baeg J. O., 'Synthesis of nanosize-necked structure $\alpha$- and $\gamma$-$Fe_2O_3$ and its photocatalytic activity', *Journal of the American Ceramic Society*, **90**, 412–414 (2007).

21. Mou F., Xu L., Ma H., Guan J., Chen D., Wang S., 'Facile preparation of magnetic $\gamma$-$Fe_2O_3$/$TiO_2$ Janus hollow bowls with efficient visible-light photocatalytic activities by asymmetric shrinkage', *Nanoscale*, **4**, 4650–4657 (2012).

22. Tang Y., Hu X., Liu C., 'Perfect inhibition of CdS photocorrosion by graphene sheltering engineering on $TiO_2$ nanotube array for highly stable photocatalytic activity', *Physical Chemistry Chemical Physics*, **16**, 25321–25329 (2014).

23. Nan Y. X., Chen F., Yang L. G., Chen H. Z., 'Electrochemical synthesis and charge transport properties of CdS nanocrystalline thin films with a conifer-like structure', *The Journal of Physical Chemistry C*, **114**, 11911–11917 (2010).

24. Wang L., Wei H., Fan Y., Gu X., Zhan J., 'One-dimensional CdS/$\alpha$-$Fe_2O_3$ and CdS/$Fe_3O_4$ heterostructures: Epitaxial and nonepitaxial growth and photocatalytic activity', *The Journal of Physical Chemistry C*, **113**, 14119–14125 (2009).

25. Jiang R., Yao J., Zhu H., Fu Y., Guan Y., Xiao L., Zeng G., 'Effective decolorization of congo red in aqueous solution by adsorption and photocatalysis using novel magnetic alginate/$\gamma$-$Fe_2O_3$/CdS nanocomposite', *Desalination and Water Treatment*, **52**, 238–247 (2014).

26. Zhang S., Xu W., Zeng M., Li J., Xu J., Wang X., 'Hierarchically grown CdS/$\alpha$-$Fe_2O_3$ heterojunction nanocomposites with enhanced visible-light-driven photocatalytic performance', *Dalton Transactions*, **42**, 13417–13424 (2013).

27. Preethi V., Kanmani S., 'Photocatalytic hydrogen production using $Fe_2O_3$-based core shell nano particles with ZnS and CdS', *International Journal of Hydrogen Energy*, **39**, 1613–1622 (2014).

28. Shi Y., Li H., Wang L., Shen W., Chen H., 'Novel $\alpha$-$Fe_2O_3$/CdS cornlike nanorods with enhanced photocatalytic performance', *ACS Applied Materials and Interfaces*, **4**, 4800–4806 (2012).

29. Wu Z., Yu H., Kuai L., Wang H., Pei T., Geng B., 'CdS urchin-like microspheres/ $\alpha$-$Fe_2O_3$ and CdS/$Fe_3O_4$ nanoparticles heterostructures with improved photocatalytic

recycled activities', *Journal of Colloid and Interface Science*, **426**, 83–89 (2014).

30. Chen Y. J., Shi X. L., Cao M. S., Zhu C. L., 'Synthesis and magnetic properties of CdS/α-Fe$_2$O$_3$ hierarchical nanostructures', *Science in China Series G: Physics, Mechanics and Astronomy*, **52**, 997–1002 (2009).

31. Kwon K. W., Shim M., 'γ-Fe$_2$O$_3$/II-VI sulfide nanocrystal heterojunctions', *The Journal of the American Chemical Society*, **127**, 10269–10275 (2005).

32. Liu J., Zhang D., Pu X., Dong D., Cai P., Seo H. J., 'Combustion synthesis and photocatalytic properties of magnetically separable Zn$_{1-x}$Cd$_x$S/γ-Fe$_2$O$_3$ composites', *Materials Letters*, **130**, 94–96 (2014).

33. Sharma G., Jeevanandam P., 'Synthesis of self-assembled prismatic iron oxide nanoparticles by a novel thermal decomposition route', *RSC Advances*, **3**, 189–200 (2013).

34. Shayan N. N., Mirzayi B., 'Adsorption and removal of asphaltene using synthesized maghemite and hematite nanoparticles', *Energy and Fuels*, **29**, 1397–1406 (2015).

35. Banisharif A., Khodadadi A. A., Mortazavi Y., Anaraki Firooz A., Beheshtian J., Agah S., Menbari S., 'Highly active Fe$_2$O$_3$-doped TiO$_2$ photocatalyst for degradation of trichloroethylene in air under UV and visible light irradiation: Experimental and computational studies', *Applied Catalysis B: Environmental*, **165**, 209–221 (2015).

36. Yang G., Zhang B., Wang J., Xie S., Li X., 'Preparation of polylysine-modified superparamagnetic iron oxide nanoparticles', *Journal of Magnetism and Magnetic Materials*, **374**, 205–208 (2015).

37. Sharma G., Jeevanandam P., 'A facile synthesis of multifunctional iron oxide@Ag core-shell nanoparticles and their catalytic applications', *European Journal of Inorganic Chemistry*, **2013**, 6126–6136 (2013).

38. Rajeswari Yogamalar N., Sadhanandam K., Chandra Bose A., Jayavel R., 'Quantum confined CdS inclusion in graphene oxide for improved electrical conductivity and facile charge transfer in hetero-junction solar cell', *RSC Advances*, **5**, 16856–16869 (2015).

39. Dimitrov R. I., Moldovanska N., Bonev I. K., 'Cadmium sulphide oxidation', *Thermochimica Acta*, **385**, 41–49 (2002).

40. Gaur R., Jeevanandam P., 'Evolution of different morphologies of CdS nanoparticles by thermal decomposition of bis(thiourea) cadmium chloride in various solvents', *Journal of Nanoparticle Research*, **17**, 156/1–156/13 (2015).

41. Sugii Y., Inada M., Yano H., Obora Y., Iwasaki Y., Arakawa R., Kawasaki H., 'Single nanosized FeO nanocrystals with photoluminescence properties', *Journal of Nanoparticle Research*, **15**, 1379/1–1379/8 (2013).

42. Fischer V., Bannwarth M. B., Jakob G., Landfester K., Muñoz-Espí R., 'Luminescent and magnetoresponsive multifunctional chalcogenide/polymer hybrid nanoparticles', *The Journal of Physical Chemistry C*, **117**, 5999–6005 (2013).

43. Kishore P. N. R., Jeevanandam P., 'A novel thermal decomposition approach for the synthesis of silica-iron oxide core-shell nanoparticles', *Journal of Alloys and Compounds*, **522**, 51–62 (2012).

44. Pandey B. K., Shahi A. K., Shah J., Kotnala R. K., Gopal R., 'Optical and magnetic properties of $Fe_2O_3$ nanoparticles synthesized by laser ablation/fragmentation technique in different liquid media', *Applied Surface Science*, **289**, 462–471 (2014).

45. Lin C. R., Chu Y. M., Wang S. C., 'Magnetic properties of magnetite nanoparticles prepared by mechanochemical reaction', *Materials Letters*, **60**, 447–450 (2006).

46. Zhang L., Papaefthymiou G. C., Ying J. Y., 'Size quantization and interfacial effects on a novel $\gamma$-$Fe_2O_3$/$SiO_2$ magnetic nanocomposite via sol-gel matrix-mediated synthesis', *Journal of Applied Physics*, **81**, 6892/1–6892/10 (1997).

47. Ahmad S., Nagarajan R., Raj P., Prakash G. V., 'Novel fluorite structured superparamagnetic $RbGdF_4$ nanocrystals as versatile upconversion host', *Inorganic Chemistry*, **53**, 10257–10265 (2014).

48. Kishore P. N. R., Jeevanadam P., 'Synthesis of silver–iron oxide nanocomposites by thermal decomposition', *Journal of Nanoscience and Nanotechnology*, **11**, 3445–3453 (2011).

49. Rastogi A. C., Dhara S., Das B. K., 'Kinetics, growth, structure, and atmospheric chemical vapor deposition of ferrimagnetic iron oxide thin films from metallorganic acetyl acetonate precursor', *Journal of Electrochemical Society*, **142**, 3148–3156 (1995).

50. Meledandri C. J., Stolarczyk J. K., Ghosh S., Brougham D. F., 'Nonaqueous magnetic nanoparticle suspensions with controlled particle size and nuclear magnetic resonance properties', *Langmuir*, **24**, 14159–14165 (2008).

51. Dutta S. K., Mehetor S. K., Pradhan N., 'Metal semiconductor heterostructures for photocatalytic conversion of light energy', *The Journal of Physical Chemistry Letters*, **6**, 936–944 (2015).

52. Wang H., Hodgson J., Shrestha T. B., Thapa P. S., Moore D., Wu X., Ikenberry M., Troyer D. L., Wang D., Hohn K. L., Bossmann S. H., 'Carbon dioxide hydrogenation to aromatic hydrocarbons by using an iron/iron oxide nanocatalyst', *Beilstein Journal of Nanotechnology*, **5**, 760–769 (2014).

53. Ikenberry M., Peña L., Wei D., Wang H., Bossmann S. H., Wilke T., Wang D., Komreddy V. R., Rillema D. P., Hohn K. L., 'Acid monolayer functionalized iron oxide nanoparticles as catalysts for carbohydrate hydrolysis', *Green Chemistry*, **16**, 836–843 (2014).

54. Kumar S. G., Rao K. S. R. K., 'Zinc oxide based photocatalysis: Tailoring surface-bulk structure and related interfacial charge carrier dynamics for better environmental applications', *RSC Advances*, **5**, 3306–3351 (2015).

55. Wang Y., Wang Q., Zhan X., Wang F., Safdar M., He J., 'Visible light driven type II heterostructures and their enhanced photocatalysis properties: A review', *Nanoscale*, **5**, 8326–8339 (2013).

56. Liu Y., Yu L., Hu Y., Guo C., Zhang F., Wen Lou X., 'A magnetically separable photocatalyst based on nest-like $\gamma$-$Fe_2O_3$/ZnO double-shelled hollow structures with enhanced photocatalytic activity', *Nanoscale*, **4**, 183–187 (2012).

57. Hsu Y. K., Chen Y. C., Lin Y. G., 'Novel ZnO/$Fe_2O_3$ core–shell nanowires for photoelectrochemical water splitting', *ACS Applied Materials and Interfaces*, **7**, 14157–14162 (2015).

58. Zhang J., Liu X., Wang L., Yang T., Guo X., Wu S., Wang S., Zhang S., 'Synthesis and gas sensing properties of $\alpha$-$Fe_2O_3$@ZnO core-shell nanospindles.', *Nanotechnology*, **22**, 185501/1–185501/7 (2011).

59. Guskos N., Glenis S., Zolnierkiewicz G., Typek J., Sibera D., Kaszewski J., Moszyński

D., Łojkowski W., Narkiewicz U., 'Magnetic study of $Fe_2O_3$/ZnO nanocomposites', *Physica B: Condensed Matter*, **405**, 4054–4058 (2010).

60. Qin L., Zhu Q., Li G., Liu F., Pan Q., 'Controlled fabrication of flower–like ZnO–$Fe_2O_3$ nanostructured films with excellent lithium storage properties through a partly sacrificed template method', *Journal of Materials Chemistry*, **22**, 7544–7550 (2012).

61. Reda S. M., 'Synthesis of ZnO and $Fe_2O_3$ nanoparticles by sol–gel method and their application in dye-sensitized solar cells', *Materials Science in Semiconductor Processing*, **13**, 417–425 (2010).

62. Lee J., Mulmi S., Thangadurai V., Park S. S., 'Magnetically aligned iron oxide/gold nanoparticle-decorated carbon nanotube hybrid structure as a humidity sensor', *ACS Applied Materials and Interfaces*, **7**, 15506−15513 (2015).

63. Maya-Treviño M. L., Guzmán-Mar J. L., Hinojosa-Reyes L., Ramos-Delgado N. A., Maldonado M. I., Hernández-Ramírez A., 'Activity of the ZnO-$Fe_2O_3$ catalyst on the degradation of Dicamba and 2,4-D herbicides using simulated solar light', *Ceramics International*, **40**, 8701–8708 (2014).

64. Hernández A., Maya L., Sánchez-Mora E., Sánchez E. M., 'Sol-gel synthesis, characterization and photocatalytic activity of mixed oxide ZnO-$Fe_2O_3$', *Journal of Sol-Gel Science and Technology*, **42**, 71–78 (2007).

65. Yin Q., Qiao R., Zhu L., Li Z., Li M., Wu W., 'α-$Fe_2O_3$ decorated ZnO nanorod-assembled hollow microspheres: Synthesis and enhanced visible-light photocatalysis', *Materials Letters*, **135**, 135–138 (2014).

66. Abdullah Mirzaie R., Kamrani F., Anaraki Firooz A., Khodadadi A. A., 'Effect of α-$Fe_2O_3$ addition on the morphological, optical and decolorization properties of ZnO nanostructures', *Materials Chemistry and Physics*, **133**, 311–316 (2012).

67. Liu Y., Sun L., Wu J., Fang T., Cai R., Wei A., 'Preparation and photocatalytic activity of ZnO/$Fe_2O_3$ nanotube composites', *Materials Science and Engineering: B*, **194**, 9–13 (2015).

68. Fu R., Wang W., Han R., Chen K., 'Preparation and characterization of γ-$Fe_2O_3$/ZnO composite particles', *Materials Letters*, **62**, 4066–4068 (2008).

69. Si S., Li C., Wang X., Peng Q., Li Y., '$Fe_2O_3$/ZnO core-shell nanorods for gas sensors',

*Sensors and Actuators, B: Chemical*, **119**, 52–56 (2006).

70. Balti I., Smiri L. S., Rabu P., Gautron E., Viana B., Jouini N., 'Synthesis and characterization of rod-like ZnO decorated with γ-Fe$_2$O$_3$ nanoparticles monolayer', *Journal of Alloys and Compounds*, **586**, S476–S482 (2014).

71. Zhou X., Xiao Y., Wang M., Sun P., Liu F., Liang X., Li X., Lu G., 'Highly enhanced sensing properties for ZnO nanoparticle-decorated round-edged α-Fe$_2$O$_3$ hexahedrons', *ACS Applied Materials and Interfaces*, **7**, 8743–8749 (2015).

72. Chu X. Y., Hong X., Zhang X. T., Zou P., Liu Y. C., 'Heterostructures of ZnO microrods coated with iron oxide nanoparticles', *The Journal of Physical Chemistry C*, **112**, 15980–15984 (2008).

73. Mo M., Ma T., Jia L., Peng L., Guo X., Ding W., 'Ferric oxide and ZnFe$_2$O$_4$ nanotubes derived from nano ZnO/FeO$_x$ core/shell structures', *Materials Letters*, **63**, 2233–2235 (2009).

74. Chandraiahgari C. R., De Bellis G., Ballirano P., Balijepalli S. K., Kaciulis S., Caneve L., Sarto F., Sarto M. S., 'Synthesis and characterization of ZnO nanorods with a narrow size distribution', *RSC Advances*, **5**, 49861–49870 (2015).

75. Ayyappan S., Gnanaprakash G., Panneerselvam G., Antony M. P., Philip J., 'Effect of surfactant monolayer on reduction of Fe$_3$O$_4$ nanoparticles under vacuum', *Journal of Physical Chemistry C*, **112**, 18376–18383 (2008).

76. Jayanthi S. A., Nathan D. M. G. T., Jayashainy J., Sagayaraj P., 'A novel hydrothermal approach for synthesizing α-Fe$_2$O$_3$, γ-Fe$_2$O$_3$ and Fe$_3$O$_4$ mesoporous magnetic nanoparticles', *Materials Chemistry and Physics*, **162**, 316–325 (2015).

77. Teja A. S., Koh P. Y., 'Synthesis, properties, and applications of magnetic iron oxide nanoparticles', *Progress in Crystal Growth and Characterization of Materials*, **55**, 22–45 (2009).

78. Morales M. P., Verdangure S. V., Montero M. I., Serna C. J., Roig A., Casas L., Martinez B., Sandiumenge F., 'Surface and internal spin canting in γ-Fe$_2$O$_3$ nanoparticles', *Chemistry of Materials*, **11**, 3058–3064 (1999).

79. Maiti D., Mukhopadhyay S., Chandra Mohanta S., Saha A., Sujatha Devi P., 'A multifunctional nanocomposite of magnetic γ-Fe$_2$O$_3$ and mesoporous fluorescent ZnO',

*Journal of Alloys and Compounds*, **653**, 187–194 (2015).

80. Maity D., Agrawal D. C., 'Synthesis of iron oxide nanoparticles under oxidizing environment and their stabilization in aqueous and non-aqueous media', *Journal of Magnetism and Magnetic Materials*, **308**, 46–55 (2007).

81. Suresh R., Giribabu K., Manigandan R., Stephen A., Narayanan V., 'Fabrication of Ni–Fe$_2$O$_3$ magnetic nanorods and application to the detection of uric acid', *RSC Advances*, **4**, 17146–17155 (2014).

82. Song Y. B., Song X. D., Cheng C. J., Zhao Z. G., 'Poly(4-styrenesulfonic acid-co-maleic acid)-sodium-modified magnetic reduced graphene oxide for enhanced adsorption performance toward cationic dyes', *RSC Advances*, **5**, 87030–87042 (2015).

83. Saffari J., Mir N., Ghanbari D., Khandan-Barani K., Hassanabadi A., Hosseini-Tabatabaei M. R., 'Sonochemical synthesis of Fe$_3$O$_4$/ZnO magnetic nanocomposites and their application in photo-catalytic degradation of various organic dyes', *Journal of Materials Science: Materials in Electronics*, **26**, 9591–9599 (2015).

84. Wu H., Wang L., 'Phase transformation-induced crystal plane effect of iron oxide micropine dendrites on gaseous toluene photocatalytic oxidation', *Applied Surface Science*, **288**, 398–404 (2014).

85. Wu P., Du N., Zhang H., Jin L., Yang D., 'Functionalization of ZnO nanorods with γ-Fe$_2$O$_3$ nanoparticles: Layer-by-layer synthesis, optical and magnetic properties', *Materials Chemistry and Physics*, **124**, 908–911 (2010).

86. Wilson J. L., Poddar P., Frey N. A., Srikanth H., Mohomed K., Harmon J. P., Kotha S., Wachsmuth J., 'Synthesis and magnetic properties of polymer nanocomposites with embedded iron nanoparticles', *Journal of Applied Physics*, **95**, 1439–1443 (2004).

87. Zhang S., Ren F., Wu W., Zhou J., Xiao X., Sun L., Liu Y., Jiang C., 'Controllable synthesis of recyclable core-shell γ-Fe$_2$O$_3$@SnO$_2$ hollow nanoparticles with enhanced photocatalytic and gas sensing properties.', *Physical Chemistry Chemical Physics*, **15**, 8228–8236 (2013).

88. Ma J., Wang K., Zhan M., 'Growth mechanism and electrical and magnetic properties of Ag–Fe$_3$O$_4$ core–shell nanowires', *ACS Applied Materials and Interfaces*, **7**, 16027–16039 (2015).

89. Nadeem K., Krenn H., Traussnig T., Würschum R., Szabó D. V., Letofsky-Papst I., 'Effect of dipolar and exchange interactions on magnetic blocking of maghemite nanoparticles', *Journal of Magnetism and Magnetic Materials*, **323**, 1998–2004 (2011).

90. Liu S., Ma C., 'Synthesis and characterization of flower-like NiCoP/ZnO composites', *New Journal of Chemistry*, **39**, 6332–6337 (2015).

91. Mikhaylova M., Kim D. K., Bobrysheva N., Osmolowsky M., Semenov V., Tsakalakos T., Muhammed M., 'Superparamagnetism of magnetite nanoparticles: Dependence on surface modification', *Langmuir*, **20**, 2472–2477 (2004).

92. Laurent S., Forge D., Port M., Roch A., Robic C., Elst L. V, Muller R. N., 'Magnetic iron oxide nanoparticles: Synthesis, stabilization, vectorization, physicochemical characterizations, and biological applications', *Chemical Reviews*, **110**, 2064–2110 (2008).

93. Mashlan M., Zboril R., Machala L., Vujtek M., Walla J., Nomura K., 'Mössbauer spectroscopy in study of thermally induced crystallization of amorphous $Fe_2O_3$ nanoparticles', *Journal of Metastable and Nanocrystalline Materials*, **20-21**, 641–647 (2004).

94. Mukherjee S., Pal A. K., Bhattacharya S., Chattopadhyay S., 'Field-induced spin–flop transitions of interacting nanosized $\alpha$-$Fe_2O_3$ particles dispersed in a silica glass matrix', *Journal of Physics: Condensed Matter*, **20**, 055204/1–055204/12 (2008).

95. Bødker F., Hansen M., Koch C., Lefmann K., Mørup S., 'Magnetic properties of hematite nanoparticles', *Physical Review B*, **61**, 6826–6838 (2000).

96. Sreeja V., Joy P. A., 'Microwave-hydrothermal synthesis of $\gamma$-$Fe_2O_3$ nanoparticles and their magnetic properties', *Materials Research Bulletin*, **42**, 1570–1576 (2007).

97. Zysler R. D., Fiorani D., Testa A. M., 'Investigation of magnetic properties of interacting $Fe_2O_3$ nanoparticles', *Journal of Magnetism and Magnetic Materials*, **224**, 5–11 (2001).

98. Amin N., Arajs S., 'Morin temperature of annealed submicronic $\alpha$-$F_2O_3$ particles', *Physical Review B*, **35**, 4810–4811 (1987).

99. Machala L., Zboril R., Gedanken A., 'Amorphous iron(III) oxides-A review', *The Journal of Physical Chemistry B*, **111**, 4003–4018 (2007).

100. Chen Y. J., Zhang F., Zhao G. G., Fang X. Y., Jin H. B., Gao P., Zhu C. L., Cao M. S., Xiao G., 'Synthesis, multi-nonlinear dielectric resonance, and excellent electromagnetic absorption characteristics of $Fe_3O_4$/ZnO core/shell nanorods', *Journal of Physical Chemistry C*, **114**, 9239–9244 (2010).

101. Si S., Li C., Wang X., Yu D., Peng Q., Li Y., 'Magnetic monodisperse $Fe_3O_4$ nanoparticles', *Crystal Growth and Design*, **5**, 391–393 (2005).

102. Tsuzuki T., Schäffel F., Muroi M., McCormick P. G., 'Magnetic properties of mechanochemically synthesized $\gamma$-$Fe_2O_3$ nanoparticles', *Journal of Alloys and Compounds*, **509**, 5420–5425 (2011).

103. Wu W., Jiang C., Roy V. A. L., 'Recent progress in magnetic iron oxide–semiconductor composite nanomaterials as promising photocatalysts', *Nanoscale*, **7**, 38–58 (2015).

104. Woo K., Hong J., Choi S., Lee H., Ahn J., Kim C. S., Lee S. W., 'Easy synthesis and magnetic properties of iron oxide nanoparticles', *Chemistry of Materials*, **16**, 2814–2818 (2004).

# CHAPTER 6

## *Applications of Nanocomposites*

**Applications of Nanocomposites**

Nanocomposites have been widely studied because of their potential applications in environmental remediation [1,2], energy storage [3], sensors [4,5], catalysis [6] and biological applications [7,8]. In the present study, various applications such as oxidation of styrene, photocatalytic degradation of rhodamine B (RhB) and congo red (CR), and photocatalytic reduction of Cr(VI) using the synthesized nanocomposites have been demonstrated (Scheme 6.1).
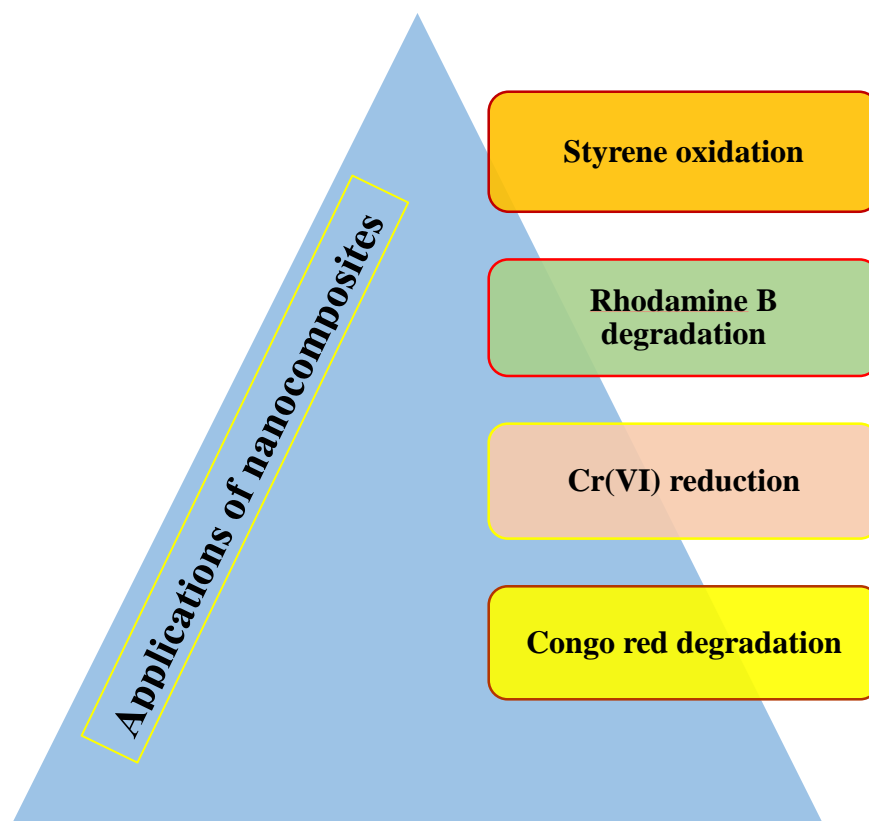


**Scheme 6.1:** Different applications studied using the nanocomposites prepared in the present study.

## 6.1 Styrene Oxidation

### 6.1.1 Introduction

Heterogeneous catalysis has advantages such as reuse of catalysts and easy separation of catalyst from the products [6,9]. Functionalization of hydrocarbons by catalytic oxidation of C-H bond to form oxygenated products under mild conditions is a major challenge now a days. This route provides key to the formation of oxygenated chemicals and pharmaceuticals [10]. Catalytic oxidation of styrene is useful from both academic and commercial point of view for

the synthesis of styrene oxide [11]. Styrene oxide, the product of oxidation, is an important intermediate for a large variety of fine chemicals [12]. Conventionally, oxidation of styrene is carried out using stoichiometric quantities of organic peracids as the oxidant [13]. However, peracids are expensive and hazardous, with poor selectivity for styrene oxide with undesirable side products. A few studies have been reported recently for greener epoxidation of styrene using safer oxidizing agents (e.g. *tert*-butyl hydroperoxide (TBHP) and hydrogen peroxide) and easily separable solid catalysts. The examples for the latter include NiO, CoO, and $MoO_3$ nanoparticles [14], nanocrystalline oxides of Cu–Ni–Co on γ-alumina [15], $Fe_3O_4$ nanoparticles [16], $Ag/Mn_3O_4$ [10], gold supported transition metal oxides [17], silica supported indium oxide [18], NiCoFe spinel-type oxide [19] and metal ion doped $TiO_2$ nanoparticles [20].

### 6.1.2 Experimental Details

In the present study, oxidation of styrene by tert-butyl hydroperoxide (TBHP) in the presence of $NiO-Al_2O_3$ nanocomposites (Chapter 3) as the catalyst was studied (Scheme 6.2) [14]. The oxidation reactions were carried out under reflux conditions at 80 $^o$C in air with stirring in a 50 mL round-bottom flask on a constant temperature oil bath. Gas chromatography-mass spectrometry (GC-MS) was used for the identification and the quantification of the products. The analysis was done on a Perkin-Elmer Clarus 680 gas chromatograph coupled with a Perkin-Elmer Clarus SQ 8T mass detector. The column (Elite–5MS) used was of length 30 m, i.d.0.25 mm, film thickness 0.25 μm and temperature range 80 to 280 $^o$C. For the catalytic test, 50 mg of the catalyst and 1 mmol of styrene were added to 10 mL acetonitrile, followed by the addition of 3 mmol of TBHP. The reaction mixture was heated at 80 °C for 6 h under continuous stirring. The products of the reaction were analyzed by GC-MS.
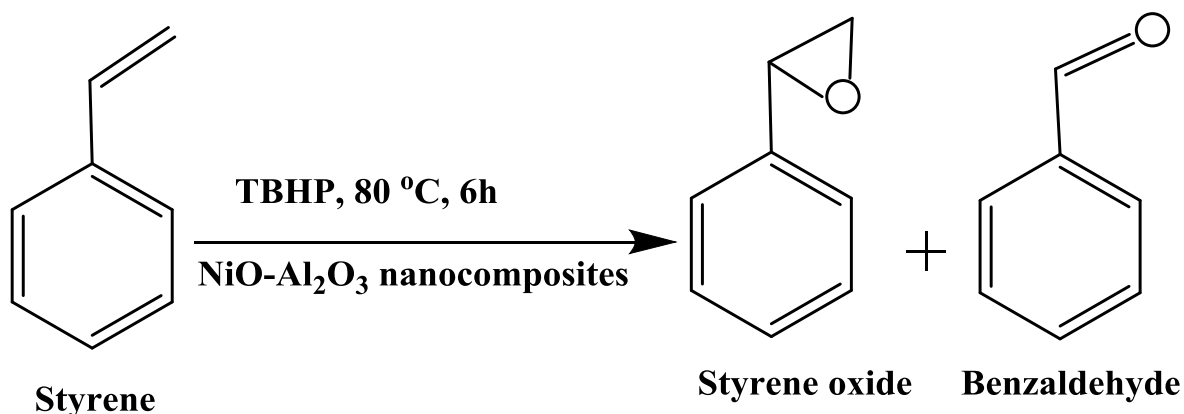


**Scheme 6.2:** Reaction products of oxidation of styrene.

### 6.1.3 Results and Discussion

The catalytic reaction was also carried out using pure NiO nanoparticles, pure $Al_2O_3$ and also in the absence of the catalyst. No products were obtained when the reaction was carried out (i) using pure alumina, (ii) in the absence of catalyst and (iii) in the absence of TBHP. The results on the epoxidation of styrene using the NiO-$Al_2O_3$ nanocomposites are given in Table 6.1.

**Table 6.1:** Results on the epoxidation of styrene by TBHP using NiO-$Al_2O_3$ nanocomposites as the catalyst. For more details on the nanocomposites, see Table 3.2.

| Sl. No. | Catalyst | Styrene oxide (%) | Benzaldehyde (%) | Total conversion (%) | Surface area ($m^2/g$) |
|---------|----------|-------------------|------------------|----------------------|------------------------|
| 1. | NiO nanoparticles | 10.8 | 28.3 | 39.1 | 25.4 |
| 2. | LN1 $[Ni^{2+}]:[Al^{3+}]$ = 0.5:1 | 52.0 | 8.2 | 60.2 | 336.7 |
| 3. | LN2 $[Ni^{2+}]:[Al^{3+}]$ = 1:1 | 4 | 18.5 | 22.5 | 293.7 |
| 4. | LN3 $[Ni^{2+}]:[Al^{3+}]$ = 2:1 | 6 | 21.8 | 27.8 | 216.6 |

From Table 6.1, one can conclude that the NiO-$Al_2O_3$ nanocomposite LN1 shows a total conversion of 60.2%, with a selectivity (selectivity (%) of a product = (concentration of product/total concentration of all products) $\times$ 100) for styrene oxide of 86.3% in a reaction time of 6 h. Ren et al. [21] have reported 69% of conversion of styrene with 78.2% selectivity for styrene oxide in a reaction time of 21 h. Choudhary et al. have reported NiO-$SiO_2$ and NiO-$Al_2O_3$ as the catalysts in the epoxidation of styrene. They obtained a total conversion of 48.8% and selectivity of 77.7% for styrene oxide by NiO-$SiO_2$. Using NiO-$Al_2O_3$, total conversion of 55.2% and selectivity of 52.2% for styrene oxide was obtained in a reaction time of 3 h [14].

### 6.1.3.1 Mechanism of styrene oxidation

Ghosh et al. [22] have explained the factors that contribute to good conversion and selectivity of styrene oxide. Solid catalysts containing transition metals act as solid Lewis acids. The Lewis acids catalyze oxidation reactions by forming acid-base adducts either with the substrate or with the oxidizing agent (in the present study, TBHP) enhancing their reactivity and selectivity towards styrene oxide [23]. The nanocomposite LN1 shows maximum conversion and selectivity for styrene oxide compared to pure NiO nanoparticles and the other two nanocomposites (LN1 and LN2). Nanocomposite LN1 has a higher surface area ($336.7 \ m^2/g$) compared to that of pure NiO nanoparticles, alumina and the other two nanocomposites (LN2 and LN3). TEM results and EDX analysis of nanocomposite LN1 show uniform dispersion of NiO nanoparticles over alumina (Chapter 3, Fig. 3.7 and Table 3.3). Due to this, nanocomposite LN1 adsorbs more styrene molecules and provides more actives sites for the epoxidation of styrene compared to the other nanocomposites. NiO possesses surface acid sites which will form acid-base adducts with the oxidizing agent (TBHP) enhancing the selectivity towards styrene oxide [23,24]. The alumina support provides mechanical strength to the NiO nanoparticles as well as increases the effective surface area.

## 6.2 Photocatalytic Degradation of Rhodamine B

### 6.2.1 Introduction

Dyes are organic pollutants and their release as waste in the environment is source of noticeable pollution and have adverse effect on aquatic life [25]. Most of the dyes are resistant to biodegradation and direct photolysis, and N-containing dyes such as rhodamine B (RhB) undergo self-reductive degradation to produce carcinogenic aromatic amines. Rhodamine B is a common dye used extensively in textile, printing, food, and cosmetic industries [26]. RhB belongs to the triphenylmethane family, which contains four N-ethyl groups at either side of the xanthene ring (Scheme 6.3) [26]. In the present study, photodegradation of rhodamine B was carried out using $CdS\text{-}TiO_2$ (Chapter 4) and $Ag_2S\text{-}TiO_2$ (Chapter 4) nanocomposites as the photocatalysts.
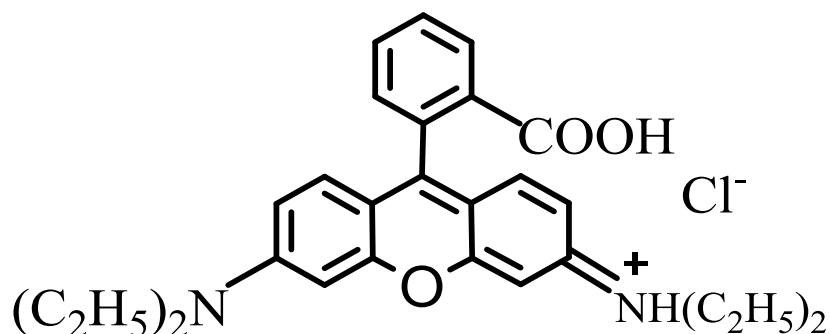
**Scheme 6.3:** Chemical structure of rhodamine B.

### 6.2.2 Photocatalytic degradation of rhodamine B by CdS-TiO₂ nanocomposites

### 6.2.2.1 Experimental Details

For the photocatalysis experiments, about 0.1 g each of CdS–TiO$_2$ nanocomposite powders was dispersed in 100 mL of aqueous rhodamine B solution ($10^{-5}$ M). The mixture was sonicated for 10 minutes and kept for 30 minutes in dark in order to reach adsorption–desorption equilibrium. The contents were irradiated under sunlight at room temperature for various time intervals (0 to 120 minutes) (Scheme 6.4). After periodic time intervals, 5 mL of the reaction mixture was taken and centrifuged to remove the dispersed photocatalyst. The concentration of rhodamine B was analyzed by checking the absorbance of the supernatant solution at 553 nm using a UV–visible spectrophotometer (Shimadzu UV–2450). Pure CdS nanoparticles and TiO$_2$ were also used as the catalysts to compare their photocatalytic activity with that of the CdS–TiO$_2$ nanocomposites.

```
┌─────────────────────────┐        ┌─────────────────────────┐
│      100 mL aqueous     │  ┌┴┐    │                         │
│  solution of RhB (1×10⁻⁵)│  ╪ ╪   │     Catalyst (0.1 g)    │
│                         │  └┬┘    │                         │
└────────────┬────────────┘        └─────────────────────────┘
             │
             │  Sonication for 10 min
             ▼
   ┌─────────────────────┐
   │  Dispersed catalyst in │
   │       aq. RhB       │
   └──────────┬──────────┘
              │
              │  Sunlight irradiation for different
              │   time intervals (0 to 120 min)
              ▼
   ┌─────────────────────┐
   │    Photodegraded    │
   │      products       │
   └─────────────────────┘
```
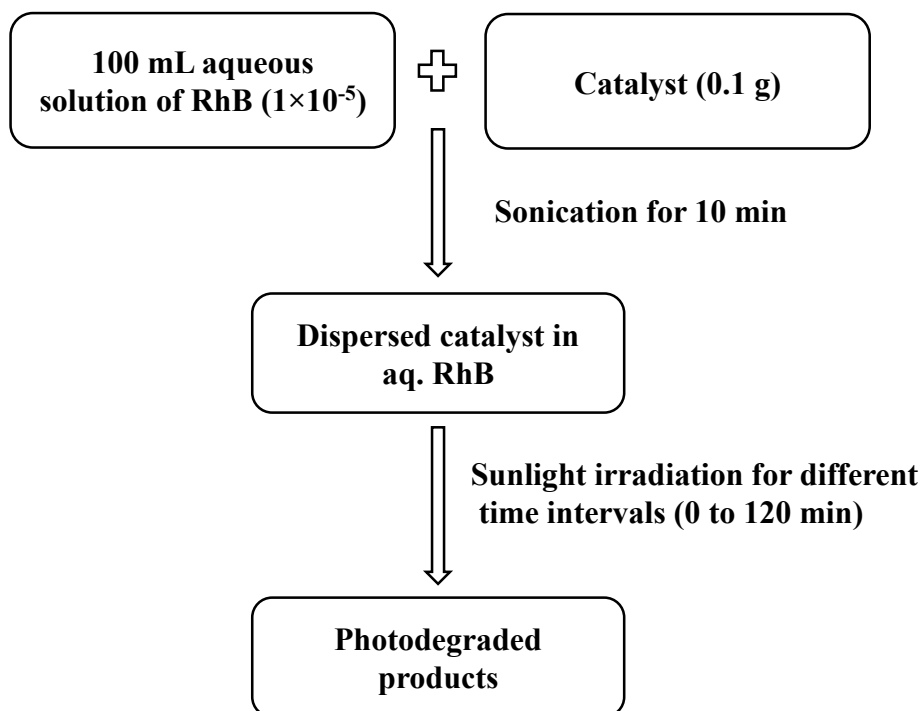
**Scheme 6.4:** Experimental steps involved in photocatalytic degradation of rhodamine B.

## 6.2.2.2 Results and Discussion

Fig. 6.1(a) shows the UV–visible spectral results on the photodegradation of rhodamine B by pure CdS nanoparticles and all the CdS-TiO$_2$ nanocomposites prepared using different TiO$_2$ samples (See Table 4.2). Nanocomposite CT4 shows maximum degradation of rhodamine B compared to pure CdS and the other nanocomposites. Fig. 6.1(b) and 6.1(c) show the kinetics of degradation of rhodamine B in the presence of pure CdS nanoparticles and sol-gel TiO$_2$ nanoparticles calcined at 500 °C, respectively. In the case of pure CdS, it can be seen that the absorption band at 553 nm is blue-shifted to 498 nm and in the case of sol–gel TiO$_2$ nanoparticles calcined at 500 °C, the intensity of absorption band at 553 nm decreases with increase in irradiation time but without any shift. Fig. 6.1(d) shows the kinetics of degradation of rhodamine B using CdS–TiO$_2$ nanocomposite CT4 as the catalyst. It can be seen that the absorption band at 553 nm is blue shifted to 498 nm. The absorbance decreases with irradiation time, and almost completely disappears after 120 minutes.
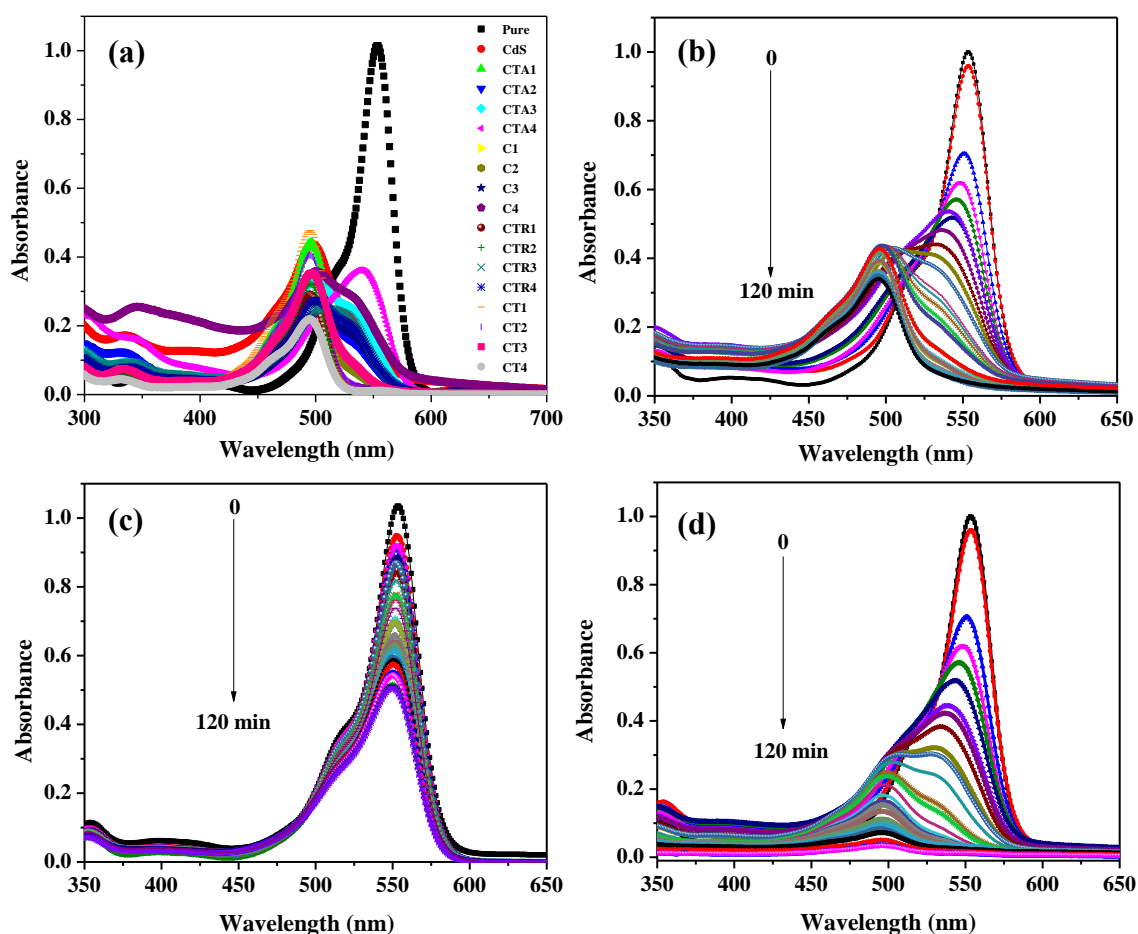
**Fig. 6.1:** (a) UV-visible spectra indicating the photodegradation of rhodamine B using pure CdS, TiO$_2$ nanoparticles and all the CdS–TiO$_2$ nanocomposites, (b) kinetic study of photodegradation of rhodamine B by CdS nanoparticles, (c) kinetic study for photodegradation of rhodamine B by TiO$_2$ nanoparticles calcined at 500 $^o$C, and (d) kinetic study for photodegradation of rhodamine B by CdS-TiO$_2$ nanocomposite CT4.

On the other hand, pure CdS and TiO$_2$ nanoparticles calcined at 500 $^o$C are unable to complete the degradation of rhodamine B in 120 min of irradiation (Fig. 6.2(a)). The photocatalytic degradation of rhodamine B by different photocatalysts under visible light irradiation follows pseudo-first-order kinetics with respect to the concentration of rhodamine B [55]; the plot of $-\ln (C_t/C_0)$ versus time yields a straight line with slope k (Fig. 6.2(b)) where $C_t$ and $C_0$ are the rhodamine B concentrations at time t = t and t = 0, respectively and k is the rate constant. The rate constant for rhodamine B degradation using CdS–TiO$_2$ nanocomposite CT4 is 0.06 min$^{-1}$ which is higher than the corresponding values for pure CdS (0.027 min$^{-1}$) and pure TiO$_2$ (0.0057 min$^{-1}$). Besides higher photocatalytic activity, the CdS-TiO$_2$ nanocomposite CT4 also showed good stability and reusability towards photodegradation of rhodamine B.
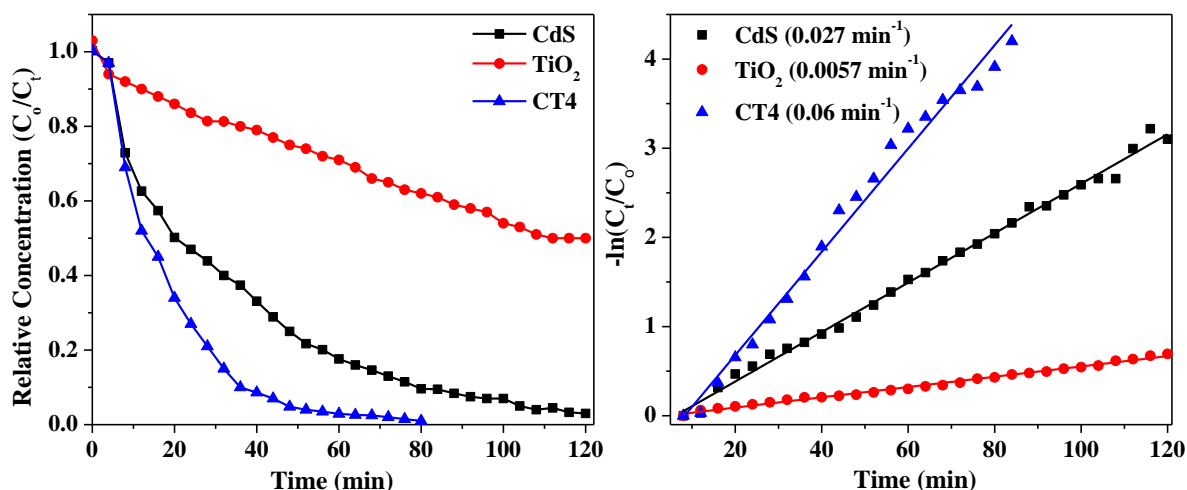
**Fig. 6.2:** (a) Comparison of photocatalytic degradation behavior of rhodamine B over pure CdS nanoparticles, $TiO_2$ and CdS-$TiO_2$ nanocomposite (CT4), and (b) pseudo-first-order kinetics of rhodamine B degradation using CdS,$TiO_2$ nanoparticles and CdS-$TiO_2$ nanocomposite (CT4) as the catalysts under visible light irradiation.

Table 6.2 lists the summary of reported results of rhodamine B photodegradation by various CdS-$TiO_2$ nanocomposites.

**Table 6.2:** Summary of reported results on the photodegradation of RhB by different CdS-$TiO_2$ nanocomposites.

| Sl. No. | Catalyst | Reaction conditions | Time required for complete degradation/ Rate constant | Reference |
|---------|----------|---------------------|------------------------------------------------------|-----------|
| 1. | CdS–$TiO_2$ heterojunctions | 100 mg of catalyst was suspended in 100 mL of RhB solution (20 mg $L^{-1}$), irradiation under 300 W Xenon lamp | 120 min | [27] |
| 2. | CdS nanocrystals decorated $TiO_2$ nanotube arrays | 50 mg of catalyst was suspended in 50 mL of RhB solution (5 mg $L^{-1}$), visible light source of 350 W Xenon lamp | 60 min/0.046 $min^{-1}$ | [28] |

| | | | | |
|---|---|---|---|---|
| 3. | CdS-TiO$_2$ nanofibers | 0.1 g catalyst in 100 mL of RhB (10 mg L$^{-1}$), visible light source of 150 W Xenon lamp | 6 h/0.011 min$^{-1}$ | [29] |
| 4. | CdS quantum dots sensitized TiO$_2$ nanotube arrays | 25 mg of catalyst was suspended in 50 mL of RhB solution (5 mg L$^{-1}$), visible light source of 500 W halogen lamp | 120 min | [30] |
| 5. | CdS-TiO$_2$ nanocomposites | 100 mg of catalyst was suspended in 100 mL of RhB solution (20 mg L$^{-1}$), visible light source of 300 W Xenon lamp | 80 min | [31] |
| 6. | CdS–TiO$_2$ heterojunctions | 50 mg of catalyst suspended in 50 mL of RhB solution (5 mg L$^{-1}$), under visible light source of 300 W Xenon lamp | 90% degradation in 30 min | [32] |
| 7. | TiO$_2$@CdS and CdS@TiO$_2$ double-shelled hollow spheres | 50 mg of catalyst suspended in 50 mL of RhB solution (10 mg L$^{-1}$), visible light source of 500 W Xenon lamp | 60 min | [33] |
| 8. | CdS–TiO$_2$ nanocomposites | 40 mg of catalyst suspended in 80 mL of RhB solution (5 mg L$^{-1}$), visible light source of 500 W halogen lamp | 94% degradation in 120 min | [34] |
| 9. | CdS@TiO$_2$ | 50 mg of catalyst suspended in 50 mL of RhB solution (10 mg L$^{-1}$), visible light source of 300 W Xenon lamp | 4h/0.021 min$^{-1}$ | [35] |
| 10. | TiO$_2$/CdS | 25 mg of catalyst dispersed in 100 mL of RhB solution (25 mg L$^{-1}$), solar light simulator (100 W cm$^{-2}$) | 60 min | [36] |

| 11. | CdS–TiO$_2$ microspheres | 50 mg of catalyst dispersed in 50 mL of RhB solution (10 mg L$^{-1}$), visible light source of 500 W Xenon lamp | 3 h | [37] |
|---|---|---|---|---|
| 12. | CdS quantum dots decorated TiO$_2$ nanotube arrays | 20 mL of RhB solution (5 mg L$^{-1}$), 300 W xenon lamp | 68.14% in 300 min /0.0033 min$^{-1}$ | [38] |
| 13. | CdS nanocrystals decorated TiO$_2$ nanotubes | 30 mL of RhB solution (5 mg L$^{-1}$), 350 W xenon lamp | 63.5% in 60 min/ 0.06476 min$^{-1}$ | [39] |
| 14. | CdS quantum dot–TiO$_2$ nanobelt | 3 mL of RhB solution (5 mg L$^{-1}$), 300 W xenon lamp | Complete degradation in 4 h/0.123 min$^{-1}$ | [40] |
| 15. | TiO$_2$/CdS hollow sphere | 70 mg of catalyst dispersed in 70 mL of RhB solution (15 mg L$^{-1}$), 300 W Xenon lamp | 94.2% in 120 min | [41] |
| 16. | CdS-TiO$_2$ nanocomposites | 100 mg of catalyst suspended in 100 mL of RhB solution (5 mg L$^{-1}$), sunlight illumination | 120 min/0.06 min$^{-1}$ | Present work |

In the reported literature, complete degradation of rhodamine B takes 30 minutes to 6 h with the highest reported rate constant of 0.123 min$^{-1}$. In the present work, complete degradation of rhodamine B takes about 120 min with a rate constant of 0.06 min$^{-1}$.

### 6.2.2.3 Mechanism of photodegradation of rhodamine B

It is proposed, in the present study, that the degradation of rhodamine B takes place by N-de-ethylation. On illumination with sunlight, electrons from the valence band of CdS get excited to its conduction band. Also, electrons transfer from the exited RhB molecules to the conduction band of CdS (Scheme 6.5) [42]. The N-de-ethylation process involves electron transfer from nitrogen atom of the excited singlet state of rhodamine B to CdS nanoparticles leading to the formation of radical cation of rhodamine B [43]. The dye radical cation

undergoes de-ethylation due to attack by one of the active oxygen species on the N-ethyl group [43,44]. A close examination of the spectral behaviour of degradation of rhodamine B by nanocomposite CT4 (Fig. 6.2(d)) suggests that RhB is de-ethylated in a stepwise manner, i.e., ethyl groups are removed one by one as confirmed by the gradual shift of absorption maximum of rhodamine B towards the blue region [45]. De-ethylation of the N, N, N′, N′-tetra ethylated rhodamine (i.e., RhB) leads to its major absorption band shifted towards the blue region (RhB ($\lambda_{max}$ = 553 nm), N, N, N′-tri-ethylated rhodamine (539 nm), N, N′-di-ethylated rhodamine (522 nm), N-ethylated rhodamine (510 nm), and rhodamine (498 nm) [43,45]. Irradiation with visible light for longer times leads to further decomposition of the de-ethylated rhodamine by destruction of chromophore as indicated by decrease in the peak intensity at 498 nm (Fig. 6.1(d)).

According to Takirawa et al. [46], the most important factor which determines the efficiency of N-dealkylation of rhodamine B is the position of the electron donating energy level of the excited RhB relative to the conduction band edge of CdS. The relative positions of the standard redox potential of the excited singlet state of rhodamine B (RhB*) is −1.09 V versus the normal hydrogen electrode [42,44,46]. CdS is an n-type semiconductor and its conduction band potential ($V_{CB}$) is about −0.7 V and its valence band potential ($V_{VB}$) is about 1.85 V [46,47]. Thus, an efficient electron transfer can occur between the excited dye (RhB*) to the conduction band of CdS (Scheme 6.5). Further, the electrons are transferred to the conduction band of $TiO_2$ nanoparticles since the $V_{CB}$ of CdS is more negative than that of $TiO_2$ (−0.5 V) [47]. The transferred electrons can be trapped by surface oxygen to give $O_2^{\bullet-}$ and active species such as $OOH^{\bullet}$ and $OH^{\bullet}$ radicals which attack N-ethyl group of the rhodamine B leading to step wise de-ethylation and further degradation.
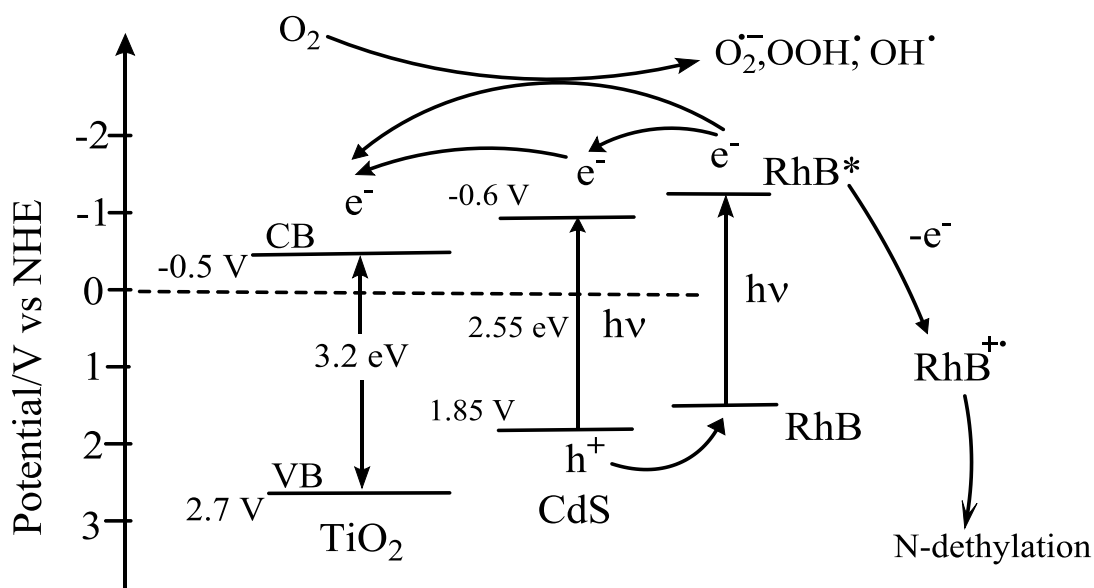
**Scheme 6.5:** Proposed mechanism for photocatalytic degradation of rhodamine B using CdS-TiO$_2$ nanocomposites as the catalyst.

### 6.2.3 Photocatalytic degradation of rhodamine B by Ag$_2$S-TiO$_2$ nanocomposites

#### 6.2.3.1 Experimental Details

Photocatalytic activity tests using the Ag$_2$S-TiO$_2$ nanocomposites (Chapter 4) were performed at room temperature. The nanocomposite powders (0.1 g each) were dispersed in 50 mL of aqueous rhodamine B solutions ($1 \times 10^{-5}$ M) in a 100 mL beaker. The mixtures were sonicated for about 10 minutes and kept for 60 minutes in dark in order to reach adsorption-desorption equilibrium. The contents were irradiated in sunlight for various time intervals (5 to 90 min) (experimental steps were same as that in scheme 6.4). After periodic time intervals, 5 mL of the reaction mixture was taken and immediately centrifuged to remove the dispersed photocatalyst. The concentration of rhodamine B in the supernatant solution was analyzed by monitoring the absorbance at 554 nm using the UV-visible spectrophotometer. Pure Ag$_2$S nanoparticles and TiO$_2$ (anatase) were also tested as the catalysts to compare their photocatalytic activity with that of the Ag$_2$S-TiO$_2$ nanocomposites.

#### 6.2.3.2 Results and Discussion

Fig. 6.3(a) shows the UV-visible spectral results on the photodegradation of rhodamine B in the aqueous solutions by pure Ag$_2$S nanoparticles, TiO$_2$ nanoparticles and all the Ag$_2$S-TiO$_2$ nanocomposites (A1-A4) (Chapter 4, Table 4.7). Nanocomposite A4 shows maximum decrease in absorbance indicating higher activity compared to pure Ag$_2$S, TiO$_2$ and the other

nanocomposites (A1, A2, A3). Detailed kinetic study was carried out using nanocomposite A4 (Fig. 6.3(b)) by monitoring the absorbance at 554 nm with irradiation time. The absorption band due to rhodamine B almost completely disappears after 90 min of irradiation, whereas $Ag_2S$ and $TiO_2$ nanoparticles are unable to complete the degradation in the same time period (Fig 6.3(c)). The photocatalytic degradation of rhodamine B by different photocatalysts under visible light follows pseudo-first-order kinetics with respect to the concentration of rhodamine B [48,49].

$$-\ln\left(\frac{C_t}{C_o}\right) = k_t t$$

The plot of $-\ln(C_t/C_0)$ versus time (t) yields a straight line with slope $k_t$ (Fig 6 (d)) where $C_t$ and $C_0$ are the rhodamine B concentrations at times t and zero, respectively, and $k_t$ is the rate constant. The rate constant for rhodamine B degradation using $Ag_2S$-$TiO_2$ nanocomposite A4 is $3.7\times10^{-2}$ $min^{-1}$ which is higher than the values of $k_t$ obtained using pure $Ag_2S$ ($1.3\times10^{-2}$ $min^{-1}$) and pure $TiO_2$ ($6.6\times10^{-3}$ $min^{-1}$) as the catalysts.
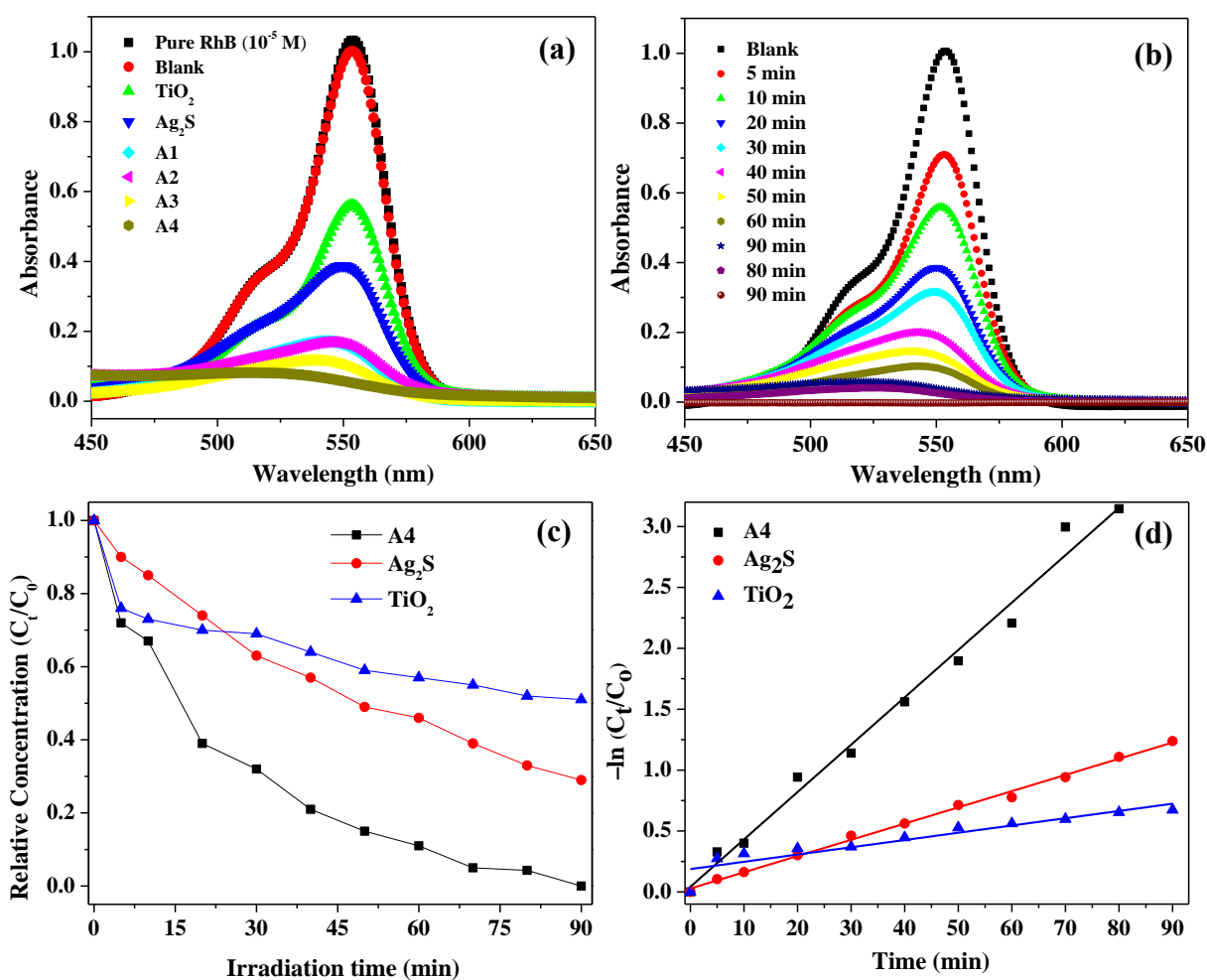
**Fig. 6.3:** (a) UV-visible spectra indicating the photodegradation of rhodamine B using pure Ag$_2$S, TiO$_2$ calcined at 500 °C and the Ag$_2$S-TiO$_2$ nanocomposites (A1-A4), (b) kinetic study of photodegradation of rhodamine B by nanocomposite A4, (c) comparison of photocatalytic degradation behavior of rhodamine B over pure Ag$_2$S, TiO$_2$ and Ag$_2$S-TiO$_2$ nanocomposite (A4), and (d) pseudo-first-order kinetics of rhodamine B degradation using TiO$_2$, Ag$_2$S and Ag$_2$S-TiO$_2$ nanocomposite (A4) as the catalysts.

Zhu et al. have reported the photodegradation of rhodamine B under UV and visible light illumination using MWCNT/Ag$_2$S-TiO$_2$ nanocomposites as the catalyst [48]. They have compared the photodegradation efficiencies using pure TiO$_2$, Ag$_2$S/TiO$_2$, CNT/TiO$_2$, and Ag$_2$S-TiO$_2$/CNT as the catalysts. The Ag$_2$S-TiO$_2$/CNT nanocomposite shows a higher efficiency compared to Ag$_2$S/TiO$_2$, CNT/TiO$_2$, and pure TiO$_2$. The authors have reported complete photodegradation of rhodamine B under visible light illumination in 160 min with a rate constant of $3.18 \times 10^{-3}$ min$^{-1}$. In the present study, the Ag$_2$S-TiO$_2$ nanocomposite A4 shows complete degradation of rhodamine B under sunlight in about 90 minutes with a rate constant

of $3.7 \times 10^{-2}$ min$^{-1}$ which is better compared to the reported results. From FE-SEM, TEM and EDX analyses (Chapter 4, Section 4.2.3) it was found that $Ag_2S$-$TiO_2$ nanocomposite A4 has uniform distribution of smaller silver sulphide nanoparticles ($8.8 \pm 1.9$ nm) over the $TiO_2$ matrix. The nanocomposite A4 possesses the highest surface area ($54.5$ m$^2$/g) among the nanocomposites ( A1, A2, A3 and A4, Chapter 4, Section 4.2.3.5) and hence possesses more active adsorption sites for rhodamine B, which improves the photocatalytic activity [49,50]. The mechanism of photocatalytic degradation of rhodamine B is given below.

### 6.2.3.3 Mechanism of photodegradation of rhodamine B

Photocatalytic degradation of rhodamine B dye is reported to takes place by two pathways (I and II) as shown in Scheme 6.6. On illumination with sunlight, electrons from the valence band of $Ag_2S$ get excited to its conduction band. Since the conduction band of $TiO_2$ is more positive than that of $Ag_2S$, electrons from the conduction band of $Ag_2S$ get transferred to the conduction band of $TiO_2$ [51]. As a result of this, there is less recombination of electrons and holes. The photogenerated electrons on irradiated $Ag_2S$ react with the surface adsorbed $O_2$ molecules to yield the $O_2^{\bullet-}$ radical anions which on protonation yields $HO_2^{\bullet-}$ radicals. The holes in the valence band of $Ag_2S$ become trapped as surface bound $OH^{\bullet}$ radicals due to oxidation of the surface hydroxyl groups or $H_2O$ molecules [44,48,52]. On illumination with sunlight, photooxidation of rhodamine B (RhB) takes place leading to the formation of radial cation (RhB$^{\bullet+}$). In pathway I, the degradation occurs by de-ethylation of RhB$^{\bullet+}$ because of attack by one of the active oxygen species ($O_2^{\bullet-}$, $HO_2^{\bullet-}$, $OH^{\bullet}$) on the N-ethyl group leading to the formation of de-ethylated intermediates (N,N,N′-tri-ethylated rhodamine, N,N′-di-ethylated rhodamine, N-ethylated rhodamine and rhodamine) with different absorption maxima [26,44,52] (as discussed in Section 6.2.2.4). Another pathway II involves the degradation of rhodamine B chromophore because of attack by $OH^{\bullet}$ radicals on its chromophoric structure leading to rapid decrease in the absorption intensity of rhodamine B at 554 nm [44,52]. Destruction of conjugated chromophore structure leads to the formation of intermediates (organic acids and various alcohols) and finally to $CO_2$ and $H_2O$ [26]. In the case of photocatalytic degradation of rhodamine B by $Ag_2S$-$TiO_2$ nanocomposite A4, in addition to decrease in the intensity, the absorption maximum ($\lambda_{max} = 554$ nm) shifts by about 25 nm (Fig. 6.3(b)). In the present study, it is proposed that both the pathways (de-ethylation as well as the destruction of the conjugated chromophore structure of rhodamine B) take place simultaneously.
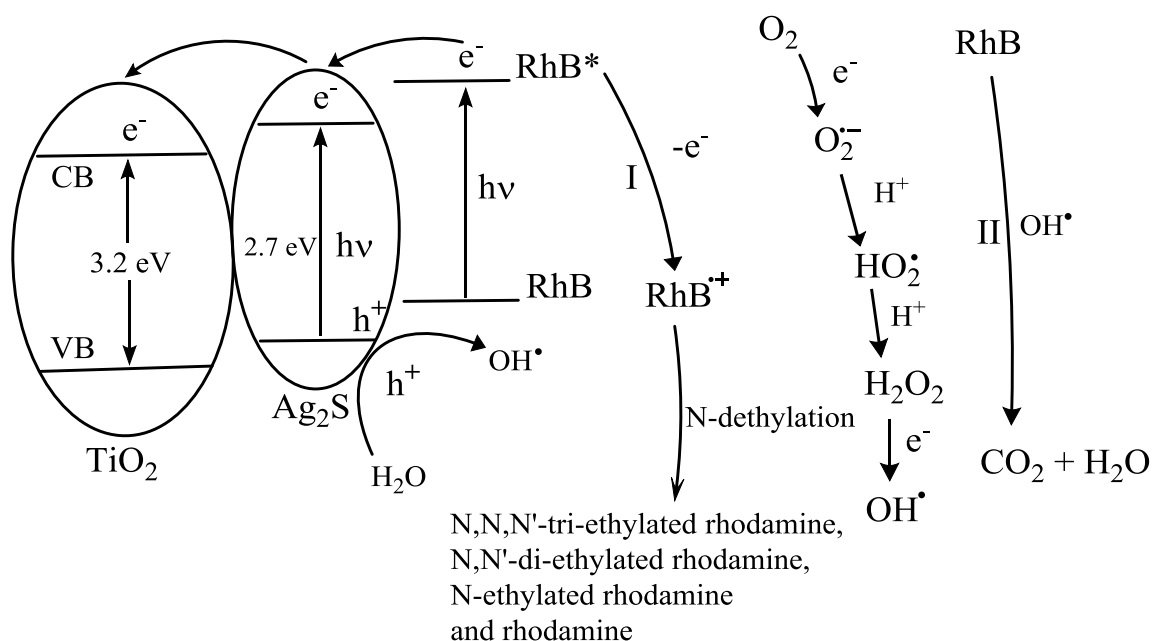
**Scheme 6.6:** Proposed mechanism for photocatalytic degradation of rhodamine B using $Ag_2S$-$TiO_2$ nanocomposites as the catalyst.

## 6.3 Photocatalytic reduction of Cr(VI)

### 6.3.1 Introduction

Water pollution by heavy metals like Cr(VI), As(V), Pb(II) is posing great threat to human health due to its hazardous effect [53]. Chromium is widely use in chemical industries for electroplating, leather tanning and painting [54]. Hexavalent chromium is highly toxic and carcinogenic and hence it is important to develop methods for the removal Cr(VI) from waste water [55]. Various methods have been used for the removal of heavy metal ions such as ion exchange, membrane separation, catalytic reduction and adsorption [56]. Among the above, catalytic reduction is an attractive method due to its simplicity and high efficiency. In present study, CdS-$TiO_2$ nanocomposites (Chapter 4) were used as photocatalyst for the reduction of Cr(VI) into less harmful Cr(III).

### 6.3.2 Experimental Details

The CdS-$TiO_2$ nanocomposites prepared using sol-gel $TiO_2$ nanoparticles calcined at 500 °C (CT1-CT4) showed better catalytic activity towards the degradation rhodamine B (section 6.2.2) and hence they were tried as the catalysts towards the photoreduction of Cr(VI). About 50 mg each of the CdS-$TiO_2$ nanocomposites (CT1-CT4) was dispersed in 50 mL of Cr(VI) solution (40 mg $L^{-1}$) which was prepared by dissolving $K_2Cr_2O_7$ in deionized water. The

suspension was first stirred in the dark for 30 minutes and then exposed to sunlight for 6 min. After certain time interval, 4 mL of the suspension was taken and centrifuged to remove the dispersed photocatalyst. The supernatant solution was analyzed by recording the UV–visible spectrum (Shimadzu UV–2450). First, a series of standard aqueous solutions of potassium dichromate with known concentrations (40 mg L$^{-1}$, 30 mg L$^{-1}$, 20 mg L$^{-1}$, 10 mg L$^{-1}$ and 5 mg L$^{-1}$) were prepared and a calibration plot was made after recording the absorbance values at 370 nm. Then, the concentration of Cr(VI) in the supernatant solutions after sunlight irradiation for 6 minutes for all the samples was estimated by measuring the absorbance values at 370 nm.

### 6.3.3 Results and Discussion

Fig. 6.4(a) shows the UV–visible spectral results on the reduction of Cr(VI) into Cr(III) by CdS, TiO$_2$ and CdS-TiO$_2$ nanocomposites (CT1–CT4) in the presence of sunlight. Nanocomposite CT4 shows the maximum reduction. The catalytic reduction carried out under similar conditions but in the absence of sunlight indicated that the reduction takes place only in the presence of sunlight. Fig. 6.4(b) shows the kinetic study for the reduction of Cr(VI) into Cr(III) in the presence of CdS nanoparticles, TiO$_2$ nanoparticles and CdS-TiO$_2$ nanocomposite CT4. Nanocomposite CT4 shows complete reduction of Cr(VI) into Cr(III) in 6 minutes whereas pure CdS and TiO$_2$ nanoparticles were unable to complete the reduction during the same time interval. The photocatalytic reduction of Cr(VI) to Cr(III) by different photocatalysts under visible light follows pseudo-first-order kinetics [57]; the plot of $-\ln(C_t/C_0)$ versus times yields a straight line with slope k (Fig. 6.4(c)). The rate constant for photocatalytic reduction of Cr(VI) to Cr(III) by CdS−TiO$_2$ nanocomposite CT4 is 0.56 min$^{-1}$ which is higher than the corresponding values for pure CdS nanoparticles (0.15 min$^{-1}$) and pure TiO$_2$ (0.0056 min$^{-1}$).
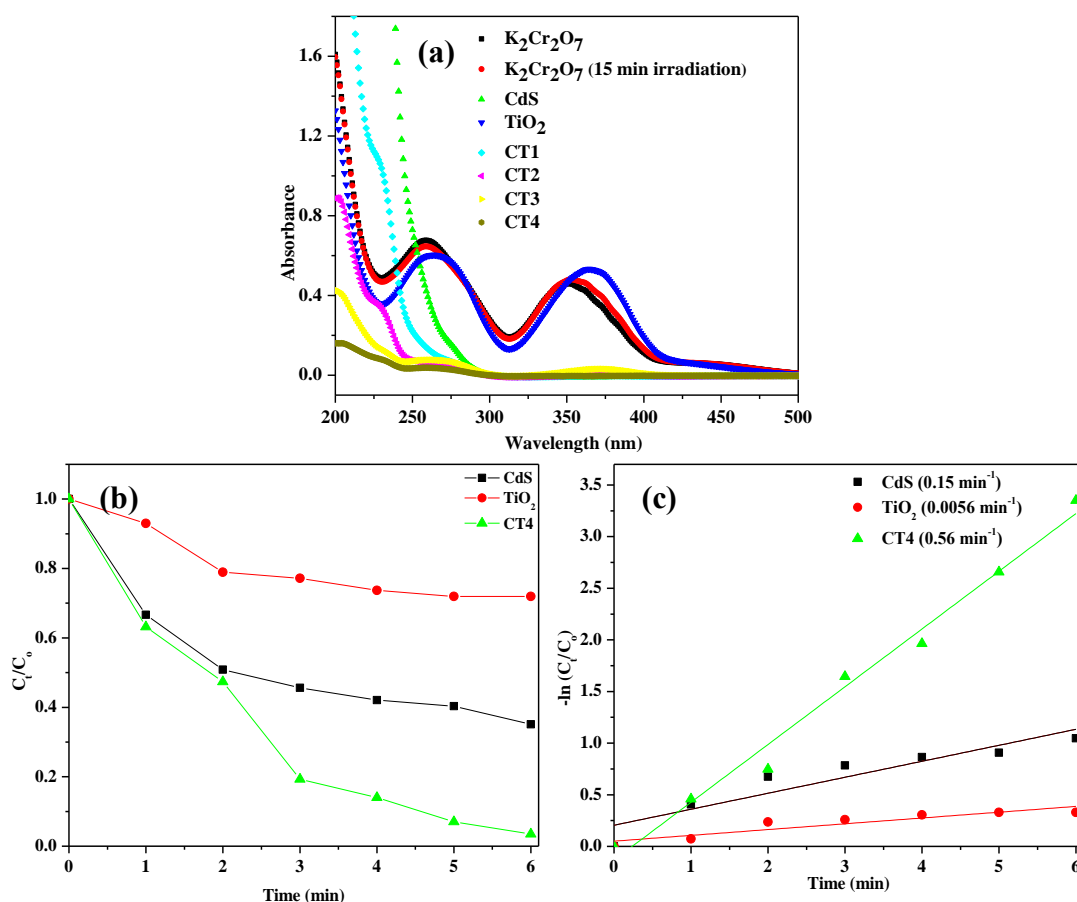
**Fig. 6.4:** (a) UV-visible spectra indicating the photocatalytic reduction of Cr(VI) to Cr(III) using pure CdS nanoparticles, TiO$_2$ nanoparticles and the CdS−TiO$_2$ nanocomposites (CT1−CT4), (b) comparison of kinetics of pure CdS nanoparticles and CdS-TiO$_2$ nanocomposite (CT4) as the catalysts under visible light irradiation, (c) pseudo-first-order kinetics for the photocatalytic reduction of Cr(VI) to Cr(III) using pure CdS nanoparticles, TiO$_2$ nanoparticles and CdS-TiO$_2$ nanocomposite (CT4).

In the present study, the initial concentration of Cr(VI) was 40 mg L$^{-1}$. After sunlight irradiation for 6 minutes, the concentration of Cr(VI) decreases to 0.26 mg L$^{-1}$ in the case of CdS-TiO$_2$ nanocomposite CT4. In the case of pure CdS nanoparticles and TiO$_2$ nanoparticles, the concentration of Cr(VI) decreases to 11.5 mg L$^{-1}$ and 30.5 mg L$^{-1}$, respectively. This clearly indicates that the CdS-TiO$_2$ nanocomposite CT4 acts as a better photocatalyst compared to pure CdS and TiO$_2$ nanoparticles. Liu et al. [58] have reported the photoreduction of Cr(VI) to Cr(III) under visible light illumination in the presence of CdS-TiO$_2$ core-shell nanocomposites. They have reported that the complete photoreduction of Cr(VI) occurs in 30 minutes. Liu et al. [57] have reported photocatalytic reduction of Cr(VI) to Cr(III) in the presence of CdS quantum

dots sensitized $TiO_2$ films. They have reported 93% photocatalytic reduction of Cr(VI) in 240 minutes with a rate constant of 0.011 min$^{-1}$. Chen et al. [59] have reported photocatalytic reduction of Cr(VI) to Cr(III) in the presence of $TiO_2$ coated-CdS spheres core-shell nanocomposites. Liu et al. [60] have reported photocatalytic reduction of Cr(VI) to Cr(III) in the presence of graphene–(CdS nanowire)–$TiO_2$ nanocomposites. They have reported photocatalytic reduction of Cr(VI) in     20 min with a rate constant of 0.185 min$^{-1}$. In the present study, the time required for the complete reduction of Cr(VI) is lower (6 minutes) with a higher rate constant (0.56 min$^{-1}$).

### 6.3.3.1 Mechanism of photocatalytic reduction of Cr(VI)

In the photocatalytic reduction of Cr(VI), CdS is excited by the visible light illumination and electrons and holes are created.

$$CdS + h\nu = h^+ + e^-$$
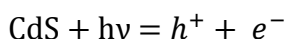
The photo-generated electrons are easily transferred from the conduction band of CdS nanoparticles to that of $TiO_2$. The Cr(VI) ions are reduced to Cr(III) ions by the photo-generated electrons, while the holes are involved in the oxidation of water to oxygen [57].

$$Cr_2O_7^{2-} + 14\,H^+ + 6e^- \rightarrow 2Cr^{3+} + 7H_2O$$

$$2H_2O + 4H^+ \rightarrow O_2 + 4H^+$$
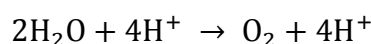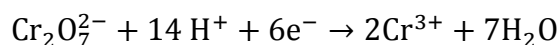
The CdS-$TiO_2$ nanocomposite CT4 acts as a good catalyst for the photodegradation of rhodamine B and reduction of Cr(VI) into Cr(III) in the presence of sunlight because it possesses the smallest CdS crystallite size (3 nm) (Chapter 4, Table 4.3) with uniform elemental distribution (as indicated by the EDX analysis, Chapter 4, Table 4.4).

### 6.4 Photocatalytic Degradation of Congo red

### 6.4.1 Introduction

Congo red (sodium salt of benzidine diazo-bis-1-naphthyl amine-4-sulphonic acid) is an azo dye which is often used as a colouring agent in textile and paper industries [61]. Congo red can cause serious environmental hazards and endanger human life due to its toxic, mutagenic and carcinogenic nature [62]. Due to its complex aromatic structure (Scheme 6.7), congo red is quite stable and it is hard to remove the dye by traditional methods of waste water treatment. The absorption spectrum of congo red is characterized by a band at 495 nm due to the azo

chromophore which leads to its dark red colour. The other two bands located at 237 nm and 343 nm are attributed to benzene ring and naphthalene ring, respectively [63]. Hence, it is necessary to develop efficient and economical processes to remove congo red from the waste water. Semiconductors based photocatalysis is considered as one of the most promising methods for wastewater treatment. This is because of its strong destructive power to mineralize toxic pollutants into $CO_2$ and $H_2O$. In the present study, the photocatalytic degradation of congo red was carried out using CdS-$\gamma$-Fe$_2$O$_3$ (Chapter 5) and ZnO@$\gamma$-Fe$_2$O$_3$ (Chapter 5) nanocomposites under sunlight irradiation.
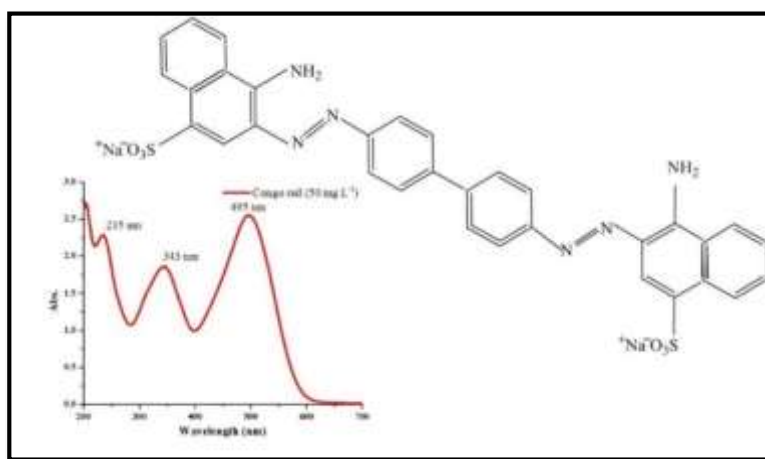


**Scheme 6.7:** Molecular structure of congo red [58] and UV-visible spectrum of an aqueous solution of congo red (50 mg L$^{-1}$).

## 6.4.2 Photocatalytic degradation of congo red by CdS-$\gamma$-Fe$_2$O$_3$ nanocomposites

### 6.4.2.1 Experimental Details

About 50 mg of each CdS-$\gamma$-Fe$_2$O$_3$ nanocomposite powders was dispersed in 50 mL of congo red solution (concentration = 50 mg L$^{-1}$). The suspension was sonicated for about 10 minutes and kept in dark for 30 minutes to reach adsorption-desorption equilibrium. Afterwards, the suspension was irradiated in sunlight at room temperature for various time intervals (0 to 60 minutes) (Scheme 6.8). Aliquots were taken from the suspension every 5 minutes and the photocatalyst powder was separated by centrifugation. The concentration of congo red in the supernatant solutions was determined by measuring the absorbance at 495 nm using the UV-visible spectroscopy (Shimadzu UV–2450). Pure CdS and $\gamma$-Fe$_2$O$_3$ nanoparticles were also explored as the photocatalysts to compare their photocatalytic activity with that of the CdS-$\gamma$-Fe$_2$O$_3$ nanocomposites.

```
┌─────────────────────────────┐       ┌─────────────────────────────┐
│   50 mL aqueous solution of │  ╬╬╬  │         Catalyst            │
│   congo red (50 mg L⁻¹)     │       │         (0.05 g)            │
└─────────────────────────────┘       └─────────────────────────────┘
                    │
                    │  Sonication for 10 min
                    ▼
        ┌─────────────────────────┐
        │   Dispersed catalyst in │
        │      aq. congo red      │
        └─────────────────────────┘
                    │
                    │  Sunlight irradiation for different
                    │  time intervals (0 to 60 min)
                    ▼
        ┌─────────────────────────┐
        │      Photodegraded      │
        │        products         │
        └─────────────────────────┘
```
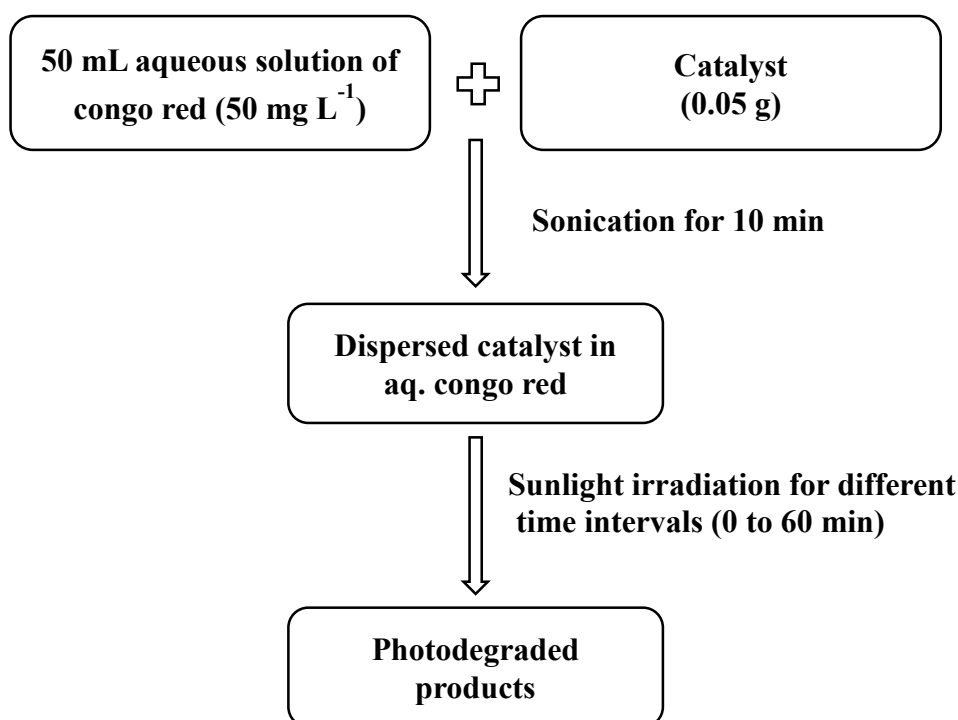
**Scheme 6.8:** Experimental steps involved in photocatalytic degradation of congo red.

### 6.4.2.2 Results and Discussion

The photocatalytic activity of the CdS-$\gamma$-Fe$_2$O$_3$ nanocomposites (FC1-FC6) was examined by studying the degradation of congo red under sunlight irradiation. Fig. 6.5(a) shows the UV–visible spectral results on the photodegradation of congo red by pure $\gamma$-Fe$_2$O$_3$, CdS nanoparticles and all the nanocomposites (FC1-FC6). It can be seen from Fig. 6.5(a) that nanocomposite FC5 shows maximum photodegradation compared to pure $\gamma$-Fe$_2$O$_3$, CdS nanoparticles and all the other nanocomposites. It is proposed that when the amount of CdS in the nanocomposites is too low (e.g. FC1), an efficient interfacial electron transfer from CdS to $\gamma$-Fe$_2$O$_3$ does not occur. Also, too much CdS on the surface of $\gamma$-Fe$_2$O$_3$ (nanocomposite FC6) blocks irradiation of Fe$_2$O$_3$ and nanocomposite FC5 contains the optimum concentration of CdS and it exhibits the maximum degradation. The BET surface area values for the CdS-$\gamma$-Fe$_2$O$_3$ nanocomposites FC1, FC2, FC3, FC4, FC5 and FC6 are 29.8 m$^2$/g, 52 m$^2$/g, 59.8 m$^2$/g, 30.7 m$^2$/g, 66.1 m$^2$/g and 65.2 m$^2$/g, respectively. The CdS-$\gamma$-Fe$_2$O$_3$ nanocomposite FC5 possesses higher surface area than that of pure $\gamma$-Fe$_2$O$_3$ (51.1 m$^2$/g), CdS nanoparticles (58.9 m$^2$/g) and all the other nanocomposites. Thus, due to an optimum concentration of CdS and high surface area, CdS-$\gamma$-Fe$_2$O$_3$ nanocomposite FC5 shows better photocatalytic activity compared to pure $\gamma$-Fe$_2$O$_3$, CdS nanoparticles and other nanocomposites.

Fig. 6.5(b) shows the kinetics of photo degradation of congo red using CdS-$\gamma$-Fe$_2$O$_3$ nanocomposite FC5 as the catalyst in comparison with pure iron oxide and CdS nanoparticles. It can be seen that the absorbance at 495 nm decreases with time, and it almost approaches zero within 60 min. On the other hand, pure $\gamma$-Fe$_2$O$_3$ and CdS nanoparticles are unable to complete the degradation of congo red even after 60 minutes of irradiation (Fig. 6.5(c)).
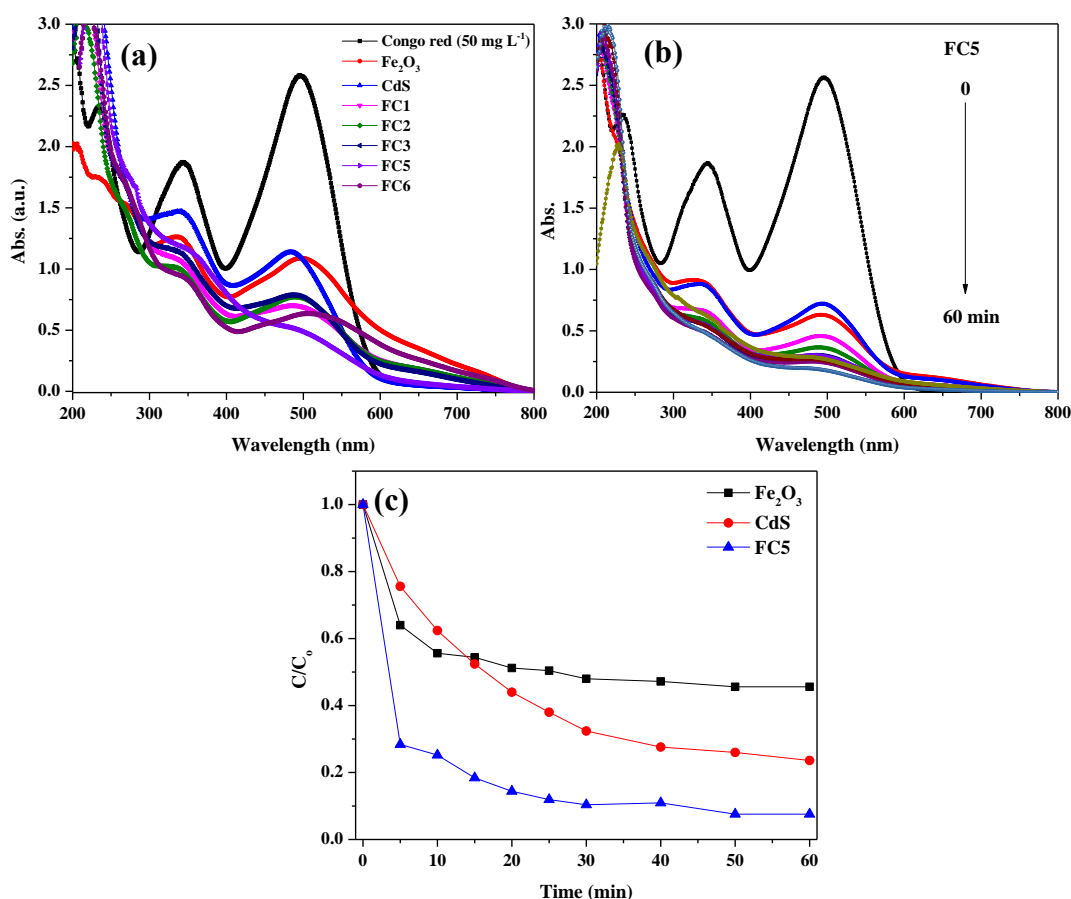


**Fig. 6.5:** (a) UV-visible spectra indicating photocatalytic degradation of congo red in an aqueous solution using pure $\gamma$-Fe$_2$O$_3$, CdS nanoparticles and the CdS-$\gamma$-Fe$_2$O$_3$ nanocomposites as the catalysts, (b) kinetics of photocatalytic degradation of congo red using CdS-$\gamma$-Fe$_2$O$_3$ nanocomposite FC5 and (c) comparison of photocatalytic degradation of congo red with pure $\gamma$-Fe$_2$O$_3$, CdS nanoparticles and CdS-$\gamma$-Fe$_2$O$_3$ nanocomposite FC5.

The pseudo-first-order and pseudo-second-order kinetics models were applied to study the kinetics of congo red photodegradation by pure $\gamma$-Fe$_2$O$_3$, CdS nanoparticles and CdS-$\gamma$-Fe$_2$O$_3$ nanocomposite FC5 (equations 1 and 2) [64].

Pseudo first order kinetics model:

$$\ln\left[\frac{C_o}{C}\right] = k_1 t \qquad (1)$$

Pseudo second order kinetics model:

$$\frac{1}{[C]} = k_2 t + \frac{1}{[C_o]} \qquad (2)$$

Where $C_o$ and $C$ represent the concentration of congo red at $t = 0$ and at any time t. $k_1$ and $k_2$ are pseudo-first and pseudo-second order rate constants, respectively. Figs. 6.6(a) and 6.6(b) show the fitting of kinetics data for the photodegradation of congo red using pure $Fe_2O_3$, CdS nanoparticles and CdS-$\gamma$-$Fe_2O_3$ nanocomposite FC5 as the catalyst. The kinetic parameters obtained by linear regression using the two kinetic models are summarized in Table 6.3.

**Table 6.3:** Estimated pseudo first order and second-order kinetic parameters for the photocatalytic degradation of congo red using pure $\gamma$-$Fe_2O_3$, CdS nanoparticles and CdS-$\gamma$-$Fe_2O_3$ nanocomposite (FC5) as the catalysts.

| Catalyst | Pseudo first-order kinetics | | Pseudo second-order kinetics | |
|---|---|---|---|---|
| | $k_1$ (min$^{-1}$) | $R^2$ | $k_2$ (mg$^{-1}$ min$^{-1}$) | $R^2$ |
| $\gamma$-$Fe_2O_3$ | 0.009 | 0.52 | 0.006 | 0.93 |
| CdS | 0.024 | 0.89 | 0.022 | 0.97 |
| CdS-$\gamma$-$Fe_2O_3$ nanocomposite (FC5) | 0.035 | 0.71 | 0.088 | 0.98 |

The higher correlation coefficient values ($R^2$) indicate a better fitting of the kinetic data using the pseudo-second-order kinetics model rather than the pseudo-first-order one. The value of second order rate constant of photodegradation of congo red using CdS-$\gamma$-$Fe_2O_3$ nanocomposite FC5 is 0.088 mg$^{-1}$ min$^{-1}$ which is higher than the values for pure $Fe_2O_3$ (0.006 mg min$^{-1}$) and pure CdS (0.022 mg$^{-1}$ min$^{-1}$). The enhanced photocatalytic activity of the CdS-$\gamma$-$Fe_2O_3$ nanocomposites is attributed to an efficient charge separation at the CdS-$Fe_2O_3$ interface.
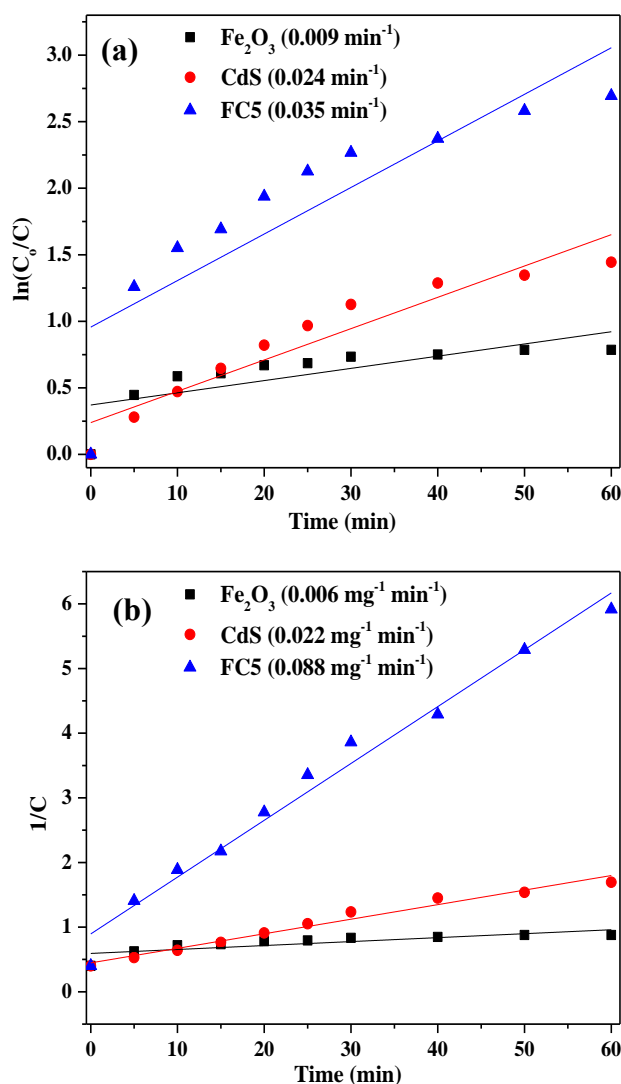
**Fig. 6.6:** Kinetics plots using (a) pseudo-first order and (b) pseudo-second order models for photo degradation of congo red in an aqueous solution. Symbols are experimental values and solid lines are the fits using the two kinetic models.

The ability to recycle a photocatalyst is very important. To investigate the reusability CdS-γ-$Fe_2O_3$ nanocomposites, the photocatalytic degradation experiment was repeated four times using the same catalyst (CdS-γ-$Fe_2O_3$ nanocomposite, FC5) again and again (Fig. 6.7). The concentration of congo red was kept constant (50 mg $L^{-1}$) with 60 minutes as the irradiation time. The photocatalyst was recovered in each cycle from the sun light irradiated solutions by centrifugation and subsequent washing with double distilled water three times and reused for the catalysis. The degradation efficiency of CdS-γ-$Fe_2O_3$ nanocomposite FC5 decreases from 93 % to 85% after three cycles.
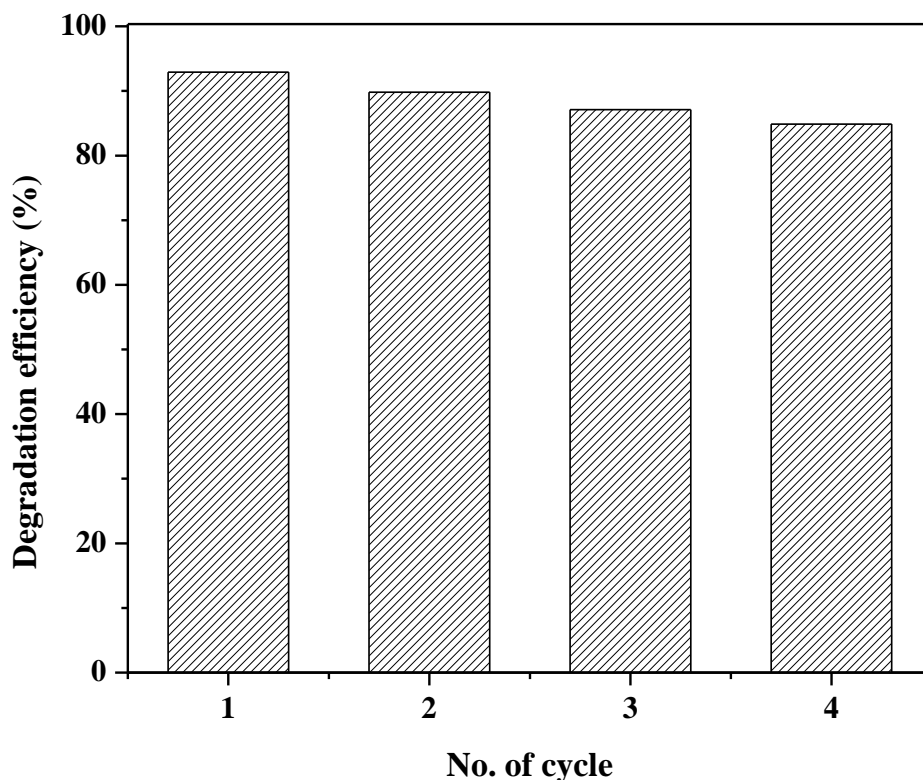
**Fig. 6.7:** Four cycles of degradation of Congo-red dye in an aqueous solution in the presence of CdS-γ-Fe$_2$O$_3$ nanocomposite (FC5)

### 6.4.2.3 Mechanism of Photodegradation of Congo Red

According to the reported literature [61,62,65], the mechanism for the photo degradation of congo red involves cleavage of C–S bond, aromatic ring opening, cleavage of –N=N– double bond and cleavage of various C–N and C–C bonds in addition to decarboxylation. Scheme 6.9 shows the possible species formed during the degradation of congo red in the presence of CdS-γ-Fe$_2$O$_3$ nanocomposites as the catalyst.
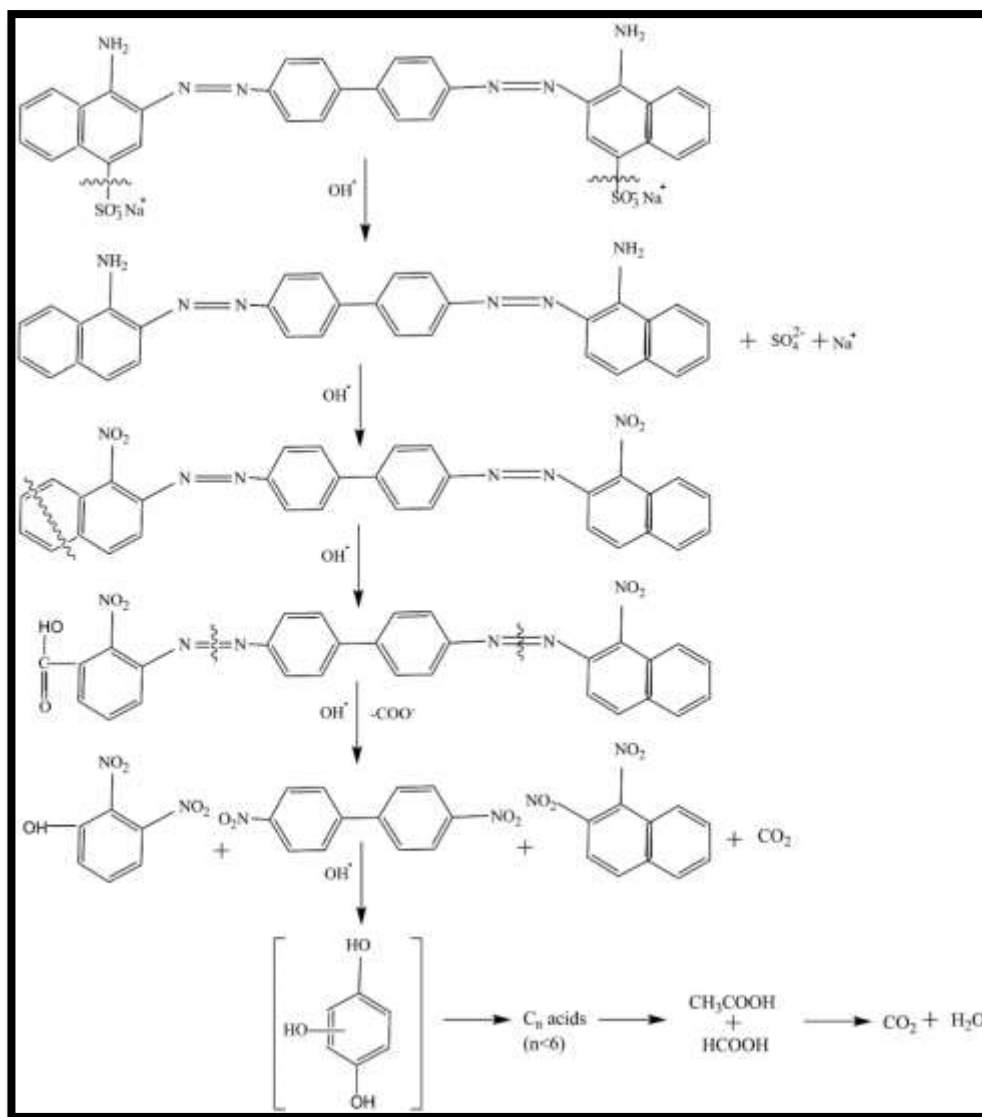
**Scheme 6.9:** Proposed mechanism and photodegradation products of congo red.

Based on the literature [66–68], the mechanism of photodegradation is described as follows (Scheme 6.10):

$$CdS - Fe_2O_3 \xrightarrow{h\nu} CdS(e^- + h^+) + Fe_2O_3(e^- + h^+)$$

$$CdS(e^- + h^+) + Fe_2O_3(e^- + h^+) \rightarrow CdS(h^+) + Fe_2O_3(e^-)$$

$$e^- + O_2 \rightarrow O_2^{\bullet -}$$

$$2e^- + O_2 + 2H^+ \rightarrow H_2O_2$$

$$H_2O_2 + O_2^{\bullet -} \rightarrow OH^\bullet + OH^- + O_2$$
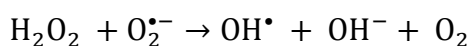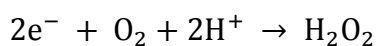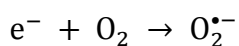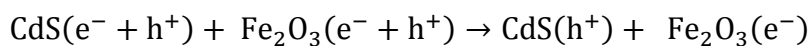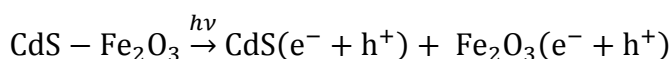
On sunlight irradiation, electrons in the valence band of CdS and $\gamma$-Fe$_2$O$_3$ are excited to their respective conduction bands. The electrons on the CB of CdS are transferred to that of $\gamma$-Fe$_2$O$_3$ while the photogenerated holes on the VB of $\gamma$-Fe$_2$O$_3$ are transferred to that of CdS [69].

The photogenerated electron–hole pairs migrate easily to the surface and can be separated efficiently at the interface of the nanocomposites with low recombination [70]. The transferred electrons are trapped by the adsorbed surface oxygen molecules to give $O_2^{\bullet-}$ and $H_2O_2$ which form active species ($OH^{\bullet}$ radicals) which attack chromophore of the congo red leading to its degradation [66,71].
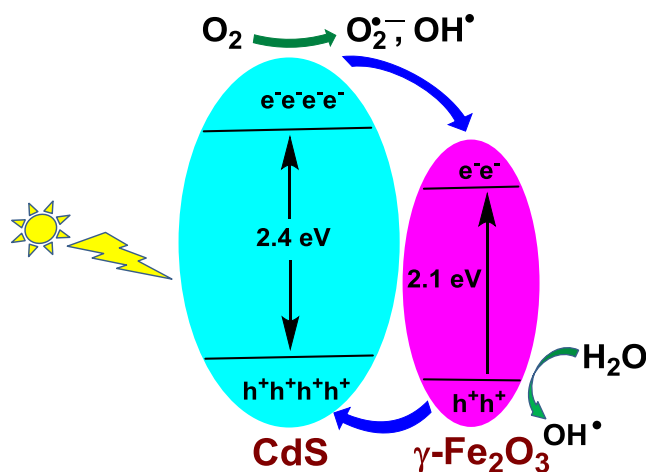


**Scheme 6.10:** Band alignment and photo-induced electron transfer in CdS-γ-Fe₂O₃ nanocomposites.

## 6.4.3 Photocatalytic degradation of congo red by ZnO@γ-Fe₂O₃ core-shell nanocomposites

### 6.4.3.1 Experimental Details

The photocatalytic experiments using ZnO@γ-Fe₂O₃ core-shell nanocomposites (Chapter 5, ZF1, ZF2, ZF3 and ZF4) as the catalysts for the photodegradation of congo red in an aqueous solution were conducted as follows: 50 mg of each of the catalyst was suspended in 50 mL of congo red solution ($50\ mg\ L^{-1}$) and the contents were stirred in dark for 60 minutes to reach adsorption-desorption equilibrium. Afterwards, the suspension was exposed to sunlight for various time intervals (0 to 90 minutes) (experimental steps were same as that in Scheme 6.8). At regular time intervals, 3 mL of the suspension was taken out and centrifuged at 3500 rpm for 5 minutes to completely remove the catalyst. The concentration of congo red in the supernatant solution was analyzed with the help of UV-visible spectroscopy (Shimadzu UV-2450) by measuring the absorbance at 495 nm. The photocatalytic activity of pure ZnO nanorods and γ-Fe₂O₃ nanoparticles towards the photodegradation of congo red were also studied for comparison with that of the ZnO@γ-Fe₂O₃ core-shell nanocomposites.

## 6.4.3.2 Results and Discussion

In order to study the photodegradation efficiency of ZnO nanorods, $\gamma$-Fe$_2$O$_3$ nanoparticles and the ZnO@$\gamma$-Fe$_2$O$_3$ core-shell nanocomposites, the photodegradation of congo red in an aqueous solution under sunlight irradiation was carried out. Fig. 6.8(a) shows the UV–visible spectral results on the photodegradation of congo red using pure ZnO nanorods, $\gamma$-Fe$_2$O$_3$ nanoparticles and all the nanocomposites (ZF1-ZF4) as the catalyst. It can be seen that ZnO@$\gamma$-Fe$_2$O$_3$ nanocomposite ZF1 shows maximum photodegradation compared to pure ZnO nanorods, $\gamma$-Fe$_2$O$_3$ nanoparticles and all the other three nanocomposites (ZF2, ZF3 and ZF4). Fig. 6.8(b) shows the effect of varying the amount of catalyst ZF1 on the photocatalytic degradation of congo red. The amount of catalyst was varied from 20 to 100 mg in 50 mL of congo red solution (50 mg L$^{-1}$). It can be seen that the solution containing 50 mg and 100 mg of catalyst show almost the same decrease in the concentration of congo red. Hence, 50 mg of catalyst (ZF1) in 50 mL of congo red solution was optimized as the best conditions to carry out further photocatalytic degradation experiments.
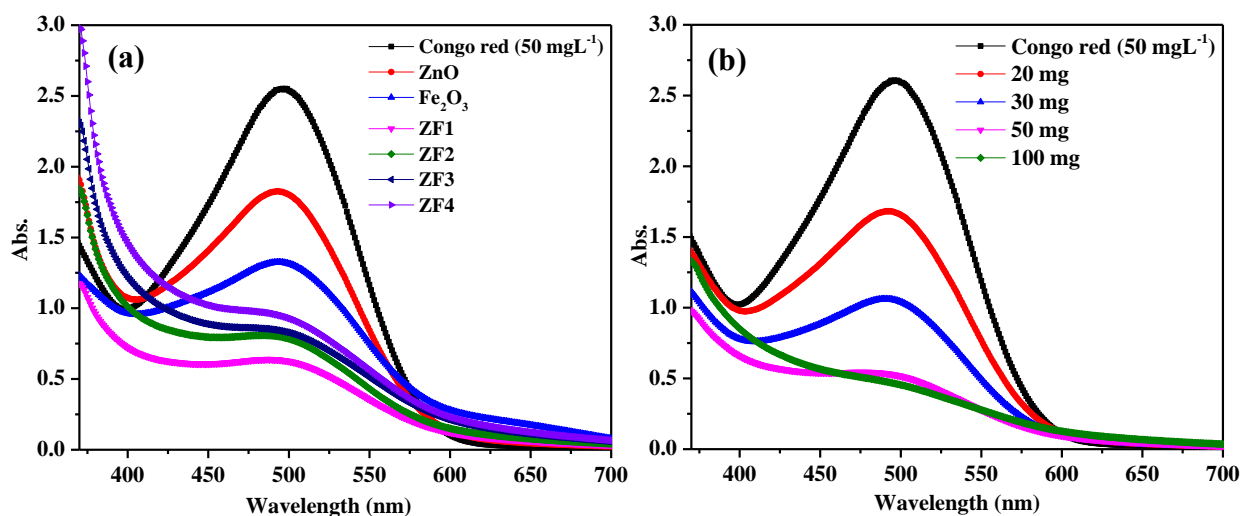


**Fig. 6.8:** (a) UV-visible spectra of photocatalytic degradation of congo red in an aqueous solution by ZnO nanorods, $\gamma$-Fe$_2$O$_3$ nanoparticles and ZnO@$\gamma$-Fe$_2$O$_3$ core-shell nanocomposites (ZF1, ZF2, ZF3 and ZF4) and (b) UV-visible spectra of photocatalytic degradation of congo red using different amounts of ZnO@$\gamma$-Fe$_2$O$_3$ core-shell nanocomposite ZF1 as the catalyst.

Fig. 6.9 shows the kinetics of photocatalytic degradation of congo red by ZnO, $\gamma$-Fe$_2$O$_3$ nanoparticles and the ZnO@$\gamma$-Fe$_2$O$_3$ core-shell nanocomposites ZF1, ZF2, ZF3 and ZF4. In the case of core-shell nanocomposite ZF1, the intensity of absorption band of congo red at 495 nm decreases with time and almost approaches zero in about 90 minutes. On the other hand, pure ZnO, $\gamma$-Fe$_2$O$_3$ nanoparticles and all the other ZnO@$\gamma$-Fe$_2$O$_3$ nanocomposites (ZF2, ZF3 and ZF4) are unable to complete the degradation during this period
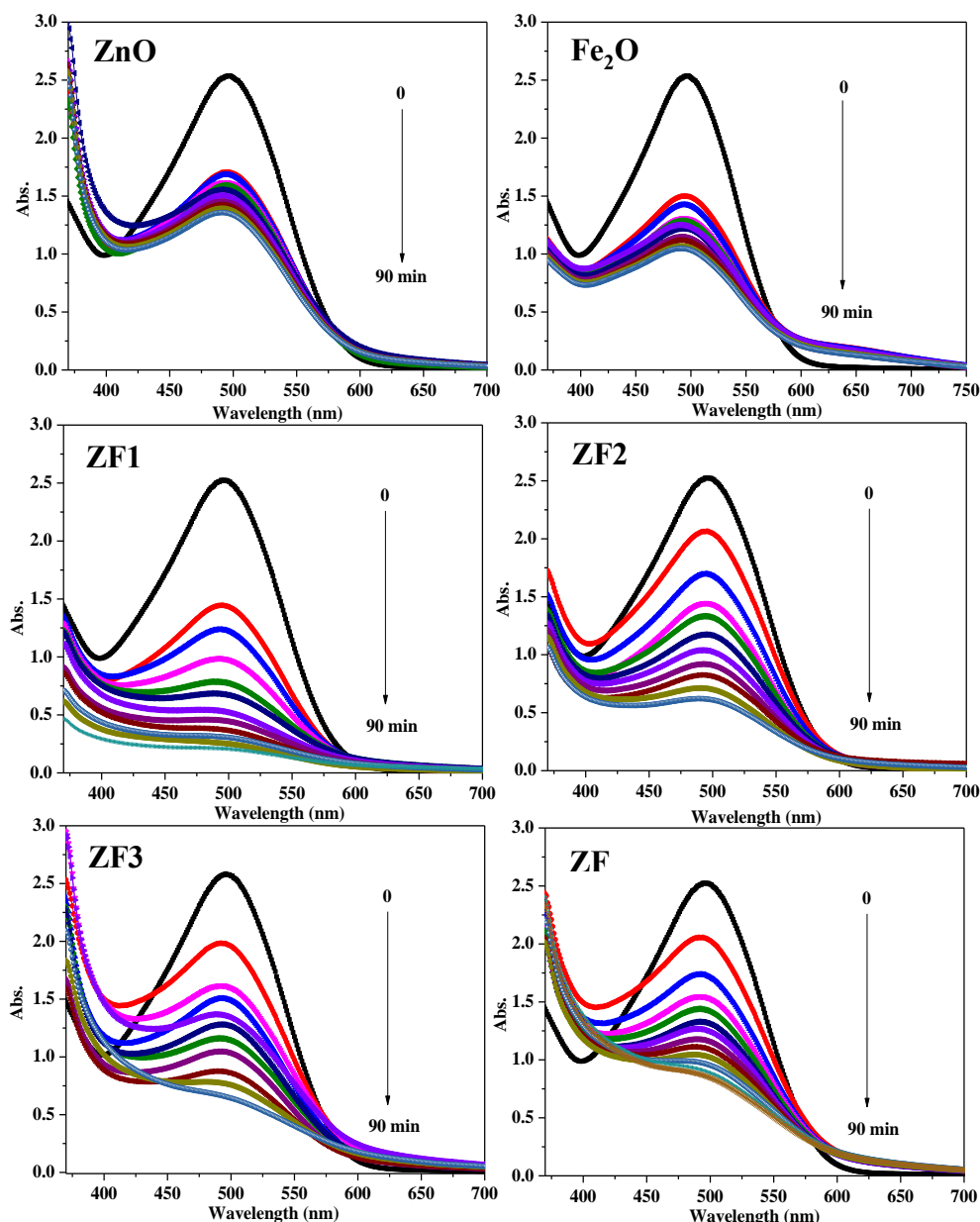


**Fig. 6.9:** UV-visible spectra of kinetics of photodegradation of congo red in an aqueous solution by pure ZnO nanorods, $\gamma$-Fe$_2$O$_3$ nanoparticles and ZnO@$\gamma$-Fe$_2$O$_3$ core-shell nanocomposites ZF1, ZF2, ZF3 and ZF4.

Fig. 6.10(a) shows the kinetics of photodegradation of congo red using ZnO, $\gamma$-Fe$_2$O$_3$ nanoparticles and the ZnO@$\gamma$-Fe$_2$O$_3$ core-shell nanocomposites as the catalyst where C$_o$ is the initial concentration of congo red and C is its concentration at different times. The photocatalytic activity of ZnO@$\gamma$-Fe$_2$O$_3$ core-shell nanocomposites decreases with an increase in the concentration of Fe(acac)$_3$ used during the preparation of the nanocomposites (Chapter 5, Table 5.5). The ZnO@$\gamma$-Fe$_2$O$_3$ core-shell nanocomposite with less amount of $\gamma$-Fe$_2$O$_3$ nanoparticles (ZF1) shows enhanced photocatalytic activity. It is proposed that using higher $\gamma$-Fe$_2$O$_3$ content causes reduction in the distance between photoelectrons and holes, which results in decrease in the photocatalytic activity due to enhancement in the recombination [72,73]. The BET surface area values for the ZnO@$\gamma$-Fe$_2$O$_3$ core-shell nanocomposites ZF1, ZF2, ZF3 and ZF4 are 62.1 m$^2$/g, 53.3 m$^2$/g, 50.3 m$^2$/g and 38.2 m$^2$/g, respectively. The surface area of core-shell nanocomposite ZF1 is higher than that of pure ZnO (24.4 m$^2$/g), Fe$_2$O$_3$ (51.1 m$^2$/g) and all the other nanocomposites. Nanocomposite ZF1 shows better activity than that of pure ZnO nanorods, $\gamma$-Fe$_2$O$_3$ nanoparticles and all the other (ZF2, ZF3 and ZF4) nanocomposites. This is because it has effective charge separation, more surface area and more number of oxygen vacancies present on its surface. As elucidated by PL studies in (Chapter 5, Fig. 5.29), nanocomposite ZF1 has enhanced defect emission compared to pure ZnO nanorods, $\gamma$-Fe$_2$O$_3$ nanoparticles and all the other ZnO@$\gamma$-Fe$_2$O$_3$ nanocomposites.

In general, the photodegradation of congo red catalyzed by the semiconductor catalysts follows pseudo first-order rate law [74].

$$\ln \left[ \frac{C_o}{C} \right] = k_1 t$$

Where C$_o$ and C represent the concentration of congo red at t = 0 and at any time t and k$_1$ is the apparent first order rate constant. Fig. 6.10(b) respectively, shows the fitting of kinetics data using pseudo first order rate law for the photodegradation of congo red using pure ZnO nanorods, $\gamma$-Fe$_2$O$_3$ nanoparticles and ZnO@$\gamma$-Fe$_2$O$_3$ core-shell nanocomposites (ZF1-ZF4) as the catalysts.
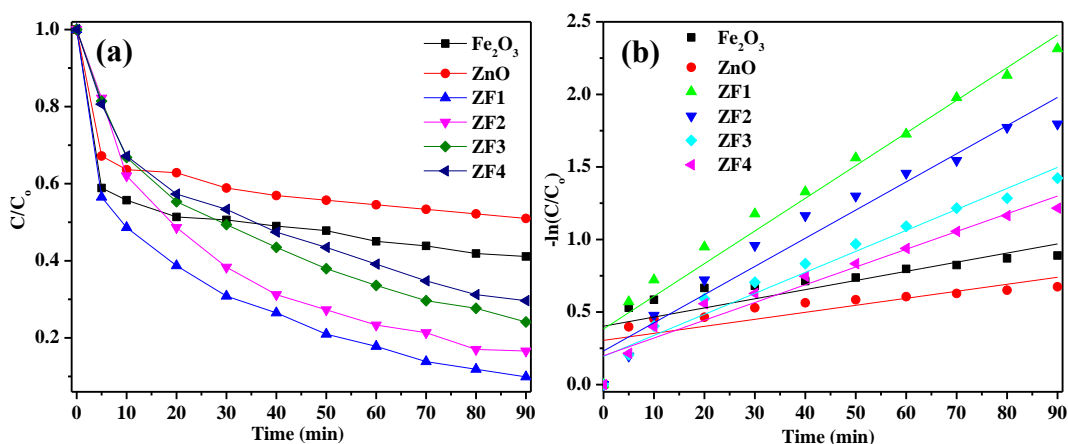
**Fig. 6.10:** (a) Comparison of photocatalytic degradation of congo red with ZnO nanorods, $\gamma$-$Fe_2O_3$ nanoparticles and ZnO@$\gamma$-$Fe_2O_3$ core-shell nanocomposites (ZF1-ZF4) ($C_o$ is the initial concentration of dye and C is the concentration of dye at different times), and (b) kinetics plots of pseudo first order for congo red dye photodegradation. Symbols are experimental values and solid lines are the fits using the pseudo first order kinetic model.

The kinetic parameters obtained by the linear fitting using the pseudo first order kinetic model are summarized in Table 6.4. The first order rate constant of congo red degradation using ZnO@$\gamma$-$Fe_2O_3$ core-shell nanocomposite ZF1 is 0.022 $min^{-1}$ which is higher than the values for pure ZnO (0.005 $min^{-1}$), pure $\gamma$-$Fe_2O_3$ (0.006 $min^{-1}$) and other ZnO@$\gamma$-$Fe_2O_3$ core-shell nanocomposites (ZF2 (0.019 $min^{-1}$), ZF3 (0.014 $min^{-1}$) and ZF4 (0.012 $min^{-1}$). The enhanced activity of the ZnO@$\gamma$-$Fe_2O_3$ core-shell nanocomposites is attributed to faster charge separation at the interface of ZnO@$\gamma$-$Fe_2O_3$ core-shell nanocomposites.

**Table 6.4:** Estimated pseudo first order kinetic parameters for the photocatalytic degradation of congo red in aqueous solution using pure ZnO, $\gamma$-$Fe_2O_3$ nanoparticles and ZnO@$\gamma$-$Fe_2O_3$ core-shell nanocomposites as the catalysts.

| Catalyst | Rate constant ($min^{-1}$) | $R^2$ |
|---|---|---|
| $Fe_2O_3$ | 0.006 | 0.80 |
| ZnO | 0.005 | 0.78 |
| ZF1 | 0.022 | 0.98 |
| ZF2 | 0.019 | 0.98 |
| ZF3 | 0.014 | 0.97 |
| ZF4 | 0.012 | 0.97 |

The ability of reusing the ZnO@$\gamma$-Fe$_2$O$_3$ core-shell nanocomposite ZF1 was evaluated by performing repeated photocatalytic degradation reactions using congo red (50 mg L$^{-1}$). The suspension was first irradiated in sunlight for 90 min. The photocatalyst was recovered from the suspension after every cycle by centrifugation and subsequent washing with doubled distilled water for three times. The recovered catalyst was dried in vacuum for overnight and was reused for the photodegradation again. The degradation efficiency of the ZnO@$\gamma$-Fe$_2$O$_3$ core-shell nanocomposite ZF1 decreases from about 97 % to 85 % after four cycles (Fig. 6.11).
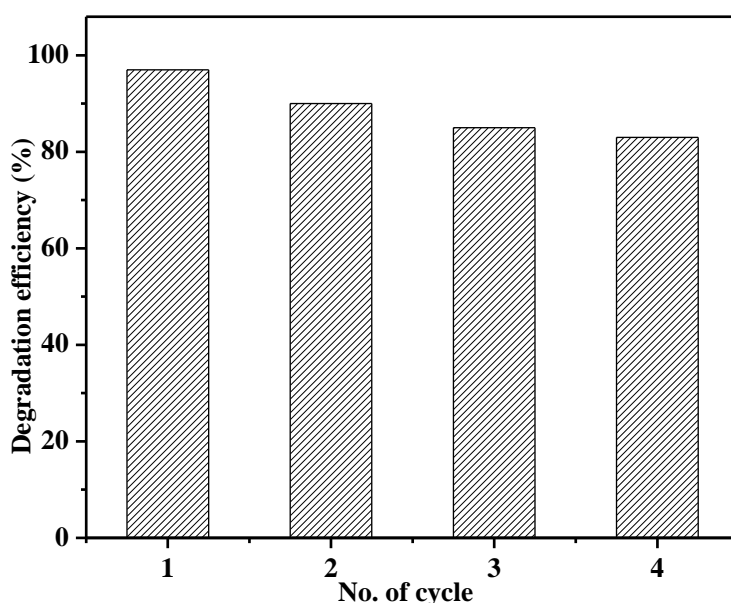


**Fig. 6.11:** Reusability of ZnO@$\gamma$-Fe$_2$O$_3$ core-shell nanocomposite ZF1 for congo red photodegradation.

**6.4.3.3 Mechanism of Photodegradation of Congo Red**

ZnO has absorption in the UV region due to its wide band gap (3.28 eV) and $\gamma$-Fe$_2$O$_3$ has absorption in the visible region due to its narrow band gap (1.9-2.2 eV) [75]. The absorption spectra of ZnO@$\gamma$-Fe$_2$O$_3$ core-shell nanocomposites have contribution from both the components. All the core-shell nanocomposites (ZF1 to ZF4) show better photocatalytic efficiency compared to pure ZnO nanorods and pure Fe$_2$O$_3$ nanoparticles. Scheme 6.11 shows the band configuration and electron–hole separation at the interface between ZnO and $\gamma$-Fe$_2$O$_3$ nanoparticles.

$O_2^{\bullet-}$

$O_2$

CB

3.3 eV  ZnO  hν

VB

2.2 eV  $Fe_2O_3$  hν

CB

VB

$H_2O$

$OH^{\bullet}+H^+$

$$\text{Congo red} + O_2^{\bullet-}, OH^{\bullet} \longrightarrow CO_2 + H_2O$$
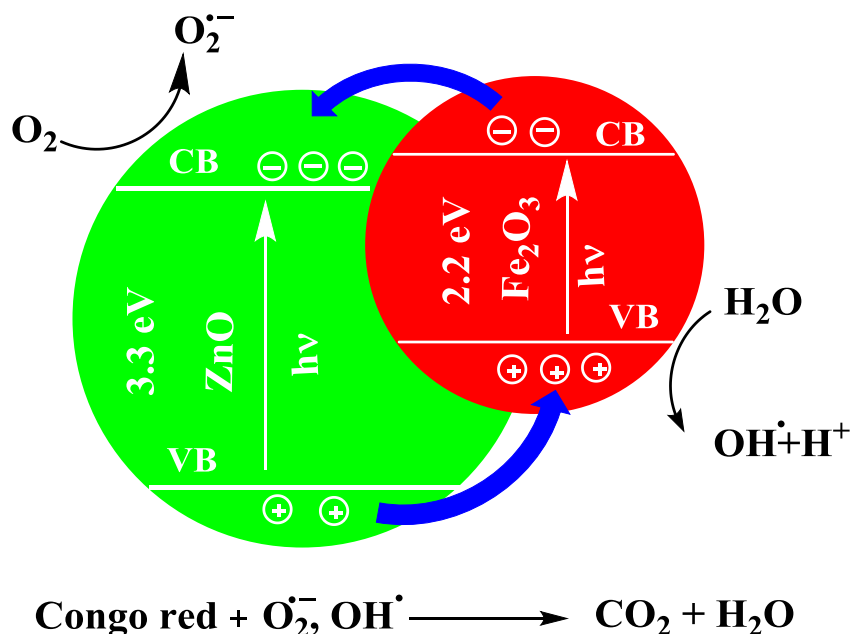
**Scheme 6.11:** Schematic diagram of band configuration and electron–hole separation at the interface between ZnO nanorods and γ-Fe$_2$O$_3$ nanoparticles under sunlight irradiation.

Under sunlight irradiation, the photogenerated electrons in the conduction band (CB) of γ-Fe$_2$O$_3$ transfer to that of ZnO while the holes in the valence band (VB) of ZnO transfer to that of γ-Fe$_2$O$_3$ [74,76]. This enables the separation of photogenerated electrons and holes, which greatly reduce the electron-hole recombination. Subsequently, the electrons in the conduction band of ZnO transfer to the surface of ZnO to react with dissolved oxygen molecules to give super oxide radicals anions ($O_2^{\bullet-}$), yielding hydroperoxyl radicals ($HO_2^{\bullet}$) on protonation and finally $OH^{\bullet}$ radicals [74,76]. The hydroxyl radicals and super oxide radicals are powerful oxidizing agents which help in the effective photodegradation of congo red into CO$_2$ and H$_2$O. The photocatalytic mechanism is summarized as follows [77]:

$ZnO/Fe_2O_3 + h\nu \rightarrow (ZnO)e^- + (Fe_2O_3)h^+$

$(ZnO)e^- + O_2 \rightarrow O_2^{\bullet-}$

$(Fe_2O_3)h^+ + HO^{\bullet-} \rightarrow OH^{\bullet}$

$O_2^{\bullet-} + H_2O \rightarrow HO_2^{\bullet} + HO^-$

$HO_2^{\bullet} + H_2O \rightarrow H_2O_2 + OH^{\bullet}$

$H_2O_2 \rightarrow 2OH^{\bullet}$

Congo red + $O_2^{\bullet-}$, $OH^{\bullet} \rightarrow$ degradation products
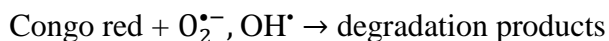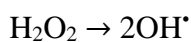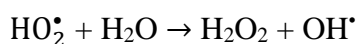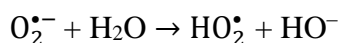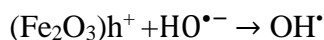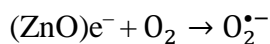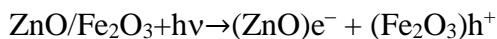
Jiang et al. [66] have reported photodegradation of congo red (20 mg $L^{-1}$) in the presence of $\gamma$-$Fe_2O_3$/CdS nanocomposite. They observed a rate constant of 0.0023 $min^{-1}$ with 91.5% of degradation in about 300 min. Mirzaie et al. [73] have reported photodegradation of congo red in the presence of ZnO/$Fe_2O_3$ nanocomposites. The nanocomposite having ($Fe^{3+}$/$Zn^{2+}$) molar ratio of 1/100 shows the highest photocatalytic activity of about 93% decolorization in 25 min compared to other nanocomposites ($Fe^{3+}$/$Zn^{2+}$ = 0.5/100, 5/100 and 10/100). Recently, many authors have reported photodegradation of congo red in the presence of different nanocomposites. Narayan et al. [78] have reported photocatalytic degradation of congo red (25 mg $L^{-1}$) in the presence of $Y^{3+}$ doped $TiO_2$ nanocomposites. They observed maximum rate constant of 0.027 $min^{-1}$ for nanocomposite $TiO_2$[$Y_2O_3$]$_{0.1}$ with 91% of degradation in about 180 min. Pouretedal et al. [79] have reported photodegradation of congo red (5 mg $L^{-1}$) in the presence of $Zn_{1-x}Cu_xS$ nanocomposites. They observed rate constant of 0.033 $min^{-1}$ for nanocomposite $Zn_{0.9}Cu_{0.1}S$ with 98% degradation in about 120 min. Guo et al. [80] have reported photodegradation of congo red (50 mg $L^{-1}$) in the presence of $TiO_2$/PANI nanocomposites. They observed maximum rate constant of 0.0007 $min^{-1}$ for nanocomposite (1:1) with 95% photodegradation in about 160 min. Farbod et al. [81] have reported photodegradation of congo red (20 mg $L^{-1}$) in the presence of Gd/$TiO_2$ nanocomposites. They observed rate constant of 0.034 $min^{-1}$ for the nanocomposite Gd(1.8%)/$TiO_2$ with complete photodegradation in about 180 min. Lin et al. [82] have reported photodegradation of congo red in the presence of ZnO/Zn nanocomposite with cellulose (ZnO-Zn)-C and starch (ZnO/Zn)-S. They observed rate constant of 0.0105 $min^{-1}$ for nanocomposite (ZnO/Zn)-S with 98% of photodegradation in about 3 h. Thiripuranthagan et al. [83] have reported photodegradation of congo red (50 mg $L^{-1}$) in the presence of Ag impregnated $TiO_2$–$SiO_2$ composites. They observed rate constant of 0.0173 $min^{-1}$ for $TiO_2$–$SiO_2$ impregnated with 1% Ag showing 85% of photodegradation in about 180 min. Liu et al. [61] have reported photodegradation of congo red (25 mg $L^{-1}$) in the presence of Ag-ZnO nanocomposites. They observed a rate constant of 0.0312 $min^{-1}$ for 3% Ag-ZnO nanocomposite with 97.3% of photodegradation in about 50 min. Li et al. [84] have reported photodegradation of congo red (10 mg $L^{-1}$) in the presence of $TiO_2$/PCNFs (porous carbon nanofibers). They observed a rate constant of 0.0158 $min^{-1}$ for nanocomposite $TiO_2$/PCNFs-4 (0.25 mL of $TiCl_4$) for complete photodegradation in about 60 min. In the present work, complete photodegradation of congo red take place in about 90 min with a rate constant of 0.022 $min^{-1}$ by the ZnO@$\gamma$-$Fe_2O_3$ nanocomposite ZF1.

## 6.5 Chemical Oxygen Demand (COD)

To understand the extent of mineralization of a dye by photocatalysis, chemical oxygen demand (COD) of the dye solution was measured [85,86]. Chemical oxygen demand gives an idea about concentration of the oxidizable matter present in a solution. If the dye is not photodegraded or mineralized, the COD value would be higher than that of the completely mineralized dye [87]. For determining the chemical oxygen demand (COD) of the dye solutions during the photocatalytic experiments, aliquots were collected after the degradation experiment. The initial solution (i.e. before photodegradation) and the solution after the photodegradation were taken for COD analysis using a standard dichromate method [88]. The tests were carried out using a sample volume of 3.5 mL digested with 1.5 mL of potassium dichromate (0.035 M) and 3.5 mL of concentrated sulfuric acid for 120 min at 100 $^{\circ}$C (Digestion unit DRB 200, HACH, USA). After this, the solutions were allowed to cool and analyzed with a COD analyzer (HACH, DR 5000, USA). On the basis of the COD results, the photocatalytic degradation efficiency was calculated using the following equation:

$$\text{Photodegradation efficiency (\%)} = \frac{COD_0 - COD}{COD_0} \times 100$$

Where $COD_0$ and COD are the chemical oxygen demand values of dye solutions before and after the photocatalytic degradation, respectively. The COD and photodegradation efficiency values for the photodegradation of rhodamine B and congo red in aqueous solutions are given in Table 6.5.

**Table 6.5**: COD and photodegradation efficiency of rhodamine B (RhB) and congo red (CR) dyes in aqueous solutions using different nanocomposites as the catalysts.

| Nanocomposite | Dye | Time of sunlight irradiation (min) | $COD_0$ initial (mg $L^1$) | COD (After sunlight irradiation) (mg $L^{-1}$) | Photodegradation efficiency (%) |
|---|---|---|---|---|---|
| CdS-TiO$_2$ CT4 | RhB | 120 | 203 | 37 | 81.7 |
| Ag$_2$S-TiO$_2$ A4 | RhB | 90 | 203 | 10 | 96.5 |

| | | | | | |
|---|---|---|---|---|---|
| CdS-$\gamma$-Fe$_2$O$_3$ FC5 | CR | 60 | 57 | 12 | 78.9 |
| ZnO@$\gamma$-Fe$_2$O$_3$ ZF1 | CR | 90 | 57 | 16 | 71.9 |

A comparison of the COD values of the initial dye solutions with that after the photodegradation using different nanocomposites as the catalyst (CT4, A4, FC5 and ZF1) indicates that the COD values are considerably reduced after the photodegradation. The reduction in COD values confirms that rhodamine B and congo red are photodegraded in the presence of nanocomposites. Ag$_2$S-TiO$_2$ nanocomposite A4 shows the maximum photodegradation efficiency (96.5%) for the photodegradation of rhodamine B.

**6.6 Conclusions**

In the present study, various applications of the synthesized nanocomposites were explored. NiO-Al$_2$O$_3$ nanocomposites show better catalytic activity in the oxidation of styrene compared to pure NiO and Al$_2$O$_3$ nanoparticles. CdS-TiO$_2$ nanocomposites were better photocatalyst in the degradation of rhodamine B and reduction Cr(VI) compared to pure CdS and TiO$_2$ nanoparticles. CdS-$\gamma$-Fe$_2$O$_3$ nanocomposites were found to be better photocatalyst in the degradation of congo red in an aqueous solution compared to pure CdS and $\gamma$-Fe$_2$O$_3$ nanoparticles and ZnO@$\gamma$-Fe$_2$O$_3$ core-shell nanocomposites show better catalytic activity in the degradation of congo red in an aqueous solution compared to pure ZnO and $\gamma$-Fe$_2$O$_3$ nanoparticles. The COD analyses for the photocatalytic experiments confirm that rhodamine B and congo red are photodegraded in the presence of nanocomposites. Ag$_2$S-TiO$_2$ nanocomposite A4 shows the maximum photodegradation efficiency (96.5%) for the photodegradation of rhodamine B.

**References**

1.  Wang Y., Wang Q., Zhan X., Wang F., Safdar M., He J., 'Visible light driven type II heterostructures and their enhanced photocatalysis properties: A review', *Nanoscale*, **5**, 8326–8339 (2013).

2.  Matějka V., Tokarský J., 'Photocatalytical nanocomposites: A review', *Journal of Nanoscience and Nanotechnology*, **14**, 1597–1616 (2014).

3.  Roy P., Srivastava S. K., 'Nanostructured anode materials for lithium ion batteries', *Journal of Materials Chemistry A*, **3**, 2454–2484 (2015).

4.  Fernandez C. de J., Manera M. G., Spadavecchia J., Maggioni G., Quaranta A., Mattei G., Bazzan M., Cattaruzza E., Bonafini M., Nergo E., Vomiero A., Carturan S., Scian C., Mea G. Della, Rella R., Vasanelli L., Mazzoldi P., 'Study of the gas optical sensing properties of Au-polyimide nanocomposite films prepared by ion implantation', *Sensors and Actuators B*, **111-112**, 225–229 (2005).

5.  Singh A. K., Kanchanapally R., Fan Z., Senapati D., Ray P. C., 'Synthesis of highly fluorescent water-soluble silver nanoparticles for selective detection of Pb(II) at the parts per quadrillion (PPQ) level', *Chemical Communications*, **48**, 9047–9049 (2012).

6.  Shi J., 'On the synergetic catalytic effect in heterogeneous nanocomposite catalysts', *Chemical Reviews*, **113**, 2139–2181 (2013).

7.  Bagga K., Brougham D. F., Keyes T. E., Brabazon D., 'Magnetic and noble metal nanocomposites for separation and optical detection of biological species.', *Physical Chemistry Chemical Physics*, **17**, 27968–27980 (2015).

8.  Wang H., Shrestha T. B., Basel M. T., Pyle M., Toledo Y., Konecny A., Thapa P., Ikenberry M., Hohn K. L., Chikan V., Troyer D. L., Bossmann S. H., 'Hexagonal magnetite nanoprisms: Preparation, characterization and cellular uptake', *Journal of Materials Chemistry B*, **3**, 4647–4653 (2015).

9.  Peña L., Xu F., Hohn K. L., Li J., Wang D., 'Propyl-sulfonic acid functionalized nanoparticles as catalyst for pretreatment of corn stover', *Journal of Biomaterials and Nanobiotechnology*, **5**, 8–16 (2014).

10. Acharyya S. S., Ghosh S., Sharma S. K., Bal R., 'Cetyl alcohol mediated fabrication of forest of $Ag/Mn_3O_4$ nanowhiskers catalyst for the selective oxidation of styrene with

molecular oxygen', *RSC Advances*, **5**, 89879–89887 (2015).

11. Klust A., Madix R. J., 'Selectivity limitations in the heterogeneous epoxidation of olefins: Branching reactions of the oxametallacycle intermediate in the partial oxidation of styrene', *The Journal of the American Chemical Society*, **128**, 1034–1035 (2006).

12. Yadav G. D., Lawate Y. S., 'Hydrogenation of styrene oxide to 2-phenyl ethanol over polyurea microencapsulated mono- and bimetallic nanocatalysts: Activity, selectivity, and kinetic modeling', *Industrial and Engineering Chemistry Research*, **52**, 4027–4039 (2013).

13. Swern D., 'Organic Peroxide', *Wiley Interscience, New York* (1971).

14. Choudhary V., Jha R., Jana P., 'Selective epoxidation of styrene to styrene oxide by TBHP using simple transition metal oxides (NiO, CoO or $MoO_3$) as highly active environmentally-friendly catalyst', *Catalysis Communications*, **10**, 205–207 (2008).

15. Valand J., Parekh H., Friedrich H. B., 'Mixed Cu–Ni–Co nano-metal oxides: A new class of catalysts for styrene oxidation', *Catalysis Communications*, **40**, 149–153 (2013).

16. Huang C., Zhang H., Sun Z., Zhao Y., Chen S., Tao R., Liu Z., 'Porous $Fe_3O_4$ nanoparticles: Synthesis and application in catalyzing epoxidation of styrene', *Journal of Colloid and Interface Science*, **364**, 298–303 (2011).

17. Patil N. S., Uphade B. S., McCulloh D. G., Bhargava S. K., Choudhary V. R., 'Styrene epoxidation over gold supported on different transition metal oxides prepared by homogeneous deposition–precipitation', *Catalysis Communications*, **5**, 681–685 (2004).

18. Rahman S., Farooqui S. A., Rai A., Kumar R., Santra C., Prabhakaran V. C., Bhadu G. R., Sen D., Mazumder S., Maity S., Sinha A. K., Chowdhury B., 'Mesoporous TUD-1 supported indium oxide nanoparticles for epoxidation of styrene using molecular $O_2$', *RSC Advances*, **5**, 46850–46860 (2015).

19. Meng G., Yang Q., Wang Y., Sun X., Liu J., 'NiCoFe spinel-type oxide nanosheet arrays derived from layered double hydroxides as structured catalysts', *RSC Advances*, **4**, 57804–57809 (2014).

20. Wang A., Jing H., 'Tunable catalytic activities and selectivities of metal ion doped $TiO_2$ nanoparticles-oxidation of organic compounds', *Dalton Transactions*, **43**, 1011–1018 (2014).

21. Ren S., Yang C., Sun C., Hui Y., Dong Z., Wang J., Su X., 'Novel NiO nanodisks and hollow nanodisks derived from $Ni(OH)_2$ nanostructures and their catalytic performance in epoxidation of styrene', *Materials Letters*, **80**, 23–25 (2012).

22. Ghosh R., Shen X., Villegas J. C., Ding Y., Malinger K., Suib S. L., 'Role of manganese oxide octahedral molecular sieves in styrene epoxidation', *The Journal of Physical Chemistry B*, **110**, 7592–7599 (2006).

23. Corma A., Garcıa H., 'Lewis acids as catalysts in oxidation reactions: From homogeneous to heterogeneous systems', *Chemical Reviews*, **102**, 3837–3892 (2002).

24. Hosseinpour N., Khodadadi A. A., Bahramian A., Mortazavi Y., 'Asphaltene adsorption onto acidic/basic metal oxide nanoparticles toward in situ upgrading of reservoir oils by nanotechnology', *Langmuir*, **29**, 14135–14146 (2013).

25. Fu H., Pan C., Yao W., Zhu Y., 'Visible-light-induced degradation of rhodamine B by nanosized $Bi_2WO_6$', *The Journal of Physical Chemistry B*, **109**, 22432–22439 (2005).

26. Yu K., Yang S., He H., Sun C., Gu C., Ju Y., 'Visible light-driven photocatalytic degradation of rhodamine B over $NaBiO_3$: Pathways and mechanism', *The Journal of Physical Chemistry A*, **113**, 10024–10032 (2009).

27. Yang G., Yang B., Xiao T., Yan Z., 'One-step solvothermal synthesis of hierarchically porous nanostructured $CdS/TiO_2$ heterojunction with higher visible light photocatalytic activity', *Applied Surface Science*, **283**, 402–410 (2013).

28. Cheng X., Pan G., Yu X., Zheng T., 'Preparation of CdS NCs decorated $TiO_2$ nano-tubes arrays photoelectrode and its enhanced photoelectrocatalytic performance and mechanism', *Electrochimica Acta*, **105**, 535–541 (2013).

29. Su C., Shao C., Liu Y., 'Electrospun nanofibers of $TiO_2/CdS$ heteroarchitectures with enhanced photocatalytic activity by visible light', *Journal of Colloid and Interface Science*, **359**, 220–227 (2011).

30. Zhou Q., Fu M. L., Yuan B. L., Cui H. J., Shi J. W., 'Assembly, characterization, and photocatalytic activities of $TiO_2$ nanotubes/CdS quantum dots nanocomposites', *Journal of Nanoparticle Research*, **13**, 6661–6672 (2011).

31. Shi J. W., Yan X., Cui H. J., Zong X., Fu M. L., Chen S., Wang L., 'Low-temperature synthesis of $CdS/TiO_2$ composite photocatalysts: Influence of synthetic procedure on

photocatalytic activity under visible light', *Journal of Molecular Catalysis A: Chemical*, **356**, 53–60 (2012).

32. Zhao K., Wu Z., Tang R., Jiang Y., Lu Y., 'One-pot hydrothermal synthesis of CdS–TiO$_2$ heterojunctions with enhanced visible light photocatalytic activity', *Research on Chemical Intermediates*, **41**, 4405–4411 (2014).

33. Meng H. L., Cui C., Shen H. L., Liang D. Y., Xue Y. Z., Li P. G., Tang W. H., 'Synthesis and photocatalytic activity of TiO$_2$@CdS and CdS@TiO$_2$ double-shelled hollow spheres', *Journal of Alloys and Compounds*, **527**, 30–35 (2012).

34. Li W., Cui X., Wang P., Shao Y., Li D., Teng F., 'Enhanced photosensitized degradation of rhodamine B on CdS/TiO$_2$ nanocomposites under visible light irradiation', *Materials Research Bulletin*, **48**, 3025–3031 (2013).

35. Jiang B., Yang X., Li X., Zhang D., Zhu J., Li G., 'Core-shell structure CdS/TiO$_2$ for enhanced visible-light-driven photocatalytic organic pollutants degradation', *Journal of Sol-Gel Science and Technology*, **66**, 504–511 (2013).

36. Gao P., Liu J., Zhang T., Sun D. D., Ng W., 'Hierarchical TiO$_2$/CdS 'spindle-like' composite with high photodegradation and antibacterial capability under visible light irradiation', *Journal of Hazardous Materials*, **229-230**, 209–216 (2012).

37. Huo Y., Zhang J., Chen X., Li H., 'Synthesis of hollow CdS-TiO$_2$ microspheres with enhanced visible-light photocatalytic activity', *International Journal of Photoenergy*, **2012**, 1–5 (2012).

38. Zhu Y., Wang Y., Chen Z., Qin L., Yang L., Zhu L., Tang P., Gao T., Huang Y., Sha Z., Tang G., 'Visible light induced photocatalysis on CdS quantum dots decorated TiO$_2$ nanotube arrays', *Applied Catalysis A: General*, **498**, 159–166 (2015).

39. Cheng X., Pan G., Yu X., 'Visible light responsive photoassisted electrocatalytic system based on CdS NCs decorated TiO$_2$ nano-tube photoanode and activated carbon containing cathode for wastewater treatment', *Electrochimica Acta*, **156**, 94–101 (2015).

40. Zhang J., Xiao F. X., Xiao G., Liu B., 'Assembly of a CdS quantum dot–TiO$_2$ nanobelt heterostructure for photocatalytic application: Towards an efficient visible light photocatalyst via facile surface charge tuning', *New Journal of Chemistry*, **39**, 279–286 (2015).
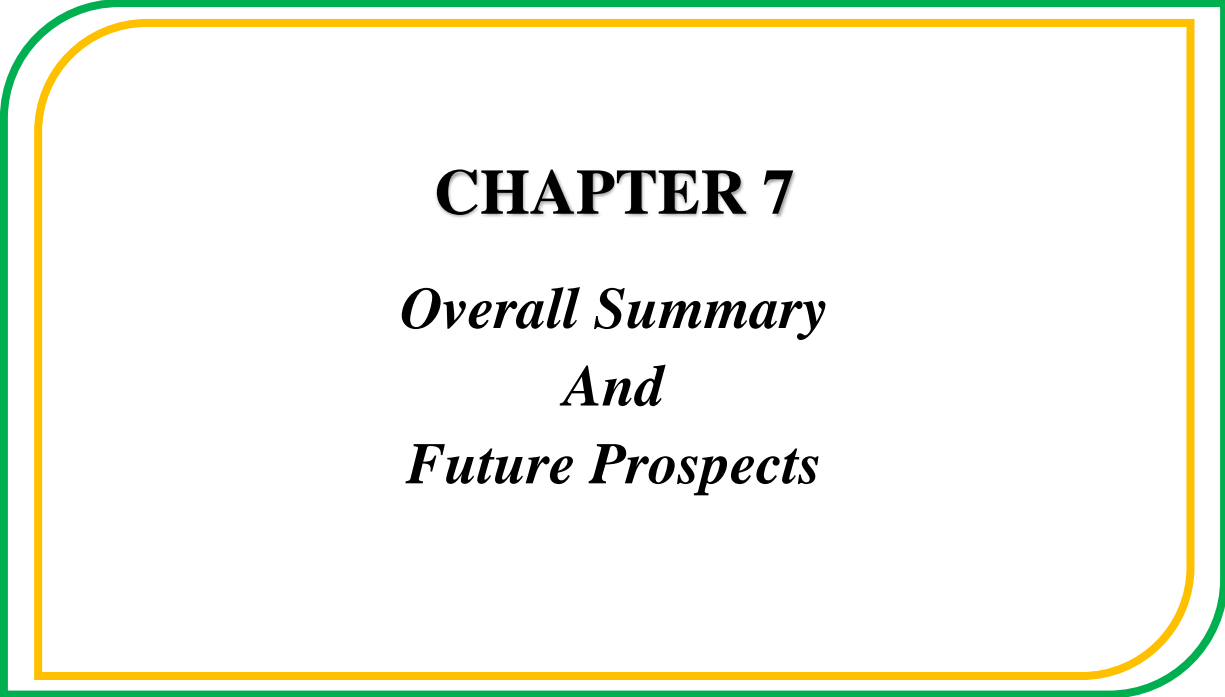
41.    Xue C., Wang T., Yang G., Yang B., Ding S., 'A facile strategy for the synthesis of hierarchical $TiO_2$/CdS hollow sphere heterostructures with excellent visible light activity', *Journal of Materials Chemistry A*, **2**, 7674–7679 (2014).

42.    Kim Y., Kim H. B., Jang D. J., 'Facile microwave fabrication of CdS nanobubbles with highly efficient photocatalytic performances', *Journal of Materials Chemistry A*, **2**, 5791–5799 (2014).

43.    Watanabe T., Takirawa T., Honda K., 'Photocatalysis through excitation of adsorbates. 1. Highly efficient N-deethylation of rhodamine B adsorbed to CdS', *The Journal of Physical Chemistry*, **81**, 1845–1851 (1977).

44.    Wu T., Liu G., Zhao J., Hidaka H., Serpone N., 'Photoassisted degradation of dye pollutants. V. Self-photosensitized oxidative transformation of rhodamine B under visible light irradiation in aqueous $TiO_2$ dispersions', *The Journal of Physical Chemistry B*, **102**, 5845–5851 (1998).

45.    Li W., Li D., Meng S., Chen W., Fu X., Shao Y., 'Novel approach to enhance photosensitized degradation of rhodamine B under visible light irradiation by the $Zn_xCd_{1-x}S$/$TiO_2$ nanocomposites', *Environmental Science and Technology*, **45**, 2987–2993 (2011).

46.    Takizawa T., Watanabe T., Honda K., 'Photocatalysis through excitation of adsorbates. 2. A comparative study of rhodamine B and methylene blue on cadmium sulfide', *The Journal of Physical Chemistry*, **82**, 1391–1396 (1978).

47.    Flood R., Enright B., Allen M., Barry S., Dalton A., Doyle H., Tynan D., Fitzmaurice D., 'Determination of band edge energies for transparent nanocrystalline $TiO_2$-CdS sandwich electrodes prepared by electrodeposition', *Solar Energy Materials and Solar Cells*, **39**, 83–98 (1995).

48.    Zhu L., Meng Z. D., Oh W. C., 'MWCNT-Based $Ag_2S$-$TiO_2$ nanocomposites photocatalyst: Ultrasound-assisted synthesis, characterization, and enhanced catalytic efficiency', *Journal of Nanomaterials*, **2012**, 1–10 (2012).

49.    Wu J. M., Zhang T. W., 'Photodegradation of rhodamine B in water assisted by titania films prepared through a novel procedure', *Journal of Photochemistry and Photobiology A: Chemistry*, **162**, 171–177 (2004).

50. Tang J., Gong W., Cai T., Xie T., Deng C., Peng Z., Deng Q., 'Novel visible light responsive Ag@(Ag$_2$S/Ag$_3$PO$_4$) photocatalysts: Synergistic effect between Ag and Ag$_2$S for their enhanced photocatalytic activity', *RSC Advances*, **3**, 2543–2547 (2013).

51. Du Y., Xu B., Fu T., Cai M., Li F., Zhang Y., Wang Q., 'Near-infrared photoluminescent Ag$_2$S quantum dots from a single source precursor', *The Journal of the American Chemical Society*, **132**, 1470–1471 (2010).

52. Chen C., Zhao W., 'Formation and identification of intermediates in the photodegradation of sulforhodamine-B dye in aqueous TiO$_2$ dispersion', *Environmental Science and Technology*, **36**, 3604–3611 (2002).

53. Gollavelli G., Chang C. C., Ling Y. C., 'Facile synthesis of smart magnetic graphene for safe drinking water: Heavy metal removal and disinfection control', *ACS Sustainable Chemistry and Engineering*, **1**, 462–472 (2013).

54. Idris A., Hassan N., Rashid R., Ngomsik A. F., 'Kinetic and regeneration studies of photocatalytic magnetic separable beads for chromium(VI) reduction under sunlight', *Journal of Hazardous Materials*, **186**, 629–635 (2011).

55. Nakagawa T., Kokubo K., Moriwaki H., 'Application of fullerenes-extracted soot modified with ethylenediamine as a novel adsorbent of hexavalent chromium in water', *Journal of Environmental Chemical Engineering*, **2**, 1191–1198 (2014).

56. Zhao J., Han Q., Zhu J., Wu X., Wang X., 'Synthesis of Bi nanowire networks and their superior photocatalytic activity for Cr(VI) reduction', *Nanoscale*, **6**, 10062–10070 (2014).

57. Liu X., Pan L., Lv T., Sun Z., 'CdS sensitized TiO$_2$ film for photocatalytic reduction of Cr(VI) by microwave-assisted chemical bath deposition method', *Journal of Alloys and Compounds*, **583**, 390–395 (2014).

58. Liu S., Zhang N., Tang Z. R., Xu Y. J., 'Synthesis of one-dimensional CdS@TiO$_2$ core-shell nanocomposites photocatalyst for selective oxidation: The dual role of TiO$_2$ shell', *ACS Applied Materials and Interfaces*, **4**, 6378−6385 (2012).

59. Chen Z., Xu Y., 'Ultrathin TiO$_2$ layer coated-CdS spheres core−shell nanocomposite with enhanced visible-light photoactivity', *ACS Applied Materials and Interfaces*, **5**, 13353–13363 (2013).

60.    Liu S., Yang M. Q., Xu Y. J., 'Surface charge promotes the synthesis of large, flat structured graphene-(CdS nanowire)-TiO$_2$ nanocomposites as versatile visible light photocatalysts', *Journal of Materials Chemistry A*, **2**, 430–440 (2014).

61.    Liu X., Li W., Chen N., Xing X., Dong C., Wang Y., 'Ag–ZnO heterostructure nanoparticles with plasmon-enhanced catalytic degradation for Congo red under visible light', *RSC Advances*, **5**, 34456–34465 (2015).

62.    Li H., Wang G., Zhang F., Cai Y., Wang Y., Djerdj I., 'Surfactant-assisted synthesis of CeO$_2$ nanoparticles and their application in wastewater treatment', *RSC Advances*, **2**, 12413–12423 (2012).

63.    Wang J., Li R., Zhang Z., Sun W., Xu R., Xie Y., Xing Z., Zhang X., 'Efficient photocatalytic degradation of organic dyes over titanium dioxide coating upconversion luminescence agent under visible and sunlight irradiation', *Applied Catalysis A: General*, **334**, 227–233 (2008).

64.    Sim L. C., Leong K. H., Ibrahim S., Saravanan P., 'Graphene oxide and Ag engulfed TiO$_2$ nanotube arrays for enhanced electron mobility and visible-light-driven photocatalytic performance', *Jounal of Materials Chemistry A*, **2**, 5315–5322 (2014).

65.    Li D., Guo Y., Hu C., Jiang C., Wang E., 'Preparation, characterization and photocatalytic property of the PW$_{11}$O$_{39}$$^{7-}$/TiO$_2$ composite film towards azo dye degradation', *Journal of Molecular Catalysis A: Chemical*, **207**, 183–193 (2004).

66.    Jiang R., Yao J., Zhu H., Fu Y., Guan Y., Xiao L., Zeng G., 'Effective decolorization of congo red in aqueous solution by adsorption and photocatalysis using novel magnetic alginate/γ-Fe$_2$O$_3$/CdS nanocomposite', *Desalination and Water Treatment*, **52**, 238–247 (2014).

67.    Zhang S., Xu W., Zeng M., Li J., Xu J., Wang X., 'Hierarchically grown CdS/α-Fe$_2$O$_3$ heterojunction nanocomposites with enhanced visible-light-driven photocatalytic performance', *Dalton Transactions*, **42**, 13417–13424 (2013).

68.    Wu Z., Yu H., Kuai L., Wang H., Pei T., Geng B., 'CdS urchin-like microspheres/ α-Fe$_2$O$_3$ and CdS/Fe$_3$O$_4$ nanoparticles heterostructures with improved photocatalytic recycled activities', *Journal of Colloid and Interface Science*, **426**, 83–89 (2014).

69.    Zhu L. P., Bing N. C., Yang D. D., Yang Y., Liao G. H., Wang L. J., 'Synthesis and

photocatalytic properties of core–shell structured $\alpha$-$Fe_2O_3$@$SnO_2$ shuttle-like nanocomposites', *CrystEngComm*, **13**, 4486–4490 (2011).

70. Li Q., Guo B., Yu J., Ran J., Zhang B., Yan H., Gong J. R., 'Highly efficient visible-light-driven photocatalytic hydrogen production of CdS-cluster-decorated graphene nanosheets', *The Journal of the American Chemical Society*, **133**, 10878–10884 (2011).

71. Guo H., Ke Y., Wang D., Lin K., Shen R., Chen J., Weng W., 'Efficient adsorption and photocatalytic degradation of Congo red onto hydrothermally synthesized NiS nanoparticles', *Journal of Nanoparticle Research*, **15**, 1475/1–1475/12 (2013).

72. Hernández A., Maya L., Sánchez-Mora E., Sánchez E. M., 'Sol-gel synthesis, characterization and photocatalytic activity of mixed oxide ZnO-$Fe_2O_3$', *Journal of Sol-Gel Science and Technology*, **42**, 71–78 (2007).

73. Abdullah Mirzaie R., Kamrani F., Anaraki Firooz A., Khodadadi A. A., 'Effect of $\alpha$-$Fe_2O_3$ addition on the morphological, optical and decolorization properties of ZnO nanostructures', *Materials Chemistry and Physics*, **133**, 311–316 (2012).

74. Wu W., Zhang S., Xiao X., Zhou J., Ren F., Sun L., Jiang C., 'Controllable synthesis, magnetic properties, and enhanced photocatalytic activity of spindlelike mesoporous $\alpha$-$Fe_2O_3$/ZnO core-shell heterostructures', *ACS Applied Materials and Interfaces*, **4**, 3602–3609 (2012).

75. Yin Q., Qiao R., Zhu L., Li Z., Li M., Wu W., '$\alpha$-$Fe_2O_3$ decorated ZnO nanorod-assembled hollow microspheres: Synthesis and enhanced visible-light photocatalysis', *Materials Letters*, **135**, 135–138 (2014).

76. Zhang S., Ren F., Wu W., Zhou J., Xiao X., Sun L., Liu Y., Jiang C., 'Controllable synthesis of recyclable core-shell $\gamma$-$Fe_2O_3$@$SnO_2$ hollow nanoparticles with enhanced photocatalytic and gas sensing properties.', *Physical Chemistry Chemical Physics*, **15**, 8228–8236 (2013).

77. Chen X., Zhang F., Wang Q., Han X., Li X., Liu J., Lin H., Qu F., 'The synthesis of ZnO/$SnO_2$ porous nanofibers for dye adsorption and degradation', *Dalton Transactions*, **44**, 3034–3042 (2015).

78. Narayan H., Alemu H., Macheli L., Thakurdesai M., Rao T. K. G., 'Synthesis and characterization of $Y^{3+}$-doped $TiO_2$ nanocomposites for photocatalytic applications', *Nanotechnology*, **20**, 255601/1–255601/8 (2009).

79.     Pouretedal H. R., Keshavarz M. H., 'Synthesis and characterization of $Zn_{1-X}Cu_XS$ and $Zn_{1-X}Ni_XS$ nanoparticles and their applications as photocatalyst in Congo red degradation', *Journal of Alloys and Compounds*, **501**, 130–135 (2010).

80.     Guo N., Liang Y., Lan S., Liu L., Zhang J., Ji G., Gan S., 'Microscale hierarchical three-dimensional flowerlike $TiO_2$/PANI composite: Synthesis, characterization, and its remarkable photocatalytic activity on organic dyes under UV-light and sunlight irradiation', *The Journal of Physical Chemistry C*, **118**, 18343–18355 (2014).

81.     Farbod M., Kajbafvala M., 'Effect of nanoparticle surface modification on the adsorption-enhanced photocatalysis of Gd/$TiO_2$ nanocomposite', *Powder Technology*, **239**, 434–440 (2013).

82.     Lin S. T., Thirumavalavan M., Jiang T. Y., Lee J. F., 'Synthesis of ZnO/Zn nano photocatalyst using modified polysaccharides for photodegradation of dyes', *Carbohydrate Polymers*, **105**, 1–9 (2014).

83.     Thiripuranthagan S., Raj D., Kannan K., 'Photocatalytic degradation of congo red on silica supported Ag impregnated $TiO_2$', *Journal of Nanoscience and Nanotechnology*, **15**, 4727–4733 (2015).

84.     Li X., Lin H., Chen X., Niu H., Zhang T., Liu J., Qu F., 'Fabrication of $TiO_2$/porous carbon nanofibers with superior visible photocatalytic activity', *New Journal of Chemistry*, **39**, 7863–7872 (2015).

85.     Mishra G., Parida K. M., Singh S. K., 'Solar light driven Rhodamine B degradation over highly active β-SiC–$TiO_2$ nanocomposite', *RSC Advances*, **4**, 12918 (2014).

86.     Bagheri M., Mahjoub A. R., Mehri B., 'Enhanced photocatalytic degradation of congo red by solvothermally synthesized $CuInSe_2$–ZnO nanocomposites', *RSC Advances*, **4**, 21757–21764 (2014).

87.     Shang M., Wang W., Sun S., Ren J., Zhou L., Zhang L., 'Efficient visible light-induced photocatalytic degradation of contaminant by spindle-like PANI/$BiVO_4$', *The Journal of Physical Chemistry C*, **113**, 20228–20233 (2009).

88.     Wang C., Song K., Feng Y., Yin D., Ouyang J., Liu B., Cao X., Zhang L., Hana Y., Wu M., 'Preparation of $NaLuF_4$:Gd, Yb, Tm-$TiO_2$ nanocomposite with high catalytic activity for solar light assisted photocatalytic degradation of dyes and wastewater', *RSC Advances*, **4**, 39118–39125 (2014).

# CHAPTER 7

*Overall Summary*
*And*
*Future Prospects*

This chapter deals with an overall summary of the present work along with the future prospects. In the present thesis, three different types of nanocomposites were synthesized and they include (i) $NiO$-$Al_2O_3$ and $PbS$-$Al_2O_3$ nanocomposites, (ii) $CdS$-$TiO_2$ and $Ag_2S$-$TiO_2$ nanocomposites, and (iii) $CdS$-$\gamma$-$Fe_2O_3$ and $ZnO@\gamma$-$Fe_2O_3$ nanocomposites. The nanocomposites were synthesized using a facile sol-gel process a two-step sol-gel process followed by thermal decomposition approach and a one-step thermal decomposition approach. The synthesized nanocomposites were explored for applications such as oxidation of styrene, photocatalytic degradation of rhodamine B, photo-reduction of Cr(VI) and photocatalytic degradation of congo red in aqueous solutions. A detailed summary on the synthesis, characterization and applications of the nanocomposites, presented in the thesis, along with their future prospects is given below.

**Chapter 1:** *Introduction*

In this chapter, a brief historical background of nanotechnology, an introduction to nanocomposites, their types, various synthetic methods for the preparation of nanocomposites and the factors affecting their optical and magnetic properties have been discussed. Various properties of the nanocomposites have been discussed with the help of suitable examples. At the end, some of the important applications of the nanocomposites in different areas have been discussed.

**Chapter 2:** *Experimental techniques*

In this chapter, the analytical techniques which were used to characterize the synthesized nanocomposites and the method of their sample preparation have been discussed. The analytical techniques include powder X-ray diffraction, Fourier transform infrared spectroscopy, Raman spectroscopy, thermal gravimetric analysis, atomic absorption spectroscopy, field emission-scanning electron microscopy coupled with energy dispersive X-ray analysis, transmission electron microscopy, selected area electron diffraction, UV-visible spectroscopy, diffuse reflectance spectroscopy, photoluminescence spectroscopy, surface area measurements and magnetic measurements using a superconducting quantum interference device (SQUID) and a vibrating sample magnetometer (VSM). The catalytic applications of the nanocomposites were studied using gas chromatography coupled with mass spectroscopy (GC-MS) and UV-visible spectroscopy.

**Chapter 3:** *Synthesis and characterization of NiO-Al₂O₃ and PbS-Al₂O₃ nanocomposites by sol-gel method*

This chapter consists of two sections and they are summarized separately below.

*3.1 Synthesis and characterization of NiO-Al₂O₃ nanocomposites by sol-gel method*

NiO−Al₂O₃ nanocomposites were prepared by sol-gel method. This method involves hydrolysis of mixture of metal precursors leading to the formation of corresponding metal hydroxides which on calcination at 500 ℃ gives NiO-Al₂O₃ nanocomposites. This synthetic method is easy and no expensive chemicals or any special apparatus was required. The present synthetic approach may be extended for the preparation of other metal oxide nanocomposites.

The nanocomposites were characterized using different sophisticated analytical techniques. The XRD results confirm the presence of small NiO nanocrystallites in the nanocomposites (mean size ~2.6 nm). The crystallite size of NiO in the nanocomposites increases with an increase in concentration of nickel acetate used during the sol-gel process. FT-IR studies on the NiO-Al₂O₃ nanocomposites show characteristic bands due to nickel oxide and alumina and Raman spectroscopy results show characteristic bands due to nickel oxide. EDX analysis shows the presence of oxygen, aluminium and nickel in the nanocomposites and TEM results suggest uniform distribution of small NiO nanoparticles on the surface of alumina with web-like morphology for the nanocomposites prepared using $[Ni^{2+}]:[Al^{3+}] = 0.5:1$ and $[Ni^{2+}]:[Al^{3+}] = 2:1$. Diffuse reflectance spectral studies indicate higher band gap of NiO in the nanocomposites (4.5 to 4.8 eV) compared to bulk NiO (4.0 eV). The band gap of NiO in the nanocomposites increases with decrease in the particle size and this is attributed to quantum size effect. The nanocomposites exhibit superparamagnetism at 5 K and show higher remanent magnetization compared to pure NiO nanoparticles. The NiO-Al₂O₃ nanocomposites are expected to be useful as good heterogeneous catalyst in industrial processes such as hydrogenation, dehydrogenation, petroleum refining, $CO_2$ reduction and fuel cells, and as protective barriers, electrochromic materials and sensors.

*3.2 Synthesis and characterization of PbS-Al₂O₃ nanocomposites by sol-gel method*

PbS-Al₂O₃ nanocomposites were prepared by the sol-gel method. The XRD results confirm the presence of small PbS nanocrystallites in the nanocomposites and the crystallite size of PbS in the nanocomposites varies from 18.2 to 40.5 nm. FT-IR studies on the nanocomposites show characteristic bands due to lead sulfide and alumina. Raman spectral studies on the

nanocomposites reveal characteristic peaks due to PbS nanoparticles and TEM studies indicate uniform distribution of lead sulfide nanoparticles on the alumina matrix. Optical studies on the PbS-Al$_2$O$_3$ nanocomposites indicate NIR absorption and emission. A blue shift of band gap of PbS in the nanocomposites (0.92 to 0.96 eV) compared to pure PbS nanoparticles and bulk PbS is observed (0.41 eV). PL studies show characteristic peaks due to excitonic emission of PbS nanoparticles in all the PbS-Al$_2$O$_3$ nanocomposites. The PbS-Al$_2$O$_3$ nanocomposites can be useful in Q-switching NIR lasers, luminescent markers, solar cells and photovoltaics.

**Chapter 4:** *Synthesis and characterization of CdS-TiO$_2$ and Ag$_2$S-TiO$_2$ nanocomposites by thermal decomposition approach*

This chapter consists of two sections and they are summarized separately below.

*4.1 Synthesis and characterization of CdS-TiO$_2$ nanocomposites by thermal decomposition approach*

CdS-TiO$_2$ nanocomposites were prepared by thermal decomposition of cadmium acetate, thiourea and three different TiO$_2$ nanoparticles (as prepared sol-gel TiO$_2$, sol-gel TiO$_2$ calcined at 500 $^{\circ}$C, sol-gel TiO$_2$ calcined at 700 $^{\circ}$C) and macro-crystalline TiO$_2$ in diphenyl ether at 150 $^{\circ}$C, in air, for about 60 min. The synthesis was carried out in a short time (60 minutes) and no special apparatus was required. The present synthetic approach may be extended for the preparation of other metal sulfide-metal oxide nanocomposites.

The nanocomposites were characterized using different analytical techniques. The XRD results confirm the presence of CdS and TiO$_2$ nanocrystallites in the nanocomposites and the crystallite size of CdS in the nanocomposites increases with an increase in the concentration of CdS precursors (cadmium acetate and thiourea) used during the preparation of nanocomposites. The FE-SEM and TEM results indicate uniform distribution of small CdS nanoparticles on the surface of TiO$_2$ in the case of nanocomposites prepared using lower concentration of CdS precursors ([Cd$^{2+}$]:[S$^{2-}$] = 0.15:0.15) and as-prepared sol–gel TiO$_2$ and sol–gel TiO$_2$ nanoparticles after calcination at 500 $^{\circ}$C. Diffuse reflectance spectral studies indicate higher band gap of CdS in all the CdS-TiO$_2$ nanocomposites with respect to bulk CdS. Photoluminescence studies indicate blue shift in band edge emission of the CdS-TiO$_2$ nanocomposites compared to pure CdS nanoparticles. The CdS-TiO$_2$ nanocomposites may be used for various applications such as photocatalytic degradation of organic pollutants (e.g. methyl orange, rhodamine B, and methylene blue), reduction of nitrobenzene derivatives,

selective oxidation of alcohols, water splitting, reduction of Cr(VI), bio-imaging and in solar cells.

*4.2 Synthesis and characterization of $Ag_2S$-$TiO_2$ nanocomposites by thermal decomposition approach*

$Ag_2S$-$TiO_2$ nanocomposites were prepared by the thermal decomposition of silver acetate, thiourea and $TiO_2$ nanoparticles (calcined at 500 °C) in diphenyl ether at 220 °C, in air, for about 60 min. The synthesis was carried out in a short time (60 minutes) and no special apparatus was required. The present synthetic approach may be extended for the preparation of other metal sulfide-metal oxide nanocomposites.

The $Ag_2S$-$TiO_2$ nanocomposites were characterized using different analytical techniques. The XRD results confirm the presence of both $Ag_2S$ and $TiO_2$ nanocrystallites in the nanocomposites and the crystallite size of $Ag_2S$ in the nanocomposites (16 to 35.3 nm) increases with an increase in the concentration of precursors (silver acetate and thiourea) used during the preparation of $Ag_2S$-$TiO_2$ nanocomposites. The FE-SEM images showed that the $Ag_2S$-$TiO_2$ nanocomposites consist of more or less uniform particles with close to spherical morphology while the energy dispersive X-ray analysis studies indicate the presence of silver, sulfur, titanium and oxygen in the nanocomposites. TEM results indicate uniform distribution of small $Ag_2S$ nanoparticles on the surface of $TiO_2$ and diffuse reflectance spectral studies indicate higher band gap of $Ag_2S$ in the nanocomposites compared to bulk $Ag_2S$. The band gap of $Ag_2S$ in the nanocomposites (2.2 to 2.7 eV) increases with decrease in the size of $Ag_2S$ nanoparticles. The $Ag_2S$-$TiO_2$ nanocomposites may be used for different applications such as photocatalytic degradation of organic pollutants (e.g. methyl orange, rhodamine B, and methylene blue), and industrial pollutants (e.g. phenol, p-xylene and chlorophenol) and water splitting.

**Chapter 5:** *Synthesis and characterization of CdS-γ-Fe₂O₃ and ZnO@γ-Fe₂O₃ nanocomposites by thermal decomposition approach*

This chapter consists of two sections and they are summarized separately below.

*5.1 Synthesis and characterization of CdS-γ-Fe₂O₃ nanocomposites by thermal decomposition approach*

CdS-γ-Fe₂O₃ nanocomposites were successfully prepared by a simple and facile thermal decomposition approach which involves thermal decomposition of iron acetylacetonate,

cadmium acetate and thiourea in diphenyl ether at 200 °C, in air, for about 35 or 70 min. The method is easy, can be carried out at low temperature (~200 °C) and no expensive chemicals or any special equipment was required.

The CdS-$\gamma$-Fe$_2$O$_3$ nanocomposites were characterized using different analytical techniques. The XRD results confirm the presence of CdS nanocrystals (1.2 to 2.9 nm) in the nanocomposites. FT-IR results on the nanocomposites show characteristic bands due to $\gamma$-Fe$_2$O$_3$ and CdS. FE-SEM results indicate more or less uniform particles with close to spherical morphology while the energy dispersive X-ray analysis studies indicate the presence of cadmium, sulfur, iron and oxygen in the nanocomposites. TEM results indicate formation of agglomerated sphere-like particles in the nanocomposites. Diffuse reflectance spectral studies of CdS-$\gamma$-Fe$_2$O$_3$ nanocomposites indicate absorbance in the visible region (1.8 to 2.5 eV) and the nanocomposites show blue shift of band edge emission compared to pure CdS due to quantum size effect. The CdS-$\gamma$-Fe$_2$O$_3$ nanocomposites exhibit superparamagnetic behaviour at room temperature. The CdS-$\gamma$-Fe$_2$O$_3$ nanocomposites show multifunctional properties (optical and magnetic) due to which they may be useful in catalysis, environmental remediation (photodegradation of organic pollutants), sensors, magnetic materials, pigments, lithium ion batteries and drug delivery.

*5.2 Synthesis of ZnO@$\gamma$-Fe$_2$O$_3$ core-shell nanocomposites by a thermal decomposition approach*

ZnO@$\gamma$-Fe$_2$O$_3$ core-shell nanocomposites were synthesized by a novel two-step thermal decomposition approach. This method involves, thermal decomposition of iron acetylacetonate and ZnO nanorods (prepared by calcination of zinc acetate at 300 °C) in diphenyl ether at about 200 °C, in air, for about 35 min. The method employed is simple, can be carried out at low temperature (~ 200 °C) and no expensive chemicals or any special apparatus was required.

The ZnO@$\gamma$-Fe$_2$O$_3$ nanocomposites were characterized with the help of an array of analytical techniques. XRD results confirm the presence of hexagonal wurtzite ZnO and XRD studies on as prepared and calcined samples suggest the phase of as prepared iron oxide nanoparticles as $\gamma$-Fe$_2$O$_3$. FT-IR studies on the as prepared iron oxide nanoparticles and ZnO@$\gamma$-Fe$_2$O$_3$ core-shell nanocomposites show characteristic IR bands due to $\gamma$-Fe$_2$O$_3$ and FE-SEM images show uniform shell formation of iron oxide on the ZnO nanorods. Transmission electron microscopy studies clearly show that ZnO exhibits rod like morphology with ~40 nm diameter

and length 1.1 μm and the TEM images of ZnO@γ-Fe$_2$O$_3$ core-shell nanocomposites show uniform shell formation of γ-Fe$_2$O$_3$ nanoparticles on the surface of ZnO nanorods. The thickness of Fe$_2$O$_3$ shell varies from 10 to 20 nm in ZnO@γ-Fe$_2$O$_3$ core-shell nanocomposites. HRTEM observations demonstrate that the constituents of the nanocomposites are crystalline with characteristic lattice spacing of γ-Fe$_2$O$_3$ (0.48 nm) and ZnO (0.24 nm). The diffuse reflectance spectra of ZnO@γ-Fe$_2$O$_3$ core-shell nanocomposites reveal extended optical absorption in the visible range 400–600 nm. The core-shell nanocomposites show red shift of the band gap absorption due to iron oxide from 2.24 eV to 1.9 eV with increase in the precursor concentration of γ-Fe$_2$O$_3$. The photoluminescence spectral studies indicate that the ZnO@γ-Fe$_2$O$_3$ core-shell nanocomposites exhibit enhanced defect emission which is expected to increase its photocatalytic activity. The ZnO@γ-Fe$_2$O$_3$ core-shell nanocomposites exhibit superparamagnetic behaviour at room temperature with maximum saturation magnetization of 2.1 emu/g. The ZnO@γ-Fe$_2$O$_3$ core-shell nanocomposites show interesting optical and magnetic properties due to which they may be useful in catalysis, waste water treatment, water splitting, sensors, magnetic materials, lithium ion batteries and solar cells.

**Chapter 6:** *Applications of Nanocomposites*

In this chapter, various applications such as oxidation of styrene, photocatalytic degradation of rhodamine B, photocatalytic reduction of Cr(VI) and photocatalytic degradation of congo red using the synthesized nanocomposites have been demonstrated.

The NiO-Al$_2$O$_3$ nanocomposites show better catalytic activity in the oxidation of styrene compared to pure NiO and Al$_2$O$_3$ nanoparticles. NiO-Al$_2$O$_3$ nanocomposite prepared using [Ni$^{2+}$]:[Al$^{3+}$] = 0.5:1 shows a total conversion of 60.2%, with a selectivity for styrene oxide of 86.3% in a reaction time of 6 h. The NiO-Al$_2$O$_3$ nanocomposites can be explored as heterogeneous catalyst for the oxidation of methane, reduction of CO$_2$, etc. The CdS-TiO$_2$ nanocomposites are better photocatalyst in the degradation of rhodamine B and reduction Cr(VI) in aqueous solutions compared to pure CdS and TiO$_2$ nanoparticles. The CdS-TiO$_2$ nanocomposite prepared using [Cd$^{2+}$]:[S$^{2-}$] = 0.15:0.15 shows complete photodegradation of rhodamine B in 120 min and complete photo-reduction of Cr(VI) in 6 min. These nanocomposites can be explored for the degradation of other dyes such as methylene blue, rhodamine 6B, methyl orange, congo red, etc. The Ag$_2$S-TiO$_2$ nanocomposites show better photocatalytic activity in the degradation of rhodamine B in aqueous solutions compared to pure Ag$_2$S and TiO$_2$ nanoparticles. The Ag$_2$S-TiO$_2$ nanocomposite prepared using

$[Ag^+]:[S^{2-}] = 0.3:0.15$ shows complete degradation of rhodamine B in 90 min. These nanocomposites can be explored for degradation of other dyes such as methylene blue, rhodamine 6B, methyl orange, congo red, etc. The CdS-$\gamma$-Fe$_2$O$_3$ nanocomposites were found to be better photocatalyst in the degradation of congo red in aqueous solutions compared to pure CdS and $\gamma$-Fe$_2$O$_3$ nanoparticles. The CdS-$\gamma$-Fe$_2$O$_3$ nanocomposite prepared using $[Fe^{3+}]:[Cd^{2+}]:[S^{2-}] = 1:0.25:0.25$ shows complete photodegradation of congo red in 60 min. These nanocomposites can be explored for degradation of other dyes such as methylene blue, rhodamine B, methyl orange, etc. The ZnO@$\gamma$-Fe$_2$O$_3$ core-shell nanocomposites show better catalytic activity in the degradation of congo red in an aqueous solutions compared to pure ZnO nanorods and $\gamma$-Fe$_2$O$_3$ nanoparticles. The ZnO@$\gamma$-Fe$_2$O$_3$ core-shell nanocomposite prepared using $[Zn^{2+}]:[Fe^{3+}] = 1:0.25$ shows complete photodegradation of congo red in 90 min. These nanocomposites can be explored for degradation of other dyes such as methyl orange, rhodamine B, methylene blue, etc. The COD analyses for the photocatalytic experiments confirm that rhodamine B and congo red are photodegraded in the presence of nanocomposites. Ag$_2$S-TiO$_2$ nanocomposite A4 shows the maximum photodegradation efficiency (96.5%) for the photodegradation of rhodamine B.